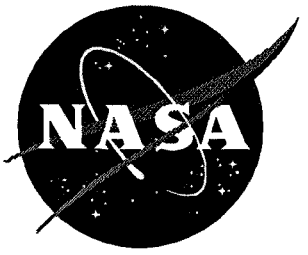

NASA Conference Publication 3336
Part 2

Third International Symposium on Magnetic Suspension Technology

Edited by
Nelson J. Groom and Colin P. Britcher

Proceedings of a symposium sponsored by the
National Aeronautics and Space Administration,
Washington, D.C., and held in
Tallahassee, Florida
December 13–15, 1995

July 1996

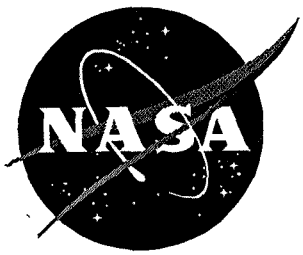

NASA Conference Publication 3336
Part 2

Third International Symposium on Magnetic Suspension Technology

Edited by
Nelson J. Groom
Langley Research Center • Hampton, Virginia

Colin P. Britcher
Old Dominion University • Norfolk, Virginia

Proceedings of a symposium sponsored by the
National Aeronautics and Space Administration,
Washington, D.C., and held in
Tallahassee, Florida
December 13–15, 1995

National Aeronautics and Space Administration
Langley Research Center • Hampton, Virginia 23681-0001

July 1996

INTRODUCTION

The 3rd International Symposium on Magnetic Suspension Technology was held at The Holiday Inn Capital Plaza in Tallahassee, Florida on December 13-15, 1995. The symposium was sponsored by the Guidance and Control Branch of the Langley Research Center in coordination with NASA Headquarters and was hosted by the National High Magnetic Field Laboratory (NHMFL) operated by Florida State University. The symposium was chaired by the following people:

Nelson J. Groom, Symposium Co-Chairman
NASA
Langley Research Center
Hampton, VA 23681-0001

Dr. Jack E. Crow, Symposium Co-Chairman
National High Magnetic Field Laboratory
Tallahassee, FL 32306-4005

Dr. Colin P. Britcher, Technical Program Co-Chairman
Dept. of Aerospace Engineering
Old Dominion University
Norfolk, VA 23529-0247

Dr. Hans Schneider-Muntau, Technical Program Co-Chairman
National High Magnetic Field Laboratory
Tallahassee, FL 32306-4005

Kendall Sherman, Administrative Co-Chairman
NASA
Langley Research Center
Hampton, VA 23681-0001

Sandy Johnson, Administrative Co-Chairman
NASA
Langley Research Center
Hampton, VA 23681-001

Janet Patten, Administrative Co-Chairman
National High Magnetic Field Laboratory
Tallahassee, FL 32306-4005

Merry Ann Johnson, Administrative Co-Chairman
National High Magnetic Field Laboratory
Tallahassee, FL 32306-4005

An international steering committee assisted in selecting and reviewing submitted abstracts and in structuring the symposium sessions. The steering committee consisted of the following people:

Dr. John Miller
National High Magnetic Field Laboratory
1800 E. Paul Dirac Drive
Tallahassee, FL 32306-4005

Dr. Hideo Sawada
Aircraft Aerodynamics Division
National Aerospace Laboratory
7-44-1 Jindaiji-higashi-machi
Chofu
Tokyo 182
JAPAN

Dr. Justin Schwartz
National High Magnetic Field Laboratory
1800 E. Paul Dirac Drive
Tallahassee, FL 32306-4005

Dr. Steve Van Sciver
National High Magnetic Field Laboratory
1800 E. Paul Dirac Drive
Tallahassee, FL 32306-4005

Dr. Roland Siegwart
Mecos Traxler AG
Gutstrasse 38
Winterthur S CH-8400
SWITZERLAND

Dr. David Trumper
Department of Electrical Engineering
Massachusetts Institute of Technology
Cambridge, MA 02139
USA

The goal of the symposium was to examine the state of technology of all areas of magnetic suspension and to review recent developments in sensors, controls, superconducting magnet technology, and design/implementation practices. The symposium included 19 sessions in which a total of 55 papers were presented. The technical sessions covered the areas of bearings, superconductivity, vibration isolation, maglev, controls, space applications, general applications, bearing/actuator design, modelling, precision applications, electromagnetic launch & hypersonic maglev, applications of superconductivity, and sensors. A list of attendees begins on page xv.

The first symposium in this series was organized by NASA Langley Research Center and held at Langley Research Center, Hampton, Virginia on August 19-23, 1991. The proceedings of the first symposium are available as NASA Conference Publication 3152, Parts 1 and 2. The second symposium in the series, also organized by NASA Langley Research Center, was held at the Westin Hotel in Seattle, Washington on August 11-13,

Research Center, was held at the Westin Hotel in Seattle, Washington on August 11-13, 1993. The proceedings of the second symposium are available as NASA Conference Publication 3247, Parts 1 and 2.

CONTENTS

*Part 1 is presented under separate cover.

SESSION 4--Maglev 1
Chairman: Harry Jones, Oxford University

SESSION 5--Controls 1 – Continued
Chairman: Bibhuti B. Banerjee, Premag Inc.

SESSION 6--Space Applications
Chairman: Nelson J. Groom, NASA Langley

SESSION 12--Precision Applications
Chairman: Karl Boden, KFA-IGV/Hideo Sawada, NAL

SESSION 13--Applications 2
Chairman: Steven Van Sciver, NHMFL

SESSION 14--Maglev 2
Chairman: Tim Lynch, Florida State University

SESSION 15--Controls 3
Chairman: Alexander V. Kuzin, MATI

SESSION 16--Electromagnetic Launch & Hypersonic Maglev
Chairman: George Dulikravich, Penn State University

SESSION 17--Applications of Superconductivity
Chairman: Justin Schwartz, NHMFL

SESSION 18--Modelling 2
Chairman: Gerald Foshage, Honeywell Corporation

SESSION 19--Sensors
Chairman: Colin P. Britcher, Old Dominion University

LIST OF ATTENDEES

Markus Ahrens
Int. Center for Magnetic Bearings
Technopark PFA F16
Pfingstweidstr. 30
Zurich 8005
SWITZERLAND
41-1-445 13 32

Nathaniel G. Albritton
Auburn University
Electrical Engineering Dept.
200 Brown Hall
Auburn University, AL 36849
334-844-1800

Dave L. Alderson
IGC Advanced Superconductors
1875 Thomaston Avenue
Waterbury, CT 06704
203-753-5215

Paul E. Allaire
University of Virginia
Mechanical Engineering Department
Thornton Hall/McCormick Road
Charlottesville, VA 22903-2442
804-924-7421

David E. Andrews
Oxford Superconducting Technology
600 Milik Street
Carteret, NJ 07008
908-541-1300

Bibhuti Banerjee
Precision Magnetic Bearing Systems
36 Green Mountain Drive
Cohoes, NY 12047
518-783-4343

Natale Barletta
EEK
Pfingstweidstr. 30
Technopark E44
Zurich CH-8005
SWITZERLAND
41-1-445 13 81

Clayton C. Bear
Revolve Technologies Inc.
300 207 10th Avenue SW
Calgary, Alberta T2ROB
CANADA
403-232-9262

Martin E. Beck
TRW
1 Space Park R9-2873
Redondo Beach, CA 90278
310-814-8013

Urs Bikle
ETH Institut IEM
ETH Zentrum
ETL G14
Zurich CH 8092
41-1-632-28-17

Mark D. Bird
NHMFL-FSU
1800 E. Paul Dirac Drive
Tallahassee, FL 32306
904-644-7709

Laurence E. Blow
Strategic Insight
1745 Jefferson Davis Hwy #511
Arlington, VA 22202
703-413-0700

Kenneth A. Blumenstock
NASA Goddard Space Flight Center
Code 723.2
Greenbelt, MD 20771
301-286-4268

Karl Boden
Forschungszentrum Juelich
GMBH KFA IGV
PF 1913
Juelich 52425
GERMANY
02461-55712

Hans J. Bornemann
Forschugszentrum Karlsruhe
Postfach 3640
D-76021 Karlsruhe
GERMANY
49-7247-82-4389

Colin P. Britcher
Old Dominion University
Dept. of Aerospace Engineering
Norfolk, VA 23529-0247
804-683-4916

Thomas C. Britton
Lockheed Martin Eng. & Sciences
NASA Langley Research Center
Mail Stop 161
Hampton, VA 23681-0001
804-864-6619

Donato Cardarelli
Milli Sensor Systems & Actuators, Inc.
93 Border Street
West Newton, MA 02165
617-965-1346

David C. Carpenter
Vector Fields, Inc.
1700 N. Farnsworth Ave.
Suite 28
Aurora, IL 60505
708-851-1734

H. Ming Chen
Mohawk Innovative Technology, Inc.
1059 Belridge Road
Niskayuna, NY 12309-4717
518-372-9547

Juan C. Cockburn
FAMU-FSU College of Engineering
Dept. of Electrical Engr.
2525 Pottsdamer Street
Tallahassee, FL 32310-6046
904-487-6462

Howard Coffey
Argonne National Laboratory
Building EES/363
9700 S. Cass Avenue
Argonne, IL 60439

Emmanuel G. Collins
FAMU/FSU
Department of Mechanical Engineering
2525 Pottsdamer Street
Tallahassee, FL 32310-6046
904-487-6373

Thomas C. Cosmus
Intermagnetics General Corporation
450 Old Niskayuna Road
Latham, NY 12110-0461
518-782-1122

David E. Cox
NASA Langley Research Center
Mail Stop 161
Hampton, VA 23681-0001
804-864-8149

Joyanne L. Craft
Rockwell
P. O. Box 21105
Kennedy Space Center, FL 32815
407-799-5507

Michael J. Cronin
Mechanical Technology Inc.
968 Albany-Shaker Road
Latham, NY 12110
518-785-2469

Jack E. Crow
National High Magnetic Field Lab
Florida State University
1800 E. Paul Dirac Dr., B-223
Tallahassee, FL 32306-4005
904-644-0311

Charles R. Dauwalter
Milli Sensor Systems & Actuators Inc.
93 Border Street
West Newton, MA 02165
617-965-1346

Kent R. Davey
American Maglev Technology Inc.
P. O. Box 10
Edgewater, FL 32132
904-427-6643

Daniel A. Davidson
GMSA Systems, Inc.
2730 Kirby Avenue NE #5
Palm Bay, FL 32905
407-728-3800

Peter C. Dent
Everson Electric Company
2000 City Line Road
Bethlehem, PA 18017-2167
610-266-2834

James R. Downer
SatCon Technology Corp.
161 First Street
Cambridge, MA 02142-1207
617-661-0540

George S. Dulikravich
The Pennsylvania State University
Dept. of Aerospace Engineering
233 Hammond Blvd.
University Park, PA 16802
814-863-0134

Horst Ecker
Duke University
Mechanical Engineering
Box 90300
Durham, NC 27708-0300
919-660-5339

Y. M. Eyssa
National High Magnetic Field Lab.
1800 E. Paul Dirac Drive
Tallahassee, FL 32306

Edmund Farino
PMS390T222
c/o NAVSEA
2531 Jefferson Davis Hwy
Arlington, VA 22202
703-602-6255

Roger A. Farrell
Intermagnetics General Corporation
450 Old Niskayuna Road
P. O. Box 461
Latham, NY 12110
518-782-1122

Salah E. Feteih
Florida State University
2525 Pottsdamer Street
Tallahassee, FL 32310
904-487-6164

Gordon Findlay
Tunnel Vac Inc.
3567 W. 117th Street
Cleveland, OH 44111-5270
216-251-3030

Gerald K. Foshage
Honeywell Satellite Systems Div.
19019 North 59th Avenue
Glendale, AZ 85308-9650
602-561-3178

Bruce H. Friedman
Allied Signal, Inc.
Route 46
Mail Stop E/D12
Teterboro, NJ 07608-1173
201-393-3262

Satoru Fukata
Kyushu University 36
Dept. of Energy and Mech. Eng.
6-10-1 Hakozaki, Higashiku
Fukuoka 812-81
JAPAN
81-92-641-1101

James R. Gaines
Superconductive Components Inc.
1145 Chesapeake Ave.
Columbus, OH 43212-2238
614-486-0261

Jameson A. Garrett
Rockwell International Space Sys. Div.
Mail Code AC59
12214 Lakewood Blvd.
Downey, CA 90241-7009
310-922-3432

Nelson J. Groom
NASA Langley Research Center
Mail Stop 161
Hampton, VA 23681-0001
804-864-6613

Cynthia Haffey
Museum of Science & Industry
4801 E. Fowler Avenue
Tampa, FL 33617-2099
813-987-6341

Joseph W. Haney
Rockwell International
12214 Lakewood Blvd.
Mail Stop AA40
Downey, CA 90241-7009
310-922-1057

Mary M. Harman
Cryomagnetics
1006 Alvin Weinberg Drive
Oak Ridge, TN 37830
615-482-9551

Yusuf S. Hascicek
NHMFL
1800 E. Paul Dirac Drive
Tallahassee, FL 32306
904-644-0859

Leo Holland
General Atomics
P. O. Box 85608
San Diego, CA 92186
619-455-3043

Benjamin Joffe
Jet Propulsion Laboratory
4800 Oak Grove Drive
MS 251
Pasadena, CA 91109-8099
818-354-6444

Graham Jones
AVCON
5210 Lewis Road #14
Agoura Hills, CA 91301
818-865-0250

Harry Jones
University of Oxford
Clarendon Laboratory
Oxford OX1 3PU
ENGLAND
44-1865-272326

Patrick S. Keogh
University of Bath
School of Mech. Engineering
Bath BA27AY
UNITED KINGDOM
44 (0) 1225 826826

Jongwon Kim
Seoul National University
Dept. of Mech. Des. & Prod.
San 56-1 Shinlim-Dong, Kwanak-Ku
Seoul, 151-742
KOREA
82-2-880-7181

Ronald W. Kipp
Kingsbury, Inc.
10385 Drummond Road
Philadelphia, PA 19154
215-824-4887

Carl R. Knospe
University of Virginia
Dept. of Mech., Aero., & Nuclear Eng.
Thorton Hall
Charlottesville, VA 22903
804-982-2603

Stewart M. Kohler
Sandia National Laboratories
P. O. Box 5800
Mail Stop 0501
Albuquerque, NM 87185
505-844-0328

Valentine N. Komarov
Scientific Research Institute
for Applied Math. & Cybernetics
10 Uljanov Str.
Nizhny Novgorod 603005
RUSSIA

Anthony S. Kondoleon
The Charles Stark Draper Lab
Mail Stop 23
555 Technology Square
Cambridge, MA 02139-3563
617-258-1537

Ladislav Kucera
Int. Center for Magnetic Bearings
Technopark PFA F16
Pfingstweidstr. 30
Zurich 8005
SWITZERLAND
41 1 445 13 33

Robert Kuklinski
NUWC DIV NPT
Code 8233 Building 1302
Newport, RI 02841
401-841-6034

Alexander V. Kuzin
Moscow Aviation-Technological Inst.
Microprocessor Systems, Electronics
& Electrical Eng., Petrovka, 27
Moskow, K-31 103737
USSR
7-095-313-5551

Bernard Lechable
Aerospatiale Espace et Defense
66 Route de Verneuil BP 2
Les Mureaux 78133
FRANCE
33-1-34 92 32 16

Yyng-Ming Lee
MSE, TA Inc.
P. O. Box 4078
Butte, MT 59701
406-494-7235

Melissa K. Less
846th Test Squadron
1521 Test Track Road
Holloman AFB, NM 88330-7847
505-679-2674

Enrico Levi
Polytechnic University
Six Metrotech Center
333 Jay Street
Brooklyn, NY 11201
718-260-3416

John Liedl
Vector Fields
4917 Water's Edge Drive
Suite 272
Raleigh, NC 27606
919-859-9364
Anders L. Lindskog
SKF Nova AB
Chalmers Teknikpark
Goteborg 41288
SWEDEN
46-31-772-4053

Tim Lynch
Florida State University
1800 E. Paul Dirac Drive
Tallahassee, FL 32306

Ki B. Ma
Texas Center for Superconductivity
University of Houston
3201 Cullen Blvd.
Houston, TX 77204-5932
713-743-8254

Eric H. Maslen
University of Virginia
Mech., Aero., & Nuclear Eng.
Thornton Hall
Charlottesville, VA 22903
804-924-6227

Manabu Matsui
Dept. of Mech. & Envir. Engr.
371-H Cannon Green Dr.
Santa Barbara, CA 93106-5070
805-893-4711

David C. Meeker
University of Virginia
Mech., Aero., & Nuclear Engr.
Thornton Hall
Charlottesville, VA 22903-2442
804-924-3292

Allan D. Miller
MSE, Inc.
P. O. Box 4078
Butte, MT 59702
406-494-7319

John J. Morena
American Maglev Star, Inc.
425 California Ave.
Stuart, FL 34994
407-288-9996

Shin-ichi Moriyama
Kyushu Institute of Technology
Dept. of Control Engineering & Science
Kawazu 680-4
lizuka, Fukuoka 820
JAPAN
81-948-29-7700

Atsushi Nakajima
National Aerospace Laboratory
7-44-1 Jindaiji-Higashi-machi
Chofu-shi
Tokyo 182
81-422-47-5911 X2548

David R. Noakes
Virginia State University
Physics Department
P. O. Box 9325
Petersburg, VA 23806
804-524-5063

Janet Patten
National High Magnetic Field Lab.
1800 E. Paul Dirac Drive
Tallahassee, FL 32306-4005
904-644-9651

Richard F. Post
Lawrence Livermore National Lab
P. O. Box 808, L-644
7000 East Avenue
Livermore, CA 94551
510-422-9853

Douglas B. Price
NASA Langley Research Center
Mail Stop 161
Hampton, VA 23681-0001
804-864-6605

Ian L. Pykett
Intermagnetics General Corporation
450 Old Niskayuna Road
Latham, NY 12110
518-782-1122

Ronald Rohner
Sulzer Electronics AG
Hegifeldstr. 30
Winterthur SH-8409
SWITZERLAND
41-52-2625284

Dick Rozycki
Lockheed Martin
P. O. Box 179
MS T320
Denver, CO 80201
303-977-1043

Alain Samuel
Aerospatiale Espace et Defense
66 Route de Verneuil BP2
Les Mureaux 78133
FRANCE
33 1 34 92 1825

Michele S. Sapuppo
Milli Sensor Systems & Actuators, Inc.
93 Border Street
West Newton, MA 02165
617-965-1346

Hideo Sawada
National Aerospace Laboratory
7-44-1 Jindaijihigashi-machi
Chofu-shi
Tokyo 182
JAPAN
81-0422-47-5911

Jim C. Schaaf
BDM International
950 Explorer Blvd.
Huntsville, AL 35806
205-922-5159

Harold J. Schmidt
Univ. of Tennessee Space Institute
B. H. Goethart Parkway
Tullahoma, TN 37388
615-393-7422

Hans Schneider-Muntau
National High Magnetic Field Lab.
1800 E. Paul Dirac Drive
Tallahassee, FL 32306-4005
904-644-0863

Venkat Selvamanickam
Intermagnetics General Corp.
450 Old Niskayuna Road
Latham, NY 12110
518-782-1122

Sevankar Sengupta
Superconductive Components Inc.
1145 Chesapeake Ave.
Columbus, OH 43212-2238
614-486-0261

Mark W. Senti
Advanced Magnet Lab, Inc.
425 California Ave.
Palm Bay, FL 34994

Yih R. Sheu
Nan-Tai College
Dept. of Electrical Eng.
No. 1 Nan-Tai Street
Jia-Ding Lane
Taiwan 701
886-06-2741820

Dongwon Shin
Seoul National University
Dept. of Mech. Des. & Prod.
San 56-1 Shinlim-Dong, Kwanak-Ku
Seoul, 151-742
KOREA
82-2-880-7144

John Stekly
Field Effects
Intermagnetic General Corporation
6 Eastern Road
Acton, MA 01720
508-264-4099

Richard E. Stelter
Dexter Magnetic Materials Division
48460 Kato Road
Fremont, CA 94538
510-656-5700, x3050

L. Scott Stephens
Louisiana State University
2508 CEBA
Baton Rouge, LA 70803-6413
504-388-5905

Haga Takahide
Ebara Research Co., Ltd.
2-1 Honfujisawa 4-chome
Fujisaw Kanagawa 251
JAPAN
0466-83-7639

R. Torti
SatCon Technology Corp.
161 First Street
Cambridge, MA 02142-1207
617-349-0875

Dau K. Tran
TRW Space & Defense
One Space Park
Redondo Beach, CA 90278
310-814-8012

David L. Trumper
Massachusetts Institute of Tech.
Room 35-016
77 Massachusetts Avenue
Cambridge, MA 02139
617-253-3481

Wilfred T. Ussery
Ussery & Associates
690 Market Street
Suite 514
San Francisco, CA 94104
415-788-6580

Steve Van Sciver
National High Magnetic Field Lab.
1800 E. Paul Dirac Drive
Tallahassee, FL 32306-4005

Don J. Wade
Hypersonic Maglev Group
1720 Orange Hill Drive
Brandon, FL 33510
813-654-5610

Roy Weinstein
Institute for Beam Particle Dyn.
University of Houston
Room 632 SR1
Houston, TX 77204-5506
713-748-0461

Philip W. Winkler
Government Systems
Air Products & Chemicals Inc.
7201 Hamilton Blvd.
Allentown, PA 18195-1501
610-481-4284

Katsuya Yamashita
Mitsubishi Heavy Industries, Ltd.
Dept. of Mech., Aero., & Nuclear Eng.
Univ. of Virginia, Thornton Hall
Charlottesville, VA 22902
804-924-6234

Kinjiro Yoshida
Kyushu University
Faculty of Engineering
10-1, 6 Chome, Hakozaki, Higashi-ku
Fukuoka 812
JAPAN
092-641-1101 X5307

John Zhang
University of Houston
Dept. of Mechanical Engineering
Houston, TX 77204-4792
713-743-4543

Dawei Zhou
General Superconductor Inc.
1663 Technology Ave.
Alachua, FL 32615
904-462-5977

Ronald B. Zmood
Royal Melbourne Institute of Tech.
124 Latrobe Street
Dept. of Electrical Eng.
Melbourne, Victoria 3000
AUSTRALIA
613-660-2100

PART 2

Session 11 -- Modelling 1

Chairman: Douglas B. Price
NASA Langley Research Center

A WIDE BANDWIDTH MODEL FOR THE ELECTRICAL IMPEDANCE OF MAGNETIC BEARINGS

David C. Meeker
Eric H. Maslen
Myounggyu D. Noh
Department of Mechanical, Aerospace, and Nuclear Engineering
University of Virginia
Charlottesville, VA

SUMMARY

Magnetic bearings are often designed using magnetic circuit theory. When these bearings are built, however, effects not included in the usual circuit theory formulation have a significant influence on bearing performance. Two significant sources of error in the circuit theory approach are the neglect of leakage and fringing effects and the neglect of eddy current effects. This work formulates an augmented circuit model in which eddy current and flux leakage and fringing effects are included. Through the use of this model, eddy current power losses and actuator bandwidth can be derived. Electrical impedance predictions from the model are found to be in good agreement with experimental data from a typical magnetic bearing.

INTRODUCTION

Maxwell's equations are generally adequate to describe the magnetic and electric fields inside a magnetic bearing. It is possible to approximately solve Maxwell's equations directly using the finite element method [1] [2] [3]. However, the computational cost of a 3-D eddy current solution is very high. Moreover, the effects of any particular design parameter may be difficult to isolate in such an elaborate model.

It is common to develop a simplified magnetic circuit analysis for design using the assumptions

- no flux fringing, or spreading out of the flux in the vicinity of air gaps in the bearing.
- no flux leakage, or flux that circulates locally around a coil through unmodeled paths.
- negligible eddy current effects
- flux density uniform in every flux-carrying cross-section

NOMENCLATURE

a	Cross-sectional area of flux path.	m	number of poles in stator.
A	Magnetic vector potential.	M	Air gap influence matrix.
B	Magnetic flux density.	n	Number of turns in coil.
b	Frequency domain magnetic flux density.	p_k	k^{th} pole in the expansion of μ_{fd}.
		r	Magnetic reluctance.
$\mathbf{B}$	Vector magnetic flux density.	s	Laplace variable.
d	Lamination thickness.	V	Voltage.
$\mathbf{E}$	Vector electric field intensity.	w	Axial length of magnetic bearing.
H	Magnetic field intensity.	z_k	k^{th} zero in the expansion of μ_{fd}.
$\mathbf{H}$	Vector magnetic field intensity.	α	$(\omega\sigma\mu d^2/2)$
I	Coil current.	ζ	$\sqrt{\sigma\mu}d/2$
j	$\sqrt{-1}$	μ	Magnetic permeability.
J	Current density.	σ	Electrical conductivity.
$\mathbf{J}$	Vector current density.	ϕ	magnetic flux.
l	length of flux path section.	ω	excitation frequency.
L	Inductance matrix.	$\Delta\Omega$	Magnetomotive force drop.

by which Maxwell's equations are reduced to a set of circuit equations [4]. The magnetic field can then be determined by solving a relatively small set of linear algebraic equations. The resulting magnetic circuit theory is commonly used in the design of magnetic bearings. However, the presence of leakage, fringing, and eddy current effects can lead to significant discrepancies between circuit theory predictions and experimental performance.

The objective of this work is to present an augmented magnetic circuit model that accounts for the effects of eddy currents, leakage, and fringing in magnetic bearings without abandoning the circuit paradigm. The development will be directed specifically towards the case of active radial magnetic bearings, as pictured in Figure 1. Corrections for eddy currents are developed from a 1-dimensional eddy current model often employed for losses in transformer cores. Extra leakage paths are proposed to account for the effects of flux leakage, and a magnetostatic finite element model is used to correct the reluctance of the air gaps for fringing effects and to identify the reluctance of leakage paths. Bearing electrical impedance predicted by the augmented circuit model is compared to experimental measurements and to predictions made using the usual circuit techniques. In this comparison, the augmented model predicts the experimental results more accurately than typical circuit methods.

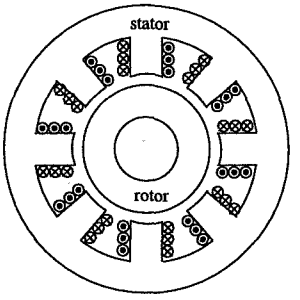

Figure 1: Active radial magnetic bearing.

RELATED WORK

A one-dimensional eddy current formulation for laminated magnetic circuits has been available since Stoll [5]. This formulation has been used more recently in several instances to analyze eddy current losses in transformers [6] [7] [8]. However, the one-dimensional analysis has not been applied to cores with complicated connectivity. Zmood [9] applied a one term expansion of the formulation in [5] to a simple magnetic bearing. The present work extends Zmood's formulation so that a bearing with an arbitrarily complex network of flux paths can be addressed with an expansion of arbitrary order.

Previous works have accounted for fringing effects at the pole tips in magnetic bearings by isolating the tip regions from the rest of the bearing and solving magnetic scalar potential in the region of the air gap [10] [11]. In these analyses, the iron is assumed to be infinitely permeable; it can then be treated solely by defining a constant value of magnetic scalar potential at the iron-air interface. The air gap reluctance deduced from this infinite permeability solution is then assumed to apply in a magnetic circuit with high (but not infinite) iron permeability.

These previous works, however, dealt with geometries in which the pole tips could be conveniently isolated from the geometry of the rest of the bearing. In a typical radial magnetic bearing, the ends of the poles are not so removed from the rest of the bearing structure as to allow an examination of the pole in isolation from the rest of the bearing. This work presents a general infinite permeability method of determining air gap reluctance based on magnetic vector potential that uses the solution of the field in all sections of the air between the rotor and stator to determine fringing corrections. In this process, the forms of additional leakage paths are suggested, and the reluctances of these leakage paths can be determined.

EDDY CURRENT CORRECTION

The use of a one-dimensional eddy current model to describe eddy currents in thin laminations has been addressed in the literature. As reported in Stoll [5], the effects of

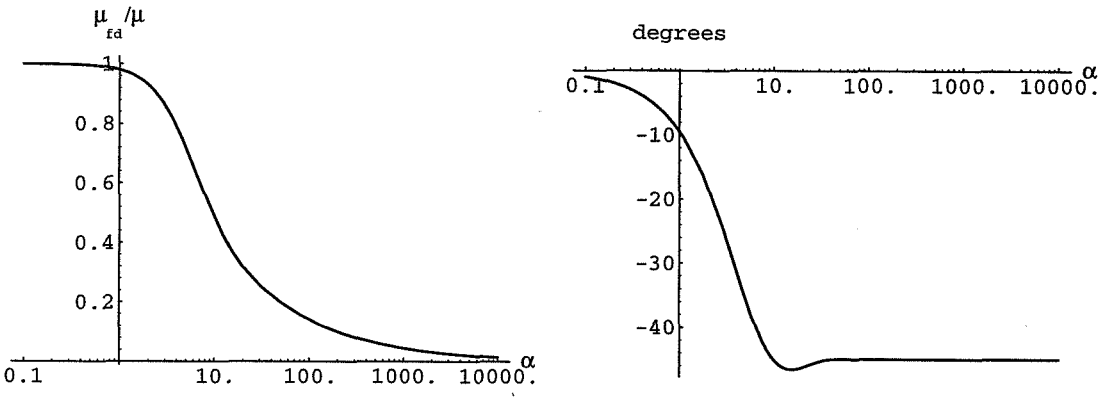

Figure 2: Magnitude and phase shift of $\mu_{fd}(j\omega)$ versus frequency.

eddy currents can be incorporated into a frequency-dependent permeability, $\mu_{fd}(s)$:

$$\mu_{fd}(s) = \mu \left[\frac{\tanh(\sqrt{s\sigma\mu}\,\frac{d}{2})}{\sqrt{s\sigma\mu}\,\frac{d}{2}} \right] \tag{1}$$

where d is lamination thickness, σ is conductivity, and μ is steady-state permeability. Permeability μ_{fd} can be used in magnetic circuit equations in a way analagous to regular permeability: magnetomotive force drop across a section of laminated iron is

$$\Delta\Omega(s) = \frac{l}{\mu_{fd}(s)}\bar{b} \tag{2}$$

where $\bar{b}$ is the average flux density in the laminated section.

If harmonic response is desired, $\mu_{fd}(j\omega)$ can be evaluated at any particular ω. Permeability $\mu_{fd}(j\omega)$ can be evaluated in terms of standard functions:

$$\mu_{fd}(j\omega) = \mu \left[\frac{(1 - e^{-2\sqrt{\alpha}} + 2e^{-\sqrt{\alpha}} \sin\sqrt{\alpha}) - j\,(-1 + e^{-2\sqrt{\alpha}} + 2e^{-\sqrt{\alpha}} \sin\sqrt{\alpha})}{\sqrt{\alpha}\,(1 + e^{-\sqrt{\alpha}} + 2e^{-\sqrt{\alpha}} \cos\sqrt{\alpha})} \right] \tag{3}$$

where

$$\alpha = \frac{\omega\sigma\mu d^2}{2} \tag{4}$$

The magnitude variation and phase shift of $\mu_{fd}(j\omega)$ are shown Figure 2. Once $\mu_{fd}(j\omega)$ is obtained, magnetic circuit analysis then proceeds with a complex permeability for the iron sections of flux path.

However, a model that remains in the Laplace domain is a necessary prerequisite for the use of many tools from control theory. If (1) is simply substituted into the set of circuit equations in symbolic form, solving the magnetic circuit equations becomes laborious. Instead, the magnetomotive force drop across a laminated section can be defined as

$$\Delta\Omega(s) = \frac{l}{\mu}\bar{b} - I_e(s) \tag{5}$$

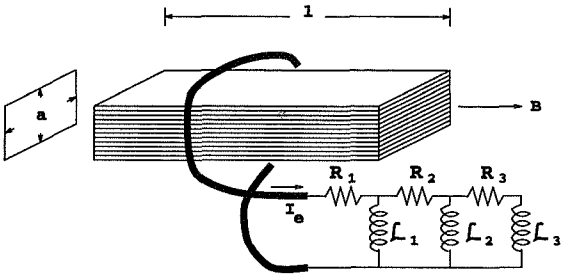

Figure 3: Equivalent circuit model for eddy currents.

From a magnetic circuit standpoint, I_e is merely a 1-turn coil wound around the laminated section of interest that carries some arbitrary current, just like the regular pole windings. The electric circuit equations for each pole winding are then written assuming that all I_e's are arbitrary inputs to the system. The current flowing in I_e is then determined by the transfer function

$$\frac{I_e(s)}{\phi(s)} = \left[\frac{l}{a\,\mu} - \frac{l}{a\,\mu_{fd}(s)}\right] \tag{6}$$

where $\phi = \bar{b}\,a$ is the total flux flowing through the laminated section. The hyperbolic tangent can be expanded in continued fraction form as [7]:

$$\tanh x = \cfrac{x}{1 + \cfrac{x^2}{3 + \cfrac{x^2}{5 + \cdots}}} \tag{7}$$

which can be substituted into (6) to yield

$$\frac{I_e(s)}{\phi(s)} = -\left(\frac{l}{\mu\,a}\right) \cfrac{s\gamma^2}{3 + \cfrac{s\gamma^2}{5 + \cdots}} \qquad \text{where} \quad \gamma = \sqrt{\sigma\mu}\frac{d}{2} \tag{8}$$

With some algebraic manipulation, (8) can be re-arranged in the form

$$\frac{I_e(s)}{\phi(s)} = \cfrac{-s}{R_1 + \cfrac{1}{\cfrac{1}{s\mathcal{L}_1} + \cfrac{1}{R_2 + \cfrac{1}{\cfrac{1}{s\mathcal{L}_2} + \cdots}}}} \tag{9}$$

where

$$\mathcal{L}_i = \frac{\mu\,a}{(4i+1)\,l} \tag{10}$$

$$R_i = \frac{4\,(4i-1)a}{\sigma l d^2} \tag{11}$$

Equation (9) can be interpreted as the transfer function of a one-turn coil driving the chain of resistors and inductors pictured in Figure 3. The effects of eddy currents can be viewed as a parasitic winding around each section of iron flux path that drives a chain of resistors and inductors. For a finite state model, the chain is simply truncated after an arbitrary number of resistor-inductor pairs.

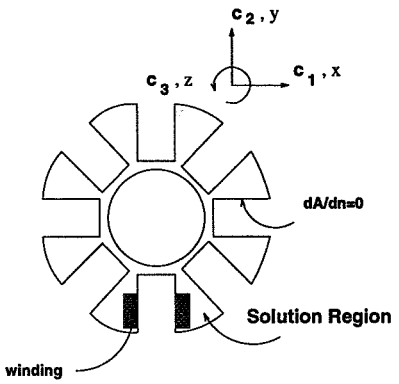

Figure 4: 2-D solution region inside a magnetic bearing.

LEAKAGE AND FRINGING CORRECTIONS

To determine an adequate network of bulk flux paths and to solve for the reluctance of the air sections in those circuit paths, the coupled coil inductances derived from a magnetostatic field solution will be compared to the inductances derived by circuit techniques. In both cases, inductance will be determined with μ of the iron in the bearing assumed to be infinity. The reluctances derived (for $\mu = \infty$) are assumed to apply for a finite but high permeability material with eddy current effects.

If a bearing is suitably long in the axial direction, axial end effects can be neglected; a 2-dimensional analysis is then sufficient to determine leakage and fringing effects. In a 2-D model, vector potential is related to flux by

$$\mathbf{B} = \frac{\partial A}{\partial y}\mathbf{c}_1 - \frac{\partial A}{\partial x}\mathbf{c}_2 \tag{12}$$

where $x, y, \mathbf{c}_1$, and $\mathbf{c}_2$ refer to Figure 4. Following the development in [12], the magnetostatic field satisfies the differential equation

$$\nabla^2 A = J \tag{13}$$

where J is the coil current density flowing in the $\mathbf{c}_3$ direction.

A great simplification in the solution of (13) is to assume that the iron in the solution region is infinitely permeable. The boundary condition

$$\nabla A \cdot \mathbf{n} = 0 \tag{14}$$

then applies at the air-iron interface where $\mathbf{n}$ is a vector normal to the interface. The field then need not be computed inside the iron sections.

In a radial magnetic bearing, the solution region assuming infinite iron permeability is then limited to the air between the rotor and stator. If the stator is symmetric and the rotor is

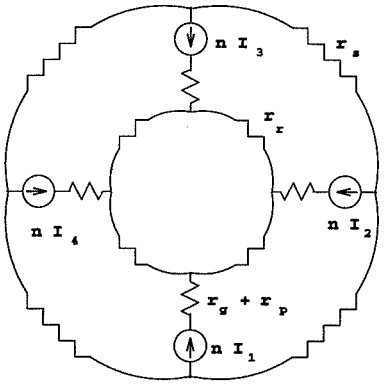

Figure 5: Equivalent circuit model of a 4 pole symmetric radial magnetic bearing.

centered, all possible flux distributions for any set of coil currents can be determined by the superposition of the solutions found with only one active coil. Such a solution domain is pictured in Figure 4 for an 8-pole radial magnetic bearing. It is then relatively straight-forward and economical to solve for A inside the air and coils using the finite element method [12].

Once the A field is determined inside the air and coils of the bearing, the mutual inductance between the i^{th} and j^{th} coils (denoted $\hat{L}_{ij}$) can be determined by the integration [13]:

$$\hat{L}_{ij} = w\frac{\iint A_i J_j \, dx \, dy}{I_i I_j} \tag{15}$$

In this integration, A_i is the contribution to A from current in the i^{th} coil, J_j is the current density contribution of the the j^{th} coil, I_i and I_j are the currents flowing in the i^{th} and j^{th} coils respectively, and w is the axial length of the bearing. The integration is taken over the entire solution domain, but the only non-zero contributions to the integral are in the area of the j^{th} coil.

Note that inductance is computed by (15) without assuming any network structure for the flux. A set of magnetic circuits must be deduced such that when the air gap reluctances in that circuit model are appropriately chosen, the circuit theory inductance closely matches the field theory inductance as $\mu \to \infty$.

The nominal equivalent circuit model used in radial magnetic bearings is pictured in Figure 5. For simplicity, a four pole symmetric radial bearing is shown instead of the usual eight-pole bearing. Symbols r_p, r_r, and r_s correspond to the reluctances in the iron of the pole, rotor, and stator respectively. These reluctances are computed from the formula

$$r = \frac{l}{\mu_{fd}(s)a} \tag{16}$$

where l corresponds to the length and a to the cross-sectional area of the segment in

question. Reluctance r_g is the air gap reluctance and has a nominal value of

$$r = \frac{l_g}{\mu_o a_g} \tag{17}$$

without the inclusion of fringing effects. The flux in any part of the bearing can be deduced by analogy to electric circuits where magnetic reluctance corresponds to electrical resistance and magnetic flux to electrical current [4].

In the circuit model, the inductance between the i^{th} and j^{th} coils (denoted L_{ij}) is

$$L_{ij} = n \frac{\partial \phi_i}{\partial I_j} \tag{18}$$

where ϕ_i is the flux passing through the i^{th} coil, I_j is the current in the j^{th} coil, and n is the number of turns in the j^{th} coil.

In the infinite permeability case, reluctances due to iron (r_r, r_s, and r_p) are all zero. For a symmetric bearing, the self inductance of each coil is

$$L_{ii} = \frac{m-1}{m}\left(\frac{n^2}{r_g}\right) \tag{19}$$

and the mutual inductance is

$$L_{ij} = \frac{-1}{m}\left(\frac{n^2}{r_g}\right) \qquad i \neq j \tag{20}$$

At this point, air gap reluctance r_g could be chosen to minimize the difference between corresponding entries in circuit theory inductance matrix L and field theory inductance matrix $\hat{L}$. However, the existence of error between L and $\hat{L}$ that cannot be eliminated by the proper choice of r_g suggests that extra leakage flux paths exist and should be modeled. In the nominal circuit model, all flux produced by a coil returns to that coil by eventually passing through another coil on the stator. The summation of the entries of any row of L is therefore zero. The sum of the row entries in $\hat{L}$, however, is generally non-zero; some of the flux travels in loops not accounted for by the usual circuit model. The chief cause of this discrepancy is a self-leakage path for each coil. Some flux makes a complete circuit flowing only in the air and iron immediately adjacent to an active coil and never crosses the air gap to link with other coils. Leakage mutual inductances also exist, but these mutual leakage paths are usually an order of magnitude more reluctant than the self-leakage path and can be neglected with little error incurred.

Fortunately, a self-leakage path is simple to incorporate into the nominal circuit model. This leakage is a short circuit path that loops around a coil without passing through the bulk reluctances associated with the pole iron and the air gap for the corresponding leg. This path is visualized in Figure 6, where r_l signifies the reluctance of the leakage path.

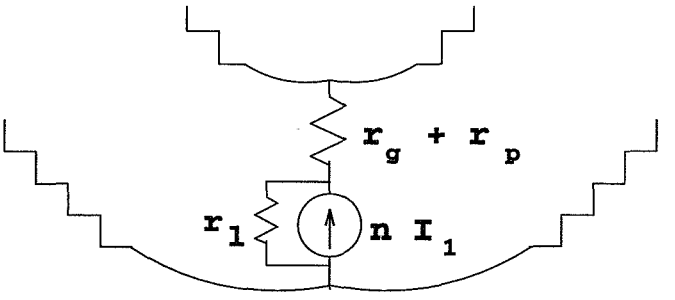

Figure 6: Equivalent circuit for self-leakage path.

Some parts of the leakage flux travel through the iron in the leg and stator adjacent to the coil of interest. However, the reluctance of the air part of the bulk leakage path is very large; the increase in the reluctance of the leakage path due to finite permeability in the iron is arguably negligibly small in comparison. The leakage flux is therefore idealized as flowing only in the coil itself and in the air around it from a circuit standpoint.

The fluxes in the gaps are identical with and without the self-leakage path; an extra flux of

$$\phi_{leak} = \frac{n}{r_l} I_i \tag{21}$$

is merely added to the flux that passes through the i^{th} coil. The only effect is to increase the self-inductance of a coil:

$$L_{ii} = \frac{m-1}{m}\left(\frac{n^2}{r_g}\right) + \frac{n^2}{r_l} \tag{22}$$

Off-diagonal terms in L remain the same as before. An over-determined set of linear equations can now be solved for r_g^{-1} and r_l^{-1} by equating L and $\hat{L}$. If the bearing is symmetric, it is sufficient to compare only the first row of L and $\hat{L}$. Denoting the first row of L as L_1, row L_1 can be decomposed as:

$$L_1' \equiv M \left\{ \begin{array}{c} r_g^{-1} \\ r_l^{-1} \end{array} \right\} \text{ where } M = \left[\begin{array}{cc} n^2\left(\frac{m-1}{m}\right) & n^2 \\ \frac{-n^2}{m} & 0 \\ \vdots & \vdots \\ \frac{-n^2}{m} & 0 \end{array} \right] \tag{23}$$

The least-squares solutions for the gap and leakage reluctances are then

$$\left\{ \begin{array}{c} r_g^{-1} \\ r_l^{-1} \end{array} \right\} = [M'\,M]^{-1}\,M'\,\hat{L}_1' \tag{24}$$

POWER LOSS AND ACTUATOR BANDWIDTH CALCULATION

A frequency-dependent bearing inductance can be obtained either by the use of $\mu_{fd}(s)$ in inductance calculation or by measurement of bearing electrical impedance. Once this inductance is determined, power loss and actuator bandwith can be deduced by relatively simple calculations.

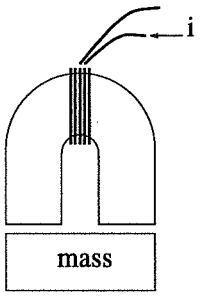

Figure 7: Simple magnetic actuator.

Power Loss

At a given frequency ω, inductance L can be separated into real and imaginary components:

$$L(j\omega) = L_r + j\,L_i \tag{25}$$

where L_r and L_i are both real numbers. In the frequency domain, the voltage drop across the bearing is

$$V(j\omega) = j\omega\,(L_r + j\,L_i)I(j\omega) \tag{26}$$

Eq. (26) implies that if the current going through a bearing is

$$I(t) = i\,\sin\omega t \tag{27}$$

the voltage drop across the bearing is

$$V(t) = \omega\,i(-L_i\,\sin\omega t + L_r\,\cos\omega t) \tag{28}$$

Noting that instantaneous power loss is $I(t)\,V(t)$, the power loss can be integrated through one cycle and divided by the cycle length to yield average power loss:

$$\text{Power Loss} = -\frac{\omega}{2}\,L_i\,i^2 \tag{29}$$

In the absence of eddy currents, L_i is zero. When eddy currents are modeled, L_i is a negative number, resulting in a power loss.

Actuator Bandwidth

Determination of actuator bandwidth will be addressed by considering a simple example; however, the method is readily extended to more complicated actuators. Specifically, consider the actuator shown in Figure 7. A single horseshoe electromagnet pulls a mass upwards against the force of gravity. The force, f, produced by this bearing is

$$f(t) = \frac{1}{\mu_o\,a}\,(\phi_b + \phi_p)^2 \tag{30}$$

pole length	l_p	0.0181 m	rotor area	a_r	$0.786 \times 10^{-4}\,\mathrm{m}^2$
pole area	a_p	$1.210 \times 10^{-4}\,\mathrm{m}^2$	lam. thickness	d	$0.635 \times 10^{-3}\,\mathrm{m}$
air gap length	l_g	$4.572 \times 10^{-4}\,\mathrm{m}$	conductivity	σ	$9.017 \times 10^{6}\,(\Omega \cdot \mathrm{m})^{-1}$
air gap area	a_g	$1.210 \times 10^{-4}\,\mathrm{m}^2$	permeability	μ	$5000\,\mu_o$
stator length	l_s	0.0366 m	turns	n	76 turns/pole
stator area	a_s	$1.210 \times 10^{-4}\,\mathrm{m}^2$	coil resistance	R_c	0.62 Ω
rotor length	l_r	0.0198 m	shunt resistance	R_s	15.35 Ω

Table 1: Kingsbury Bearing Dimensions

where ϕ_b is a constant bias flux and ϕ_p is perturbation flux. If ϕ_b is chosen to exactly counteract gravity and the magnitude of ϕ_p is assumed small, the net force on the mass is

$$f(t) \approx \frac{1}{\mu_o\, a}\phi_b\phi_p \tag{31}$$

Perturbation flux $\Phi_p(s)$ is related to perturbation current $I_p(s)$ by

$$\Phi = \frac{L(s)}{n} I_p \tag{32}$$

implying that the relation between force and current in the Laplace domain is

$$F(s) = \left(\frac{\phi_b}{\mu_o\, a\, n}\right) L(s)\, I_p(s) \tag{33}$$

From eq. (33), it can be concluded that the bearing bandwidth is identical to the bandwidth of the frequency-dependent inductance.

EXPERIMENTAL COMPARISON–FREQUENCY RESPONSE

To test the accuracy of the augmented circuit methods, performance predictions made using the circuit method were compared to experimental results from an 8-pole radial bearing made by **Kingsbury, Inc.** The dimensions of this bearing are described in Table 1. For testing purposes, only one leg of the stator is wound with a 76-turn coil.

A two-dimensional finite element analysis of the bearing and coil was performed. Since the bearing and all windings are symmetric, it is sufficient to consider only the first row of $\hat{L}$, denoted $\hat{L}_1$. The first entry in this row corresponds to the self-inductance of the test coil, and the other entries in the row correspond to the mutual inductances that would be obtained if identical coils lay on each of the other legs. The following $\hat{L}_1$ was obtained by the finite element model:

$$\hat{L}_1' = \{2.0069, -0.2772, -0.2735, -0.2732, -0.2729, -0.2732, -0.2735, -0.2772\} \text{ mHenries}$$

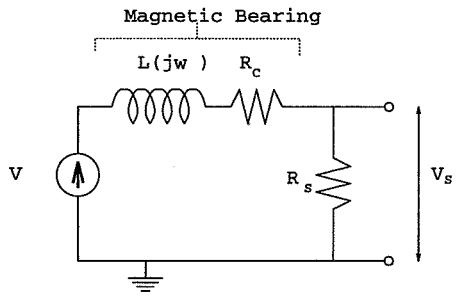

Figure 8: Test circuit.

Solving for r_g and r_l via (24) yields

$$r_g = 2.631 \times 10^6 \ \frac{\text{Wb}}{\text{A}} \qquad\qquad r_l = 6.701 \times 10^7 \ \frac{\text{Wb}}{\text{A}}$$

For comparison purposes, the air gap reluctance predicted by the nominal magnetic circuit model without leakage and fringing corrections is

$$r_{g,nominal} = \frac{l_g}{\mu_o g} = 3.007 \times 10^6 \, \frac{\text{Wb}}{\text{A}} \tag{34}$$

Fringing effects reduce the predicted air gap reluctance by 12.5 percent relative to the nominal reluctance. Leakage effects add another 0.086 mH of inductance, amounting to 4.30 percent of the total predicted self-inductance including leakage and fringing corrections when $\mu = \infty$.

Reluctances of the iron sections are computed from (16):

$$r_p = \frac{l_p}{\mu_{fd} a_p} = \frac{150.0\,\text{m}^{-1}}{\mu_{fd}} \qquad r_s = \frac{l_s}{\mu_{fd} a_s} = \frac{298.8\,\text{m}^{-1}}{\mu_{fd}} \qquad r_r = \frac{l_r}{\mu_{fd} a_r} = \frac{249.4\,\text{m}^{-1}}{\mu_{fd}} \tag{35}$$

For any particular frequency of interest, $\mu_{fd}(j\omega)$ is evaluated via (3).

The test bearing is included in a measurement circuit as pictured in Figure 8. Resistance R_c is the intrinsic resistance of the wire in the bearing's coil. Resistance R_s is an arbitrarily chosen current shunt resistance. In the present case, a 15.35 Ω resistor was employed. The input to the circuit is the voltage V. The measured output of the circuit is the voltage V_s. The transfer function of the electric circuit model is

$$\frac{V_s}{V} = \frac{R_s}{s\,L(s) + (R_s + R_c)} \tag{36}$$

The test bearing was subjected to a sine wave sweep varying from 100 Hz to 10^5 Hz. The output signal was convolved with the input signal to determine the magnitude and phase shift of the output.

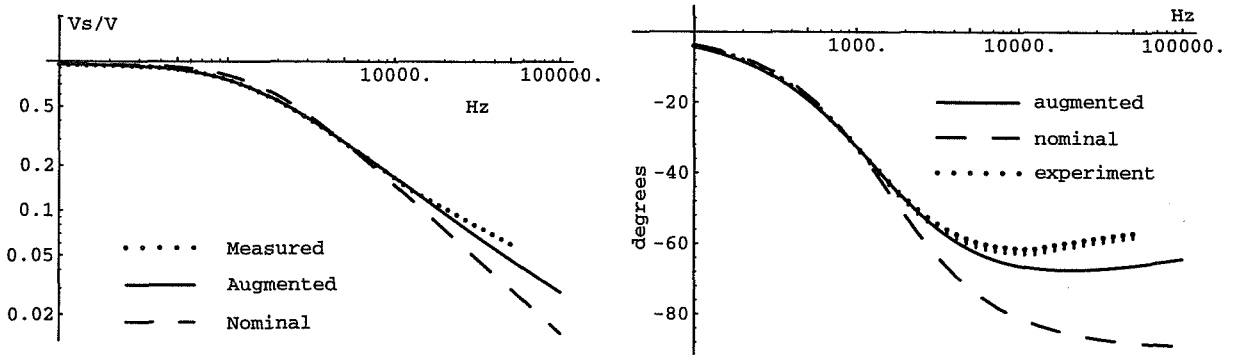

Figure 9: Frequency response of test circuit.

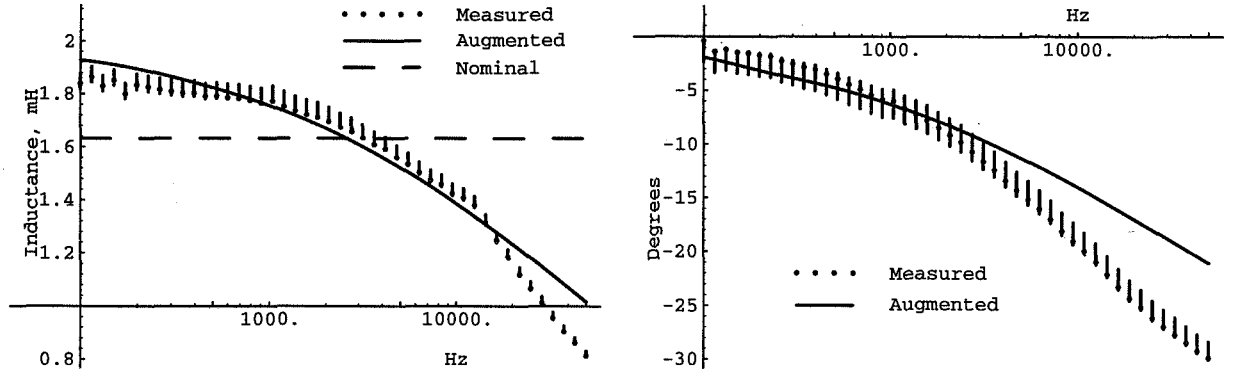

Figure 10: Response of frequency-dependent inductance.

A direct comparison of the measured transfer function $\frac{V_s}{V}$ can now be made with the transfer functions predicted by the augmented circuit model and the nominal circuit model. Figure 9 is a comparison of predicted and measured frequency response of test circuit. By substituting experimentally measured values of V_s/V into (36), one can solve for the frequency-dependent inductance of the bearing. Experimentally derived and predicted $L(j\omega)$ are compared to the nominal magnetic circuit model inductance in Figure 10. In each figure, the error bars associated with the measured data represent the maximum deviations expected due to experimental uncertainty.

At low frequencies (less than 1000 Hz), eddy current effects are negligible; the differences between the augmented and nominal models are due solely to leakage and fringing effects. In this frequency region, the augmented model shows an improvement in predictive accuracy over the nominal model. The nominal model underestimates the inductance in this region, but the corrected gap and leakage reluctances yield an inductance at low frequency that closely agrees with the experimentally derived inductance. The augmented

model also correctly predicts the "corner frequency" at which the magnitude response suddenly decreases; the nominal model over-predicts the corner slightly.

At higher frequencies, eddy currents become a significant effect. Figure (10) shows that a significant drop in inductance is predicted by the augmented model at higher frequencies. Experiment verifies this drop. Most significantly, eddy currents induce a recovery in phase in a situation where a simple inductor model predicts a terminal phase lag of 90^o as $\omega \rightarrow \infty$. The augmented model predicts the recovery of phase fairly well, with some loss of accuracy at the highest frequencies considered. Discrepancies between the augmented model and experiment at high frequency could be due to any of several effects:

- a breakdown in the accuracy of the leakage and fringing model due to a low effective permeability,
- capacitive effects in the test coil,
- saturation effects caused by concentration of flux near the sides of the lamination,
- mechanical resonance effects in the test apparatus.

An interesting phenomenon predicted by the augmented model is a terminal phase lag of $45°$. This result is possible because of the infinite number of poles and zeros associated with $\mu_{fd}(s)$. Far out on the negative real axis, poles and zeros are placed increasingly close together (on a log scale) to yield a terminal 45^o lag. The experiment corroborates this prediction.

CONCLUSIONS

An augmented magnetic circuit model was presented to account for eddy current, leakage, and fringing effects in radial active magnetic bearing. Although leakage and fringing corrections are derived from a bearing model in which the iron is assumed infinitely permeable, a good correspondence with experimental data was observed when these correction factors were applied to a model with complex iron permeability. The eddy current corrections, derived from a 1-D eddy current model, were also found to adequately account for a drop in bearing inductance with frequency. The eddy current correction can be evaluated at a specific frequency when frequency response is desired, or truncated into a finite-state model for use in transient response calculations or control applications. In both instances, a structure of arbitrarily complicated connectivity can be addressed. In summation, the augmented magnetic circuit model provides an improvement in the prediction of bearing performance over usual circuit methods without resorting to computationally expensive 2-D or 3-D finite element eddy current models.

REFERENCES

[1] Carpenter, C. J.: Comparison of Alternative Formulations of 3-Dimensional Magnetic-Field and Eddy-Current Problems at Power Frequencies. *Proc. IEE*, vol. 124, no. 11, Nov. 1977, pp. 1026-1034.

[2] Biro, O.; and Preis, K.: On the Use of Magnetic Vector Potential in the Finite Element Analysis of Three-Dimensional Eddy Currents. *IEEE Trans. Mag.*, vol. MAG-25, no. 4, July 1989, pp. 3145-3159.

[3] Williamson, S.; and Chan, E. K. C.: Three-Dimensional Finite Element Formulation for Problems Involving Time-Varying Fields, Relative Motion, and Magnetic Saturation. *IEE Proc-A*, vol. 140, no. 2, Mar. 1993, pp. 121-130.

[4] Plonus, M.: *Applied Electromagnetics.* McGraw-Hill, 1978.

[5] Stoll, R. L.: *The Analysis of Eddy Currents.* Oxford University Press, 1974.

[6] Avila-Rosales, J.; and Alvarado, F.: Nonlinear Frequency Dependent Transformer Model for Electromagnetic Transient Studies in Power Systems. *IEEE Trans. PAS*, vol. PAS-101, no. 11, Nov. 1982, pp. 4281-4288.

[7] Tarasiewicz, E. J. *et al.*: Frequency Dependent Eddy Current Models for Nonlinear Iron Cores. *IEEE Trans. Power Systems*, vol. 8, no. 2, May 1993, pp. 588-597.

[8] de Leon, F.; and Semlyen, A.: Time Domain Modeling of Eddy Current Effects for Transformer Transients. *IEEE Trans. Power Delivery*, vol. 8, no. 1, Jan. 1993, pp. 271-280.

[9] Zmood, R. B.; Anand, D. K.; and Kirk, J. A.: The Influence of Eddy Currents on Magnetic Actuator Performance. *Proc. IEEE*, vol. 75, no. 2, 1987, pp. 259-60.

[10] Walowit, J. A.; and Pinkus, O.: Analytic and Experimental Investigation of Magnetic Support Systems. Part 1: Analysis. *J. of Lubrication Technology*, vol. 104, July 1982, pp. 418-428.

[11] Tuschiya, K. *et al.*: Anisotropic Stiffness Effect of Stability of a Magnetically Suspended Momentum Wheel. *J. of Guidance, Control, and Dynamics*, vol. 14, no. 2, pp. 330-336.

[12] Hoole, S. R.: *Computer-Aided Analysis and Design of Electromagnetic Devices.* Elsevier, 1989.

[13] Rogers, W. E.: *Introduction to Electric Fields, A Vector Analysis Approach.* McGraw-Hill, 1954.

Modeling and Identification of a Large Gap Magnetic Suspension System

David E. Cox * and Nelson J. Groom †
NASA Langley Research Center, Hampton, Virginia 23681-0001

Min-Hung Hsiao‡, Jen-Kuang Huang§
Old Dominion University, Norfolk, VA 23529-0247

Abstract

This paper presents the results of modeling and system identification efforts on the NASA Large-Angle Magnetic Suspension Test Fixture (LAMSTF). The LAMSTF consists of a cylindrical permanent magnet which is levitated above a planar array of five electromagnets mounted in a circular configuration. The analytical model is first developed and open-loop characteristics are described. The system is shown to be highly unstable and requires feedback control in order to apply system identification. Limitations on modeling accuracy due to the effect of eddy-currents on the system are discussed. An algorithm is derived to identify a state-space model for the system from input/output data acquired during closed-loop operation. The algorithm is tested on both the baseline system and a perturbed system which has an increased presence of eddy currents. It is found that for the baseline system the analytic model adequately captures the dynamics, although the identified model improves the simulation accuracy. For the system perturbed by additional unmodeled eddy-currents the analytic model is no longer adequate and a higher-order model, determined through system identification, is required to accurately predict the system's time response.

*Research Engineer, Guidance and Controls Branch
†Senior Research Engineer, Guidance and Controls Branch
‡Ph.D. student, Dept. of Mechanical Engineering
§Associate Professor, Dept. of Mechanical Engineering

1 Introduction

The Large Angle Magnetic Suspension Test Fixture (LAMSTF) has been assembled by the NASA Langley Research Center for a ground-based experiment that will be used to investigate the technology issues associated with magnetic suspension at large gaps. This technology is applicable to future efforts that range from magnetic suspension of wind-tunnel models to advanced spacecraft isolation and pointing systems.

The LAMSTF system consists of a planar array of five electromagnets which actively suspend a small cylindrical permanent magnet (see Figure 1). The cylinder is a rigid body and has six independent degrees of freedom, namely, three displacements (x, y and z) and three rotations (pitch, yaw and roll). The roll axis of the cylinder is uncontrollable and is assumed to be motionless. A position sensing system is used to indirectly sense the pitch, yaw, x, y, and z position of the cylinder. It consists of six pairs of laser sheet sensors and photo-detectors mounted on a platform surrounding the suspended element. Therefore, the inputs consist of five currents into the electromagnets and the outputs are six voltage signals from the photo-detectors. The input currents to the electromagnets generate a magnetic field which produces a net force and torque on the suspended permanent magnet. Bias currents produce a force to counteract gravity. However, the field distribution about the suspension point produces forces which cause the suspension to be unstable. The linear model describes the systems dynamics in a region about this unstable equilibrium point. References [1] and [2] give a more complete description of the LAMSTF and some of the control approaches which have been investigated.

The analytical state-space model of LAMSTF is developed in Section 2. It has three highly unstable real poles and two low-frequency stable oscillatory modes. Experimental results obtained with controllers designed using the analytical model show reasonable agreement with simulation results. However, there are differences in predicted frequency and level of damping in the pitch axis. The differences are believed to be due to eddy-currents induced in the electromagnet's iron cores which are not considered in the system model. The objective of this paper is to derive the analytical model for a large-gap magnetic suspension system, and to demonstrate system identification as a method of eliminating model errors due to eddy-currents.

In the past few decades, a great variety of system identification methods have been studied. The choice of an identification method depends on the nature of the system and the purpose of identification. For control of a dynamic system, the state-space model is usually preferred. Recently, some methods were introduced [3] - [5] to identify a state-space model from a finite difference model. The difference model, called Auto-Regressive with eXogenous input (ARX) model, is derived through Kalman filter theories. This derivation is based on a deterministic approach. For identifying linear stochastic systems, projection filters are required as developed in [6] and [7]. There, the relationship between the state-space model and the ARX model was derived based on optimal estimation theory. In Section 4 this relationship is re-derived in a much simpler way through a z-transform of the ARX model.

Since the LAMSTF system is highly unstable, feedback control is required to ensure overall system stability while obtaining input/output data. The identification algorithm is applied to identify a state-space model from the plant input to the plant output. This system identification includes the following steps. First, the coefficient matrices of an ARX model, which can represent the corresponding state-space model, are estimated from the plant input/output data via the least-squares method. Second, the system and Kalman filter Markov parameters are computed from the estimated coefficient matrices of the ARX model in a recursive way. Third, the system matrices are realized from Hankel matrices formed by the system Markov parameters via the singular-value decomposition method [8], [9].

Experimental results are presented in Section 5. Step responses from simulations and test data are used to compare the accuracy of identified models of the baseline and perturbed system with the analytic model. It is found that the analytical model has a deficiency which is most evident in the dynamics of the pitch axis. Previous work with this system [2], [10] showed that increasing eddy-currents by placing an aluminum ring around the suspended element increases the modeling error in the pitch dynamics. For the baseline system the analytic model adequately captures the dynamics, although the identified model improves the simulation accuracy. For the system perturbed by an aluminum ring the unmodeled eddy-currents produce larger errors in pitch response and a higher-order model, determined through system identification, is required to accurately predict the system's time response.

2 System Modeling

A representation of this system is shown in Figure 1. The motion of the cylinder is defined by the body fixed axes, $\bar{x}, \bar{y}, \bar{z}$, that define the motion of the cylinder with respect to fixed inertial axes x, y, z. The development here follows the approach detailed in [11] and [12].

In a large-gap magnetic suspension system torques on the suspended element in the inertial coordinate system can be approximated as,

$$T_c = \int_V (M \times \mathcal{B}) dV \approx \nu (M_o \times \mathcal{B}_o) \tag{1}$$

and forces as,

$$F_c = \int_V (M \cdot \nabla) \mathcal{B} dV \approx \nu (M_o \cdot \nabla) \mathcal{B}_o = \nu [\partial \mathcal{B}_o] M_o \tag{2}$$

where ν is the volume of the permanent magnet core, M is the magnetization of the core, $\mathcal{B}$ is the flux density, and $\partial \mathcal{B}$ is a matrix of gradients. The approximation assumes that the magnetization is uniform over the core volume and that the higher order terms, obtained by expanding $\mathcal{B}$ about the origin of the core axis system are negligible.

In body fixed coordinates, the torque becomes

$$\bar{T}_c \approx \nu \left(\bar{M}_o \times T_m \mathcal{B}_o \right) \tag{3}$$

and the corresponding force,

$$\bar{F}_c \approx \nu T_m [\partial \mathcal{B}_o] T_m^{-1} \bar{M}_o \tag{4}$$

where T_m is an Euler transformation matrix between the inertial and body fixed coordinate systems. Under small angle and rate assumptions we can write the angular and linear acceleration of the suspended element, $\dot{\bar{\Omega}}, \dot{\bar{V}}$ in the body fixed coordinates as

$$\dot{\bar{\Omega}} = I_c^{-1} \left(\bar{T}_c + \bar{T}_d \right) \tag{5}$$

$$\dot{\bar{V}} = m_c^{-1} \left(\bar{F}_c + \bar{F}_d \right) \tag{6}$$

where I_c, m_c is the inertia and mass, respectively, of the suspended element; $\bar{T}_c$ and $\bar{F}_c$ denote the control torques and forces produced by the electromagnets; and $\bar{T}_d$ and $\bar{F}_d$ denote external disturbance torques and forces. For LAMSTF the only significant disturbance acting on the suspended element is along the z-axis and is equal to its weight

$$\bar{F}_g = T_m \begin{bmatrix} 0 & 0 & -m_c g \end{bmatrix} \tag{7}$$

where g is the acceleration due to gravity.

The control torques and forces are functions of position and orientation as well as the input currents, thus the equations of motion are in the form

$$\dot{x} = f(\tilde{x}, I) = \begin{Bmatrix} I_c^{-1} \bar{T}_c(\tilde{x}, I) \\ m_c^{-1} \left(\bar{F}_c(\tilde{x}, I) + \bar{F}_d \right) \end{Bmatrix} \tag{8}$$

where,

$$x = \begin{bmatrix} \tilde{x} & \Omega_{\bar{y}} & \Omega_{\bar{z}} & V_{\bar{x}} & V_{\bar{y}} & V_{\bar{z}} \end{bmatrix}^T, \tag{9}$$

and $\tilde{x}$ is the position and orientation of the body fixed reference frame with respect to the inertial frame. The equation can be linearized around the nominal operation point (x_o, I_o) by performing a Taylor series expansion. Neglecting second-order terms and subtracting out x_o results in

$$\delta \dot{x} = A \delta x + B \delta I, \tag{10}$$

where $A = \frac{\partial f}{\partial x}\Big|_{x_o, I_o}$ and $B = \frac{\partial f}{\partial I}\Big|_{x_o, I_o}$. The eigenvalues and mode shapes of the analytic model for LAMSTF are shown in Table 1 and Figure 2, respectively.

The development above yields a linear system model which is valid under the stated assumptions. In practice these assumptions are not overly constraining and are met by the LAMSTF system. The planar arrangement of electromagnets leads to a symmetric field distribution, and the suspended element is a uniform cylindrical magnet. Another factor, however, which is not considered in the model is the dynamic effects of nearby conductors on the magnetic fields. The actuator coils in LAMSTF contain iron cores which greatly improve their efficiency. The field in the cores is kept below the saturation level for that material so hysteresis effects are minimal. However, eddy currents due to changing magnetic fields can add dynamics to the actuator. Currently the system is modeled using a numerical package

Analytic Model	Nominal Identified	Perturbed Identified
0.00 - 0.96i	1.04 - 12.09i	0.54 - 10.22i
0.00 + 0.96i	1.04 + 12.09i	0.54 + 10.22i
0.00 - 7.97i	0.75 - 7.38i	2.02 - 9.22i
0.00 + 7.97i	0.75 + 7.38i	2.02 + 9.22i
-9.78	-6.71	-6.16
9.78	6.53	7.16
-57.81	-56.95	-57.95
57.81	61.72	60.33
-58.78	-58.14	-58.48
58.78	62.76	62.65
		-256.2

Table 1: Continuous plant eigenvalues for analytic model and identified models, under nominal and perturbed conditions.

which considers the static effect iron cores have on the field distribution of each actuator. The software cannot, however, predict the dynamic effect of eddy-currents in the iron cores.

In general eddy current effects are difficult to model because the relevant material properties vary with frequency and the resulting field distortion depends upon the conductor's geometry. Within a conductor the effect of eddy-currents is purely dissipative. Fields arise from eddy-currents which exactly oppose the inducing fields and are proportional to the inducing fields time rate-of-change. However, at points outside the conductor, fields may add in-phase with the suspension fields. For applications where magnetic suspension systems must operate in the vicinity of complex conductors, detailed modeling of eddy-currents is difficult if not impossible. For this reason it is desirable to investigate the use of system identification to refine the analytic models of these systems.

3 Relation Between State-Space and ARX Models

A finite-dimensional, linear, discrete-time, time-invariant system can be modeled as:

$$x_{k+1} = Ax_k + Bu_k + w_k, \tag{11}$$

$$y_k = Cx_k + Du_k + \nu_k, \tag{12}$$

where $x \in R^{n\times 1}$, $u \in R^{s\times 1}$, $y \in R^{m\times 1}$ are state, input and output vectors, respectively; w_k is the process noise, ν_k the measurement noise; $[A, B, C, D]$ are the state-space parameters. Sequences w_k and ν_k are assumed Gaussian, white, zero-mean, and stationary with covariance matrices Q and R, respectively. One can derive a steady-state filter innovation model [6]

$$\hat{x}_{k+1} = A\hat{x}_k + Bu_k + AK\epsilon_k, \tag{13}$$

$$y_k = C\hat{x}_k + Du_k + \epsilon_k \tag{14}$$

where $\hat{x}_k$ is the a priori estimated state, K is the steady-state Kalman filter gain and ϵ_k is the residual after filtering: $\epsilon_k = y_k - C\hat{x}_k - Du_k$. The existence of K is guaranteed if the system is detectable and $(A, Q^{1/2})$ is stabilizable. Substituting (14) into (13), one has

$$\hat{x}_{k+1} = \bar{A}\hat{x}_k + \bar{B}u_k + AKy_k, \tag{15}$$

where $\bar{A} = A - AKC, \bar{B} = B - AKD$, and $\bar{A}$ is guaranteed to be asymptotically stable because the steady-state Kalman filter gain K exists. Taking the z-transform of (15) and (14), one has

$$\hat{x}(z) = (z - \bar{A})^{-1}(\bar{B}u(z) + AKy(z)), \tag{16}$$

$$y(z) = C\hat{x}(z) + Du(z) + \epsilon(z). \tag{17}$$

Substituting (16) into (17) yields,

$$y(z) = C(z - \bar{A})^{-1}(\bar{B}u(z) + AKy(z)) + Du(z) + \epsilon(z) \tag{18}$$

Taking the inverse z-transform of (18) with $(z - \bar{A})^{-1} = \sum_{i=1}^{\infty} \bar{A}^{i-1}z^{-i}$, one has

$$y_k = \sum_{i=1}^{\infty} C\bar{A}^{i-1}AKy_{k-i} + \sum_{i=1}^{\infty} C\bar{A}^{i-1}\bar{B}u_{k-i} + Du_k + \epsilon_k \tag{19}$$

Since $\bar{A}$ is asymptotically stable, $\bar{A}^i \approx 0$ if $i > q$ and q is chosen large enough. Thus (19) becomes

$$y_k \approx \sum_{i=1}^{q} a_i y_{k-i} + \sum_{i=0}^{q} b_i u_{k-i} + \epsilon_k, \tag{20}$$

where, $a_i = C\bar{A}^{i-1}AK, b_i = C\bar{A}^{i-1}\bar{B}$, and $b_o = D$.

The model described by (20) is called the Auto-Regressive with eXogenous input (ARX) model which directly represents the relationship between output and input without state variables. The coefficient matrices a_i and b_i can be estimated through least-squares methods from random excitation input u_k and the corresponding output y_k. From (20) and for l points of the input/output data, one can have

$$\xi \approx \theta\Phi + \Xi \tag{21}$$

where,

$$\begin{aligned}
\xi &= \begin{bmatrix} y_{q+1} & y_{q+2} & \cdots & y_l \end{bmatrix}, \\
\theta &= \begin{bmatrix} b_o & a_1 & b_1 & a_2 & b_2 & \cdots & a_q & b_q \end{bmatrix}, \\
\Xi &= \begin{bmatrix} \epsilon_{q+1} & \epsilon_{q+2} & \cdots & \epsilon_l \end{bmatrix}, \\
\Phi &= \begin{bmatrix} u_{q+1} & u_{q+2} & \cdots & u_l \\ \phi_q & \phi_{q+1} & \cdots & \phi_{l-1} \\ \phi_{q-1} & \phi_q & \cdots & \phi_{l-2} \\ \vdots & \vdots & \ddots & \vdots \\ \phi_1 & \phi_2 & \cdots & \phi_{l-q} \end{bmatrix}, \text{ and } \phi = \begin{bmatrix} y \\ u \end{bmatrix}
\end{aligned}$$

From (21) it can be seen that parameters of the ARX model are linearly related to the input/output data. Therefore, solving for an ARX model involves solving a linear system involving an over determined set of equations. The batch least-square solution for the coefficient matrices a_i and b_i is

$$\theta = \xi \Phi^{\dagger} \tag{22}$$

where $\Phi^{\dagger}$ is the pseudoinverse of the Φ matrix.

4 Markov Parameters and State-Space Realization

The previous section presents the relation between an ARX model and a state-space model. The ARX model can be estimated through the least-squares method. The estimated ARX model has to be transformed back to a state-space model for system model comparisons or controller designs. First, the system and Kalman filter Markov parameters are calculated from the estimated coefficient matrices of the ARX model. Then a state-space realization can be obtained by using singular-value decomposition for a Hankel matrix formed by the system Markov parameters.

4.1 System and Kalman Filter Markov Parameters

Taking the z-transform of state-space model (13), one has

$$\hat{x}(z) = (z - A)^{-1}(Bu(z) + AK\epsilon(z)). \tag{23}$$

Substituting (23) into the z-transform of the output equation (14) yields

$$\begin{aligned} y(z) &= C(z - A)^{-1}(Bu(z) + AK\epsilon(z)) + Du(z) + \epsilon(z) && (24) \\ &= \sum_{k=0}^{\infty} Y(k) z^{-k} u(z) + \sum_{k=0}^{\infty} N(k) z^{-k} \epsilon(z) && (25) \end{aligned}$$

where $Y(0) = D$ and $Y(k) = CA^{k-1}B$ are called system Markov parameters, $N(0) = \tilde{I}$ an identity matrix, and $N(k) = CA^{k}K$ the Kalman filter Markov parameters.

Taking the z-transform of the ARX model (20), one has

$$\left(\tilde{I} - \sum_{i=1}^{q} a_i z^{-i}\right) y(z) = \sum_{i=0}^{q} b_i z^{-i} u(z) + \epsilon(z) \tag{26}$$

Applying long division to (26), one has

$$\begin{aligned} y(z) &= (b_0 + (b_1 + a_1 b_0) z^{-1} \\ &+ (b_2 + a_1(b_1 + a_1 b_0) + a_2 b_0) z^{-2} + \ldots) u(z) \\ &+ (\tilde{I} a_1 z^{-1} + (a_1 a_1 + a_2) z^{-2} + (a_1(a_1 a_1 + a_2) + a_2 a_1 + a_3) z^{-3} + \ldots) \epsilon(z) \end{aligned} \tag{27}$$

By comparing with (25), the system and Kalman filter Markov parameters can be recursively calculated from the estimated coefficient matrices of the ARX model as follows

$$Y(k) = b_k + \sum_{i=1}^{k} a_i Y(k-i) \tag{28}$$

$$N(k) = \sum_{i=1}^{k} a_i N(k-i) \tag{29}$$

It is noted that $Y(0) = b_0$, $N(0) = \tilde{I}$, and $a_i = b_i = 0$, when $i > q$. One may obtain (28) and (29) from (20) and the definition of the Markov parameter [4],[5]. However, the derivation is much more complex. The Markov parameters of the Kalman filter can be used to design an optimal estimator without requiring noise statistics. The system Markov parameters are used in the following section to form the state-space model.

4.2 State-Space Realization

To obtain the open-loop state-space model, the realization through Singular Value Decomposition (SVD) method [8], [9] is used. The first step is to form a Hankel matrix from the system Markov parameters as follows:

$$H(j) = \begin{bmatrix} Y(j) & Y(j+1) & \cdots & Y(j+\beta) \\ Y(j+1) & Y(j+2) & \cdots & Y(j+\beta+1) \\ \vdots & \vdots & \ddots & \vdots \\ Y(j+\gamma) & Y(j+\gamma+1) & \cdots & Y(j+\gamma+\beta) \end{bmatrix} \tag{30}$$

where $Y(j)$ is the j-th Markov parameter. From the measurement Hankel matrix, The realization uses the SVD of $H(1)$, $H(1) = U\Sigma V^T$, to identify an n-th order discrete state-space model as

$$A = \Sigma_n^{-1/2} U_n^T H(2) V_n \Sigma_n^{-1/2}, B = \Sigma_n^{1/2} V_n^T E_s, C = E_m^T U_n \Sigma_n^{1/2}, D = Y(0) \tag{31}$$

where matrix Σ_n is the upper left hand $n \times n$ partition of Σ containing the n largest singular values along the diagonal. Matrices U_n and V_n are obtained from U and V by retaining only the n columns of singular vectors associated with the n singular values. Matrix E_m is a matrix of appropriate dimension having m columns, all zero except that the top $m \times m$ partition is an identity matrix. E_s is defined analogously.

5 Numerical and Experimental Results

A number of experimental tests were conducted to both validate the analytic modeling procedure and to demonstrate system identification as a method of generating models which

include eddy current effects. A control law was designed, based on the analytic model, to achieve approximate pole-placement [13]. The continuous control design was then converted to a discrete system via a tustin approximation. Real-time code implemented the controller at 250 Hz and provided reference inputs and data storage. A system simulation was also developed. The simulation was based on the discrete controller and used both the analytic and identified models for comparison.

To validate the analytic model a series of step responses were taken and compared to simulation. Inputs were placed at the system's sensors to achieve a unity feedback tracking system, as shown in Figure 3. The tracking signal was a series of steps in θ_y, θ_z, x, y and z with magnitudes of 2 degrees angular and 1 mm linear. Although the system does not track the reference perfectly, for most degrees of freedom simulation results match the experimental results as shown in figure 4. The analytical model lacks some cross-coupling in yaw, and has a different damping and frequency in pitch dynamics. A step response in pitch is shown in Figure 5 along with its simulation.

System identification tests were run to try and improve the model accuracy. A white noise reference input was placed at the control coils as shown in Figure 3. Data was recorded from the plant input and plant output. The recorded data length was 6000 points for each of the five actuators and six sensors. The model order was chosen to be 15, large enough to capture the dynamics of the system. From the Markov parameters a 10th order state-space model was derived. Using this identified model the tracking response was simulated. The simulated response compared well with the experimental response even in pitch, which is shown in Figure 6.

In order to study the effects of eddy-currents a conductive structure was added to perturb the nominal system. The perturbed system included an aluminum ring around the suspended element, as shown in Figure 7. The aluminum ring produces eddy-currents in response to changes in the magnetic fields but does not cause a static warping of the fields. This adds dynamics which are not considered in the analytic model. Previous experiments (which used an aluminum ring to mount the sensor array) had shown this geometry to cause modeling errors primarily in dynamics of the pitch axis. Using the same controller as before, step responses were taken for the perturbed configuration. The experimental pitch response of both the nominal and perturbed systems are shown in Figure 8. As evidenced from the figure, the effect of the aluminum ring is dramatic, causing a significant loss of damping in the closed-loop response.

System identification tests were repeated on the perturbed system. As before, white noise was injected at the systems actuators and a total of 6000 data points were taken at the input and output of the plant. The resulting system model included the effects of eddy-currents and was able to accurately predict the response in pitch as well as in other degrees of freedom. The pitch response of the experimental perturbed system and the simulation with the identified model are shown in Figure 9.

The eigenvalues of the analytic model, the identified model of the nominal system, and the identified model of the perturbed system are compared in Table 1. Two points are to be

noted here. First is that the perturbed model has an additional real pole. It was not possible to obtain a 10th order model which would accurately match the system's time response. An 11th order model, however, with an additional real pole, did match the experiment quite well. Although the pole is much higher in frequency than the nominal model dynamics, it is important for the closed-loop dynamics and adds the type of phase errors expected from eddy-current effects.

The second point is that the neither identified model contains the low frequency stable eigenvalues corresponding to the analytic model. This is believed to be an error in the identified model which has a negligible effect on the closed-loop performance. In obtaining bounded input/output data for identification, feedback control is required to provide overall system stability. Under closed-loop operation, however, it is difficult to guarantee sufficiently rich input to the plant to excite all the systems dynamics. In practice it was found that the low frequency oscillatory modes associated with the motion in the z-axis were difficult to identify. It is believed that, due to the controllers large low frequency gain, the white noise input, which acts as a disturbance, did not induce sufficient low frequency power at the plant input.

6 Concluding Remarks

An analytical model is derived for an unstable large-gap magnetic suspension system. This model is linearized to provide an analytic state-space model. The linear model dynamics are described and validated through experimental testing. A method of system identification is also described. The relation between the state-space and ARX models is derived through z-transforms. This derivation provides physical interpretation of the mapping from input/output data to the state space and the explicit meanings of the ARX parameters. Applying the system identification algorithms to the experimental system yields models with improved fidelity. Experimental tests are also conducted to show the effect of unmodeled eddy-currents on the closed-loop system. Applying system identification yields models for the perturbed system which include eddy-currents. These models are also validated through comparison of closed-loop step responses.

References

[1] N. J. Groom, and C. P. Britcher: *A Description of a Laboratory Model Magnetic Suspension Test Fixture with Large Angular Capability.* Proceedings of the First IEEE Conference on Control Application, Sept. 13-16, 1992 Dayton, OH, Vol. 1, pp. 454-459.

[2] C. P. Britcher and L. E. Foster: *Some Further Developments in the Dynamic Modeling and Control of the Large Angle Magnetic Suspension Test Fixture.* Proceedings of the Second International Symposium on Magnetic Suspension Technology, Seattle WA, August 1993, pp. 367-377.

[3] C. W. Chen, J.-K. Huang, M. Phan, and J.-N. Juang: *Integrated System Identification and Modal State Estimation for Control of Flexible Space Structures.* Journal of Guidance, Control and Dynamics, 1992, Vol 15, No.1, 88-95.

[4] M. Phan, L. G. Horta, J.-N. Juang, and R. W. Longman: *Linear System Identification via an Asymptotically Stable Observer.* AIAA Guidance, Navigation and Control Conference, 1991.

[5] J. N. Juang, M. Phan, L. G. Horta, and R. W. Longman: *Identification of Observer/Kalman Filter Markov Parameters: Theory and Experiments.* AIAA Guidance, Navigation and Control Conference 1991, and NASA TM-104069.

[6] C. W. Chen, J.-K. Huang, and J.-N. Juang: *Identification of Linear Stochastic Systems Through Projection Filters.* AIAA Structures, Structural Dynamics and Materials Conference 1992, pp. 2330-2340. Also to appear in Journal of Guidance, Control and Dynamics.

[7] C. W. Chen, J.-N. Juang, and J.-K. Huang: *Adaptive Linear System Identification and State Estimation.* Control and Dynamic Systems: Advances in Theory and Applications, Vol. 57, Multidisciplinary Engineering Systems: Design and Optimization Techniques and Their Application, edited by C. T. Leondes. New York: Academic Press, Inc., 1993, pp. 331-368.

[8] C. T. Chen, 1984, Linear System Theory and Design, Second Edition, Chapter 6, CBS College Publishing, New York.

[9] J. N. Juang, and R. S. Pappa: *An Eigensystem Realization Algorithm for Modal Parameter Identification and Model Reduction.* Journal of Guidance, Control, and Dynamics, 1985, Vol. 8, No. 5, 620-627.

[10] K. B. Lim, and D. E. Cox: *Experimental Robust Control Studies on an Unstable Magnetic Suspension System.* Proceedings of the American Control Conference, Baltimore, MD, July 1994, pp. 3198-3203.

[11] N. J. Groom: *Analytical Model of a Five Degree-Of-Freedom Magnetic Suspension and Positioning System.* NASA TM-100671, 1989.

[12] N. J. Groom, and C. P. Britcher: *Open-Loop Characteristics of Magnetic Suspension Systems Using Electromagnets Mounted in a Planar Array.* NASA TP-3229, 1992.

[13] N. J. Groom: *A Decoupled Control Approach for Magnetic Suspension Systems Using Electromagnets Mounted in a Planar Array.* NASA TM-109011, 1993.

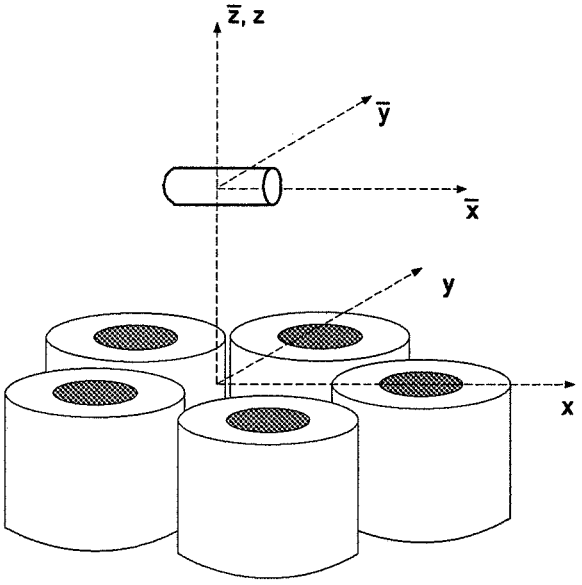

Figure 1: LAMSTF Physical system

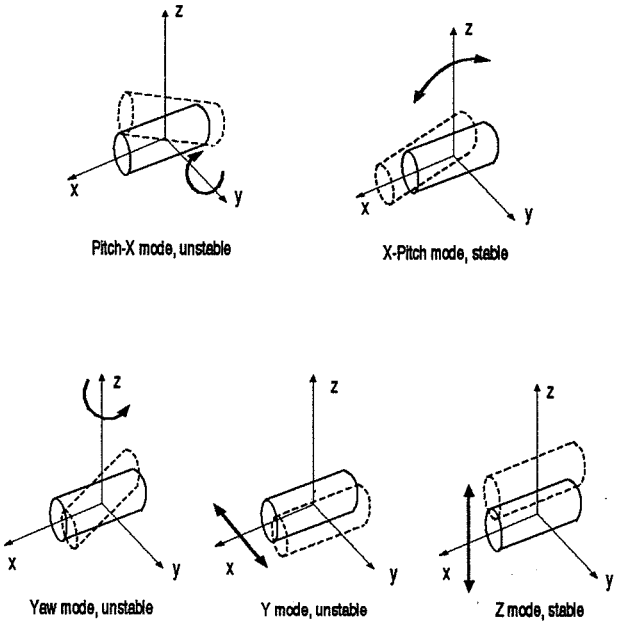

Figure 2: LAMSTF Modeshapes

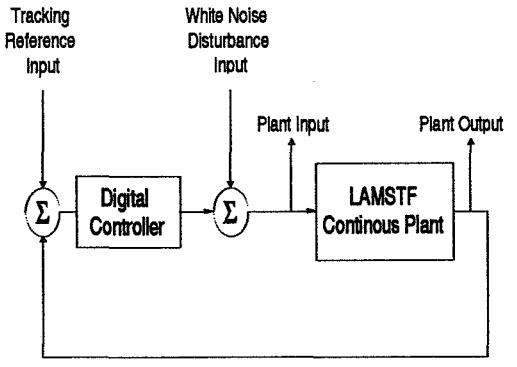

Figure 3: Block diagram for experimental LAMSTF system

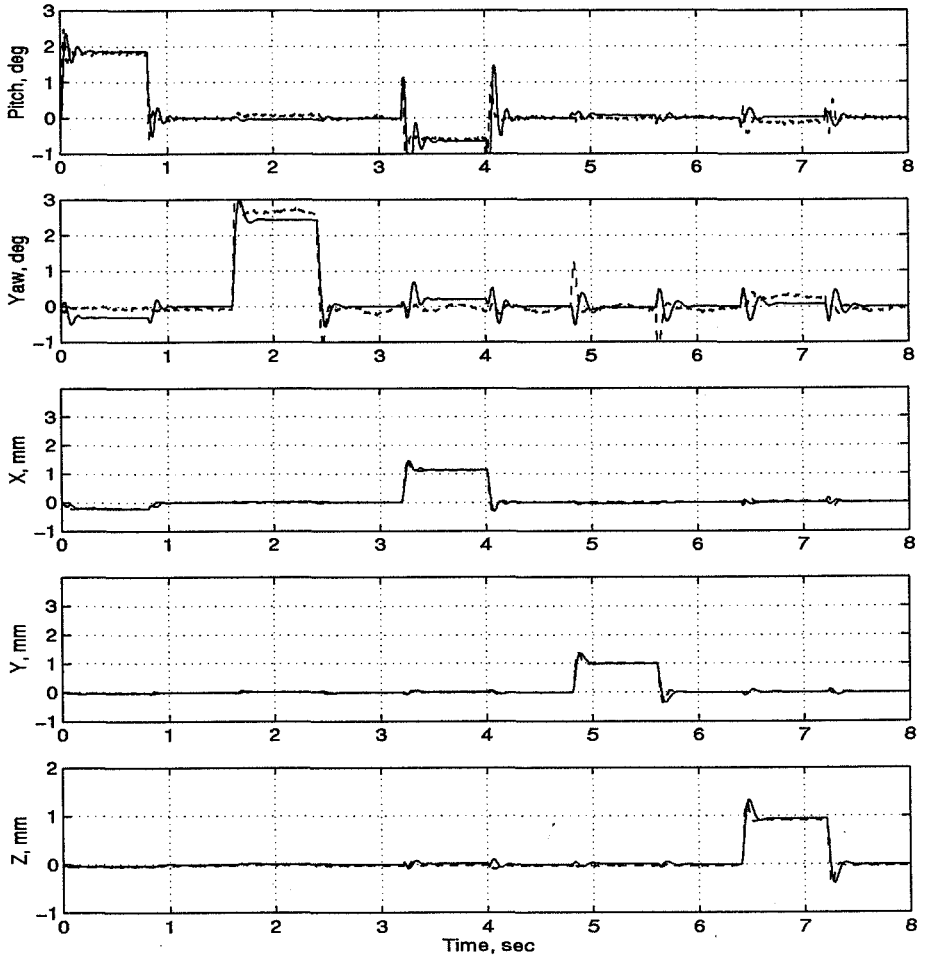

Figure 4: Analytic model simulation (solid) and experiment (dashed)

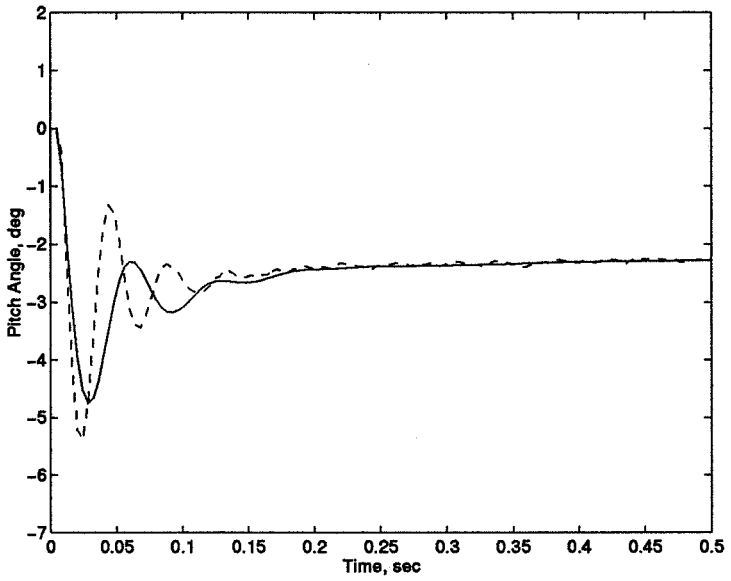

Figure 5: Analytic model simulation (solid) and experiment (dashed), pitch step response

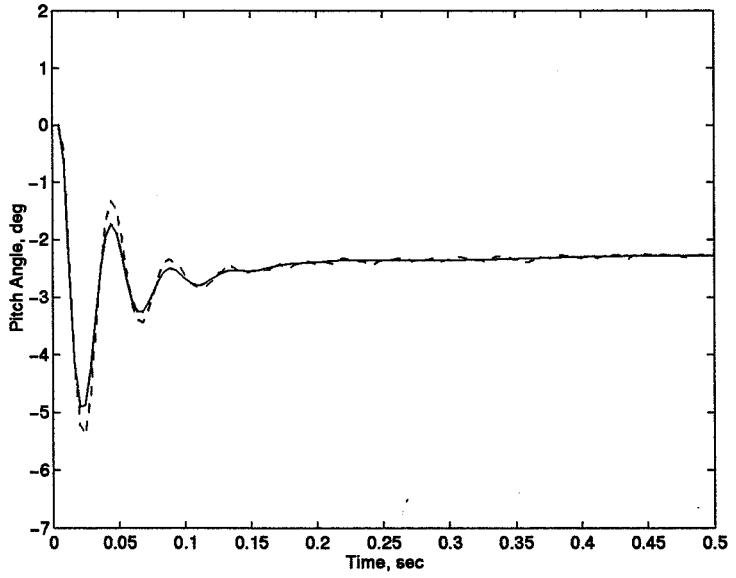

Figure 6: Identified model simulation (solid) and experiment (dashed), pitch step response

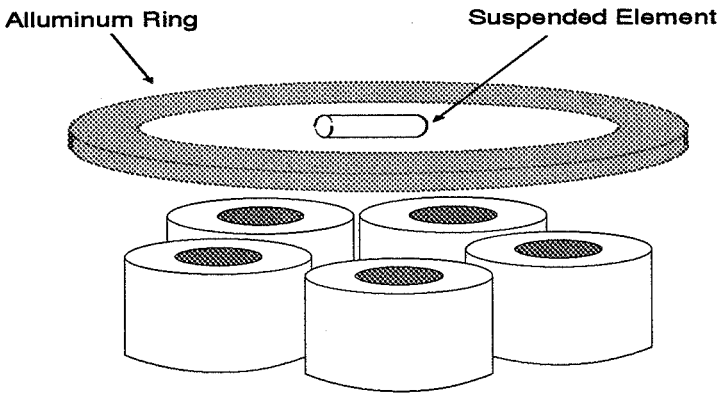

Figure 7: Perturbed LAMSTF system with aluminum ring to provide source of eddy-currents

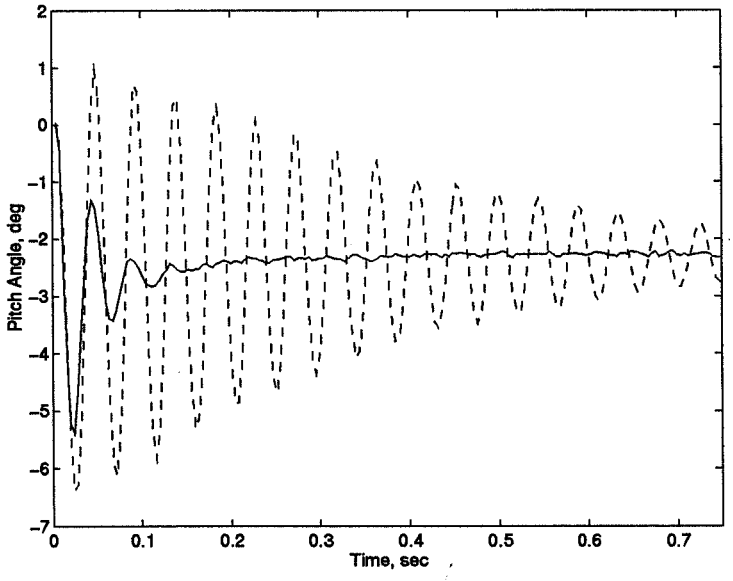

Figure 8: Nominal experiment (solid) and perturbed experiment (dashed), pitch step response

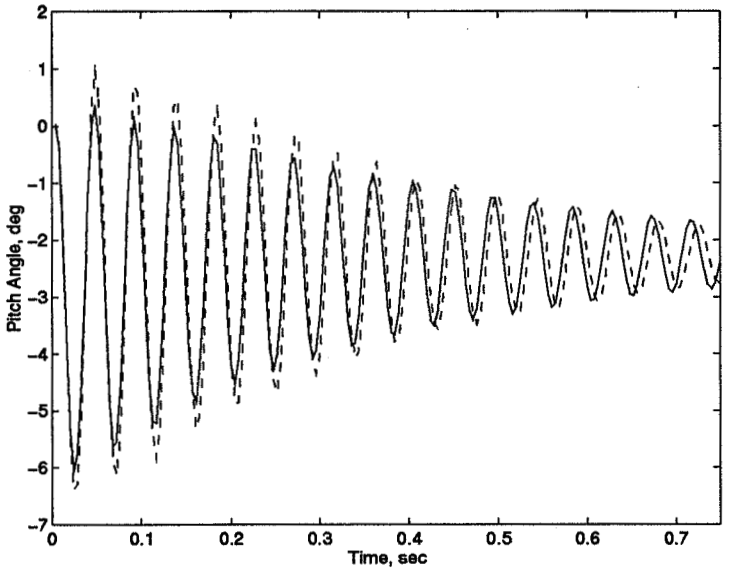

Figure 9: Identified model simulation (solid) and perturbed experiment (dashed), pitch step response

A MODEL FOR AXIAL MAGNETIC BEARINGS INCLUDING EDDY CURRENTS

Ladislav Kučera
International Center for Magnetic Bearings, ETH Zurich
Switzerland

Markus Ahrens
International Center for Magnetic Bearings, ETH Zurich
Switzerland

ABSTRACT

This paper presents an analytical method of modelling eddy currents inside axial bearings. The problem is solved by dividing an axial bearing into elementary geometric forms, solving the Maxwell equations for these simplified geometries, defining boundary conditions and combining the geometries. The final result is an analytical solution for the flux, from which the impedance and the force of an axial bearing can be derived. Several impedance measurements have shown that the analytical solution can fit the measured data with a precision of approximately 5%.

INTRODUCTION

Modelling magnetic bearings is necessary to achieve reasonable results for magnetic force and bearing losses in order to design bearings and amplifiers. Furthermore, controller design is based on a model of the plant including magnetic bearings. Magnetic bearings are usually modelled as equivalent electrical circuits. With simple models neglecting eddy currents, hysteresis, saturation and material nonlinearities, it is possible to achieve approximations for the magnetic force which are sufficient for most applications. Nevertheless, better modelling can improve bearing design and system behaviour. For some applications such as self sensing bearings a more precise model is necessary.
The absolute permeability μ describes the relationship between the magnetic flux density B and the magnetic field strength H (see equation (5)). The relative permeability μ_r is material dependent, the permeability of vacuum μ_0 is constant. For simple models μ_r can be assumed to be constant, but for real materials μ_r depends on the magnetic field strength (i.e. $\mu_r = \mu_r(H)$). With increasing magnetic field strength the gradient μ decreases (to a limit value μ_0). Therefore, the magnetic flux density is nearly constant for high field strengths (*saturation*). While increasing and decreasing H, the flux density B has different values for forward or backward loops due to *hysteresis* of the material. There are complex mathematical models such as the Preisach model [May91] to describe hysteresis, but these do not have an analytical solution.
Changing magnetic fields inside conducting materials cause currents to flow. These *eddy currents* have a large influence on the behaviour of magnetic bearings. The main goal of this paper

is to achieve an analytical description of a bearing model including eddy currents. Nonlinear material behaviour is considered in numerical calculations. Hysteresis is neglected in this paper. For elementary geometric forms, analytical solutions for eddy currents can be found. These solutions are sufficient to describe the behaviour of axial bearings. The elementary geometric forms are a semi-infinite plate, a rotationally symmetric plate and a semi-infinite cylinder.

ELEMENTARY GEOMETRIC FORMS

Electromagnetic fields and, therefore, eddy currents also can be described using Maxwell's equations ([Küp90], [Jac83]). In order to achieve analytical solutions it is necessary to divide an axial bearing into elementary geometric forms. Contrary to numerical results,analytical solutions can be more useful for bearing and controller design. Finite Element analysis can solve two or three-dimensional problems and more complex geometric forms. These numerical calculations are therefore used to verify analytical results and simplifications.

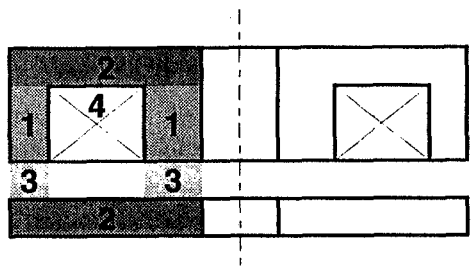

(1) Semi-infinite cylinder
(2) Rotational symmetric plate
(3) Air gap
(4) Coil with N turns

Figure 1: Cross section of an axial bearing. The bearing is divided into elementary forms.

Maxwell's Equations

Considering that the frequencies of the currents and fields are sufficiently low so that we can neglect the displacement current $\partial \boldsymbol{D}/\partial t$, Maxwell's equations can be written as

$$\mathrm{curl}\boldsymbol{E} = -\frac{\partial \boldsymbol{B}}{\partial t} = -\frac{\mathrm{d}\boldsymbol{B}}{\mathrm{d}\boldsymbol{H}}\frac{\partial \boldsymbol{H}}{\partial t} \tag{1}$$

$$\mathrm{curl}\boldsymbol{H} = \boldsymbol{J} \tag{2}$$

$$\mathrm{div}\boldsymbol{B} = 0 \tag{3}$$

Here $\boldsymbol{E}$ is the electric field strength and $\boldsymbol{J}$ the current density. The generalized Ohm's law, with the electric conductivity σ is given by:

$$\boldsymbol{J} = \sigma \boldsymbol{E} \tag{4}$$

The material equation is:

$$\boldsymbol{B} = \mu_0 \mu_r \boldsymbol{H} = \mu \boldsymbol{H} \tag{5}$$

Combining equations (1), (2), (4) and (5) we obtain:

$$\mathrm{curl}(\mathrm{curl}\boldsymbol{H}) = -\mu\sigma\frac{\partial \boldsymbol{H}}{\partial t} \tag{6}$$

A sinusoidal variation of the fields enables the transformation of equation (6) into the Fourier space. $\partial/\partial t$ can be replaced by $j\omega$ giving:

$$\mathrm{curl}(\mathrm{curl}\boldsymbol{H}) = -j\omega\mu\sigma\boldsymbol{H} = -\alpha^2\boldsymbol{H} \tag{7}$$

where:

$$\alpha = \sqrt{j\omega\mu\sigma} = (1+j)\sqrt{\frac{\omega\mu\sigma}{2}} \tag{8}$$

Maxwell's equations (2) and (3) can be integrated using the theorems of Stokes and Gauss (Θ: magnetomotive force , Φ: magnetic flux) to give:

$$\Theta = \int_{\partial A} \boldsymbol{H}\mathrm{d}\boldsymbol{s} = \sum \boldsymbol{I} + \int_{A} \boldsymbol{J}\mathrm{d}\boldsymbol{A} \tag{9}$$

$$\Phi = \int_{\partial V} \boldsymbol{B}\mathrm{d}\boldsymbol{A} \tag{10}$$

In the following sections, solutions for the elementary geometric forms *semi-infinite plate*, *rotational symmetric plate* and *semi-infinite cylinder* are given.

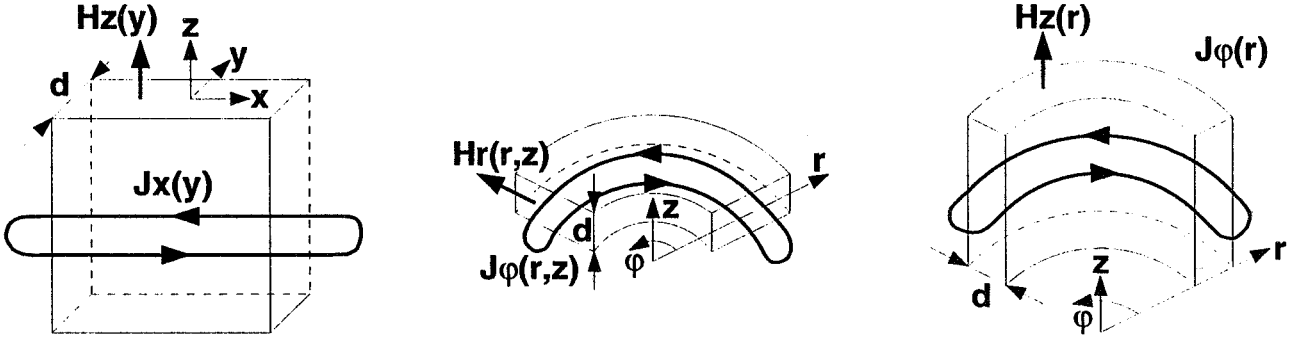

Figure 2: Cross section of
(a) a semi-infinite plate, (b) a rotational plate, (c) a semi-infinite cylinder

Semi-infinite Plate

A very long plate with thickness d and a magnetic field only in the z-direction has an eddy current flow in the x-direction. Equation (7) leads to the following differential equation:

$$\mathrm{curl}\begin{pmatrix} 0 \\ 0 \\ H_z \end{pmatrix} = \begin{pmatrix} \frac{\partial H_z}{\partial y} \\ 0 \\ 0 \end{pmatrix} = \begin{pmatrix} J_x \\ 0 \\ 0 \end{pmatrix} \tag{11}$$

$$\operatorname{curl}\begin{pmatrix} \frac{\partial H_z}{\partial y} \\ 0 \\ 0 \end{pmatrix} = \begin{pmatrix} 0 \\ 0 \\ -\frac{\partial^2 H_z}{\partial y^2} \end{pmatrix} = \begin{pmatrix} 0 \\ 0 \\ -\alpha^2 H_z \end{pmatrix} \tag{12}$$

$$\frac{\partial^2 H_z}{\partial y^2} = \alpha^2 H_z \tag{13}$$

with the general solution:

$$H_z(y) = c_1 e^{\alpha y} + c_2 e^{-\alpha y} \tag{14}$$

$$J_x(y) = \frac{\partial H_z}{\partial y} = c_1 \alpha e^{\alpha y} - c_2 \alpha e^{-\alpha y} \tag{15}$$

Rotational Symmetric Plate

$$\operatorname{curl}\begin{pmatrix} H_r \\ 0 \\ 0 \end{pmatrix} = \begin{pmatrix} 0 \\ \frac{\partial H_r}{\partial z} \\ 0 \end{pmatrix} = \begin{pmatrix} 0 \\ J_\varphi \\ 0 \end{pmatrix} \tag{16}$$

$$\operatorname{curl}\begin{pmatrix} 0 \\ \frac{\partial H_r}{\partial z} \\ 0 \end{pmatrix} = \begin{pmatrix} -\frac{\partial^2 H_r}{\partial z^2} \\ 0 \\ \frac{1}{r}\frac{\partial}{\partial r}\left(r\frac{\partial H_r}{\partial z}\right) \end{pmatrix} = \begin{pmatrix} -\alpha^2 H_r \\ 0 \\ 0 \end{pmatrix} \tag{17}$$

Equation (17) represents the following two differential equations:

$$\frac{\partial^2 H_r}{\partial z^2} = \alpha^2 H_r \tag{18}$$

$$\frac{1}{r}\frac{\partial H_r}{\partial z} + \frac{\partial^2 H_r}{\partial z \partial r} = 0 \tag{19}$$

The solution for the differential equations (18) and (19) can be found by separation of the variables:

$$H_r(r, z) = \mathcal{R}(r)\mathcal{Z}(z) \tag{20}$$

Equation (18) can be transformed to:

$$\frac{\partial^2 \mathcal{Z}}{\partial z^2} = \alpha^2 \mathcal{Z} \tag{21}$$

with the general solution:

$$\mathcal{Z}(z) = z_1 e^{\alpha z} + z_2 e^{-\alpha z} \tag{22}$$

Equation (19) can be transformed to:

$$\frac{1}{r}\mathcal{R} + \frac{\partial \mathcal{R}}{\partial r} = 0 \tag{23}$$

with the general solution:

$$\mathcal{R}(r) = r_1 \frac{1}{r} \tag{24}$$

Equation (22) and (24) lead to:

$$H_r(r,z) = \frac{1}{r}(c_1 e^{\alpha z} + c_2 e^{-\alpha z}) \tag{25}$$

Without regard for r, equation (25) is similar to equation (14) (the case of the semi-infinite plate).

Semi-infinite Cylinder

$$\operatorname{curl}\begin{pmatrix} 0 \\ 0 \\ H_z \end{pmatrix} = \begin{pmatrix} 0 \\ -\frac{\partial H_z}{\partial r} \\ 0 \end{pmatrix} = \begin{pmatrix} 0 \\ J_\varphi \\ 0 \end{pmatrix} \tag{26}$$

$$\operatorname{curl}\begin{pmatrix} 0 \\ -\frac{\partial H_z}{\partial r} \\ 0 \end{pmatrix} = \begin{pmatrix} 0 \\ 0 \\ -\frac{1}{r}\frac{\partial}{\partial r}\left(r\frac{\partial H_z}{\partial r}\right) \end{pmatrix} = \begin{pmatrix} 0 \\ 0 \\ -\alpha^2 H_z \end{pmatrix} \tag{27}$$

$$\frac{\partial^2 H_z}{\partial r^2} + \frac{1}{r}\frac{\partial H_z}{\partial r} - \alpha^2 H_z = 0 \tag{28}$$

The substitution $\bar{r} = \alpha r$ transforms the differential equation (28) into Bessel's equation:

$$\bar{r}^2 \frac{\partial^2 H_z}{\partial \bar{r}^2} + \bar{r}\frac{\partial H_z}{\partial \bar{r}} - \bar{r}^2 H_z = 0 \tag{29}$$

with the general solution:

$$H_z(\bar{r}) = c_1 I_0(\bar{r}) + c_2 K_0(\bar{r}) \tag{30}$$

or written without substitution:

$$H_z(r) = c_1 I_0(\alpha r) + c_2 K_0(\alpha r) \tag{31}$$

Here, I_0 is the modified Bessel function of first type and zeroth order and K_0 is the modified Bessel function of second type and zeroth order. More detailed information can be found in [AS65]. For calculations with Bessel functions, especially with complex arguments, a power series expansion is necessary. A solution without Bessel functions is therefore desirable.
It can be clearly seen that equation (31) leads to equation (14) when $R_i \gg d$ (R_i: inner radius of the cylinder). A numerical comparison of the results for equation (31) and equation (14) shows that the difference between these two equations is only significant for unrealistically small values of R_i ($R_i < d$).

An analysis of the cases of the semi-infinite cylinder and the rotational symmetric plate shows that these cases can be described with the equations of the semi-infinite plate. The problem of eddy currents in a semi-infinite plate is well known in the literature ([Sto74], [Küp90]), because the choice of lamination thickness is important for high power transformers and electrical machines.

BOUNDARY CONDITIONS

Solutions of differential equations require definitions of boundary conditions. Current field lines have to be closed. This is valid for eddy currents too. It is therefore assumed that eddy currents in a semi-infinite plate turn back at infinity. Eddy currents flow in one direction at one edge and in the other direction at the second edge (see figure 3 (a)). This solution is given in the literature ([Sto74], [Küp90]).
For a semi-infinite cylinder a second solution is possible. Contrary to a plate, a cylinder is geometrically closed and therefore eddy currents can flow in one direction (see figure 3 (b)). Calculations with the Finite Element program FEMAG ([Ins94]) produce this solution by default.

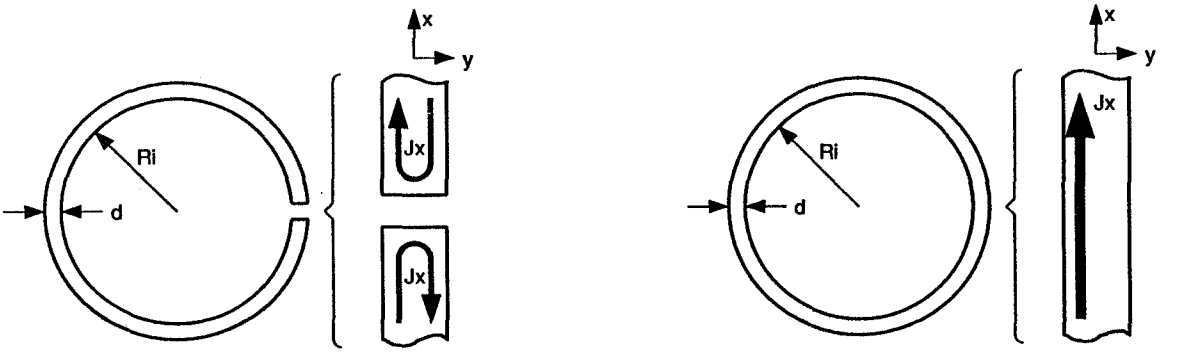

Case (a): A cylinder with an intersection. Eddy currents flow in two directions.

Case (b): A cylinder without an intersection. Eddy currents flow in one direction.

Figure 3: The two different boundary conditions. Cylinders with or without intersection.

Cylinder with intersection

The constants c_1 and c_2 of equations (14) and (15) can be found by defining two boundary conditions. The first boundary condition is given by

$$H_z(-\frac{d}{2}) = H_0 \tag{32}$$

The second boundary condition can be derived using Kirchhoff's law. The sum of all the currents has to be 0.

$$\int_{-\frac{d}{2}}^{\frac{d}{2}} J_x(y)\mathrm{d}y = 0 \tag{33}$$

Equation (33) can be written as:

$$H_z(\frac{d}{2}) = H_z(-\frac{d}{2}) \tag{34}$$

The solutions for H_z, J_x and the flux Φ with the boundary condition of a cylinder with intersection are as follows (A is the area of the cross section of a cylinder):

$$H_z(y) = H_0 \frac{\cosh(\alpha y)}{\cosh(\alpha \frac{d}{2})} \tag{35}$$

$$J_x(y) = \alpha H_0 \frac{\sinh(\alpha y)}{\cosh(\alpha \frac{d}{2})} \tag{36}$$

$$\Phi = \int_{-\frac{d}{2}}^{\frac{d}{2}} B \mathrm{d}A = \mu \frac{A}{d} \int_{-\frac{d}{2}}^{\frac{d}{2}} H_z(y) \mathrm{d}y = A \mu H_0 \frac{\tanh(\alpha \frac{d}{2})}{\alpha \frac{d}{2}} \tag{37}$$

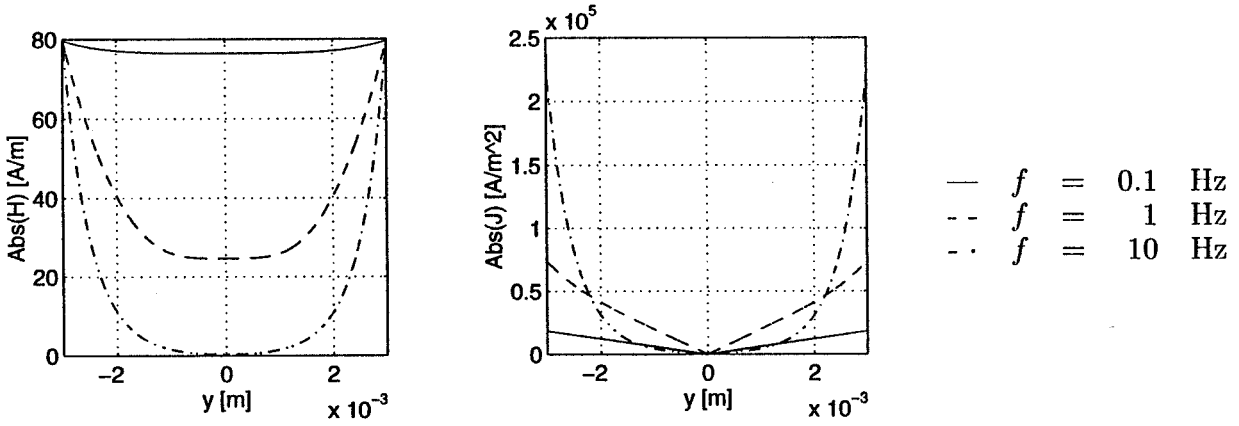

Figure 4: $|H_z(y)|$ and $|J_x(y)|$ for a cylinder with intersection.

Figure 4 shows the decrease of the H-field in the middle of the core and the increase of eddy currents near the surface of the core with increasing frequency. The following model parameters have been used.

d	=	$6 \cdot 10^{-3}$	m
A	=	$1.39 \cdot 10^{-3}$	m^2
μ_0	=	$4\pi \cdot 10^{-7}$	H/m
μ_r	=	5000	
H_0	=	79.6	A/m
B_0	=	$\mu_0 \mu_r H_0 = 0.5$	T
σ	=	$2 \cdot 10^7$	$(\Omega\mathrm{m})^{-1}$

Cylinder without intersection

In the case of a cylinder without intersection the start and end of the plate are fixed together and therefore eddy currents can have closed field lines and flow in one direction (the opposite

direction of the coil current).[1] The eddy current density at the outer surface of the core is zero.

c_1 and c_2 in equations (14) and (15) can be found by defining two boundary conditions. The first boundary condition is given by:

$$H_z(-\frac{d}{2}) = H_0 \tag{38}$$

The second boundary condition is given by:

$$J_x(\frac{d}{2}) = 0 \tag{39}$$

The solutions for H_z, J_x and Φ with the boundary condition of a cylinder without intersection are

$$H_z(y) = H_0 \frac{\cosh(\alpha\frac{d}{2} - \alpha y)}{\cosh(\alpha d)} \tag{40}$$

$$J_x(y) = \alpha H_0 \frac{\sinh(\alpha\frac{d}{2} - \alpha y)}{\cosh(\alpha d)} \tag{41}$$

$$\Phi = A\mu H_0 \frac{\tanh(\alpha d)}{\alpha d} \tag{42}$$

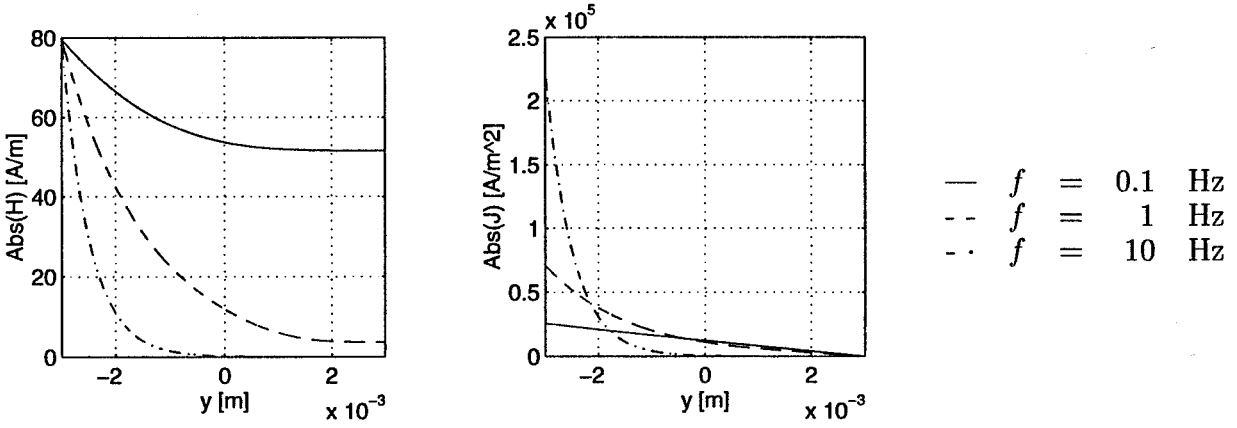

Figure 5: $|H_z(y)|$ and $|J_x(y)|$ for a cylinder without intersection

Figure 5 shows the decrease of the H-field near to the outer surface of the core and the increase of eddy currents near to the inner surface of the core with increasing frequency. The model parameters of the preceding section have been used.

[1]The unidirectional eddy current flow reminds us of a transformer with a shorted secondary winding. With the transformer equation, a model for eddy currents would be very simple. A transformer however has two windings and one core. Currents flow inside the windings and the core is only used as a magnetic material. An axial bearing has one winding and the core has two functions (for conducting and as a magnetic material). The transformer equation therefore would lead to an unacceptable error.

Comparison of the two boundary conditions

The generalized form of the flux equation can be written as:

$$\Phi = \Phi_0 \frac{\tanh(\gamma)}{\gamma} \tag{43}$$

with $\Phi_0 = A\mu H_0$ and with $\gamma = \alpha\frac{d}{2} \ldots \alpha d$.

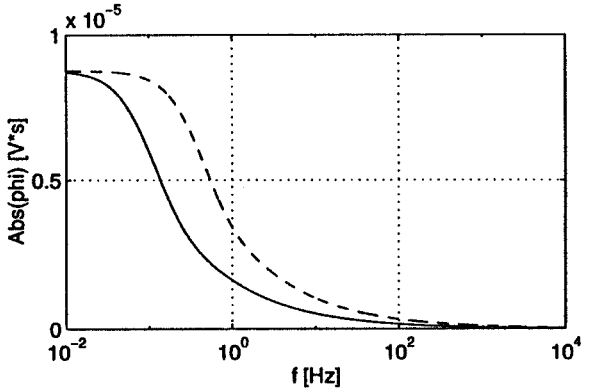

Figure 6: $|\Phi(f)|$ — cylinder without intersection
- - cylinder with intersection

A comparison of the flux equations (36) and (42) shows that γ is two times larger for unidirectional than for bidirectional eddy currents. Figure 6 shows the frequency dependent flux for both cases with the same Φ_0.
The flux bandwidth of bidirectional eddy currents is 4 times higher (see figure 6). This does not correspond to measurements which only show a factor of 2. This difference is caused by the frequency dependence of Φ_0.
In the case of bidirectional eddy currents, Φ_0 is constant for all frequencies. The H-field only changes inside the core and the boundary conditions at the surface of the core remain the same. This leads to frequency independance of the global H-field.
For unidirectional eddy currents the boundary conditions change at the surface of the core. This leads to a global change of the H-field and, therefore, to a change of Φ_0. In order to achieve analytical solutions it is necessary to expand the problem of modelling eddy currents with the problem of modelling inductances. Calculation of inductances can be done for simple geometric setups, but for complex geometries such as axial bearings analytical models are not available.
Several measurements have shown that the flux curves are similar for both eddy current cases. Therefore, the equations for bidirectional eddy currents can be used for unidirectional eddy currents too. It is clear that axial bearings with screw-holes or other gaps have uni- and bidirectional eddy currents and, therefore, the flux curve is between the two extreme eddy current cases.

The last boundary value H_0 can be found by closing the magnetic circuit. In order to build the complete magnetic circuit different materials have to be combined. Solutions for the flux are independent from the depth of the core (i.e. from the z-direction). Different materials lead to different solutions. It is clear that the flux changes in a transition region from one solution to the other. Finite Element analysis is used to calculate the flux distribution in a transition region between different materials. Figure 7 shows that the flux in the air gap is homogeneous even for high frequencies and that the transition region in the iron is small. Combining several materials is possible because the flux density distribution inside one material has little influence on the flux density distribution inside the next material.

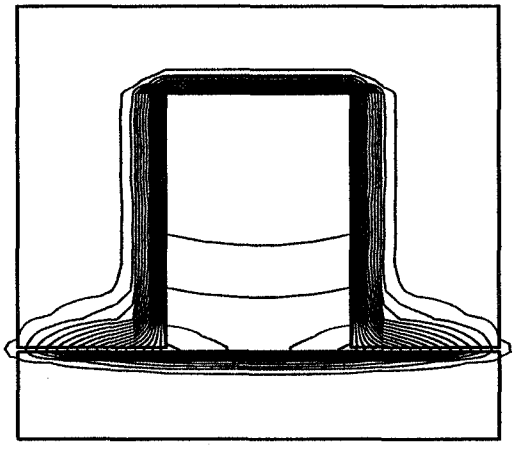

Figure 7: The flux inside the air gap is homogeneous even with a highly nonhomogeneous flux inside the unlaminated core ($f = 1\text{KHz}$).

For calculations with eddy currents, it is useful to define the cut-off frequency f_g of the flux decrease inside the core. In the literature f_g is called the cut-off frequency of the lamination (see also [Küp90]).

$$f_g = \frac{1}{\pi\sigma\mu d^2} \tag{44}$$

Axial bearing materials normally have either a very low f_g (unlaminated iron) or a very high f_g (laminated iron, special magnetic core materials such as Corovac[2] and air ($f_{g,air} \to \infty$)).

$$\oint H\mathrm{d}l = \sum_{m=1} H_m x_m = NI \tag{45}$$

$$\Phi = \int B_m \mathrm{d}A_m = A_m \mu_0 \mu_{r,m} H_m \frac{\tanh(\gamma_m)}{\gamma_m} \tag{46}$$

[2]Corovac is a high frequency core material with $\sigma \approx 5 \cdot 10^5 \text{S/m}$ and $\mu_r \approx 130$. The μ_r of Corovac is low compared to ferrite cores which are used for high frequency transformers. The machinability of Corovac is however much better.

Solving the system of equations (45) and (46) leads to the flux equation (for n different materials):

$$\Phi = \frac{\mu_0 N I}{\sum_{m=1}^{n} \frac{x_m}{\mu_{r,m} A_m} \frac{\gamma_m}{\tanh(\gamma_m)}} \tag{47}$$

The modelling of axial bearings cannot be improved using more than two terms of the sum. The first term represents all materials with low f_g and the second term includes all materials with a behaviour as air (f_g is very high and $\tanh(\gamma_m)/\gamma_m = 1$). This simplification is based upon the fact that a connection of two materials with similar f_g leads to:

$$a_1 \frac{\tanh(\gamma_1)}{\gamma_1} + a_2 \frac{\tanh(\gamma_2)}{\gamma_2} \approx a_3 \frac{\tanh(\gamma_3)}{\gamma_3} \tag{48}$$

The reduced flux equation is:

$$\Phi = \frac{\mu_0 N A I}{2x + \frac{l_{fe}}{\mu_r} \frac{\gamma}{\tanh(\gamma)}} = \mu_0 N A I \frac{1}{2x} \frac{1}{1 + \frac{1}{a_{fe}} \frac{\gamma}{\tanh(\gamma)}} \tag{49}$$

with:

$$a_{fe} = \mu_r \frac{2x}{l_{fe}} \tag{50}$$

All areas are normalized to the area of the air gap A. x is the length of the air gap (including lengths of materials with very high f_g) and l_{fe} is the length of the unlaminated core.

Saturation

In the previous calculations μ_r has been assumed to be constant. Saturation of the magnetic material leads to a limit value for the flux. The solution for the flux therefore gives unrealistically high values at the surface. Even with simple models for saturation (e.g. Fröhlich model [Sto74]), it is not possible to derive an analytical solution for the differential equations. Numerical calculations have shown that the behaviour of the H-field with saturation is very similar to the behaviour without saturation. It is therefore not necessary to include saturation into a model for eddy currents.

Equivalent Electrical Circuit

When x is assumed to be constant, the impedance of an eddy current affected coil can be written as:

$$Z = \frac{U}{I} = \frac{N \frac{\mathrm{d}\Phi}{\mathrm{d}t}}{I} = j\omega L_0 \frac{1}{1 + \frac{1}{a_{fe}} \frac{\gamma}{\tanh(\gamma)}} \tag{51}$$

with:

$$L_0 = \mu_0 N^2 A \frac{1}{2x} \tag{52}$$

Forces

The magnetic force is proportional to the square of the flux. Therefore a reduction of the flux due to eddy currents will also reduce the force to:

$$F = \frac{\Phi^2}{\mu_0 A} = \frac{K}{4}\frac{I^2}{x^2}\frac{1}{\left(1 + \frac{1}{a_{fe}}\frac{\gamma}{tanh(\gamma)}\right)^2} \tag{53}$$

with:

$$K = \mu_0 N^2 A \tag{54}$$

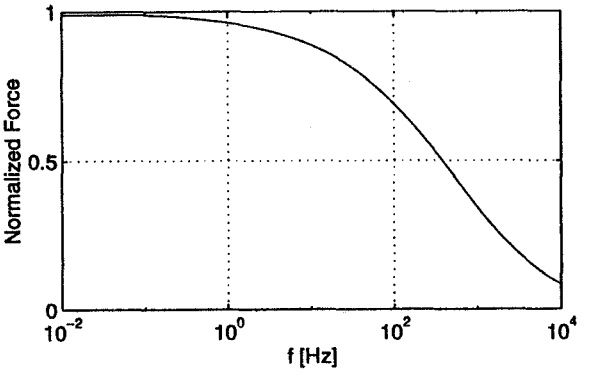

Figure 8: Normalized force dynamics $|F/F_{DC}|$ of an axial bearing ($f_g \approx 0.02$Hz, $a_{fe} \approx 200$)

NONLINEAR PARAMETER IDENTIFICATION

Parameter Identification

It is clear that the impedance of a coil not only depends on the inductance affected by the eddy currents. An impedance model must also include the coil resistance R_{cu}, the coil inductance L_{cu} and the coil capacitance C_{cu} (see figure 9). The last two parameters are necessary to model the frequency range above 10kHz. Thus, the total impedance is:

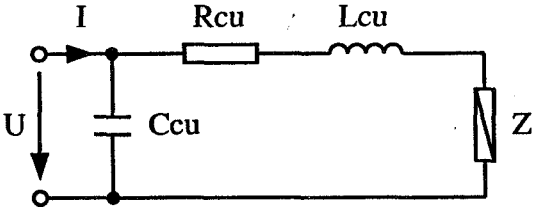

Figure 9: Complete equivalent electrical circuit

$$Z_{tot} = \frac{1}{j\omega C_{cu}} || (Z + R_{cu} + j\omega L_{cu}) \tag{55}$$

Robustness of the identification can be improved by defining the constraints. The authors used the constraint algorithm from the MATLAB Optimization Toolbox. The parameter range described below is sufficient to approximate all measured axial bearings. Less stringent constraints are possible, but computational time increases.
All parameter ranges excluding R_{cu} are written with exponential notation. The fitting algorithm therefore fits the exponent of the parameters. This method avoids the value 0 and guarantees convergence.

The ranges of the fitted parameters are given below.

$$\begin{array}{lllll} R_{cu} & = 0 & \ldots & 2 & \Omega \\ C_{cu} & = 1 \cdot 10^{-12} & \ldots 1 \cdot 10^{-9} & & F \\ L_{cu} & = 1 \cdot 10^{-6} & \ldots 1 \cdot 10^{-3} & & H \\ L_0 & = 1 \cdot 10^{-3} & \ldots 1 \cdot 10^{0} & & H \\ a_{fe} & = 1 \cdot 10^{0} & \ldots 1 \cdot 10^{3} & & \\ f_g & = 1 \cdot 10^{-3} & \ldots 1 \cdot 10^{1} & & Hz \end{array}$$

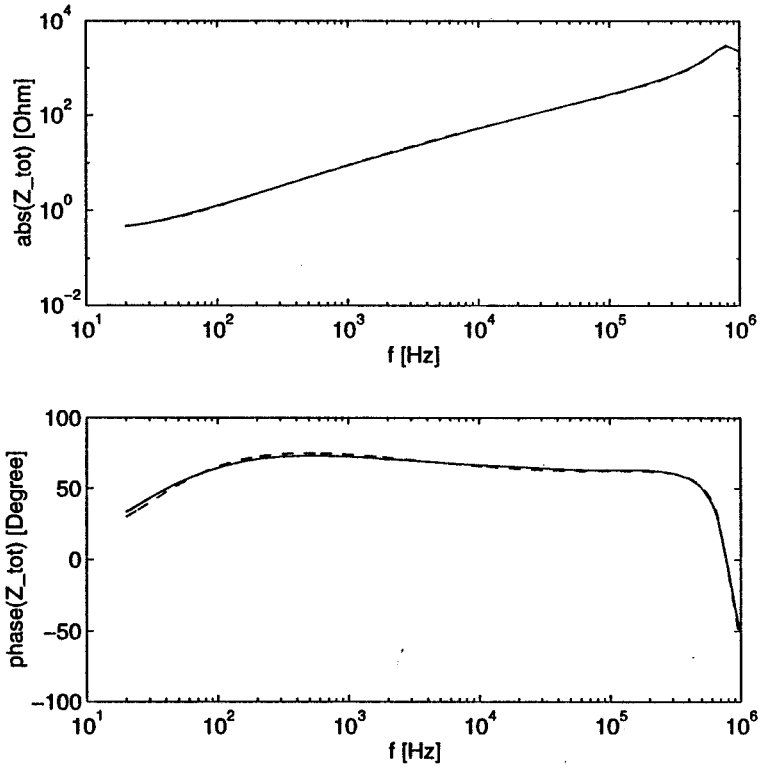

Figure 10: Example 1: Axial bearing with unlaminated core and target.
— : calculated data, - - : measured data
Identified parameters: $R_{cu} \approx 1.5\Omega, C_{cu} \approx 800pF, L_{cu} \approx 120\mu H, L_0 \approx 12mH, a_{fe} \approx 3, f_g \approx 7Hz$

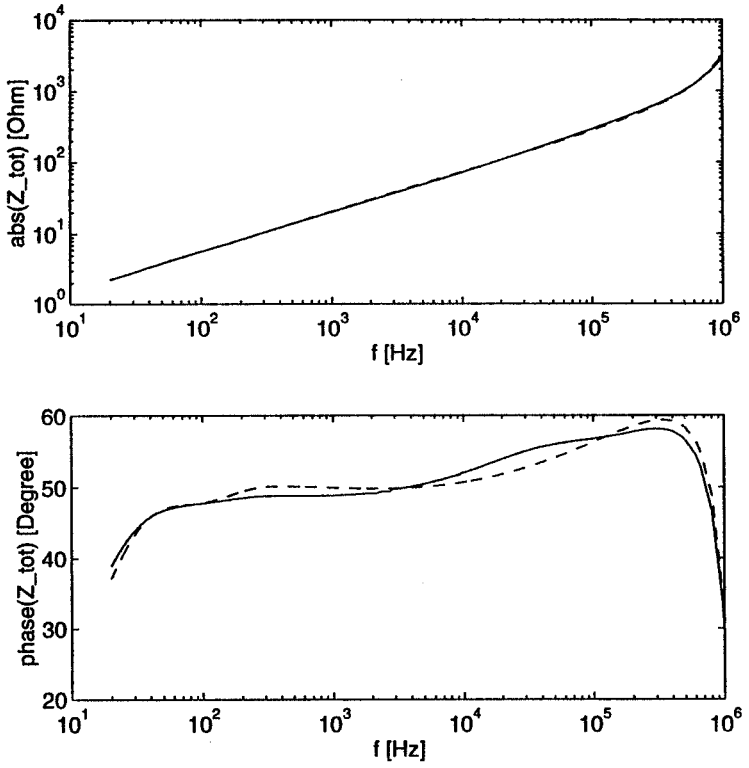

Figure 11: Example 2: Axial bearing with a Corovac core and an unlaminated target.
— : calculated data, - - : measured data
Identified parameters: $R_{cu} \approx 0.4\Omega, C_{cu} \approx 150pF, L_{cu} \approx 120\mu H, L_0 \approx 1.4mH, a_{fe} \approx 150, f_g \approx 0.12Hz$

The fitting error e is approximately 5% with the usual air gap and increases up to 10% when the air gap is small and the flux is saturated and is given by:

$$e = \sqrt{\frac{1}{n}\sum^{n}\left|1 - \frac{Z_{fit}}{Z_{meas}}\right|^2} \tag{56}$$

where n is the number of measured values, Z_{fit} the fitted impedance and Z_{meas} the measured impedance.

Losses

The spectral losses of an axial bearing are given by:

$$P = \text{real}(U\text{conj}(I)) = |U|^2\text{real}(\text{conj}\left(\frac{1}{Z_{tot}}\right)) \tag{57}$$

Figure 12 shows normalized loss based on impedance measurements of an axial bearing with a Corovac core. At low frequencies losses are very high due to R_{cu}. With increasing frequency

losses decrease. It is therefore useful to choose the switching frequency of an amplifier as high as possible. As mentioned in section *Comparison of the two boundary conditions*, a radial intersection of an axial bearing can increase the bandwidth of the flux and leads to lower losses. It is only sufficient to intersect unlaminated parts of the core with low f_g, i.e. in most cases the axial bearing target. An axial bearing without intersection suffers more than 40% higher loss than one with intersection at frequencies typically used for switching amplifiers (20 - 200 kHz).

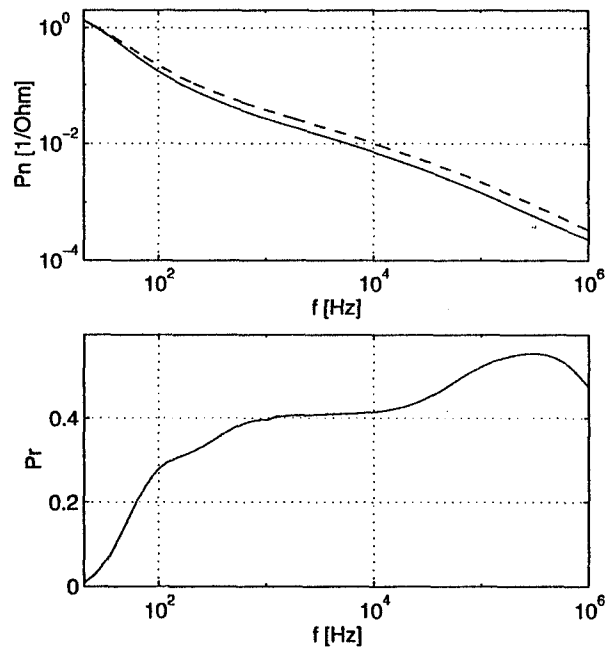

Figure 12: upper plot: normalized losses $P_n = P/|u|^2$ of an axial bearing with Corovac core and steel target (— P_1: target intersected , - - P_2: target not intersected)
lower plot: relative difference between the two curves of the upper plot $P_r = (P_2 - P_1)/P_1$

Measurement

Measurements of axial bearing impedances are made with a LCR-meter (HP 4284A) including a power current source (HP 42841A). The LCR-meter has the possibility to measure with logarithmically sweeped frequencies from 20Hz up to 1MHz. A host computer controls the measurement via GPIB-interface.
The power current source allows measurements of very high inductances and can superpose the measurement signal with a DC-bias current of up to 20A.

CONCLUSIONS

A model for eddy currents in axial bearings has been derived which can describe the behaviour for a wide frequency range. From the analytical solution for the flux, the impedance, the magnetic force and the losses can be calculated. Measurements have shown that the model is very precise.

REFERENCES

[AS65] Milton Abramowitz and Irene A. Stegun. *Handbook of Mathematical Functions.* Dover Publications, Inc., New York, 1965.

[Gro78] Emil Grosswald. *Bessel Polynomials.* Springer-Verlag, Berlin, 1978.

[Haf87] Christian Hafner. *Numerische Berechnung elektromagnetischer Felder.* Springer-Verlag, Berlin, 1987.

[Hec75] Carl Heck. *Magnetische Werkstoffe und ihre technischen Anwendungen.* Hüthig, Heidelberg, 1975.

[Ins94] Institut für Elektrische Maschinen, ETH Eidgenössische Technische Hochschule, Zürich. *FEMAG Benutzeranleitung*, 1994.

[Jac83] John D. Jackson. *Klassische Elektrodynamik.* de Gruyter, Berlin, 1983.

[Küp90] Karl Küpfmüller. *Einführung in die theoretische Elektrotechnik.* Springer-Verlag, Berlin, 1990.

[KXMH92] J. Knight, Z. Xia, E. McCaul, and H. Hacker. Determination of Forces in a Magnetic Bearing Actuator: Numerical Computation With Comparison to Experiment. *Journal of Tribology*, 114, 1992.

[LD89] Dimitris Labridis and Petros Dokopoulos. Calculation of Eddy Current Losses in Nonlinear Ferromagnetic Materials. *IEEE Transactions on Magnetics*, 25, May 1989.

[May91] I.D. Mayergoyz. *Mathematical Models of Hysteresis.* Springer-Verlag, New York, 1991.

[MH94] T. Mizuno and T. Higuchi. Experimental Measurement of Rotational Losses in Magnetic Bearings. In *Fourth International Symposium on Magnetic Bearings*, Zurich, 1994.

[Sto74] Richard Stoll. *The analysis of eddy currents.* Clarendon Press, Oxford, 1974.

[TK85] J.A. Tegopoulos and E.E. Kriezis. *Eddy Currents in Linear Conducting Media.* Elsevier, Amsterdam, 1985.

[Tra86] Alfons Traxler. *Eigenschaften und Auslegung von berührungsfreien elektromagnetischen Lagern.* PhD thesis, ETH Eidgenössische Technische Hochschule, Zürich, 1986.

Session 12 -- Precision Applications

Chairman: Karl Boden
KFA-IGV/Hideo Sawada, NAL

Development of a Wafer Positioning System for the Sandia Extreme Ultraviolet Lithography Tool

John B. Wronosky
Tony G. Smith
Joel R. Darnold

Sandia National Laboratories
Albuquerque, NM 87185-0501

Abstract

A wafer positioning system was recently developed by Sandia National Laboratories for an Extreme Ultraviolet Lithography (EUVL) tool[1]. The system, which utilizes a magnetically levitated fine stage to provide ultra-precise positioning in all six degrees of freedom, incorporates technological improvements resulting from four years of prototype development.[2] This paper describes the design, implementation, and functional capability of the system. Specifics regarding control system electronics, including software and control algorithm structure, as well as performance design goals and test results are presented. Potential system enhancements, some of which are in process, are also discussed.

[1] The EUVL program, including the subject positioning system, being performed at Sandia National Laboratories is supported by ARPA DALP and by the US Department of Energy under contract DE-AC04-94AL85000.

[2] Results of a joint program between GCA Corporation and Sandia National Laboratories with partial funding provided by SEMATECH.

Introduction

Magnetic levitation (maglev) is emerging as an important technology for wafer positioning systems in advanced lithography applications. The advantages of maglev stem from the absence of physical contact. The resulting lack of friction enables accurate, fast positioning. Maglev systems are mechanically simple, accomplishing full six degree-of-freedom suspension and control with a minimum of moving parts. Power-efficient designs, which reduce the possibility of thermal distortion of the platen, are achievable.

History of Maglev Positioning at Sandia

In the late 1980s, a concept for a magnetically levitated fine positioning technique was developed at MIT by Dr. David Trumper. The technique appeared to offer numerous advantages over conventional approaches. The maglev technique is frictionless, generates no wear particles, and requires no lubrication. A maglev system requires relatively simple fabrication techniques, offering cost advantages. Designs with extremely high power efficiency are readily achievable to minimize the possibility of thermal distortion of the platen. GCA Corp. viewed this new technology as very promising for lithography applications. They began implementing a plan to incorporate maglev positioning technology into GCA steppers. However, barriers to this plan included several difficulties in the application of the technology, such as the nonlinear aspects of the actuators, and implementing the multi-input, multi-output control strategy which is required. These difficulties prompted GCA and SEMATECH, through the Sandia/SEMATECH Cooperative Research and Development Agreement (CRADA), to seek assistance from Sandia in the development of a maglev fine stage control system. The first part of our effort, during CY '92, was the development of a control system for a prototype maglev fine stage. By the time of GCA's demise in mid-1993, proof-of-concept testing of the stage system had been successfully accomplished at Sandia. Peak-to-peak positioning noise of less than 20 nm was demonstrated. The ARPA Advanced Lithography Program funded a study that specified control system improvements needed for commercial application. Knowledge gained during these efforts has been applied to the development of the wafer stage system for the EUVL program.

The EUVL Project

The demand for smaller critical dimensions in integrated circuits has driven projection lithography to shorter wavelengths. Deep ultraviolet systems, operating at 248 nm, are commercially available and 193 nm lithography is under development. Research and development to extend this trend to extreme ultraviolet (EUV) wavelengths, in the range of 11 nm to 14 nm, is underway at Sandia National Laboratories in Livermore, California. The EUVL project is supported by the Department of Energy through a CRADA between Sandia National Laboratories and AT&T Bell Laboratories and by the ARPA Advanced Lithography Program. An EUVL laboratory tool using a 10x reduction Schwarzchild camera and magnetically levitated wafer stage driven by a digital feedback controller facilitate this research. Figure 1 shows a drawing of the tool[1]. This system represents the first attempt at integrating all major subsystems into an EUVL laboratory tool, suitable for device fabrication experiments. Further development

of EUV technology is aimed at the goal of building a practical lithography tool capable of producing microelectronics devices having critical dimensions of less than 0.13 μm.

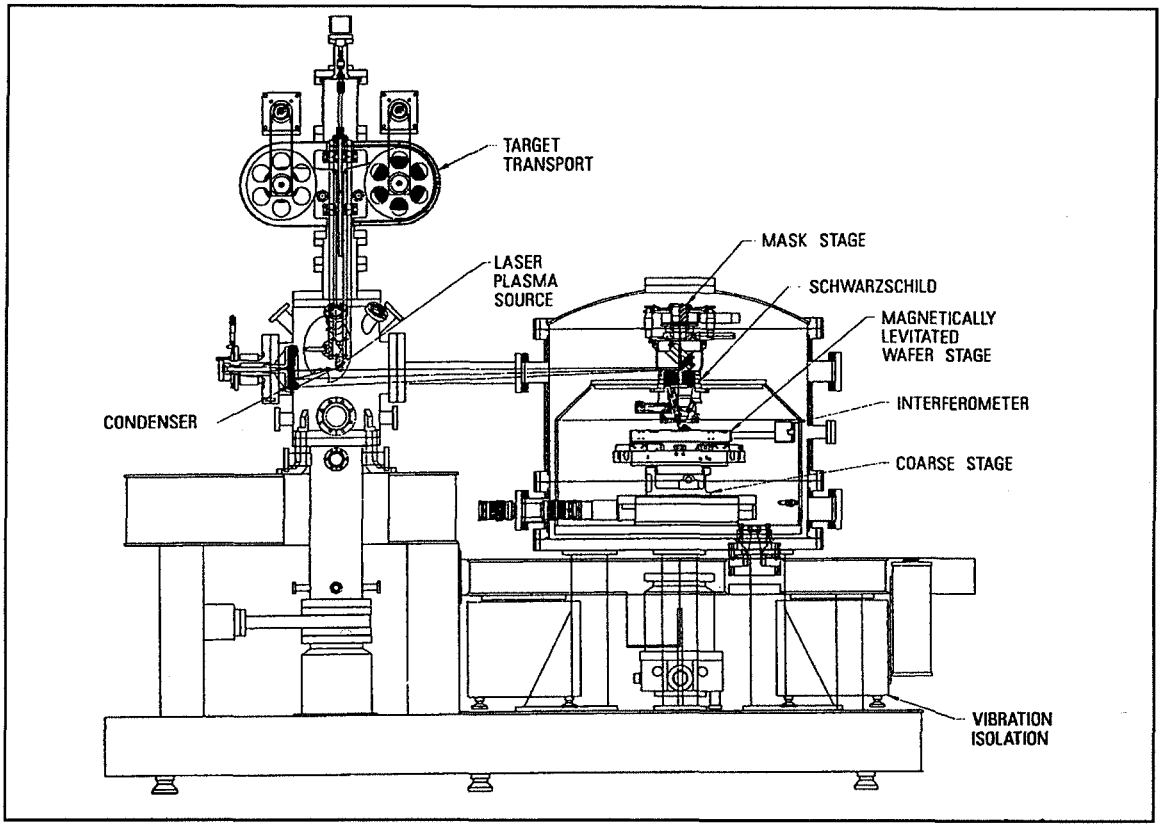

Figure 1. Drawing of EUV Lithography tool

The EUVL Wafer Positioning System

Operational Requirements

The wafer positioning system for the EUVL system represents the first use of maglev technology for fabrication of integrated circuits. The system must provide a highly stable and accurate platform for the successful imaging of 0.1 micron features. The following attributes are necessary for achieving this goal.

Overall positioning range: The EUVL system requires a limited positioning range. It will be used for creation of small footprint devices and does not need to cover the full range indicated by the size of silicon wafers. The coarse stage travel is limited to ± 37 mm in the Y axis and ± 50 mm in the X axis, X and Y being horizontal axes, in the plane of the wafer. The coarse stage is controlled to position the center of the fine stage to within 2 μm of the final position.

Fine stage range: The fine stage, as designed, is accurate over a ±150 μm range in both X and Yaxes.

Stability: The positioning system must be capable of holding a target wafer sufficiently still to allow creation of a 100nm feature with no appreciable smearing. For this implementation, X/Y positioning noise of up to 10nm p-p (at a high probability) of X/Y image motion was deemed acceptable.

Absolute position: Errors of less than 10nm @ 3 sigma for 1 cm travel.

Interface: The stage control system must be able to communicate with the EUVL executive computer system. It also must provide the interface to the grazing incidence focus system and indirect alignment system.

Operating environment: The stage assembly and position measuring laser interferometers must reside in a vacuum chamber. All mechanical and electrical components of these assemblies must be compatible with vacuum operation.

Focus: The system must provide a Z axis resolution comparable to that of the X and Y axes in order to accurately return a wafer to within ½ wavelength of a position previously established. This requirement necessitates a dual focus methodology that includes a "coarse" focus system for repositioning a wafer and an interferometry - controlled "fine" position system to maintain the position accuracy and stability required.

Positioning bandwidth: The initial requirements for positioning bandwidth (a measure of the positioner's repositioning speed used to indicate wafer throughput capability) are liberal due to the research nature of the tool. A 30 Hz bandwidth was considered acceptable.

System Configuration

The wafer positioning system for the EUVL research tool consists of the maglev stage, two long travel coarse position stages, an electronics rack and a high resolution interferometry

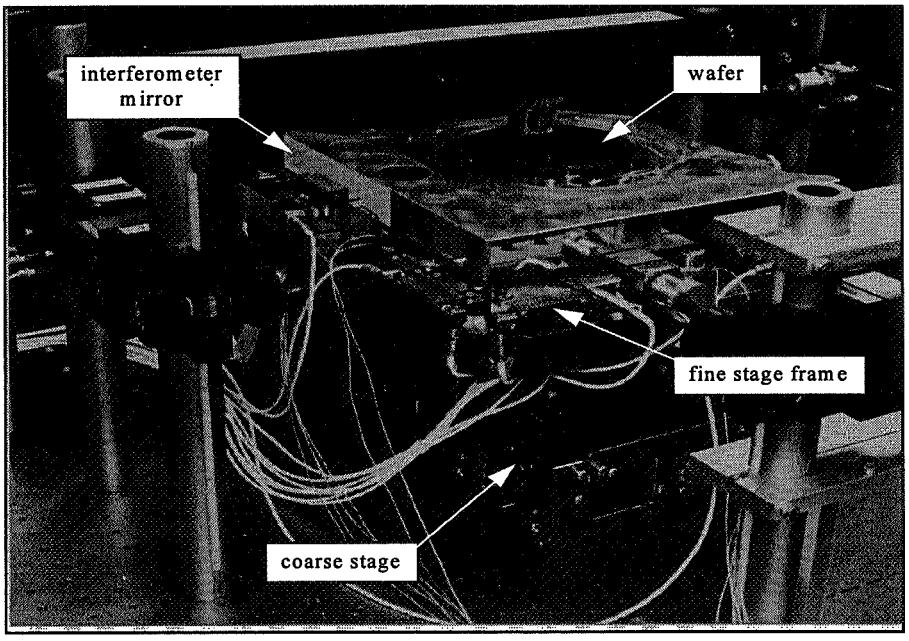

Figure 2: EUVL Stage Assembly

system. The photograph of Figure 2 shows the stage assembly on a test table prior to installation into the EUVL tool.

Maglev Fine Stage

The design of the maglev fine stage for the EUVL system is essentially unchanged from that originally developed by GCA and MIT. This design was described in a paper presented at the Second International Symposium on Magnetic Suspension Technology in August, 1993[2]. Figure 3 is a photo of the stage. Since 1993, extensive refinements have been applied to the electronics and software used to operate and control the system and to provide interfaces required by the EUVL system.

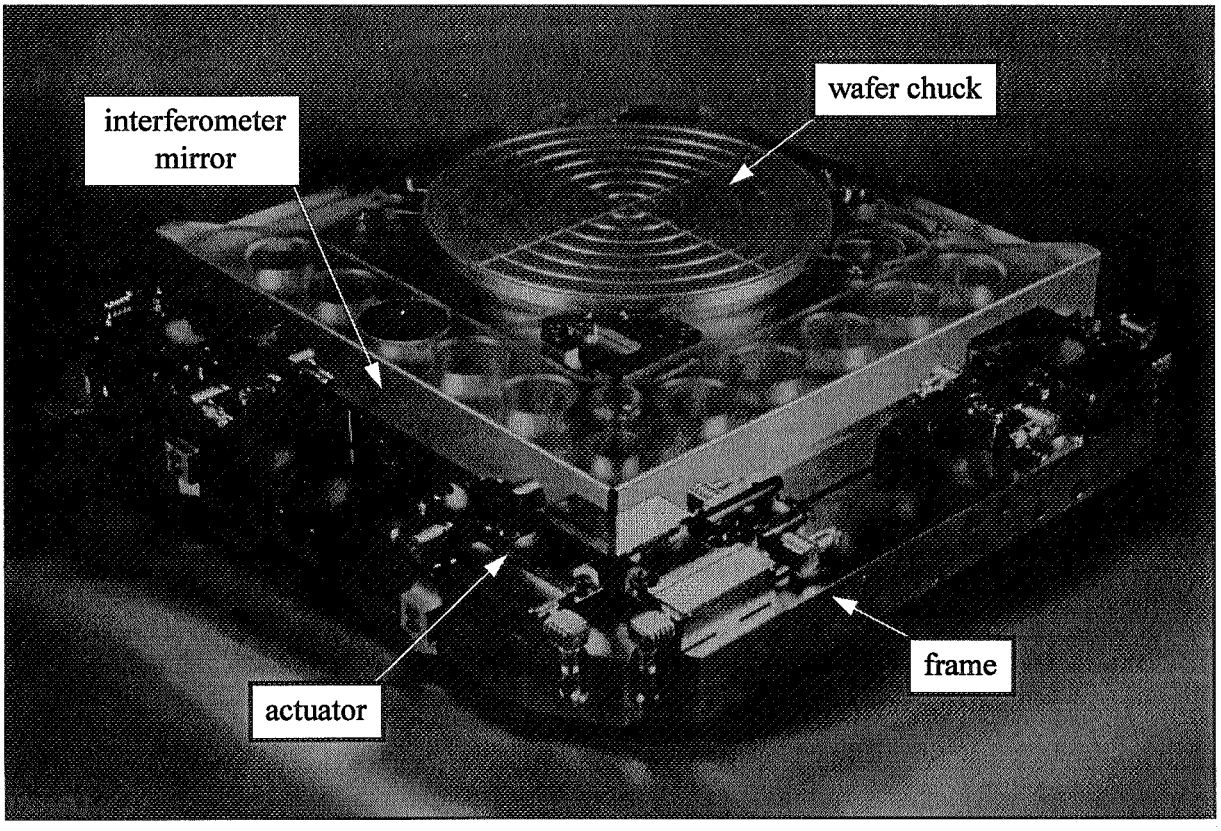

Figure 3: Maglev Fine Stage

Coarse Stages

Two Anorad lead screw stages mounted perpendicular to each other are used to provide positioning over the full range of motion. These stages are controlled independently of the fine stage. They include linear encoders for position detection and incorporate rotary encoders in the drive motors for motion stability. These stages have a stated resolution of 0.1μm.

Interferometry

A Hewlett Packard Laser interferometry system consisting of five interferometers, two laser sources, beam benders, optical receivers, and high resolution laser axis boards provide position information in all six degrees of freedom. The interferometry can resolve to 0.625nm in X and Y and 1.25 nm in Z. The Z axis requires that a wafer be in place to provide a reflecting surface for the light beam.

Capacitive "Gap" Sensing

The maglev fine stage utilizes six capacitive sensors for determination of the "gap" between the movable platen and stationary frame. This information is used to linearize the maglev actuator force characteristics for control purposes. The fine stage can be controlled and positioned using only these sensors for feedback, but with less accuracy than that obtainable with

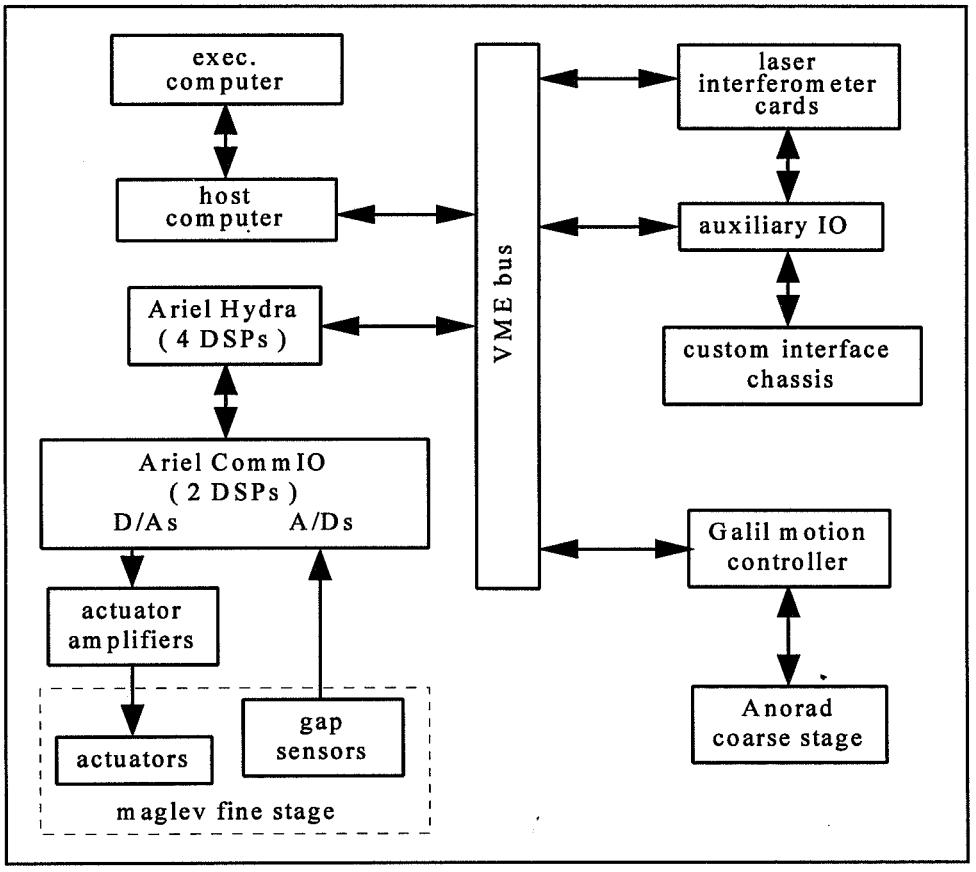

Figure 4: System Block Diagram

the interferometers. Capacitive sensors are used for Z axis measurement and control in the absence of a wafer.

Electronics

Two computers are used in the implementation of the EUVL wafer positioning system. An embedded VME-based 486 PC provides the user interface. The electronics include six TMS320C40 DSPs for data acquisition, manipulation, and control. Figure 4 is a diagram showing the major system elements.

Host computer: The host computer is an embedded PC subsystem that mounts in the VMEbus chassis. It provides a critical interface between the operator and the positioning system. Two methods are available for human interface. A user can access the system using a monitor and keyboard for complete control. This also provides the interface required for development and modification of the system operating characteristics. The second method of interface is via a TCP/IP network served by the executive computer of the EUVL system. This is the interface that is used during normal operation.

DSP computer: The digital signal processing computer consisting of four TMS320C40 DSPs located on a Hydra™ computer board (by Ariel Corp.) and two additional TMS320C40 DSPs on two Ariel CommIO™ interface boards provide the necessary processing power for the positioning system. This is the stage control computer for the system.. Analog-to-digital I/O is used to gather gap information from the capacitive sensors as well as other EUVL system data. Sixteen channels of digital-to-analog I/O control the current amplifiers which drive the electromagnetic actuators.

Custom interface: Custom electronics is provided for interfacing the components of the coarse and fine stage to the computer electronics. The chassis includes power supplies, enabling relay circuitry, I/O analog filtering, and interface matching circuitry.

Coarse stage control: The two coarse stages are controlled using a dedicated control computer (Galil DMC1320). This computer is programmed for optimum stage performance and receives commands from the host computer when it is necessary to travel beyond the range of the maglev fine stage.

Actuator amplifiers: Custom current amplifiers are used to supply drive current to the sixteen electromagnetic actuators. They are 1 amp limited, but capable of up to 100 volts output. This provides the inductive magnetic actuator with a fast force response thereby allowing high bandwidth positioning.

Control System Design

Figure 5 is a block diagram of the stage control system. A complete simulation of the system was constructed using the Matlab Simulink® environment. Included in the simulation are the dynamics of the levitated platen, the nonlinearities associated with the actuators, the voltage limitations associated with the transimpedance amplifiers, quantization errors, computational delays associated with the control computer, and changes in the interferometer measurement equations due to displacement of the platen. A simplified model of the coarse stage is also

included. Small motions are assumed, allowing the dynamics and the transformations between the positions and the measurements to be approximated as linear.

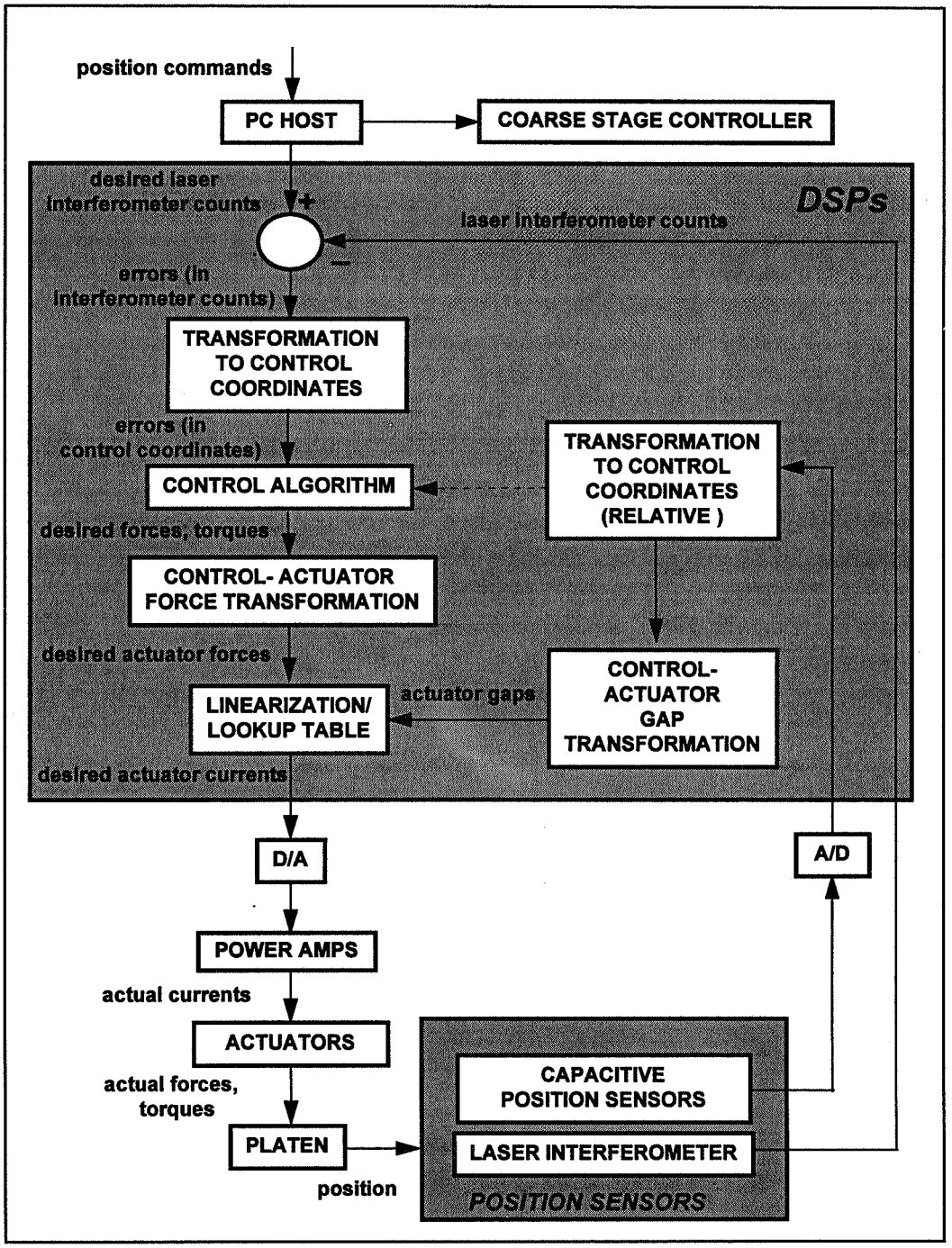

Figure 5 : Stage Control System Block Diagram

To allow the use of SISO linear controller design techniques, the system is considered to consist of six independent subsystems, each corresponding to one of the six

degrees of freedom (x, y, z, θ_x, θ_y, θ_z). In the control computer, the measurements are transformed to give the positions of, and rotations about, the center of mass. These are the quantities that the controller regulates. The outputs of the controller are six resultant forces and torques to be applied to the levitated platen. The control computer then calculates a set of forces that, when applied at the 16 actuators, will produce the desired forces and torques. Since the outputs of the control computer, in conjunction with the transimpedance amplifiers, produce the currents flowing in the actuators, the desired actuator forces must be transformed into representative actuator currents. For small forces, the following equation is a good fit.

$$i = \sqrt{f(a_0 + a_1 g + a_2 g^2)}$$

f is the desired force from a given actuator, g is the gap between the actuator and its associated target, the a_i are constants determined empirically, and i is the current. If the desired forces are large, the actuator will be driven nearer to saturation, and a lookup table is used to compute the needed current given the actuator gap and the desired force.

By using the ideas outlined above, the controller sees six linear, decoupled systems, and any controller design technique can be used. For each of the six axes, we are using a PID (Proportional-Integral-Derivative) controller with an additional high-frequency pole. Because of the compliance of the mechanical structure supporting the interferometers and their reference mirrors, the closed-loop bandwidth was limited to 30Hz to prevent unacceptable excitation of structural noise. The final controller implemented also has notch filters for eight different resonances excited by the control loop.

We verified the behavior of the combined plant and compensator by comparing the response of the system with the simulation. Agreement was excellent.

Software Design

Software Requirements

As might be expected with a research system, the stage control system software requirements are very broad. The throughput of the system must be sufficiently high in order to limit system phase delays. The user interface must be flexible enough to allow easy system development, user control, and system diagnostics. And finally, an interface to the EUVL executive computer is required to give a remote user limited system control and information feedback.

The stage control system software is made up of C and assembly language code written and compiled for use on 486 PC and TMS320C40 DSP processors. Additionally, a text based language is used for programming the Galil motion control board used for controlling the coarse stages. Vendor-supplied board-specific routines are used where possible. Each DSP of the Hydra board executes a distinct program allowing individual processor task tailoring. Controller

timing, controller synchronization, host communications, and system state are controlled by one of the four DSPs on Hydra in a master/slave relationship.

Host Computer Software

The Host PC software is responsible for several aspects of system operation. It handles system startup and initialization sequences, user interface functions, EUVL executive computer communications, coarse stage controller interface, and coordinates system data collection and analysis.

If a coarse move is required a simple command to the Galil motion controller is made by the Host PC. After the coarse stage move is complete, the maglev fine stage makes the required position error corrections.

All data collection and system diagnostics are coordinated by the Host PC. The user, through the user interface, can configure the DSPs on Hydra to capture "snapshots" of real time data of interest. The "snapshot" is triggered by a system command or user input allowing flexible performance monitoring and system diagnostics. The "snapshot" data can then be transferred to the Host PC and written to disk. The user interface screen contains important controller and system data which are updated automatically every second.

DSP Computer Software

The DSP software is primarily responsible for executing the fine stage controller tasks. These tasks include gathering position sensor data, executing controller algorithms, and outputting to actuators. Other responsibilities of the DSP software are to initialize hardware under its control at startup, handle error situations, and deliver data to the Host PC when commanded.

During system startup, the DSP software handles initialization of the fine stage controller subsystems. These subsystems include the CommIOs and their A/D and D/A modules, the laser interferometer cards, and the multifunction card which controls the custom interface chassis.

After the system has been initialized, the DSP software begins executing the control loop. The controller sequence is simplified by breaking it into seven sequential tasks:

1. Gather sensor data (capacitive pickoffs and laser interferometers).
2. Calculate stage relative position and actuator gaps.
3. Calculate stage absolute position and form modal errors.
4. Execute controller difference equations to determine required modal force outputs.
5. Resolve modal forces into actuator forces.
6. Linearize actuator output based on present actuator gap and required output force (either linearization algorithm or lookup table).
7. Output actuator voltage (apply forces).

The capacitive pickoff sensor data are collected by sampling six A/Ds on CommIO boards. The laser interferometer data are collected by triggering and then reading position registers in the laser axis boards via the VME bus.

As part of the process for determining the desired force at a given actuator, linearization is performed. When the desired actuator current data are available, they are written out the sixteen D/As on the CommIO which controls the actuators.

The controller tasks are distributed among the four DSPs on the Hydra card to maximize system throughput. Much of the previously described sequence occurs in parallel.

The control loop timing is generated by an internal timer of the master DSP. The timer generates an interrupt to the master DSP at a programmable rate. When the master DSP services the interrupt, it transmits commands over the communication ports to the other DSPs on Hydra signaling the beginning of a cycle thus synchronizing the four processors. All controller data are passed between processors via the C40 communication ports which give complete interconnectivity between the four processors.

The control loop has three states in which it can execute: the X-Y-Z capacitive pickoff feedback state, the X-Y laser, Z capacitive pickoff feedback state, and the X-Y-Z laser feedback state. The three possible system states determine which instruments are being used to measure the position of the stage. During the control cycle, several sensor status checks are made. Any sensor errors cause system state changes which prevent hardware damage.

Performance Testing Results

The original performance requirement for image stability was, as given earlier in this paper, 10nm peak-to-peak with high probability. Figure 6 shows a plot of the laser interferometer data for the *x*-axis. As can be seen, this has a peak-to-peak displacement of less than 10nm. The corresponding Y axis data had less than 9nm peak-to-peak displacement. From the figure, it can be seen that a large component of the displacement is low frequency (about 5Hz). The clean room is located on an isolated slab that has a mode near 5Hz, and the isolated table that holds this system has a mode at 5Hz. The commercial isolated table we are using has active vibration damping that should provide better suppression of this 5Hz mode when the equipment is working properly, which we anticipate in the near future. This could reduce the peak-to-peak displacements by several nm.

The data shown in Figure 6 are typical for times when there is no activity in the clean room. The standard deviation of the distance of the image from the desired location on the wafer surface is less than 2.5nm ($\sigma < 2.5$nm). During exposures, when there is generally more activity in the clean room and more equipment running, $3\text{nm} < \sigma < 4\text{nm}$. The EUVL project team was able to demonstrate 0.1 micron lithographic-quality features with operational positioning stability of $\sigma \approx 4$ nm.

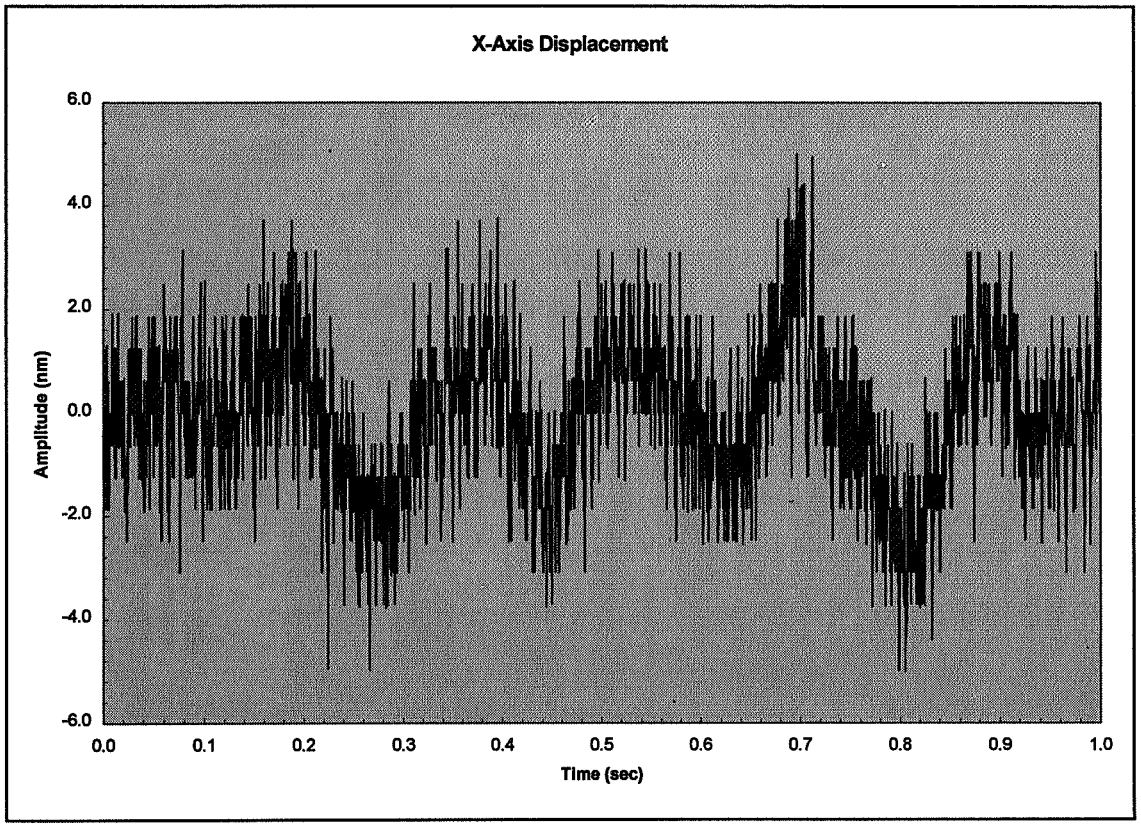

Figure 6: Laser interferometer data

We have not yet determined the overall system accuracy. The next set of experiments on the EUVL project will entail overlaying one exposure on top of another. The absolute positioning accuracy will be very important for these experiments.

Future Enhancements

System enhancements that are being implemented on a follow-on project include optimization of the electronics for faster data input and output, greater compression of the software by redistribution of tasks and additional use of assembly language, and coordination of target moves between the coarse and fine stages for enhanced response. Progress to date includes the implementation of optimized IIR filter routines written in assembly code which has greatly decreased controller computing time. The IIR filter routines can be used for filtering sensors, filtering controller outputs, and performing controller compensation tasks. Other software enhancements included targeting time consuming system tasks written in C and rewriting them in assembly utilizing the DSP hardware circular buffering, zero overhead looping, and single-cycle parallel instructions where possible. The final area of software improvements is improved task distribution among processors which creates more communication overhead and system complication but has greatly increased system throughput. At present, the follow-on system throughput is over three times faster than the EUVL system.

1. Tichenor, G. D. Kubiak, S. J. Haney, R. P. Nissen, K. W. Berger, R. W. Arling, A. K. Ray-Chaudhuri, K. B. Nguyen, R. H. Stulen, J. B. Wronosky, J. D. Jordan, T. G. Smith, J. R. Darnold, P. M. Kahle, A. A. Jojola, S. M. Kohler, R. S. Urenda, D. R. Wheeler, J. E. Bjorkholm, O. R. Wood, II, G. N. Taylor, and R. S. Hutton, "Recent results in the development of an integrated EUVL laboratory tool," **Proc. of the SPIE Symp. on Electron-Beam, X-Ray, and Ion-Beam Submicrometer Lithographies for Manufacturing V**, vol. 2437, 292 (1995).

2. R. W. Arling, S. M. Kohler: "Six Degree of Freedom Fine Motion Positioning Stage Based on Magnetic Levitation", Second Annual Symposium on Magnetic Suspension Technology, Seattle, WA., August 11-13, 1993.

Precision Magnetic Bearing Six Degree of Freedom Stage

M.E.Williams, D.L.Trumper

Dept. of Mechanical Engineering
Massachusetts Institute of Technology
Cambridge, Mass. 02139

SUMMARY

Magnetic bearings are capable of applying force and torque to a suspended object without rigidly constraining any degrees of freedom. Additionally, the resolution of magnetic bearings is limited only by sensors and control, and not by the finish of a bearing surface. For these reasons, magnetic bearings appear to be ideal for precision wafer positioning in lithography systems. To demonstrate this capability a linear magnetic bearing has been constructed which uses variable reluctance actuators to control the motion of a 14.5 kg suspended platen in five degrees of freedom. A Lorentz type linear motor of our own design and construction is used to provide motion and position control in the sixth degree of freedom. The stage performance results verify that the positioning requirements of photolithography can be met with a system of this type. This paper describes the design, control, and performance of the linear magnetic bearing.

INTRODUCTION

Lithography steppers currently produced use a combination of mechanical stages to achieve control of the wafer location in six degrees of freedom. In these stages, the wafer is carried on a fine stage which provides six degree of freedom control with approximately 100 μm travel. This fine stage is then mounted on a coarse mechanical stage which provides X-Y positioning with approximately 200 mm travel. The fine stage is typically comprised of multiple piezo-actuators and or voice coil drives which are used to position a platen mounted on flexures. These mechanical stages generally suffer from poor dynamics, a result of the compound flexures used. This method of X-Y positioning can become very complicated and could be approaching its maximum speed and resolution capabilities. In comparison magnetic bearings can provide speed and simultaneous control of six degrees of freedom with a single moving element. This eliminates the complicated flexures and mechanical actuators used in the current mechanical designs. Additionally, magnetic bearings have no mechanical contact. This makes them ideal for clean room use where particle generation from mechanical friction is a major source of contamination.

STAGE DESCRIPTION

A six degree of freedom magnetically suspended X-Y stage has been constructed which uses variable reluctance actuators to control the motion of a 14.5 kg platen in five degrees of freedom (three rotational and two translational) and a unique permanent magnet Lorentz type linear motor to control motion in the sixth degree of freedom. For fine focusing the stage can provide 400 μm of travel normal to the wafer surface and milliradian rotations around three axes. The linear motor has 200 mm of X travel and consists of a permanent magnet Halbach array attached to the underside of the platen and a planar, ironless, six phase stator fixed in the machine frame [2]. A conventional mechanical linear slide will be used to provide 200 mm of travel in the other major axes (Y). This design increases power efficiency and yields increased performance by capitalizing on the typical operation of a lithography X-Y stage. Typical operation of a stage is to step in the X direction 10 - 20 times along a row of die sites, before a single step is made in the Y direction to the next row of die sites. Since the stage operation is dominated by X positioning, this mechanical-magnetic bearing stage design results in a simple magnetic bearing structure while simultaneously increasing the stage precision and throughput. The stage is sized to accommodate an eight inch wafer and platen dimensions are 25 cm x 20 cm.

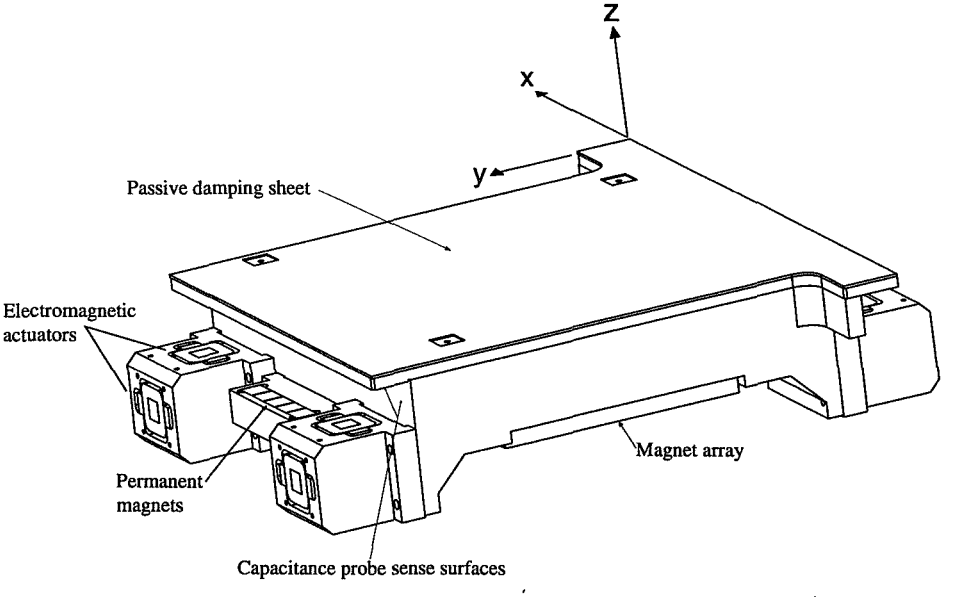

Figure 1: Assembled platen with actuators, lift magnets, and magnet array

The electromagnetic actuators that comprise the magnetic bearings consist of E type laminations and a single copper coil. The lamination material is a 49% nickel/51% iron alloy. This alloy was selected for its negligible hysteresis and moderately high saturation flux density. Negligible hysteresis is critical to ensure that the actuator force is single

valued on the control current. In addition to the core material, the lamination size can be optimized for power. The dimensions of the core lamination can optimize force by sizing the pole face area in relation to the core length and height. Thus, for an optimum square pole face area the maximum force can be obtained for a given power level [1]. A theoretical model for the actuator force-current-airgap relationship can be derived from classical magnetic circuit theory. However, this is accurate only at very small airgaps and low flux densities. As the gap and the coil current increase, the actuator core saturates and the theoretical model is no longer effective. To obtain an accurate model, the actuator can be characterized for its force-current-airgap relationship [3]. This characterization data can be linearized in real time and implemented in a digital control algorithm. The actuators are located on the moving platen to provide a constant force

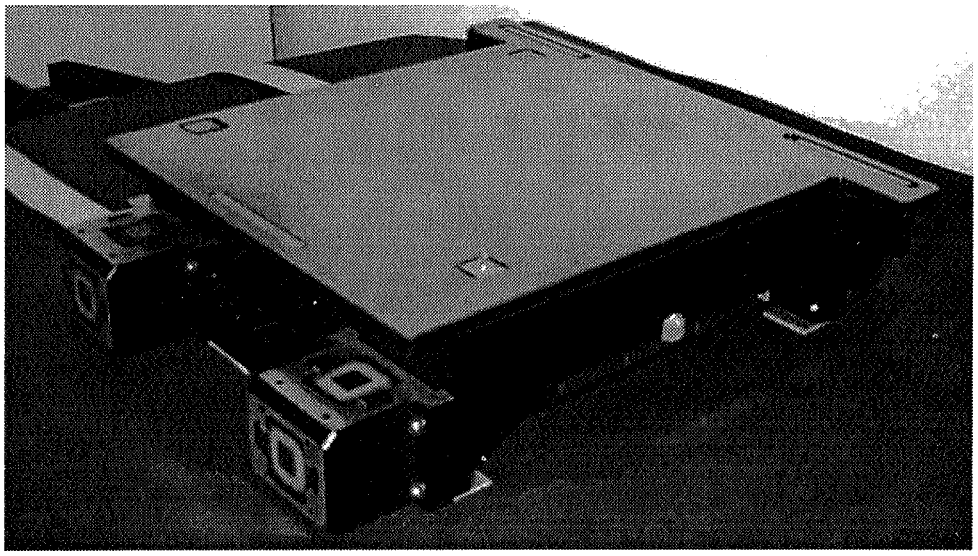

Figure 2: View of platen which shows the actuators and permanent magnet housing

relative to the platen center of gravity. Located at each corner of the platen is a housing which contains three E-core and coil assemblies. Within this housing the actuators are arranged at 90° intervals. This provides a total six pair of opposing push-pull actuators which provide five-degree of freedom control of the platen. The actuators have a nominal bearing air gap of 300 μm with displacements of $\pm$200 μm from the nominal in the Y and Z translational direction. Rotations of about one milliradian are possible around all three axes. These translational and rotational ranges are sufficient to provide the local alignment, focus, and leveling required in typical lithography equipment. The actuator control current is passed to the moving platen through a highly flexible flat conductor which rolls under the platen. The bend radius of the flexible conductor is consistent throughout the platen travel to help minimize any disturbance force.

Located between the actuator housing on each side of the platen are rare earth permanent magnet Halbach arrays. These lift magnets offset the mass of the platen and allow the vertical actuators to dissipate power only for platen position control. The

permanent lift magnets are operated at a relatively large airgap so the force is not a strong function of position. This results in a slow open loop time constant associated with the lift magnets allowing the actuators easier stabilization of the system. The actuators

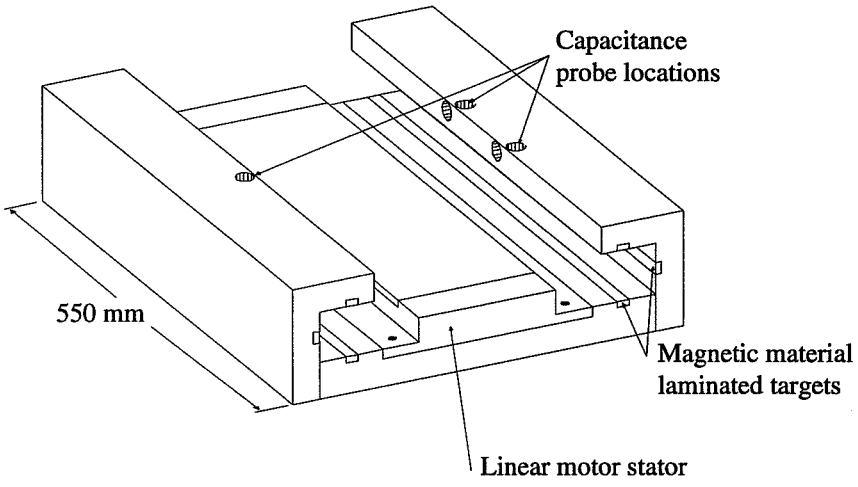

Figure 3: Stage base with linear motor stator

and the lift magnets act upon a laminated magnetic material target rail that runs the length of the machine base. The machine base is mounted on three points and is kinematically constrained using a system of brackets and Belleville washer stacks.

The stage parts were machined from 6061-T6 aluminum and are hard coat anodized. The fundamental resonant frequency of the suspended platen is located at 1030 Hz. While this mode is well above the control system crossover frequency, it is very lightly damped ($\zeta = 0.02$) and is easily excited even with a closed loop bandwidth of 100 Hz. This characteristic was anticipated from finite element modeling and a viscoelastic constrained layer damper was designed. This damper consists of a stainless steel plate machined to fit the top surface of the platen. The plate is 0.125" thick with a 0.05" thick layer of viscoelastic adhesive material which attaches it to the platen. This provides an order of magnitude better damping which effectively eliminated the resonant problem within the control bandwidth.

Since five platen degrees of freedom are controlled by the actuators, five independent position measurements are required. This is achieved by locating capacitance probes in the stationary frame which sense relative to a flat ground surface located on the platen. Laser interferometry is used to measure platen displacement along the X-axis. For lithography operations the stage would be positioned and locally focused using six axes of laser metrology.

To reduce the stage power dissipation the linear motor stator winding thickness is power optimized and a Halbach type magnet array is used which doubles the power efficiency of the motor. The key concept in the Halbach array is that the magnetization

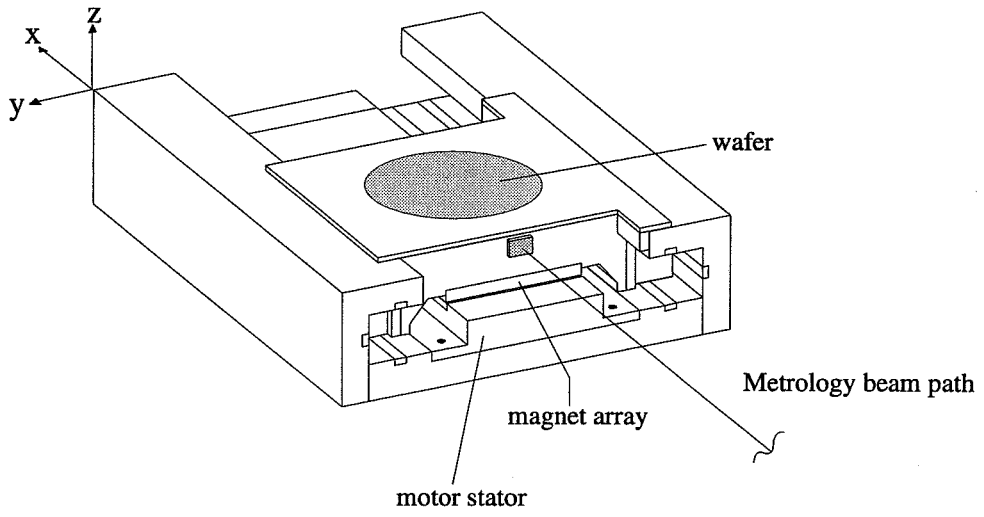

Figure 4: Suspended platen in base

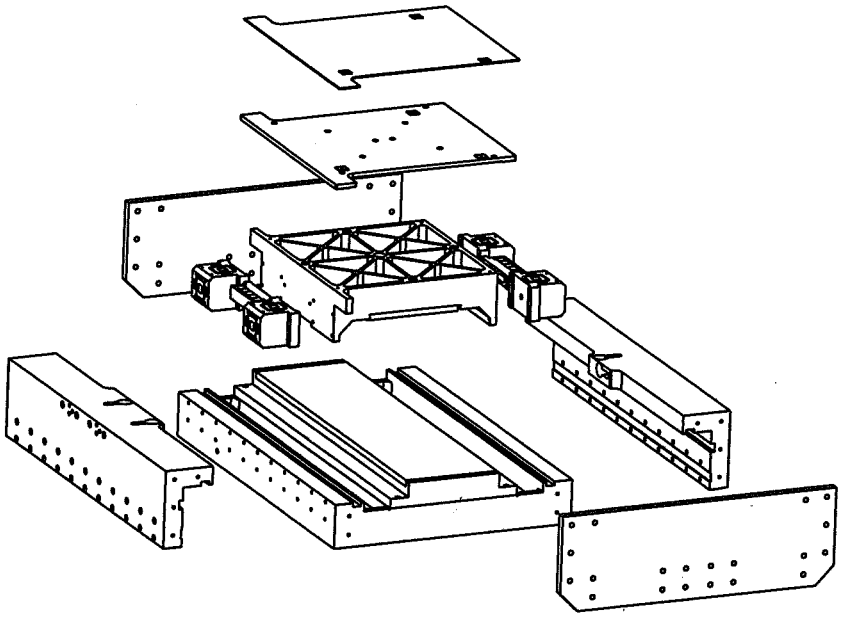

Figure 5: Complete stage assembly

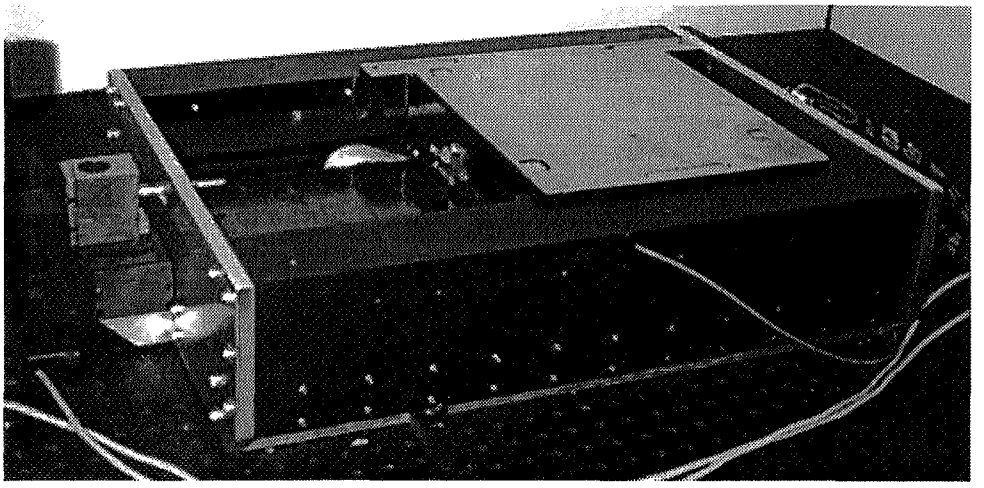

Figure 6: Overall view of assembled platen in the stage base

vector should rotate as a function of distance along the array. In fact if the vector rotates continuously, the field on one side of the array will be identically zero, while the field strength on the opposite side of the array is doubled relative to an array with a sinusoidally varying purely vertical magnetization [2]. While the ideal case calls for continuous rotation, in practice it is not possible to construct magnetic material with a continuously rotating magnetization vector. Therefore, each spatial wavelength of the magnet array is constructed of four uniform blocks of magnets, square in cross section each rotated by 90°. This geometry achieves 90% of the ideal continuously rotating field and is easily manufactured. The magnet sections are sized to provide one full rotation in one spatial period of the stator winding. The magnet array is 150 x 250 x 12.7 mm in size and is constructed of sixty individual rare earth magnet elements. The motor is designed to accelerate the 14.5 kg mass at 5 m/sec^2 while dissipating 6 watts of electrical power. In the photograph (Figure 7) the magnet array is visible. Also shown in Figure 7 are actuators and the flexible cable and cable connectors.

STAGE CONTROL

The linear motor and the linear magnetic bearing are digitally controlled using a TMS320C30 floating point digital signal processor implemented on a VME chassis. The structure of the bearing control scheme is to use decoupled equations of motion about the stage center of gravity. This is accomplished with modal transformations performed in real time on the digital control platform. The modal transformations are a function of stage position since the feedback sensor positions change relative to the stage center of

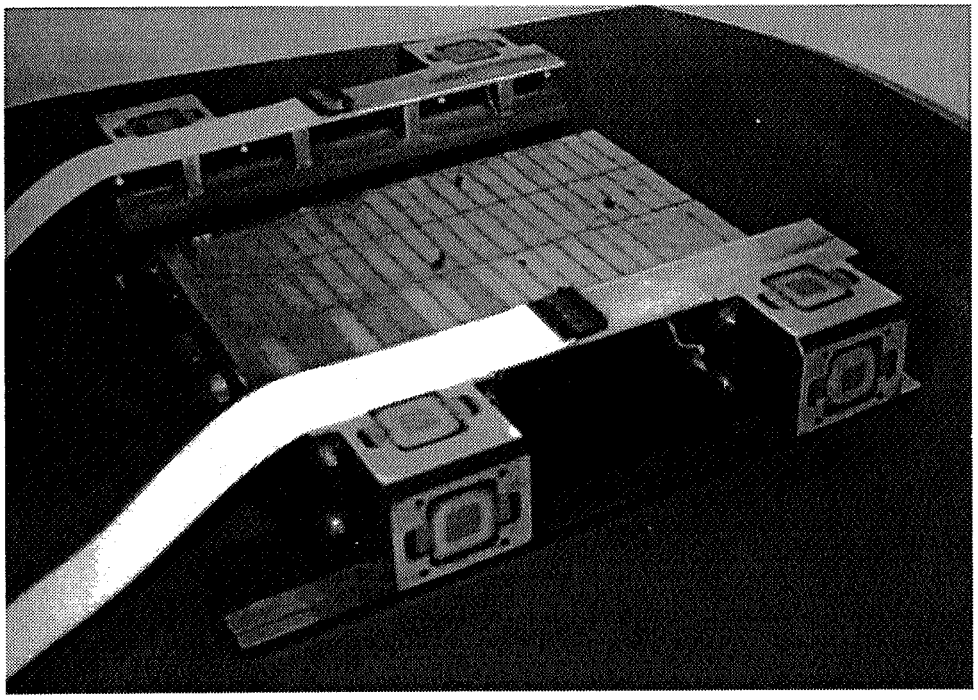

Figure 7: Underside of platen showing linear motor magnet array and actuators

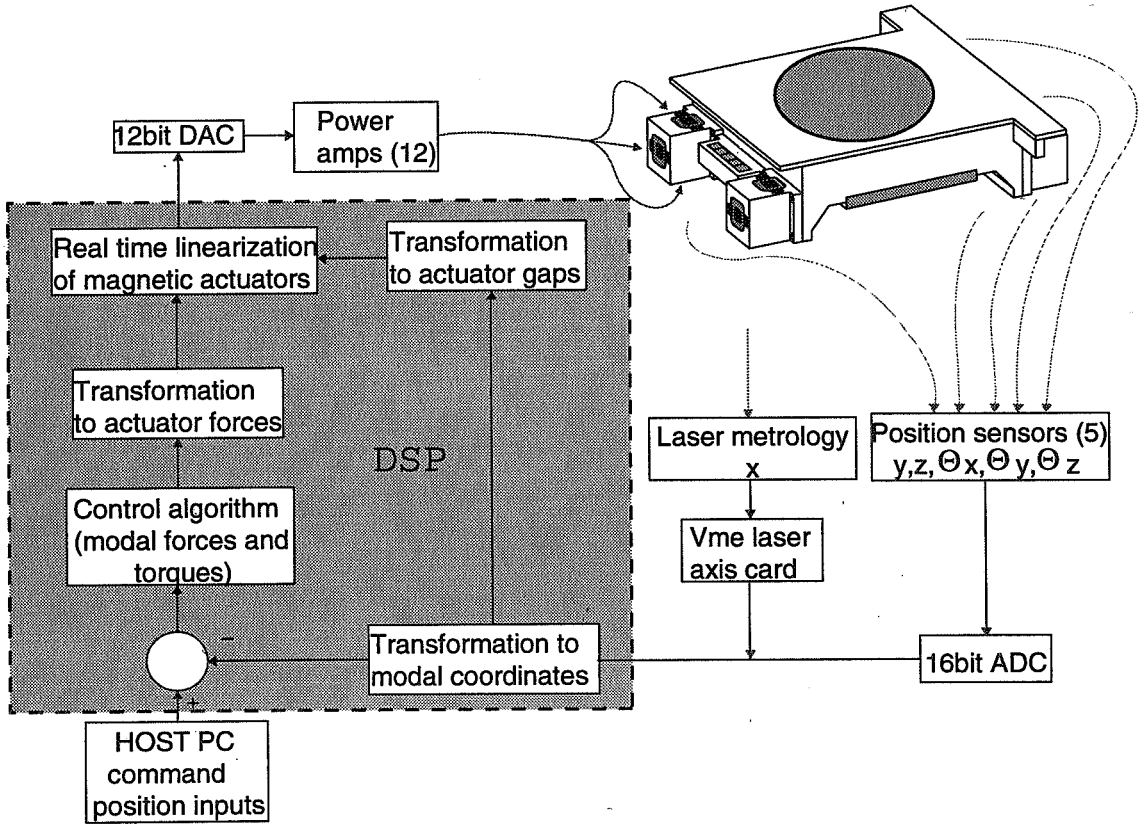

Figure 8: Bearing control flow diagram

gravity. The control algorithm used is a lead-lag compensator with two second order digital filters in each feedback path. The control bandwidth of the bearing axes is presently 100 Hz with a future goal of 200 Hz crossover frequency. The control bandwidth is currently limited to 100 Hz by the resonant modes of the pnuematic vibration isolation table that the stage is on. Figure 8 is a representation of the bearing control system algorithm. The linear motor is controlled as a single degree of freedom actuator which is

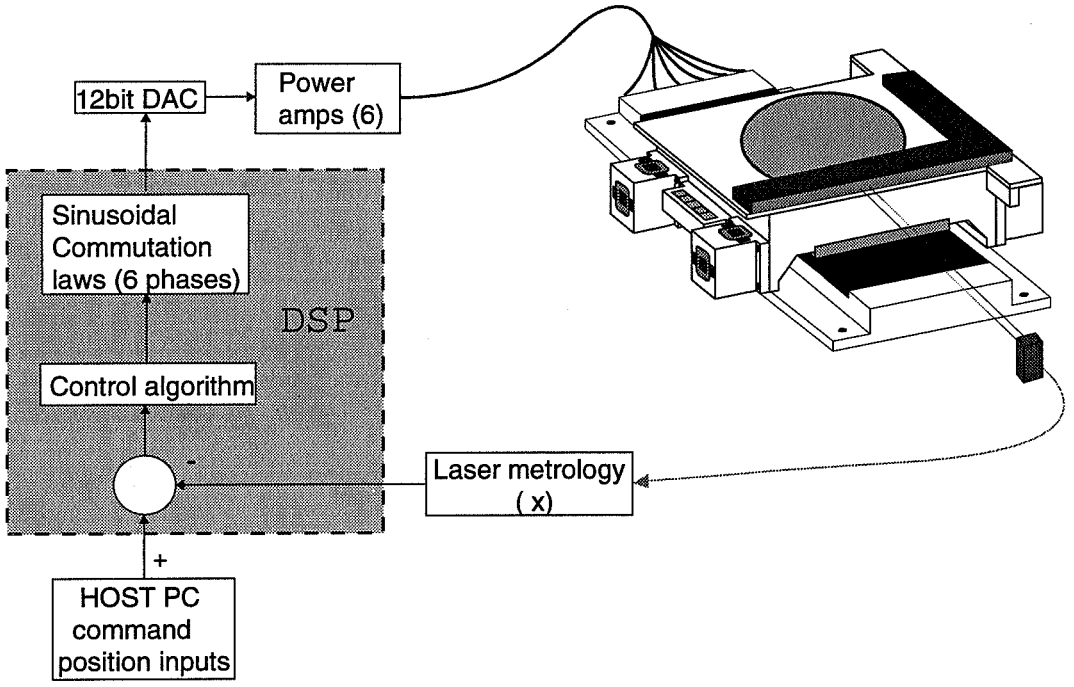

Figure 9: Linear motor control flow diagram

designed to be mostly decoupled from the bearing axes. This axis decoupling is accomplished through the platen design. The platen center of gravity was placed as closely coaxial with the linear motor force as was possible. The center of gravity is located at a position on the centerline of the stage about 1 cm above the plane of the motor force. This offset is accounted for in the modal transformations. The linear motor is a six-phase Lorentz type sinusoidally commutated motor. The motor controller is a lead-lag compensator with a bandwidth of 40 Hz. Figure 9 is a schematic representation of the linear motor control loop.

STAGE PERFORMANCE

Step response curves for both the bearing and linear motor are shown in the curves. A 100 nanometer step is shown in Figure 10. The peak-to-peak positioning noise is approximately 100 nm. The level of this noise can be attributed to the 16 bit analog to

digital converter that is used to sample the capacitance probe voltage levels. The ADC has 7-8 least counts of inherent noise This noise limits the position resolution of the bearing degrees of freedom and translates to approximately 70-80 nm (10 nm/count). The other four bearing degrees of freedom exhibit similar behavior.

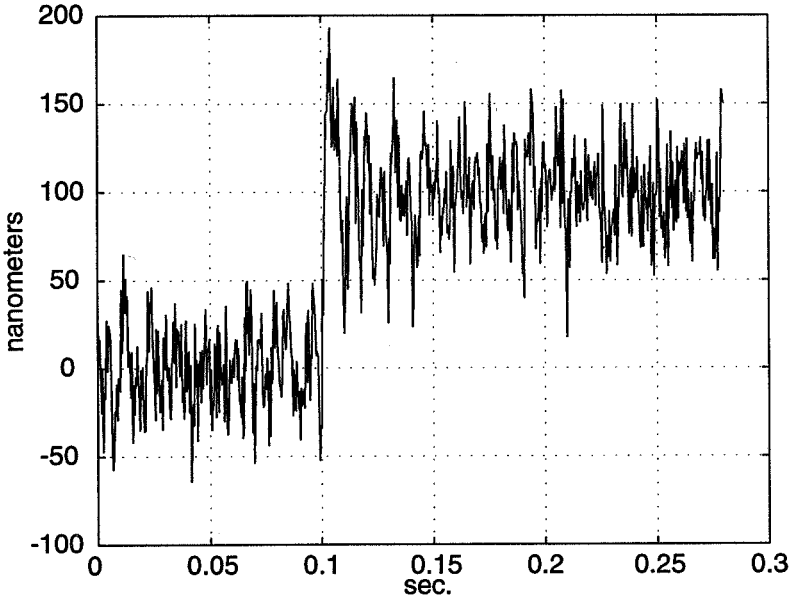

Figure 10: 100 nm bearing step in Z-direction

Figure 11 is a 20 nm step of the linear motor in the X direction. The peak-to-peak positioning noise in this axis is approximately 15 nm. This noise is dominated by noise from the bearing degrees of freedom being injected into the X-axis. There is also a 4 Hz component of noise that is directly attributable to rocking of the vibration isolation table. Figure 12 is a 2 cm step response that is a typical photolithography step size. The response shows that the stage will step and settle in 130 msec with no overshoot. However, the fine settling includes a 4 Hz component due to the optical table rocking mode.

CONCLUSIONS

We have presented the performance of a six degree of freedom stage which demonstrates that magnetic bearings have the capabilities for precision X-Y positioning at the level required for photolithography. We have demonstrated bearing resolution of

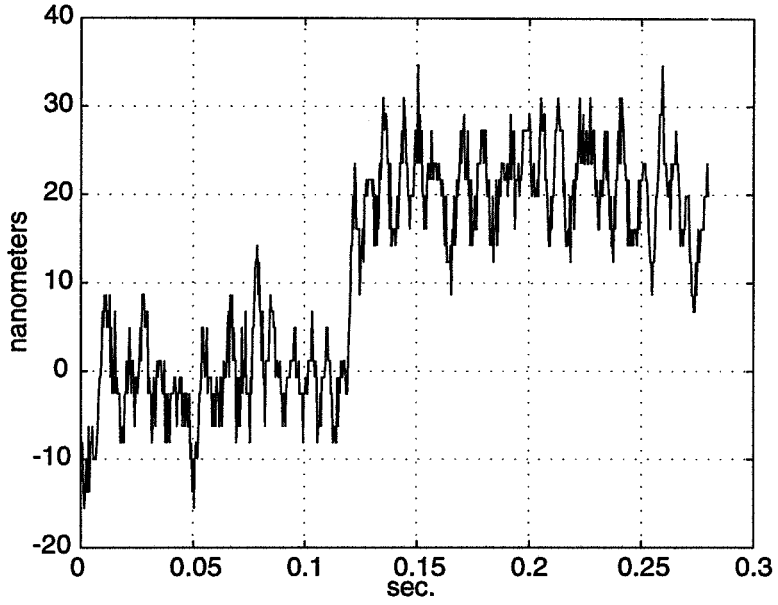

Figure 11: 20 nm linear motor step

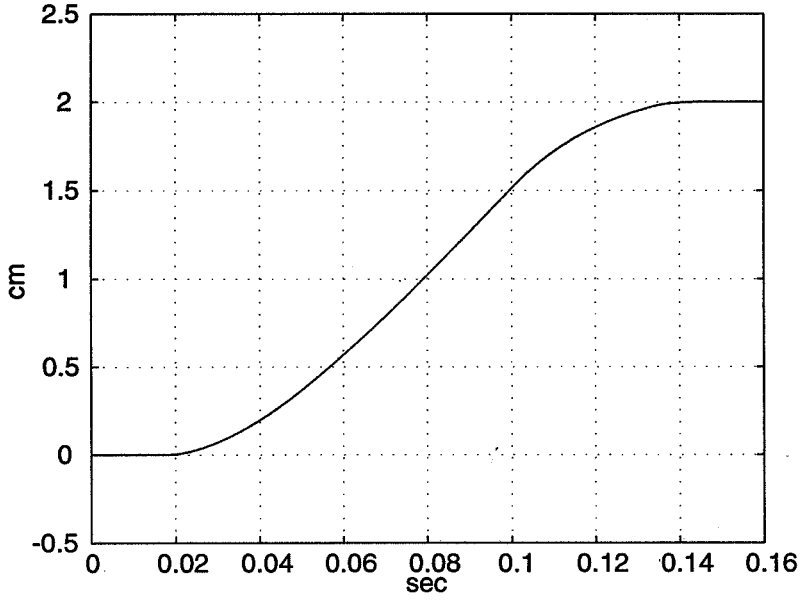

Figure 12: 2 cm linear motor step

100 nm peak-to-peak which is at the noise level of the ADC. The linear motor position resolution is at 15 nm peak-to-peak. The stage step and settle is at 130 msec., a dramatic improvement over the current state of the art in lithography steppers. Using laser metrology to feedback the stage position could significantly improve the baseline noise in all degrees of freedom. In the present configuration the stage performance is well within the position requirements of lithography with significant improvements made in manufacturability, speed, and durability.

Acknowledgments

This work is covered by Patent number 5,196,745. This research is being supported by Sandia National Laboratories, Albuquerque, NM and Integrated Solutions Inc, Tewksbury, MA

References

[1] Williams,M.E. and Trumper, D.L., "Materials For Efficient High Flux Magnetic Bearing Actuators," NASA 2nd International Symposium on Magnetic Suspension Technology, Seattle, Washington, Aug. 11-13,1993.

[2] Trumper, D.L., and Williams,M.E., "Magnet Arrays for Synchronous machines," IEEE Industrial Applications Society Annual Meeting., Toronto, Canada, Oct.,1993

[3] Poovey,T., and Holmes,M., "A Kinematically Coupled Magnetic Calibration Fixture." Precision Engineering, 16(2), Apr 1994.

Session 13 -- Applications 2

Chairman: Steven Van Sciver
NHMFL

DESIGN AND PERFORMANCE IMPROVEMENTS OF THE PROTOTYPE OPEN CORE FLYWHEEL ENERGY STORAGE SYSTEM*

D. Pang
Hua Fan College of Humanities and Technology
Shihtin, Taiwan

D. K. Anand
Professor of Mechanical Engineering
University of Maryland

J. A. Kirk
Professor of Mechanical Engineering
University of Maryland
College Park, MD 20742 USA

ABSTRACT

A prototype magnetically suspended composite flywheel energy storage (FES) system is operating at the University of Maryland. This system, designed for spacecraft applications, incorporates recent advances in the technologies of composite materials, magnetic suspension, and permanent magnet brushless motor/generator. The current system is shown in Figure 1 and is referred to as an Open Core Composite Flywheel [OCCF] energy storage system.

This paper will present design improvements for enhanced and robust performance. The control aspects of the OCCF magnetic bearings are discussed in a separate paper, "Parameter Design And Optimal Control Of an Open Core Composite Flywheel Energy Storage System."

Initially, when the OCCF prototype was spun above its first critical frequency of 4,500 RPM, the rotor movement would exceed the space available in the magnetic suspension gap and touchdown on the backup mechanical bearings would occur. On some occassions it was observed that, after touchdown, the rotor was unable to re-suspend as the speed decreased. Additionally, it was observed that the rotor would exhibit unstable oscillations when the control system was initially turned on. Our analysis suggested that the following problems existed:

1. The linear operating range of the magnetic bearings was limited due to electrical and magnetic saturation,

2. The inductance of the magnetic bearings was affecting the transient response of the system,

---

* This research was partially supported by a contract from NASA-Goddard Space Flight Center and FARE, Inc.

3. The flywheel was confined to a small movement because mechanical components could not be held to a tight tolerance,

4. The location of the touchdown bearing magnifies the motion at the pole faces of the magnetic bearings when the linear range is crucial.

In order to correct these problems an improved design of the flywheel energy storage system was undertaken. The magnetic bearings were re-designed to achieve a large linear operating range and to withstand load disturbances of at least 1 g. The external position transducers were replaced by a unique design which were resistant to magnetic field noise and allowed cancellation of the radial growth of the flywheel at high speeds. A central rod was utilized to ensure the concentricity of the magnetic bearings, the motor/generator, and the mechanical touchdown bearings. In addition, the mechanical touchdown bearings were placed at two ends of the magnetic bearing stack to restrict the motion at pole faces. A composite flywheel was made using a multi-ring interference assembled design for a high specific energy density. To achieve a higher speed and better efficiency, a permanent magnet DC brushless motor was specially designed and fabricated. A vacuum enclosure was constructed to eliminate windage losses for testing at high speeds.

With the new improvements the OCCF system was tested to 20,000 RPM with a total stored energy of 15.9 WH and an angular momentum of 54.8 N-m-s (40.4 lb-ft-s). Motor current limitation, caused by power loss in the magnetic bearings, were identified as causing the limit in upper operating speed.

INTRODUCTION

A magnetically suspended composite flywheel energy storage (FES) system was developed, for spacecraft applications, incorporating recent advancements in the technologies of composite materials, magnetic suspension, and permanent magnet brushless motor/generator. Kirk and Anand [1] suggested that a magnetically suspended composite flywheel energy storage system is a viable and superior alternative to batteries for spacecraft applications. The system can easily achieve the specific energy density (SED) of 20 WH/kg, which exceed a typical 14 WH/kg of the electrochemical system and has a long lifetime of 10 to 15 years. The proposed system was designed for a low earth orbit (LEO) satellite with a 90-minute cycle. The flywheel is accelerated during a 60-minute interval (charge cycle) when the satellite is exposed to sunlight. The flywheel is spun down during a 30-minute interval (discharge cycle) when the satellite is exposed to darkness. The system during this darkness must supply power at a constant voltage of 150±2% volts DC. With efficient power electronics, the system can accomplish an efficiency of 90% for each cycle. The FES system utilized an open core flywheel made of multi-ring graphite/epoxy composites which was interference assembled to maximize the specific energy density (SED). Two permanent magnet/electromagnet (PM/EM) magnet bearings were stacked in the center for magnetic suspension of the flywheel. The motor/generator mounted between two magnetic bearings was used to provide power transfer into and out of the system.

The overall design of the FES system was based on a pancake-shaped PM/EM magnetic bearing and a spokeless composite flywheel proposed by Kirk and Studer [2]. They described general design requirements for a magnetically suspended composite flywheel energy storage system. Anand, Kirk, and Iwaskiw [3] developed a detailed design of a 500 WH magnetically suspended composite flywheel energy

storage system for a low earth orbit (LEO) satellite. A prototype of this design was constructed at the University of Maryland's Magnetic Bearing Laboratory and is shown in Fig. 1.

When this prototype was spun slightly above its first critical frequency of 4,500 RPM, the magnetic suspension would fail and touchdown would occur. It was sometimes observed that the system failed to self-suspend or exhibited unstable oscillations when the control system was initially turned on. Analysis suggested that the following problems existed:

1. the linear operating range of the magnetic bearings is limited due to electrical and magnetic saturation,
2. the inductance of the magnetic bearings affects the transient response of the system,
3. the flywheel is confined to a small movement because mechanical components could not be held to a tight tolerance,
4. the location of the touchdown bearing magnifies the motion at the pole faces of the magnetic bearings when the linear range is crucial.

In order to correct these problems an improved design of the flywheel energy storage system was attempted [4,5,6]. The magnetic bearings were re-designed to achieve a large linear operating range and to withstand load disturbances of at least 1 g. The external position transducers were replaced by the inner ones to cancel the radial growth of the flywheel at high speeds. A central rod was utilized to ensure the concentricity of the magnetic bearings, the motor/generator, and the mechanical touchdown bearings. In addition, the mechanical touchdown bearings were placed at two ends of the magnetic bearing stack to restrict the motion at pole faces. A composite flywheel was made using a multi-ring interference assembled design for a high specific energy density. To achieve a higher speed and better efficiency, a permanent magnet DC brushless motor was specially designed and fabricated. A vacuum enclosure was constructed to eliminate windage losses for testing at high speeds. A final prototype was built along with a display panel, which includes all control electronics and a data acquisition system. This has been reported in earlier literature [7,8].

The FES system was tested to 20,000 RPM with a total stored energy of 15.9 WH and an angular momentum of 54.8 N-m-s (40.4 lb-ft-s). Additional specifications are shown in Table 1. Motor current limitation, caused by power loss in the FES system, prevented testing to a higher speed. The spin-down test and magnetization tests have indicated that the major power losses are due to eddy currents in the magnetic bearing return rings. The test results and theoretical analysis are discussed in [9]. This work shows that the performance was not robust and several critical improvements are necessary.

The objective of this continued research is principally to analyze the magnetic bearing system for nonlinear effects in order to increase the region of stability, as determined by high speed and large air gap control. This is achieved by four tasks: (1) physical modeling, design, prototyping, and testing of an improved magnetically suspended flywheel energy storage system, (2) identification of problems that limits performance and their corresponding solutions, (3) development of a design methodology for magnetic bearings, and (4) design of an optimal controller for future high speed applications.

This paper is concerned with an improved design methodology leading to system improvements for enhanced and robust performance. The control aspects are discussed in a separate paper.

IMPROVED DESIGN

Central to the design methodology is an appropriate model. The mathematical model of the PM/EM magnetic bearing can be represented by both a reluctance model and a stiffness model. In the reluctance model, magnetic circuit theory and bearing geometric dimensions are used to analyze the magnetic flux in the bearing. In the stiffness model, stiffness and force equilibrium equations are utilized to describe the bearing characteristics. By combining the two models, the performance of the bearing can be predicted given the geometric dimensions, the power electronics, the permanent magnets, and the electromagnetic coils.

The linear range is determined not only by the maximum control current to the EM coils but by the current/displacement ratio C of the control system as well. The active stiffness and the maximum restoring force are also dependent on the current/displacement as illustrated in Fig. 2.

The EM coil design is based on the stability and the force slew rate considerations, which determine the number of turns for the coils, and the power amplifier voltage and current. The stability consideration is derived from a nonlinear control system analysis, which is used to remove the limit cycle oscillation and to improve the robustness of the bearing. The force slew rate consideration is derived from the dynamic requirements of the magnetic bearing under either the external force or mass unbalance condition. From both experimental results and theoretical analysis, the power amplifier voltage and the number of turns of the EM coils have greater roles in stabilizing the bearing and responding to any disturbance.

It was found that when the power of the magnetic bearing was turned on, the flywheel not only failed to self-suspend but often broke into self-sustaining oscillations unless the mechanical touchdown gap was well adjusted. Also, the magnetic bearing flywheel system broke into a limit cycle oscillation due to a large disturbance. It has been shown that the oscillation is due to the combined effects of the power amplifier saturation, the passive radial stiffness, the touchdown gap, and the inductance of the EM coil. The mathematical representation of the model has been developed in detail in [9] and is used in the design procedure discussed further.

The flowchart for the new design methodology of the PM/EM bearing is shown in Fig. 3. The design procedures start with performance requirements for the magnetic bearing including the mass of the flywheel, axial force, radial force, and linear operating range. There are some initial inputs such as the saturation flux density of the magnetic material, the recoil permeability of the PM material, the operating flux density of the permanent magnet, the useful flux ratio, and power amplifier voltage. These values can be updated or changed with the choice of the specific materials and designs. The bearing design is an iterative process so the number of steps just shows a possible sequence.

The flux densities in any section of the magnetic bearing are limited by the saturation value of the magnetic material so the combined flux densities from the PM and EM are less than the saturation value. If there are equal flux densities from the PM and EM, the bearing can generate a maximum force. For a linear attractive force, the flux density from the PM is greater than that from the EM.

There are a few constraints on the geometric dimensions of the bearings due to physical limitations and engineering considerations. For example, the size of the permanent magnets is limited to a quadrant of the magnetic plate. Since our PM/EM bearing is a small gap suspension design, the linear

range is expected to be less than 15% of the air gap. To avoid large leakage flux between the pole faces of the return ring and two magnet plates, the pole face thickness is at least 3 times that of the air gap.

The magnetic bearing can be designed to satisfy the force requirements by using the flux densities and the geometric dimensions. Because of our radial active bearing design, the load capability in the axial direction is weaker than the radial direction. If the bearing is used to handle the same force in both directions, the axial force requirement becomes dominant.

To avoid the possibility that a larger axial drop may worsen the magnetic properties of the bearing, the ratio of the axial drop and the pole face thickness is limited to 20%.

After satisfying the performance requirement and physical constraints, a feasible design is chosen which includes the flux densities from the PM and EM, the mean radius, the air gap, the pole face thickness, and other dimensions.

Using the information from the previous step, the parameters of the permanent magnet design such as the magnet strength, thickness, and cross section area can be determined. Based on the stability and force slew rate considerations, the number of turns for the EM coils as well as the voltage and current for the power amplifier can finally be determined.

An optimization model was developed and in order to keep the design problem manageable, the scope of the optimization is concentrated on the most important design variables of the bearing.

The design goals for the magnetic bearings in the flywheel energy storage system are that the bearing has a 2 g axial load capacity, can withstand 2 g radial force, the axial drop is less than 10% of the pole face thickness and that the stable range of the bearing is maximized. The magnetic bearings are expected to handle a 2 g load from the flywheel at both the axial and radial directions. The axial drop ratio requirement is based on past work showing that the large axial drop will reduce the useful magnetic flux and affect all the magnetic properties of the bearing. The last requirement seems to be hard to observe because the bearing should be designed for a large linear range, a higher active stiffness and a greater radial force. Notice that the linear range, active stiffness, and radial force are dependent on the control system design and impose conflicting requirements. For example, a control system with a large linear range will have a lower active stiffness. In order to fundamentally improve the properties of the bearing, the stable range, which is independent of the control system, should be as large as possible. The objective of the optimization design is to maximize the stable range of the bearing, and select 12 design variables.

The equations for the objective function and the design constraints are developed in [9]. In these equations there are parameters in the model that most be specified by the designer. These parameters include the weight of the flywheel, the axial force, the radial force, the maximum mean radius of the bearing, the axial drop ratio, the useful flux ratio, the operating flux density of the permanent magnet, the saturation value of the magnetic material, the maximum current output, the maximum numbers of turns for the EM coil and the minimum air gap. The model can be further simplified by eliminating 6 equality constraints so that the 12 design variables become 6 independent variables.

Three optimization methods, the Monotonicity analysis, the Generalized Reduced Gradient (GRG) method and the Augmented Lagrange Multiplier (ALM) method, have been developed to find the optimal magnetic bearing design. The monotonicity analysis can check if the optimization model is well

bounded. If all design variables are bounded, the model is well defined. This analysis can improve the modeling of the problem and satisfy the necessary condition of existence of a solution before trying to compute the solution. The GRG and ALM methods are used to solve the nonlinear constraint problems numerically. A commercial software package GRG2, developed by Lasdon [10], is used in the optimization process. The ALM method is a kind of penalty algorithm to solve a constrained optimization problem as an unconstrained problem. A computer program is developed using the ALM method, the Fletcher-Reeves conjugate direction method, and the golden section method to find the optimal point of the pseudo-objective function.

The results from these three methods [9] are remarkably close. They show the constraints of the axial force, the axial drop, the control current, the number of turns for the EM coil, the space for the permanent magnet, and the bearing diameter are active constraints. It comes as no surprise that the axial performance requirements are dominant for the radial active bearing, because the axial direction has passive control and its performance is limited. The control current output is restricted by the existing power amplifier but the objective function can be improved by relaxing this constraint. The number of turns for the EM coil is restricted by the stability and force slew rate considerations. The geometric limitations for mean radius of bearing and the permanent magnet are inherited from the design of the flywheel system so the restrictions are hard to ease physically.

SYSTEM IMPROVEMENTS

During the development of a magnetically suspended FES system, many system performance limitations were identified and corrected. The problems limiting system performance include magnetic bearing perturbation force, third harmonic noise, power amplifier voltage saturation, structure vibration, mass imbalance, electronic unreliability, impedance mismatch between motor controller and motor/generator, and time delay of motor commutation sensors. Although all these are discussed in detail in [9], two of the areas of investigation are discussed here.

Since the old magnetic bearing from the earlier prototype did not meet the radial load requirement in the linear operating range, a new magnetic bearing was designed following the design methodology proposed here. In order to improve the bearing performance in the radial direction, the design must maximize the bearing stable range for a fixed control current. Due to the constraints (magnetic bearing diameter, the number of turns for EM coils, maximum control current, and permanent magnet material), the pole face thickness and the permanent magnet diameter were identified as the two most important design parameters. In order to improve the bearing performance, the new pancake bearing was built using the pole face thickness of 3.05 mm (0.12 in) and permanent magnet diameter of 31.75 mm (1.25 in), compared to 1.65 mm (0.065 in) and 34.29 mm (1.35 in) for the old bearing. The experimental testing results for the old magnetic bearing and new pancake bearing are discussed in detail in [9] but it is suffice to say that considerable improvements in bearing performance is noted. Specifically

1. The new pancake bearing can stand at least 1 g load of 36 N (8 lb) in axial and radial directions.

2. When both bearings have almost the same linear range due to the same gain in the control system, the new pancake bearing exhibits a higher active stiffness and a greater radial force.

3. Both bearings show a similar active stiffness when the new pancake bearing has a gain at 125 KΩ and the old bearing at 250 KΩ. The linear range of the new pancake bearing is almost doubled.

4. Both bearings have a similar axial drop around 20% of the pole face thickness at 1 g load.

The new pancake bearing was tested using a single magnetic bearing setup and was spun up to 3400 RPM with a runoff error of less than 0.02 mm (0.0008 in). The new pancake showed impressive performance in the radial direction and is satisfactory in the axial direction. It was therefore chosen for the final prototype of the magnetically suspended flywheel energy storage system.

The rotor orbit in the FES system can be observed using an X-Y plot of two perpendicular displacement sensor outputs. Because of eccentricities and disturbances, a circular shaped orbit was expected similar to the one shown in Fig. 4 using a single pancake bearing setup. When the flywheel supported by two stack bearings was spun, rectangular and diamond shaped orbits from the top and bottom stack bearings were observed as shown in Fig. 5.

These orbits are caused by a third harmonic superimposed on a first harmonic. The third harmonic noise was observed at all speed ranges. Sometimes, the third harmonic component becomes very large and the orbit had sustained loops. The third harmonic noise is undesirable because it demands unnecessary voltage and current outputs from the control system.

For a bearing stiffness of 350 N/mm (2000 lb/in), the third harmonic noise is very small but it distorts the flywheel motion. Also, the third harmonic noise demands unnecessary control voltage and current, and causes extra difficulties for mass balancing of the flywheel. Because the first harmonic from the magnetic bearing force is superimposed by mass imbalance, sensor error, and geometric error, there are different shaped orbits for the top and bottom stack bearings throughout the speed range.

Mathematical modeling and experimental analysis confirmed that the magnetic bearing return ring operating in the nonlinear region caused the third harmonic noise. The pancake return ring has the best performance because it does not cause any third harmonic noise at either the pancake bearing or the top stack bearing. The return ring causes a large third harmonic noise at either bearing. The different characteristics of the return rings were possibly due to the batch variation of the magnetic materials since all the rings follow the same machining and heat treatment processes.

In order to find out the best return rings for the magnetic bearing stack, the return rings were assembled into a one-ring composite flywheel for spinning test and frequency analysis. The one-ring composite flywheel did not have the permanent magnet ring so the motor/generator did not affect the testing. Because there are less third harmonic noises generated using the pancake return rings this arrangement was chosen for the final prototype of the FES system. Results of a variety of improvements in the final prototype are given in Table 2.

For flywheel energy storage applications, the power loss of the magnetic bearing system is very important. Unexpected large power losses during spin down tests prompted further theoretical analysis and experimental studies.

Considering the experimental tests and theoretical analysis [9] we conclude:

1. The major power loss is caused by the skin effect of the eddy currents in the magnetic bearing return rings.

2. Non-laminated return rings have similar DC magnetic properties as the manufacturer's laminated specimens but differ greatly from AC magnetic properties. Because of the skin effect, the return rings have a large magnetic field, a low peak permeability, and a huge core loss at the same flux density level and cycling frequency.

3. If the flux density distribution is uniform throughout the cores, the hysteresis and eddy current losses are proportional to the frequency and the square of the frequency of the magnetic field. The hysteresis and eddy current components of the core loss can be separated by testing at different frequencies and the knowledge of their relative magnitude can be used to reduce the power loss.

CONCLUSIONS

The problems limiting performance of the magnetically suspended flywheel energy storage system were identified. With the improvements done on the magnetic bearing, motor/generator, composite flywheel, system electronics, and system mechanical structure, the FES system achieved a maximum speed of 20,000 RPM with a total stored energy of 15.9 WH and a DN number greater than 2.1 million which exceeds the capability of most mechanical bearings.

In order to improve bearing performance, a new magnetic bearing with larger load capability has been designed and manufactured. The improved magnetic bearing can handle at least 1 g load in both axial and radial directions, and has a linear operating range over the mechanical touchdown gap. Because the third harmonic noise affects the stability of the FES system, theoretical analysis and experimental testing were conducted. The results showed that the third harmonic noise is caused by the magnetic bearing return ring operating in the nonlinear region. In order to eliminate the noise, all the return rings were tested and the best return rings were selected in the final prototype of the FES system.

The research has been primarily concerned with nonlinear effects of a magnetically suspended flywheel energy storage system in order to increase the region of stability at high speed and large air gap.

The FES system was unable to reach a higher speed because power losses in the magnetic bearing exceeded the power capability of the motor controller. Experimental and theoretical studies have shown the major power loss is due to the skin effect of the eddy currents in the non-laminated return rings.

REFERENCES

1. Kirk, J.A.; Anand, D.K.: The Magnetically Suspended Flywheel as an Energy Storage Device. NASA Pub. 2484. *Space Electrochemical Research and Technology (SERT),* pp. 137-146, 1987.

2. Kirk, J.A.; Studer, P.A.: Flywheel Energy Storage Part II - Magnetically Suspended Superflywheel. *International Journal of Mechanical Science,* vol. 19, No. 4, pp. 233-245, 1977.

3. Anand, D.K.; Kirk, J.A.; Iwaskiw, P.: Magnetically Suspended Stacks for Inertial Energy Storage Flywheel. *Proceedings of 22nd Intersociety Energy Conversion Engineering Conference,* Philadelphia, PA, August 10-14, 1987.

4. Anand, D.K.; Anjanappa, M.; Kirk, J.A.; Jeyaseelan, M.: CAD for Active Magnetic Bearings. *Mechanical Engineering,* vol. 112, No. 12, December, 1990.

5. Anand, D.K.; Kirk, J.A.; Zmood, R.B.; Pang, D.; Lashley, C.: Final Prototype of Magnetically Suspended Flywheel Energy Storage System. *Proceedings of 26th Intersociety Energy Conversion Engineering Conference,* Boston, MA, August 4-11, 1991.

6. TPI, Inc. Magnetically Suspended Flywheels for Inertial Energy Storage. Final Report, NASA Contract No. NAS5-30091, Goddard Space Flight Center, Greenbelt, MD, January 31, 1991.

7. FARE, Inc. A Composite Material Flywheel for Energy Storage. Final Report, NASA Contract No. NAS5-31704, Goddard Space Flight Center, Greenbelt, MD, July 23, 1993.

8. Johnson, R.G.; Pang, D.; Kirk, J.A.; Anand, D.K.: Computer-Aided Modeling and Analysis of a Magnetic Bearing System. *Proceedings of 27th Intersociety Energy Conversion Engineering Conference,* San Diego, CA, August 3-7, 1993.

9. Pang, D.: Magnetic Bearing System Design for Enhanced Stability. Ph.D. Dissertation, University of Maryland, College Park, MD, 1994.

10. Lasdon, L.S.; Waren, A.D.; Margery, W.R.: GRG2 User's Guide. 1983.

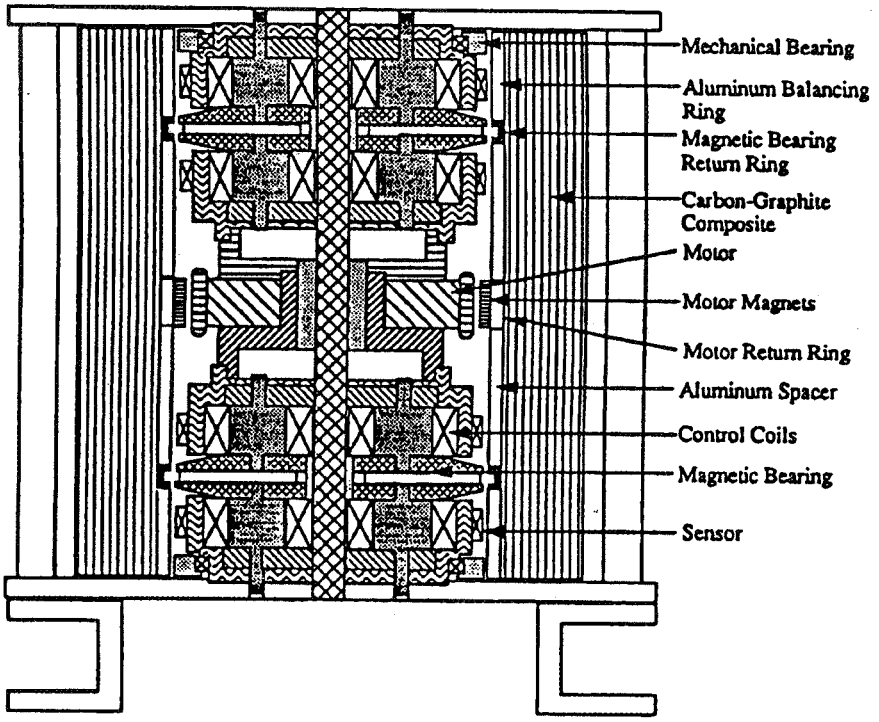

Figure 1 - Cross section of OCCF Components

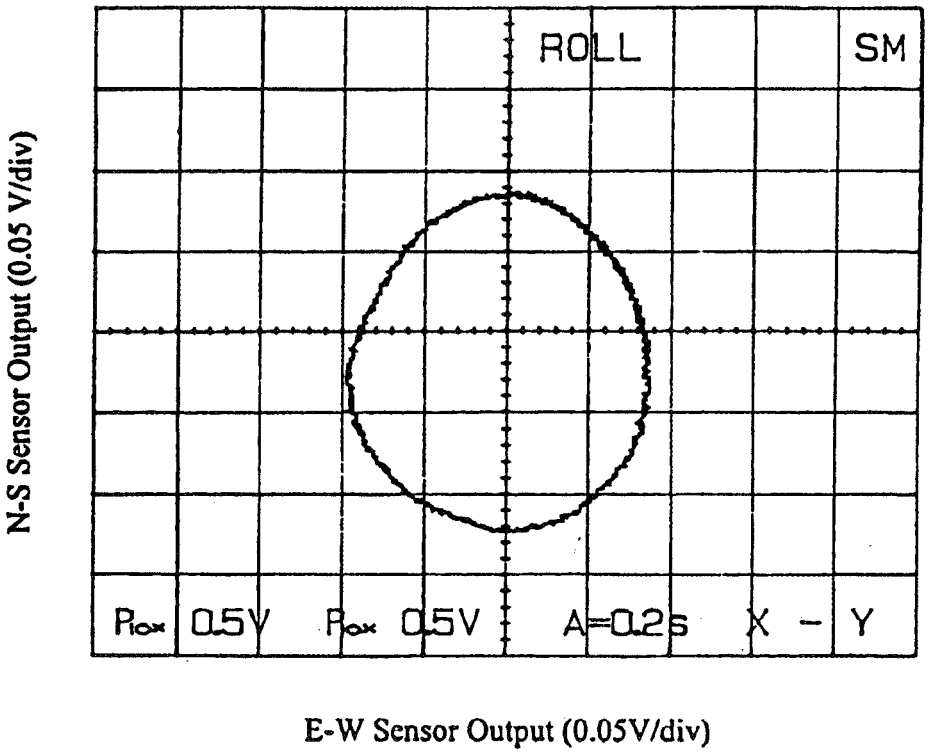

Figure 4 - Pancake Magnetic Bearing Displacement Output

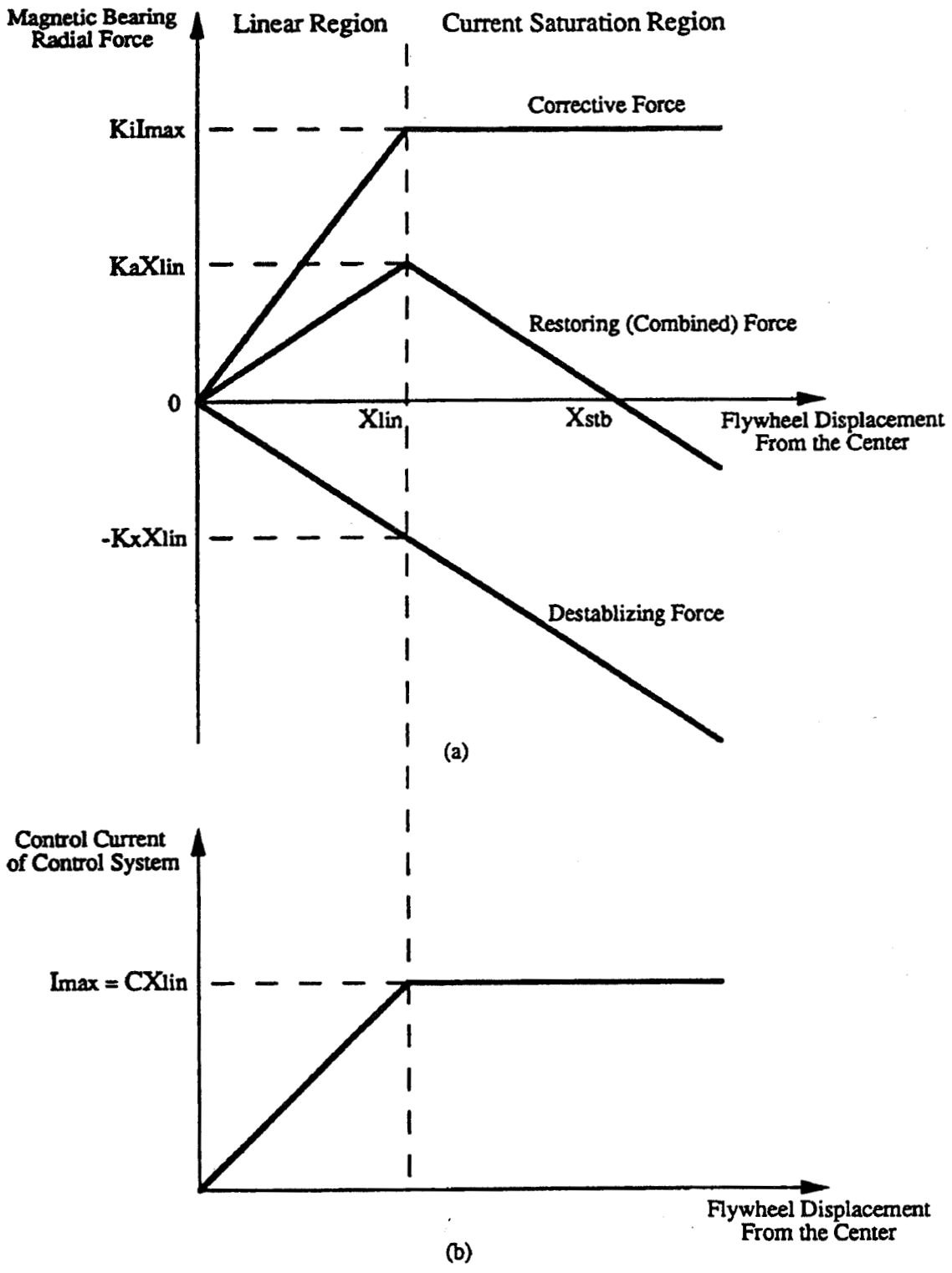

Figure 2 - Radial Forces and Control Current Output of Magnetic Bearing

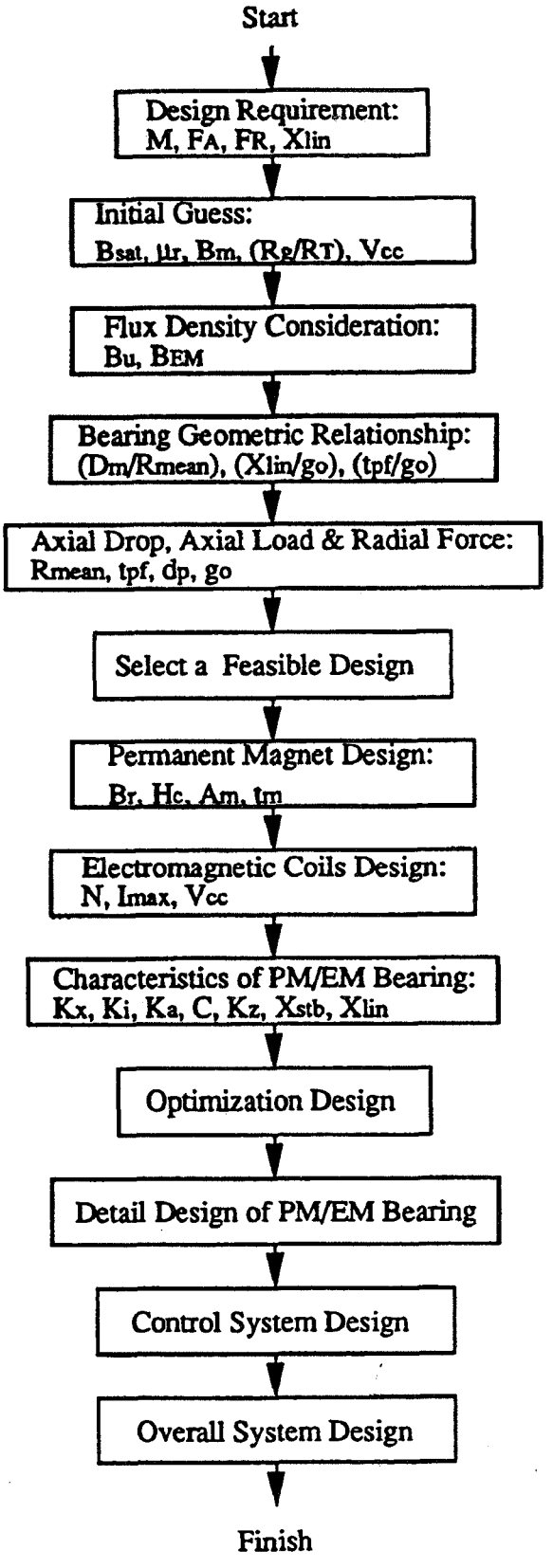

Figure 3 - Design Methodology Flowchart of PM/EM Magnetic Bearing

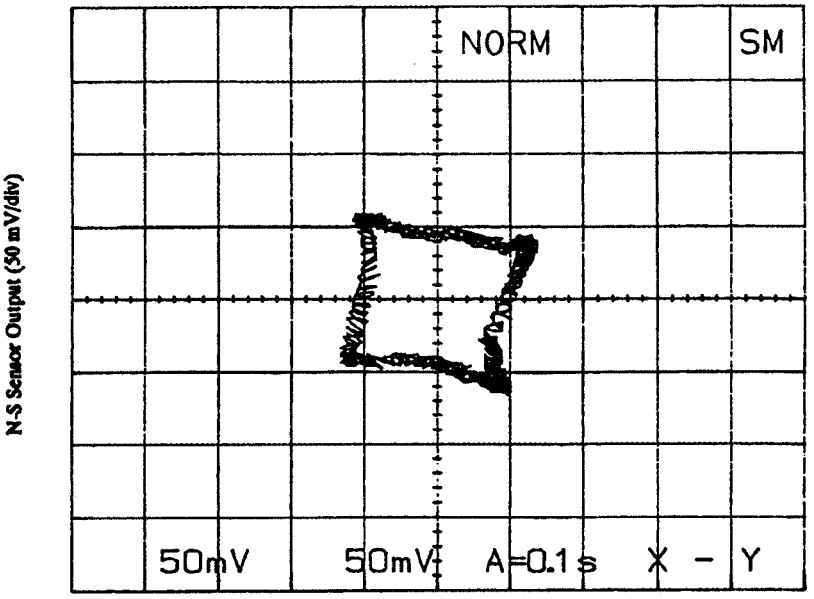

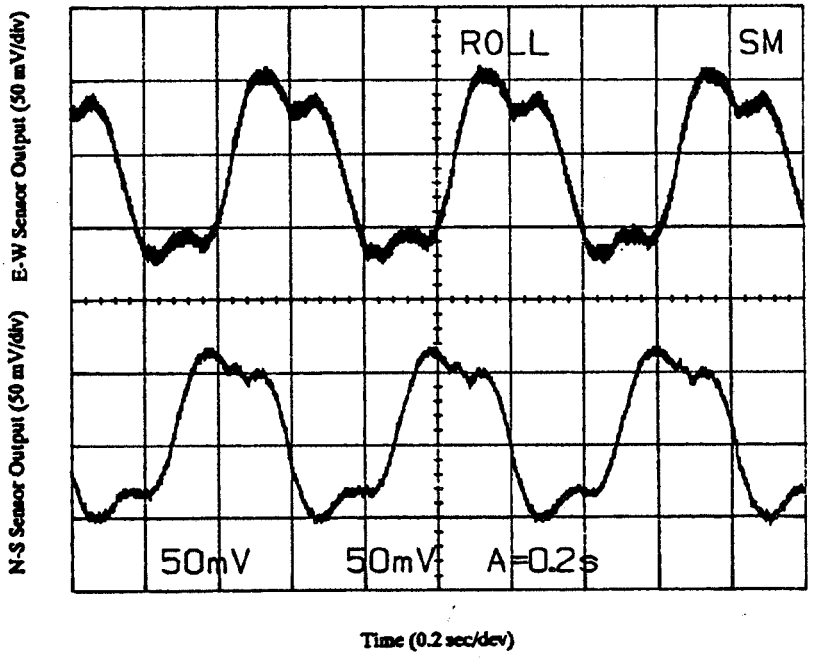

Figure 5 - Top Stack Bearing Displacement Sensor Output

TABLE 1

SPECIFICATIONS OF MAGNETICALLY SUSPENDED FLYWHEEL ENERGY STORAGE SYSTEM

FES Systems Designs Specifications

Deliverable Energy:	171 Wh
Useful Flywheel S.E.D.:	30.2 Wh/Kg
Operating Speed:	37,875 - 75,750 RPM
Cycle Period:	90 Minutes (60-minute Charge Cycle, 30-minute discharge cycle)
Power Line Output:	150±2 V DC
System Efficiency:	85%

FES System Specifications

Max. Operating Speed:	20,000 RPM
Stored Energy:	15.9 Wh at 20,000 RPM
Angular Momentum:	54.75 N-m-sec (40.38 lb-ft-sec) at 20,000 RPM
Flywheel Tip Speed:	165 m/s at 20,000 RPM
Runoff Error:	<0.038 mm (0.0015 in)
Vacuum Condition:	~10^{-4} Torr
Power Loss:	~70 W at 16,000 RPM

TABLE 2

DEVELOPMENT OF FLYWHEEL ENERGY STORAGE SYSTEM

Rotating Speed (RPM)	Test Conditions	Limiting Factors	Corrective Actions
	Old FES System	Poor Magnetic Bearing Performance	Design of New Magnetic Bearings & FES System
All Speed Range	Magnetic Saturation of Return Rings	3rd Harmonics Affecting Stability	Selection of Return Rings with Minimum Magnetic Saturation
4,000	±24 V Power Amplifiers & 750-turn EM Coils	Magnetic Bearing Power Amplifier Voltage Saturation	(1) ±90 V Improved Howland Bridge Amplifier Installed, (2) Use of 500-turn EM Coils to Reduce Inductance
6,000	Undamped Structure	Structure Vibration	Rubber Vibration Isolators Installed
6,000	Flywheel as Manufactured	Mass Unbalance	Balancing Flywheel Using Displacement X-Y Orbit
8,000	FES System Operating in Air	Windage Loss	Vacuum System Implemented
10,000	PM DC Brushless Motor Controller	Motor Current Limitation due to Impedance Mismatch Between Motor and Motor Controller	(1) Use of Variac to Adjust Motor Controller Input Voltage, (2)Dummy Inductors Added to Motor Inputs
12,000	Hand Wired Electronics Boards for Controllers, Sensors, & Power Amplifiers	(1) Inconvenient to Adjust Stiffness & Damping of Magnetic Bearings (2) Reliability	(1)Adjustable Stiffness & Damping Controller Implemented, (2)Use of Print Circuit Boards for All Electronics
15,000	Phototransistor Reflective Optical Sensor with 1 ms Response Time	Time Delay of Motor Commutation Signal	Photodarlington Reflective Optical Sensor and Schmitt Trigger Installed with 0. I ms Response Time
20,000	Existing FES System with Improved Components	Motor Current Limitation	(1) Power Loss Analysis Suggesting Lamination of Magnetic Bearings, (2) Future Improvements on Motor & Motor Controller

MAGNETIC LEVIATION SYSTEM DESIGN AND IMPLEMENTATION FOR WIND TUNNEL APPLICATION

Chin E. Lin
Institute of Aeronautics and Astronautics
National Cheng Kung University
Tainan, Taiwan, R.O.C.

Yih-Ran Sheu
Department of Electrical Engineering
Nan-Tai College, Tainan, Taiwan, R.O.C.

Hui-Long Jou
Institute of Aeronautics and Astronautics
National Cheng Kung University
Tainan, Taiwan, R.O.C.

ABSTRACT

This paper presents recent work in magnetic suspension wind tunnel development in National Cheng Kung University. In this phase of research, a control-based study is emphasized to implement a robust control system into the experimental system under study. A ten-coil 10 cm x 10 cm magnetic suspension wind tunnel is built using a set of quadrant detectors for six degree of freedom control. To achieve the attitude control of suspended model with different attitudes, a spacial electromagnetic field simulation using OPERA 3D is studied. A successful test for six degree of freedom control is demonstrated in this paper.

I. INTRODUCTION

Magnetic Suspension and Balance Systems (MSBS) are being developed for wind tunnels to support aircraft models operating free from flow interference caused by the conventional mechanical supports. There are several MSBS's operated for wind tunnel tests described in the literature. A typical MSBS consists of an array of electromagnets around the wind tunnel test section, generating electromagnetic forces and moments on the suspended model. The suspended model is designed with several permanent magnets embedded inside the non-metallic envelope. MSBS's of this type are inherently open-loop unstable, i.e., the position and attitude of the

suspended model should be continuously monitored with adjustment and control of the magnetic field within the wind tunnel test section via a feedback control system [1,2]. From the literature, the MSBS for wind tunnel application requires a dedicated electromagnetic loop design and a feedback control system. These two major parts are dominant to the success of the MSBS in wind tunnel operation. To accomplish such a development, a control-based study for developing a modern position and attitude control technology should be emphasized. In preparation for this research development, a comprehensive force model has been developed to look into more correlated problems in the large-gap MSBS [3,4]. From basic control approaches, we understand that many conventional control technologies can be adopted in the MSBS for wind tunnel applications. The control methodology can become useful knowledge in our laboratory from previous studies [5]. This paper presents an MSBS for wind tunnel applications from the view of the control-based study and implementation. A test system, consisting of an array of ten electromagnets for 10 cm x 10 cm wind tunnel test section, has been built and tested. The configuration of typical MSBS consists of power supplies, position sensing system, dynamic model, and feedback controller. The power supply system consists of ten PWM switching power units. Each power unit uses the high gain current feedback method to shift the poles of the electromagnet coil far from the imaginary axis. The electromagnet dynamics is neglected [2]. The position sensing system is composed of a laser optical circuit, quadrant detectors, and lateral offset detectors. The system can measure the motion of the suspended model with six degrees of freedom in wide range operation. Its accuracy is proved by experimental testing. The operating rate of the system is above 1 KHz such that the stiffness in model control is high. The dynamic model in our case indicates the relationship between the electromagnetic coil currents and the motion of suspended model. The electromagnetic field is simulated by the OPERA 3D magnetic field simulation software to look into the electromagnetic field problem, and the magnetic forces and moments in relation with magnetic field are calculated by the theoretical electromagnetic formulas. After the equations of motion are introduced [3], the linearized system dynamic model at a normal operation point is obtained. From the Bode plot of the linearized system dynamic model, we can consider the system to be decentralized since each motion of degree of freedom is dominated by its corresponding electromagnets. Then, the PID controllers are used in the decentralized system for stable regulation control. This controller is simple and easy to implement. Combining the decentralized PID controller with the optical position sensing system, the proposed system does a good job to achieve control requirements in the MSBS.

II. SYSTEM DYNAMIC MODELING

The sketch of the electromagnet circuit and its system coordinates are shown in Fig. 1. It is composed of ten electromagnet coils and a suspended model. Two air cored coils, No. 1 and No. 2, and the other eight iron cored coils, from No. 3 to No. 10, generate the electromagnetic forces and moments acting on the suspended model against the aerodynamic drag force, moment and the gravity force. The size of test section is 10 cm x 10 cm. The symmetric arrangement of the ten electromagnet coils is arranged to have a uniform magnetic field distribution in the test section. The system dynamic model gives the relationship of coil currents and the positions and attitudes of the controlled suspended model. The ten coils of the MSBS are divided into six

groups. The input coil currents are I_1, I_2, I_3, I_4, I_5, and I_6, individually. The system outputs are the positions of x, y, z, and the attitude of pitch, yaw and roll. The coil currents will produce magnetic field and exert the magnetic forces and moments on the suspended model such that motion in six degrees of freedom can be generated. As the equations of motion are introduced [6] and are generally linearized for use, the system dynamic model at its normal operation point is obtained. The magnetic field in our experiments is simulated by the OPERA 3D magnetic field simulation software to understand the magnetic field problem, and the electromagnetic forces and moments in relation with magnetic field are calculated by the improved theoretical electro-magnetic formulas. The formulas are simple and their accuracies are proved by experimental measurements [4]. This process is valuable to understand the relationship of coil currents to each desired model position and attitude. Using different test conditions as inputs, the simulation results quickly show the correct direction for test preparations and control gain setting.

III. POSITION SENSING SYSTEM

The position sensing system is composed of a laser optical circuit, quadrant detectors, and lateral offset detectors. The configuration of the system is shown in Fig. 2. The laser beam from the laser tube passes through a spatial filter and a convex lens, and then extends to parallel beams. The light beam is marked by a covered sheet to form a slender rectangular beam. It goes through a splitter and then divides into two light beams. One beam goes in y-axis direction and the other in z-axis direction as shown in Fig. 5, each will be detected by a quadrant detector located at the center of the sensing position. The quadrant detector is a cell which is composed of four photo-diodes for each different direction. As the light intensity on the cell is balanced, the output of sensor voltage is zero. For the suspended model in the test section, part of the light beam will be blocked by the model and the residual light will still be received by the quadrant detector. If the model is located at the center position in z-axis direction, the top part of the residual light is the same as the bottom part and the output voltage of the detector is zero. If the model moves down in z-axis position, the top part is larger than the bottom part and the output voltage is negative, or vice versa.

This is the example for the z-axis displacement measurement. Similarly, from the residual light of the left part and the right part, the y-axis displacement can be measured. In pitch angle and yaw angle measurement, the angle variation is proportional to the sum of the unmarked light intensity by a sinusoidal function. We can pick up the data of the sum of the unmarked light to obtain the model attitude. The x-axis displacement and roll motion is measured using the lateral offset detector. The lateral offset detector is first applied to the model position sensing in MSBS. It is like the CCD position sensing system to measure the position of the marked light points on the suspended model [7], but its outputs are analog voltages with relative to the x position of the reflected light point on the detectors. The resolution and speed are much higher than CCD, and its operation is simpler.

The sensing system is calibrated by several experiments. The experimental instruments are built-up by two 0.01 mm accuracy height gauges, a 0.01 mm accuracy meter gauge, and a 10000

pulses per cycle photo-encoder. The height gauges are used to measure the y, z, pitch, and yaw displacements of the model, the meter gauge is used to measure the x-axis displacement, and the photo-encoder is used to measure the roll displacement. As the positions, and attitudes are changed, the data from the detector signal amplifier is picked up. The calibration results, which is the relationship of amplifier output signal and attitude change, and its error analysis, which is obtained from the differences between the picked-up data and the fitted curves, are shown in Fig. 3. Fig. 3(a) is the result of x-axis displacement, Fig. 3(b) is the z-axis displacement, Fig. 3(c) is the pitch angle, and Fig. 3(d) is the roll angle. The y-axis displacement and yaw angle rotation calibration result are similar to the z-axis displacement and pitch angle. We can see that the accuracy of x displacement is limited in 0.04 mm, z displacement is limited in 0.01 mm, and pitch angle is limited in 0.2 degree. The operation ranges of the sensing system follows: the pitch angle is +/= 25°, the yaw angle is +/= 25°, and the roll angle is +/= 20°.

Concerning the position sensing system, there are several problems to be discussed. One is the coupling problem between the measurements in each degree of freedom, for example, the movement of z-axis will effect the measurement of roll displacement. But in the real application of the wind tunnel, the mass center of the model is fixed such that the coupling problem is not considered here. Another problem is about the sensitivity of the analog devices. They are effected by the light intensity variation and noise, mainly produced by the computer. In practice, the output signal of the amplifier is normalized by the light intensity to have the signal relatively insensitive to intensity changes and the accuracy is acceptable considering the noisy environment. To summarize, the advantages of the position and attitude sensing system are high bandwidth, accuracy, robustness, easy realization, and wide range in operation.

IV. SYSTEM IMPLEMENTATION

Based on theoretical analysis, since each electromagnetic coil contributes a different effect to position and attitude control of the suspended model, a decentralized control can be implemented on a PC-based control system. The decentralized control commands coils No. 1 and No. 2 acting on the x displacement, coils No. 3, No. 4, No. 5 and No. 6 acting on the z displacement and pitch motion control, and then coils No. 7, No. 8, No. 9 and No. 10 acting on the y displacement and yaw and roll angle control. The suspended model has embedded a cylindrical permanent magnet inside its aerodynamic envelope for magnetic field vector control. The envelope of our experiment model is a rocket of 90 mm length with total mass of 100 g, embedded with five high flux density permanent magnets of 10 mm diameter. The measured value of the magnetization is equal to 839250 A/m.

By an integration of the decentralized PID controller with loop closed from the position sensing system, the suspended model in the test section is stable in regulation control. The photograph of configuration of the MSBS is shown in Fig. 4 and its control results is shown in Fig. 5. Six PID controllers for six degrees of freedom of motion control are realized using an Intel 486-33 personal computer. The highest system sampling rate is 2 KHz, determined by

stiffness of the suspended model. The higher sampling rate can provide higher operation stiffness, and the lower sampling rate is more difficult to design the controller to meet system stability requirement.

V. CONCLUSION

In this paper, the implementation of a magnetic suspension wind tunnel using effective measurement and control is demonstrated. The objective of the proposed idea accomplishes the operation requirements of a model position and attitude measurement and control for six degrees-of-freedom. By calibration procedures, the accuracy of the proposed measurement system using an integration of quadrant detector and lateral offset detector has achieved an acceptable level [8]. Other advantages of such an implementation are beneficial operation range, bandwidth, stiffness, and stability, in addition to its high accuracy with low cost. This magnetic suspension wind tunnel is used for low speed model tests under continuous attitude changes as a simulation of real flight conditions. Also, the measurement system is established for other related research projects to test their developing control methods for such nonlinear and unstable characteristics of magnetic suspension system.

REFERENCES

[1] C. P. Britcher; and M. J. Goodyer: "Digital Control of Wind Tunnel Magnetic Suspension and Balance System," ICIASF '87 Record, Williamsburg, VA, June 22-23, 1990.

[2] C. E. Lin; and L. A. Lee: "Dynamic Control of Magnetic Suspension System," IEEE Advanced Motion Control Conference, Tokyo, Japan, March 30, 1990.

[3] N. J. Groom: "Analytical Model of a Five Degree-of-Freedom Magnetic Suspension and Positioning System," NASA TM-100671, March 1989.

[4] C. E. Lin; and H. L. Jou: "A Dynamic Method for Magnetic Torque Measurement of Permanent Magnet," IEEE Instrumentation and Measurement Technology Conference IMTC '94, Hamamatsu, Japan, May 9-12, 1994.

[5] C. E. Lin; and Y. R. Sheu: "A Hybrid Control Approach for Large-Gap Magnetic Suspension System," CAC Journal of Control Systems and Technology, Vol. 2, No. 1, Jan. 1994, pp. 1-9.

[6] Nelson J. Groom: "Analytical Model of a Five Degree of Freedom Magnetic Suspension and Positioning System," NASA TM-100671, March 1989.

[7] C. E. Lin; and A. S. Hou, "A Real Time Position and Attitude Sensing Using CCD in Magnetic Suspension System Application," IEEE Trans. on Instrumentation and Measurement," Vol. 44, No. 1, pp. 8-14, February 1995.

[8] C. E. Lin; J. H. Jou; and Y. R. Sheu: "System Implementation of Measurement and Control for a Magnetic Suspension Wind Tunnel," IEEE Instrumentation and Measurement Technology Conference 95, Boston, April 23-26, 1995.

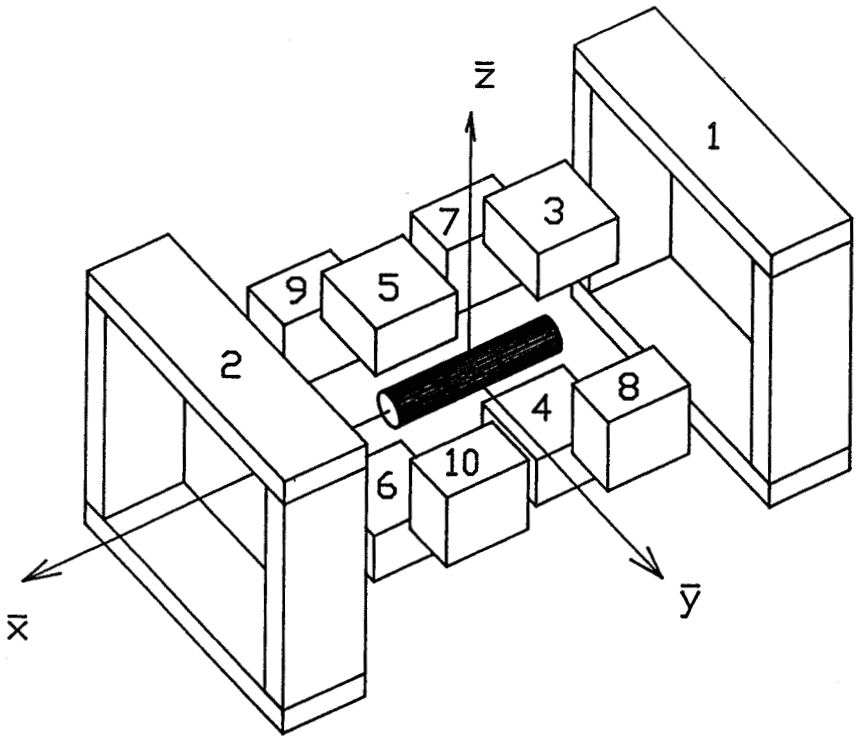

Fig. 1 Sketch of the MSBS and its system coordinate.

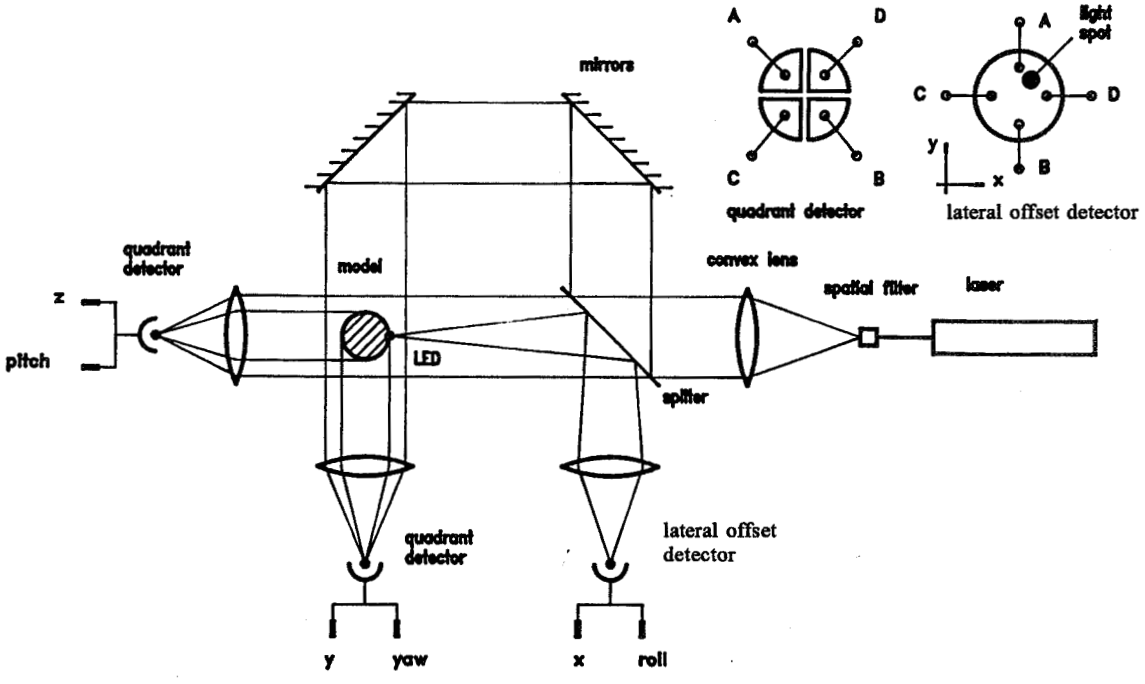

Fig. 2 Sketch of the position sensing system.

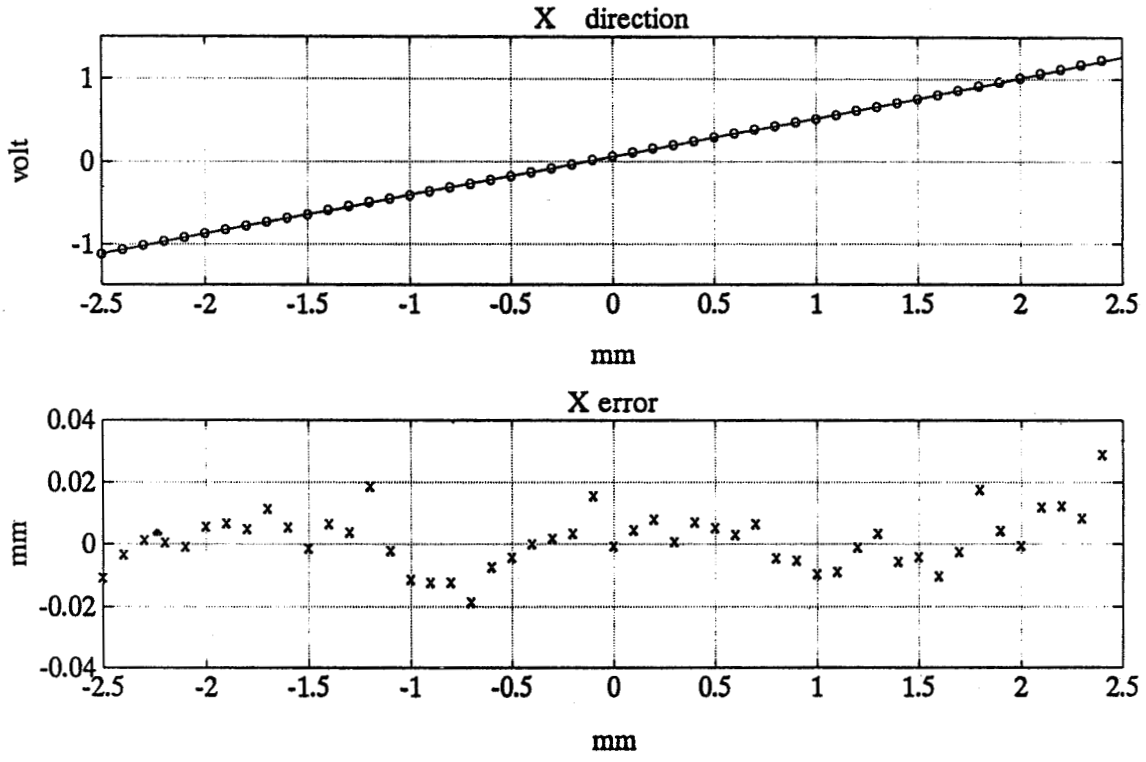

(a)

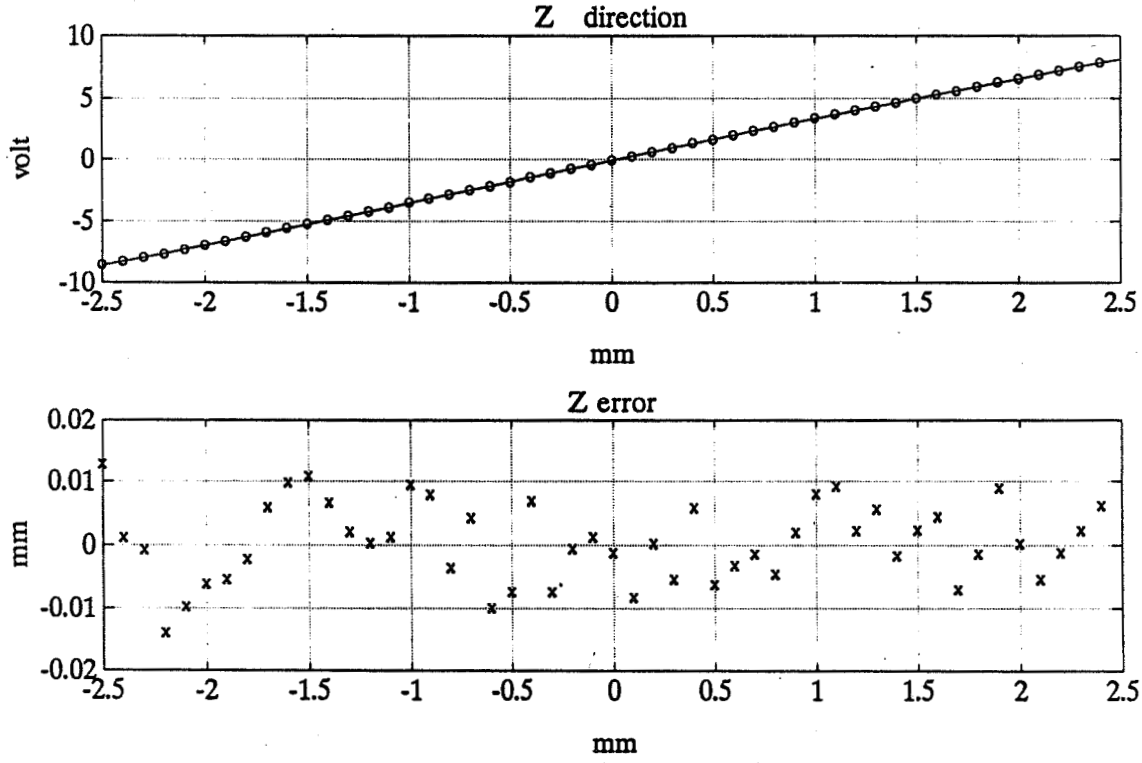

(b)

Fig. 3 Calibration results of position sensing system.

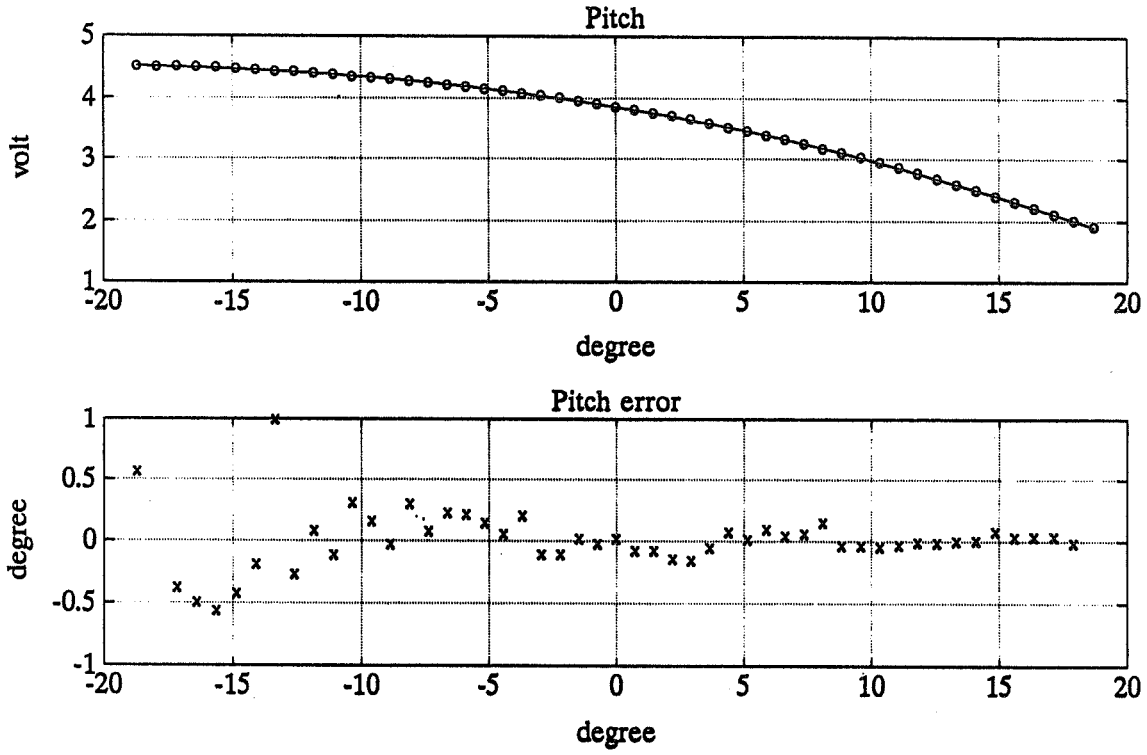

(c)

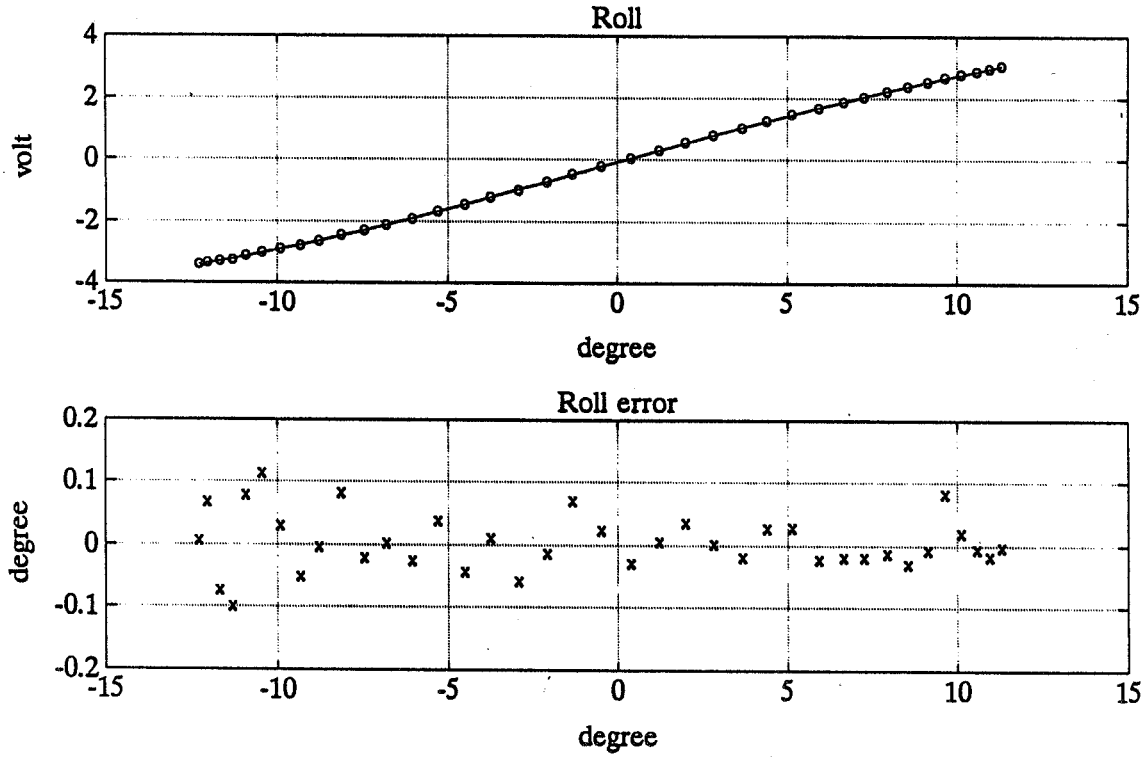

(d)

Fig. 3 Calibration results of position sensing system.

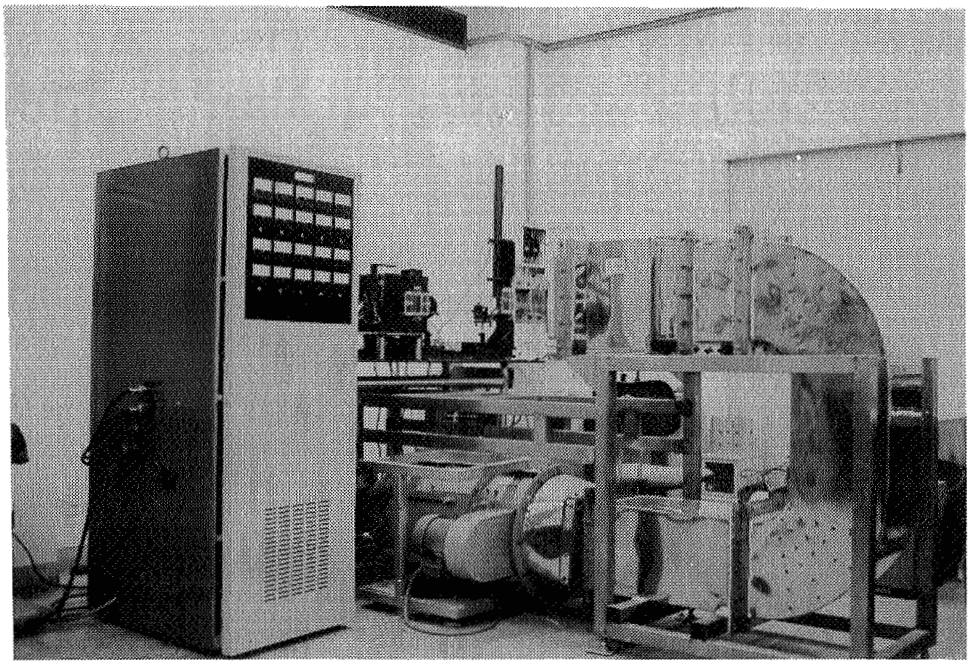

Fig. 4 Photograph of the configuration of the MSBS.

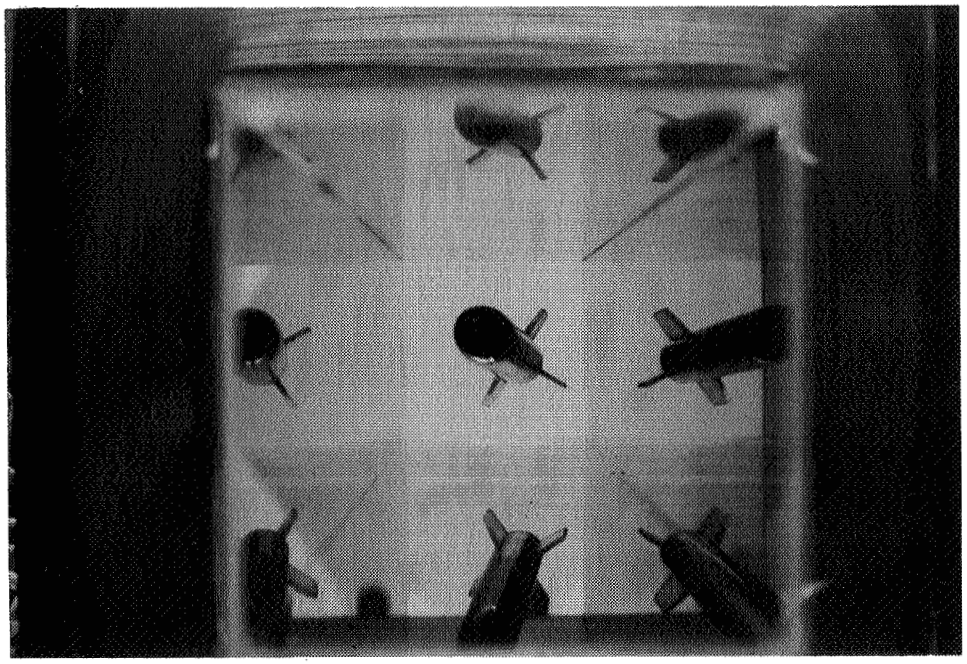

Fig. 5 Photograph of the control results of the MSBS.

FORCE MEASUREMENTS IN MAGNETIC SUSPENSION AND BALANCE SYSTEM

Alexander Kuzin
Moscow Aviation Technological Institute
Moscow, Russia

George Shapovalov
Central Aero-Hydrodynamic Institute
Moscow region, Russia

Nikolay Prohorov
MERA LTD Company
Moscow, Russia

SUMMARY

The description of an infrared telemetry system for measurement of drag forces in Magnetic Suspension and Balance Systems (MSBS) is presented. This system includes a drag force sensor, electronic pack and transmitter placed in the model which is of special construction, and receiver with a microprocessor-based measuring device, placed outside of the test section. Piezosensitive resonators as sensitive elements and non-magnetic steel as the material for the force sensor are used. The main features of the proposed system for load measurements are discussed and the main characteristics are presented.

INTRODUCTION

Experimental aerodynamicists extensively test aircraft models in wind tunnels. The behavior of models in a confined flow with specified parameters indicates how a real aircraft will behave in flight. Similarity to real conditions is thus of paramount importance in an aerodynamic experiment. The mechanical components (strings, tension members, struts, etc.) used to support the models block the wind tunnel and disturb the airflow. Assessing the effects they have on the experimental results is extremely difficult because of their diversity and ambiguity. Thus, support systems that do not disturb the airflow in the wind tunnel are stiff and yet accurately transmit the aerodynamic loads borne by the model to measurement devices. These requirements are met by magnetic suspension and balance systems [1]. The mechanical connections are

replaced by the forces in the electromagnetic field, and all mechanical contacts with the suspended object are completely removed while the potential for accurate measurement is retained.

Most aerodynamic experiments are aimed at determining the aerodynamic forces and moments on the model. They are derived from the electromagnetic forces and moments counter-balancing them. The electromagnetic forces and moments are determined by the currents in the electromagnets and the model's spatial coordinates relative to the electromagnets. Only the currents and the model coordinates can be measured directly. To find the aerodynamic forces and moments, the relationship between the electromagnetic forces, the currents, and the model coordinates must be established. Since this relationship is hard to calculate with the required accuracy (which is determined by the accuracy of measuring the aerodynamic loads) it has to be established experimentally (from a calibration procedure).

Traditionally, the aerodynamic loads are derived from the variations in the currents in the windings of the corresponding magnets. These currents are automatically regulated to balance the aerodynamic forces and to hold the model at a constant static position. The calibration procedure involves loading the model with a known external load close to that expected (Figure 1) and measuring the currents in the electromagnets with no airflow past the model.

To automate the process and to decrease the calibration measurements, some mathematical relation between the magnetic forces (or moments) and the currents is assumed. Based on certain assumptions, it could be the squared form:

$$P_{qm} = \frac{1}{2}\sum_{k=1}^{n}\sum_{s=1}^{n}\frac{\partial L_{ks}}{\partial q} i_k i_s, \tag{1}$$

where $P_{qm} = \{F_{xm}, F_{ym}, F_{zm}, M_{xm}, M_{ym}, M_{zm}\}$ are magnetic forces and moments; $q = \{x, y, z, \gamma, \psi, \theta\}$ are coordinates of the model; L_{kk} - inductance of electromagnet ($k=1,...,n$); $L_{ks} = L_{sk}$ - mutual inductances of electromagnets; i_k is the current in the k-th electromagnet; n is the number of electromagnets.

With other assumptions, the relation between the magnetic forces and currents could be described as linear:

$$P_{qm} = \sum_{k=1}^{n} A_{qk}(i_k - i_{k0}), \tag{2}$$

where $A_{qk} = \left(\frac{\partial P_{qm}}{\partial i_k}\right)_{i_0, q_0}$; i_{k0} is the initial current in the k-th electromagnet (that is required to support the model when there is no load).

An adequate way of finding the calibration relations (for example, for linear relation (2)) is to load the model with n values of the multicomponent load, measure the currents in every electromagnet for each value of the load, and to solve the system of n equations linear in unknowns A_{qk}.

During wind-tunnel tests of a model, the currents in the electromagnets are measured and the acting aerodynamic load is found from the calibration relations.

To improve MSBS calibration, it has been proposed [1] that intra-model strain gauges be used which, in the absence of airflow, would be suspended in the magnetic field together with the model; known load components are applied to the balance through the calibration rod. One end of the balance is fastened to the model and the calibration rod is attached to the other end.

A promising modification of this method is to use an intra-model strain-gauge balance to measure the aerodynamic loads in MSBS wind-tunnel tests. This technique will eliminate calibration of the MSBS system which is time-consuming and requires complicated equipment. The MSBS is then used only to support the model. The challenge is to get contactless transmission of the signals carrying information of the loads being measured by the intra-model balance from the model to the detection and processing equipment. Investigation of that problem is the subject of this paper.

SYSTEM DESCRIPTION

A schematic of the drag force measurement telemetry system is shown in Figure 2. A model of special construction was developed to house the telemetry package and measure drag force. The model consists of a non-magnetic housing and magnetic core that is connected with the housing through two bars of non-magnetic steel. One of these bars is the force sensor (product of Mera LTD). The model is placed in a wind tunnel and its position is stabilized because of the interaction of the core with an automatically controlled magnetic field generated by magnets situated outside the test section. When the external force is applied to the model in the x direction, the force sensor is in a strained condition because the external force is applied to the non-magnetic housing of the model, but the magnetic force is applied to the magnetic core of the model. Construction of the force sensor is shown in Figure 3. Two piezo-sensitive resonators are placed on the surface of the bar by means of elastic glue. One of the resonators is in the strained condition under load and the other one is in a compressed condition. Construction of the force sensor removes the influence of applied moments on the measurement result. The resonators are chosen in such a way that the differences between their resonance frequencies is equal to 2-7 KHz and the first one has a working frequency in normal condition (without load) about 10 Mhz. Each of the resonators is included in a generator circuit. Figure 4 shows a schematic of the signal conditioner. The output signals of the generators are multiplied in a multiplier and then passed through a low-pass filter. The output signal of the filter is proportional to the difference between the resonance frequencies of the resonators. The resonant

frequency of each resonator linearly depends on the load, and the difference between their frequencies depends on the load also. The amplified signal, the frequency of which is proportional to the load force, feeds the infrared light emitting diode (LED). A frequency-modulated optical signal from the LED crosses the test section of the wind tunnel and is received by the silicon photodiode located outside the test section. The signal of photodiode is read by the microprocessor-based measuring device that transforms frequency into binary equivalent and shows the measured drag force on the indicator.

The power supply for the drag force measurement telemetry system is a battery of 8 V. The battery and conditioner pack are placed inside of the model housing. The LED is glued in the hole through the side of the model housing.

CALIBRATION OF THE DRAG FORCE MEASUREMENT SYSTEM

The calibration procedure involves applying known loads to the force sensor at a constant temperature and measuring the frequency-modulated signal by the microprocessor-based measuring device connected with the photodiode. The calibration results are presented in Figure 5 and show that the output frequency of the force sensor linearly depends on load for constant temperature.

The effect of varying the battery voltage on the output frequency of the force sensor is presented in Figure 6 and shows that output frequency is independent of the battery voltage over a wide operational range. The application of a compact integral regulator of battery voltage will increase the operational time of the system.

The differential system of sensitive elements is thermally balanced. The thermal influence is 0.1% per 1^0C of the maximum calibration load of 20 N.

EXPERIMENTAL RESULTS

Figure 7 shows the MSBS at MAI-TsAGI [2] that was used for the drag force measurement experiment. The drag force measurements were taken for a model with a 400 mm length and 40 mm diameter over the velocity range from 0 m/s to 50 m/s. The results are presented in Figure 8. The experiment indicates good repeatability of two sets of measured data. The standard deviation of data from the mean is less than 1% of the maximum calibration load of 5 N. Figures 9 and 10 show the model that was used for drag force measurements.

CONCLUSIONS

An infrared telemetry system for measurement of drag force in magnetic suspension and balance systems has been developed. The experimental results prove the possibility of application of the intra-model balance for contactless force measurements in MSBS. The construction technique can be developed for multicomponent force measurements.

REFERENCES

1. Kuzin, A.V.: Electromagnetic Suspension Systems in Experimental Aerodynamics: State of the Art and Prospects. *Instruments and Experimental Techniques*, No. 3, 1992, pp. 403-416.

2. Kuzin, A. V.; Vyshkov, Y. D.; Shapovalov, G. K.: Progress of magnetic suspension and balance systems for wind tunnels in the USSR. Proceedings of International Symposium on Magnetic Suspension Technology, NASA CP-3152, 1992, pp. 65-74.

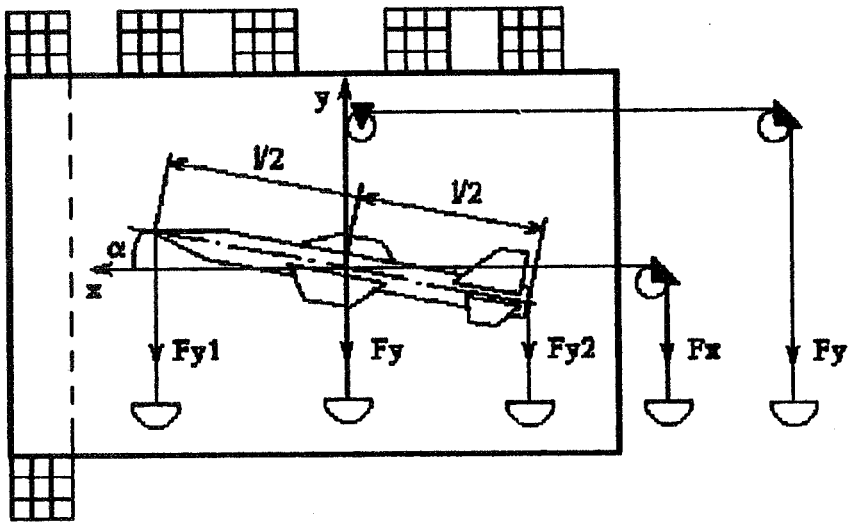

Figure 1. Calibration set-up of MSBS.

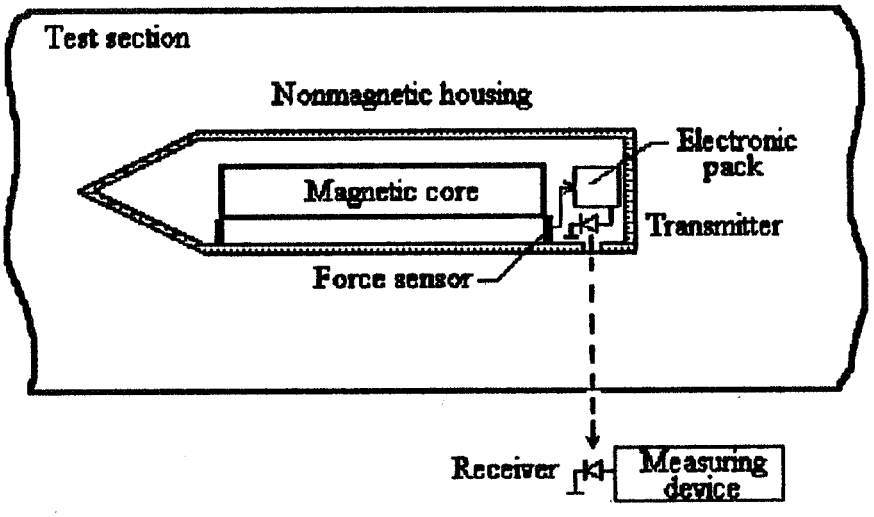

Figure 2. Schematic of drag force measurement telemetry system.

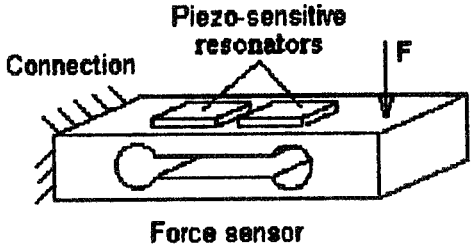

Figure 3. Construction of force sensor.

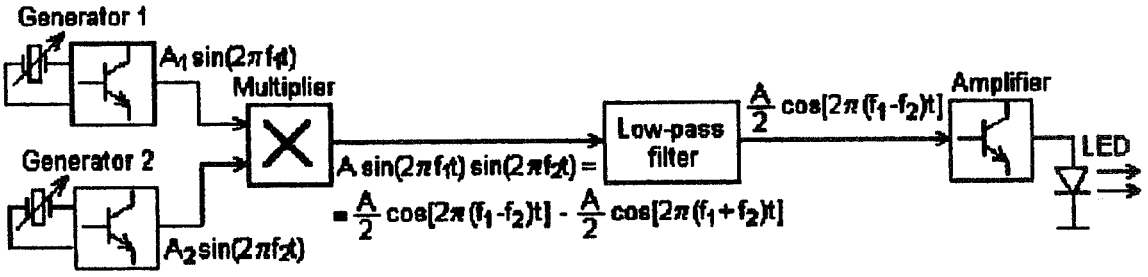

Figure 4. Schematic of signal conditioner.

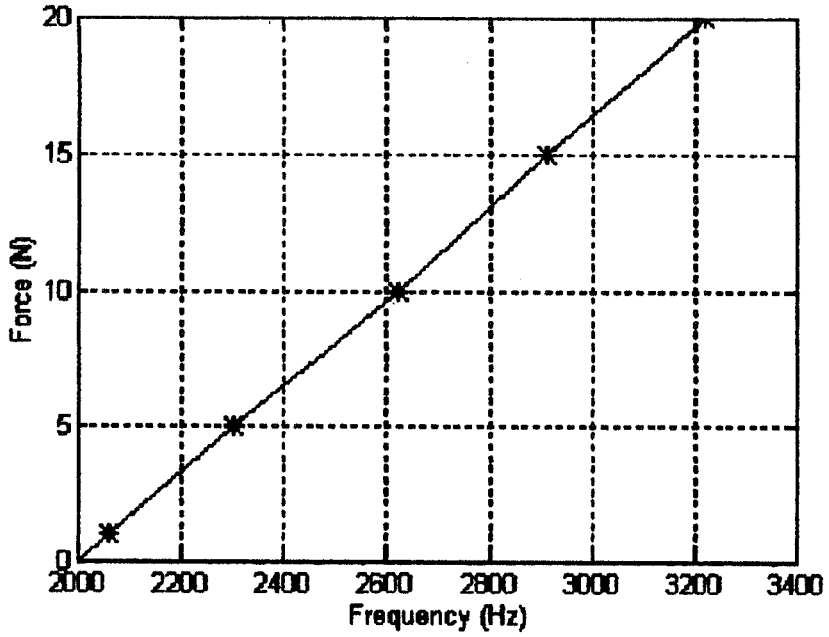

Figure 5. Drag force measurement telemetry system calibration curve.

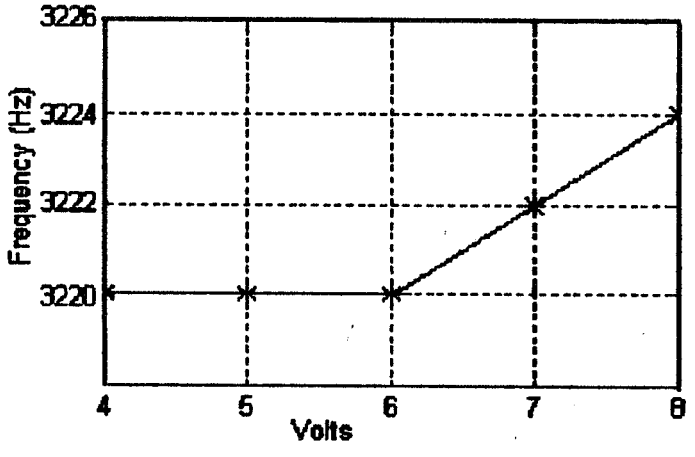

Figure 6. Effects of battery voltage on output frequency.

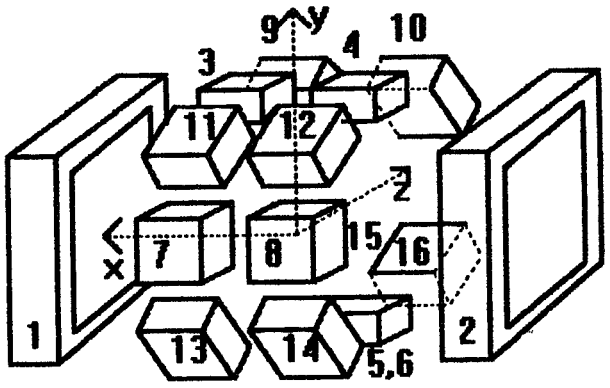

Figure 7. Magnetic Suspension and Balance System of MAI-TsAGI.

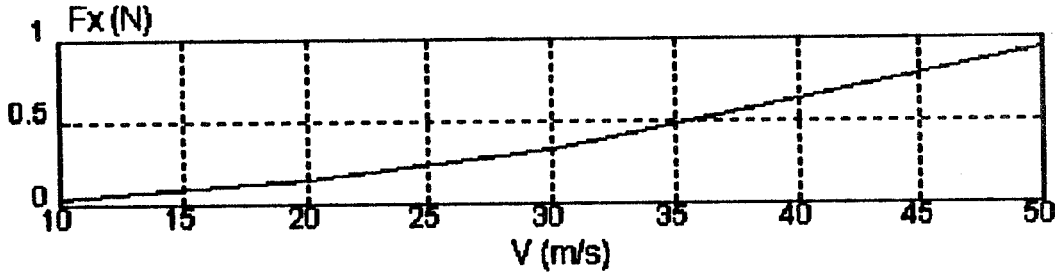

Figure 8. MSBS drag force measurements.

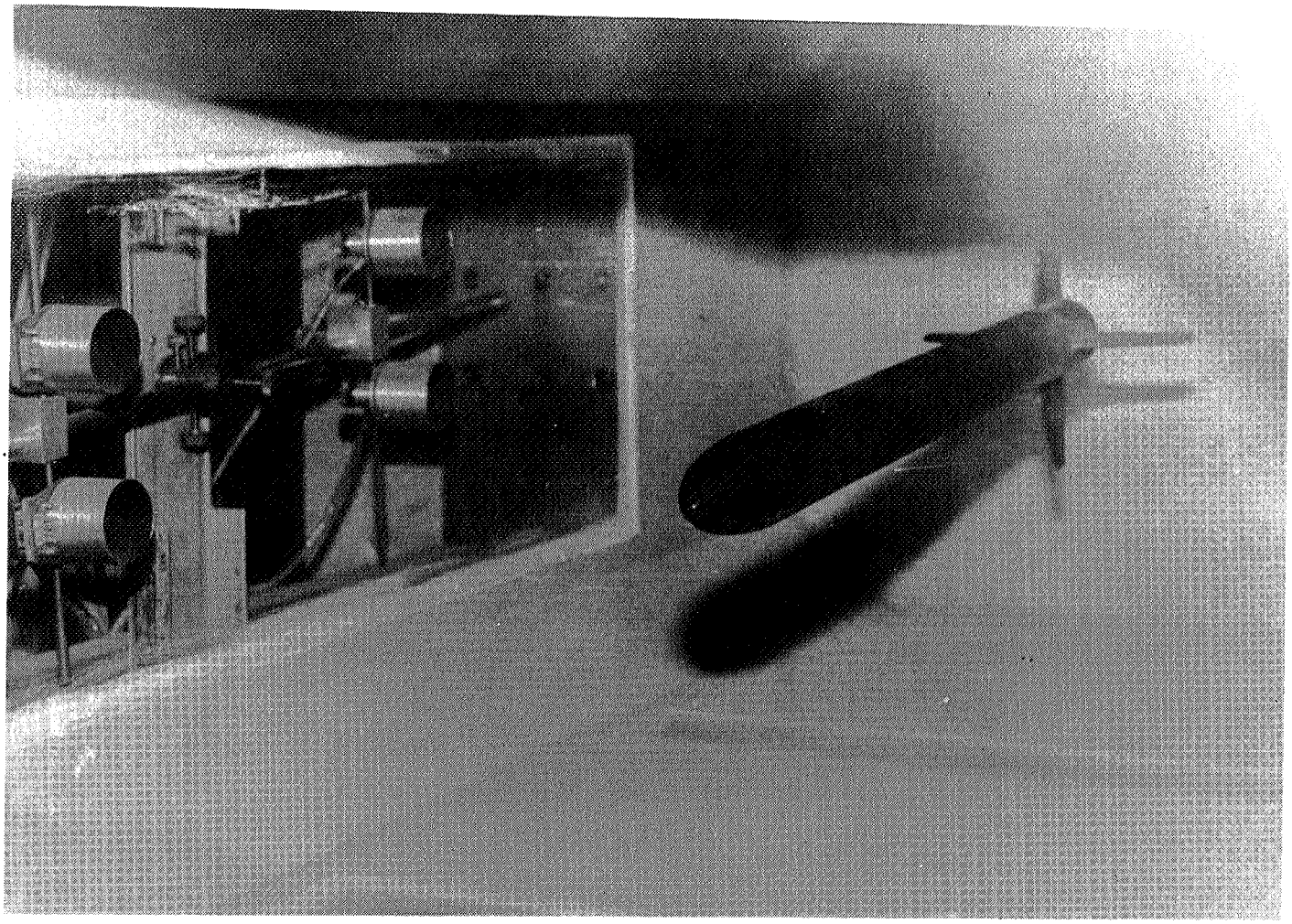

Figure 9. Photograph of model in magnetic suspension of MAI-TsAGI.

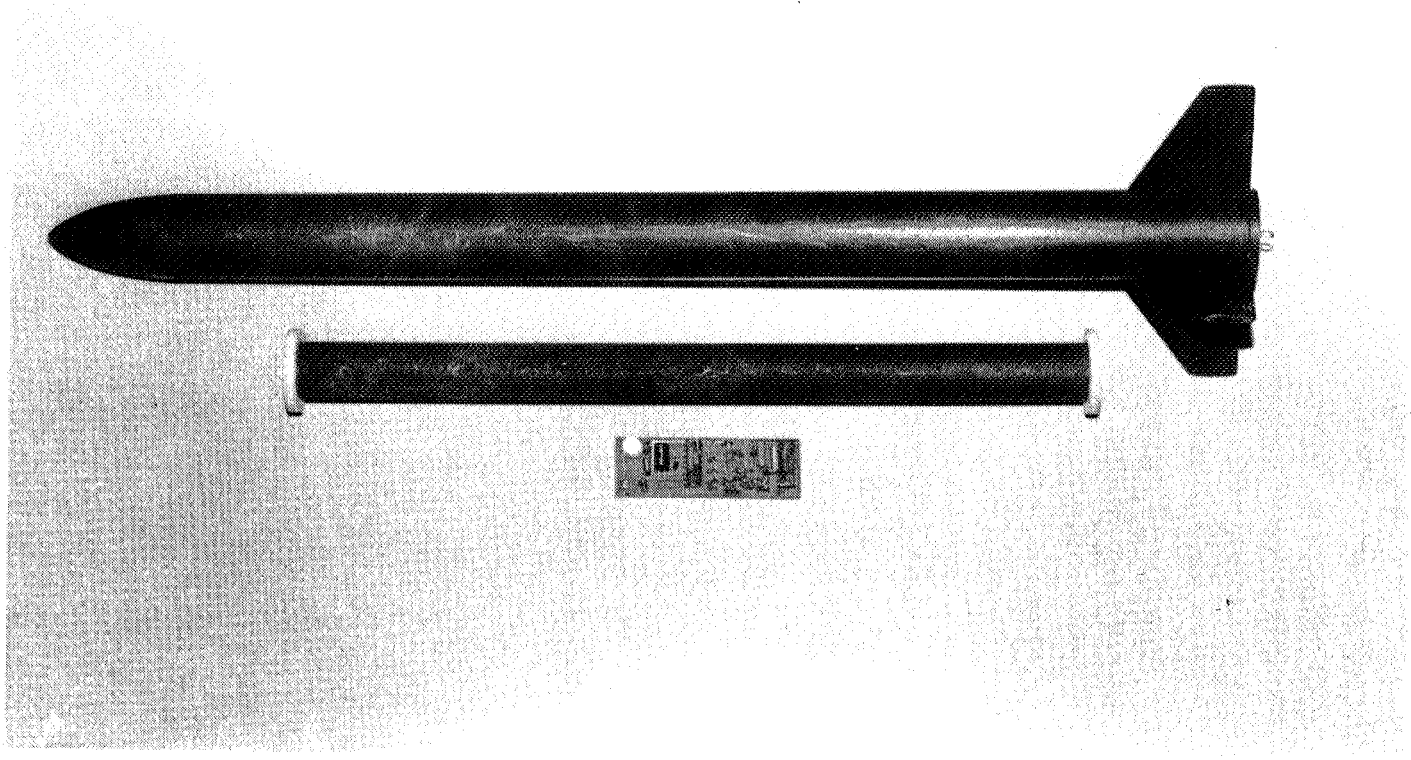

Figure 10. Photograph of model with telemetry system and magnetic core.

STATUS OF MSBS STUDY AT NAL IN 1995

Hideo SAWADA, Hisasi SUENAGA, Tetuya KUNIMASU, Takashi KOHNO
National Aerospace Laboratory (Japan)
7-44-1 Jindaijihigashi-machi Chofu-shi Tokyo 182, Japan

SUMMARY

Magnetic field intensity and currents passing through the coils of the National Aerospace Laboratory (NAL) 10cm Magnetic Suspension and Balance System (MSBS) were measured while a cylindrical model was oscillated along x,y,z and also about y and z axes, respectively. The model was made of alnico 5 and was 8mm in diameter and 60mm long. Two kinds of tests were carried out. Amplitude of the oscillation was varied at a frequency of 10Hz. Frequency was varied from 1 to 50Hz in the other test. Results of the tests show that the relation between coil currents and magnetic force acting on the model is affected by frequency. They also show that the relation between measured magnetic field intensity and the force in vertical direction is independent of the frequency below 30Hz. Using the measured magnetic field intensity, the vertical force can be evaluated at the MSBS instantaneously when a model moves at frequencies below 30Hz. A static drag force calibration test was carried out at the 60cm MSBS. Obtained relationships between measured drag coil currents and loads shows large hysteresis.

INTRODUCTION

Magnetic Suspension and Balance Systems (MSBS) are a kind of model support system of wind tunnels for supporting a model in flow with magnetic force. It can avoid the model support interference because the flow field in a test section will not be affected by the magnetic field except for some very high speed flow, etc. Magnetic field for suspending a model is generated by currents passing through some coils arranged around a test section. Then the magnetic force acting on the model corresponds to the currents. When the model is at a fixed position in the flow, the magnetic force must balance with the aerodynamic force acting on the model plus the gravity force. This means that the system can work as a balance for the aerodynamic force by measuring the coil currents. The relation between the magnetic force and coil currents can be decided uniquely by some calibration tests (static force calibration tests) in almost all cases. In case of a model in motion, the difference between the magnetic force and the aerodynamic force places the model in motion. Then the aerodynamic force can be evaluated by subtracting the force driving the model motion from the magnetic force. The inertia force can be estimated by measuring model motion. This means that the system can measure dynamic force. It is also easy for the system to get accurate model position because it uses the position data for its control. It is easy to create suitable forces on a model by placing the model in suitable motion in the system. The tests corresponding to the magnetic force to coil currents are called dynamic force calibration tests. Dynamic calibration tests can replace static force tests because there is no difference between the

force driving the model motion and the force by pulling with threads in the sense of the force acting on the model. Some dynamic force calibration tests were carried out at the 10cm MSBS. Preliminary static force calibration tests were conducted at the 60cm MSBS.

SYMBOLS

g gravity acceleration (= 9.8m/sec^2)
H magnetic field intensity, (H_x, H_y, H_z) (T)
Hi a magnetic field intensity component at a position along the coil no.i axis. (T) See Figure 2.
$H_{monitor}$ x component of the magnetic field intensity inside test section (T)
H_{drag}, H_{side}, H_{lift}, H_{pitch}, H_{yaw} See equation (1)
I_i current passing through coil no.i (A)
I_{drag}, I_{side}, I_{lift}, I_{pitch}, I_{yaw} See equation (1)
I_{yy}, I_{zz} moment of inertia about the y and z axis, respectively. (kgm^2)
K_{drag}, K_{side}, K_{lift}, K_{pitch}, K_{yaw} proportional constant between force and magnetic field intensity combination. See equations (2) and (3).
m model mass (kg)
m_x x component of magnetic moment (Wbm)
(x,y,z) coordinate system. See Figure 1.
θ angle about the y axis.
ϕ angle about the z axis

DYNAMIC FORCE CALIBRATION TEST

Experimental Design

Magnetic field around the test section together with coil currents was measured with Hall sensors during dynamic force calibration tests. Some preliminary test results have been published. As mentioned in References 1 and 2, even the most suitable combination of measured coil currents showed differences from model position in the sense of phase. The difference was observed to depend on the motion frequency. On the contrary, a suitable combination of measured magnetic field intensity components appeared completely in phase with the model position. In this dynamic calibration test, forced oscillations of a model were performed in two ways. Frequency varied from 1 to 50Hz along the x, y and z axes and about the y and z axes in one way. The amplitude of 10Hz oscillation varies in the other way. In order to avoid the effect of eddy currents on metal test section walls, the test section was removed during the test.

The model is 60mm long and 8mm in diameter and of alnico 5 permanent magnet. In order to measure the model position, the model was wrapped with thin white paper. The paper measured 0.2g +/- 0.1g in mass. The shape is 60mm high x 52mm wide x 0.1mm thick. A 4mm wide black line was printed along the center line of the paper. The line is used to measure the x position of the model. The whole mass of the model including the paper was measured as 23.8g +/- 0.1g with

a balance. The inertia moment of the model was evaluated at 2.87 x 10^5kgm^2 about an axis through the gravity center normal to the model axis by calculation from the model shape and mass. The model was supported by the control of 5 degrees of freedom except for rolling motion about the model axis. Besides, constant currents of 4 A in magnitude pass through the 4 side coils to generate an additional constant magnetic field which makes model position stable in y and ϕ.

The model was suspended at the center of the 10cm MSBS which is the coordinate system origin. All oscillations were pure sinusoidal, pure heaving and pure pitching motions. In the pitching (and yawing) motions, the center of gravity was controlled to be kept at the origin.

Coil currents were measured from monitor outputs of 10 power amplifier units. In order to evaluate the monitor output accuracy, they were compared between 0 to 50Hz with the currents measured with a zero inductance Shunt type resistance of 0.1 Ω and of 0.1% accuracy. The monitor outputs are less than the coil currents by about 1.2% but the difference is independent of the frequency. The monitor outputs were delayed against the real coil currents by 0.5 degree at the highest frequency of 50Hz.

The monitor outputs were measured and recorded in a personal computer with 12 bit AD converters with sample and hold function which are 0.2% accurate over a +/- 10V range. All converters were adjusted to 5mV error at most in their whole range with a reference voltage generator of 0.01% accuracy. The coil currents and the magnetic field intensity components were measured at the same time.

The Hall sensors, THC126 (Toshiba), were used to measure the magnetic field intensity components at the 8 points shown in Figure 2. H_x is symbolized as H_9 here. Although the measurement of H_9 is not disturbance-free against the flow field, it is possible to measure H_9 like a wake survey in wind tunnel tests without serious affect on the test result. The sensors were driven in the constant current mode. They were calibrated with the model 9903 of F.W. BELL which is 0.1%FSR accurate. They showed good linearity between the Hall sensor outputs and the Gauss meter output. An example of the calibration test results are shown in Figure 3.

The model position was measured with an in-house-developed model position sensing system. The system was described in detail in Reference 3. The position sensor was calibrated by a calibration model of 8mm diameter wrapped with the same paper as the dynamic force calibration model. It was positioned on a stage which can very all positions in 6 degree of freedom. Some examples of the position sensor calibration test are shown in Figure 4. There are some interferences between measured positions, particularly in y and ϕ. The interference will induce some unexpected motion of the model.

The control speed of the MSBS measured 489.8Hz. The obtained model position by the sensor is delayed by 3.0ms from the measuring time of the coil currents because it is estimated

with CCD sensors as presented in Figure 5. The times and frequencies shown in the figure were measured with a universal pulse counter.

Dynamic Force Calibration Analysis

The model is assumed a perfect cylinder and is also assumed to be magnetized along the model axis like (m_x, 0, 0). The magnetic force components along the x, y and z directions acting on the suspended model can be approximated by the magnetic field intensity gradient about the model multiplied with m_x. The moments about the y and z axes can be also approximated by the magnetic field intensity about the model multiplied with (m_x, 0, 0). Then the moment components about the y and z axes are approximately proportional to the averaged H_z and H_y over the model, respectively. To monitor the magnetic field intensity about the model, the following combinations of the measured magnetic field intensity components are defined:

$$H_{drag}=\frac{H_1+H_2-H_3-H_4+H_5+H_6-H_7-H_8}{8},$$

$$H_{monitor} = H_9, \qquad I_{drag} = \frac{I_0+I_9}{2},$$

$$H_{side} = \frac{H_2 + H_4 - H_6 - H_8}{4}, \quad I_{side} = \frac{I_2 + I_4 + I_6 + I_8}{4}, \qquad \ldots (1)$$

$$H_{lift} = \frac{H_1 + H_3 - H_5 - H_7}{4}, \quad I_{lift} = \frac{I_1 + I_3 + I_5 + I_7}{4},$$

$$H_{pitch} = \frac{H_1+H_3+H_5+H_7}{4}, \quad I_{pitch} = \frac{I_1+I_3-I_5-I_7}{4},$$

$$H_{yaw} = \frac{H_2+H_4+H_6+H_8}{4}, \quad I_{yaw} = \frac{I_2+I_4-I_6-I_8}{4}.$$

The motion of the model gravity center satisfies the following equations:

$$m\ddot{x} = K_{drag} \cdot H_{drag}, \quad or \quad m\ddot{x} = K_{monitor} \cdot H_{monitor},$$
$$m\ddot{y} = K_{side} \cdot H_{side}, \qquad \ldots (2)$$
$$m\ddot{z} = K_{lift} \cdot H_{lift} - mg,$$

where K's are proportional constants between the quantities defined above and the corresponding force. The motion of model rotation about the y and z axes at the gravity center satisfies the following equations:

$$I_{yy}\ddot{\theta} = K_{pitch} \cdot H_{pitch},$$
$$I_{zz}\ddot{\psi} = K_{yaw} \cdot H_{yaw}, \qquad \ldots (3)$$

where K's are the similar ones as above mentioned. If motion is sinusoidal, the force driving the model motion varies sinusoidally as the motion. Besides, the motion and the force must be in

phase. The model was forced to make as pure a sinusoidal motion as possible in the dynamic force calibration test. By examining the phase between the motion and the quantities defined in the above equations, it can be estimated whether or not the quantities are suitable for evaluating the dynamic force.

Dynamic Force Calibration Test Results

Heaving Motion

Figure 6 shows trajectories of H_{lift}, I_{lift} and z position of the model with respect to time during a 10Hz heaving motion. The three quantities are normalized with their rms values. H_{lift} and z are perfectly in phase. The waveforms of the two also look like a single frequency sinusoidal oscillation. Figure 7 shows also H_{lift}, I_{lift} and z vs. time during a 20Hz heaving motion. The same observation can be remarked as in the 10Hz motion. This fact confirms that H_{lift} is directly proportional to the force in the z direction. On the contrary, there is observed apparent phase difference between $-I_{lift}$ and z. This suggests that I_{lift} is not proportional to the force unlike H_{lift}.

The rms value of the force during the heaving motion was evaluated from the measured z position of the model. Figure 8 shows the relation between H_{lift} and the force in their rms values. The symbol of x shows the case of changing amplitude of 10Hz heaving motion. A dotted line in the figure is a least square approximation line fitted to the results in the amplitude change case. The symbol of an open circle shows the case of changing frequency between 1 to 30Hz with various amplitudes. The open circles are on the approximation line except for frequencies less than 5Hz. The results at frequencies higher than 30Hz are not on the line. One of the causes is poor magnetic field control because of large induced electromotive force. The maximum error of the dynamic force balance in the z direction reduces to about 2.4% in the region of the figure. The error is observed in a 1Hz heaving motion and its value is 2mN. The change of coil currents is about the resolution of the current amplifier units at the frequency. Then, suitable control of the magnetic field cannot be expected. The fact suggests that a core permanent magnet must be chosen to meet test requirements. When a small force in the z direction is measured, a weaker and light magnet must be used.

Figure 9 also shows that relation between the force and I_{lift} in their rms values. The symbols are the same as in Figure 8. Although the results in the case of amplitude change are on a line, the results in the case of frequency change are not. They show a frequency dependence when the frequency is higher than 10Hz. It means that the obtained data must be compensated by the effect of frequency dependence if dynamic force is estimated with I_{lift}. The magnetic circuits of the 10cm MSBS are made of iron blocks and have hysteresis loss dependent on frequency. This is suspected to be the cause of the frequency dependence.

Pitching Motion

Figure 10 shows trajectories of H_{pitch}, I_{pitch} and θ of the model attitude with respect to time during 10Hz pitching motion. The three quantities are normalized with their rms values. H_{pitch} and θ are in phase. The waveforms of the two also look like single frequency sinusoidal oscillations. Figure 11 shows also H_{pitch}, I_{pitch} and θ vs. time during 20Hz pitching motion. Although H_{pitch} and θ are in phase independently of frequency, H_{pitch} trajectory differs from a pure sinusoidal waveform around its peaks. H_{pitch} is approximately proportional to the torque about the y axis according to the figures. On the contrary, there is observed apparent phase difference between I_{pitch} and θ. This suggests that I_{pitch} is not proportional to the torque unlike H_{pitch}.

The rms value of torque about the y axis (pitching moment) was evaluated from the measured θ. Figure 12 shows the relation between the pitching moment and H_{pitch} in their rms values. The symbols are the same as in the case of the heaving motion test. The open circles are not on the approximation line. The similar difference between the two kinds of tests is found in the relation between pitching moment and I_{pitch} as shown in Figure 13. The difference is larger than in Figure 12 with pitching moments larger than 0.7mNm. It suggests that the frequency dependence lies in the moment evaluation by I_{pitch} as in the heaving motion test. The open circles and cross symbols in the range less than the pitching moment of 0.2mNm are not on a line. The cause is that I_{pitch} and H_{pitch} are very small and nearly out of the controllable range. Figure 14 shows the H_{pitch}, I_{pitch} and θ vs. time during 4Hz pitching motion. The model position is controlled but H_{pitch} and I_{pitch} are scattered around the pitch angle trajectory. The other open circles are approximately on a line but the line is different from the line approximated by the cross symbols. It means the relation between pitch angle and H_{pitch} depends on the frequency. The cause of it has not yet been isolated.

Oscillation in the x direction

Figure 15 shows H_{drag}, I_{drag}, and $H_{monitor}$ and x position with respect to time during 10Hz oscillating motion in the x direction. The four quantities are normalized with their rms values. Either of four is not perfectly in phase with z. $H_{monitor}$ is the most in phase with z of the three. The rms value of the force in the x direction was evaluated from the measured x position of the model. Figures 16, 17, and 18 show the relations between the force and H_{drag}, I_{drag}, $H_{monitor}$, in their rms values. Results in the frequency change are nearly on a line approximated by those in amplitude change at 10Hz in the case of using $H_{monitor}$. The other two cases show the frequency dependency. But results in the case of frequency change are nearly on a line approximated by those in amplitude change only around 10Hz in case of using I_{drag}. One of the causes is the air-cored drag coils without the hysteresis loss by iron cores.

Oscillations in the y direction and about the z axis

Figure 19 shows H_{side}, I_{side} and y position of the model with respect to time during 10Hz oscillation in the y direction. The three quantities are normalized with their rms values. Three waveforms do not look sinusoidal at all. It means that the control is not adequate. Cause of the distorted waveforms is the poor accuracy in y of the model position sensor. The rms value of force in y was evaluated from the measured y position of the model. Figures 20 and 21 show the relations between the force in the y direction and H_{side}, I_{side} in their rms values. Results in the two test cases are scattered around a line which is approximated by the amplitude change tests at 10Hz.

Figure 22 shows H_{yaw}, I_{yaw} and ϕ position of the model with respect to time during 10Hz oscillating motion about the z axis. The three quantities are normalized with their rms values. Three waveforms do not look sinusoidal. It means that the control is not adequate. Cause of the distorted waveforms is the poor accuracy in ϕ of the model position sensor. The rms value of yawing moment was evaluated from the measured ϕ of the model. Figures 23 and 24 show the relations between the yawing moment and H_{yaw}, I_{yaw} in their rms values. Results in the two test cases are scattered around a line which is approximated by amplitude change tests at 10Hz.

STATIC FORCE CALIBRATION TEST AT THE 60CM MSBS

A preliminary static force calibration test was carried out at the 60cm MSBS. The 60cm MSBS is the largest in its test section size, which is described in References 1 and 2. It is operated in 5 degree of freedom control. But y position and yaw angle control is very slow because of poor accuracy of the model position sensor in those directions. Only axial force was calibrated by pulling the model with 100g scale weights and measuring the drag coil currents. Figure 25 shows a picture of the test. The model is 381mm long and 55mm diameter and it contains a cylindrical permanent magnet core of Fe-Cr-Co magnet which is 50mm diameter and 300mm long. In order to measure the model position, the model was wrapped with a thin white paper as in the case of the 10cm MSBS model. The whole mass of the model measured 5.1kg. The model was supported by the control of 5 degree of freedom except for rolling motion. Drag coil current was measured with monitor output of a power amplifier unit for the drag coil. The monitor outputs of the 5 power amplifiers are accurate of 0.1% FSR up to 75A for constant output. The monitor output was measured and recorded by a FFT analyzer. The model position was measured with the same typed model position sensing systems at the 10cm MSBS. The position sensor was calibrated with the model. It was positioned on a stage which can very all positions in 6 degree of freedom. The control speed of the MSBS measured 248Hz. The obtained relation between the drag coil current and applied load is shown in Figure 26. Apparent hysteresis is observed. Drag force calibration tests were carried out several times. Hysteresis is observed every time. Figure 27 shows the results of another test in which the axial load increases and decreases in small steps of about 10g. Large hysteresis is observed.

REMARKS

Magnetic field intensity and coil currents of the 10cm MSBS were measured when a cylindrical model was oscillated along x, y, z and also about y and z axes, respectively. Two kinds of tests were carried out. Amplitude of the oscillation varies with constant frequency of 10Hz in one mode. Frequency varies from 1 to 50Hz in the other mode.

In case of heaving motion, H_{lift} and z position are in phase but I_{lift} and z are out of phase. The relation between H_{lift} and the force in z direction is very linear in the tested range and is also independent of the frequency below 30Hz at the 10cm MSBS. On the contrary, the relation between I_{lift} and the force is not linear but also depends on the oscillation frequency. H_{lift} can be used for estimating lift force acting on a model in motion.

In case of pitching motion, θ trajectory looks like a pure sinusoidal waveform but H_{pitch} trajectory differs from a pure sinusoidal waveform around its peaks although H_{pitch} and θ are in phase. I_{pitch} and θ are out of phase. The relation between H_{pitch} and pitching moment is linear but depends on the test modes. The cause of the test mode dependence has not been isolated yet. The relation between I_{lift} and the moment is not linear but also depends on the frequency.

x position trajectory looks like a good sinusoidal waveform but H_{drag}, $H_{monitor}$ and I_{drag} trajectories do not look like good sinusoidal waveforms. x and either of the three is not apparently in phase. The relation between H_{drag} and the force in the x direction is linear but depends on the two test modes. $H_{monitor}$ and the force is linear and is also independent of the test mode. It suggests that the relation is independent of the frequency. The relations between I_{drag} and the force and between H_{drag} and the force are linear but depend on the test modes.

Oscillations in the y direction and about the z axis are not pure sinusoidal ones because of poor accuracy in y and ϕ of the model position sensing device at the 10cm MSBS. The relations between H_{side} and the force in the y direction and between I_{side} and the force look linear but are not reliable to estimate the force from the measured H_{side} or I_{side}. The relations between H_{yaw} and the yawing moment and between I_{yaw} and the moment also look linear but are not reliable either.

At the 60cm MSBS, drag force calibration tests were carried out. The results show large hysteresis between load and drag coil current. The cause has not been isolated yet.

REFERENCES

1. Sawada, H.; Suenaga, H.; Suzuki, T.; and Ikeda, N.: Status of MSBS Study at NAL. NASA CP-3247, May 1994, pp. 275-289.

2. Sawada, H. and Suenaga, H.: Magnetic Suspension and Balance Systems at NAL. Conference Proceedings of PICAST' 1, December 1993, pp. 1014-1021.

3. Sawada, H.; Kanda, H.; and Suenaga, H.: The 10cm x 10cm Magnetic Suspension and Balance System at the National Aeronautical Laboratory. AIAA91-0397, January 1991.

4. Eskin, J.: An Investigation into Force/Moment Calibration Techniques Applicable to a Magnetic Suspension and Balance System. NASA CR-181695, August 1988.

5. Kohno, T.; Sawada, H.; Suenaga, H.; and Kunimasu, T.: NAL 0.6m x 0.6m MSBS - the Latest Development. Proceedings of the 33rd Aircraft Symposium, November 1995, pp. 345-348.

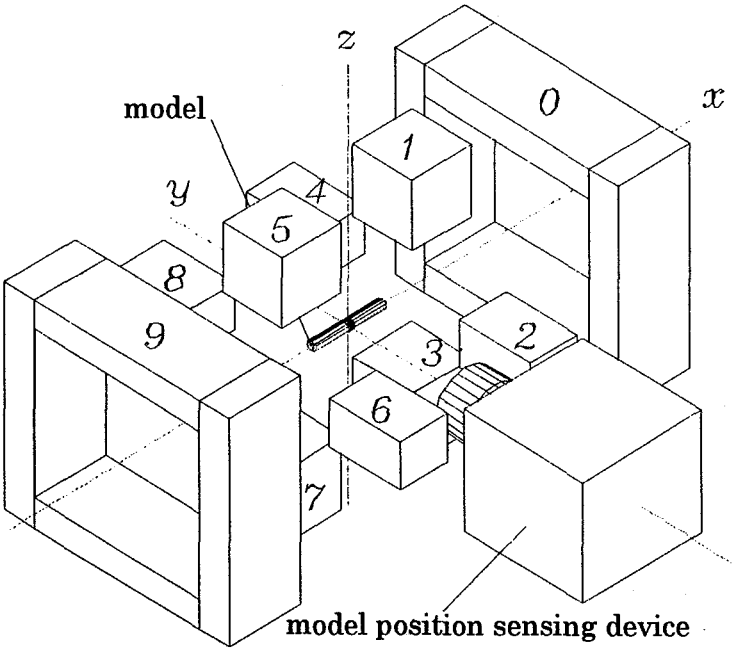

Figure 1 coil number at the 10cm MSBS

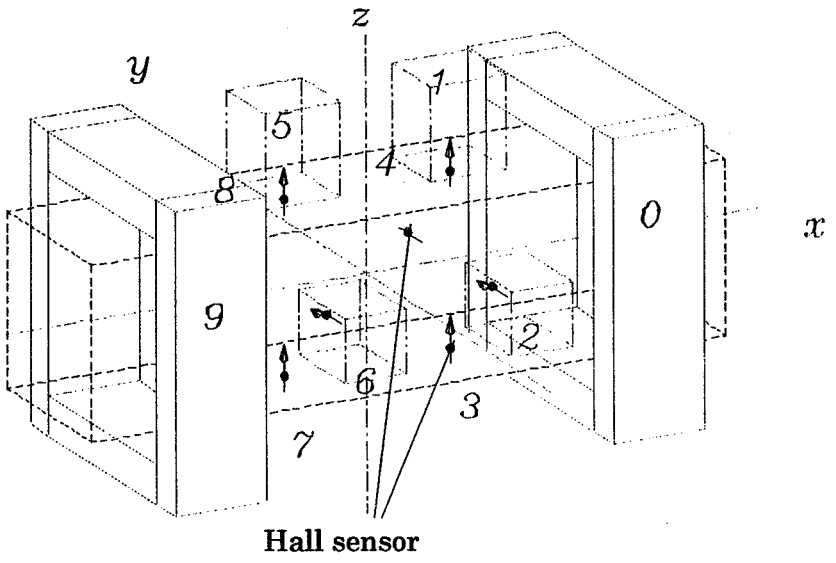

Figure 2 Hall sensor position

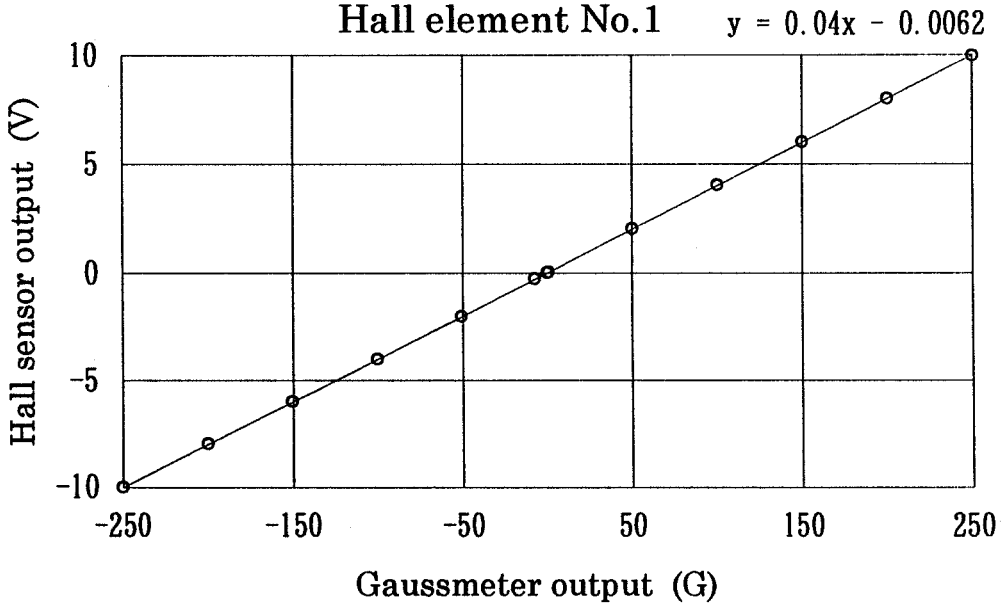

Figure 3 Hall sensor calibration test result

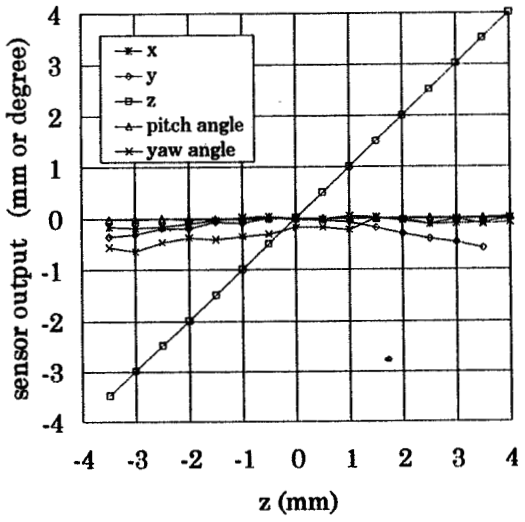

Figure 4 model position sensing device calibration test result

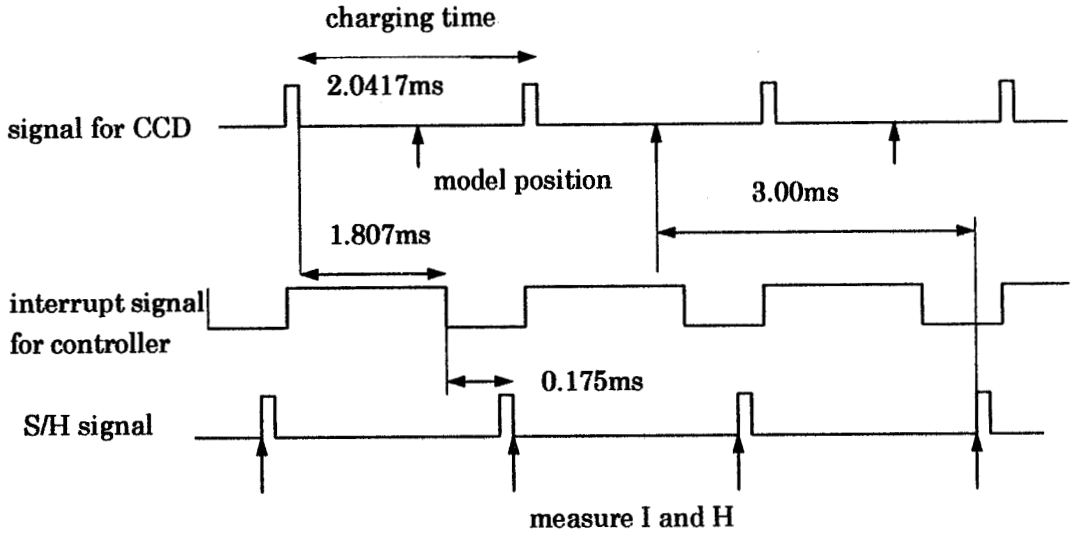

Figure 5 data acquisition timing diagram

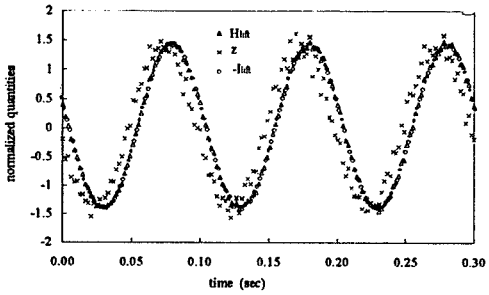

Figure 6 z,H_{lift},I_{lift} vs. time (10Hz)

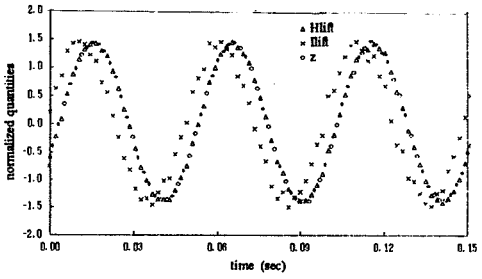

Figure 7 z,H_{lift},I_{lift} vs. time (20Hz)

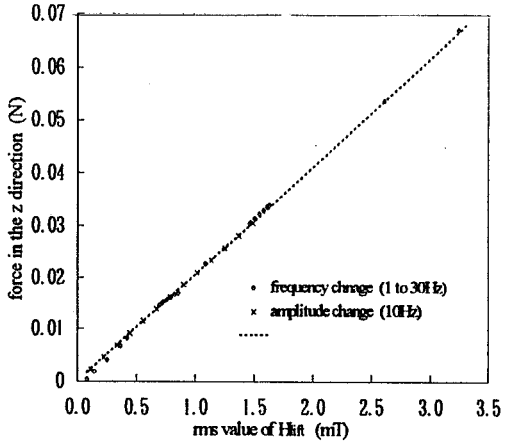

Figure 8 relation between H_{lift} and vertical force

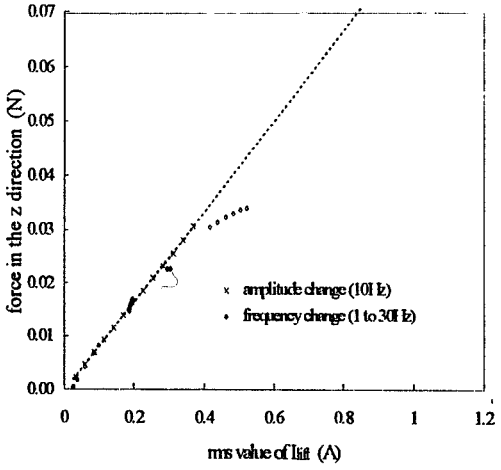

Figure 9 relation between I_{lift} and vertical force

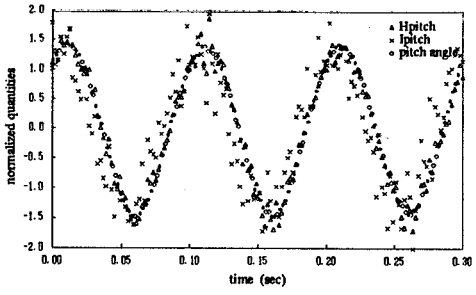

Figure 10 θ ,H_{pitch},I_{pitch} vs. time (10Hz)

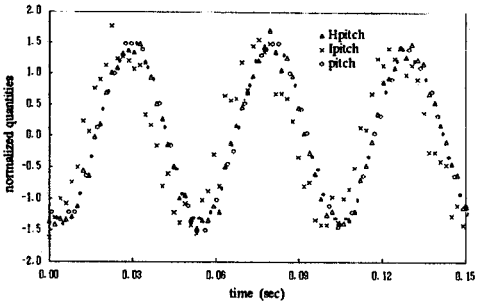

Figure 11 θ ,H_{pitch},I_{pitch} vs. time (20Hz)

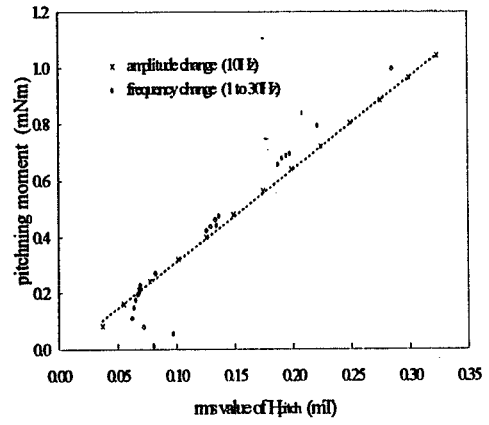

Figure 12 relation between H_{pitch} and pitching moment

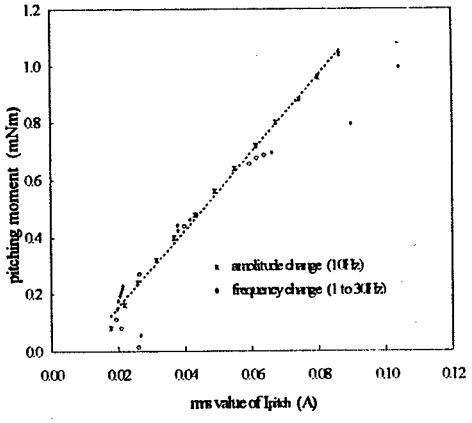

Figure 13 relation between I_{pitch} and pitching moment

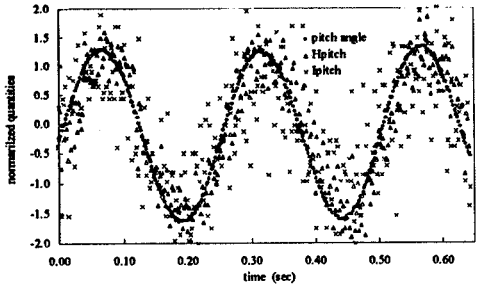

Figure 14 θ ,H_{pitch},I_{pitch} vs. time (4Hz)

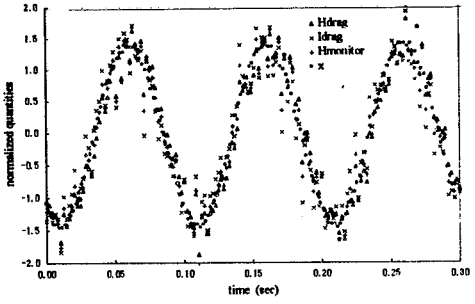

Figure 15 x,H_{drag},$H_{monitor}$,I_{drag} vs. time (10Hz)

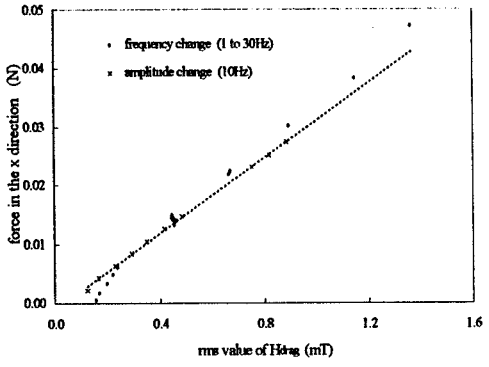

Figure 16 relation between H_{drag} and force in the x direction

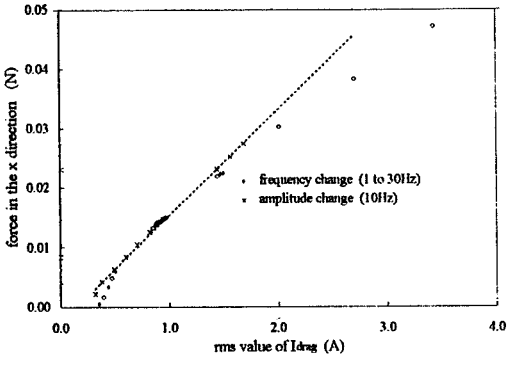

Figure 17 relation between I_{drag} and force in the x direction

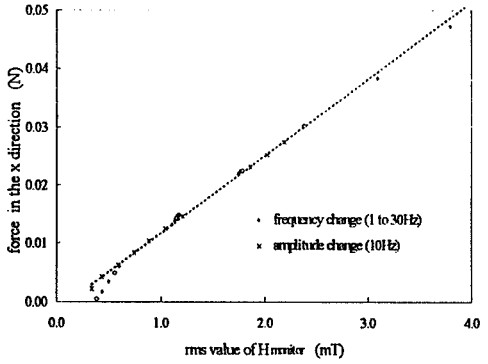

Figure 18 relation between $H_{monitor}$ and force in the x direction

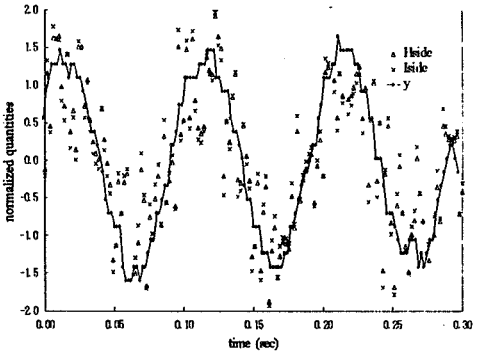

Figure 19 y, H_{side},I_{side} vs. time (10Hz)

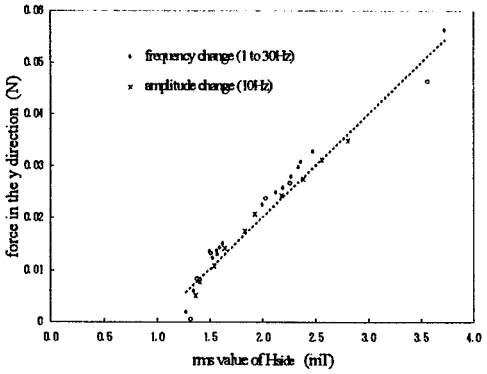

Figure 20 relation between H_{side} and force in the y direction

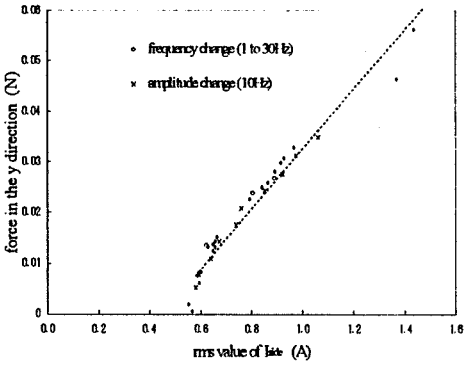

Figure 21 relation between I_{side} and force in the y direction

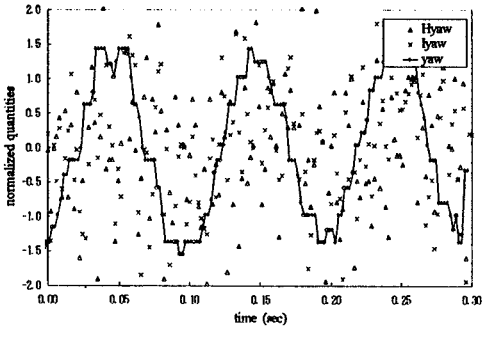

Figure 22 ϕ ,H_{yaw},I_{yaw} vs. time (10Hz)

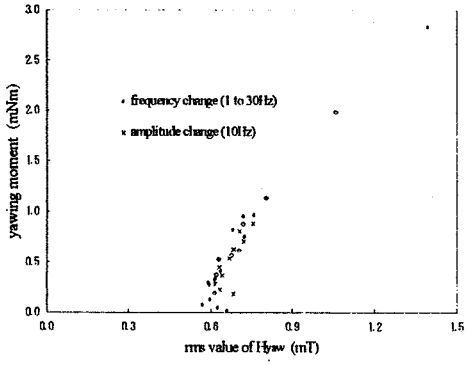

Figure 23 relation between H_{yaw} and yawing moment

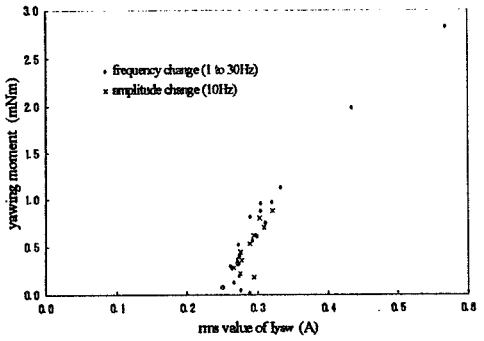

Figure 24 relation between I_{yaw} and yawing moment

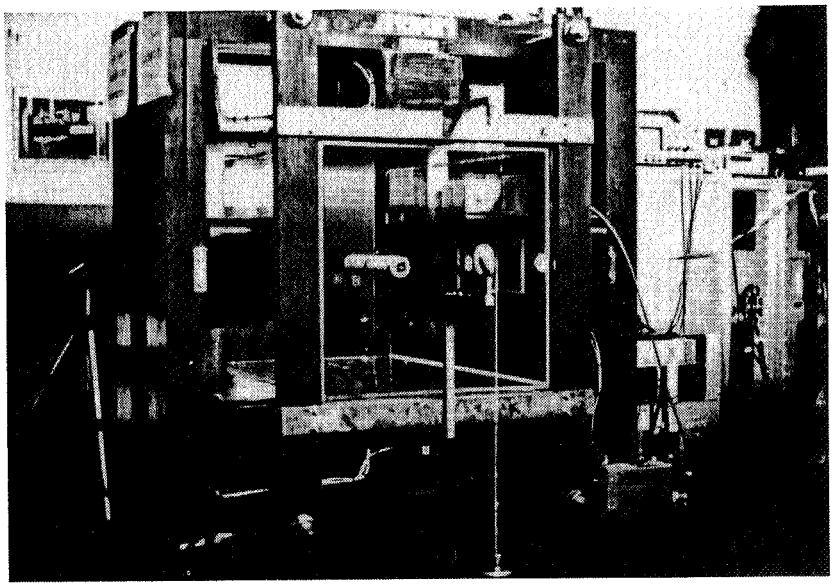

Figure 25 drag force calibration test

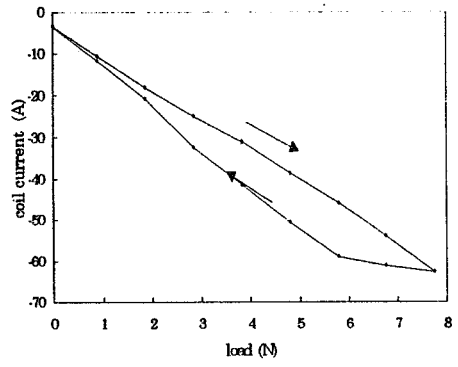

Figure 26 drag coil current vs. load (wide range)

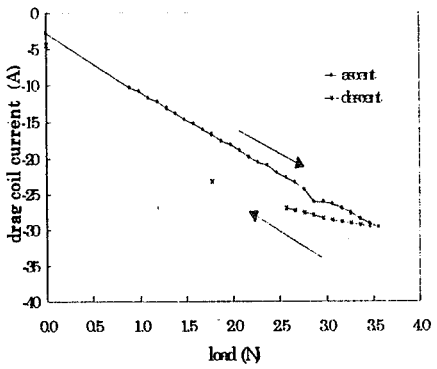

Figure 27 drag coil current vs. load (small steps)

Session 14 -- Maglev 2

Chairman: Tim Lynch
Florida State University

DEVELOPMENT OF A LARGE SCALE, HIGH SPEED WHEEL TEST FACILITY

Anthony Kondoleon & Donald Seltzer
C. S. Draper Laboratory
&
Richard Thornton & Marc Thompson
Massachusetts Institute of Technology
Cambridge, MA 02139

ABSTRACT

Draper Laboratory, with its internal research and development budget, has for the past two years been funding a joint effort with the Massachusetts Institute of Technology (MIT) for the development of a large scale, high speed wheel test facility. This facility was developed to perform experiments and carry out evaluations on levitation and propulsion designs for MagLev systems currently under consideration. The facility was developed to rotate a large (2 meter) wheel which could operate with peripheral speeds of greater than 100 meters/second. The rim of the wheel was constructed of a non-magnetic, non-conductive composite material to avoid the generation of errors from spurious forces. A sensor package containing a multi-axis force and torque sensor mounted to the base of the station, provides a signal of the lift and drag forces on the package being tested. Position tables mounted on the station allow for the introduction of errors in real time. A computer controlled data acquisition system was developed around a Macintosh IIfx to record the test data and control the speed of the wheel.

This paper describes the development of this test facility. A detailed description of the major components is presented. Recently completed tests carried out on a novel Electrodynamic (EDS) suspension system, developed by MIT as part of this joint effort are described and presented. Adaptation of this facility for linear motor and other propulsion and levitation testing is described.

BACKGROUND

Magnetically levitated high speed ground transportation technology (MagLev) was experiencing an increased interest in the United States in the early 1990's as a potential solution to increasing highway and air corridor congestion. The Intermodal Surface Transportation Efficiency Act of 1991 (ISTEA) had mandated the development of a prototype MagLev demonstration system in the United States. During the period of 1991 and 1992, Draper Laboratory was involved in study contracts from the Department of Transportation (DOT) in the high speed ground transport area. One study (1) was in the area of aerodynamic forces on MagLev vehicles. This study produced a low drag nose profile, the relationship of width to length ratio on passenger energy, the effect of lift and drag due to wing surfaces on the vehicle body, and the effect of wing surfaces on ride quality. A second contract (2) carried out a comparison of EDS and Electromagnetic (EMS) levitation concepts.

In 1991, Draper Laboratory and MIT joined the Bechtel team for one of four System Concept Definition contracts awarded by the DOT. Other members of our team included G. M. Electromotor Division and Hughes Ground System Group (3). Our team concept was an EDS system which used a novel configuration of vehicle mounted, flux canceling magnets. The vehicle contained six sets of eight superconducting magnets per side which straddled a concrete box-beam

guideway. The interaction of the vehicle magnets and the guideway sidewall, which contained a laminated aluminum ladder design, generated lift. A similar interaction with guideway mounted null-flux coils provided the guidance. The vehicle's propulsion was generated by a Linear Synchronous Motor (LSM) whose windings were also attached to the guideways sidewalls. Centrally controlled wayside stations provided the required variable-frequency, variable-voltage power for the LSM drive. The teams vehicle consisted of a single car with an inner tilting shell. It was designed to use aerodynamic control surfaces to augment the magnetic guidance forces. The guideway consisted of a post-tensioned concrete box girder. The switch was to be a bendable beam constructed from fiber reinforced plastic (FRP).

PROBLEM AREA

The Bechtel team concept for the MagLev vehicle was based on a EDS system for levitation and guidance using superconducting magnetics on the vehicle and an arrangement of electrical conductors on the guideway. The magnetic suspension system was the most important, but least understood part of our proposed EDS MagLev system. Thorough understanding of such systems, with verified analytical design techniques, were essential to formulating improved designs for successful full scale systems. While the EDS technology has many positive features, the ability to operate with large gaps for one, major questions are unanswered. A major question has to do with the particular aspect of the interaction between the superconducting magnets on the vehicle and the conductors on the guideway.

The technological cornerstone of the claimed superiority of the EDS MagLev system is the superconducting magnet. One of the critical issues affecting the potential viability of such systems is that of the magnitude and effects of AC losses in the superconducting coils which provide the levitation and guidance for the vehicles (while superconductors have zero losses for DC currents, losses do occur for AC currents). These losses, caused by the AC magnetic fields resulting from the variations of the electrical currents in the guideway which provides the levitation and guidance forces, have at least two effects that are significant for EDS MagLev systems. First, they increase the thermal load on the cryogenic refrigeration system, either reducing the safety margin, or requiring the use of more powerful (larger, more expensive, higher power) refrigeration systems. Second, and potentially more serious, they may result in the decrease of the magnet current over time; and if sufficiently rapid, cause touchdown during motion.

We felt that it was important to establish early on the nature and extent of such AC losses in superconducting coils used for MagLev levitation, and guidance, so that their implications for the design and operation of EDS MagLev systems could be understood and addressed.

SOLUTION PLAN

In 1992, Draper with its Internal Research and Development budget undertook a multi-year project to formulate a series of experiments to provide some needed quantitative information on AC losses in superconducting coils for EDS MagLev systems. The initial approach was to examine the use of Draper's centrifuge for near full size testing of MagLev suspension and propulsion designs (4). The centrifuge with its long arm (35 ft.) and high G (200), and high load (7500 lbs) capacity was found suitable for use. Unfortunately, neither a firm design or firm outside funds were available to pursue this facility further. Draper and MIT in 1993 chose to develop a facility which would be more cost effective to construct while being large enough in size to avoid many problems involved with sub-scale testing.

MAGNETIC SCALING PROBLEM

Scale model experiments involving magnetic structures face a fundamental difficulty due to dimension scaling problems. If all dimensions are increased by a factor *d*, the forces and power loss scale in different ways with efficiency improving as size increases. For example, an induction generator has an efficiency that decreases as the size decreases until for a sufficiently small machine the power loss exceeds the power generated and no net power generation is possible! In contrast, a 1 Megawatt version of this same machine can generate power with an efficiency of 98%. Dealing with these scaling problems is a fundamental issue that must be addressed in the design. We do not know of any other test facility that has dealt with the magnetic scaling laws in a satisfactory way.

The objective is to design a facility that has high enough performance that we can operate on the high speed side of the drag peak. The drag force (D) for virtually all EDS systems has the form:

$$D = abu/(b+u)^2$$

where *a* and *b* are design parameters and *u* is the vehicle speed. Parameter *a* has dimensions of force and is proportional to the square of the vehicle coil current. This constant increases with size, but the scaling laws are simple so we can extrapolate from measurements of small forces. Parameter *b* is the speed at which the drag reaches its maximum value and it scales inversely with size. Hence a 1/5 scale model will have its drag peak at 5 times the speed of the drag peak for a full size system. The full size version of our SCD suspension had an estimated drag peak of 20m/s. A 1/5 scale model would have this peak at 100m/S. For meaningful test data, it is important to operate to the high side of the drag peak, hence a maximum speed above 100 m/s would be the goal for a 1/5 size test facility.

FACILITY DEVELOPMENT

The joint Draper, MIT effort was to design and build a high speed wheel test facility which would operate above the drag peak of the proposed 1/5 scale EDS suspension systems. This wheel facility was designed to assure that the characteristics necessary for successful execution of a test program were realized. Requirements for the facility included the following:

1. Protection/containment provisions as necessary to ensure safe operation of the apparatus. This is essential due to the high surface speed of the wheel.

2. Peripheral speed of the order of 100 meters/second.

3. The wheel rim, where the simulated guideway conductors would be mounted, would be non-magnetic and non-conductive material to avoid generation of spurious forces and power losses.

4. Provisions for mounting an instrumented sensor package for measurement of forces and torques on the simulated vehicle.

5. Flexible design for accommodating a wide range of suspension/propulsion systems concepts as practical. Capability for testing both EMS systems and EDS systems.

6. Provisions for introducing errors and movement to the vehicle while the wheel is rotating. Position errors in the X, Y, Z and ø axis.

All the above requirements were met with the design of the system (Figure 1). The drive system for the wheel is a variable speed 10 Hp motor with a brake system which has driven the wheel assembly up to 1200 RPMs, > 115 m/s. The main shaft of the wheel is 8 feet long and 3 inches in diameter. One end contains the belt drive system attached to the motor drive system. The second side contains a four foot diameter, 1 inch thick aluminum disk which holds the test rim being rotated. The maximum diameter of the test rim is 68 inches to accommodate the width of the test pit where the facility is located (Figure 2). The static part of the test article is mounted to a multi-axis force sensor assembly. This sensor can read in real time the three components of the force and 3 components of torque being exerted on the assembly during test. Located in this base package are proximity sensors for magnetic air gap measurements and linear and rotary tables for error introduction in real time.

The Test Data Acquisition System is a computerized station for real time acquisition, processing, display, and storage of sensor data during tests in the facility. The system is comprised of a Macintosh IIfx, data acquisition computer, electronics console, motor controllers, specialized software and external sensors. Key parameters are monitored during tests in the facility. Summary data is recorded in the form of plots and spreadsheet compatible data files. Sensors include the multi-axis force sensor to measure forces and torques acting upon the test article, gap sensors to measure the magnetic air gap, rotation sensors to measure wheel speed, and temperature sensors to measure shaft bearing temperature. Figure 3 shows the system inter-connections. The data acquisition and control computer contains 8M RAM and a 20M hard drive, a National Instruments NB-MIO-16 analog/digital interface card with 16 multiplexed channels of analog input, 8 bits of digital I/O, and 3 counter/timers. Four analog channels are used to acquire gap and temperature sensor data, eight channels have been allocated for coil current measurement and two of the counters for measuring wheel speed. The computer also has two serial ports. One of these is used for communicating with the digital interface of the multi-axis force sensor using RS-232 protocol, while the other port is connected to the main motor controller.

The data acquisition computer software was developed in HyperCard, which is a combined development and run-time programming environment. The data acquisition software is organized as sixteen cards, grouped into six backgrounds. Some of the cards are specifically designed as high-level operator screens. The others are means of grouping similar intermediate procedures and tables. Status information for numerical data, such as sensor readings, is shown in a text field. Status data can also be displayed as an icon attached to a button. The displayed icon can be switched either by hiding or showing the button, changing the highlight of the button, or by changing the icon assigned to the button. Other information is presented in graphical form. This includes input sensor data from the six axis force sensor. The processed data are plotted together against time on the "Plot" screen.

Actions of the systems are initiated by the operator clicking on a command button. This includes starting or stopping data recording, changing an operating mode, or switching operator screens. The operator may also enter or change parameters in certain text fields by first selecting the parameter and then typing the new value. The HyperCard environment automatically saves its state when the program terminates. Upon restarting, most data and operating modes will be retained. For permanent storage of data, there are command buttons for saving data as ASCII text fields with tab elimination of fields, which can be directly imported into a spreadsheet program.

Figure 4 shows the Main Menu screen. On this screen, the operator can run tests in which all of the sensors are periodically sampled. Sensor signal readings are displayed, along with the average value, minimum value, and maximum value recorded during the test run. Each sensor reading is also checked against previously set minimum and maximum limits. Sampling can be halted at any time, and later resumed. The results of a test run can also be stored to a disk file.

Figure 5 shows the Plot Screen. This screen provides an alternative data collection method to the Main Menu screen. The New Data button triggers a 5 second period during which force data is collected at 19 Hz. Any combination of the six force and torque components can be plotted versus time on the screen. The resulting plots can be printed, or the numerical data saved to a disk file in spreadsheet format.

SUSPENSION DEVELOPMENT

The suspension design for testing in the facility was developed by MIT under a two year Draper IR&D grant. This design would replace the two separate coil circuits required for the original SCD study with one for both guidance and levitation. This suspension design is based on the use of high temperature superconducting coils in a flux-canceling arrangement. One side of one section of this design is shown in Figure 6. The guideway is composed of multiple conductive aluminum coils. When the train is in the vertical null position (Figure 6a) at $z = z_o$ and traveling in the +y direction, there is no net time-varying magnetic flux through the levitating coils, and no net current induced around the loop. However, if the train's vertical position deviates from equilibrium (Figure 6b), the net changing flux through the coil loop induces currents in the loop. The resulting Lorentz force is a restoring force in this structure, and for small deviations from the null position, the train behaves like a mass and linear spring (Figure 6c). Eddy currents and circulating currents create a drag force acting on the train in the -y direction. This drag force must be overcome by the propulsion system in an actual MagLev system. There is also a sideways force (+x) generated by this suspension. In the full size MagLev train, there will be another octapole on the other side of the train, and the sideways force will be used to center the train in the guideway.

The original guideway design of this suspension was to be four layers of .050 thick aluminum with alternative patterns from layer to layer (Figure 7a). The structure built was two layers with each layer being .090 thick aluminum of one alternating pattern. The resulting pattern would form a closed conductive circuit when the pattern was passed through the magnetic field of the coils. The linear pattern was changed to a circular pattern for testing on the wheel. This pattern is shown in Figure 7b. The challenge of mounting this circular structure to the wheel was accomplished by imbedding the structure inside the composite rim. This eliminated the need for costly assembly procedures and costly hardware. The mounting hardware would need to have been non-magnetic as well as non-conductive. The original choice was to be number 8 or 10 titanium bolts and inserts numbering in the hundreds. The process chosen eliminated these components. The design also produces a smooth surface on the rim, thereby lowering the aerodynamic forces which would be generated by the wheel motion. Before being inserted into the rim, an insulation layer between the cutouts of the two layers was installed to prevent shorting of the top layer to the bottom except at the edges where it was desired. The two layers were riveted and spot welded together to form the contact necessary for the suspension to work. The vehicle coils were spaced at the pole pitch of .126 meters for the linear model and then curved to match the circular pattern of the suspension. The resulting vehicle coil assembly, with copper coils, and proximity sensors are shown in Figure 8.

PHASE I TEST PROGRAM

The objective of the Phase I Test Program was to verify the workings of the facility and the basic concept of the novel suspension. Both of these goals were met. The basic suspension was to utilize high temperature superconductor coils, but for this first phase program, standard copper coils would suffice.

The tests were carried out with a nominal magnetic air gap of .5 inches. The physical air gap between the face of the coils and the rim surface was approximately .050 inches. The tests were carried out by first setting the magnetic air gap and the elevation of the coil assembly to the

base. The elevation settings were altered in .5 inch increments from 0 to 2.5 inches. The speed would be increased to the desired level with the no coil current. Data would be taken with the coils not energized, in order to generate a baseline database of aerodynamic forces vs. wheel peripheral speed. Data would then be taken for 5 seconds as the coil was energized. This procedure was carried out for speeds up to 1100 rpms (108 m/s), past the design goal of 1000 rpms. The data showed the lift force changed as the null position was approached and changed sign as it was passed through. The maximum lift force occurred between the offset values of .75 and 1.25 inches from null. Above the 1.25 value, the lift force decreased. The drag force increases for these offsets as does the lateral or guidance forces which confirms the working of the system. Figure 9 shows sample data.

PHASE II TESTING

A cryostat and liquid nitrogen delivery system has been designed, constructed and tested, which will allow operation of the magnet assembly in a liquid nitrogen bath (Figure 10). Phase II testing will consist of testing the copper magnet in a bath of liquid nitrogen. The resistance of the copper coils at liquid nitrogen temperature will be significantly lower than at room temperature, therefore, more current and hence more magnetic field and forces may be generated without damaging the coils.

The existing magnet assembly retro-fitted with high temperature superconducting coils, and a one degree of freedom flexure will be installed so that movement will be allowed in the vertical direction. System dynamics and superconducting coil losses will be monitored under test conditions that would mimic actual train operating conditions. The viability of replacing a mechanical secondary suspension with an active magnetic suspension for the full-scale MagLev vehicle will be investigated. The mechanical flexure which allow movement in the vertical direction have been constructed and is currently under test.

PHASE III TESTING

High temperature superconducting (HTSC) coils are currently under construction. After successful completion of Phase II testing, the copper magnets will be retro-fitted with the HTSC coils, and Phase III testing will begin. The fixture will be used to characterize the behavior of a control system for a HTSC magnetic suspension, which is not well understood.

CONCLUSIONS

The multi-year effort to design and fabricate a large scale wheel test facility and test a proposed EDS MagLev suspension design has successfully been completed. A maximum wheel speed of 1100 rpm (108 m/s) surpassed the goal of 1000 rpms. Force and torque data were recorded for various offsets from the null position for coil currents up to 7 amps per coil.

The design of a cryostat bath for first testing the coil assembly at superconducting temperatures has been completed. The next two phases will carry out tests at these temperatures.

The facility can also be retro-fitted for linear propulsion testing. The addition of a generator to the drive system, for loading, and a slip ring assembly to the wheel for power is all that is required. Currently discussions are under way to utilize this facility for this type of testing.

Maglev Wheel Test Station

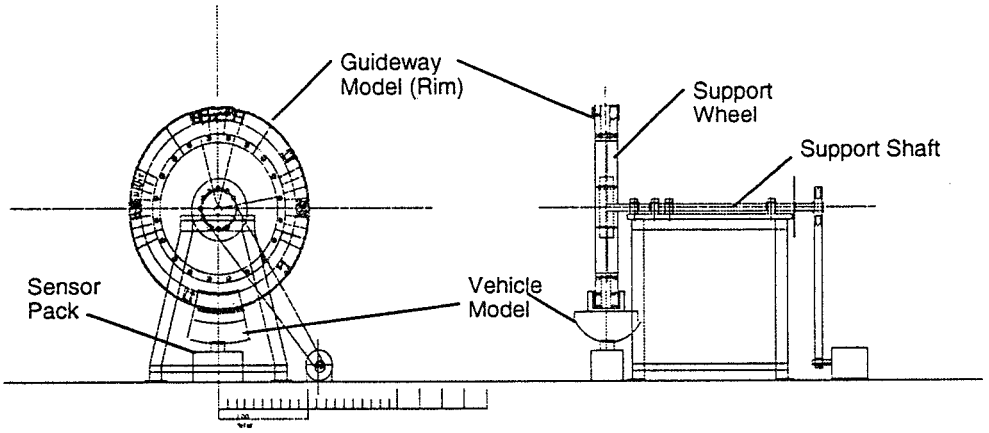

FIGURE 1

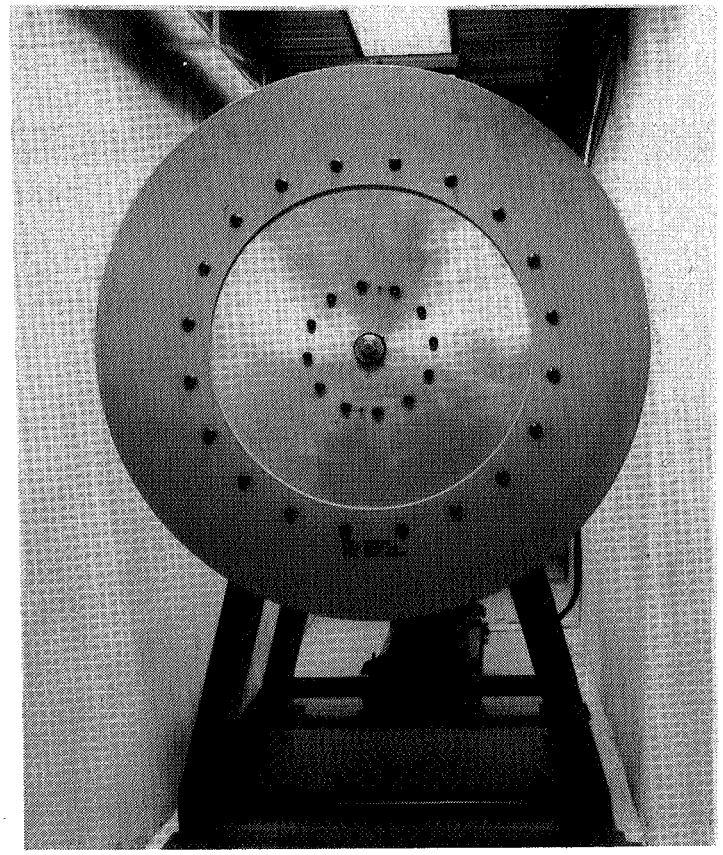

FIGURE 2

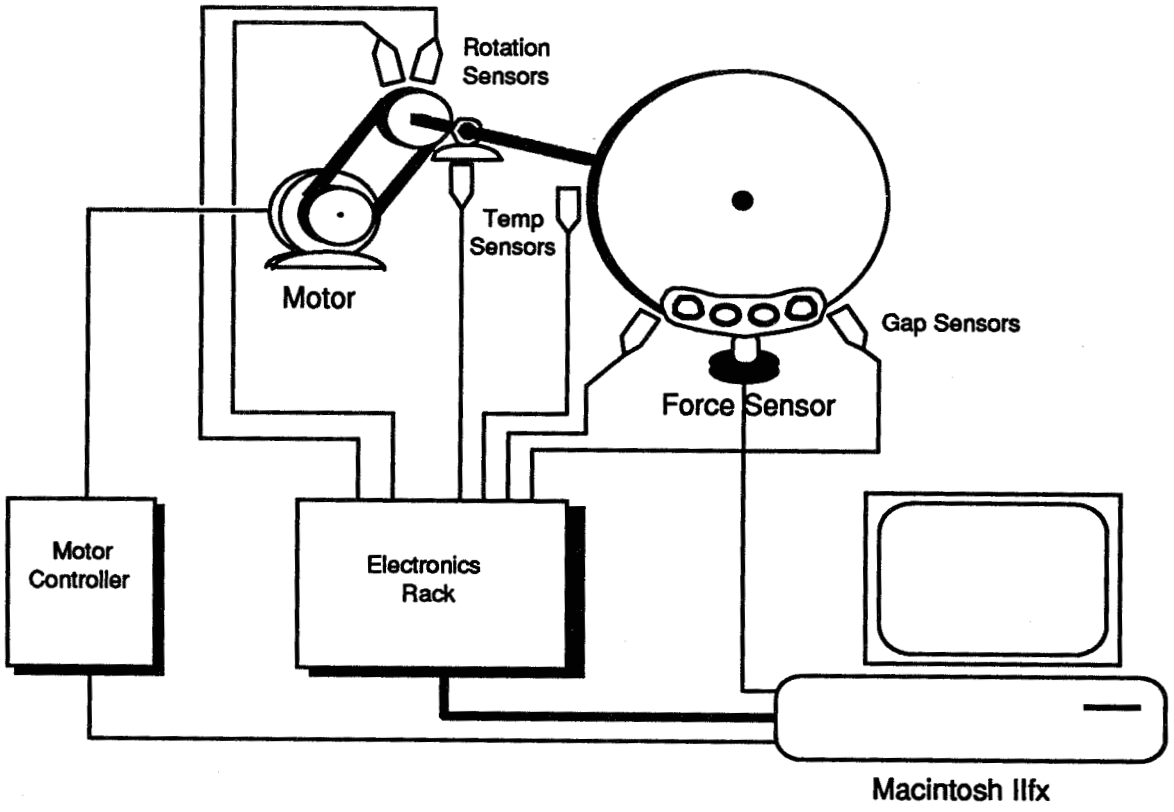

FIGURE 3

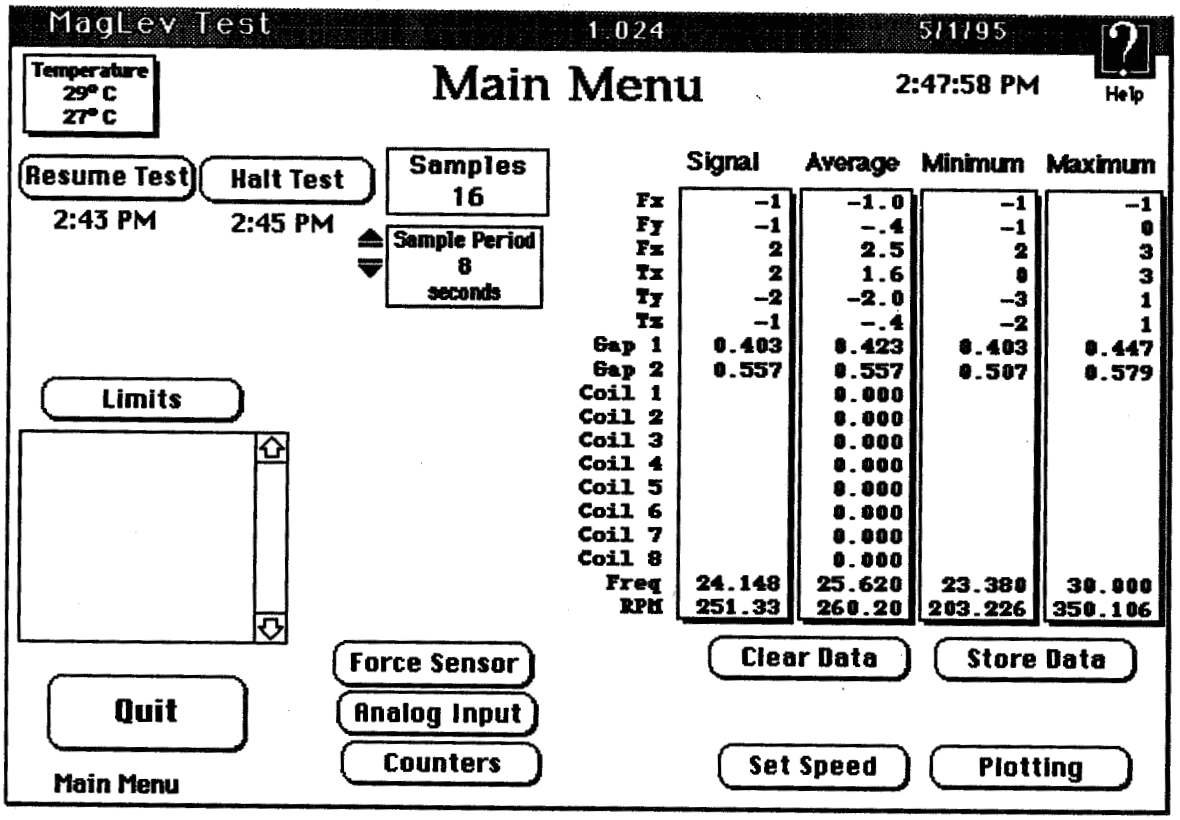

FIGURE 4

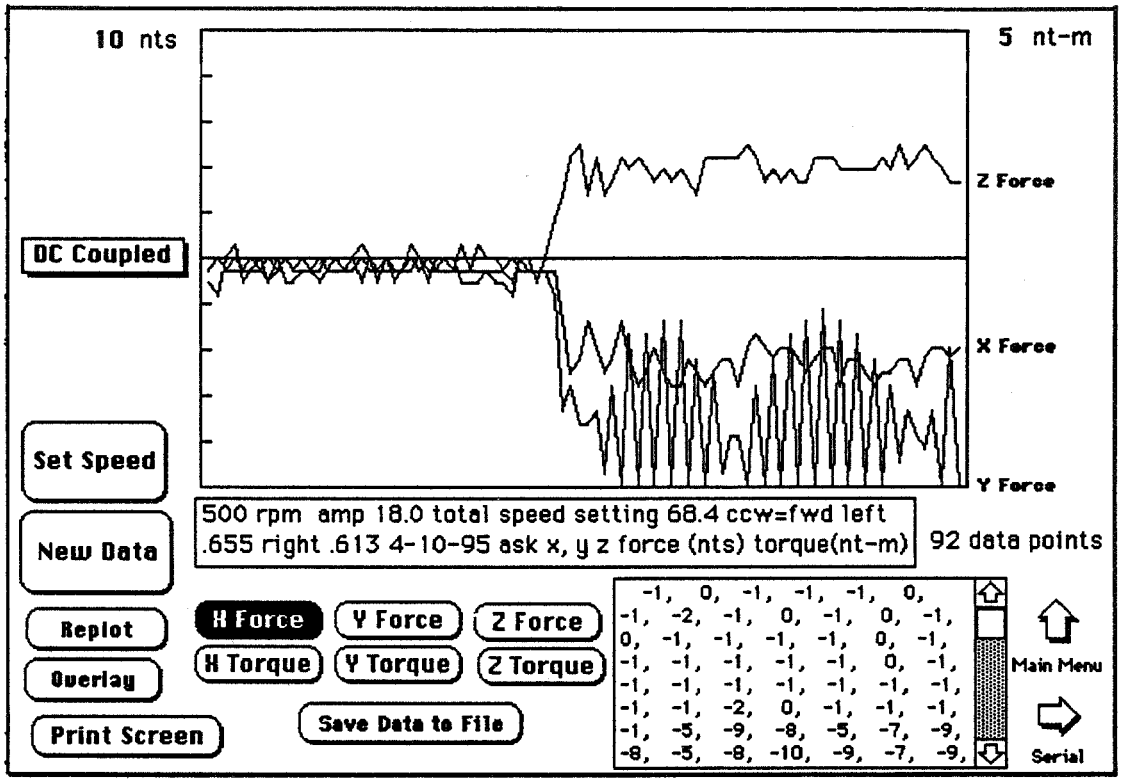

FIGURE 5

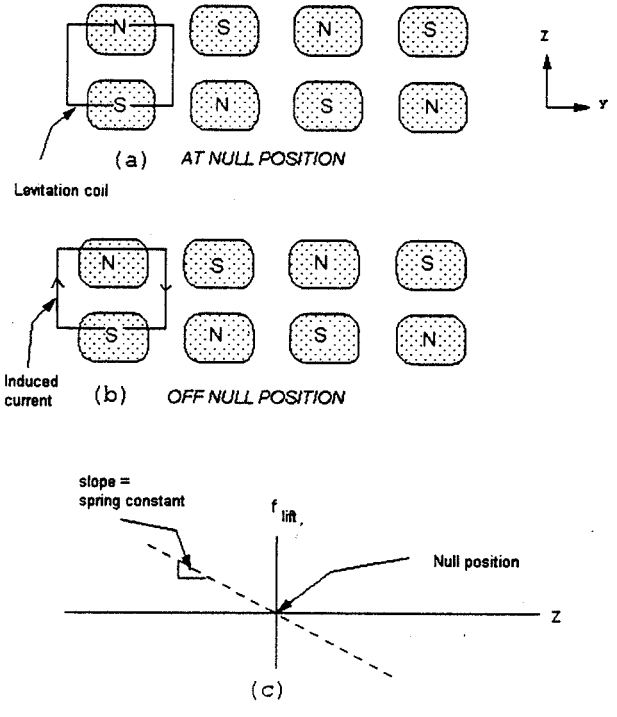

FIGURE 6

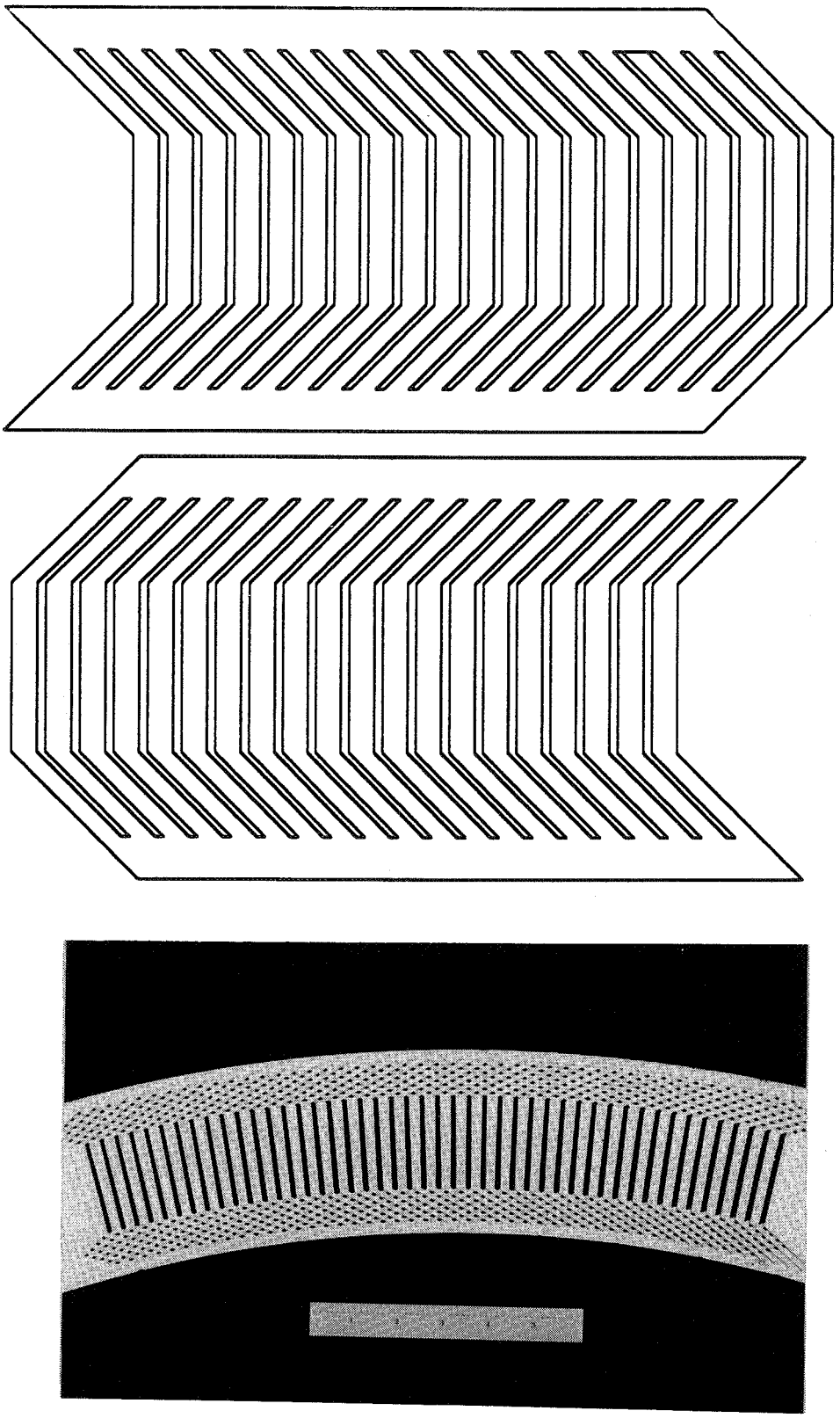

FIGURE 7

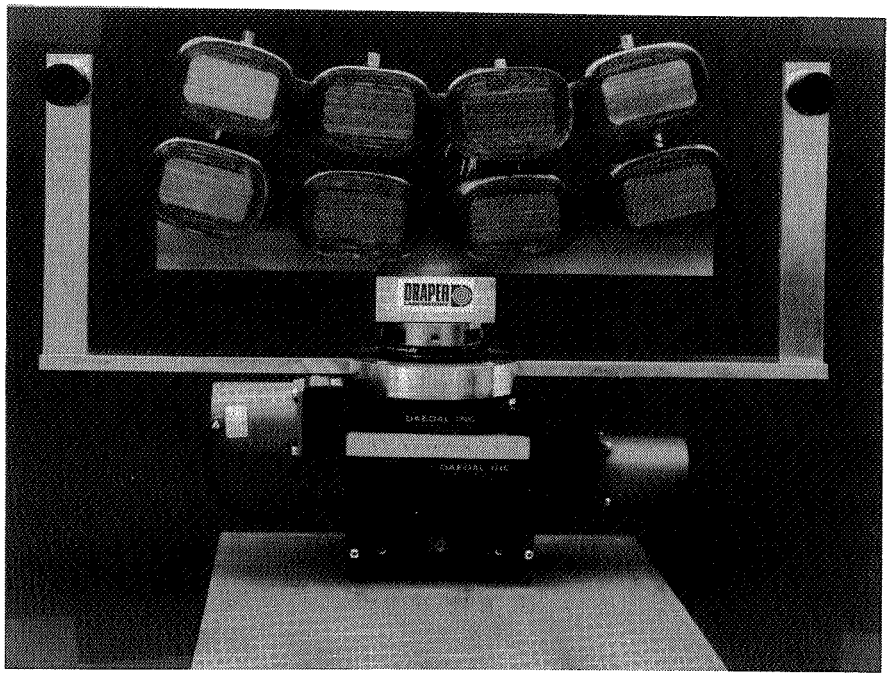

FIGURE 8

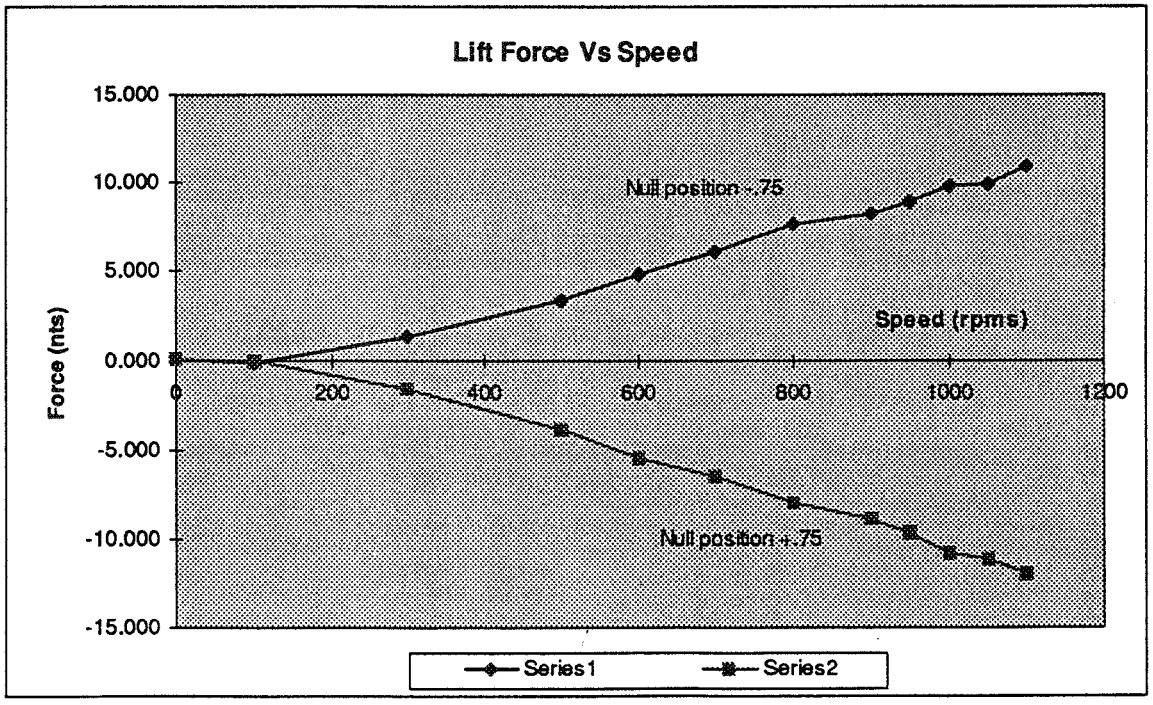

FIGURE 9

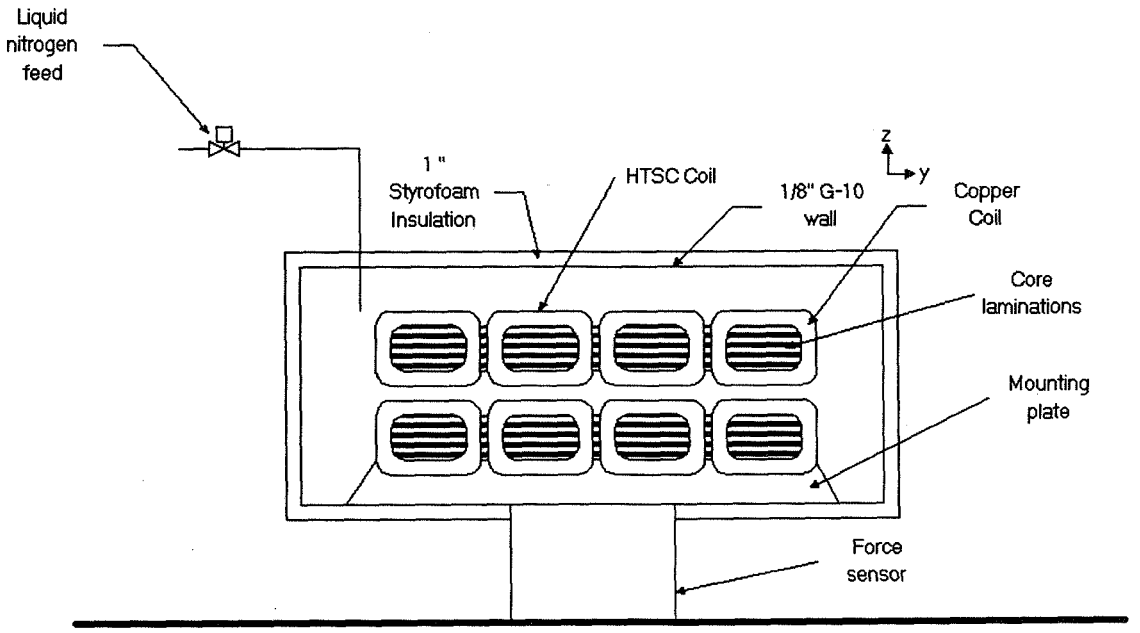

FIGURE 10

REFERENCES

1. Barrows, T.; McCallum, D.; Mark, S.; and Castellino, R.: "Aerodynamic Forces on MagLev Vehicle", DOT/FRA/NMI-92/21; December 1992.

2. Brown, W.; Dauwalter, C.; Heger, F.; and Weinberg, M.: "Comparison of Major Parameters in Electrodynamic and Electromagnetic Levitation Transport Systems, DOT/FRA/NMI-92/15, September 1992.

3. Final Report on National MagLev Initiative, September 1993.

4. Dauwalter, C.: "Loss and Guideway Interaction Force Measurements on a Superconducting Magnet for MagLev Applications", 12th International Conference on Magnetically Levitated Systems and Linear Drives, Argonne National Laboratory, May 1993.

High Temperature Superconducting Magnets with Active Control for Attraction Levitation Transport Applications

Harry Jones and Richard G. Jenkins
University of Oxford, Clarendon Laboratory, Oxford OX1 3PU, UK

Roger M. Goodall, Colin Macleod and Abdallah A. El Abbar
Loughborough University of Technology, Loughborough LEH 3TU, UK

Archie M. Campbell
University of Cambridge, IRC in Superconductivity, Cambridge CB3 0AE, UK

SUMMARY

A research programme, involving 3 British universities, directed at quantifying the controllability of High Temperature Superconducting (HTS) magnets for use in attraction levitation transport systems will be described. The work includes measurement of loss mechanisms for iron cored HTS magnets which need to produce a flux density of ~ 1 tesla in the airgap between the magnet poles and a ferromagnetic rail. This flux density needs to be maintained and this is done by introducing small variations of the magnet current using a feedback loop, at frequencies up to 10 Hz to compensate for load changes, track variation etc. The test magnet assemblies constructed so far will be described and the studies and modelling of designs for a practical levitation demonstrator (using commercially obtained HTS tape) will be discussed with particular emphasis on how the field distribution and its components, eg the component vector normal to the broad face of the tape, can radically affect design philosophy compared to the classical electrical engineering approach. Although specifically aimed at levitation transport the controllability data obtained have implications for a much wider range of applications.

INTRODUCTION

Superconductors for use in levitation transport systems are not new. Probably the most well known system in operation is the test track in Myazaki Prefecture, Kyushu, Japan where for some years, a series of test vehicles with on-board superconducting magnet systems, wound from the conventional Low Temperature Superconductor (LTS) material NbTi, and the associated liquid helium cryogenics are used to produce electrodynamic suspension (EDS) for high speed transportation. This programme is now being extended and sections of track are being built between Tokyo and Osaka for commercial evaluation[1]. High Temperature Superconductors (HTS) are still not sufficiently advanced to play a role in this type of system, in spite of the attractive advantages of their much simpler cryogenic requirements, as the high excitation and flux densities required are not obtainable yet with HTS working at a temperature in the liquid nitrogen regime $\geq$ 64K.

Electromagnetic suspension (EMS) systems are another matter however. In these the

ferromagnetic track implicitly restricts the magnetic flux density to ~1 tesla. This is normally provided by iron cored, copper wound electro-magnets which provide the lift for low speed vehicles used in "people mover" systems. A good example of these is the one at Birmingham airport, UK which has been in operation for over a decade and is the world's only commercially operating maglev system[2] Here the use of HTS has potential to provide ampere turns whilst retaining the iron core which means that the excitation required and flux density experienced by the superconductor are low enough to stay within the limiting parameters of critical current and critical field presently achievable with state of the art practical conductors (typically tapes) in the LN2 temperature range.

The Benefits of HTS Coils

At first sight the main advantage of superconducting coils is the zero power requirement when the coils are excited in steady state for lift. For EMS however, the dominating power requirement is in the propulsion system and not in the suspension. The benefits are indirect. For normal coils (Cu or Al) their design is dominated by the thermal aspects and maximum allowable current densities of ~2-3 A mm^{-2}. These are reflected in the size and weight of the coils and core. With HTS, current desities of ~10 A mm^{-2} are possible (this is a conservative figure) and this results in a smaller, lighter coil and a reduction in the slot size and therefore the mass of the iron. In a recent paper[3] Goodall et al make some estimates of the impact of HTS on the design of the magnets for the Birmingham Maglev. The relevant parameters are presented in Table 1. From this it is apparent that an increase in lift/weight ratio from 9:1 to 16:1 is possible and this is without any optimisation of the superconducting coil - a topic that will be addressed below.

The control issues

As a maglev vehicle moves along its track the magnet current, and consequently its inductive and resistive (if any) voltage, must be changed appropriately so that the flux density in the airgap is maintained in order that the vehicle follows the track at low frequencies (1 - 10 Hz) but provides isolation from the high frequency irregularities so that a good ride quality can be achieved. For magnetic suspension, using LTS magnets, the loss mechanisms resulting from these changes would make this approach very difficult as small losses result in big temperature changes at these low temperatures at which specific heat capacities are very small. This brings the risk of "quenching" of the magnets -the sudden transition from superconducting to normal state with huge energy dissipation in the liquid helium. With HTS, conditions, on the face of it, are much less fragile but, although there is some information available on losses in High Tc due to changes in current, virtually no work had been done on iron cored HTS magnets before the work reported here.

Active magnet control

To our knowledge the approach we propose to achieve control has not been studied before for iron cored superconducting magnets used in maglev. We are advocating direct control of the magnet current in closed loop feedback with sensors (such as search coils or position sensors) that can detect changes in flux resulting from track irregularities. The only other related work seems to be that reported by Kalsi et al[4] in which an LTS magnet working in persistent mode is used to provide the lift but control is achieved using adjacent normal coils. The main feature of our approach is that it involves only HTS coils which fulfill both lift and control functions.

THE EXPERIMENTAL PROGRAMME

At Loughborough University there has been for some time a demonstration rig which comprises a normal, ie, copper, wound iron cored elctromagnet which is mounted at the end of an arm pivoted at its other end. A ferromagnetic rail is positioned above the magnet pole faces and this is mounted on a frame which in its turn is mounted on an independent platform that is capable of being oscillated relative to the magnet. This arrangement permits the demonstration and study of a number of control functions under different conditions. For instance, when the magnet is powered up, it is attracted to the rail and levitates with an airgap of 10 mm and the control electronics can be configured so that when the rail is vertically oscillated the magnet stays where it is or can follow the rail with the air gap being kept constant.

The main aim of this project is to replace the normal coil electromagnet with one incorporating HTS coils and the necessary refrigeration, ie, a LN_2 pool boiling cryostat after an investigation into the loss mechanisms to see which were dominant. The proposed arrangement is shown in Fig. 1.

The superconductor

At Oxford we have an in - house programme for the development and characterisation of technical HTS superconductors. Over some 5 years, 3 departments, Physics - The Clarendon Laboratory, Materials Science and Engineering Science, have collaborated, and been jointly funded, in investigating a number of routes to produce wires and tapes incorporating BiSrCaCuO superconducting ceramic. Two phases of this are of practical interest; $Bi_2Sr_2Ca_1Cu_2O$ and $Bi_2Sr_2Ca_2Cu_3O$. The first of these is known informally as 2212 BSCCO and has a critical temperature, T_c, of $\sim$90K, the second is known as 2223 BSCCO and has a T_c of $\sim$105K. A characteristic feature of most HTS materials is that they only coexist with Ag, to all intents and purposes, so most practical conductors developed so far are composites of the HTS and Ag. At first sight, 2223 BSCCO seems by far the best choice because of its relatively high T_c and it is indeed preferable. Unfortunately, unlike 2212 BSCCO, it does not lend itself to the partial melt processing which gives good current carrying properties. Rather it has to be mechanically textured and thus the "powder in tube" approach wherein the ceramic powder is packed into a Ag tube and is drawn, rolled and pressed into tapes, has to be used. Because 2212 has good low temperature performance in high magnetic fields there is still an interest in developing it and so at Oxford good progress had been made in producing 2212 tapes by coating methods, ie, electropheretic coating[5] or dip coating[6] onto Ag tape. The early pancake coils that were used in this work were wound using this in-house produced tape.

Commercially produced HTS tape. Meanwhile Intermagnetics General Corporation, IGC, had developed a quality commercial product in 2223 BSCCO tape manufactured by the powder in tube method. We have obtained a batch of this tape and are using it for our second generation coils for the demonstrator magnet which will be described in some detail below. Apart from the good supercurrent carrying capacity of this tape (typically $\sim$15 A at 77K over 100 m, $\sim$30 A over short sample lengths) it can be wound down to 38 mm diameter without strain degradation and probably down to 25 mm with tolerable degradation. This opened up the prospect of our being able to use the "react and wind" route in producing our pancake coils compared to the wind and react method which needs to be employed with most 2212 BSCCCO tapes - ie winding the coils out of unreacted tapes and then reacting them, at temperatures on the order of 850 C, with all the inherent technological difficulties.

Anisotropy in HTS tapes. One of the inherent drawbacks in the highly textured BSCCO

conductors is that of anisotropic behaviour with respect to ambient magnetic field. The texture is such that the ab plane of the structure lies parallel to the broad face of the tape. It is well established that magnetic field which is normal to the ab plane (or parallel to the c axis. B $\|$ c) has a much greater effect on the depression of critical current I_c than that applied parallel. For a set of pancake coils this is good as in the median plane of the solenoid the field lines are indeed parallel to the tape face but at the ends of the coil the radial field component is large and it is this component which is normal to the ab plane. Consequently this aspect has to be taken into account when designing and modelling HTS coils and is probably the biggest departure from classical electrical engineering considerations when designing an HTS / iron electromagnet.

Measurement of the loss mechanisms A set of four 2212 coils was used to build two experimental test magnets. The bore of these coils was only 10 mm and the iron circuits had to comply accordingly. The second and best design is shown in Fig 2. In this the back iron is rectangular. Both solid and laminated cores were tried. The main thrust of the experiments with these test magnets was to determine what happened when a small ac current was superimposed on a dc bias current - representing the lift current in a real device - at frequencies from 0 to 100 Hz. This simulates the sort of conditions experienced by an actively controlled magnet in a maglev situation. The results were very clear; the resistive losses were negligible, as might be expected and the HTS losses were also extremely small. The overall losses are dominated by eddy current losses in the core and Ag but these are still insignificant when compared with the total losses in a normal wound magnet under similar conditions. In figure 3 we show an example of the total loss measurement as a function of frequency for both normal and laminated cores. It is worth noting that even at 100 Hz, an order of magnitude greater than that expected in practice, the loss is less than 1 mW. A simple calculation shows that if the coils were made entirely of copper the resistive loss alone, at a dc current of 0.5 A, would be 3.6 mW at all frequencies, ie 4 times that of the dynamic losses of the HTS coils at 100 Hz and two orders of magnitude greater than at a more realistic 10 Hz and this calculation assumes that the copper is at 77K. In practice, the room temperature, or greater, resistivity of the copper would yield at least another order of magnitude difference. Finally, this observation is for a very small test magnet and iron circuit. In fact the dc currents would be more like 10 A so the difference would be even more dramatic between the copper and HTS illustration.

Coil construction The pancake modules consist of a pair of pancakes wound in contrary sense on a hat shaped frp former. Pancake to pancake electrical connection is made by axial straps using indium solder at the inner windings. Inter turn insulation is Mylar ribbon $\sim$0.01 mm thick. These double pancake modules are then vacuum impregnated with paraffin wax. Electrical connection between modules is accomplished by straps on the outer turn. More details are given by Jenkins et al[7].

The control system

This paper concentrates on the general aspects and those specific to the Oxford partners. The control engineering expertise rests entirely with the Loughborough partners and will not be addressed here, but in a recent paper Goodall and Mcleod[8] deal with these aspects in some detail. Suffice to say the work at Loughborough showed that there are no real problems in achieving the necessary control.

HTS COILS FOR THE MAGLEV DEMONSTRATOR

Initial performance targets for the maglev demonstrator were that it should generate a flux density of 1T in the 5mm air gaps between 25mm diameter pole pieces and the iron rail, thus producing a lift force of approximately 390N and requiring 8000 ampere-turns.

$$\text{Lift force} = B^2A/2\mu_0 \qquad (1)$$

where B is the pole flux density and A is the total area of the poles.

In addition the current density in the windings should exceed $10A/mm^2$ (to better the performance of copper coils in the same application) and the iron yoke should be at room temperature.

In designing the HTS coils and iron yoke to meet these requirements we are faced with two important factors:

1) The critical currents of HTS composite tapes are highly sensitive to the magnitude and direction of magnetic field. The anisotropic critical current dependence on applied field for a short sample of IGC tape is shown in Fig. 4. When designing a superconducting magnet incorporating isotropic conductor one is normally concerned only with $|B|$ which is a maximum at the inner windings on the coil midplane. However, when the coil is to be wound from HTS tape with an anisotropic $I_c(B)$ one must also take into account the radial component of field (which is perpendicular to the tape surface and therefore in the weak "pinning" direction) which for a simple air-cored solenoid is a maximum at the middle turns at the ends of the coil. Maximum operating current is determined by plotting load lines for peak radial field (Br) and peak axial field (Bp) together with the tape critical current as a function of parallel and perpendicular applied fields. An example is shown in Fig 5. In this case it is the Br load line and $I_c(B \| c)$ which intersect at the lower current, hence it is the radial component of field which determines the maximum operating current of the coil.

2) The presence of iron can greatly alter the field distribution within the windings compared with that found for the same coil(s) in free space (e.g. in the final demonstrator design shown in Fig. 6 the flux over the majority of the coil windings is in the opposite direction to that for the same solenoid with an air core. This has implications for stress in the conductor.) To calculate the field distribution within the HTS windings we used commercial finite element electromagnetic design software.

Thus for each proposed design the calculated field distribution in the windings was compared with the measured critical current data. Although strictly the most important factor in the performance of the final magnet is the total losses, in the design stage it was easier and more practicable to use the criterion that nowhere should the operating current exceed the local critical current.

As a starting point for a coil/yoke design solution we began by looking at an "optimised" conventional arrangement i.e. incorporating copper coils. This is shown in Fig. 7. The ratio of slot depth to width is 1:2, the coils are pole-wound and the windings fill the slot. Fringing at the poles leads to very high flux densities ($>0.9T$ compared with 1T in the gap) in the "corners" of the windings and renders the geometry unsuitable for HTS.

By lengthening the pole pieces these high fringe fields can be kept away from the coils but the windings are still subjected to unacceptably high perpendicular components (0.25T) due to increased

flux in the now reduced-reluctance path from one pole piece to the other. A better solution is to increase the length of both the pole pieces and the slot, maintaining the same 1:2 ratio. The pole length and slot width were now 60mm and 120mm respectively. From the viewpoint of cryogenic engineering, if the iron is to be at room temperature then this pole-wound configuration is non-ideal, demanding either two simple annular cryostats or one of more elaborate design. This led to a move away from conventional geometry and the positioning of a single coil on the back iron in a single annular cryostat.

In such an arrangement the HTS windings are positioned in a region of relatively low flux density, enabling high lossless currents to be carried. Unfortunately however it does impose limitations on the achievable pole flux densities. As the number of ampere turns on the back of the yoke is increased, the iron in this region is driven into saturation, but the pole flux density remains below around 0.7T. With a 25mm diameter yoke, 60mm pole lengths and a 120mm slot width, we were unable, with a back-wound coil, to generate the target 1T pole flux density; in fact with the available IGC HTS composite tape we were limited to around 0.5T and a lift force of approximately 100 N. Therefore design targets were revised; greatest emphasis was now placed on the generation of 400N lift with the available HTS material.

This target has now been met, and the design is shown in Fig. 8 and its specification in Table 2. The cross section of the iron yoke has increased from 25 to 44 mm diameter, and the increase in pole area has enabled the higher lift force to be achieved. Coil id has also increased, from 37 to 65 mm, thus the risk of any winding strains which would cause degradation in I_c is totally eliminated.

Future work: We propose to scale up an order of magnitude to a 500Kg demonstration "vehicle" with increased emphasis on optimizing with respect to lift/weight ratio. This will in part be achieved by maximizing current densities in the HTS coils, thereby enabling their size to be reduced. Increased I_c will result from operating at lower temperature possibly using electro-mechanical "cryocoolers" (the IGC conductor at 64K exhibits a critical current approximately 1.6 times larger than that at 77K), and the use of compensation coils to reduce radial field components.

CONCLUSIONS

This project so far has demonstrated that direct active control of an HTS/iron magnet is easily possible for EMS applications. It has also shown that the magnet design is dictated by the unique characteristics of HTS conductors but with careful optimisation efficient magnets can be produced.

ACKNOWLEDGEMENTS

The authors gratefully acknowledge the funding provided by the UK's Engineering & Physical Sciences Research Council (GR/J40089). They would also like to pay tribute to the technical skills of Robert Storey for the realisation of some of the hardware. Miss Miriam Avery prepared the final version of this paper and is thanked accordingly.

REFERENCES

1. Sawada, K.: Development of Magnetically Levitated High Speed Transport System in Japan. Paper presented to 14th International Magnet Technology Conference (MT14), Tampere, Finland 1995. *IEEE Trans. Magn.* In press.

2. Taylor, P.R.D.; Goodall, R.M.; and Oates, C.D.M.: Theoretical and Practical Considerations in the Design of the Suspension System for Birmingham Maglev. *I.Mech.E. Conf. Pub.* 1984-12 paper C14/84, pp 185-192 1984.

3. Goodall, R.; Macleod, C.; El-Abbar, A.A.; Jones, H.; Jenkins, R.; and Campbell, A.: The potential for EMS Maglev using High Temperature Superconductors. *Proc. Maglev '95 Bremen, Germany.*

4. Kalsi, S.; Proise, T.; Schulthüss.; and Dawkins, B.: Iron Core Superconducting Magnet Design and Test Results for Maglev Application. *IEEE Trans. Appl. Supercond.*, 5, (1995) pp 964-967.

5. Yang, Ming.; Goringe, M.J.; Grovenor, C.R.M.; Jenkins, R.; and Jones, H.: The Fabrication of Bi-based Superconductor Tape by Electrophoretic Deposition and Melt-Texturing Techniques. *Supercond. Sci. Technol.* 7 (1994) 378-388.

6. Burgoyne, J.W.; Eastell, C.; Morgan, C.G.; East, D.; Jenkins, R.G.; Young, M.; Dew-Hughes, D.; Jones, H.; Grovenor, C.R.M.; and Goringe, M.J.: A Novel Continuous Process for the Production of Long Lengths of BSCCO-2212/Ag Dip Coated Tape. Proc. EUCAS Edinburgh July 1995. IOP Conference Series *Applied Superconductivity* 1995 - in press.

7. Jenkins, R.G.; Jones, H.; Young, M.; Belenli, I.; Grovenor, C.R.M.; and Goringe, M.J.: Prototype Coils Wound from High Tc Superconducting Composites. *Paper 259 Proc. MT13 IEEE Trans. Mag.* 30 (1994) 1813-1816.

8. Goodall, R.M.; and Macleod, C.: Control Considerations Relating to the use of Superconducting Coils in Maglev Suspensions. *IEEE Conf. on Control and its applications (CCA '95).* Albany NY Sept. 1995.

Table 1. Comparison of Normal and HTS Coils with reference to the Birmingham Maglev

	Normal	HTS
Current density	2 - 3 A mm^{-2}	10 A mm^{-2} (1)
Packing factor	0.5	0.5
Slot size	230 x 115 mm	100 x 50 mm
Mass of core	59 kg	37 kg
Total magnet mass	112 kg	63 kg (2)
Lift/weight ratio	9:1	16:1

(1) Conservative figure but makes some allowance for cryostat. (2) Estimate assuming coil is entirely Ag

Table 2. Coil Data and Performance for Maglev Demonstrator

Coil Data		**Performance @ I = 5A**	
No. of double pancake modules:	9	ampere turns (nI):	4770
total no. of turns:	954	Bgap from 3D model:	0.54 T
inner winding diam.:	65 mm	Bgap from simple calc: ($B = \mu_0 nI/g$)	0.60 T
outer winding diam.:	95.6 mm		
length:	90 mm	lift force ($B^2A/2\mu_0$):	449 N
overall turns density:	80 cm^{-2}		
operating temp.:	77.3 K		
max. operating I (Ic):	5 A		

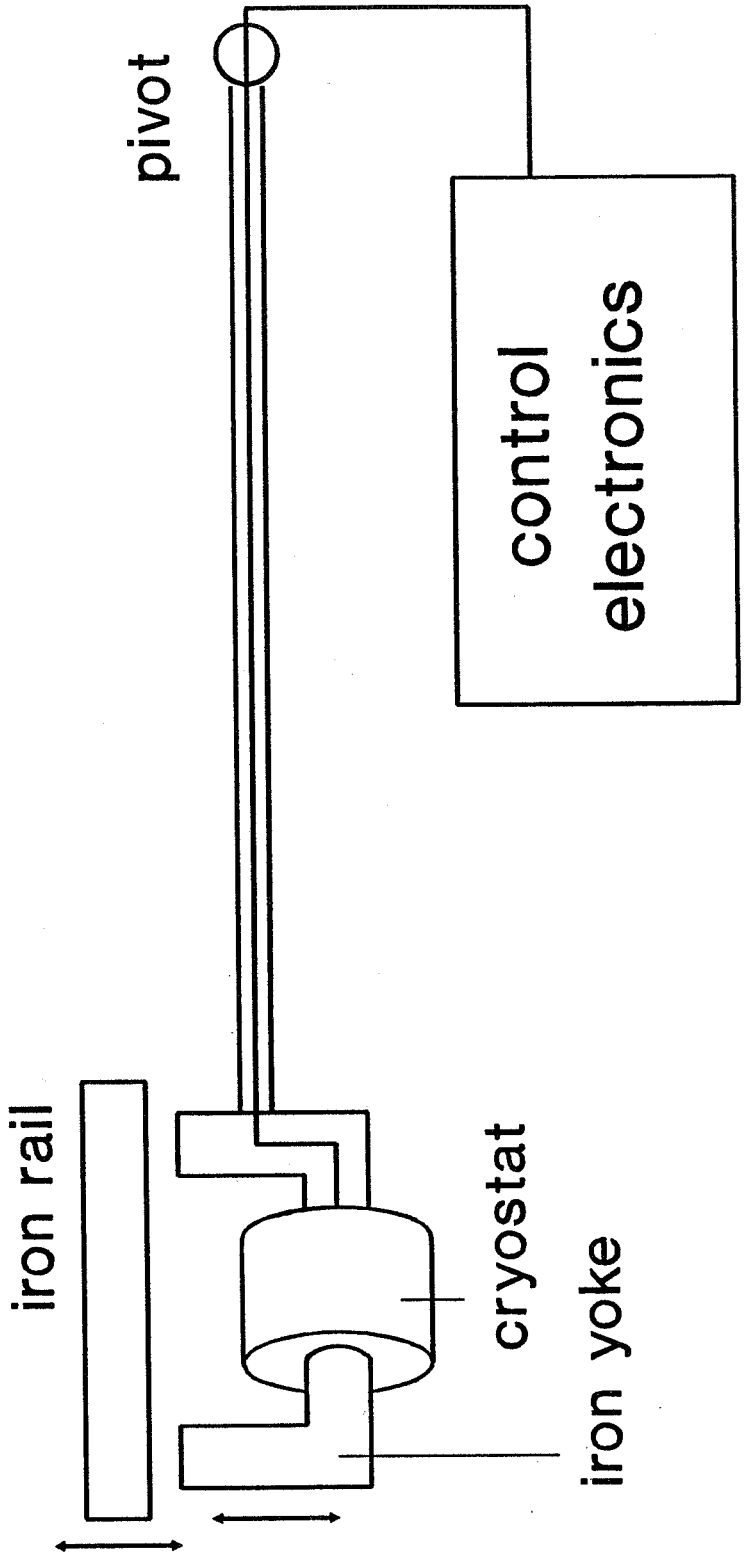

Figure 1. The maglev demonstrator incorporating HTS coils. Control of magnet current enables suspension of the iron yoke (attached to a hinged support arm) beneath a moving section of rail.

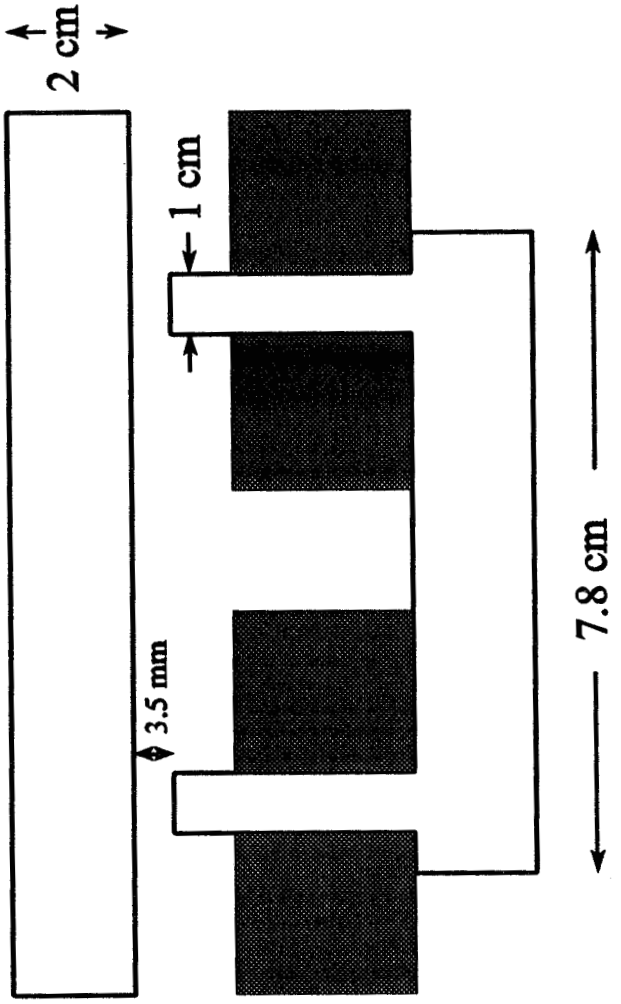

Figure 2. The improved version of the experimental magnet for loss investigations. The back iron is rectangular. Both solid and laminated versions of the iron circuit were made.

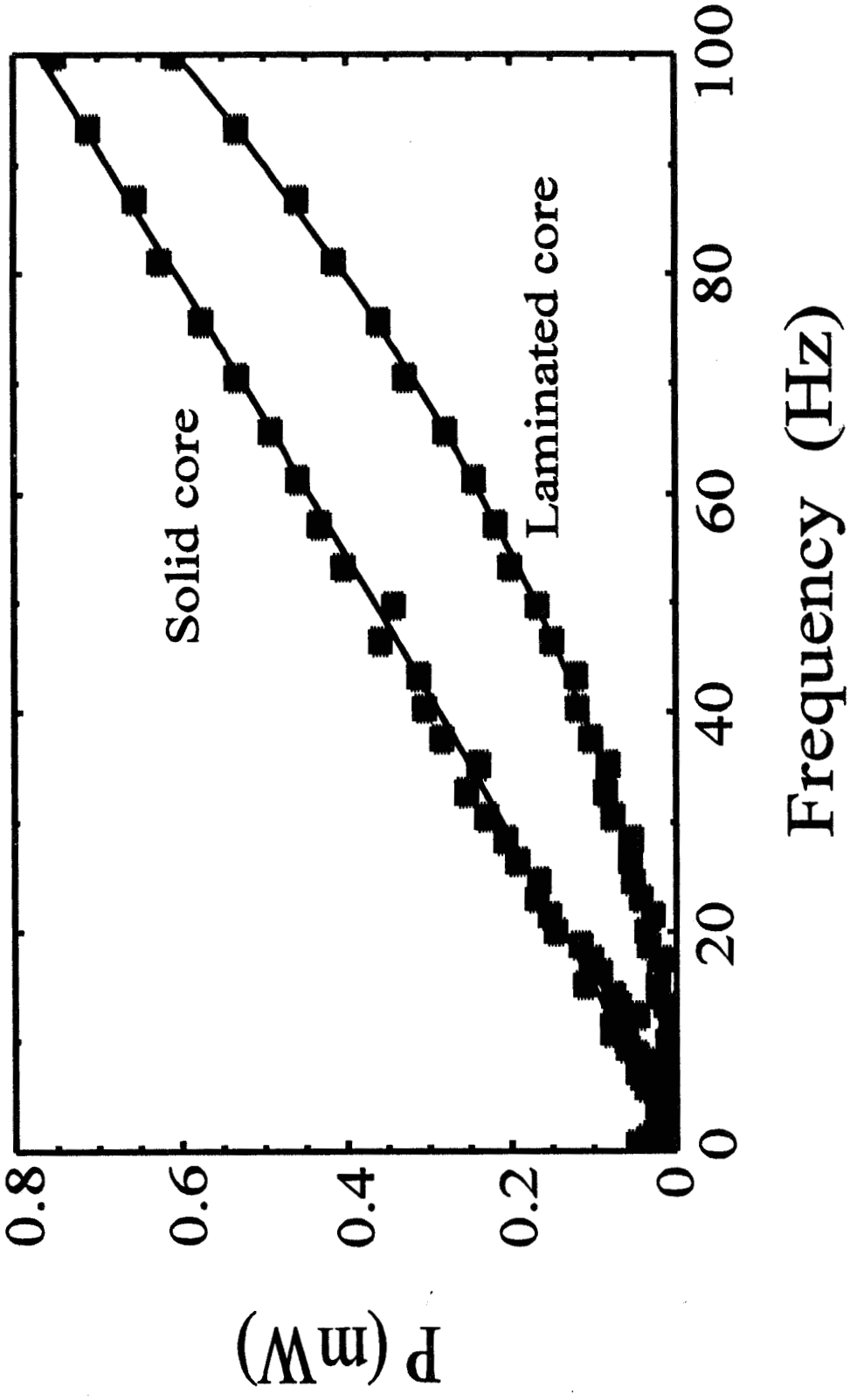

Figure 3. Losses (in mW) vs frequency for a superimposed ac current of 0.04 A (rms) on a 0.5 A d.c. current for the test magnet shown in Figure 2.

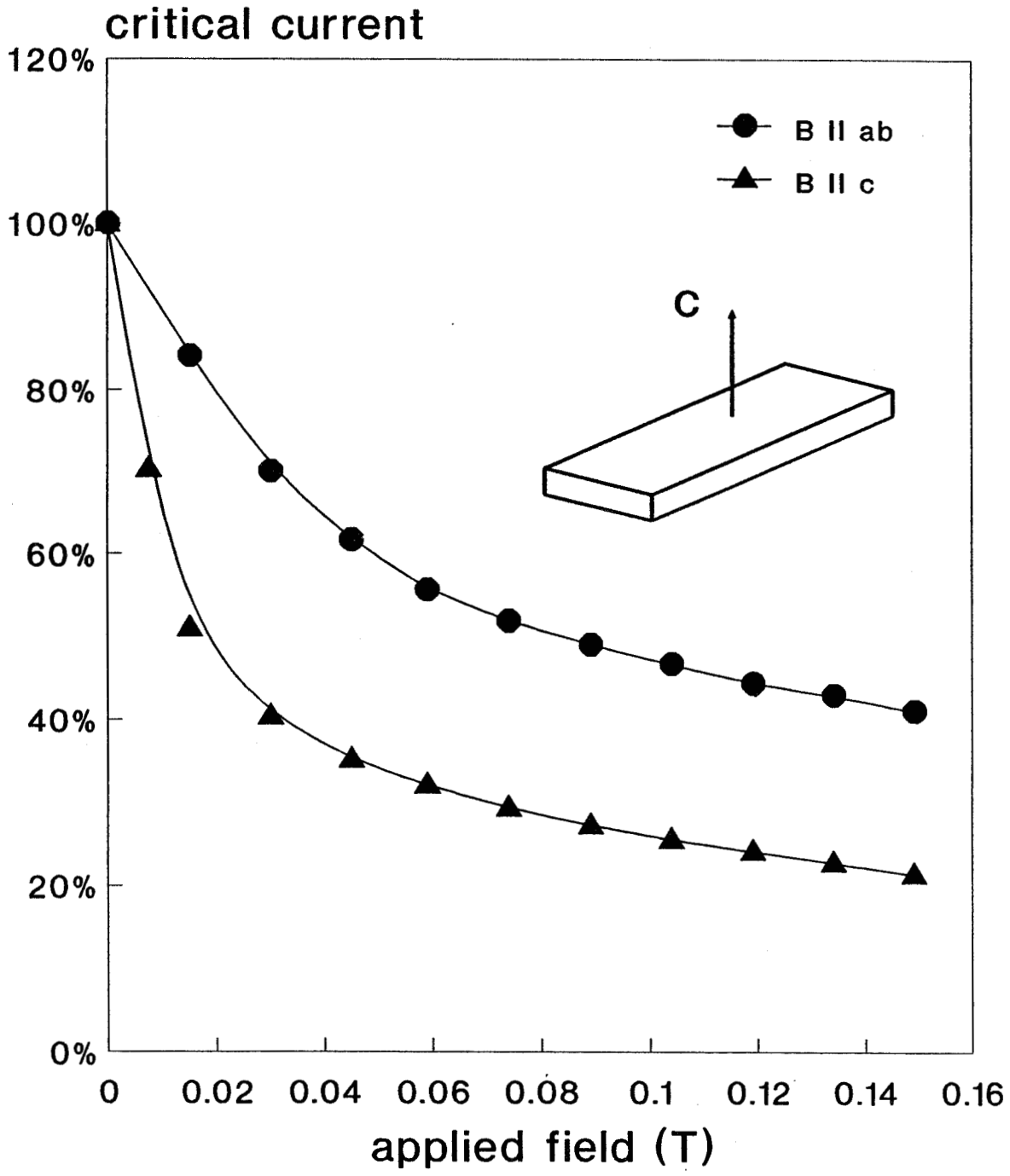

Figure 4. Normalised critical current at 77.3 K as a function of applied magnetic field for a short sample of IGC HTS tape from which the maglev demonstrator coils will be wound.

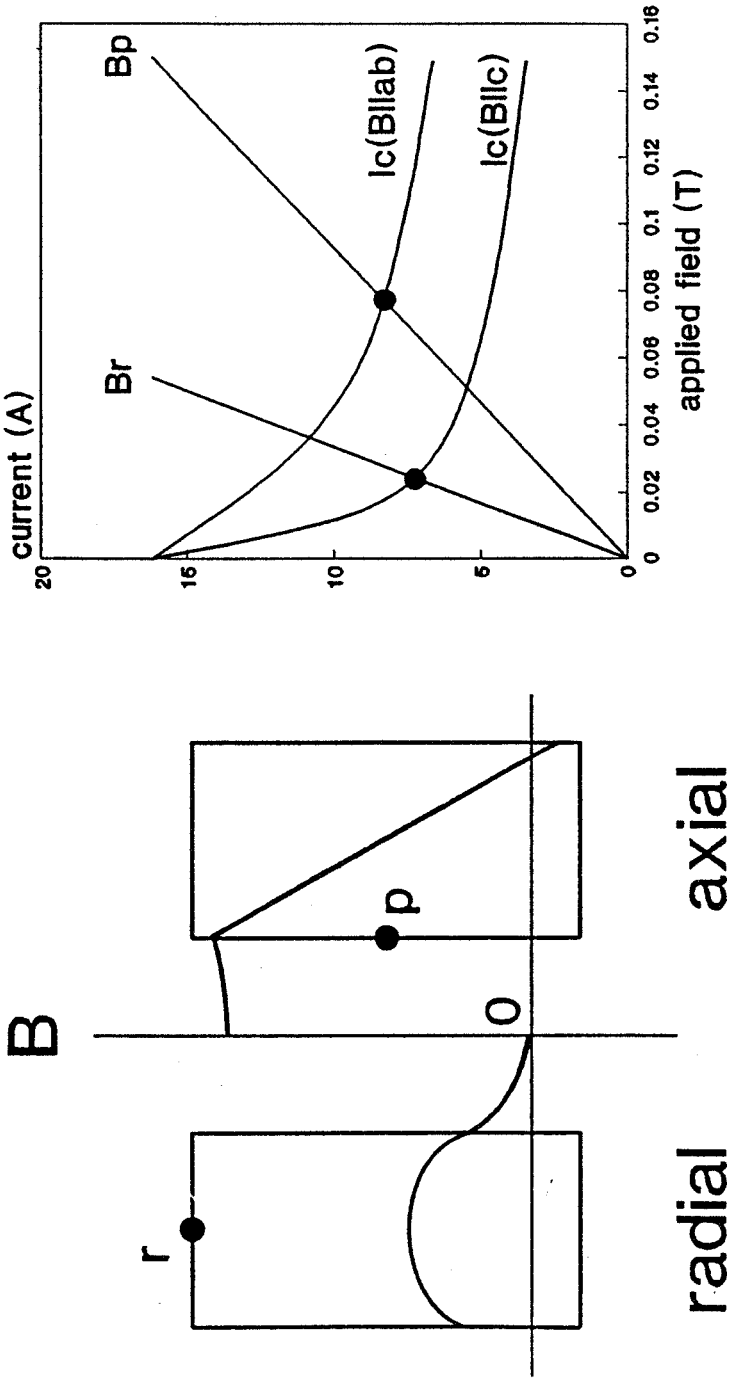

Figure 5. Axial and radial field profiles in the windings of a simple solenoid: peak values occur at points p and r respectively. Load lines plotted with anisotropic Ic(B) data show that for this example it is the radial component which limits the maximum operating current of the magnet.

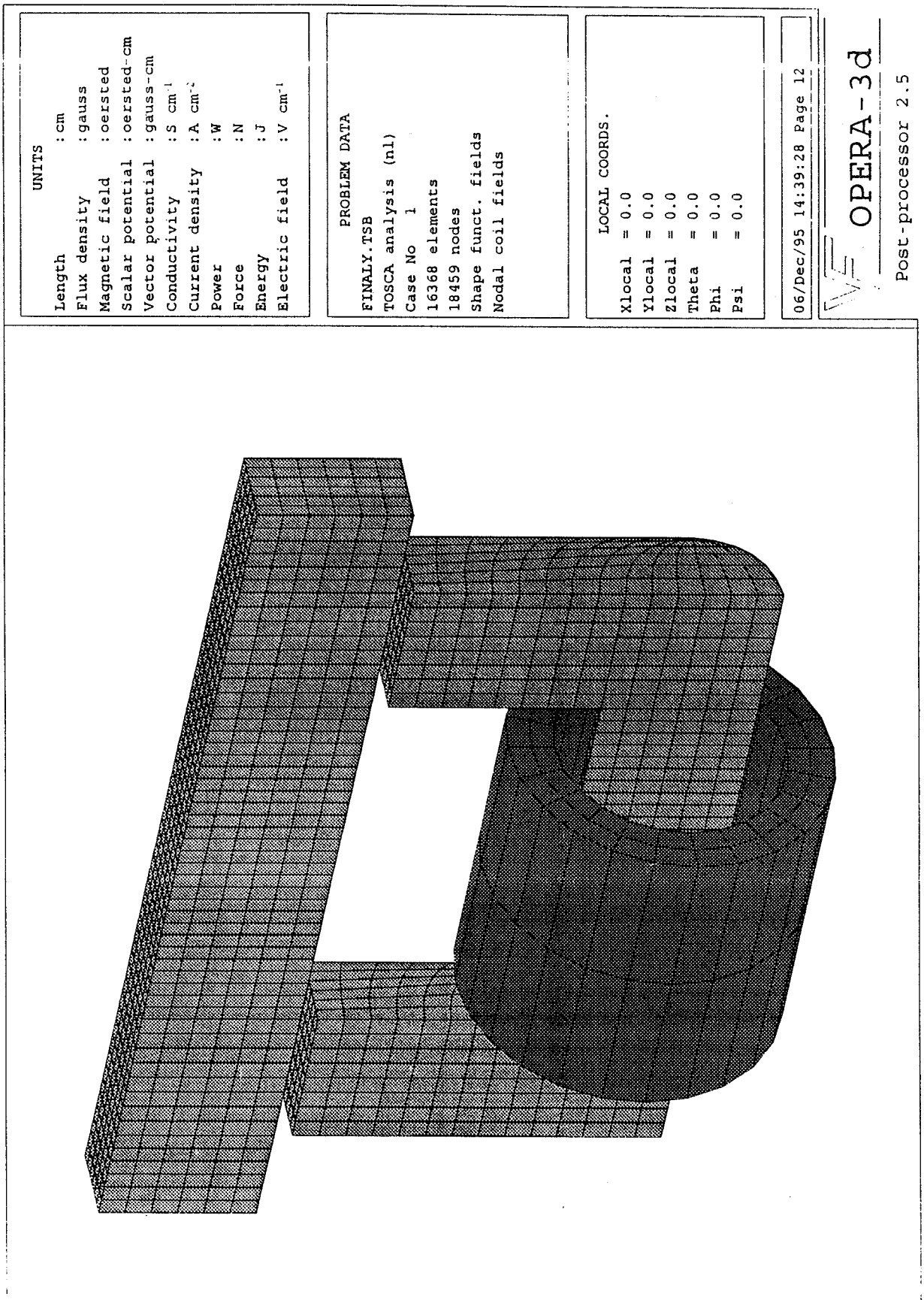

Figure 6. The final design for the iron yoke and HTS coil for the maglev demonstrator. Only half of the yoke and rail are shown, divided into elements for modelling.

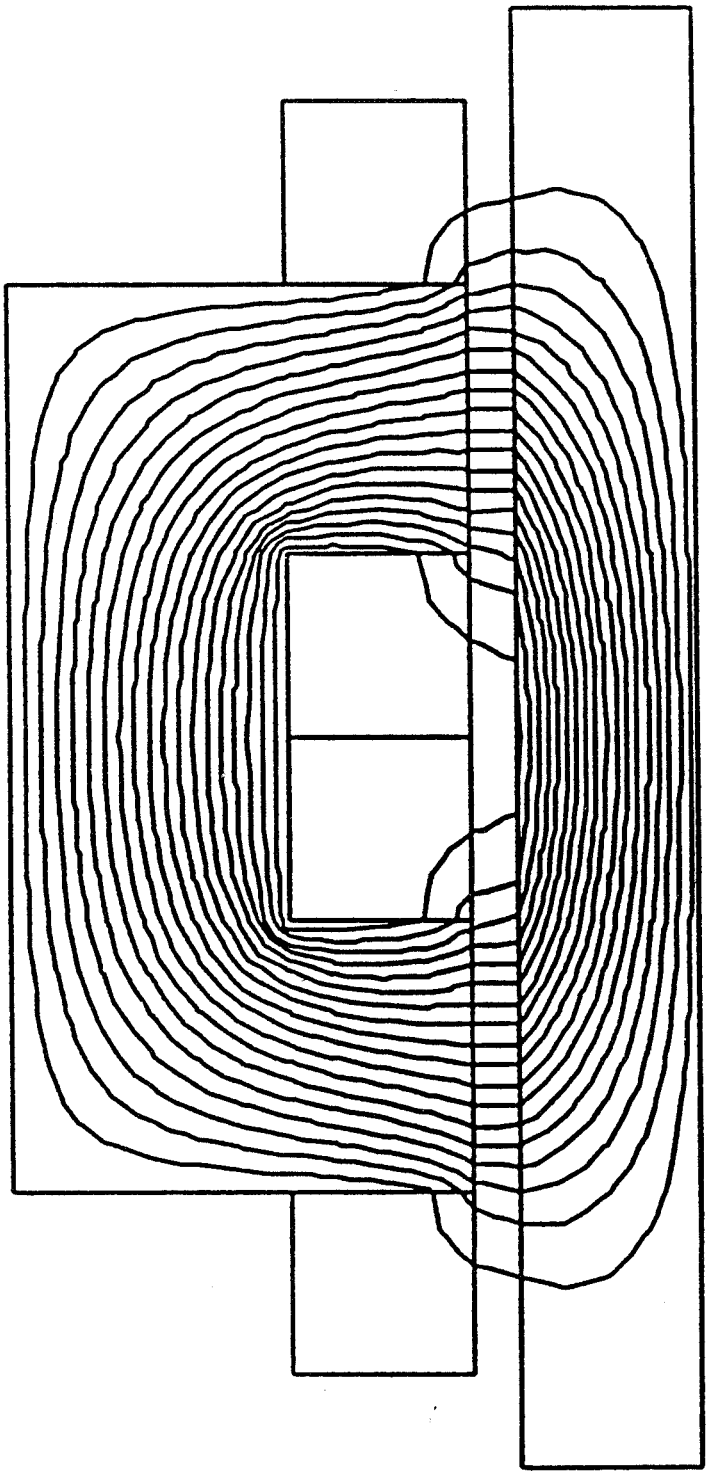

Figure 7. Flux distribution in a conventional maglev demonstrator design incorporating pole-wound coils. Fringing at the poles makes this geometry unsuitable for HTS windings.

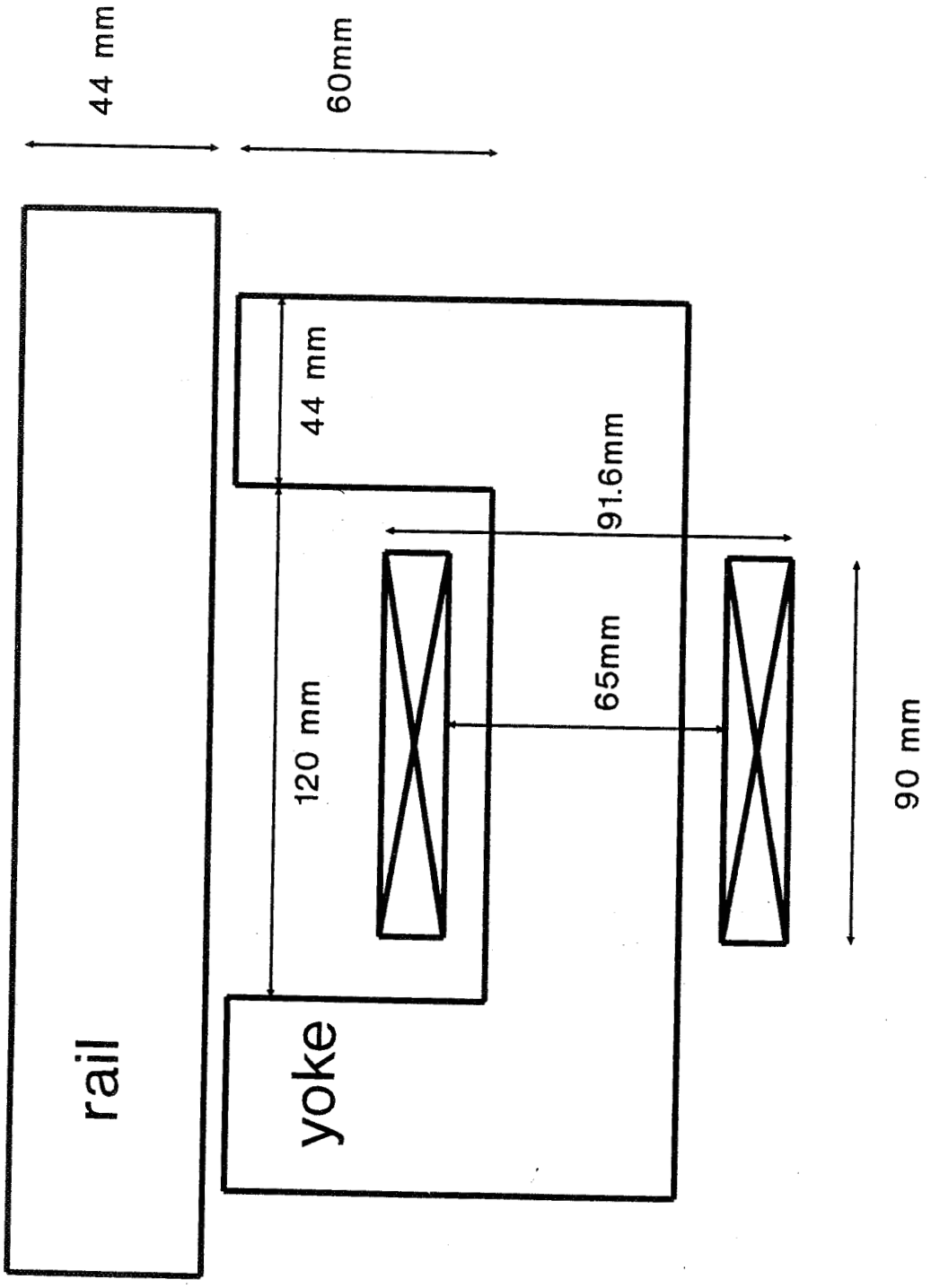

Figure 8. Cross section of the HTS coil and iron yoke for the demonstrator.

A CONCEPT FOR THE USE AND INTEGRATION OF SUPER-CONDUCTING MAGNETS IN STRUCTURAL SYSTEMS IN GENERAL AND MAGLEV GUIDEWAY MEGA-STRUCTURES IN PARTICULAR

BY: Wilfred T. Ussery

In Association With:
Drs. Eric and Johnetta MacCalla, Dr. Mahjoub Elnimeiri, Myron Goldsmith
Sharon Madison Polk, Mozella Jenkins, Dr. Robert H. Bragg

INTRODUCTION

Recent breakthroughs in several different fields now make it possible to incorporate the use of superconducting magnets in structures in ways which enhance the performance of structural members or components of structural systems in general and Maglev guideway mega-structures in particular. The building of structural systems which connect appropriately scaled superconducting magnets with the post-tensioned tensile components of beams, girders, or columns would, if coupled with 'state of the art' structure monitoring, feedback and control systems, and advanced computer software, constitute a distinct new generation of structures that would possess the unique characteristic of being heuristic and demand or live-load responsive. The holistic integration of powerful superconducting magnets in structures so that they do actual structural work, creates a class of 'technologically endowed' structures that, in part - literally substitute superconductive electric power and magnetism for concrete and steel. The research and development engineering, and architectural design issues associated with such a 'technologically endowed' structural system can now be conceptualized, designed, computer simulated, built and tested.

The Maglev guideway mega-structure delineated herein incorporates these concepts, and is designed for operation in the median strip of U.S. Interstate Highway 5 from San Diego to Seattle and Vancouver, and possibly on to Fairbanks, Alaska. This system also fits in the median strip of U.S. Interstate Highway 55 and 95 North-South, and 80 and 10, East-West. As a Western Region "Peace Dividend" project, it could become a National or Bi-National research, design and build, super turnkey project that would create thousands of jobs by applying superconducting, material science, electronic, aerospace and other defense industry technologies to a multi-vehicle, multi-use Maglev guideway mega-structure that integrates urban mass transit Lower Speed (0-100 mph), High Speed (100-200 mph), Super Speed (200-400 mph), and Hypersonic evacuated tube (400-10,000 mph) Maglev systems.

GENERAL CONCEPT

Recent breakthroughs in the fields of low and high temperature superconductivity make the idea of incorporating superconducting magnets in the foundations, columns, beams, and girders of some structural systems both conceptually and technologically viable. The theoretical underpinning of the idea of using superconducting magnets to enhance the performance of structural members or components is closely related to progress being made in understanding the physics of superconductivity and magnetism, the production of superconducting wires and cables that can superconductively transmit large amounts of electric current, the design of superconducting magnets, and the concurrent development of small Superconducting Magnetic Energy Storage (SMES) devices and/or flywheel motor/ generators.

The rapid progress being made in the field of super-conductivity is complimented by parallel advancement in the development and use of super computers; computer network systems; fuzzy logic

computer software enhancements; neural-like network designs; lightwave-based data transmission and memory systems; electronic and laser-based diagnostic structure monitoring, feedback and control systems; Computer Aided Design (CAD) and Computer Aided Manufacturing (CAM); and the potential use of magnetically inert non-ferrous composite materials and structural polymers in structural systems. Given the 'state of the art' of such innovative systems and technological developments, it is now possible to 'technologically endow' some structural systems with a systemically integrated set of components which combine and synergize the primary attributes of the ten different compatible areas of interest enumerated above. The related research and development, engineering, and architectural design issues associated with such 'technologically endowed' structural systems can now be conceptualized, designed, computer simulated, built and tested. This potentially historic, unachieved, structural characteristic of 'technologically endowed' structures is attributable to the synthesis of the special attributes of the following seven disparate, heretofore, unrelated principles or areas of technological achievement:

- The electrodynamic relationship of "ampere turn" or "the amount of magnetomotive force produced by an electric current flowing around one turn of a wire coil" to varying amounts of superconductive electric current. This phenomenon, with proper controls, can become demand or live load responsive to do actual structural work by the use of magnets whose power is a function of the number of windings and the amount of superconductive electric current flow around the magnet;
- The electrodynamic relationship of the direction of electric current flow through the windings around a magnet to changes in polarity of the magnets. This phenomenon with proper electronic controls can be used to engage or disengage sets of appropriately scaled shear pins in precast structural components and some architectural window wall systems.
- The ability to arrange magnets in linear, circular or spiral patterns so that the polarity of adjacent magnets is aligned to produce both repulsive and attractive 'magnetomotive force,' that simultaneously create push and pull forces that can be converted to 'mechanical force,' which acts in a common direction along a common axis. This phenomenon with proper engineering can be used to aggregate the 'magnetomotive force' of smaller magnets attached, alternatively, to the surrounding structure and directly, along the full length of tensile components of structural members.
- The electrodynamic relationship of attractive and repulsive 'magnetomotive force' produced by magnets that can be arranged, radially and spatially relative to an appropriately scaled source of repulsive 'magnetomotive force,' in a variety of geometrically stable patterns. This phenomenon with proper electronic controls, calibration of the number of windings and amount of superconductive electric current flow to each concentric array of magnets, and, the addition, in some cases, of rotation sufficient to impart appropriate amounts of centrifugal force, can be used to design and build a class of small micro-electronic devices, and a unique class of large scale, light weight, parabolic thin film structures in space.
- The currently accepted theory of elasticity: Hooke's Law, which states that the amount an elastic body bends or stretches out of shape (strain), is in direct proportion to the force (stress) acting on it. This law applies as long as the body is still elastic and has not been stressed beyond this elastic limit which will result in permanent change in the shape of the body;
- The history of research and engineering effort to optimize utilization of the tensile strength attributes of iron and steel as well as some magnetically inert non-ferrous composite materials and structural polymers -- and the compressive strength attributes of concrete in structural systems; and
- The availability of super computers, parallel processors, computer hardware networks, and the related software technology capable of providing a "distributed real-time, self-monitoring adaptive control system" to govern a heuristic, demand or live-load responsive flow of superconductive electric power to sets of superconducting magnets incorporated in a particular structural member, component, or system.

One of the most significant new opportunities for utilizing the special attributes and characteristics of a 'technologically endowed' structural system is to address the recurring guideway alignment and dynamic behavior problems associated with the movement of one or more high speed, super speed, or hypersonic evacuated tube Maglev vehicles on an elevated guideway.

The arrival and departure of a contact-fee, magnetically levitated, vehicle (Maglev) at a particular structural bay of an Intra-Continental, multi-use Maglev guideway mega-structure is a predictable event. Appropriate diagnostic instrumentation and telemetry systems are now available which could ascertain and report guideway alignment and the Maglev vehicle's speed and weight prior to, and, as it moves through a particular structural bay. This would provide engineers the necessary information base to design the primary structural members or components of a Maglev guideway mega-structure not only for dead load and seismic forces, but also offer the unique, possibly historic possibility of having the structure respond heuristically and in a demand responsive way to the live load and other dynamic forces induced by the vehicles movement and presence in the bay.

One of the most important objectives to be achieved by a heuristic live-load responsive, guideway mega-structure would be the reduction or elimination of any live load induced deflection of primary structural members or components that would either incite undesirable periodicity problems or be reflected or transposed into a discernable heaving up-down motion of the Maglev vehicle as it moves at high or super speed through a low point of a longitudinal beams deflection in a particular structural bay. Superconducting magnets can be incorporated and used in structural members or components in ways that provide a solution of this special, recurring, condition - whose magnitude is in direct proportion to the length of the column bay.

The live load induced deflections or periodicity episodes initiated by the arrival and departure of one of more Maglev vehicles at a particular structural bay can now be reduced or eliminated by the incorporation and use of superconducting magnets in configurations which allow them to enhance the performance of structural members or components of Maglev guideway mega-structures. A structure with these attributes and characteristics is similar in principle to a room whose lights or mechanical systems are electronically controlled to go on and off when someone enters or leaves the room.

This can be achieved by having an "engagement" fuzzy logic enhanced protocol at the front end of the electrified, magnetized segment of the guideway that propels the Maglev vehicles. Activation of the "engagement" protocol initiates a calibrated increase in superconducting electric power around a set of superconducting magnets located at the end of the beams, girders and columns which respond by increasing the tension on the post tensioned cables in the structural members in advance of the vehicle's arrival at a given structural bay. The calibration of additional tension at the ends of the post tensioned cables is scaled to eliminate any deflection of the primary structural member, guideway misalignment, dynamic behavior, or periodicity problems for the guideway mega-structure.

There would also be a "disengagement" fuzzy logic enhanced protocol at the tail end of the electrified, magnetized segment of the guideway that propels the trailing Maglev vehicle. Activation of the "disengagement" protocol initiates a calibrated increase in superconductive electric power around a set of superconducting magnets located appropriately at the end of beams, girders, and columns which respond by decreasing the tension on the post tensioned cables in the structural member that was imposed by the "engagement" protocol.

A DISTRIBUTED REAL-TIME, SELF-MONITORING, ADAPTIVE CONTROL SYSTEM

The basic components of the distributed control feedback system required to govern a heuristic, demand or live load responsive flow of superconductive electric power to sets of superconducting magnets incorporated in a particular structural member, or components of the proposed multi-level, multi-use transit guideway mega-structure must be capable of monitoring and determining on a real-time basis all of the forces, both transient and periodic, currently acting on a particular structural member or component of the structural system. See Figures 1 and 2. It must also have memory capacity adequate enough to allow it to be able to compare the effects of its effort to past efforts, real-time. Finally, it must have the ability to iteratively calculate consecutive force equations to determine the necessary counter-action to be applied.

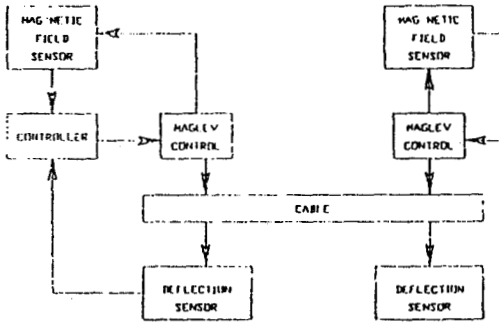

Figure 1

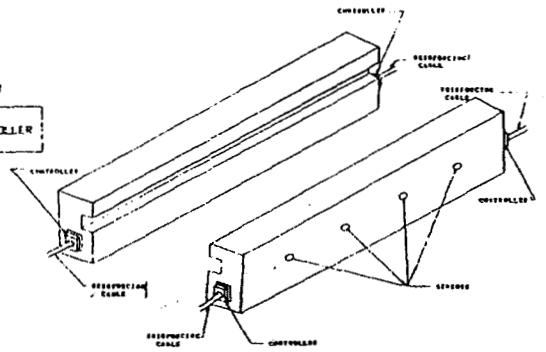

Figure 2

A very extensive set of feedback sensors is needed. These sensors must be accessible for maintenance purposes and capable of not only detecting microscopic flexing of members, but also follow the effect of the magnetically induced field on the tensile elements in the structural members and components. These sensors must be capable of collecting this data on a continuous basis. They must also be self-calibrating or capable of maintaining calibration over long time periods. There must be nearly as many sensors as there are controlled forces or the equations will be ill-conditioned and consequently not as responsive to distributive adaptive control.

The final component that is needed for the practical application of adaptive control to the use of "magnetomotive force" to "mechanical force" controlled enhancement of the performance of structural members or components of structural systems so that they become heuristic and demand or live load responsive, is a fail-safe fallback system in the event of electrical failure. If distributed adaptive control becomes an integral component of the system for enhancing the performance of structural members or components of the structural system, some method must be available for converting that effort from an active to a passive system when the real-time response is unavailable. This approach is known as graceful degradation and applied to all man missions in the aerospace arena.

Distributive adaptive control is the essence of the neural-network learning model. In it a primarily complex coupled force equation is decoupled through the use of a large quantity of independent computers each with selective feedback that is tied to the axis controlled by that computer. By operating a large quantity of these control loops in tandem, complex adaptive learning is achieved.

This approach is also applicable because of the large distances over which the system must operate. By utilizing the distributed control concept, a global problem has been essentially converted into a local problem with very tightly coupled, highly responsive feedback loops providing detailed adjustments all along the structural members. Additional models of superconductive magnets are utilized to characterize linear motion of the members. Adaptive control is applied through use of feedback sensors to estimate and predict positions and apply appropriate amounts of current to the superconducting elements. Fail safe design is utilized through use of redundancy in embedded controllers.

Sensors are used to detect position and conditions in the system. The necessary forces needed are determined through the mathematical model of the system and feedback from sensors providing feedback on the various system states. These sensors are used to determine structural integrity, temperature perturbations, stress, and physical perturbations. The guideway variations are monitored, diagnosed, and controlled through these distributed elements.

The use of distributed computing means that the non-linearity inherent in the structure are handled basically through the decoupling of independent axes. Each axis is controlled by a pair of controllers, the outputs of which are literally summed together. This is very similar to the neural-network or adaptive beam shaping approach. In fact the adaptive algorithms proposed are based on those used except we propose the digital version of those analog algorithms. Optical scanning is used as a non obstructive medium compatible with the magnetic fields generated in Maglev applications. These sensors are used to align, monitor, and control the dynamic and steady state conditions of the structural members.

Through use of distributed processors using embedded computers, appropriate modeling, distributed processing architectures, and sensor technology, the resulting system could become both economical and readily implemented through integration of presently available technology. Predictive algorithms are used and verified through an embedded communication link tying the distributed processors together over extended distances. This adds to the failsafe characteristics of the system. Power efficiency, material selection optimization, and superconductive elements are optimized through economic use of mathematical models, feedback controls, and the redundant distributed processors.

This heuristic, demand or live load responsive system, with its full array of components for a distributed control feedback system and related set of superconducting magnets also could have other modes of use for responding fully through a programmed response to any episodes of guideway alignment and dynamic behavior, foundation settling, periodicity or harmonic oscillation damping, or earthquake or wind induced motion in the multi-level, multi-use transit guideway mega-structure.

SOFTWARE FOR 'TECHNOLOGICALLY ENDOWED' STRUCTURES

When developing an appropriate monitoring, feedback, and control system,installed as an integral part of a particular structural system, numerous software related factors need to be taken into consideration. They include:

- Quality of applications produced;
- Speed of application development;
- Quality of technical support;
- Ease of use;
- Strength of programming language;
- Responsiveness of vendor service;
- Value for the dollar - cost effectiveness;
- Integration of functions within the product;
- Support for multiple server databases;
- Support for client/server communications protocols;
- Training time required to use the product;
- Quality of code generation facilities;
- Support for dividing processing tasks between client and server;
- Amount of money required; and
- Support for multiple front ends.

Consideration must also be given to Source-Routing Transparency,which supports both source-route bridging and transparent bridging. This is important to determine whether a data packet is intended for a node on the same physical ring. SRT supports both schemes in one physical box.

The comparison of protocols, interfaces, throughput, and parallel network access to relational databases can give one the increased speed needed for multiple processing. Selecting on-demand packet switched connections will facilitate being at the forefront of the newest and latest technology.

CONCEPT FOR AN INTRA-CONTINENTAL, MULTI-LEVEL, MULTI-USE MAGLEV GUIDEWAY MEGA-STRUCTURE

The multi-level, multi-use mega-structure described herein, is designed to facilitate a multi-tiered use of the median strip rights of way of the U.S. Interstate Highway System by "second or third generation" American designed and built Maglev vehicles.

The coffered foundation system and multi-level, multi-use mega-structure described herein, is also designed to accommodate the future installation of non-transit infra-structure and uses that are capable of meeting several local, regional, and national needs which are generally perceived and installed as independent systems and structures. These seemingly unrelated, separate, components of non-transit infra-structure and uses are undergoing major transformation due to recent innovations or pending breakthroughs in science and technology. These seemingly unrelated, separate, components of non-transit infra-structure and uses also enjoy an untapped, underutilized, symbiotic relationship with each other and are rendered synergistic when holistically integrated in the proposed multi-level, multi-use transit guideway mega-structure. The proposed mega-structure, more importantly, provides several unique advantages that are not attainable with a guideway system designed for single vehicle, non-consist, transit operation.

The primary modular, structural, architectural, electrical, and mechnical components for a typical structural bay of the proposed multi-level, multi-use transit guideway mega-structure include:

- A modular, precast, 1300 Cm x 1300 Cm coffered foundation system composed of four (4) subcomponents, see Figs. 3, 4, 5 and 6, that are structurally bonded by a 40 Cm wide pour strip between the subcomponents. Integral to the pour strips between the subcomponents is a 220 Cm octagonal element in the center of the foundation that is sized to accommodate the placement of a precast column over its entire length which shall extend from the bottom of the coffer to 140 Cm below the top of the foundation. See Figs. 7 and 10.
- The 20 Cm space between the inside face of the 100 Cm thick, 460 Cm wide, octagonal, precast column of the primary structural component of the transit guide-way megastructure and the octagonal 110 Cm wide x 320 Cm high element in the center of the foundation, and the space between the bottom of the precast column and the coffer shall be adjusted to accommodate an arrangement of superconducting magnets designed with sufficient power to:

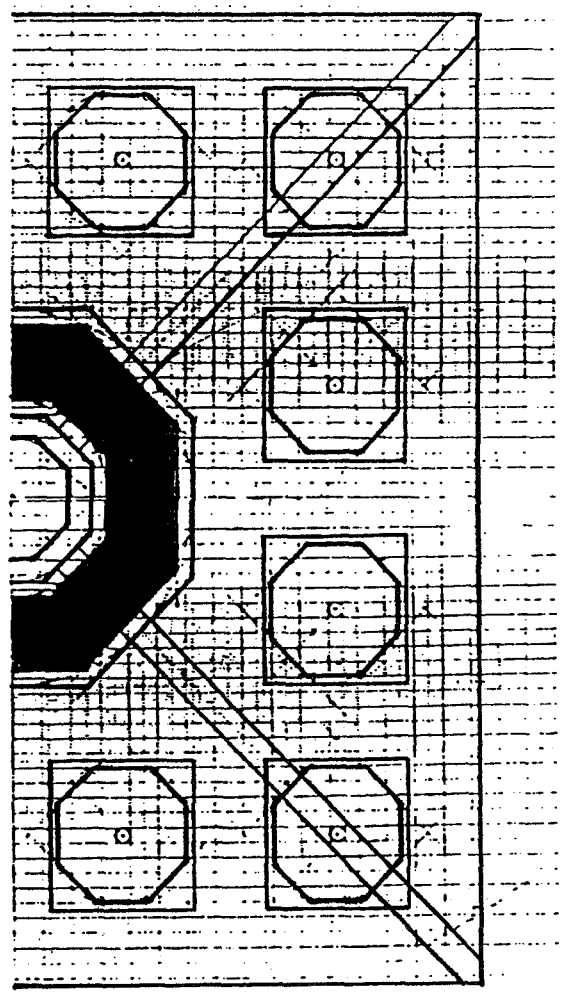

Figure 3

* Isolate the precast column of the primary structural component of the guideway mega-structure and the poured in place octagonal element in the center of the foundation, yet hold it with structural integrity in a position of proper alignment; See Figs. 6, 7 and 18.
* Isolate the precast column of the primary structural component of the transit guideway mega-structure from direct contact with the bottom of the coffer, yet hold it with structural integrity, through the use of self-aligning magnetically activated components, in a position of proper alignment. See Figs. 7, 10 and 18.
* Induce motion according to a pre-programmed fuzzy logic computer software program, to dampen, reduce or eliminate a range of periodicity problems associated with the variety of dynamic events to which the transit guideway mega-structure is subjected - including high winds and earthquakes. See Figs. 7, 10, and 18.

o The twelve (12), 200 Cm x 200 Cm x 650 Cm deep, coffers, which are produced by assembly of the four (4) modular CAD CAM, precast foundation components are configured to accommodate a specially designed, modular, CAD CAM 180 Cm wide x 400 Cm high, octagonally shaped SMES unit and/or flywheel motor/generator set whose mass is situated so that it acts integrally with the mass of the foundation itself and, which in the aggregate on a regionally scaled superspeed (200-400 MPH) or hypersonic evacuated tube Maglev vehicle system (400-10,000 MPH) offers the following possibilities: See Figs. 5, 7, 10, and 11.
* Provides a space in each foundation to build into the guideway mega-structure a modular, redundant source of superconductive electric power for each structural bay of the system.
* Provides a location for housing a network of 180 Cm octagonal SMES units capable of being a part of a program to decentralize the storage of electric power for local, regional or national electric power grid. See Figs. 4 and 7.

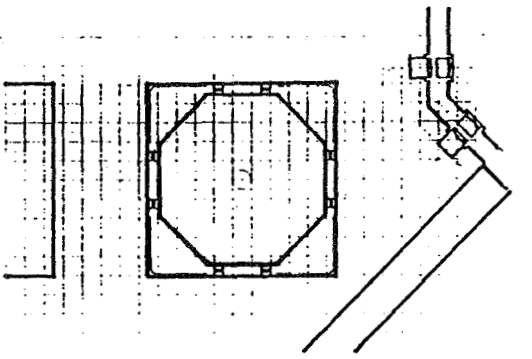

Figure 4

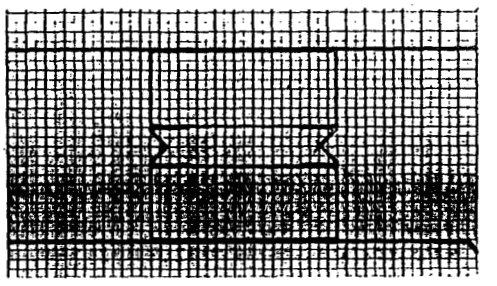

Figure 5

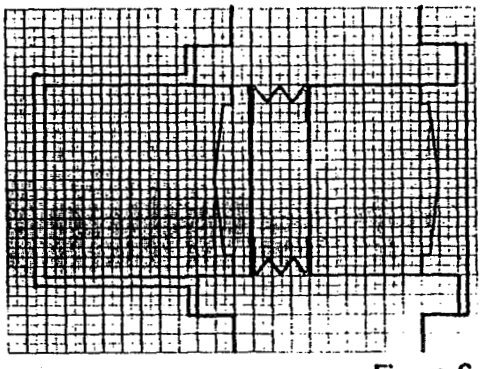

Figure 6

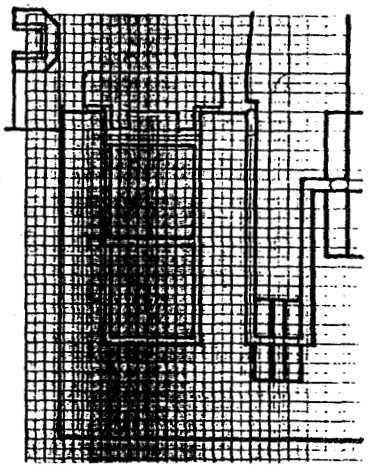

Figure 7

* Provides a triangular space at four sides of each SMES unit which shall be reserved for a series of lightwave based data transmission memory bank and capacity distance achievement functions, which if integrated with the fiber optic cables housed in the primary longitudinal girders of the guideway megastructures can, in addition to the potential of becoming an integral part of the Clinton-Gore proposed one gigabit per second, super data highway project, and also become the primary memory bank components of a regional or national information utility. This dual amenity is highly synergistic and a potential major source of non-transit revenue. This special amenity could also be made available to a broad range of potential corporate and government clients such as banks, and financial institutions, defense contractors, and local, state and federal governmental entities that would benefit from maintaining redundant, safely stored, readily accessible banks of information whose storage or redundancy was important to their organization. See Fig. 4.

- A modular, CAD CAM, octagonally shaped precast column that is designed to fit over the poured in place central octagonal element of the coffered foundation that are spaced 50 meters apart, and whose 15 meter length - above grade - is long enough to allow appropriate clearance of Interstate Highway overpass structures. See Fig. 10.
- A modular, CAD CAM, precast pair of 200 Cm wide, elongated, octagonally shaped primary structural components, designed to be secured to the top of the modular, CAD CAM, octagonally shaped precast column by superconducting magnets in attraction and a set of self aligning magnetic shear pins; See Fig. 8.
- A pair of 125 Cm wide x 200 Cm deep x 2470 Cm long rectangular, post tensioned, transverse beam components that are supported on both sides of the elongated octagonally shaped primary structural component at the mid point, bisecting it in two equal parts. The set of beams also projects beyond the outside face of the elongated, octagonally shaped primary structural components

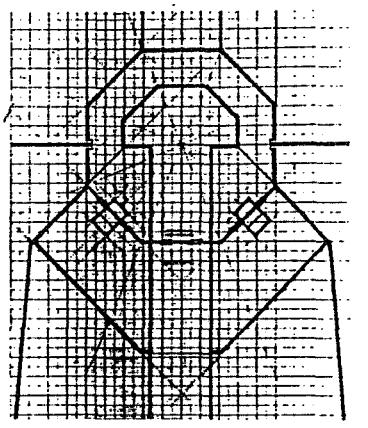

Figure 8

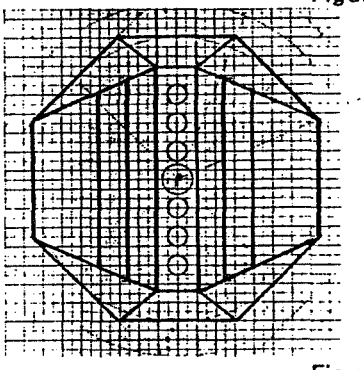

Figure 9

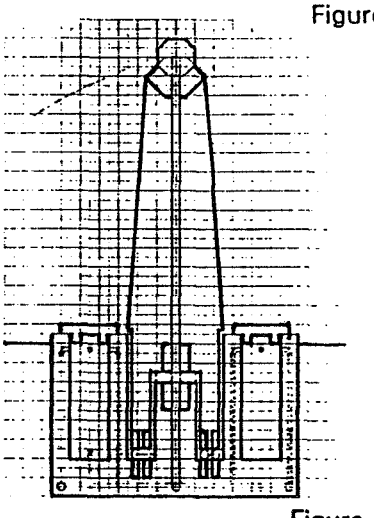

Figure 10

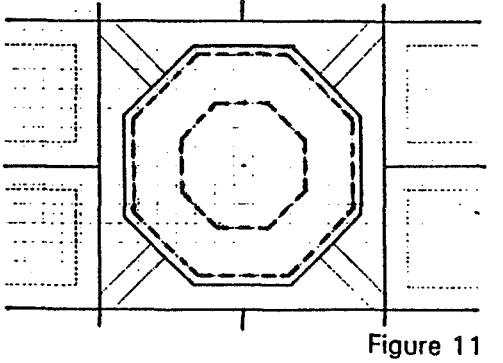

Figure 11

so that it provides support for the cambered, longitudinal, post tensioned exterior beams which are located to accommodate a 400 Cm wide superspeed Maglev vehicle on the top side of the transverse beam system and by use of the Zabar, Levi and Birenbaum air-core linear induction motor suspension and propulsion system, or use of a cylindrical Maglev system proposed by Howard Coffey of Argonne National Laboratory's Center for Transportation Research, support a 400 Cm wide intermediate to high speed Maglev system which could operate using urban stop criteria used by BART in the San Francisco Bay Area, WMATA in Washington, D.C. or Marta in Atlanta, Georgia. See Figs. 16, 18, and 19.

- The octagonal 200 Cm wide, elongated octagonally shaped primary structural component at 750 Cm wide x 1600 Cm high, inside face to inside face, is wide and high enough to accommodate, when bisected a future 4450 Cm long x 672 Cm wide-body Maglev vehicle, which after a period of 5 to 20 years of research and development, can be enclosed in solid-state electrochromatic glass for further development as an evacuated tube or vacuum, tilt-body, hypersonic Maglev system. This arrangement of transverse beams also creates a 200 Cm wide x 200 Cm deep x 750 Cm long space between the inside faces of the elongated octagonally shaped primary structural components and the transverse beams that can be used as the mechanical bay for housing a modular family of mechanical, electrical, and electronic or lightwave-based equipment designed to meet the needs of each structural bay; See Fig. 16, 18 and 19.
- A pair of cambered, 400 Cm wide x 560 Cm deep, post tensioned girders - the primary longitudinal structural components of the proposed Maglev mega-structure - that are designed to span from one elongated octagonally shaped primary structural component to the next; See Fig. 14, 18, and 19.
- A pair of cambered, 240 Cm wide x 560 Cm deep post tensioned, exterior beams, See Figs. 15 and 16, supported at the ends of the 125 Cm x 200 Cm rectangular transverse beams and whose

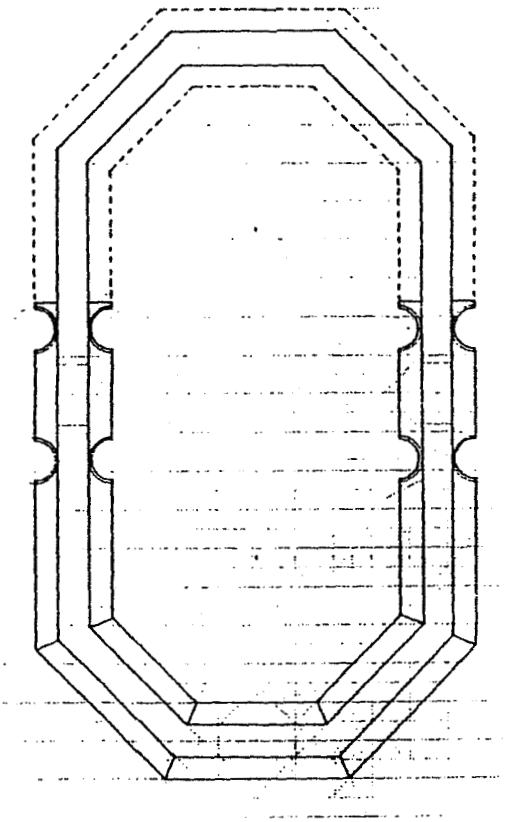

Figure 12

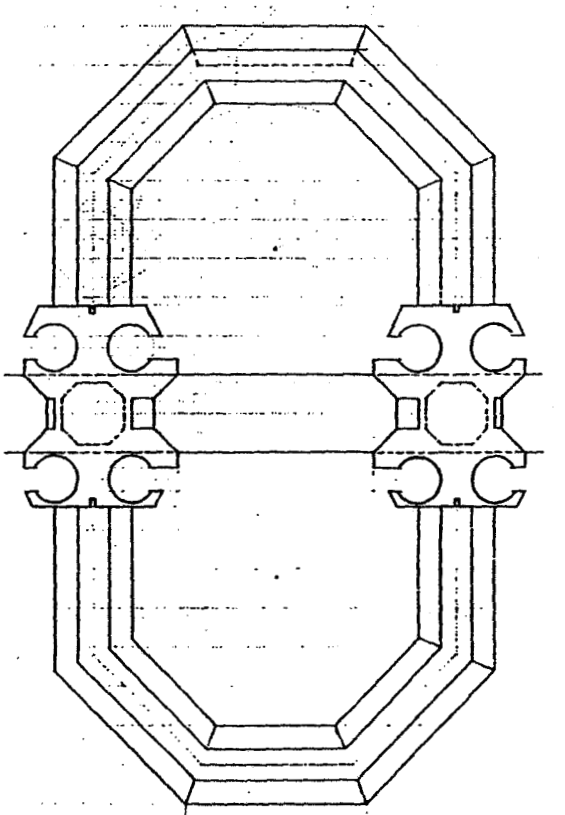

Figure 13

length, although centered on the elongated, octagonally shaped primary structural component is one third of the 50 meter span between the elongated, octagonally shaped primary structural components which in turn supports:

* A pair of transverse, cambered post tensioned beams of similar cross section to the ones adjacent to the elongated, octagonally shaped primary structural components which in this instance are also fixed in place between the exterior beams and primary longitudinal girders with a set of magnetically activated self-aligning shear pins; See Fig. 18 and 19.

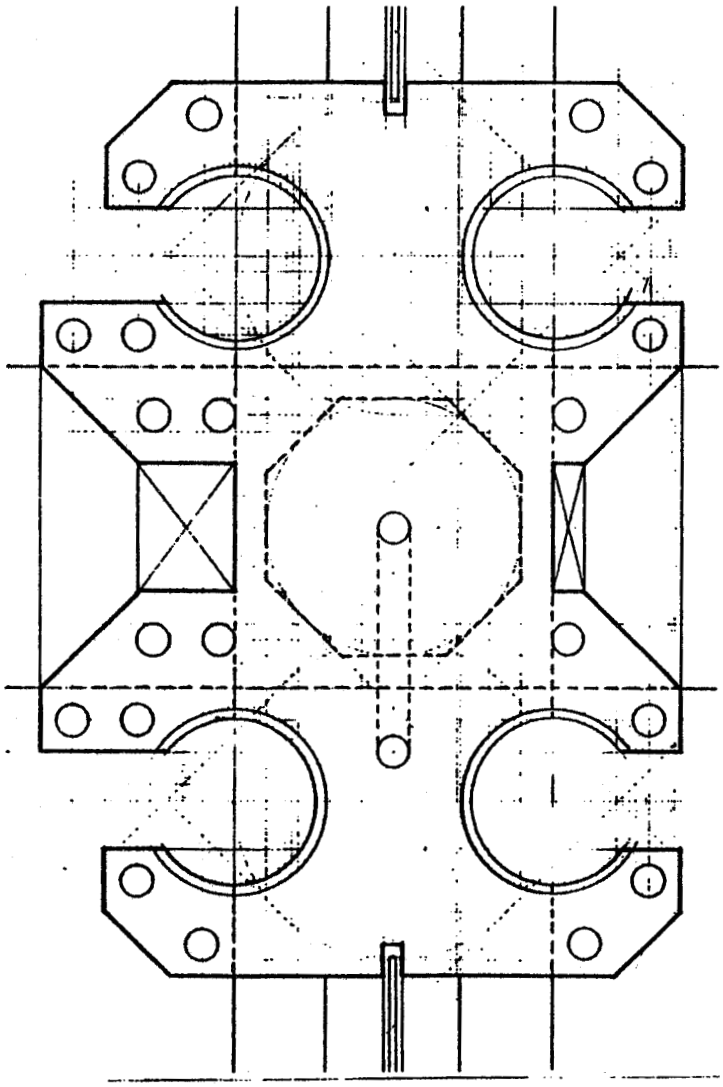

Figure 14

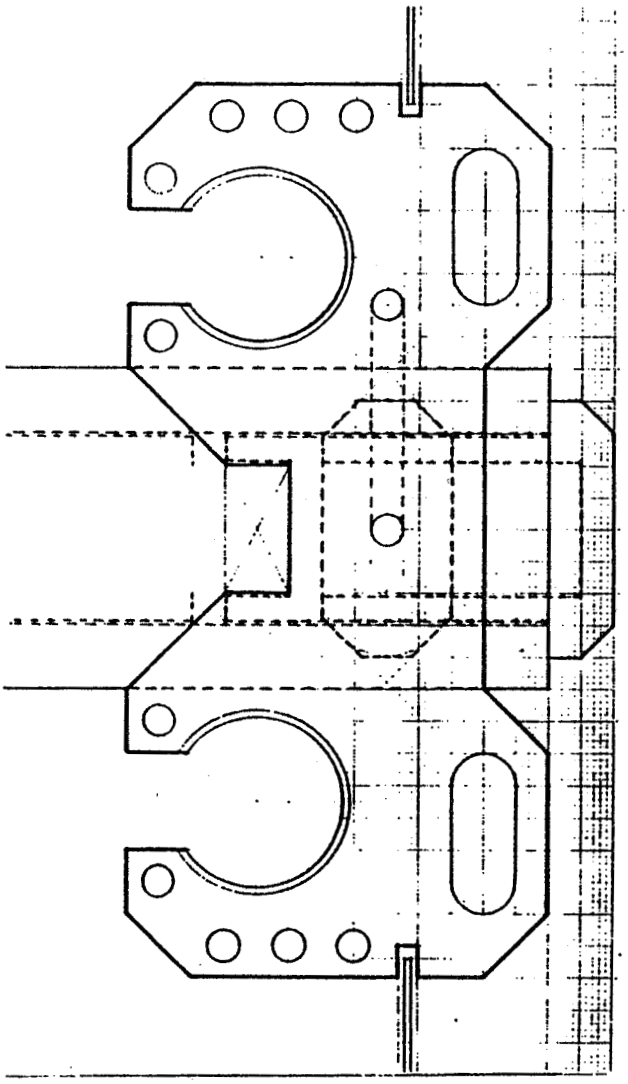

Figure 15

- Provide a series of cavities in the flange and web of both the primary girders and exterior longitudinal beams that are capable of accommodating a variety of non-transit uses that can become significant generators of revenue of sufficient amount to offset the additional costs associated with the coffered foundation and larger multi-level, multi-use guideway mega-structure such as:
  * Fiber optic cable space large enough to meet the needs of the proposed one gigabit per second, National Research and Education Network (NREN), and other users of fiber optic cable such as AT&T, local Bell Systems, Sprint, MCI, and the proposed High Definition Television (HDTV) ground based fiber optic network; See Fig. 14.
  * Superconducting electric power transmission cable space, reserved for the initial increment of programs to retrofit local, regional, and the nation's electric power grid to superconducting electric power transmission lines; See Fig. 14 and 15.
  * A vacuum tube system that could be operated by the U.S. Postal Service, United Parcel, or Federal Express, for developing a "same day" delivery service for letters and small parcels between major metropolitan centers. See Fig. 15.
  * Dedicated space and/or external piping systems designed to accommodate the transport of deep aquafur, special spring, or Alaskan sourced high quality drinking water, petroleum products, and cryogenic liquids produced as a by-product of the maintenance of the solid-state electrochromatic glass enclosed evacuated tube or vacuum for the Hypersonic Maglev Vehicle System; and also capacity to accommodate the future exponential increase in the need to transport nitrogen and other cryogenic liquids associated with an ever-expanding low and high temperature superconductivity industry.

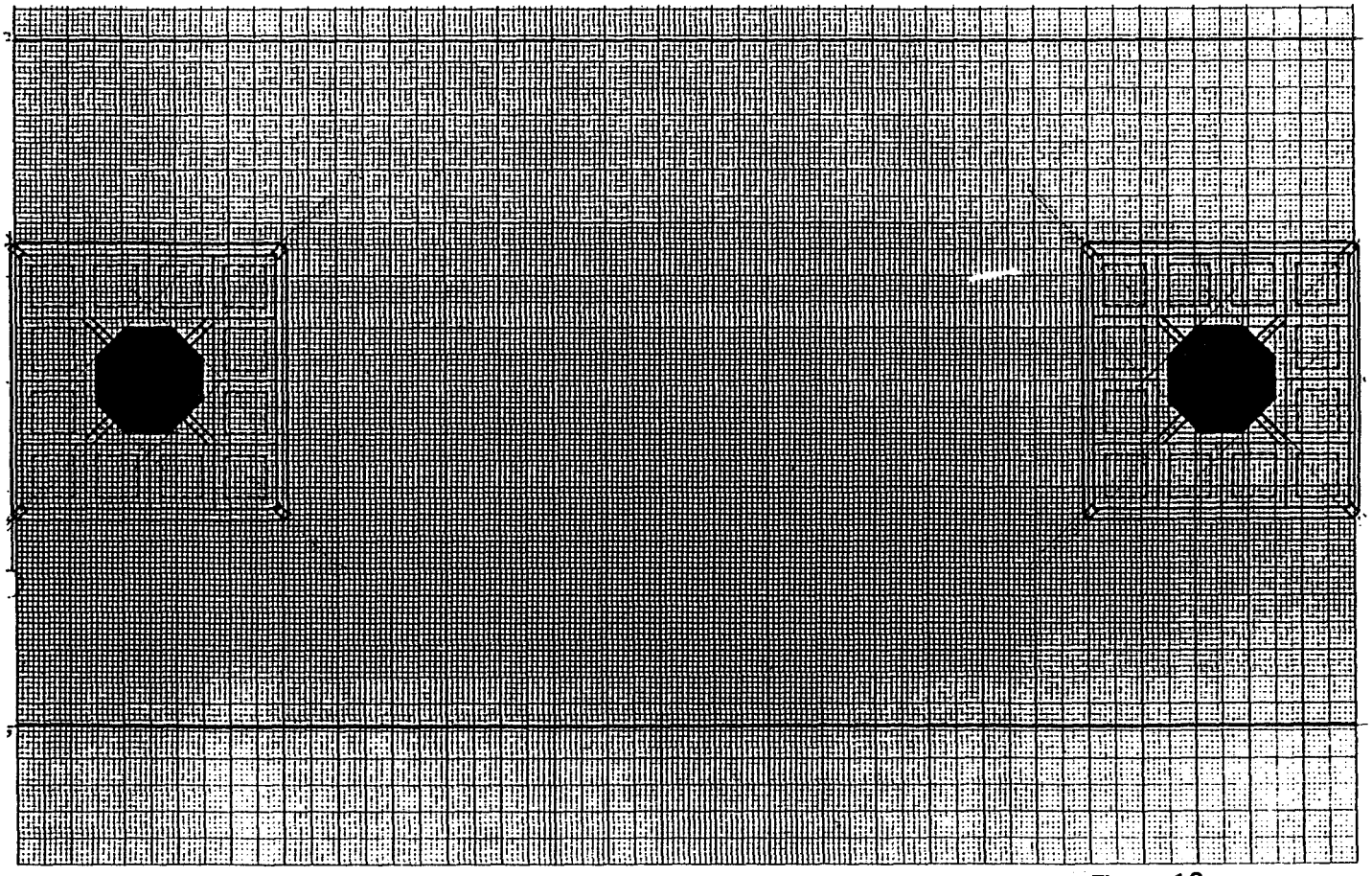

Figure 16

METHODOLOGY TO DEFINITIVELY EVALUATE CONCEPT OF A 'TECHNOLOGICALLY ENDOWED' STRUCTURE

The idea of a 'technologically endowed' structure is to utilize powerful superconducting magnets as generators of 'magnetomotive force' that can be converted to 'mechanical force', and when regulated and channeled properly, can be used advantageously to control the response of structures to live load induced deflections and or excitations of a particular structural member or component of a structural system. The objective is to be able to reduce or altogether eliminate any live load induced deflections and or excitations of the primary structural members. The process of control and regulation can be achieved by the utilization of a 'state of the art' distributed real-time, self-monitoring, adaptive control system - coupled with 'state of the art' micro and super computer systems. This distributed control feedback system is required to govern a heuristic, demand or live load responsive flow of superconductive electric power to the windings of sets of superconducting magnets incorporated in a particular structural member or components.

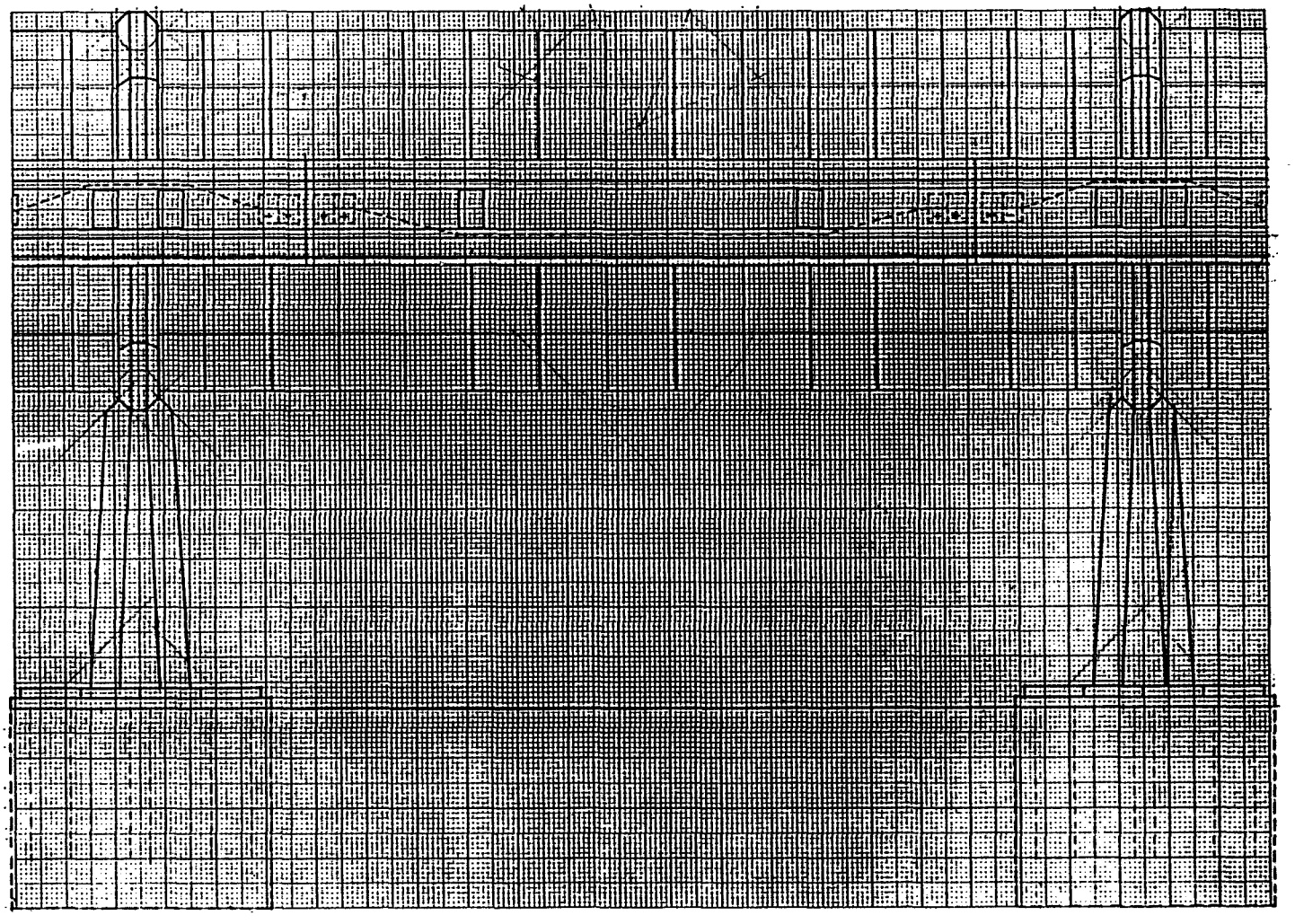

Figure 17

Because of the complexity, symbiotic relationships, and potential synergy of the proposed 'technologically endowed' structural system for the proposed multi-vehicle, multi-use Maglev guideway mega-structure, the following ten areas of research should be undertaken:

1. Study and evaluate the possibility of transferring, in structurally significant values, 'magneto-motive force' into appropriately agile 'mechanical force' and the relationship of the direction of electric current flow to polarity that will include the following experimental approach:
   - Small scale lab models;
   - Large scale (full size) models.
2. Computer simulation of live-load responsive structural members, superconductively activated structural components, and the proposed 'technologically endowed' structural system relative to geometric design, size and power of superconducting magnets needed to do actual structural work - a major numerical undertaking.
3. Surveying of 'state of the art' of available research and development of the interaction between structural materials including structural polymers and some magnetically inert non-ferrous composite materials which might be used as possible substitutes for concrete and steel.
4. Study and evaluate applicability of the 'technologically endowed' structure concept to spans longer than 50 meter spacing of the proposed structure:
   - 100 meter span
   - 250 meter span
   - 500 meter span
   - 1,000 meter span
5. Study and evaluate the applicability of 'technologically endowed' live-load responsive structural systems for use on space-based platforms or structural systems.
6. Study and evaluate utilizing 'state of the art' electronic and laser based diagnostic structure monitoring feedback and control systems in the prototype structural system.
7. Study and evaluate capabilities of the prototype structure to compatibly provide additional space for the lightwave-based data transmission and memory systems associated with the Clinton-Gore proposed one gigabit per second Super Data Highway Project.
8. Study and evaluate the feasibility and economic advantages of utilizing 'state of the art' Computer Aided Design (CAD) and Computer-Aided Manufacturing (CAM) technology for the prototype 'technologically endowed' structure.
9. Study and evaluate the feasibility of generating electric power from photo voltaic cells located in the exterior surfaces of the guideway structure and on the roof of the Maglev vehicles sufficient to service the hotel functions of the guideway and vehicle systems.
10. Study and evaluate the feasibility of locating a network of satellite receivers on the guideway structure sufficient to facilitate it becoming a linear teleport.

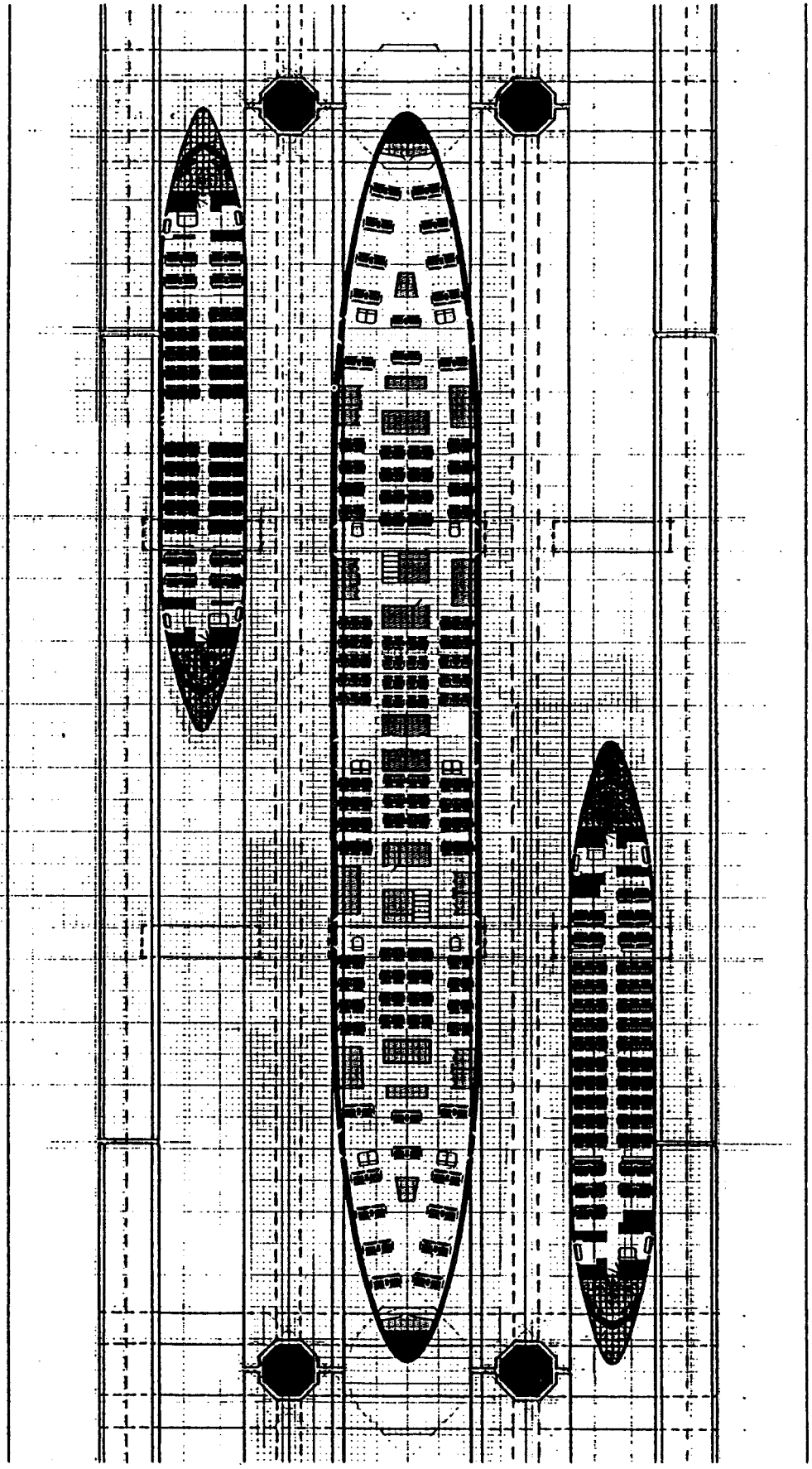

Figure 18

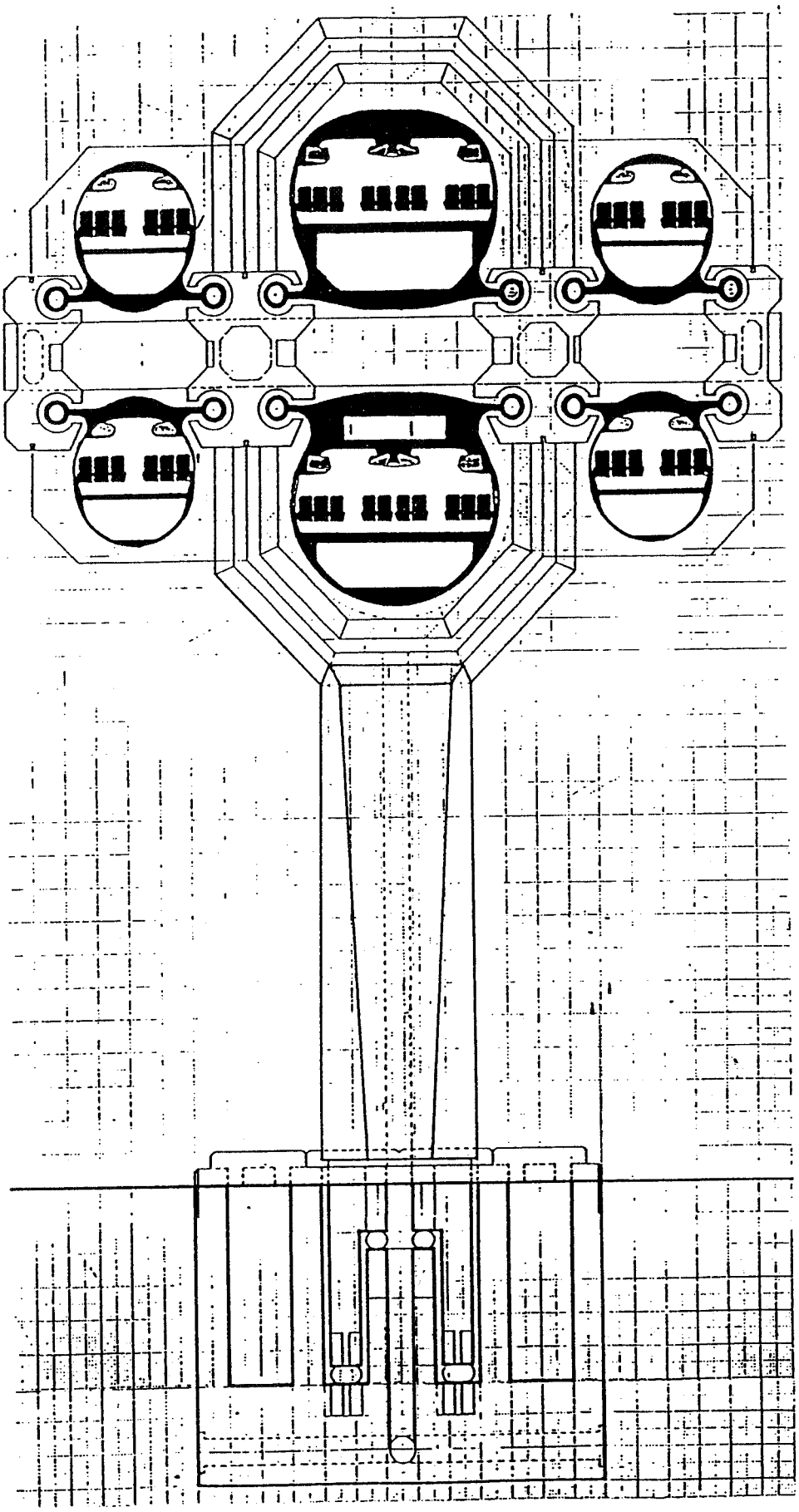

Figure 19

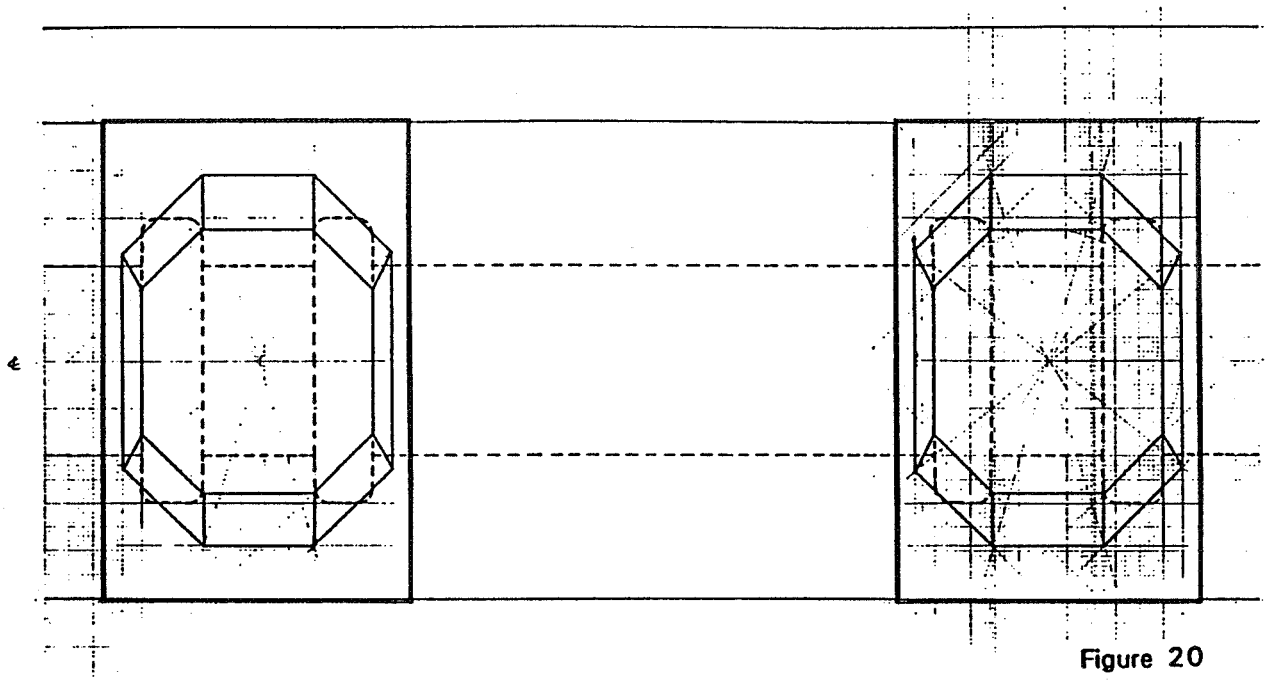

Figure 20

RECOMMENDATIONS AND CONCLUSIONS

Several recommendations regarding determining the feasibility of 'technologically endowed' structural systems are worthy of consideration. They include the following:

- A consortium of private sector and public sector members, including universities and national research laboratories, should be organized to conduct the ten point research study proposed herein, as a methodology to definitively evaluate the concept of a 'technologically endowed' structure;
- Conduct a definitive evaluation of the people moving and cargo carrying capabilities of the Maglev guideway mega-structure delineated herein, and determine whether or not a "technologically endowed" Maglev mega-structure designed to achieve multiple transit and non-transit goals would radically transform the economics of Maglev guideway systems by providing several unique income-generating capabilities that are unattainable with smaller guideway systems designed for single vehicle, non-consist, transit operation; and
- Identify the optimum North-South and East-West Interstate Highway Systems whose median strip rights of way are the natural location for multi-level, multi-vehicle, Maglev guideway mega-structures, similar in scale to the one delineated herein, which should not be pre-empted with the premature installation of bi-directional, single vehicle Maglev systems.
- Conduct an evaluation of the axiomatic relationship of mobility to military force structure and the potential to achieve a prudent reduction in U.S. military force structure as a consequence of installation of the proposed multi-vehicle, multi-use Maglev guideway megastructure in the median strip of U.S. Interstates 5, 55, and 95 North-South and 80 and 10 East-West.

The building of 'technologically endowed' structural systems constitutes the beginning of the epoch of a new generation of structures. Each new generation of 'technologically endowed' structures should improve the ability to address a broad variety of performance enhancements in structural members, components and systems, including the use of superconducting magnets in shims and self-aligning shear pins for facilitating the erection and/or disassembly of CAD/CAM precast structural systems. Over time, succeeding generations of 'technologically endowed' structural systems can be expected to achieve even greater efficiency in the art of substituting superconductive electric power and magnetism for concrete and steel.

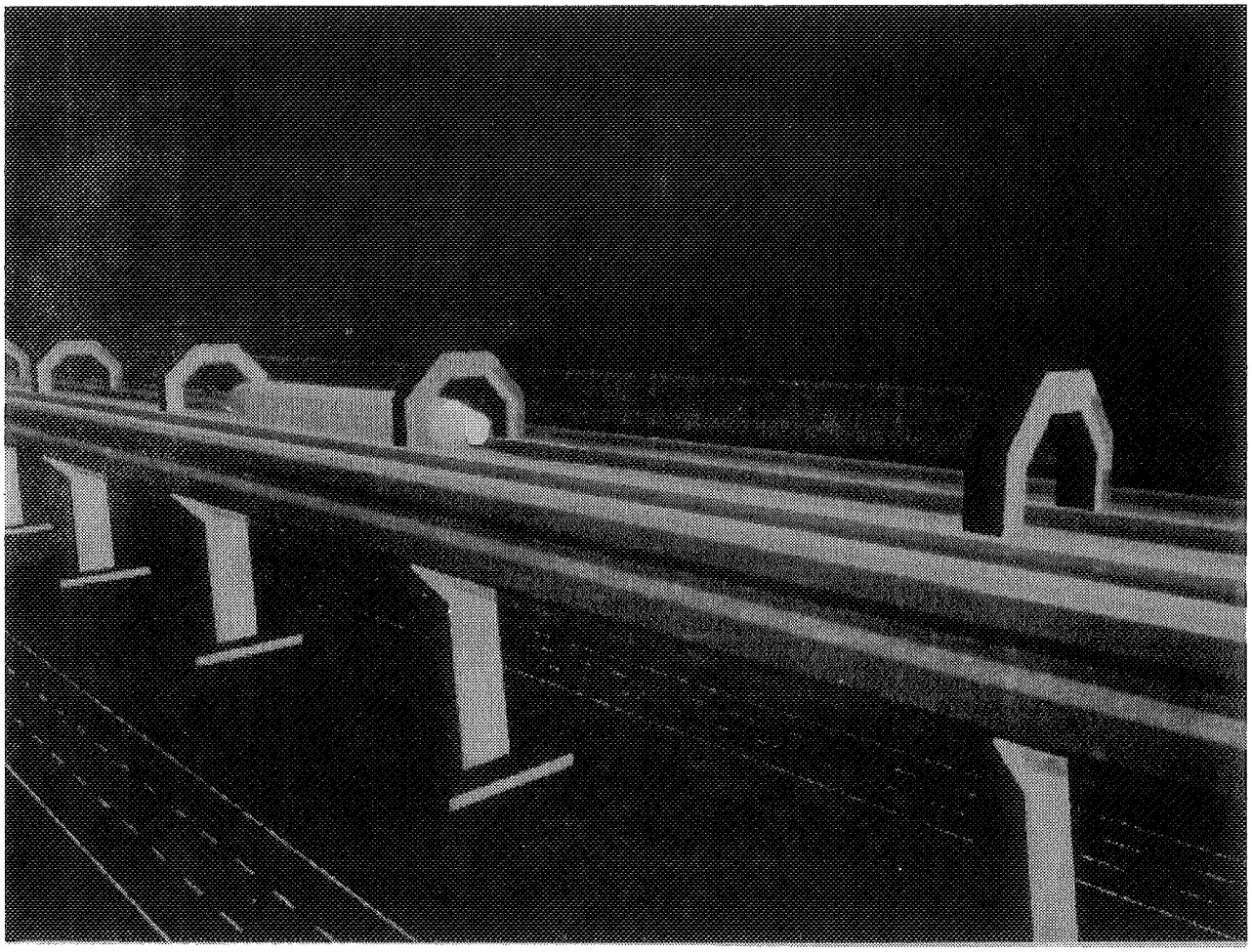

FIGURE 21

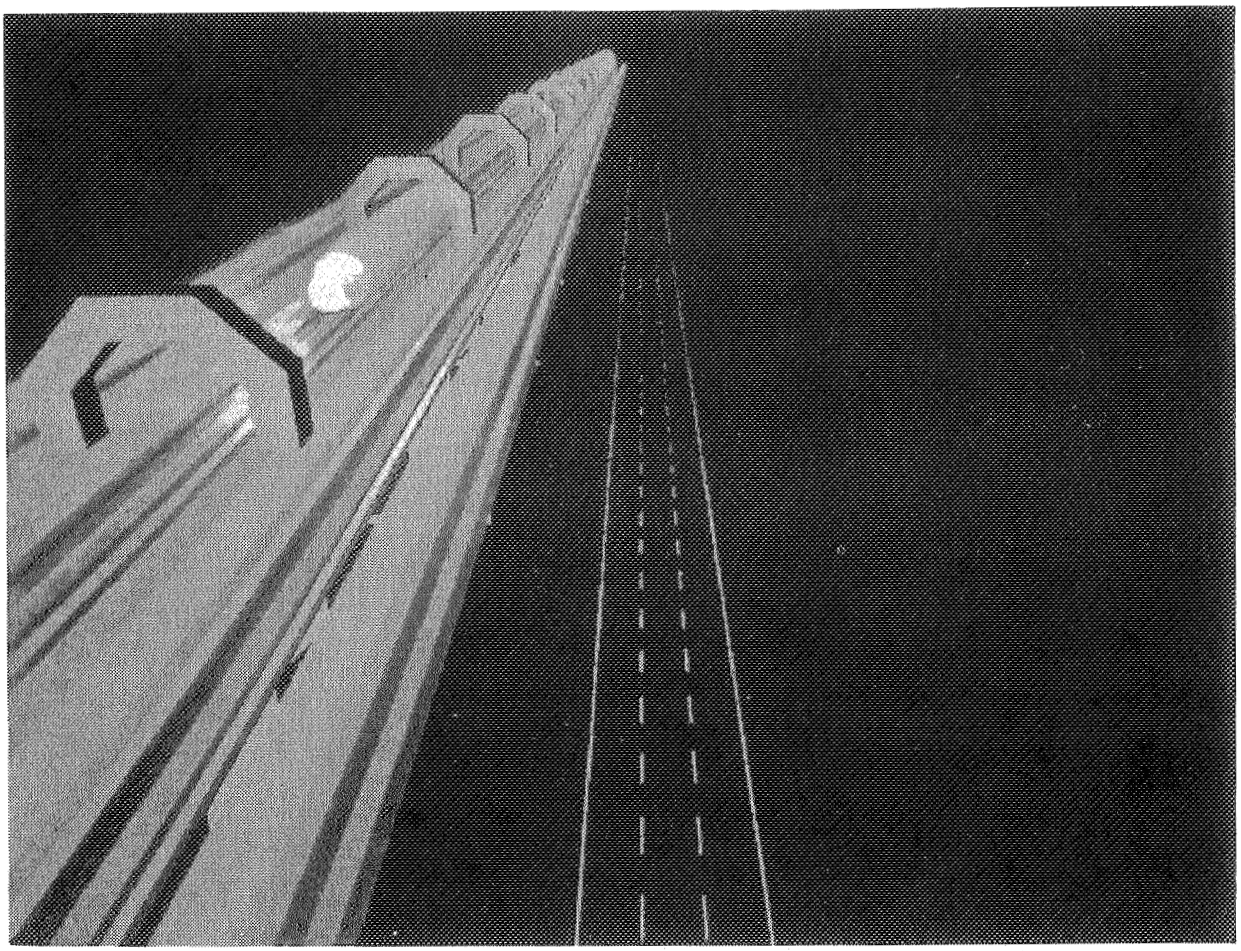

FIGURE 22

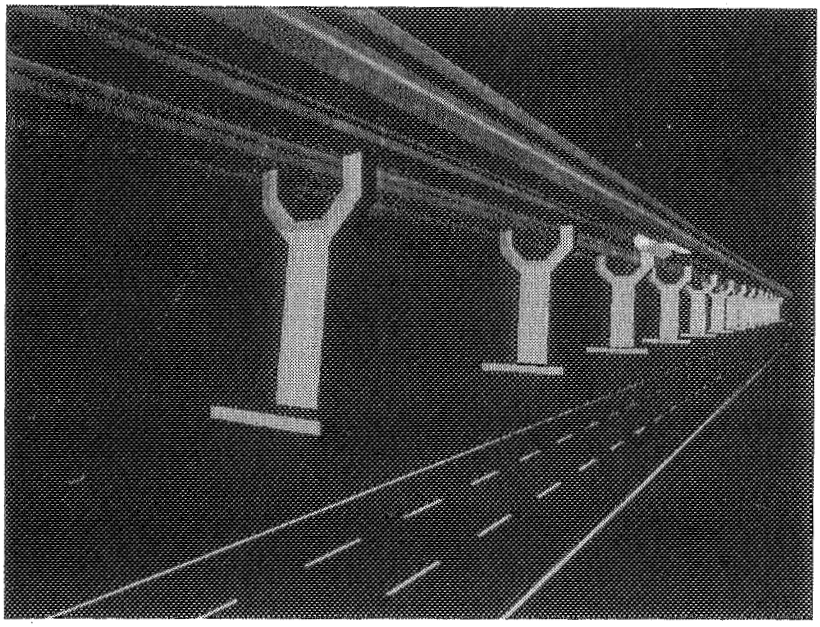

FIGURE 23

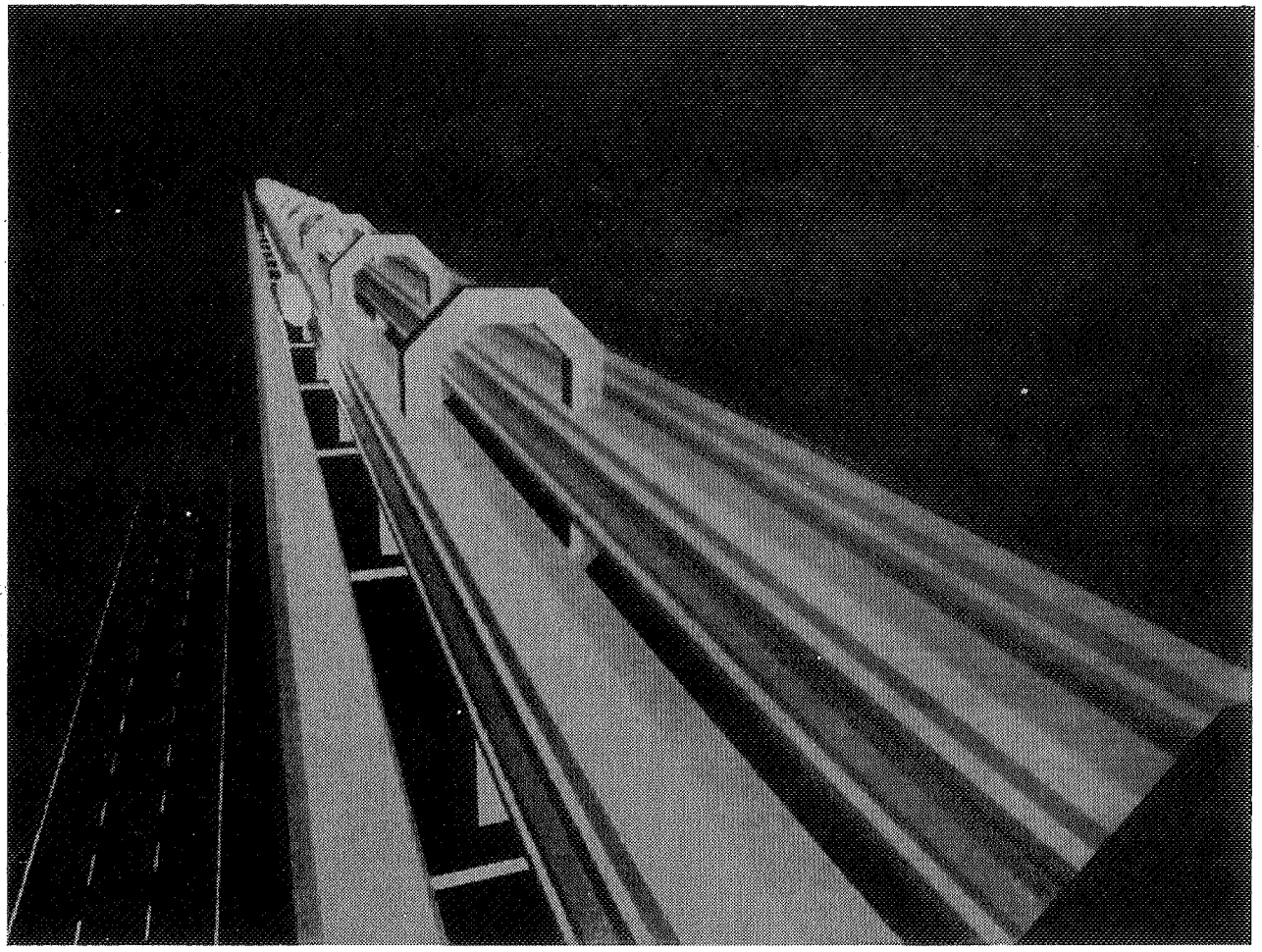

FIGURE 24

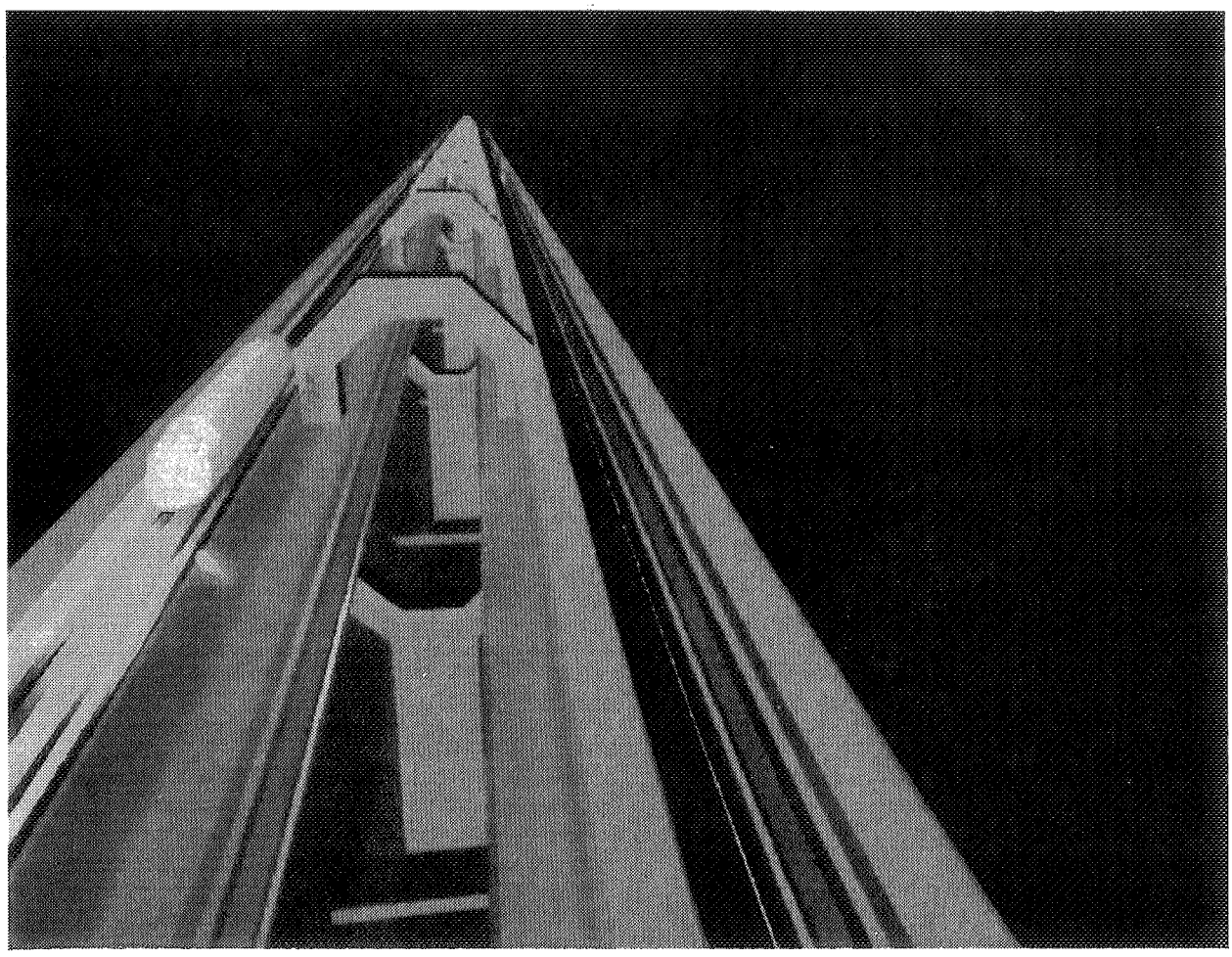

FIGURE 25

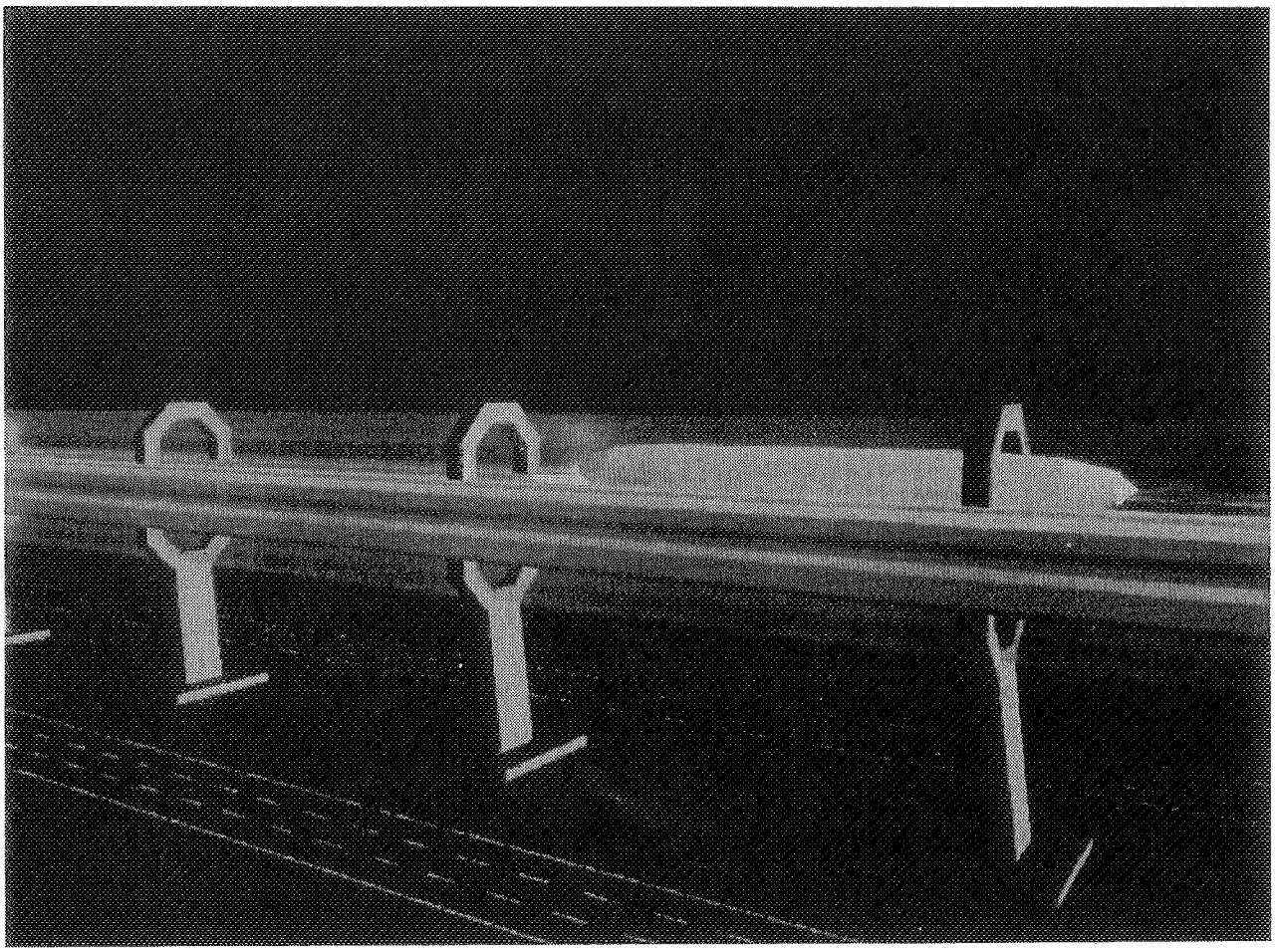

FIGURE 26

Session 15 -- Controls 3

Chairman: Alexander Kuzin
Moscow Aviation Technological Institute (MATI)

APPROACH TO SYNCHRONIZATION CONTROL OF MAGNETIC BEARINGS USING FUZZY LOGIC

Li-Farn Yang*
Department of Mechanical Engineering
National Chung Cheng University
Chia-Yi, TAIWAN, R.O.C.

ABSTRACT

This paper presents a fuzzy-logic approach to the synthesis of synchronization control for a magnetically suspended rotor system. The synchronization control enables a whirling rotor to undergo synchronous motion along the magnetic bearing axes; thereby avoiding the gyroscopic effects that degrade the stability of rotor systems when spinning at high speed. The control system features a fuzzy controller acting on the magnetic bearing device, in which the fuzzy inference system is trained through fuzzy rules to minimize the differential errors between four bearing axes so that an error along one bearing axis can affect the overall control loop for the motion synchronization. Numerical simulations of synchronization control for the magnetically suspended rotor system are presented to show the effectiveness of the present approach.

INTRODUCTION

Active magnetic bearings, which permit non-contact suspension of levitated objects, have received increasing attention in recent years. The contactless nature of magnetic bearings brings many advantages over the conventional bearings, such as energy efficiency, low wear, longer life span, absence of lubrication and mechanical maintenance, and wide range of working temperature. Also, closed-loop control of magnetic bearings enables active vibration suppression and on-line control of bearing stiffness. Studies [1-3] performed so far indicate that magnetic bearings have been very effectively used for the suspension of high-speed rotating machines, essentially at speeds over 10,000 rpm. For instance, NASA has employed magnetic bearings to support the high-speed turbopumps for use in space shuttle main engines. On the other hand, magnetic bearings have been installed on momentum wheels and CMG devices at NASA [1-5] as the gyrotorquers for the attitude control and momentum arrangement of space structures. Other industrial applications of actively controlled magnetic bearings include high-speed centrifuges, magnetic spindles, vacuum pumps, micromachines, etc. [1-2].

Magnetic bearing dynamics are inherently nonlinear as the result of nonlinearities in the electromagnetic fields and force coupling effects among the various axes. These nonlinear characteristics require an increase in the complexity of modeling, estimation, and control of the

* Associate Professor, AIAA Member.

magnetic bearings. In addition, the control performance of magnetic bearings is very sensitive to unpredictable disturbances and the plant uncertainties, wherein the classical feedback control does not seem entirely effective and satisfactory for such purposes. Various control strategies have been studied for the adaptive control of magnetic bearings when disturbed with uncertain dynamics or unknown parameters. Some of them reviewed as references here are adaptive control [6], time delay control [7], sliding mode control [3], and learning control [8]. The investigation of these papers was aimed at using different approaches to adapt the respective controller to changes in the parameters of magnetic bearings so as to continuously strive to optimize the control performance. Once a controller is activated, the magnetically suspended rotor will experience the conical and translatory whirl modes when whirling about the central axis as shown in Fig. 1. The conical whirl mode gives rise to the unbalanced torque's twisting the rotor which in turn triggers the gyroscopic effects, and thereby effecting the instability of the rotor system if not properly controlled. However, the translatory whirl mode yields the synchronous motion along the radial directions, important for a spinning rotor especially for use in high-precision, fine-cutting process. The purpose of this paper is thus to explore the synchronization problem of the magnetically suspended rotor system from the viewpoint of fuzzy-logic control [9,10].

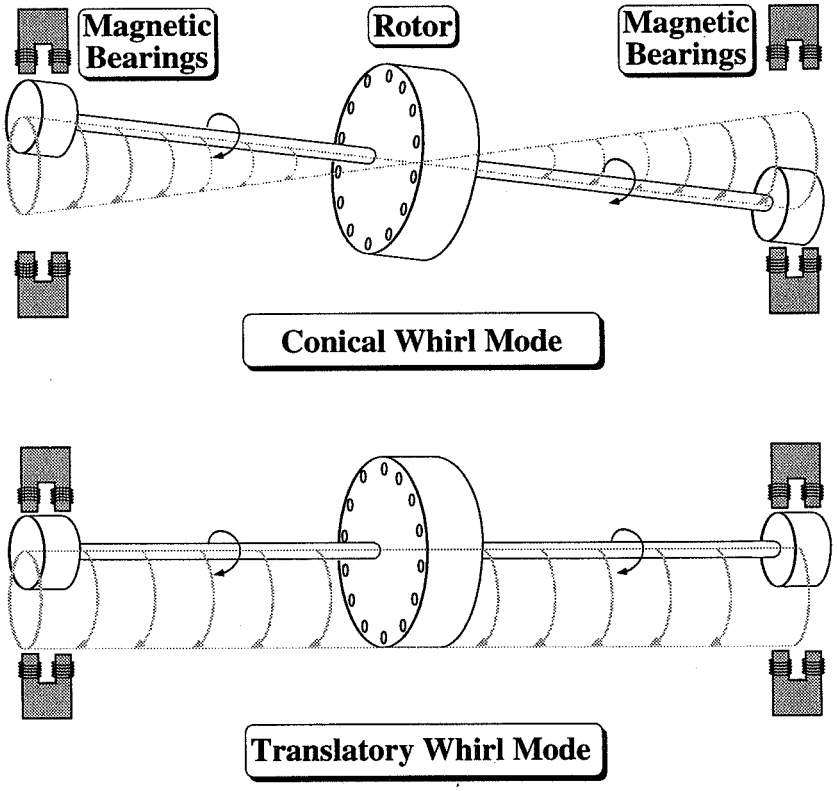

Figure 1: Whirl modes of a rigid rotor in magnetic bearings

In this paper, we introduce a fuzzy-logic scheme for the adaptive synchronization of the magnetic bearing system, which consists of a local disturbance compensator and a coupling controller for each bearing axis. The local compensator balances the rotor against disturbances, while the

coupling control responds to the synchronization error, i.e., the difference between the two motion errors along the bearing axes. The fuzzy inference system is trained through fuzzy rules for the synchronization control, in which each fuzzy controller fuzzifies the inputs by the trapezoidal membership function, applies an "AND" logic operator to handle multiple fuzzified inputs, shapes the consequent set by a fuzzy associated memory (FAM) matrix, and aggregates all outputs during defuzzifying. The defuzzification method is the centroid computation which involves the computation of centroid values of regions defined by overlapping membership functions.

The content of this paper will be outlined as follows: First, the description of the system dynamics is presented for a rotor system equipped with magnetic bearings. Then, the derivation of the fuzzy controller is detailed and applied to the synthesis of synchronization control for rejecting gyroscopic effects as well as disturbances from the rotor system. Finally, simulation results are presented for discussion.

SYSTEM DYNAMICS

In this section, the dynamics of a rotor system and magnetic bearings are studied and incorporated into a rotor-bearing system. This system is composed of a disk mounted on a rigid shaft which is actively positioned in the radial directions through the use of the magnetic bearings located at two shaft ends. This paper considers the utilization of radial magnetic bearings as an actuating device onboard the rotor system. Let's start with the description of rotor dynamics to serve as the background for the investigation of this paper.

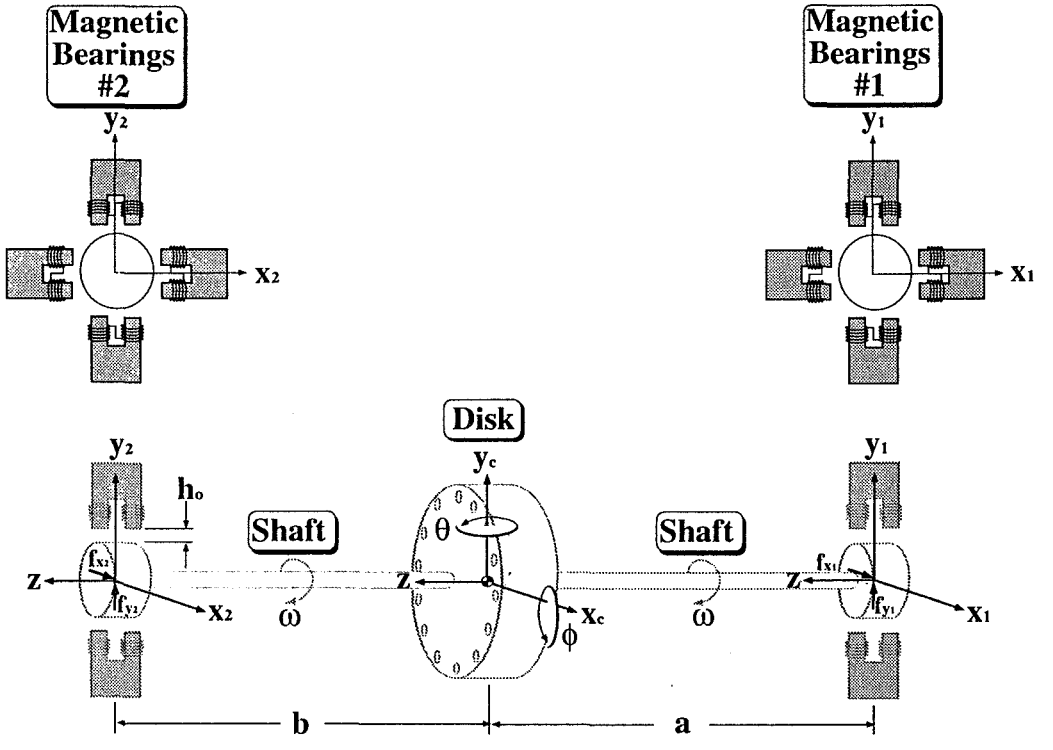

Figure 2: A rigid rotor system with actively controlled magnetic bearings

As demonstrated by Fig. 2, the rotor is modeled as a disk constantly spinning about the principal z-axis of the shaft while simultaneously suspended by two sets of magnetic bearings. Assume x_c and y_c denote the displacements of the center of mass of the rotor along the x and y directions as shown in Fig. 2, and ϕ and θ indicate (roll and pitch) angles of rotation about the x and y axes, respectively. These angles are normally assumed to be very small due to the restriction of narrow air gap within the magnetic bearings. The equations of motion of this rotor-bearing system can then be derived in the following matrix form.

$$\begin{bmatrix} m & 0 & 0 & 0 \\ 0 & m & 0 & 0 \\ 0 & 0 & I_{rr} & 0 \\ 0 & 0 & 0 & I_{rr} \end{bmatrix} \begin{bmatrix} \ddot{x}_c \\ \ddot{y}_c \\ \ddot{\theta} \\ \ddot{\phi} \end{bmatrix} + I_{zz}\omega \begin{bmatrix} 0 & 0 & 0 & 0 \\ 0 & 0 & 0 & 0 \\ 0 & 0 & 0 & 1 \\ 0 & 0 & 1 & 0 \end{bmatrix} = \begin{bmatrix} 1 & 1 & 0 & 0 \\ 0 & 0 & 1 & 1 \\ a & -b & 0 & 0 \\ 0 & 0 & -a & b \end{bmatrix} \begin{bmatrix} f_{x_1} \\ f_{x_2} \\ f_{y_1} \\ f_{y_2} \end{bmatrix} \tag{1}$$

where m is the rotor mass, I_{rr} is the moment-of-inertia of the rotor in the radial direction, I_{zz} is the moment-of-inertia about the z-axis, and ω is the spinning rate of the rotor about the z-axis. The second term in Eq. (1) can readily be recognized as the gyroscopic momenta depending on the spinning rate ω.

As for the input in Eq. (1), the f_{xi}'s and f_{yi}'s represent the magnetic forces provided by two sets of magnetic bearings each made of an eight pole electromagnet. The electromagnets, when charged, are capable of inducing coupled magnetic forces along the x and y axes. The coupling effects of magnetic forces across two axes can be neglected without loss of generality so that the magnetic force along each axis is derived independently of the displacement and current along the other axis. Figure 2 demonstrates the magnetic bearings #1 and #2 located at distances a and b from the disk. Assume that the control current signals along the x-axis are denoted by i_{x1} and i_{x2} for the bearings #1 and #2, respectively, while those along the y-axis indicated by i_{y1} and i_{y2}, accordingly. Also, the displacements of the shaft from the bearing center are described by x_i and y_i at two bearing ends. Based on Maxwell's law, the magnetic forces due to the electromagnet along the x and y axes can be modeled by:

$$\begin{aligned} f_{x_1} &= G\left[\frac{(I_o+i_{x_1})^2}{(h_o-x_1)^2} - \frac{(I_o-i_{x_1})^2}{(h_o+x_1)^2}\right], \quad f_{x_2} = G\left[\frac{(I_o+i_{x_2})^2}{(h_o-x_2)^2} - \frac{(I_o-i_{x_2})^2}{(h_o+x_2)^2}\right], \\ f_{y_1} &= G\left[\frac{(I_1+i_{y_1})^2}{(h_o-y_1)^2} - \frac{(I_o-i_{y_1})^2}{(h_o+y_1)^2}\right] - \frac{b}{a+b}mg, \quad f_{y_2} = G\left[\frac{(I_2+i_{y_2})^2}{(h_o-y_2)^2} - \frac{(I_o-i_{y_2})^2}{(h_o+y_2)^2}\right] - \frac{a}{a+b}mg \end{aligned} \tag{2}$$

where h_0 is the nominal air gap at equilibrium and G is an electromagnet constant. The I_0 is a bias current in Eq. (2), whereas the bias currents I_1 and I_2 account for balancing the weight of the disk and they can be written by :

$$I_1 = \frac{h_o}{\sqrt{G}}\sqrt{\frac{GI_o^2}{h_o^2} + \left(\frac{b}{a+b}\right)mg} \quad \text{and} \quad I_2 = \frac{h_o}{\sqrt{G}}\sqrt{\frac{GI_o^2}{h_o^2} + \left(\frac{a}{a+b}\right)mg} \tag{3}$$

Since the air gap is restricted to be very narrow, the magnetic forces in Eq. (2) can be linearized and arranged into a matrix form given by:

$$\begin{bmatrix} f_{x_1} \\ f_{x_2} \\ f_{y_1} \\ f_{y_2} \end{bmatrix} = \frac{2GI_o}{h_o^2} \begin{bmatrix} 2 & 0 & 0 & 0 \\ 0 & 2 & 0 & 0 \\ 0 & 0 & 1+\frac{I_1}{I_o} & 0 \\ 0 & 0 & 0 & 1+\frac{I_2}{I_o} \end{bmatrix} \begin{bmatrix} i_{x_1} \\ i_{x_2} \\ i_{y_1} \\ i_{y_2} \end{bmatrix} + \frac{2GI_o^2}{h_o^3} \begin{bmatrix} 2 & 0 & 0 & 0 \\ 0 & 2 & 0 & 0 \\ 0 & 0 & 1+(\frac{I_1}{I_o})^2 & 0 \\ 0 & 0 & 0 & 1+(\frac{I_2}{I_o})^2 \end{bmatrix} \begin{bmatrix} x_1 \\ x_2 \\ y_1 \\ y_2 \end{bmatrix} \quad (4)$$

which decouples control currents and displacements for the magnetic forces. Moreover, the following relations are generated from the geometry illustrated in Fig. 2.

$$\begin{matrix} x_c = \frac{bx_1+ax_2}{a+b} \\ y_c = \frac{by_1+ay_2}{a+b} \end{matrix} \quad \text{and} \quad \begin{matrix} \theta = \frac{1}{a}(x_1 - x_c) \\ \phi = \frac{1}{a}(y_c - y_1) \end{matrix} \quad (5)$$

Substituting the disk variables (x_c , y_c , θ, ϕ) in Eq. (1) with those relative to the bearing axes yields:

$$\ddot{\mathbf{x}} = \mathbf{C}\dot{\mathbf{x}} + \mathbf{K}\mathbf{x} + \mathbf{B}\mathbf{u} \quad (6)$$

where the state variable vector is given by $\mathbf{x} = [x_1 , x_2 , y_1 , y_2]^T$, and the input vector by $\mathbf{u} = [i_{x1} , i_{x2} , i_{y1} , i_{y2}]^T$. In Eq. (6), the damping, stiffness, and input matrices are:

$$\mathbf{C} = (\frac{w}{a+b})(\frac{I_{zz}}{I_{rr}}) \begin{bmatrix} 0 & 0 & a & -a \\ 0 & 0 & -b & b \\ a & -a & 0 & 0 \\ -b & b & 0 & 0 \end{bmatrix},$$

$$\mathbf{K} = \frac{2G}{h_o^3} \begin{bmatrix} 2I_o^2(\frac{1}{m}+\frac{a^2}{I_{rr}}) & 2I_o^2(\frac{1}{m}-\frac{ab}{I_{rr}}) & 0 & 0 \\ 2I_o^2(\frac{1}{m}-\frac{ab}{I_{rr}}) & 2I_o^2(\frac{1}{m}+\frac{b^2}{I_{rr}}) & 0 & 0 \\ 0 & 0 & (I_o^2+I_1^2)(\frac{1}{m}+\frac{a^2}{I_{rr}}) & (I_o^2+I_2^2)(\frac{1}{m}-\frac{ab}{I_{rr}}) \\ 0 & 0 & (I_o^2+I_1^2)(\frac{1}{m}-\frac{ab}{I_{rr}}) & (I_o^2+I_2^2)(\frac{1}{m}+\frac{b^2}{I_{rr}}) \end{bmatrix},$$

$$\mathbf{B} = \frac{2G}{h_o^2} \begin{bmatrix} 2I_o(\frac{1}{m}+\frac{a^2}{I_{rr}}) & 2I_o(\frac{1}{m}-\frac{ab}{I_{rr}}) & 0 & 0 \\ 2I_o(\frac{1}{m}-\frac{ab}{I_{rr}}) & 2I_o(\frac{1}{m}+\frac{b^2}{I_{rr}}) & 0 & 0 \\ 0 & 0 & (I_o+I_1)(\frac{1}{m}+\frac{a^2}{I_{rr}}) & (I_o+I_2)(\frac{1}{m}-\frac{ab}{I_{rr}}) \\ 0 & 0 & (I_o+I_1)(\frac{1}{m}-\frac{ab}{I_{rr}}) & (I_o+I_2)(\frac{1}{m}+\frac{b^2}{I_{rr}}) \end{bmatrix}$$

Equation (6) is the model of a rotor system equipped with magnetic bearings as necessary for the derivation of the fuzzy-based synchronization controller in the next section.

CONTROL DESIGN

In this paper, the control objective of the magnetic bearing system is to synchronize the motion of a suspended rotor during whirling, so as to insure the rotor system against the unbalance and gyrostatics. In doing so, we present a synchronization control concept that makes concurrent use of a fuzzy-logic control and a coupling control, and assesses its applicability to the magnetic control of the rotor system. An integrated cross-coupled, fuzzy-based controller is developed with the respective merits of each particular control included. First, it is known that fuzzy control is very effective in adapting nonlinear systems to the plant uncertainties and unpredictable disturbances. Then, adding the coupling control in conjunction with the fuzzy adaptation can enable the resulting control system to perform the motion synchronization for the multi-axis system.

Figure 3 shows the control block diagram of a fuzzy-based synchronization controller for the magnetically suspended rotor system. The fuzzy inference system consists of four local compensators that are cross-coupled to one another by using three coupling controllers to compromise the differential errors between the bearing axes. The local compensators are applied to the four bearing coordinates in balancing the rotor around the center of rotation. The coupling controllers link the x_1 - x_2 , y_1 - y_2, and x_1 - y_1 axes, respectively; in response to the synchronization errors as defined by:

$$\begin{aligned} e_x(t) &= x_1(t) - x_2(t), \quad \dot{e}_x(t) = \dot{x}_1(t) - \dot{x}_2(t), \\ e_y(t) &= y_1(t) - y_2(t), \quad \dot{e}_y(t) = \dot{y}_1(t) - \dot{y}_2(t), \\ e_{xy}(t) &= x_1(t) - y_1(t), \quad \dot{e}_{xy}(t) = \dot{x}_1(t) - \dot{y}_1(t) \end{aligned} \tag{7}$$

which in fact represent the differences between the two motion errors along the bearing axes. The first two equations in Eq. (7) attempt to synchronize the motion of the rotor in parallel to the directions of x_1 - x_2 and y_1 - y_2 respectively, whereas the last equation cross-couples that between the x_1 - y_2 axes. It can be seen that each controller collects the information of displacement and velocity of the rotor as inputs to the fuzzy system that outputs a control current to the magnetic bearings. Also, note that the synchronization errors drive the two sets of local fuzzy controllers in opposite directions, which will result in fast removal of the synchronization errors.

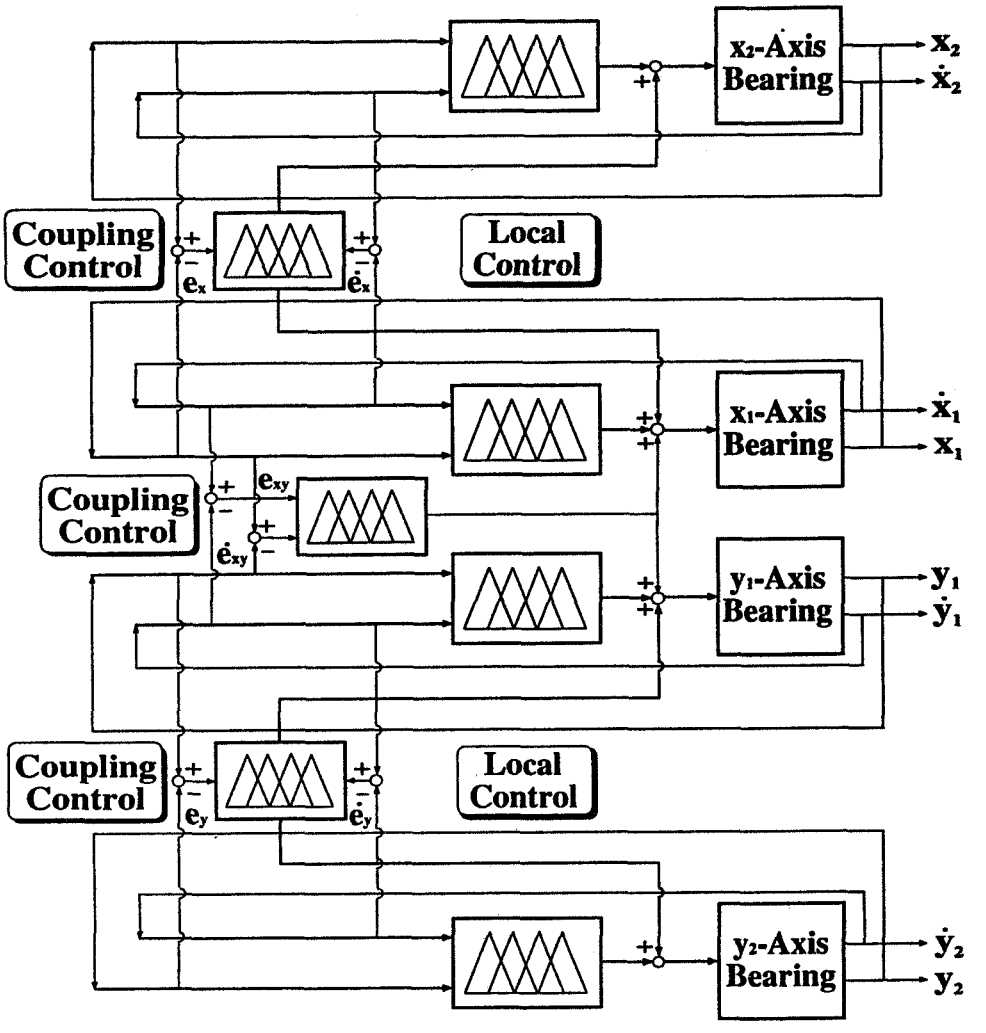

Figure 3: Control Block diagram of a fuzzy-based synchronization control

The fuzzy inference system is guided through the fuzzy rules in order to train the entire control system as for the motion synchronization. In this paper, the fuzzy controller fuzzifies the inputs by a trapezoidal membership function, applies "AND" logic operator to sort out multiple fuzzified inputs, shapes the consequent set by a FAM matrix, and aggregates all outputs during defuzzifying. Figure 4 demonstrates the membership functions and FAM matrices for the displacement and velocity of the rotor in each bearing axis. Three fuzzy sets that are specified for the input variables (x_1, $\dot{x}_1$, e_x, $\dot{e}_x$, etc.) are "Positive" (P), "Zero" (ZE), and "Negative" (N), and five fuzzy sets are assigned for the output variables (i_{x1}, i_{x2}, i_{y1}, i_{y2}) including "Positive Large" (PL), "Positive Small" (PS), "Zero" (ZE), "Negative Small" (NS), and "Negative Large" (NL). Then, the fuzzy intersection (AND) operator is applied to aggregate two membership grades such that:

$$\mu_{P\cap N}(x_1, y_1) = \mu_P(x_1) \otimes \mu_N(y_1) = min[\mu_P(x_1), \mu_N(y_1)] \tag{8}$$

where $\mu P(x_1)$ stands for the value of a membership function for the input x_1 according to the fuzzy set "Positive". The outcome from Eq. (8) is used to weight each entry in the FAM matrix, for instance:

$$w_{PL}(x_1, \dot{x}_1) = \mu_N(x_1) \otimes \mu_N(\dot{x}_1) \tag{9}$$

for the first entry in the x_1 - $\dot{x}_1$ FAM matrix. As for the output defuzzified from the fuzzy system, the centroid computation is conducted to calculate the centroid values of regions defined by overlapping membership functions. For instance, for the x_1 - $\dot{x}_1$ fuzzy system the output is defuzzified by:

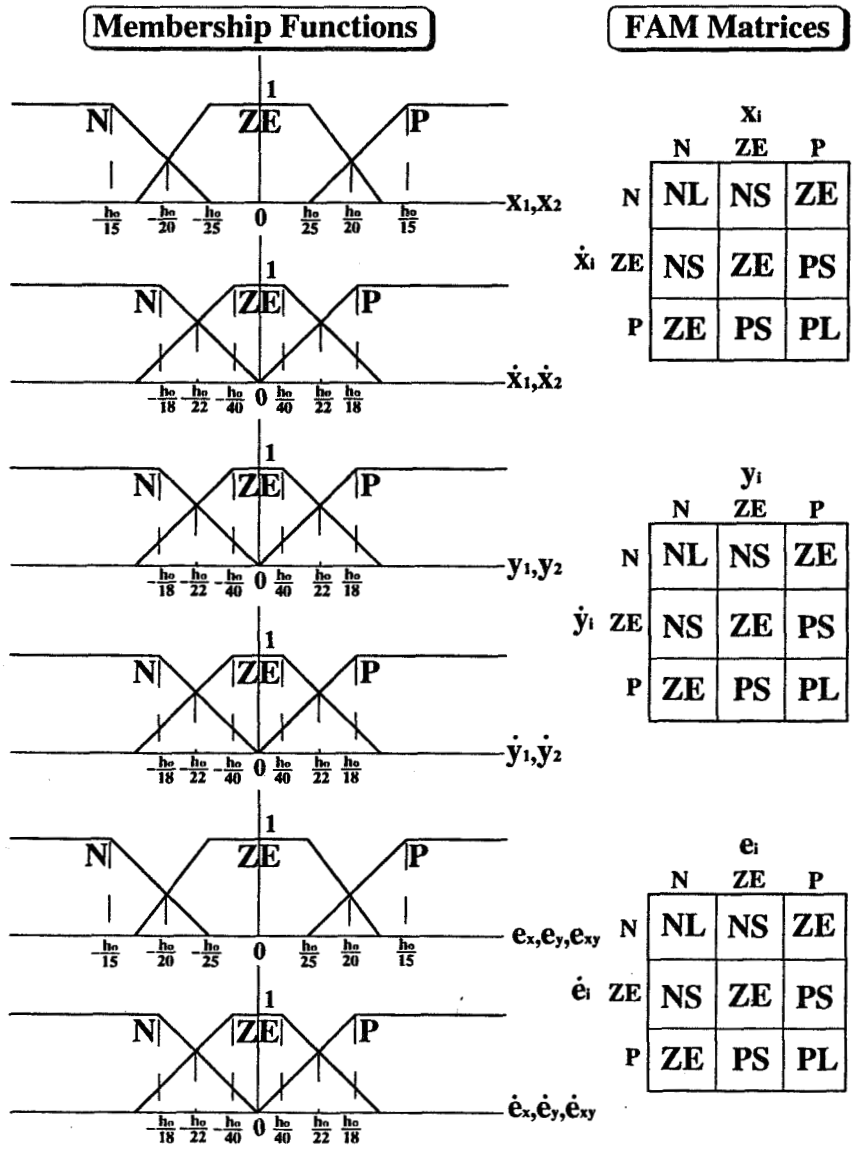

Figure 4: Input/output membership functions and FAM matrices

$$i_{x_1} = \frac{1}{\sum_i w_i}(w_{\mathrm{PL}} \cdot \mathrm{PL} + w_{PS} \cdot \mathrm{PS} + w_{\mathrm{ZE}} \cdot \mathrm{ZE} + w_{\mathrm{NS}} \cdot \mathrm{NS} + w_{\mathrm{NL}} \cdot \mathrm{NL}) \qquad (10)$$

which provides the control current for the x_1 axis. In this way, the control currents for the other axes can be defuzzified from the respective fuzzy system. Note that the total control current for each bearing axis must include those from the coupling controllers, although they are not explicitly expressed here.

The cross-coupled, fuzzy-logic control synthesis is then accomplished in this section for the synchronization control design onboard the magnetic bearing system. A closed-loop system is then obtained for the implementation of the numerical simulations, which will be the subject in the following section.

SIMULATION RESULTS

The model parameters of the rotor system with magnetic bearings for simulations are summarized in Table 1. A fuzzy-based synchronization controller has been applied to the rotor-bearing system to implement 2-second simulations subject to: (i) a sequence of impulsive disturbances on the four axes of bearings #1 and #2, and (ii) the sudden change of speed on the spinning rotor, respectively.

Table 1: Model parameters of a rotor-bearing system

Disk:		Magnetic Bearings:	
m=0.75	Kg	G=1.2×10^{-4}	N-m^2/Amp^2
I_{rr}=2.5×10^{-3}	Kg/m^4	h_o=1.5×10^{-3}	m
I_{zz}=5.0×10^{-3}	Kg/m^4	I_o=1.0	Amp
e=0.01	m	I_1=1.0361	Amp
ω=100.0	rad/sec	I_2=1.0361	Amp
a=0.5	m	b=0.5	m
Fuzzy Control Parameters:			
PL=0.01	Amp	PS=0.005	Amp
ZE=0.0002	Amp	NS=-0.005	Amp
NL=-0.01	Amp		

Figure 5 illustrates the numerical results of a control simulation along with four force impulses imposed on the four axes of bearing #1 and #2. The forces are of magnitude +/-10.0 N acting on axes x_1, x_2, y_1, and y_2 around 0.5, 0.6, 1.0, and 1.1 seconds, respectively. It can be seen in Figs. 5(a) - 5(d) that the four displacements respond synchronously to each other under the synchronization control. This implies the interactive dynamics reaction between the bearing axes due to the coupling control law. Above all, the peak magnitudes in Figs. 5(a) - 5(d) are considerably reduced within the range of 0.1 mm. Furthermore, the attendant oscillations are damped out within 0.4 seconds. Therefore, one disturbed axis can rapidly be recovered by other undisturbed axes in the presence of the fuzzy-based synchronization control. Figures 5(e) and 5(f) show the responses of the control currents. As can be seen, the amplitudes of the currents are restricted within the range of 0.015 Amp.

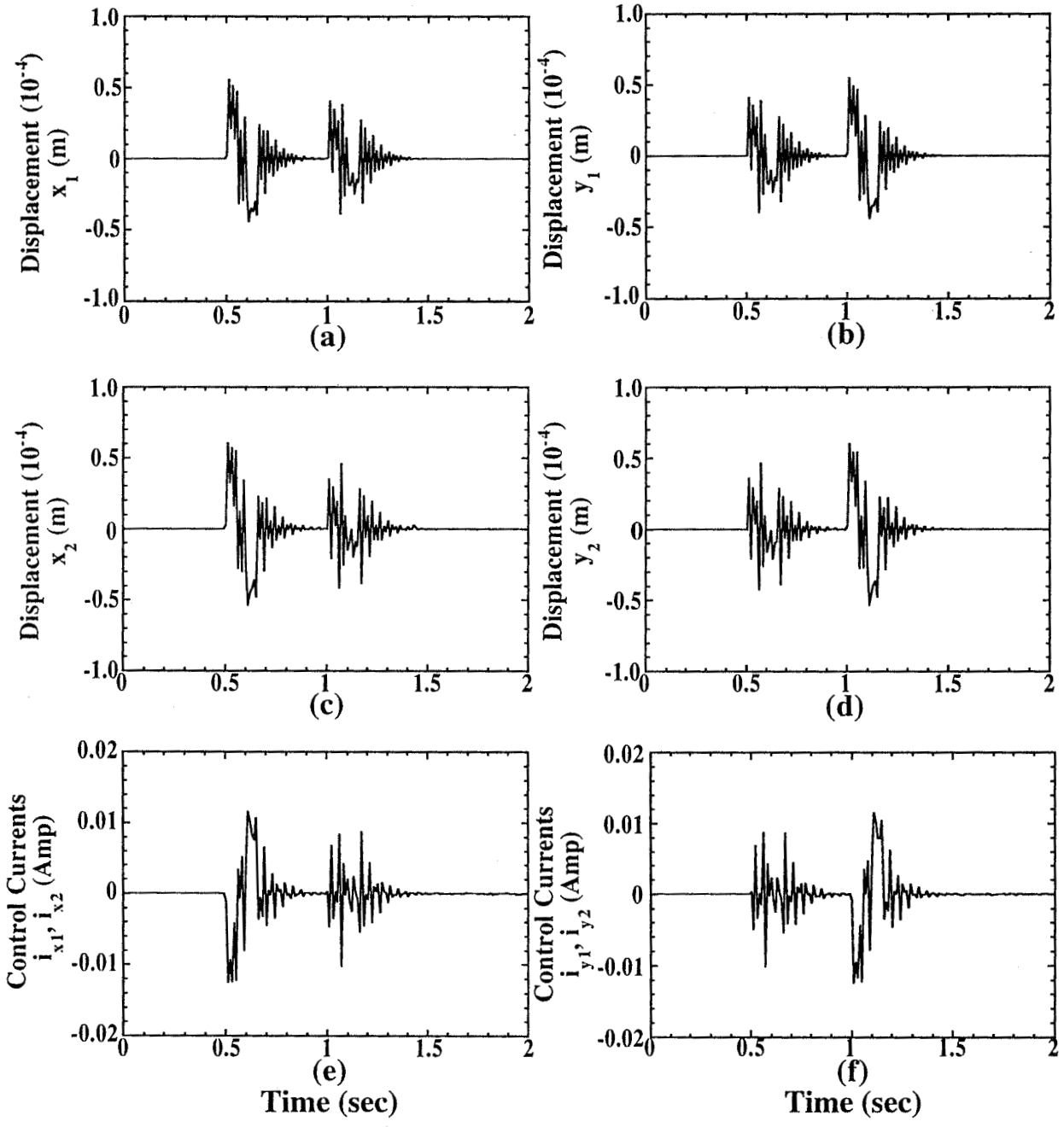

Figure 5: Simulation results subjected to impulsive disturbances

Another simulation demonstrates the capability of the proposed controller in handling the parametric change of the rotor-bearing system. Assume that the spinning speed of the rotor is suddenly changed from 1000.0 to 1010.0 rad/s around 0.4 seconds. The corresponding results are shown in Figure 6. Figures 6(a) - 6(d) show the transient responses of the displacements that are greatly eliminated with fast convergence. The corresponding time-histories of four control currents are illustrated in Figs. 6(e) and 6(f), respectively.

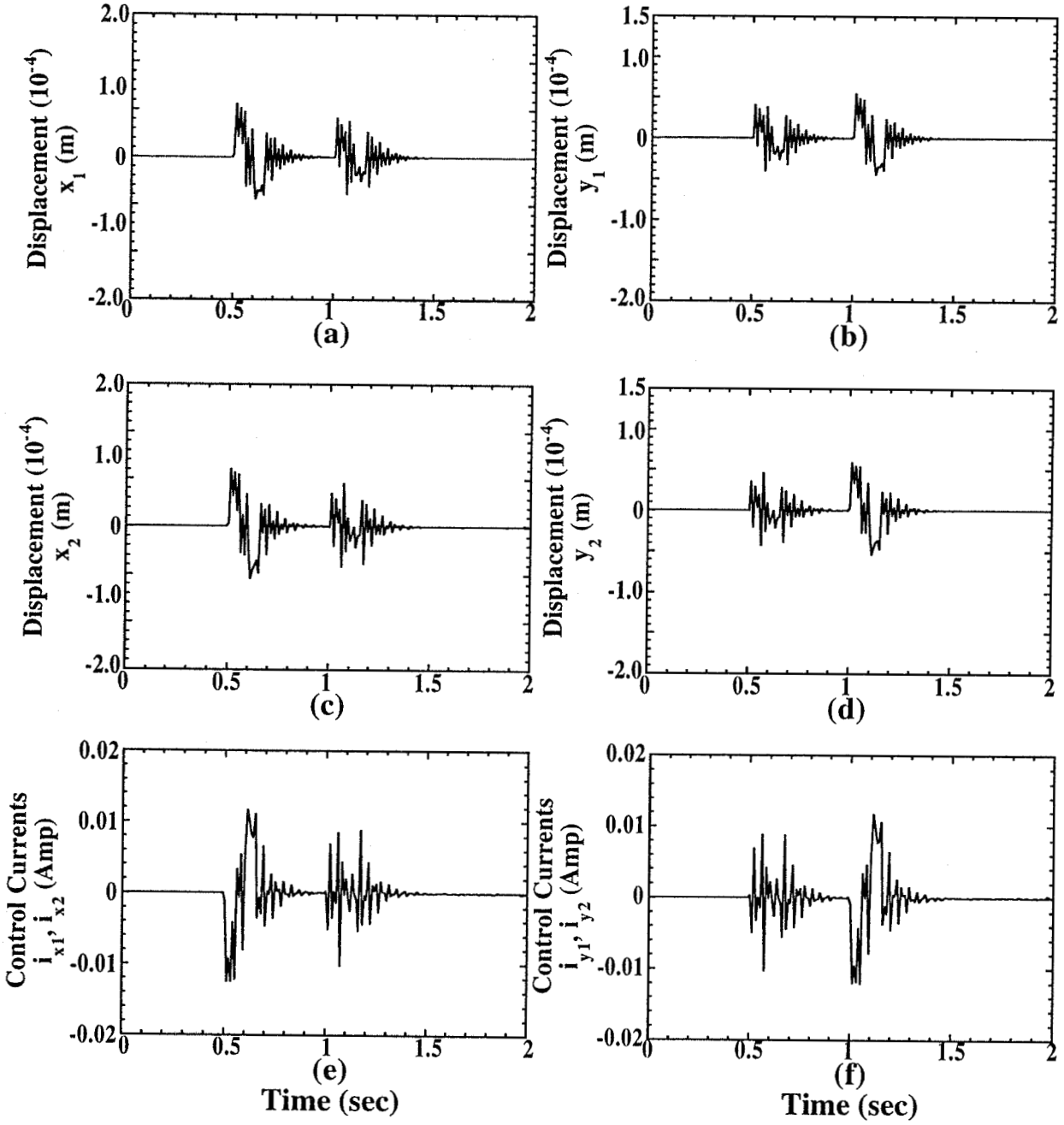

Figure 6: Simulation results subjected to the change of rotor speed

The motion of a whirling disk, under the presence of disturbances and plant parameter variations, has been shown to converge to the translatory whirl mode for fast recovery when the fuzzy-based synchronization control law is invoked. The errors appearing in synchronization have been effectively suppressed through the fuzzy control system. The simulation results in Figs. 5 and 6 thus validate the potential applicability of the proposed control design for the high-speed magnetic bearing system.

CONCLUSIONS

The problem of synchronizing the rotor motion in the magnetic bearings has been proposed and analyzed under fuzzy-logic control. An investigation of a fuzzy-based synchronization controller has been conducted for the magnetically suspended rotor system subject to disturbances and parametric variations. The fuzzy inference system was constructed by four local disturbance compensators cross-coupled to one another by using three coupling controllers in order to compromise the differential errors between the bearing axes. The stability of a rotor system can greatly be improved due to the elimination of unbalanced momenta and gyroscopic effects. The fuzzy-logic controller as designed through the synchronization process has shown to be suitable for the magnetic bearing device in rejecting the disturbances and compensating for the parametric changes. Simulation results demonstrated the effectiveness of the current approach in motion synchronization for the rotor system in cooperation with magnetic bearings. Much work needs to be done before one contemplates to evaluate the proposed strategy on a real-board prototype. They include the robustness issue, actual hardware cost-effectiveness, and power efficiency, among others. We intend to address these aspects in the future.

ACKNOWLEDGMENTS

The author wishes to acknowledge the support of this investigation through NSC Grant No. 85-2212-E-194-001 from Taiwan National Science Council.

REFERENCES

1. Dussaux, M.: The Industrial Applications of Active Magnetic Bearings Technology. *Proceedings of the 2nd International Symposium on Magnetic Bearings*, 1990, pp. 33-38.

2. Youcef-Toumi, K. and Reddy, S.: Dynamic Analysis and Control of High Speed and High Precision Active Magnetic Bearings. *ASME Journal of Dynamic Systems, Measurement, and Control*, Vol. 114, 1992, pp. 623-633.

3. Sinha, A.; Meese, K.; and Wang, K. W.: Sliding Mode Control of a Rigid Rotor Via Magnetic Bearings. *Proceedings of ASME Biennial Conference on Mechanical Vibration and Noise,* Miami, FL, 1991.

4. Dzielski, J.; Rowell, D.; and Wormley, D.: Approach to Control Moment Gyroscope Steering Using Feedback Linearization. *AIAA Journal of Guidance, Control, and Dynamics,* Vol. 14, No.1, 1991, pp. 96-106.

5. Yang, L.-F.; Mikulas, M.M., Jr.; Park, K. C.; and Su, R.: Slewing Maneuvers and Vibration Control of Space Structures By Feedforward/Feedback Moment-Gyro Controls. Will appear in *ASME Journal of Dynamic Systems, Measurement, and Control,* 1995.

6. Youcef-Toumi, K. and Ito, O.: Controller Design for Systems With Unknown Dynamics. *ASME Journal of Dynamic Systems, Measurement, and Control,* Vol. 112, No. 1, 1990, pp. 133-142.

7. Youcef-Toumi, K. and Reddy, S.: Stability Analysis of Time Delay Control with Application to High Speed Magnetic Bearings. *M.I.T. Laboratory for Manufacturing and Productivity,* Report No. LMP-90-004, 1990.

8. Hac, A. and Tomizuka, M.: Application of Learning Control to Active Damping of Forced Vibration for Periodically Time Variant Systems. *ASME Journal of Vibration and Acoustics,* Vol. 112, 1990, pp. 489-496.

9. Takagi, T. and Sugeno, M.: Fuzzy Identification of Systems and Its Applications to Modeling and Control. *IEEE Journal of Systems, Man, and Cybernetics,* Vol. SMC-15(1), 1985, pp. 116-132.

10. Welstead, S. T.: *Neural Network and Fuzzy Logic Applications in C/C++, John Wiley and Sons, Inc.,* New York, NY, 1994.

A DIGITAL CONTROL ALGORITHM FOR MAGNETIC SUSPENSION SYSTEMS*

Thomas C. Britton
Lockheed Martin Engineering & Sciences
Hampton, VA

ABSTRACT

An ongoing program exists to investigate and develop magnetic suspension technologies and modelling techniques at NASA Langley Research Center. Presently, there is a laboratory-scale large air-gap suspension system capable of five degree-of-freedom (DOF) control that is operational and a six DOF system that is under development. Those systems levitate a cylindrical element containing a permanent magnet core above a planar array of electromagnets, which are used for levitation and control purposes. In order to evaluate various control approaches with those systems, the Generic Real-Time State-Space Controller (GRTSSC) software package was developed. That control software package allows the user to implement multiple control methods and allows for varied input/output commands. The development of the control algorithm is presented. The desired functionality of the software is discussed, including the ability to inject noise on sensor inputs and/or actuator outputs. Various limitations, common issues, and trade-offs are discussed including data format precision; the drawbacks of using either Direct Memory Access (DMA), interrupts, or program control techniques for data acquisition; and platform dependent concerns related to the portability of the software, such as memory addressing formats. Efforts to minimize overall controller loop-rate and a comparison of achievable controller sample rates are discussed. The implementation of a modular code structure is presented. The format for the controller input data file and the noise information file is presented. Controller input vector information is available for post-processing by mathematical analysis software such as MATLAB[1].

* Work done on contract to NASA Langley Research Center at Lockheed Martin Engineering & Sciences, NAS1-19000.

[1] Use of names of products in this report does not constitute an official endorsement of such products, either expressed or implied, by the National Aeronautics and Space Administration or Lockheed Martin Engineering & Sciences.

INTRODUCTION

In order to investigate magnetic suspension technologies and modelling techniques, a laboratory-scale large air-gap magnetic suspension system was developed at NASA-Langley Research Center. The laboratory system, the Large Angle Magnetic Suspension Test Fixture (LAMSTF), consists of an array of five electromagnets arranged in a circular planar configuration and a suspended element that is magnetized along the long axis of the cylinder [1,2], see Figure 1. The planar array is used to provide both levitation and control of the suspended element in five degrees-of-freedom. A six degree-of-freedom (DOF) suspension system is under development. Various control approaches [3,4,5,6] have been investigated with the LAMSTF suspension system, each requiring individual control algorithms to be developed. In order to simplify the overall control system design process, the Generic Real-Time State-Space Controller (GRTSSC) software package was developed. The software package allows for the implementation of varied control algorithms without the need for code development for each algorithm, and was achieved by forming the desired control method into a standardized state-space format. By using that format, multiple types of control methods may be loaded and investigated in sequence. The developed state-space control algorithm is able to be paced at varied rates with the use of an interrupt service routine (ISR). Due to the nature of the state-space based control algorithm, the GRTSSC has other applications besides the control of magnetic suspension systems.

SOFTWARE DESIGN CRITERIA

An interrupt-driven control system is discussed in [7], but is limited in use due to the control algorithm that was implemented. Other approaches have used high-powered DSP processor chips to execute the control law [8], with custom hardware in some situations to handle the data acquisition process [9]. The use of those powerful DSP processors allow high controller sample rates to be achieved, but at a relatively high cost. Certain requirements had to be met in the development process of the GRTSSC. Those requirements were primarily driven by the need for versatility of the software and ease of use. Based on the system under control, the software package needed to be configurable by the user. Certain input and output conditions were required of the control algorithm, and other requirements of the software package were due to the desired use of the GRTSSC as an investigative tool. Thus, the emphasis of this system was not driven by the type of the system hardware, but by the design and the method of implementation of the control system software.

User Configurability

The most important requirement of the software package was to allow the user to configure the GRTSSC to handle different types and sizes of systems, by specifying the number of sensor inputs, actuator outputs, and the number of degrees-of-freedom of the system under control. This was required due to the differences between the LAMSTF and the six DOF suspension system, which is being developed. The LAMSTF consists of a state-space plant model with a ten-element state vector and requires a control system capable of handling five sensor inputs and five actuator outputs. Also, the six DOF suspension system consists of a state-space plant model with a twelve-element state vector and requires a controller that can handle a larger number of sensor inputs and actuator outputs.

Control Algorithm Functionality

The control algorithm was required to be able to handle the injection of noise on sensor inputs and actuator outputs, in addition to being able to apply sensor and actuator reference commands. The noise injection is handled off-line by initializing a data structure from a user supplied data file containing the noise information. The command reference inputs for the sensors and actuators can be calculated either on-line or supplied in a data file similiar in format to the noise data file. The ability to individually select the desired command reference channel was required in order to be able to preload setpoint data for all reference channels and, then, to be able to investigate each channel individually. Another requirement of the control algorithm was the ability to save pertinent data for post-processing with mathematical analysis software.

Software Package Functionality

In order to easily evaluate controllers with different design characteristics, the ability to select from multiple control methods that are loaded during the initialization sequence was required. The GRTSSC software package must have the ability to dynamically switch between control systems during suspension. The control algorithm should be paced by a timed interrupt, which would imply that each controller that was loaded could execute at different sample rates. It was also required that the software package provide a concise summary of commands and the status of the control system to the user. Another requirement of the GRTSSC was the indepen-

dent pacing of the data acquisition system. This was to help minimize the dependence of the software package upon a particular data acquisition system. A final requirement of the GRTSSC was for the source code to be portable between platforms.

LIMITATIONS AND TRADE-OFFS

To achieve the best code efficiency possible, a variety of areas were studied. Those included the precision of the data variables, the differences between compilers, the machine architectures, the methods of acquiring the sensor input data, and the general code optimizations. Some advantages and disadvantages exist for each of these areas.

Data Precision

The precision of the data variables that are used to process the control algorithm can affect both the speed and the amount of memory usage of the algorithm. Typically, machines perform memory access at a faster rate by using single precision data, thus increasing the speed of memory intensive routines. The state-space representation of the control system was represented by floating-point memory pointers. That allows dynamic memory allocation for each controller, thereby maximizing the efficiency of the memory usage. Single precision floating-point numbers are used, resulting in approximately a fifty percent reduction in the memory usage that was required for data and variable storage.

Machine Architectures and Compilers

The original version of the GRTSSC software package was developed on an Amiga A3000T system by Commodore Business Machines, which was based on the MC68030 microprocessor with MC68881 coprocessor support. The SAS/C compiler [10], version 6.55, that was used produced faster code with the large memory model and used double precision data. However, the current version of the software was developed on a standard 486 DX2/66 class PC by using the Microsoft C compiler [11], version 6.0. Faster code was produced by using the large memory model and single precision data. It is widely known that different compilers can produce significantly different code, both in speed and size of the executable file. For example, in a comparison

of version 6.0 of the Microsoft C compiler and the freeware GNU/C compiler, experimental results with other software suggest that a 20 percent increase in speed is achievable with the use of the GNU/C compiler.

A significant advantage that the A3000T platform possessed was the flat memory model inherent in the architecture and the true pre-emptive multitasking operating system. Also, the data acquisition subsystem was executed by a plug-in 386-PC CPU board, independent of the main processor of the A3000T. Acquired data was transmitted through dual-port random access memory (RAM), which existed on the 386-CPU board. That relieved the main processor of the A3000T of the task of data acquisition, and thus it could be dedicated to the control algorithm. The flat memory model allowed data storage space to be allocated up to the total amount of free RAM that remained. This allowed the code to save controller input, output, and state vectors for step responses on each degree of freedom of the suspension system. Data runs long enough to be able to perform system identification techniques on the linear plant model were achievable. However, sample rates on the order of 1000 Hz will be required for initial control designs for the six DOF suspension system. The A3000T using an accelerator board with a 40 MHz MC68040 was able to achieve a sample rate of approximately 500 Hz.

The PC class machine proved quite capable of generating the required controller sample rates for the six DOF suspension system. A comparison of achievable sample rates is shown in Figure 2. The data presented for the five DOF LAMSTF system was obtained with the required number of system inputs and outputs. The data presented for the six DOF suspension system was obtained with assumed number of sensor inputs of seven and assumed number of actuator outputs of eight. The plots shown in Figure 2 demonstrate the effect that the number of controller states has upon the maximum achievable controller sample rate. The affect of the number of controller inputs and outputs can also be seen by the difference between the two suspension systems that are compared. One disadvantage of a standard PC class machine is the segmented memory architecture due to the 80x86 chipset. As a result of the segmented memory architecture, most common compilers, such as the Microsoft C compiler, are limited by the operating system to the lower 640 kilobytes (KB) of RAM. In order to access the memory beyond one megabyte (MB), 32-bit compilers with a DOS-extender must be used, such as the GNU/C compiler. Unless a 32-bit compiler is used, limitations are placed on the amount of data that can be stored real-time, due to the limited amount of memory that would be available. In order to save the required number of data samples to perform system identification, only the measured sensor signals are stored for further post-processing. Other disadvantages of this class of machine are the need of the CPU to handle the data acquisition cycle and the necessity of a separate high resolution timer to provide the pacing for the timed interrupt of the control algorithm.

Data Acquisition Interface

Data acquistion is performed by a plug-in analog-to-digital convertor (ADC) data acquisition PC card. Those types of cards typically offer several programming modes, including DMA data transfer, interrupt driven data acquisition, and program control techniques. The program control technique for data acquisition is the most straight-forward of all approaches. It also tends to be slower and also must take place within the control algorithm's iterative loop. Another approach deals with the use of interrupts to acquire data. That approach has the benefit of occuring outside of the control loop and typically has a higher data transfer rate than the program control method. Significantly higher data transfer rates are achievable with the use of DMA. DMA data transfer also has the benefit of occuring as a background process relative to the control loop. The large throughput rates that are achievable by using DMA can adversely affect the timing of other interrupts due to the fact that during a single DMA transfer, the CPU address, data, and control buses are under the control of the DMA controller. It should be noted that this discussion of DMA is specific to the standard PC class computer. The DMA process can vary between platforms. As the need for faster controller sample rates increases, there exists the possibility of the time skews between acquired data samples becoming large relative to the controller sample rate. This can be detrimental to the designed control method under investigation. A simultaneous sample-and-hold can be utilized to eliminate that effect. There is a certain amount of overhead involved in using the general purpose driver software provided by the vendors. If the use of the general purpose vendor software is not desired, it is necessary to develop routines to handle the interface to the ADC board through its command registers.

Code Optimizations

Several approaches can be used to minimize the loop time of the control algorithm cycle. One method that can be used is to apply the use of boolean logic to control events within the algorithm, instead of the use of conditional statements. That has the effect that the same amount of code would be executed every iteration of the control loop, thus preventing variances in the loop time of the control algorithm. Other steps that can be taken is to remove variable declarations or equations that are constant from within any iterative loop. Another step that can be performed is to enable optimizations within the compiler, primarily any time-based optimizations. This can result in significant increases in the speed of routines that are computationally intensive. Any duplicate code that can be written as a separate routine should be implemented

as separate function calls, allowing the compiler optimizer to function efficiently.

ALGORITHM IMPLEMENTATION

The GRTSSC software package is composed of three distinct processes. The foreground process provides for user interface with the GRTSSC software package. The process consists of routines that load controller initialization information, save measured data information, allow for parameter modification by the user between control runs, and provide a status update of the software to the screen. The data input process provides for the data acquisition of the sensor inputs from the magnetic suspension system. The control algorithm process of the GRTSSC performs the control law calculations of the desired control algorithm.

A modularized approach was used in developing the GRTSSC software package. The approach minimizes the amount of modifications required for implementing the package on various platforms. Any machine dependencies due to hardware or architecture were implemented in separate routines, where possible. It would be left up to the user to write the necessary routines for a new platform. Those routines deal primarily with the data acquisition subsystem, the pacing of the control algorithm via interrupt, and some user interface via the keyboard. The software was implemented in C and adheres to the ANSI compliance standard, with the exception of platform dependent code.

Foreground Process

The foreground process of the GRTSSC software package provides a menu from which the user can load controller state-space information, modify reference input/output parameters, save acquired data to a file, and execute the control algorithm. Two configuration files exist, which cannot be altered while the software is running. The structure of those configuration files is presented in Table I. The first of the files determines the number of system inputs, system outputs, degrees-of-freedom of the system under control, and certain setpoint reference data for the sensors and actuators. The second configuration file provides the data necessary for noise injection on either the sensors or actuators. During run-time, the user may load pre-calculated controller state-space information from an input data file. The controller input data file is summarized in Table II. That file contains specific information concerning the size of the input, output, and state vector of the controller; initial conditions for various vectors; and the control system state-

space matrices. By using the format specified, beginning with the number of controller states, n_x, multiple controllers can be appended to the end of the controller input data file. The format for the data output file is presented in Table III. A time base and measured sensor inputs are written to the file for post-processing by MATLAB.

Data Input Process

An existing DAS-40 ADC card by Keithley-Metrabyte [12] is utilized for data input functions. The card provides 12-bit 16-channel single-ended/8-channel differential input capabilities and can achieve a 250 KHz throughput rate by using DMA to transfer acquired data from the ADC to buffer memory residing on the PC. By using the on-board pacer clock for the DMA data transfer process, the card is programmed with vendor provided routines to sample a sequence of channels continuously. The acquistion of each channel and the DMA transfer is paced at 70 KHz per channel by the on-board pacer clock. The data input process starts prior to the beginning of the control algorithm process and terminates at the end of the control algorithm process.

Control Algorithm Process

The control algorithm process is summarized in Figure 3. The control algorithm executes in an ISR paced by an interrupt generated by a CIO-CTR05 Counter/Timer board by ComputerBoards [13]. The timer board possesses a one MHz oscillator and a single Am9513 counter timer chip with five 16-bit counters. By using register level programming, a single counter is enabled to decrement from a loaded value and generates a CPU interrupt upon reaching zero. The number of counts required is a function of the oscillator frequency and the desired sample rate, as shown in equation (1).

$$Counts = \frac{fosc/2}{\tau} \tag{1}$$

The ADC input routine, shown in Figure 3, consists of copying the measured sensor data from the DMA memory buffer to memory pointers used by the control algorithm. A CIO-DAC16/12 digital-to-analog convertor (DAC) card by ComputerBoards [14] is used for the data output of the control algorithm. That card provides 12-bit 16-channel single-ended/8-channel differential output capabilities for the control system. The DAC output routine, shown in Figure 3, outputs the calculated control actuator commands, using register level programming.

The control algorithm implements the discrete-time state-space equations shown in equations (2) and (3).

$$\{X_{c_{k+1}}\} = [A_c]\{X_{c_k}\} + [B_c]\{U_{c_k} + U_{noise} - U_{ref}\} \tag{2}$$

$$\{Y_{c_k}\} = [C_c]\{X_{c_k}\} + [D_c]\{U_{c_k} + U_{noise} - U_{ref}\} + \{Y_{noise}\} - \{Y_{ref}\} \tag{3}$$

Note that the discrete-time state-space equations are written from the standpoint of the control computer. The input vector, $\{U_{c_k}\}$, is the measured sensor signals, and the output vector, $\{Y_{c_k}\}$, is the calculated control actuator commands to the plant model. Noise injection occurs via the sensor and actuator noise inputs, U_{noise} and Y_{noise}. Reference inputs are provided for the sensors and actuators, U_{ref} and Y_{ref}, see Figure 4. A state-space model in modal canonical form is utilized in the control algorithm. That significantly reduces the amount of matrix-vector multiply and addition operations performed by the control algorithm. The controller system matrix, $[A_c]$, is ordered as shown in equation (4).

$$[A_c] = \begin{bmatrix} a_{11} & a_{12} & 0 & \cdots & \cdots & \cdots & 0 \\ a_{21} & a_{22} & a_{23} & 0 & & & \vdots \\ 0 & a_{32} & a_{33} & a_{34} & 0 & & \vdots \\ \vdots & \ddots & \ddots & \ddots & \ddots & \ddots & \vdots \\ \vdots & & 0 & a_{n-2n-3} & a_{n-2n-2} & a_{n-2n-1} & 0 \\ \vdots & & & 0 & a_{n-1n-2} & a_{n-1n-1} & a_{n-1n} \\ 0 & \cdots & \cdots & \cdots & 0 & a_{nn-1} & a_{nn} \end{bmatrix} \tag{4}$$

Without the modal canonical form of the state-space controller, the $[A_c]$ matrix would require n^2 multiplications and $n(n-1)$ additions, where n is the number of states of the controller. By using the modal canonical form, the number of multiplications can be reduced to $3n-2$, and the number of additions can be reduced to $2(n-1)$.

The input and output operations of the control algorithm take place as close to the same time point as possible. That has the effect of minimizing the amount of computational processing time, δ, that occurs between input and output. The majority of control calculations then occur after the output of the actuator control command, but before the next sensor input during the next control iteration, refer to Figure 5. This allows the user to implement control algorithms with or without frame delays, simply by including the delays in the state-space model The feedthrough of the measured sensor inputs via the controller state-space matrix, $[D_c]$, is the only calculation required between the input and output functions. The larger the ratio of the computational processing time, δ, to that of the controller sample rate, τ, the more adverse the

effects upon the system, if not properly modelled during the controller design phase. The computational processing time, δ, can be modelled as a transport delay in simulation efforts for the closed-loop system.

CONCLUSIONS

A digital control algorithm for magnetic suspension systems has been developed, and design criteria for the software package has been presented and discussed, including the limitations and trade-offs inherent in any design. Due to the nature of the design of the GRTSSC, applications towards other types of systems exist. System hardware requirements were presented and discussed. Development of the control software package was discussed, including the design of the control algorithm. The efforts involved in producing the fastest possible control sample rate are discussed. The resulting package has a versatile configuration and can be used to investigate a variety of control approaches and applications without the need of developing separate source code for each control approach.

ACKNOWLEDGEMENTS

The author wishes to acknowledge the assistance of Nelson J. Groom and David E. Cox of the Guidance & Control Branch, Flight Dynamics & Controls Division at NASA Langley Research Center

REFERENCES

1. Groom, N.J.: *Analytical Model of a Five Degree of Freedom Magnetic Suspension and Positioning System.* NASA TM-100671, March 1989.

2. Britcher, C.P.; Ghofrani, M.; Britton, T.C.; and Groom, N.J.: *The Large Angle Magnetic Suspension Test Fixture.* International Symposium on Magnetic Suspension Techonology, NASA Langley Research Center, NASA CP-3152, August 1991.

3. Britcher, C.P.; Ghofrani, M.; Haj, A.; and Britton, T.C.: *Analysis, Modelling and Simulation of the Large-Angle Magnetic Suspension Test Fixture.* Proceedings of the Third International Symposium on Magnetic Bearings, July 1992.

4. Groom, N.J.; and Britcher, C.P.: *A Description of a Laboratory Model Magnetic Suspension Test Fixture with Large Angular Capability.* The First IEEE Conference on Control Applications, Dayton, OH, September 1992.

5. Cox, D.; Groom, N.J.: *A Decoupled Control Approach for a Large-Gap Magnetic Suspension*

System. 2nd International Symposium on Magnetic Suspension Technology, Seattle, WA, August 1993.

6. Lim, K.B.; and Cox, D.E.: *Experimental Robust Control Studies on an Unstable Magnetic Suspension System.* Proceedings of the 1994 American Control Conference, June 1994.

7. Lawson, M.A.; and Gillies, G.T.: *Interrupt-Driven Digital Controller for a Magnetic Suspension System.* Rev. Sci. Instrum., vol. 60, no.3, March 1989, pp.456-465.

8. Sinha, A.; Wang, K.W.; and Mease, K.L.: *Robust and Real-Time Rotor Control with Magnetic Bearings.* AIAA-91-3626, 1991.

9. Wassermann, J.: *A Very Fast Digital Processing Controller System for Magnetic Bearing Research.* Proceedings of MAG '95: Magnetic Bearings, Magnetic Drives and Dry Gas Seals, 1995, pp.101-108.

10. *SAS/C Development System User's Guide, Version 6.5,* SAS Institute Inc., Cary, NC, 1993.

11. *Microsoft C Reference, Version 6.0,* Microsoft Corporation, 1990.

12. *User Guide for the DAS-40G1 & DAS-40G2 A/D & D/A Data Acquisition Boards, Revision B,* Keithley Metrabyte Corp., Taunton, MA, 1991.

13. *CIO-CTR User's Manual, Revision 2.0,* ComputerBoards Inc., Mansfield, MA, 1994.

14. *CIO-DAC16/12 User's Manual, Revision 2.0,* ComputerBoards Inc., Mansfield, MA, 1994.

Table I. Format Summary of Configuration Files

System.cfg		Noise.cfg	
Line #	Data	Line #	Data
1	# sensors (Pts_{sen})	1	input pts (Pts_{in})
2	# actuators (Pts_{act})	2	output pts (Pts_{out})
3	# DOF's	3	recyle input (0/1)
4	# saved data (Pts_{sav})	4	recyle output (0/1)
5	sensor zero bias	5	input noise data
6	auto DOF cycle (0/1)	⋮	⋮
7	initial sensor ref	5+Pts_{in}-1	input noise data
8	max sensor ref	5+Pts_{in}	output noise data
9	min sensor ref	⋮	⋮
10	# sens ref pts	5+Pts_{in}+Pts_{out}-1	output noise data
11	# sens delay counts		
12	sens ref recycle (0/1)		
13	initial actuator ref		
14	max actuator ref		
15	min actuator ref		
16	# act ref pts		
17	# act delay counts		
18	act ref recycle (0/1)		
19	P2S Matrix		
⋮	⋮		
19+Pts_{sen}-1	P2S Matrix		

Table II. Format Summary of Controller Input Data File

Filename = Ctrl_dat.m	
Line #	Data
1	Suspension Currents
2	Amplifier Gain Adjust
3	# of Controller State (n_x)
4	# of Controller Inputs (n_u)
5	# of Controller Outputs (n_y)
6	Controller Sample Rate (τ)
7	Initial Controller State Vector
8	$[A_c]$ Matrix
⋮	⋮
8+n_x-1	$[A_c]$ Matrix
8+n_x	$[B_c]$ Matrix
⋮	⋮
8+2*n_x-1	$[B_c]$ Matrix
8+2*n_x	$[C_c]$ Matrix
⋮	⋮
8+2*n_x+n_y-1	$[C_c]$ Matrix
8+2*n_x+n_y	$[D_c]$ Matrix
⋮	⋮
8+2*n_x+2*n_y-1	$[D_c]$ Matrix

Table III. Format Summary of Saved Data Output File

Filename = Out_dat.m	
Line #	Data
1	Time Vector Header
2	Time Vector Data
⋮	⋮
2+Pts_{sav}-1	Time Vector Data
2+Pts_{sav}	Time Vector Trailer
2+Pts_{sav}+1	Measured Data Header
2+Pts_{sav}+2	Measured Data, U_{c_k}
⋮	⋮
2+2*Pts_{sav}+1	Measured Data, U_{c_k}
2+2*Pts_{sav}+2	Measured Data Trailer

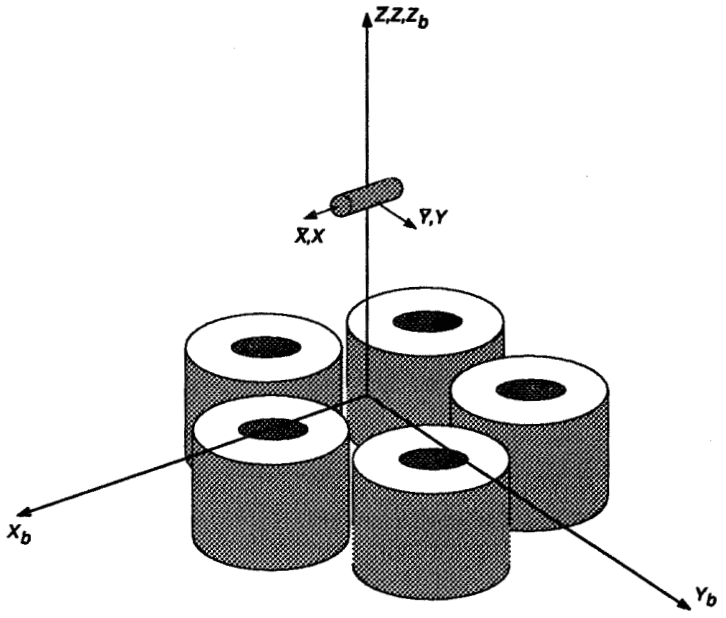

Figure 1. Coil layout of the LAMSTF suspension system.

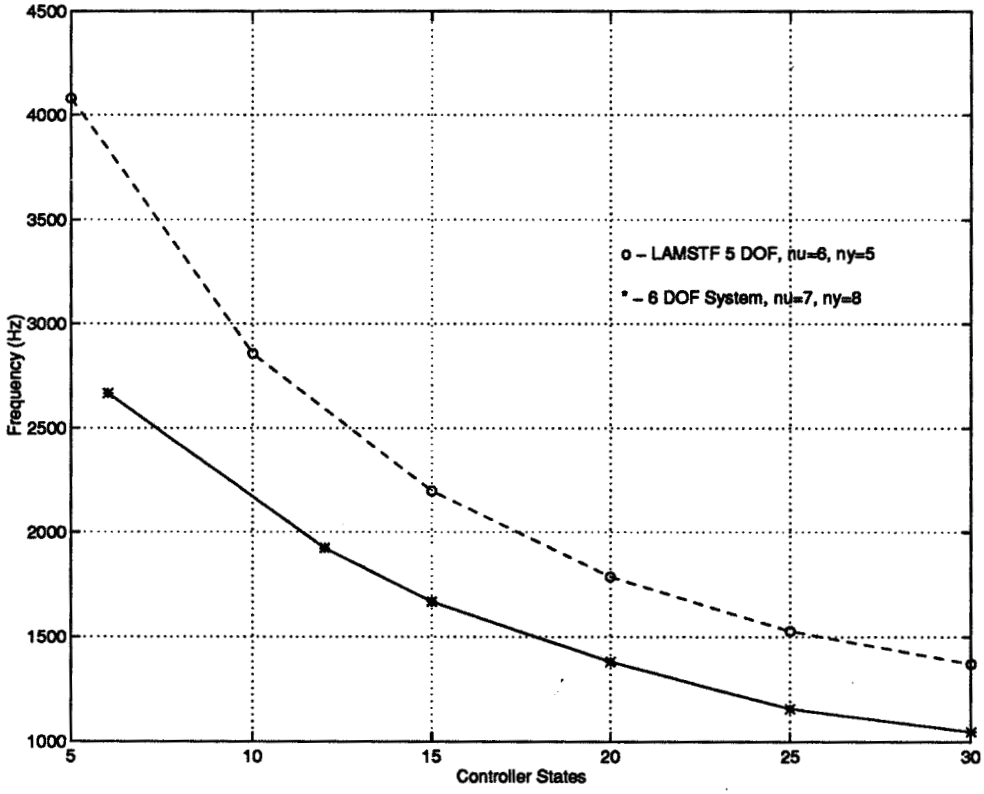

Figure 2. Maximum achievable controller sample rates, using a 486 DX2/66 PC.

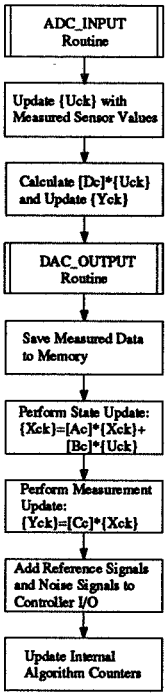

Figure 3. Control algorithm flow diagram.

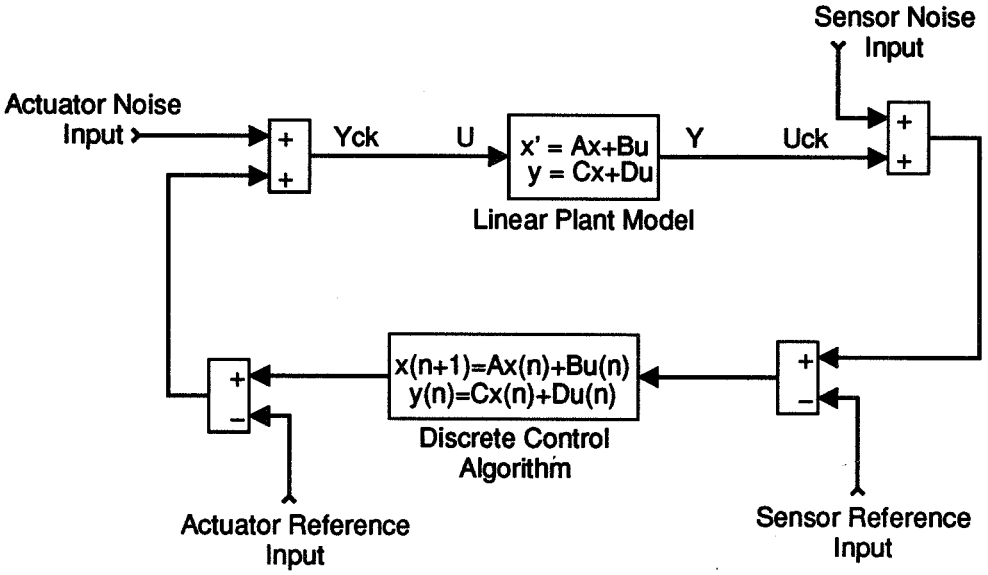

Figure 4. Closed-loop block diagram.

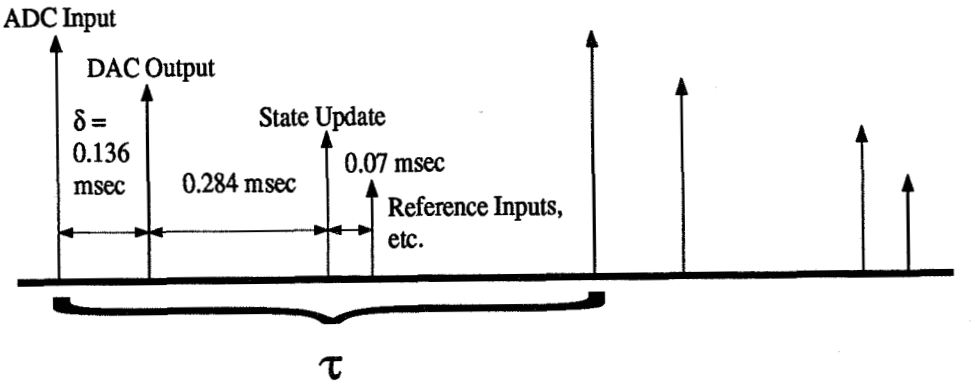

Figure 5. Timeline of control algorithm.

Session 16 -- Electromagnetic Launch & Hypersonic Maglev

Chairman: George Dulikravich
Penn State University

ISSUES ASSOCIATED WITH A HYPERSONIC MAGLEV SLED

J.W. Haney
Rockwell International
Downey, California

J. Lenzo
Holloman AFB
Alamogordo, New Mexico

INTRODUCTION

Magnetic levitation has been explored for application from motors to transportation. All of these applications have been at velocities where the physics of the air or operating fluids are fairly well known. Application of Maglev to hypersonic velocities (Mach > 5) presents many opportunities, but also issues that require understanding and resolution. Use of Maglev to upgrade the High Speed Test Track at Holloman Air Force Base in Alamogordo New Mexico is an actual hypersonic application that provides the opportunity to improve test capabilities. However, there are several design issues that require investigation. This paper presents an overview of the application of Maglev to the test track and the issues associated with developing a hypersonic Maglev sled. The focus of this paper is to address the issues with the Maglev sled design, rather than the issues with the development of superconducting magnets of the sled system.

CURRENT TESTING APPROACH

History of the test track

High speed test track facilities have been in operation for nearly half a century. The first track in the United States was commissioned in 1946 at the Naval Weapons Center in California. During the 50's, tracks were built in France and England and, in the early 60's in Russia.

The High Speed Test Track at Holloman AFB, New Mexico, became operational in 1950 when a 1,082 meter section of test track was constructed for operation as a Snark missile launching facility. The test track was extended to 1,546 meters in 1955 and to 10,690 meters in 1956. In 1972, the track was further extended to 15,480 meters in length. It is the longest and most precisely aligned track in the United States. The facility

consists of two 171 lb/yd crane rails spaced 2.13 meters apart for its total length. In the northern 5,000 meters of the track, a third rail forms a 0.67 meter rail gauge with one of the other two rails. The rails are continuously welded and prestressed to remain under tension at temperatures below 60 degrees Centigrade. A south to north view of the Holloman test track is shown in Figure 1.

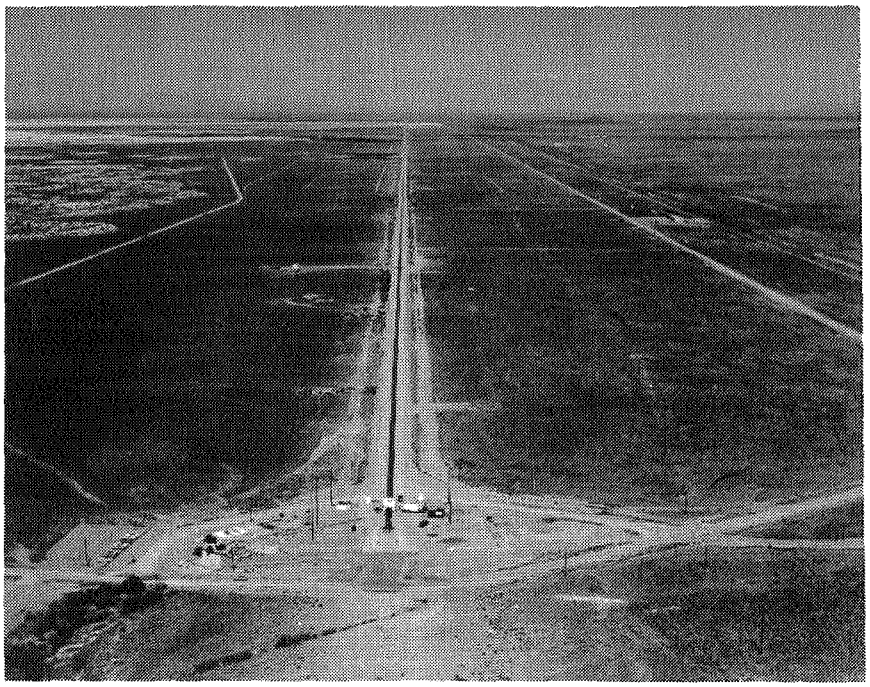

Figure 1. South-North View of the Holloman Track

High speed test tracks have been used to test a variety of aerospace hardware, such as guidance systems, crew escape systems, missile seekers and control systems, warheads, missile lethality and vulnerability, and rain erosion effects on radomes, just to name a few. Advancements in technology have created a need for higher and higher test velocities. Figure 2 is a collage of pictures showing a Theater Missile Defense interceptor impacting a simulated re-entry threat vehicle at hypersonic velocity after release from the test track.

High Speed Test Track System

The operation of vehicles in close proximity to the ground from low subsonic speeds up to hypersonic velocities produces aerodynamic ground interference effects which result in Mach number dependent lift loads and pitching moments. Therefore, it is necessary to control the biasing loads on sleds within certain limits to maintain captive flight. The means by which sled vehicles transfer loads to the rail and thus guide the vehicle are through structural hardware called slippers. Basically, the slippers are structural components fitted around the top flange of the rails with a maximum all around clearance of 1.524 mm, Figure 3. The rail gap is required because of small irregularities in rail alignment and rail surface imperfections. Due to the loads acting on the sled vehicles and

the presence of the slipper gaps, sled vehicles translate through the slipper gap and the steel slippers impact the rail causing high vibration loads in the sled vehicles. The steel slippers also wear as they travel along the steel rail. This slipper wear allows excessive clearance at the slipper-rail interface and, along with the high vibration loading, can lead to catastrophic failure of the sleds.

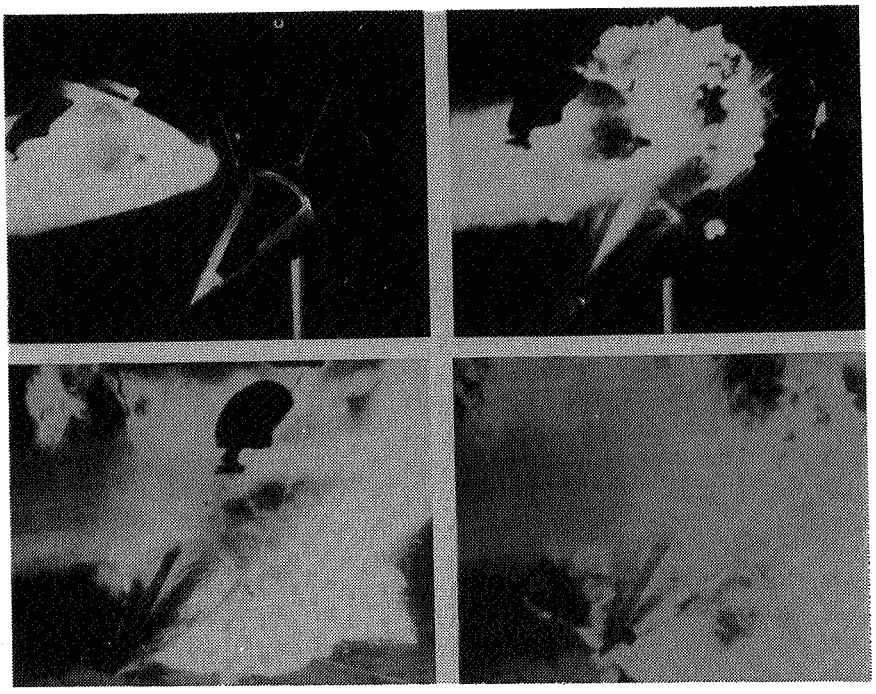

Figure 2. Impact of a Theater Missile Defense interceptor

Issues Associated with the Current Test Track

Currently, sled test velocities are theoretically limited by the combination of sled weight, drag, and thrust. With the present day techniques, the maximum theoretical velocity achievable on the Holloman test track is between 3.0 and 3.5 km/sec. In reality, sled velocities are limited by slipper wear and vibration environment along with weight, drag, and thrust resulting in theoretical velocities being impossible to achieve. To routinely obtain sled test velocities of 3.0 km/sec and higher, new ways of guiding sleds must be considered.

Aerodynamics also has a large effect on hypersonic monorail testing. The sled geometry is tailored to counteract aerodynamic lift loads, to minimize shock waves, and to prevent ram air at stagnation temperatures and pressures from entering the slipper rail gap. Structural materials and ablative or refractory coatings are selected to withstand the high enthalpy airflow encountered in the dense air at ground levels.

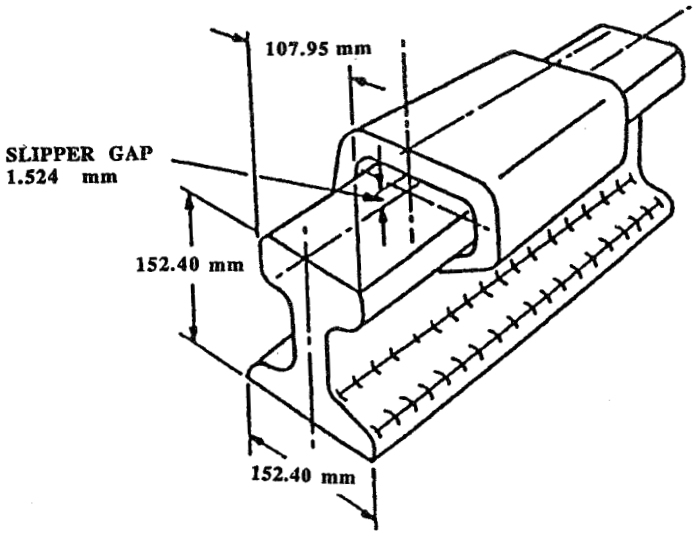

Figure 3. Test Track Slipper System

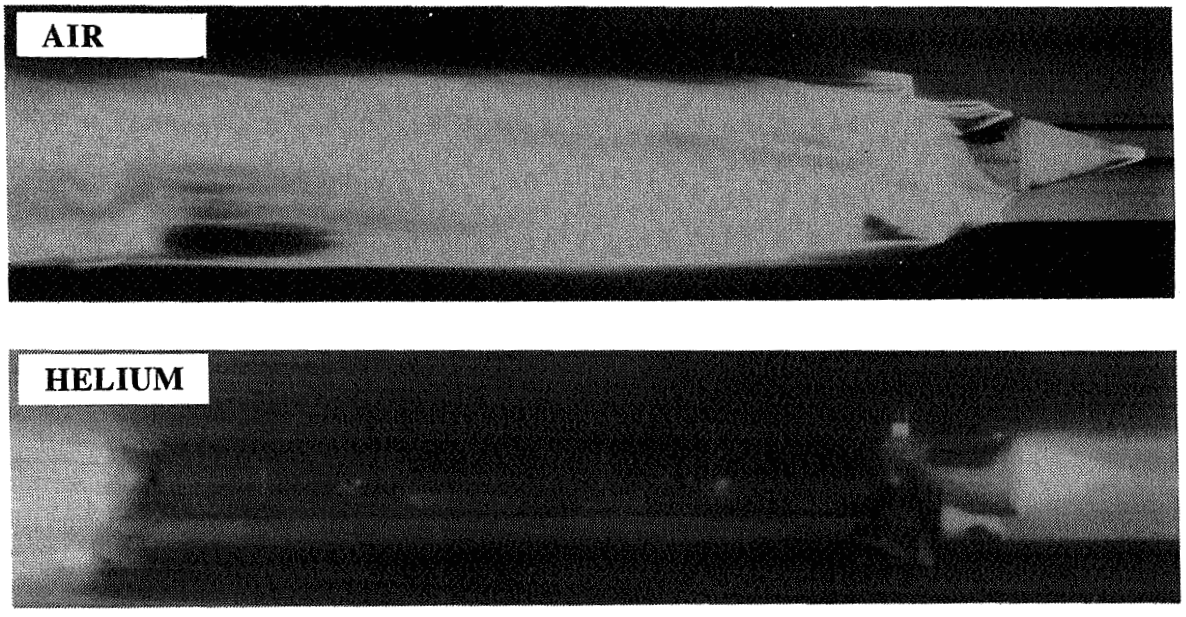

Figure 4. Image Motion Compensation Photograph of Sled in Helium Environment

Low-density operations, consisting of a helium tunnel encompassing a portion of the test rack, are also used to reduce the aerodynamic drag and aeroheating effects of hypervelocity testing. Figure 4 is an Image Motion Compensation photograph taken in a helium environment showing the cooling effect of the helium atmosphere. A slipper-rail impact can also be seen in Figure 5. It can clearly be seen in the bottom photograph that the slipper sheared from the sled bulkhead, causing a catastrophic failure. This was due to the previously discussed vibration environment.

Currently, the world land speed record of 2.71 km/sec is held by the Holloman High Speed Test Track. Sled tests in excess of 1.8 km/sec are routinely conducted and tests in excess of 2.5 km/sec are occasionally conducted with limited success, primarily due to the high vibration environment and slipper wear problems.

A promising approach to achieving the higher velocity, reducing vibration, and eliminating slipper wear is provided by magnetic levitation.

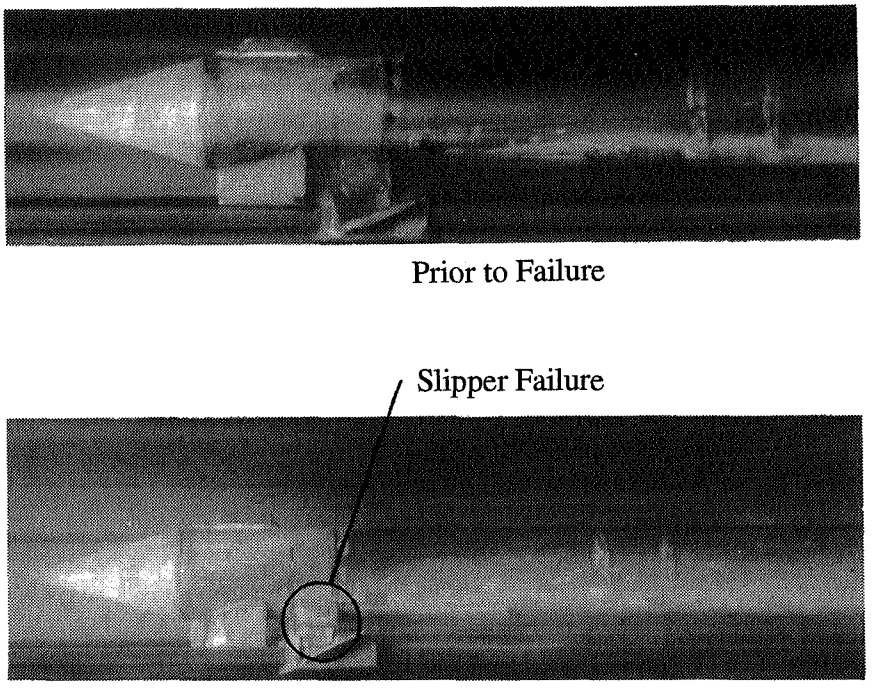

Figure 5. Slipper-Rail Impact and Slipper Failure

MAGLEV SLED APPROACH

Goal of the Maglev System

The overall goal of the Maglev sled system for the High Speed Test track is two fold. First to provide a capability for the Department of Defense, DoD, to conduct realistic hypersonic testing of warhead lethality and propulsion systems at an affordable price.

Second, to provide a capability to non DoD users, such as the Federal Railroad Administration, to test superconducting magnetic designs and fabrication, and to verify computer codes which predict dynamic magnetic fields for commercial transportation.

To achieve these goals the Holloman High Speed Test Track is being upgraded to provide magnetic levitation of payloads from 1000 kg to 25 kg with velocities ranging from subsonic to hypersonic speeds. This upgrade is required to provide higher test velocities than are achievable with the current system and to reduce the level of vibration during test. The near term approach is to accomplish this using magnetic levitation with solid rocket propulsion boosters. However, electromagnetic propulsion will be demonstrated during the upgrade. The upgraded capability will also provide magnetic braking capability.

Maglev Concept

The hypersonic Maglev sled used as a focal point of this paper is being developed under a Phase 1 contract led by General Atomics for Holloman Air Force. The Maglev sled design will continue to evolve under the Phase 2 Air Force contract, however this Phase 1 concept provides a mechanism to discuss the associated sled issues.

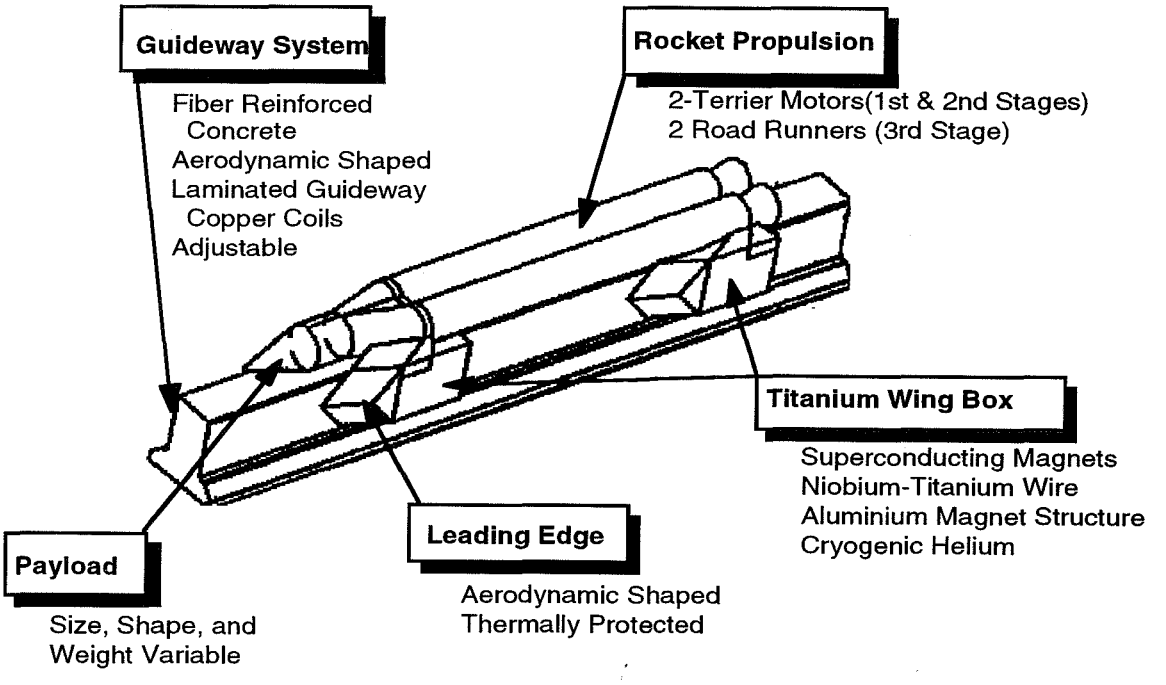

Figure 6. Phase 1 Sled Concept

The concept for a hypersonic sled is to magnetically levitate the sled by use of superconducting magnets and propel the sled along the test track using expendable solid

rocket motors. Essentially, the steel slippers of the existing system are replaced with magnetic slippers. Figure 6 illustrates the Phase 1 sled concept. The sled is comprised of rocket motors, a payload for the final stage, sled-wing attachment structure, and wings. The wings are made up of a wing box that houses the magnetic system and a leading edge fairing. The left and right wing boxes, leading edges, and wing-rocket attachment structure comprise a wing assembly. Each sled has a forward and aft wing assembly. Three stages are used to propel the payload to the hypersonic test velocities. The sled is levitated over a concrete guideway which contains copper coils to transmit the fluxes generated by the superconducting magnets and allow the restoring forces which control the sled. The Phase 1 sled-guideway Maglev system is depicted in Figure 7.

The ability to achieve hypersonic maglev testing with rocket propulsion is a systems design study involving rocket thrust (thrust to weight); the magnetic system's weight and its capability to generate the required forces; and the sled's weight and its generated lift and drag forces.

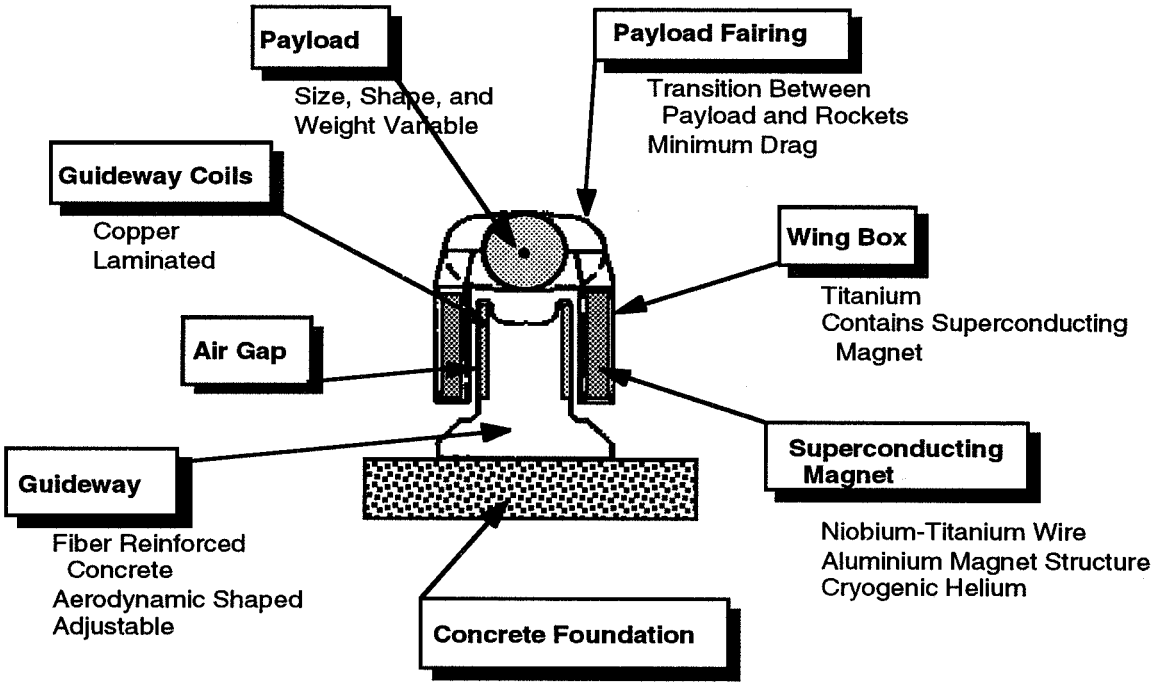

Figure 7. Maglev System

Issues Associated with Maglev Sled Development

In developing a Maglev system, optimization must occur at the system level rather than at the component level. The interplay between the component weights and the component associated forces require a careful balance to achieve an efficient system. In fact, it is require to achieve a successful system. If the sled is viewed as one of the overall Maglev system components there are several issues that have to be investigated and understood so they can be part of the overall system design.

Evolving from a captive sled (steel slipper to rail) system to a free flying system at hypersonic speeds presents unique challenges to the sled design and development, Figure 8. These challenges or issues can be categorized in broad groups such as: Aerodynamics, Flow Field definition, Stability & Control, Aeroheating, Thermal Management, Structural Design, and Integration (guideway and superconducting magnet). Each of these broad categories are composed of a subset of factors that need to be studied. The remainder of this paper will discuss these categories and the accompanying factors. System Integration/Guideway Integration by its very nature is discussed in several sections.

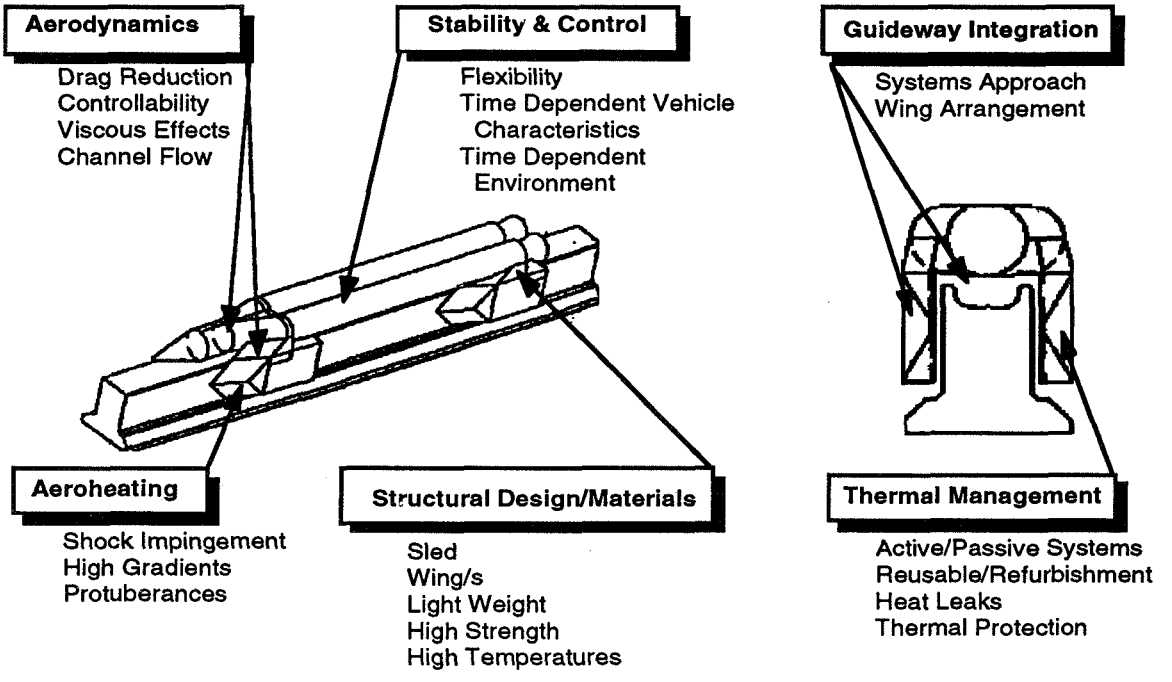

Figure 8. High Speed Sled Design Issues

Aerodynamics. In developing a hypersonic sled with magnetic levitation properties two major sled design issues are in the forefront; weight and drag. Aerodynamic design and analysis plays a major role in developing a successful system. There are several aerodynamic issues involved in sled design as shown in Figure 9, of which the major aerodynamic influence is that of sled drag. The more drag, the more propulsion power required or the less maximum speed that is achievable. Lift is also another major driver in that it imparts moments that must be resolved by the magnet system. Sled shaping is one way to reduce aerodynamic drag. Optimizing the payload to rocket fairing concept as well as how the wings attach to the sled are extremely important. Drag control and reduction also impacts the shape, radius, and sweep of the wing leading edges.

Another major aerodynamic issue is the interaction of the sled flow field with the guideway and ground plane. Flow between the wing and guideway can result in a strong shock system and choke the flow resulting in increases both in pressure and heat transfer.

In addition, reflected shocks from the guideway or ground plane can reflect back onto the sled creating forces and moments that are difficult for the magnetic system to restore. A careful system analysis of the sled and guideway is required to properly establish the correct aerodynamic configuration and how the sled should integrate with the guideway.

In evaluating this interaction, consideration must be given to whether the wings will be inside the guideway as investigated in earlier studies, or whether the wings will be outside of the guideway as selected for the Phase 1 concept. This selection has a direct impact on channel flow and magnetic performance. The orientation of the wings to the guideway; vertical, horizontal, or somewhere in between needs to be traded. In addition, the distance between the wing and guideway must be studied. All of these studies trade performance against aerodynamic forces.

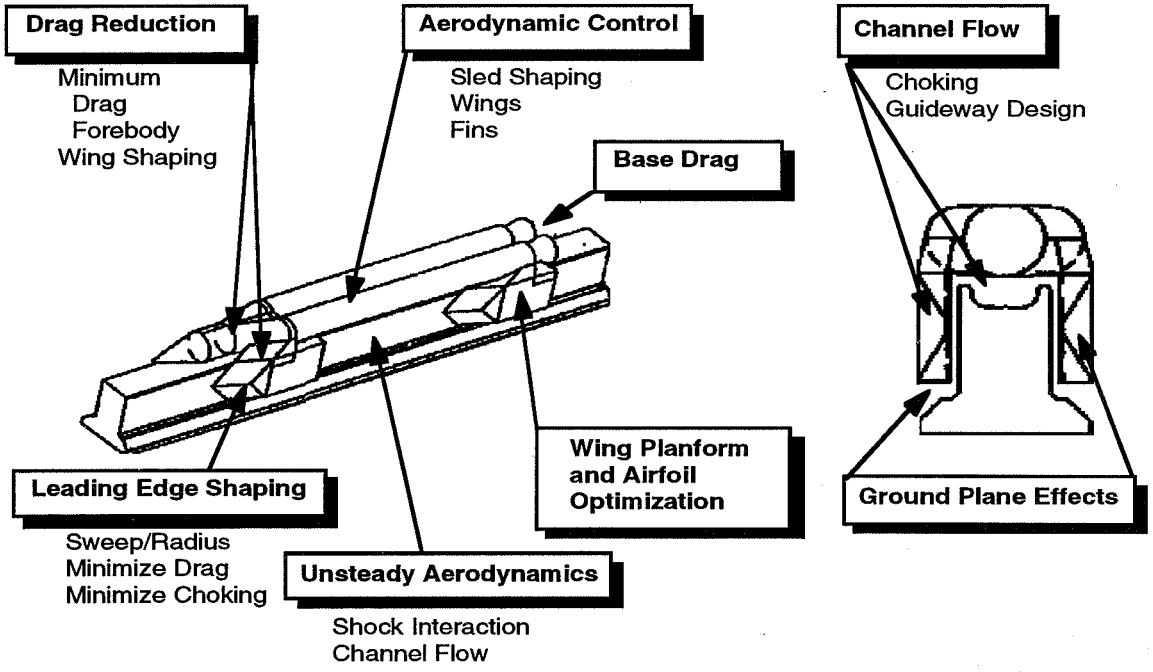

Figure 9. Aerodynamic Design and Modeling Issues

To model the resultant flow fields and capture the physics of the high speed flow requires tools other than conventional aerodynamic engineering codes. Computational Fluid Dynamics (CFD) is required to model the complex flow interactions between the sled, guideway, and ground plane. This is critical because the forces generated by reflected shocks or the viscous effects in the guideway gap can drive magnetic power requirements. These issues and requirements are indicated in Figure 10.

Computational Fluid Dynamics must be able to capture both the basic three dimensional structure of the flow around the sled which requires the ability to simulate multi-bodies, but it also must capture the viscous effects of the flow field. A computational fluid dynamics code must be able to analyze the sled from subsonic to hypersonic speeds. Also, solutions

must crisply capture shock patterns and impingement including separated flow effects and heat transfer. In developing CFD solutions advanced gridding techniques will be required to capture not only the basic sled geometry, but to be able to model geometric details and the flow between the wing and the guideway. A reliable, versatile, and accurate CFD tool is a necessity for the Maglev sled design.

The importance of this capability is depicted in the flow field solution of the General Atomics feasibility study concept where the wings are located inside a guideway channel, Figure 11. This inviscid CFD solution presents the pressure flow field about the sled at 3400 m/s in an atmosphere of helium. Several features of the basic flow are evident such as the shock generated by the payload forebody and the subsequent expansion fan aft of the payload. Close inspection of the wing (with the guideway removed) shows a pressure rise associated with subsonic flow resulting from choked channel flow due to shock interactions. Also evident, though not as obvious, is the varying flow field along the wing. To correctly model the aerodynamic forces and moments of the sled in the presence of the guideway obviously requires the application of CFD.

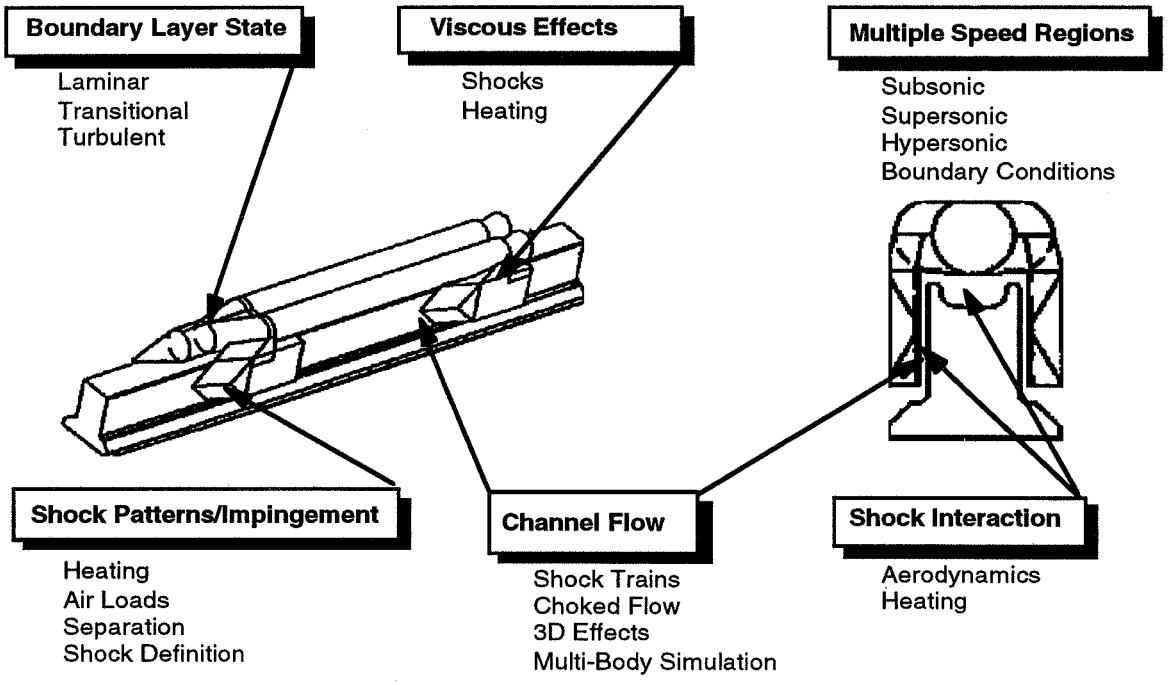

Figure 10. Flow Field Issues Associated with Sled Design

Stability & Control. Maintaining the sled in level and controllable flight with a passive (magnetic) control system while flying within an inch of a concrete guideway at hypersonic speeds is a major challenge. The only variables for the designer are aerodynamic shaping of the sled and the magnetic restoring forces.

To achieve stable and controllable flight requires definition of all the induced forces and moments due to aerodynamics, rocket propulsion, magnetic levitation, and external environments, Figure 12. In addition, transient effects such as entering and exiting a

helium bag with a significantly different atmosphere, including ignition and burnout of the rocket motors must be included in the simulation model. The effects of the interaction of the sled with the guideway and ground plane must be considered.

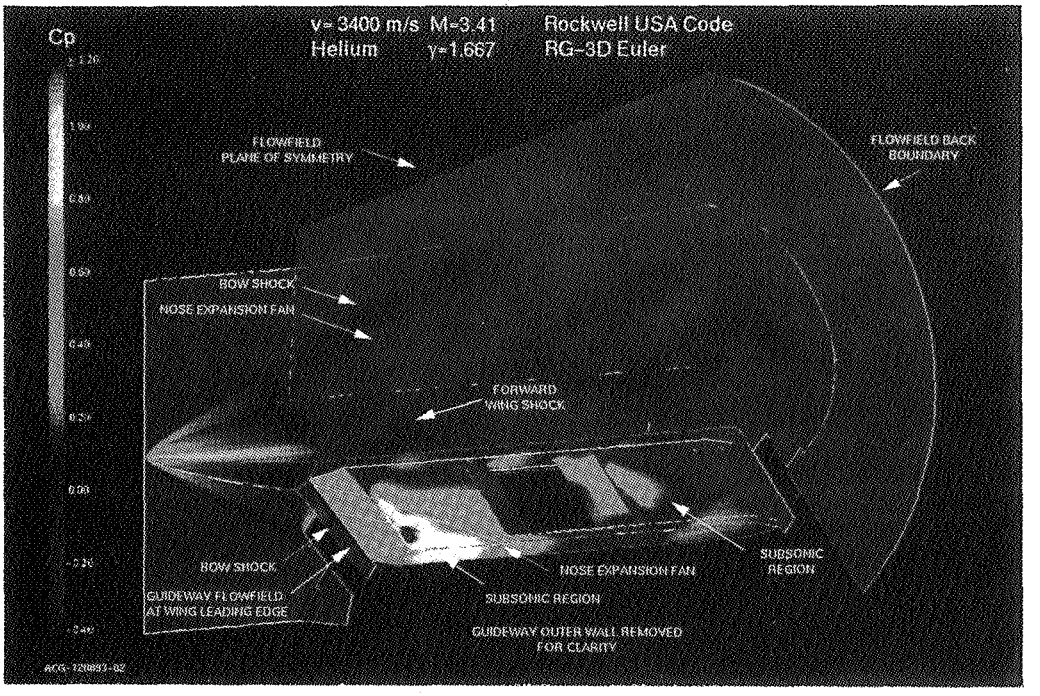

Figure 11. Pressure Flow Fields of a Sled with Guideway Effects

Time variation in forces and moments must be modeled as well as changes in overall sled weight due to expending solid rocket propellant. Simulation of these features requires a six degree-of-freedom simulator to accurately model and verify sled stability. If the sled isn't stable, changes will be required in the aerodynamic design, the sled-guideway arrangement, and/or in the magnetic power.

Aeroheating. As the speed of the sled increases into the hypersonic velocity range, heat transfer due to boundary layer forces/friction and shock impingement become an important design consideration. This requires the accurate prediction of heat transfer rates and the location and magnitude of impinging shocks. Sled design trades can be conducted to reduce heating effects by considering such design parameters as wing leading edge sweep and radius, guideway integration (guideway shaping and the wing-guideway gap), and structural attachments to the rocket motors, Figure 13. As the sled design matures, aerodynamic heating impacts due to system penetrations and protuberances associated with the superconducting magnetic system must be considered. Use of another atmosphere such as the helium tunnel at Holloman provides a reduction in both aerodynamic heating rates and aerodynamic forces. The heating rate estimates impact where and how much thermal protection is required on the sled and have a direct impact on the overall system weight.

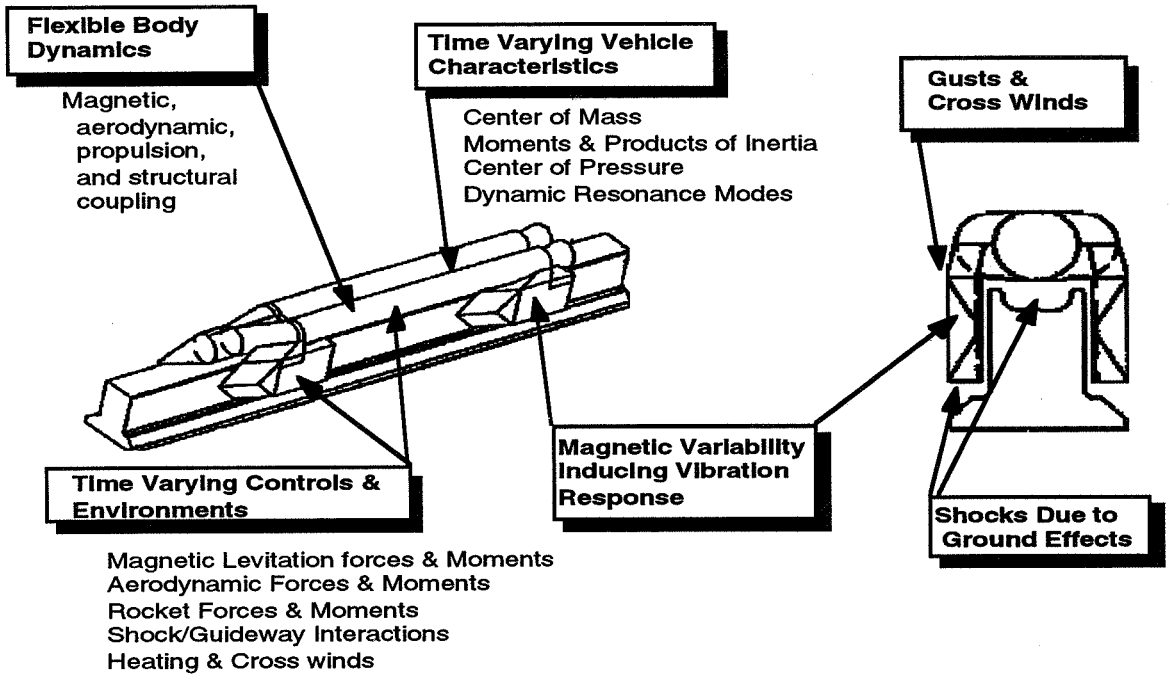

Figure 12. Stability & Control Sled Issues

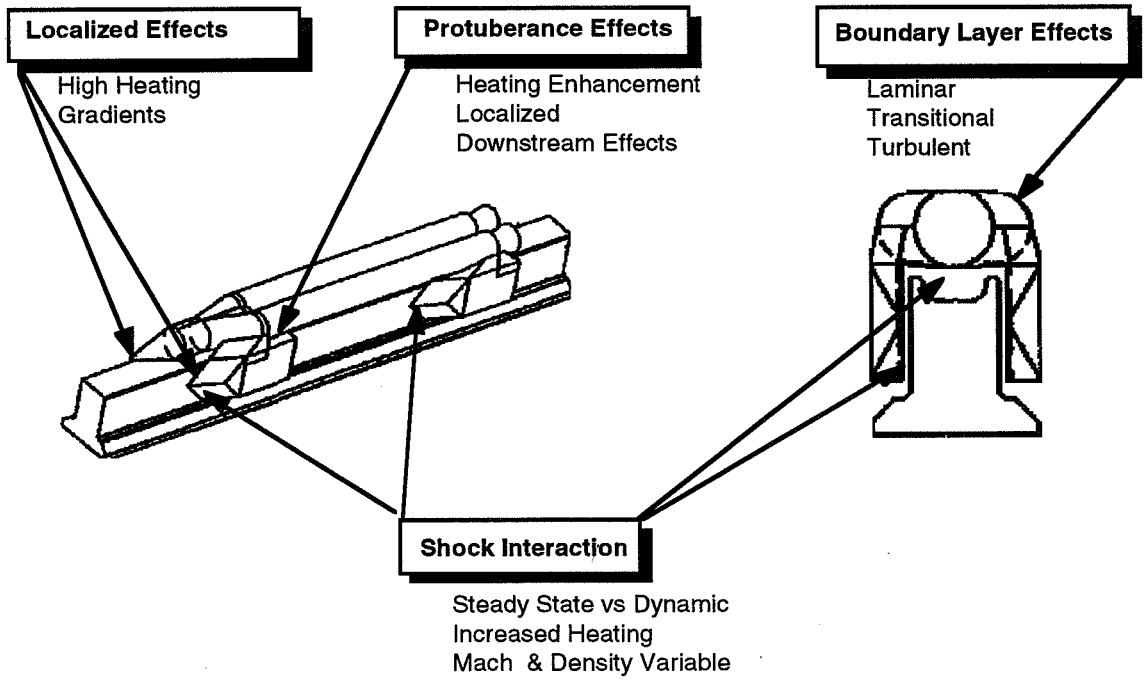

Figure 13. Aerodynamic Heating Issues

Thermal Management. Induced heating rates and loads must be accommodated to protect the basic sled structure as well as the superconducting magnets. Gradients due to shocks and the cryogenic liquids need to be included in the thermal modeling. Thermal management is challenged to protect the structure and components while minimizing the impact on the overall system weight and system refurbishment time and cost, Figure 14.

Thermal analysis must consider the transient nature of the problem where essentially the sled is in equilibrium prior to flight (Alamogordo temperature environments and cryostat temperatures) and then in a matter of seconds peak temperatures are reached. A metallic surface could see a rise of 900 °F on the side of the wing box, or a 2200°F rise on the wing leading edge in just 6 seconds. The sled must be able to withstand not only the peak temperatures, but the soak back while coasting to a stop or finally at rest.

For system operability, the desire is to maximize the use of unprotected metals by using materials such as titanium. However, leading edges and regions of high heat transfer require thermal protection. In these regions trades are required on density, reusability (ablator and susceptibility to damage), refurbishment capability (repair and replacement time), ability to attach to the structure, and material costs. Thermal analysis will require not only one and two-dimensional modeling, but possible three dimensional modeling in areas of severe thermal gradients.

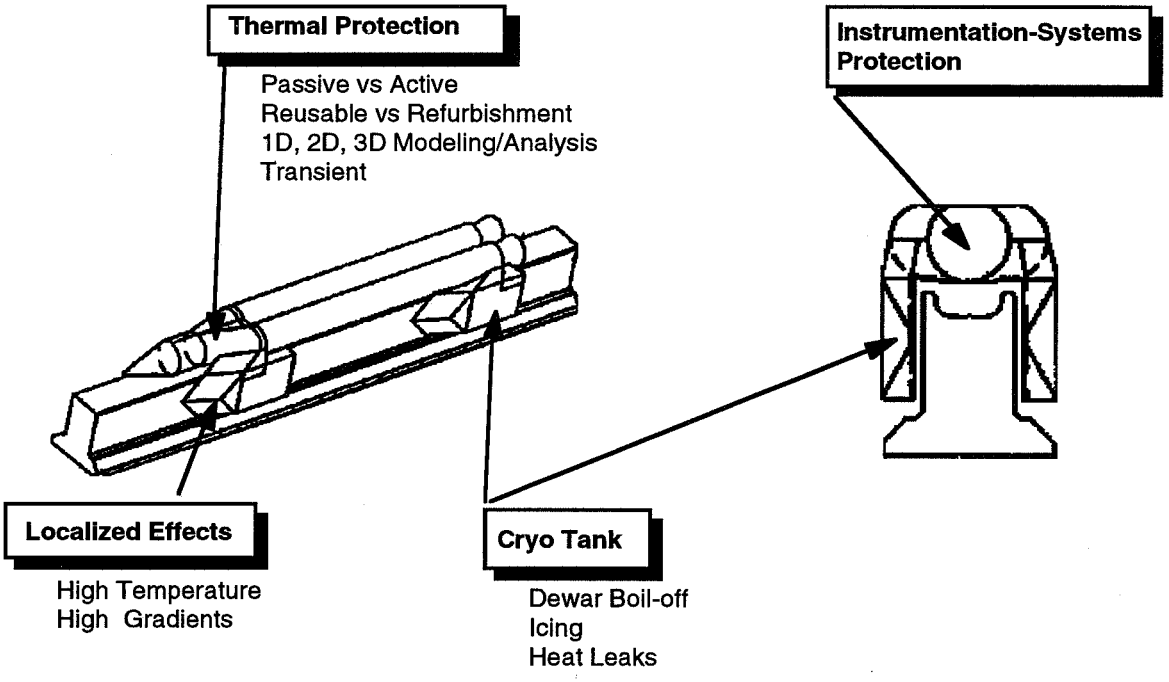

Figure 14. Thermal Management Issues

Structural Design. As mentioned in the aerodynamics discussion, weight and drag are two major design drivers. However, weight has a stronger influence on system performance (maximum velocity). The structural design or concept must strive to have the lightest weight system. Structural design and analysis must deal with some system unique issues, Figure 15. Basic construction needs to utilize non-magnetic materials which possess high strength, high temperature capability, and low density. Structural design is continually challenged to accommodate the system loads while accomplishing this with the minimum weight system. Loads from the magnet restoring forces must be transmitted from the magnets into the wing box and into the wing-rocket attachment structure to finally arrive at the rocket motor casing. Structural analysis must include all of the aerodynamic, propulsion, and magnetic forces and moments to define the total loads that the superconducting magnets must be able to restore. Stress analysis needs to trade the strength of the structural design and surface deflection limits against weight growth. In a system that is driven to obtain the lowest possible weight, care must be exercised in developing a robust but light weight design. Basic approaches of just increasing material thickness may not be the appropriate solution. Dynamic structural analysis of the sled system is required to consider the transient nature of these forces and to determine any fatigue issues. The sled experiences vibration from both aerodynamic and propulsion inputs. The long term effects of this environment has to be understood and included in the structural design. The structural design must also consider interfacing with the magnetic system so that tolerance build-up does not result in a loose magnetic installation or a crush condition. Design drawings must provide enough details to allow for quality products from both in-house and out-source manufacturing. In developing the sled design, high quality, low cost manufacturing must be achieved.

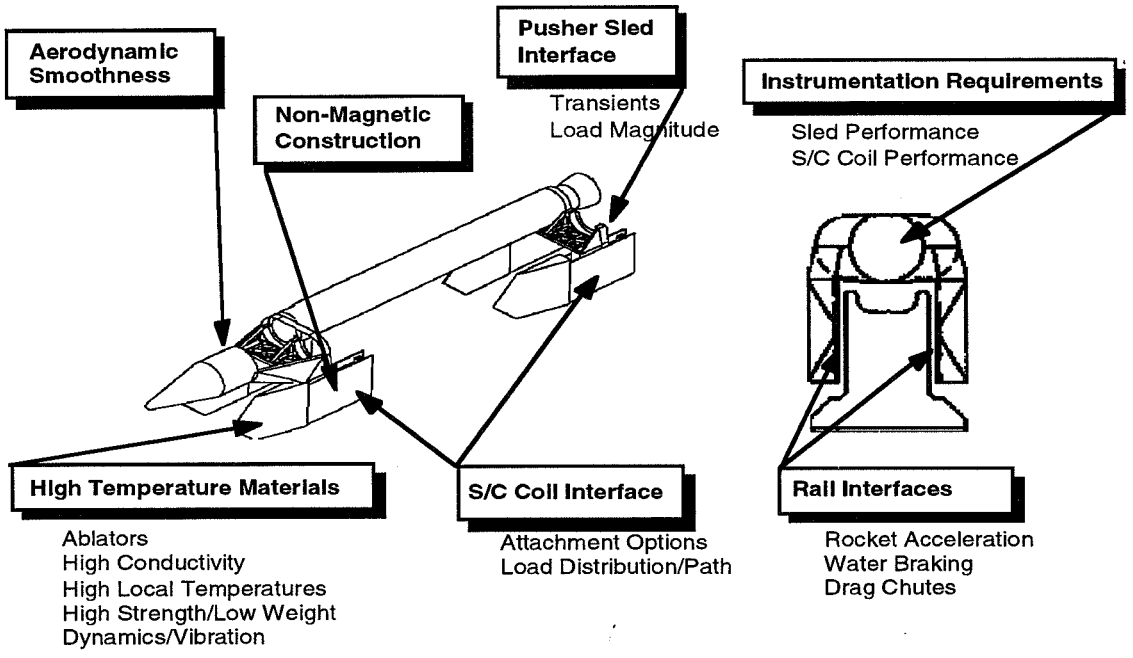

Figure 15. Structural Design Issues

SUMMARY

The Holloman High Speed Test Track has a 45 year history rich in high speed testing activities. This capability is being enhanced by the incorporation of magnetic levitation providing higher test velocities and reduced vibration. However, in the development of the hypersonic maglev sled there are several design and modeling issues that need to be addressed and understood. These issues associated with aerodynamics, flow fields, stability and control, aeroheating, thermal management, and structures/materials have been highlighted. As the Maglev sled design evolves and matures, these issues will be addressed and accommodated in the sled design.

ELECTROMECHANICAL DYNAMICS SIMULATIONS OF SUPERCONDUCTING LSM ROCKET LAUNCHER SYSTEM IN ATTRACTIVE - MODE

Kinjiro Yoshida, Kengo Hayashi, Hiroshi Takami
Depart. of Electrical Engineering
Faculty of Engineering, Kyushu University
10 - 1 6-chome Hakozaki Higashi - ku
Fukuoka, 812 JAPAN

SUMMARY

Further feasibility study on a superconducting linear synchronous motor (LSM) rocket launcher system is presented on the basis of dynamic simulations of electric power, efficiency and power factor as well as the ascending motions of the launcher and rocket. The advantages of attractive-mode operation are found from comparison with repulsive-mode operation. It is made clear that the LSM rocket launcher system, of which the long-stator is divided optimally into 60 sections according to launcher speeds, can obtain high efficiency and power factor.

INTRODUCTION

In previous papers [1], [2], we proposed a vertical type superconducting linear synchronous motor (LSM) rocket launcher system of which four acceleration guideways with double-layer armature-windings are arranged symmetrically along a shaft of about 1,500 m under the ground. From our feasibility study, it was found that the linear launcher made the rocket attain the speed of 700 km/h at the height of 100 m above the ground, at which the payload could be increased more than 15 % by substituting it for the first-step acceleration rocket. The novel armature-current control method proposed previously by us was successfully applied in a repulsive-mode operation to ascend and guide simultaneously the linear launcher with control of the Coriolis force. The current control method can be applied to an attractive-mode operation by selecting a demand value of mechanical load-angle to be slightly smaller than half the pole-pitch.

This paper presents electromechanical dynamic simulations of a superconducting LSM rocket launcher system which is operated in an attractive-mode with control of the Coriolis force. Dynamic simulations of the ascent of the 4-ton-launcher with a 1-ton-rocket are carried out to meet the same acceleration pattern of quick acceleration and deceleration rates as that of the repulsive-mode operation used in our previous papers [1], [2]. After the rocket is released at a peak speed of about 900 km/h, the linear launcher is stopped in a very short time of 5 s by a rapid control of deceleration. During the deceleration phase, the launcher is controlled quite stably with no deflection in the center of the guide shaft while it showed an under-damped oscillation in the repulsive-mode operation. The maximum value of armature-current at a peak speed of 900 km/h is decreased to a great extent as compared with that in the repulsive-mode operation.

Electrical dynamics of induced voltages and terminal voltages are simulated when the armature-windings of the 1,500-m-long stator are all excited as one section for power supply. Electrical efficiency and power factor are also evaluated qualitatively for a more practical feasibility study. The design of section lengths greatly influences electric power, power factor and efficiency of the LSM rocket launcher system. The section length should be designed taking into account its important dependence on launcher speeds. It is shown from comparison with a one-section power supply system that an optimal design of all the section lengths along the long-stator guideway leads to high efficiency and power factor of the system.

SUPERCONDUCTING LSM ROCKET LAUNCHER SYSTEM

Figure 1 shows a concept of a large-scale superconducting LSM-controlled rocket launcher system, which has the acceleration guide tube of about 1,500 m deep under the ground. The concept is based on our theoretical works on a superconducting LSM-controlled ground-based zero-gravity facility with the drop shaft of about 800 m [3]. In Fig. 1, the LSM armature-windings installed all along the acceleration guide tube are used to drive and guide the linear launcher.

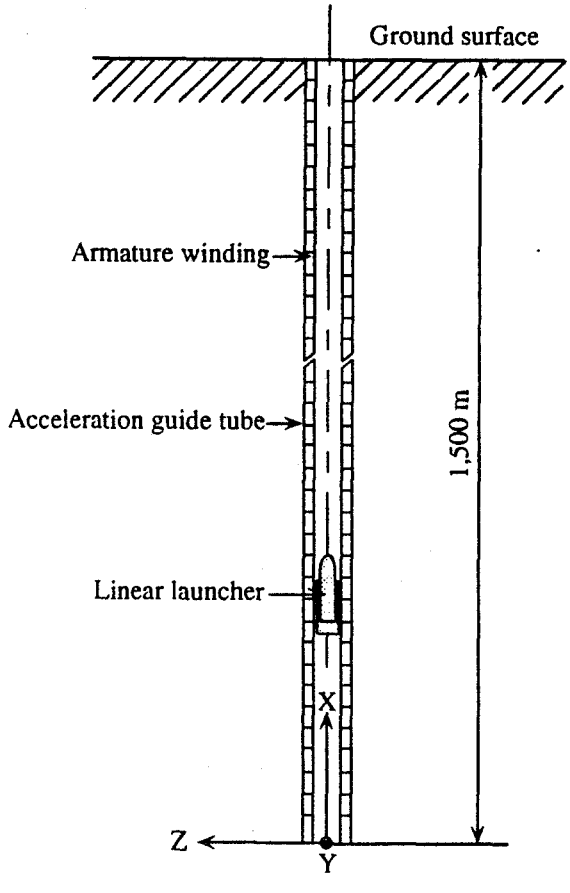

Figure 1. Vertical type superconducting-LSM controlled rocket launcher system.

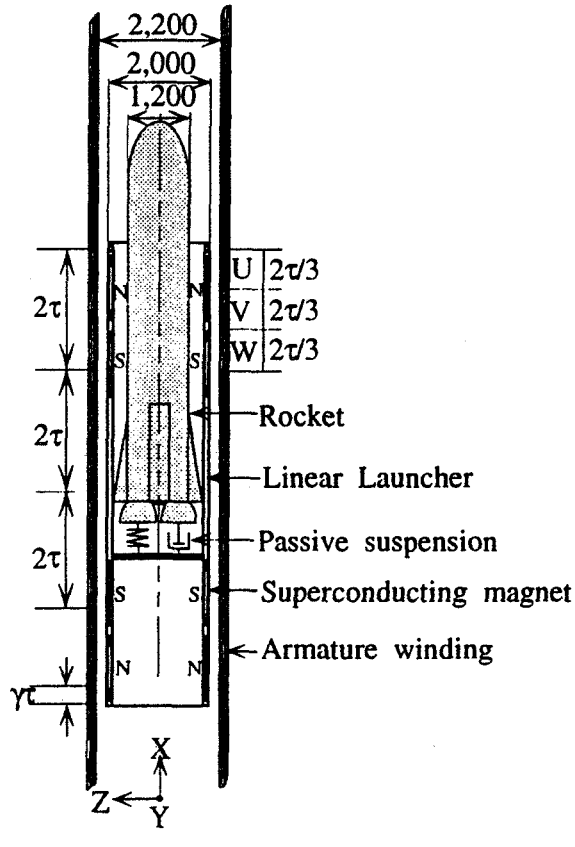

Figure 2. Acceleration guide tube of LSM armature and rocket launcher with superconducting magnets.

Figure 2 shows double-layer windings of the LSM armature which are composed of inside and outside coils, and the linear launcher on which the rocket is mounted through the use of passive suspension. The superconducting magnets are arranged with two poles facing the armature-windings in the front and rear portions of the linear launcher vehicle.

Figure 3 shows a cylindrical configuration of the LSM launcher system which has four LSM's in symmetrical positions to produce guidance forces in the Y- and Z-directions. In the figure, the linear launcher is deflected by ΔY in the Y-direction and by ΔZ in the Z-direction. Inside and outside coils of each LSM armature are connected in series and each LSM is controlled independently using each armature-current in their coils.

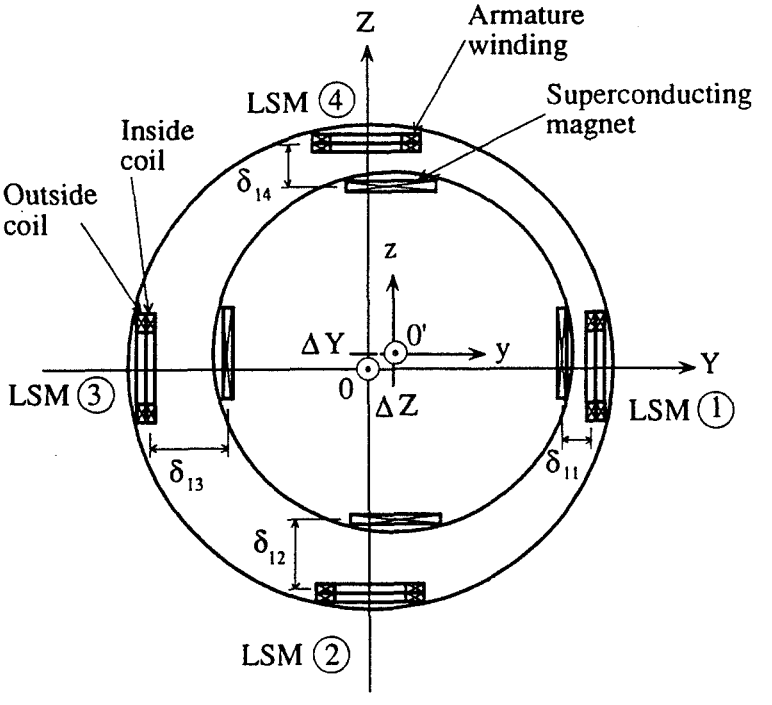

Figure 3. Model for analysis of rocket launcher showing cross-section of acceleration guide tube and four LSM's.

ASCENT AND GUIDANCE MOTION CONTROL OF LINEAR LAUNCHER AND ROCKET

The linear launcher is accelerated to a peak speed, loaded with the rocket, and after releasing the rocket, it is decelerated with no-load to be brought to rest at the end of guide tube near the earth's surface. On the other hand, during the acceleration phase, the rocket is fixed to the launcher through a passive suspension, but after separation from the launcher, it ascends freely in the guide tube. According to the armature-current control method proposed in Reference (1), the ascending motions in the X-direction of the launcher and the rocket are controlled together with the guidance motions in the Y-Z plane. When the Z-axis is assumed to be in an eastward direction, the Coriolis force can be taken into account as an external disturbance force in the Z-directed motions of the linear launcher and the rocket.

After the rocket is released from the launcher and takes off with a high initial-speed, the

rocket continues to ascend with no control subject to the Corioli's force in the Z-direction under the force of gravity in the X-direction.

The effective value of armature-current for each LSM in Fig.3 is controlled to meet the command acceleration pattern. The linear launcher should be controlled simultaneously to ascend at the synchronous speed V_{X0} of the travelling magnetic field, by producing the LSM thrust F_X. The mechanical load-angle is controlled for all the four LSM's to produce the sufficiently strong attractive force due to the resultant guidance forces F_Y and F_Z. When the launcher receives any disturbance forces in the Y- and Z-directions, the LSM guidance forces can compensate automatically and keep it at the center of the four LSM's.

ANALYSIS OF ELECTRICAL DYNAMICS

For an arrangement of the four superconducting LSM's shown in Fig. 3, each LSM can be treated independently from the viewpoint of electrical dynamics. In any LSM, a voltage equation is described for 6 armature-windings of inside and outside 3-phase-windings. Under the condition that 3-phase armature-windings and supplied voltages are all balanced and inside and outside windings are connected in series, a system of voltage equations for an arbitrary section-length is derived in the following matrix form:

$$\begin{bmatrix} v_u \\ v_v \\ v_w \end{bmatrix} = 2R \begin{bmatrix} i_u \\ i_v \\ i_w \end{bmatrix} + \frac{d}{dt} \begin{bmatrix} 2(L - M_2 + M_4) & M_5 + M_6 & M_5 + M_6 \\ M_5 + M_6 & 2(L - M_2 + M_4) & M_5 + M_6 \\ M_5 + M_6 & M_5 + M_6 & 2(L - M_2 + M_4) \end{bmatrix} \begin{bmatrix} i_u \\ i_v \\ i_w \end{bmatrix} + \begin{bmatrix} e_{u01} + e_{u02} \\ e_{v01} + e_{v02} \\ e_{w01} + e_{w02} \end{bmatrix} \quad (1)$$

where
v_v = instantaneous value of v-phase terminal-voltage
i_v = instantaneous value of v-phase armature-current
e_{v01}, e_{v02} = instantaneous value of v-phase induced-voltage in inside and outside windings
R = resistance per phase of inside or outside armature-windings
L = self inductance per phase of inside or outside armature-windings
M_2 = mutual inductance between neighbouring inside and outside armature-windings
M_4 = mutual inductance between inside and outside armature-windings of the same phase
M_5, M_6 = mutual inductance between inside and outside armature-windings of lagging and leading phases
v = u, v, w

Note that the mutual inductances M_2, M_5 and M_6 can be referred to Fig. 4.

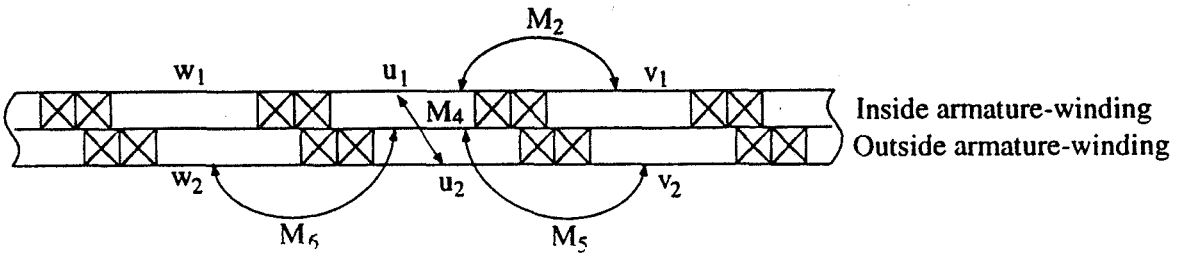

Figure 4. Mutual inductances with respect to u-phase armature-winding.

In the 3-phase armature-windings connected to satisfy the condition of $i_u + i_v + i_w = 0$, each phase-voltage equation is decoupled according to equation (1). By applying vector analysis, the terminal voltage per phase $\dot{V}$ is derived in the following vector expression:

$$\dot{V} = 2R\dot{I} + 2j\omega\left(L - M_2 + M_4 - \frac{M_5 + M_6}{2}\right)\dot{I} + \dot{E}_0 \tag{2}$$

with

$$\dot{E}_0 = E_0\, e^{j(\pi/2 - \pi/\tau\, x_0)} \tag{3}$$

where $\dot{I}$ = vector of phase current
$\dot{E}_0$ = vector of induced voltage
E_0 = effective value of induced voltage
x_0 = mechanical load-angle
$\omega = 2\pi f$ = angular velocity
f = supply frequency

The active power P_0, power loss P_l and the reactive power P_Q for each LSM system are described as follows:

$$P_0 = 3E_0 I \sin\frac{\pi}{\tau}x_0 \tag{4}$$

$$P_l = 6RI^2 \tag{5}$$

$$P_Q = 6\omega\left(L - M_2 + M_4 - \frac{M_5 + M_6}{2}\right)I^2 + 3E_0 I\cos\frac{\pi}{\tau}x_0 \tag{6}$$

where I = effective value of phase current.

Apparent power P_a, the efficiency η and power factor $\cos\phi$ are thus calculated using equations (4) - (6).

$$P_a = \sqrt{(P_0 + P_l)^2 + P_Q^2} \tag{7}$$

$$\eta = \frac{P_0}{P_0 + P_l} \times 100 \tag{8}$$

$$\cos\phi = \frac{P_0 + P_l}{P_a} \times 100 \tag{9}$$

DESIGN OF SECTION-LENGTH

It is of practical significance to design the section-length of the long-stator along the guideway which depends strongly on launcher speeds. Before the launcher enters the next section, the armature-current in that section is required to be at a steady state. The time constant is the same in all sections, so that the more the speed of the launcher increases, the larger the section-length should be. Figure 5 shows a design of section-length which includes 19-divisions with 30-, 60-, and 99-m-sections. The three regions of different section-length are

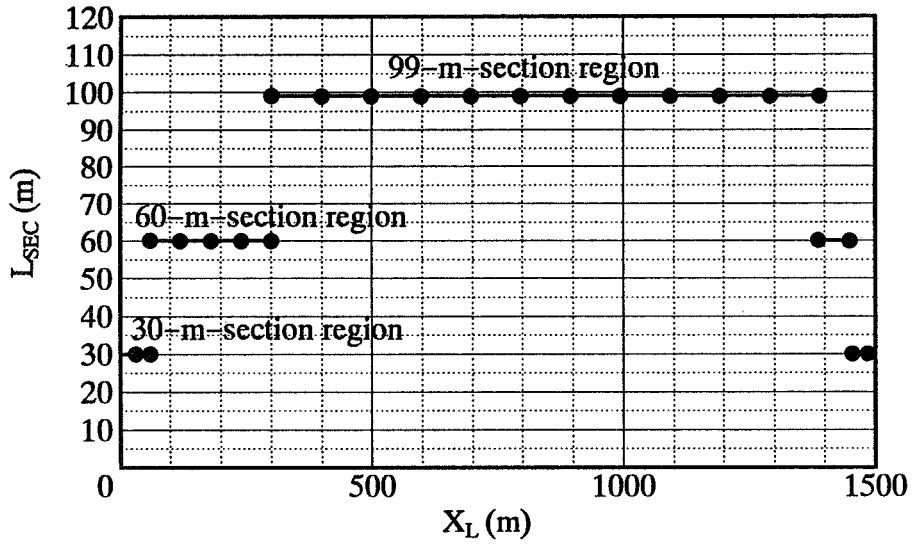

Figure 5. The 19 sections designed along the guideway

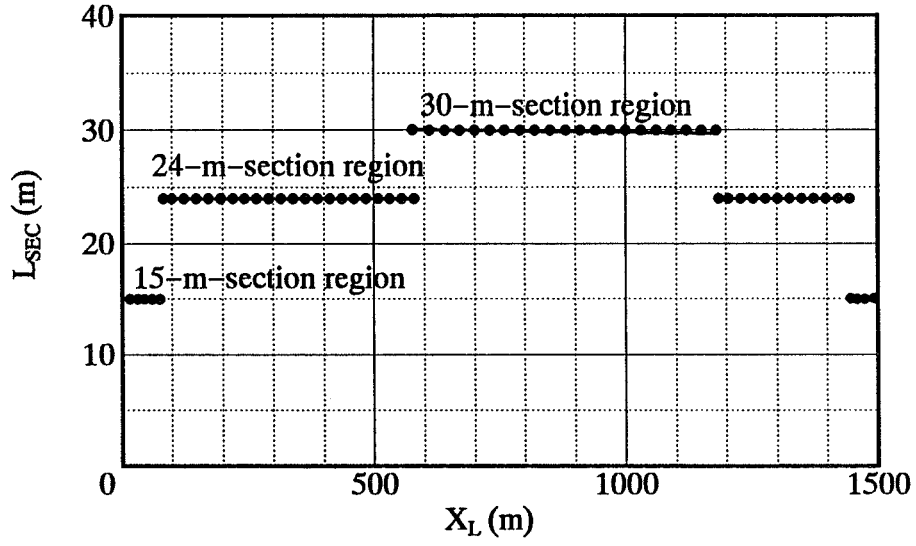

Figure 6. The 60 sections designed along the guideway

determined using the time (170 ms) enough to converge switch-on-transient phenomena, which is about five times larger than the time constant $\tau = 32.9$ ms as shown in Table 1. Figure 6 shows an optimal design of section-length which includes the 60 divisions with 15-, 24-, and 30-m-sections. This is

Table 1. Resistance, inductances and time constant in each section

section / parameter	30-m-section	60-m-section	99-m-section
R (Ω)	0.1176	0.2352	0.3881
L - M_2 + M_4 (mH)	4.8000	9.5990	15.8300
M_5 + M_6 (mH)	0.1874	0.3748	0.6185
τ (sec)	0.0329	0.0329	0.0329

calculated for the time constant of $\tau = 32.9$ ms. Even for a short time of 32.9 ms, the armature-current can be excited sufficiently by supplying a suitable voltage smaller than its maximum value which is required at a peak speed of 900 km/h.

NUMERICAL EXPERIMENTS

The superconducting LSM rocket launcher system (see Table 2) is designed for the 1-ton rocket to attain a speed of 700 km/h at the height of 100 m above the ground. In the limited length of LSM armature guide tube, the linear launcher is controlled to meet the command acceleration pattern, which has the 6.6-s-acceleration-phase with a quick variation from zero to 4 G's for 0.5 s and 4 G's kept for 6.1 s, and the 4.67-s-deceleration-phase with a very quick variation from 4 G's to -7.5 G's for 1.3 s, -7.5 G's kept for 2.87 s and a very quick variation from -7.5 G's to zero for 0.5 s.

Simulated Motions of LSM Launcher and Rocket

Fig. 7 (a) and (b) show that the rocket is released from the launcher just after the peak speed at the location of 1,000 m, launches with an initial speed of about 900 km/h, flies out the LSM guide tube with a speed of about 720 km/h and then attains the command speed of 700 km/h at the height of 100 m above the ground. An instance when the rocket is released is known from an instance for $\Delta H = 0$ in Fig. 7 (d). As shown in Fig. 7 (c), the launcher is controlled to follow very well the command acceleration pattern according to the command mechanical load-angle in Fig. 7 (e). The required armature-current and thrust force are shown in

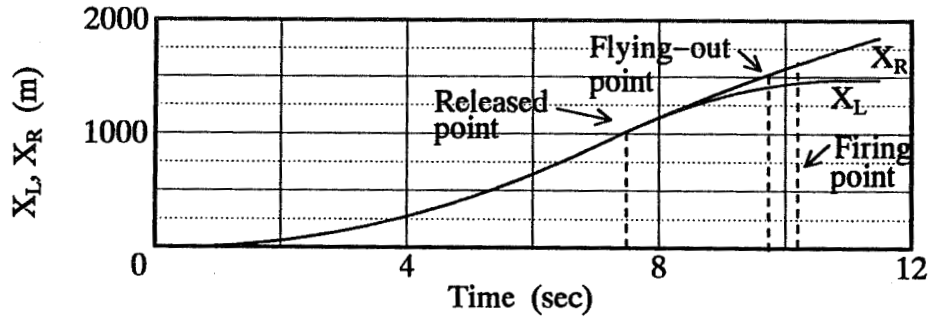

(a) Positions of ascending launcher and rocket

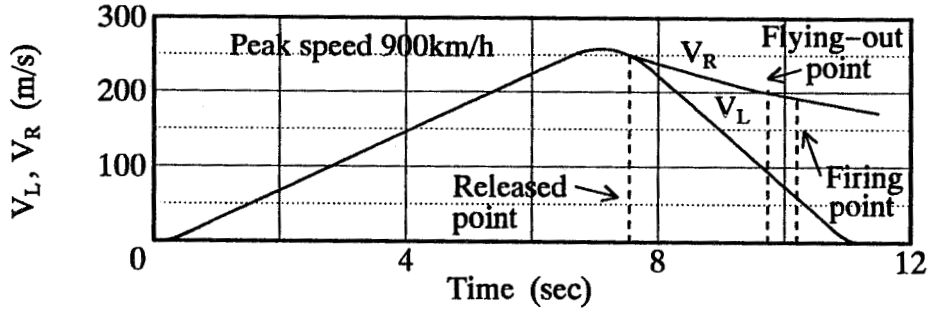

(b) Speeds of ascending launcher and rocket

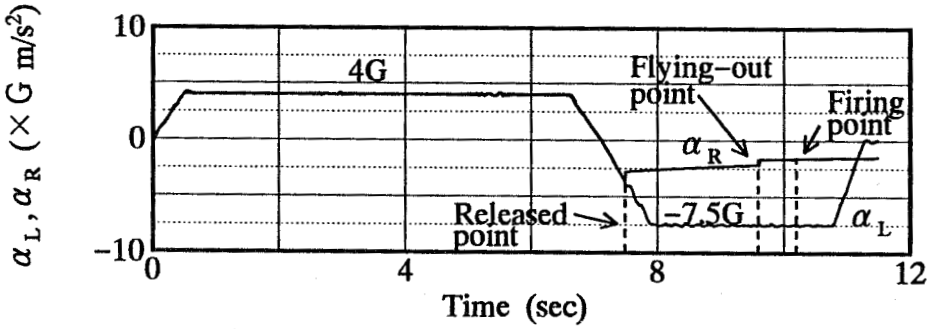

(c) Acceleration of ascending launcher and rocket

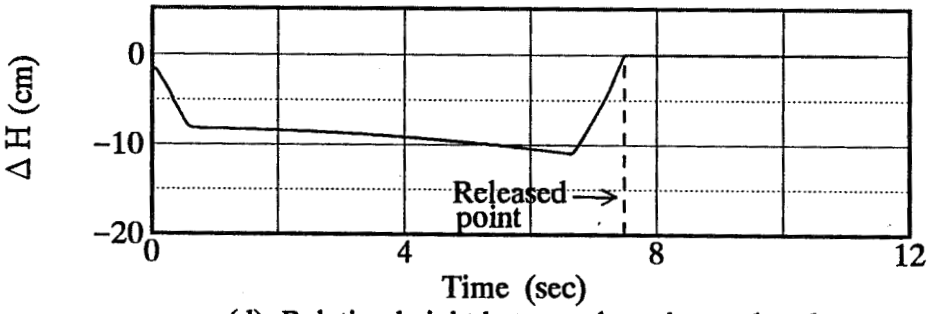

(d) Relative height between launcher and rocket

Figure 7. Ascending motion of LSM rocket launcher

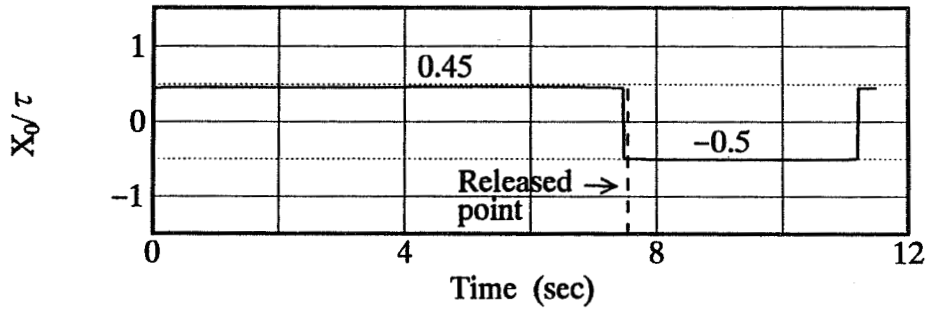

(e) Mechanical load–angle of inside armature winding

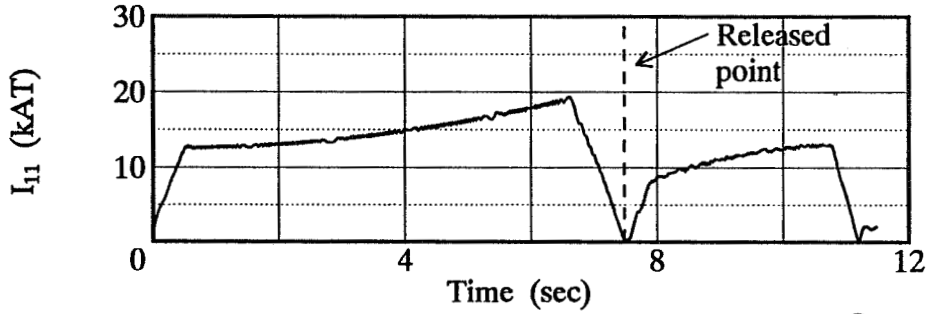

(f) Current of inside armature–winding in LSM①

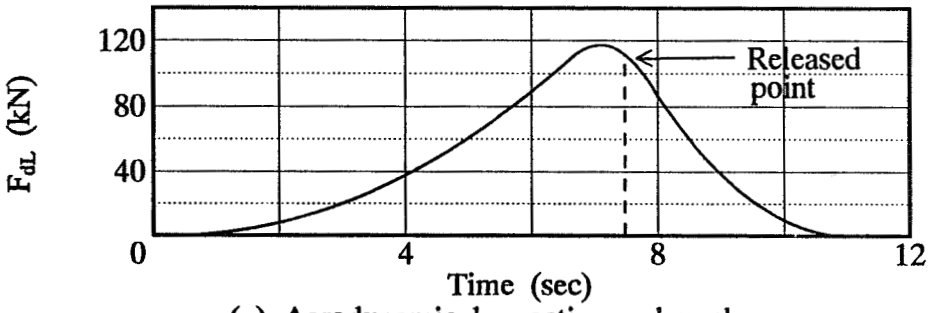

(g) Aerodynamic drag acting on launcher

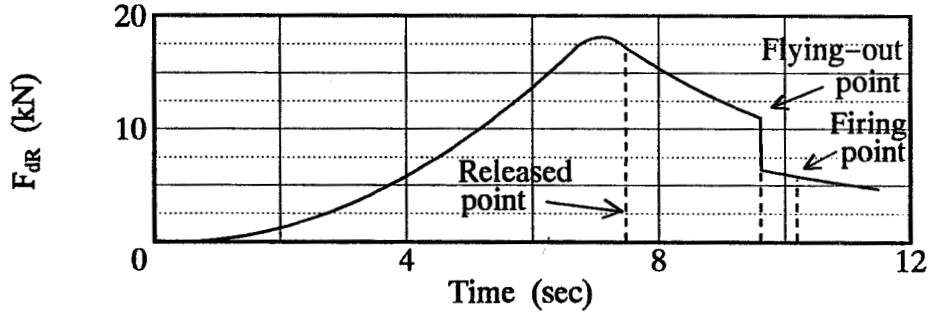

(h) Aerodynamic drag acting on rocket

Figure 7. Ascending motion of LSM rocket launcher

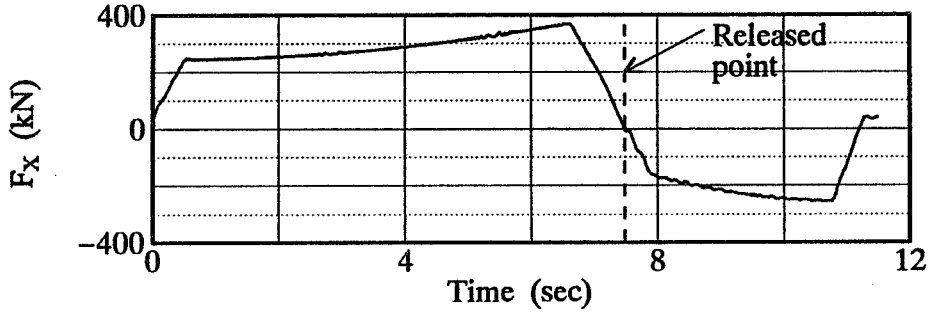

(i) Total thrust force in the X–direction

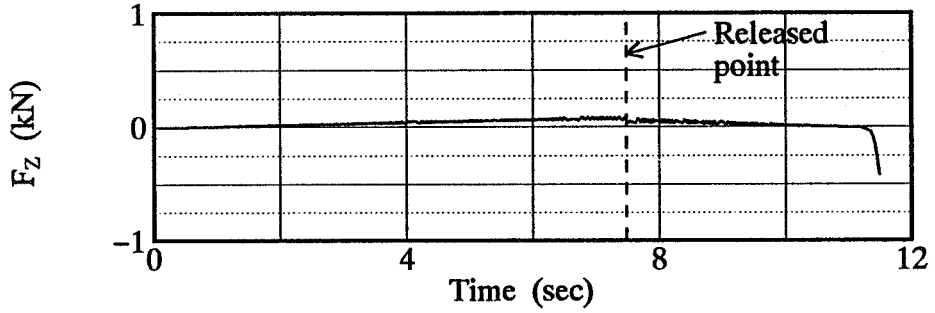

(j) Total guidance force in the Z–direction

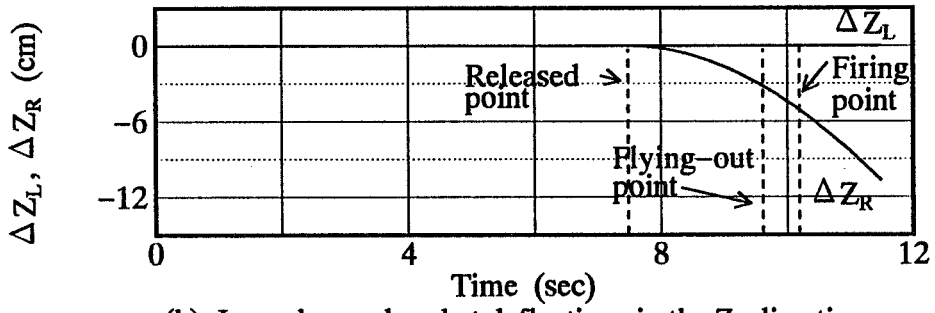

(k) Launcher and rocket deflections in the Z–direction

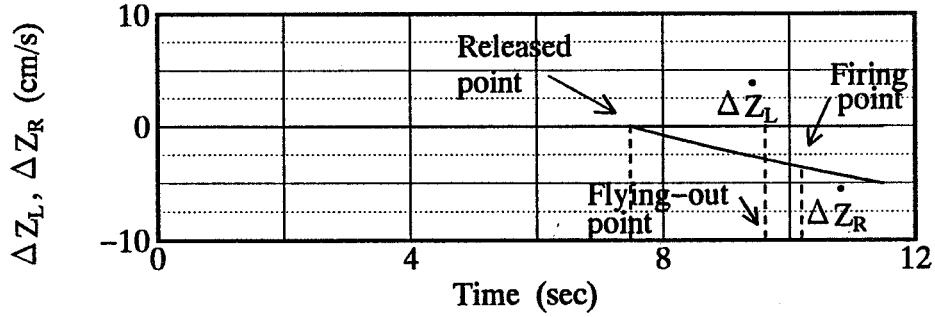

(l) Launcher and rocket speeds in the Z–direction

Figure 7. Ascending motion of LSM rocket launcher

Figs. 7 (f) and (i).

Table 2. Design data of superconducting LSM rocket launcher.

Guide Tube :		Total weight	4 ton
Total length	1,500 m	No. of Superconducting Magnets	16
Diameter	4 m	Superconducting Magnets per one LSM :	
LSM Armature Guide Tube :		No. of poles	4
Total length	1,500 m	Coil length	1.3 m
Inside diameter	2.4 m	Coil width	0.5 m
Outside diameter	2.6 m	MMF	700 kAT
No. of LSM Armature	4	Pole pitch	1.5 m
Coil length	0.8 m	Rocket :	
Coil width	0.6 m	Total weight	1 ton
Linear Launcher :		Clearance Gap :	
Total length	9 m	Electrical gap between coil centers	20 cm
Diameter	2 m	Mechanical gap	10 cm

Figure 7 (k) shows that the Coriolis force in the Z-direction is compensated completely using the guidance force in Fig. 7 (j) before the release point and after that the launcher itself is controlled quickly and stably in the center of the LSM guide tube while the rocket is deflected in the reverse direction of the Z-axis, *i. e.* in the westward direction, by 3.8 cm at the flying-out point of the guide tube end. The deflection is sufficiently small compared with the mechanical clearance between the rocket and the inside coil of LSM armature, such that the rocket does not come into collision with the wall of the inside coils. Figure 7 (l) shows that the launcher makes no motion in the Z-direction and the rocket is moved quite slowly in the westward direction due to the Coriolis force.

Electrical Dynamics Simulations

Figure 8 shows simulated results for terminal voltage, active-, reactive- and apparent-powers, power loss, efficiency and power factor per LSM in a basic case of a one-section power supply system where the 1500-m-long-stator of armature-windings are all excited simultaneously. The terminal voltage per phase becomes a maximum value of 180 kV at a peak speed of 900 km/h, as shown in Fig. 8 (a). It is known from Figs. 8 (b), (c), (d) and (e) that reactive power P_Q and apparent power P_a are about 1,000 MVA and are extremely large as compared with the active (output) power P_0 of 25 MW and power loss P_l of 47.5 MW. As a result, efficiency and power factor are generally very low, as shown in Figs. 8 (f) and (g). Figure 9 shows very important effects of section-length on electro-dynamical performance characteristics as mentioned concerning Fig. 8. It is found from Fig. 9 (a) that the maximum value of terminal voltage can be decreased by 79 % and 90 % by adapting the 19-section and 60-section power supply systems where the long-stator for each LSM is divided into 19 and 60 sections along the guideway as shown in Figs. 6 and 7, respectively. As the section-length becomes shorter, resistance and leakage inductances become smaller and reactive power P_Q and power loss P_l are dramatically decreased with active power P_0 kept constant as shown in Figs. (c), (d) and (e). Consequently, efficiency η

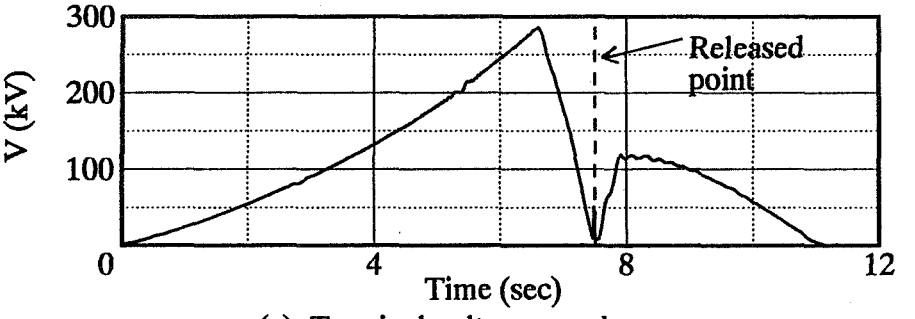

(a) Terminal voltage per phase

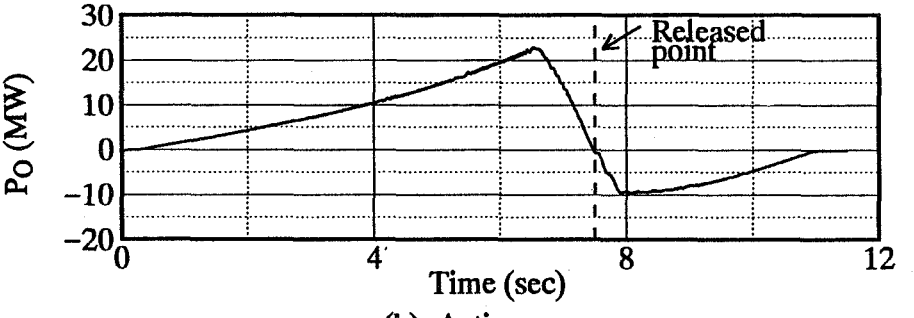

(b) Active power

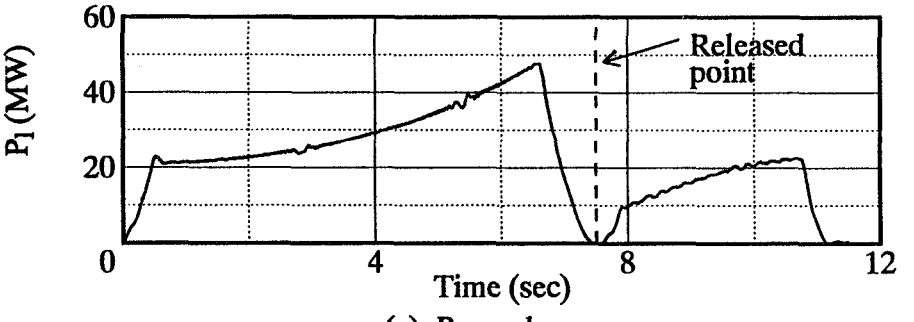

(c) Power loss

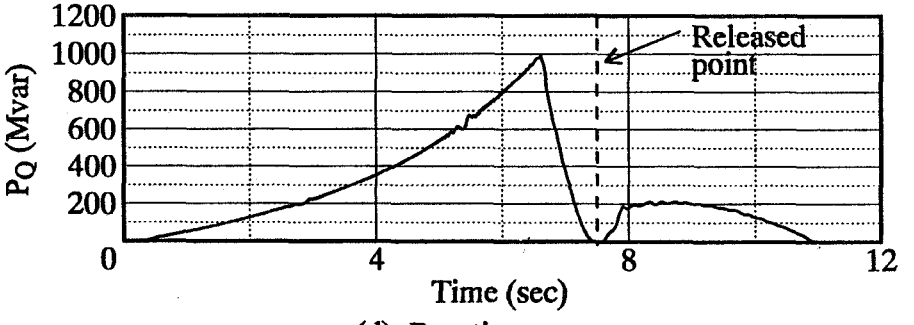

(d) Reactive power

Figure 8. Terminal voltage and electric powers in one-section power supply system

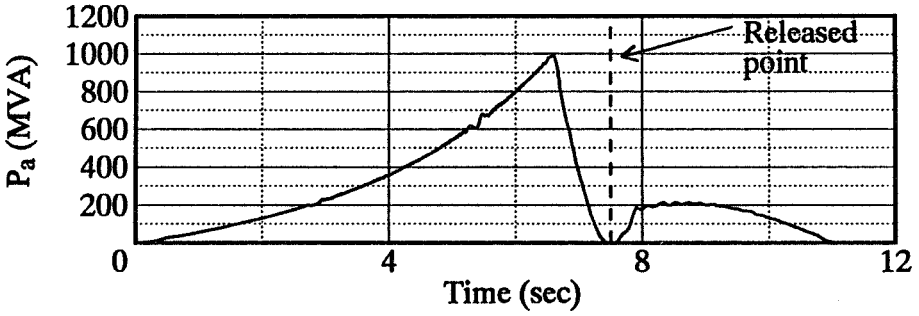

(e) Apparent power

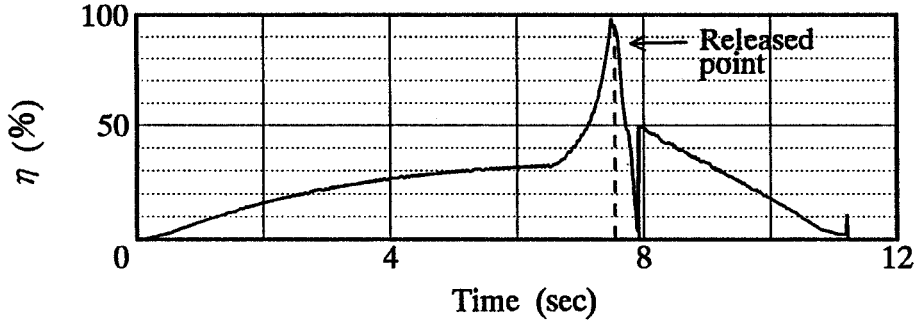

(f) Efficiency

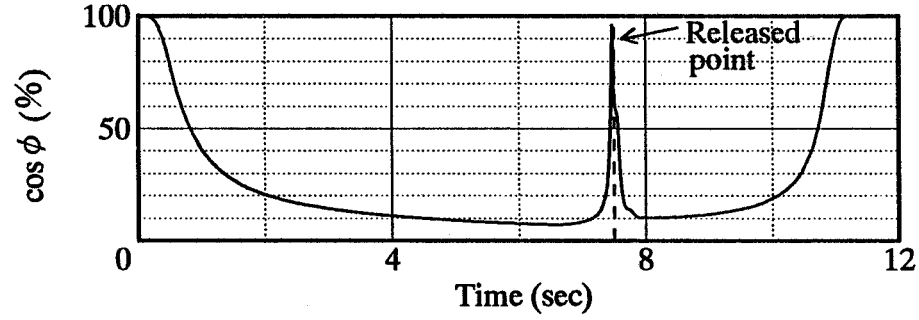

(g) Power factor

Figure 8. Terminal voltage and electric powers in one-section power supply system

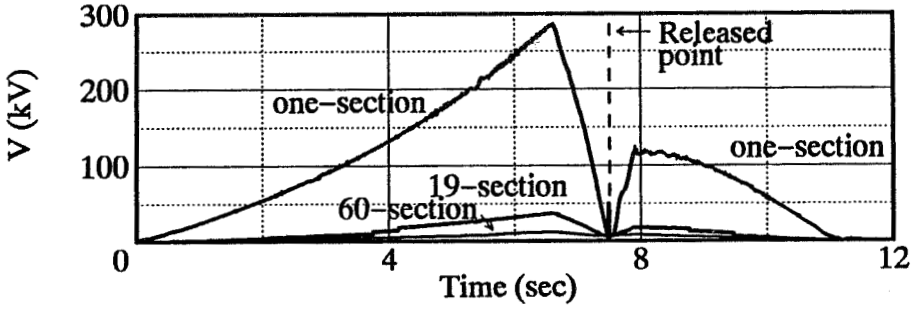

(a) Terminal voltage per phase

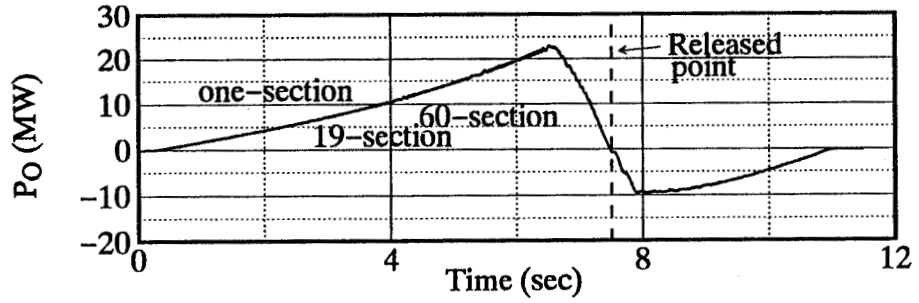

(b) Active power

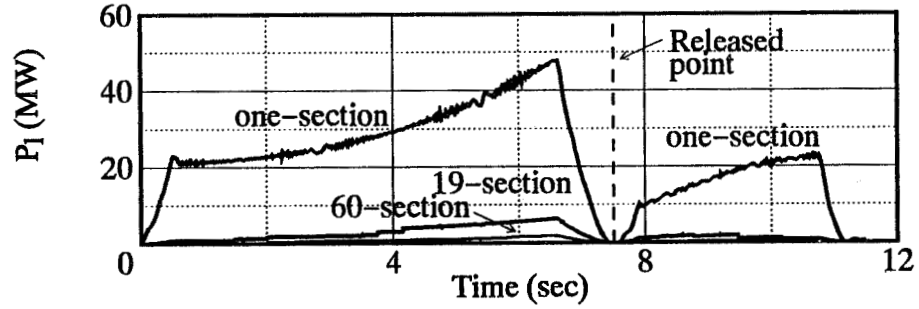

(c) Power loss

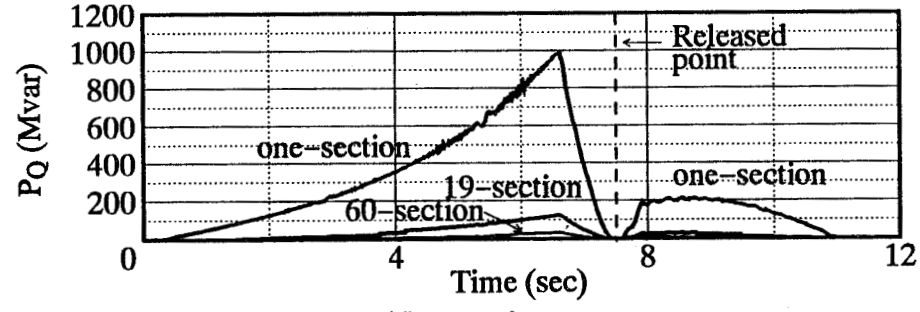

(d) Reactive power

Figure 9. Comparison of terminal voltage and electric powers among one- ,19- and 60-section power supply systems

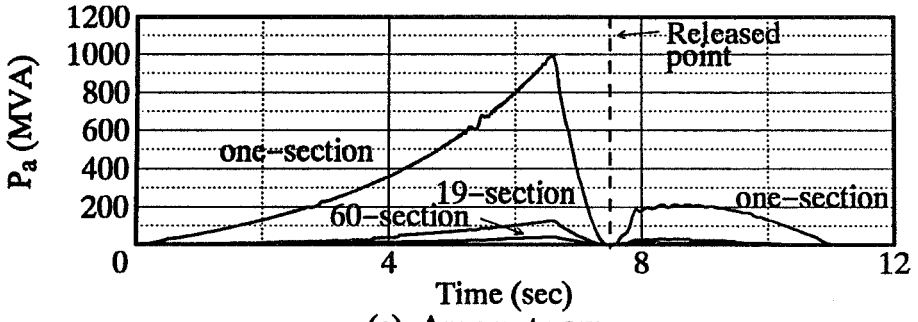

(e) Apparent power

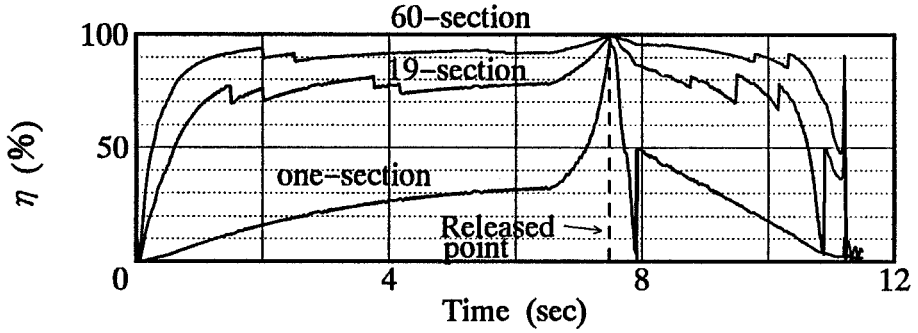

(f) Efficiency

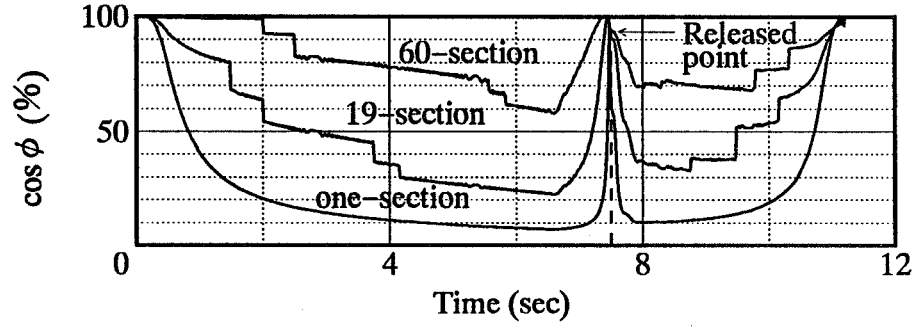

(g) Power factor

Figure 9. Comparison of terminal voltage and electric powers among one- ,19- and 60-section power supply systems

and power factor cos ϕ can be increased considerably as shown in Figs. 9 (f) and (g). Most notably, the 60-section power supply system can maximize power factor to obtain its value of 60% at lowest as compared with 22-%-power factor in the 19-section power supply system.

CONCLUSIONS

A vertical type superconducting LSM rocket launcher system under the ground which is operated in an attractive-mode is proposed and an optimal section-length of the long-stator is designed in a practical feasibility study. A computer program for simulating electromechanical dynamics of the system is developed by which the section-lengths can be designed optimally all along the guideway taking into account their dependence on the launcher speeds.

The following results are obtained from the simulation study :

(1) The novel armature-current control method proposed previously by us was also successfully applied in an attractive-mode operation for the 4-ton-launcher with 9-ton-rocket to meet the same acceleration pattern as that of the repulsive-mode used in our previous papers.

(2) The launcher is controlled quite stably with no deflection in the center of the guide shaft while compensating the Coriolis force, especially during the deceleration phase when it showed an under-damping oscillation in the repulsive-mode operation. The maximum value of armature-current at a peak speed of 900 km/h is also deduced to 73 % as compared with that in the repulsive-mode operation.

(3) The maximum values of terminal voltage per phase and apparent power for each LSM become 180 kV and 1,000 MVA and efficiency and power factor for the system are also 31 % and 8 % in a basic case of one-section power supply system. It is found that an optimal design of the 60-section-length power supply system enable the system to obtain 15 kV, 40 MVA, 92 % and 60 % for terminal voltage per phase, apparent power, efficiency and power factor, respectively.

REFERENCES

1. K. Yoshida, T. Ohashi, K. Shiraishi and H. Takami : Feasibility Study of Superconducting LSM Rocket Launcher System, NASA Conference Publication 3247 Part 2, May 1994, pp. 607 - 621
2. K. Yoshida, T. Ohashi, K. Shiraishi and H. Takami : Dynamics Simulations of Superconducting LSM Rocket Launcher System, J. of Space Tech. and Science, Vol.9 No.2, Autumn 1993, pp. 13 - 28
3. K. Yoshida, A. Kunihiro and T. Ohhashi : Superconducting LSM Dynamics in Ground - Based Zero - Gravity Facility, Proc. of Inter. Conf. on the Evolution and Modern Aspects of Synchronous Machines, Zurich, Aug. 1991, Part 3, pp. 797 - 802

AIR-CORED LINEAR INDUCTION MOTOR FOR EARTH-TO-ORBIT SYSTEMS

Zivan Zabar, Enrico Levi, and Leo Birenbaum
Polytechnic University
Six MetroTech Center
Brooklyn, NY 11201

SUMMARY

The need for lowering the cost of Earth-to-Orbit (ETO) launches has prompted consideration of electromagnetic launchers. A preliminary design based on the experience gained in an advanced type of coilgun and on innovative ideas shows that such a launcher is technically feasible with almost off-the-shelf components.

INTRODUCTION

In 1990, a seminar was held in Arlington, VA[1] on the subject of Earth-to-Orbit electromagnetic launchers. It was based on the following set of launcher parameters: velocity = 5 to 6 km/s; acceleration = < 1500 Gee's; mass = 500 to 2,000 kg; cycle time = 10 minutes (~ 500 launches per week).

If the proposed limitation on the allowable acceleration a, that is, $a < 1500$ Gee's, is accepted, then the resultant length of the barrel l_b must exceed 833 m.[2] It has been suggested that such a launcher should be built on a mountain having the proper slope and orientation - not a very practical proposition! Probably for this reason the idea was not pursued further at the time. The idea has been revived recently by the Maglev (magnetic levitation) community under a specially coined name, Maglift (or Maglifter*).

The problem of an extremely long barrel, however, will remain, unless a much larger acceleration is allowed. The reason for the original limitation on the acceleration was the low tolerance of the delicate electronic components in the payload, but hardened electronics, as used in artillery shells, can take a = 30,000 Gee's. NASA, in a proposed Advanced Hypervelocity Aerophysics Facility, would have allowed a much larger acceleration, a = 50,500 Gee's, in the fully instrumented models.

Taking the lower value, a = 30,000 Gee's, would reduce the length of the barrel to less than 50 m, and this would allow vertical take-off.

At the Polytechnic, we have developed a linear induction launcher (LIL), the principle of which we now propose be employed for earth-to-orbit launches: The launch vehicle is driven by a set of long air-cored linear induction motors, positioned vertically, or inclined from the vertical, and symmetrically placed around the axis of the vehicle launch path. These motors provide the necessary guidance and levitation forces as well as the propulsion force to the launcher vehicle, to which the motor secondaries are attached during the launch phase.

*Editors note: Maglifter, as currently envisioned by NASA Headquarters, requires relatively low "release" velocities, with chemical propulsion assistance for the climb to orbit.

Each air-cored linear induction motor has a primary winding consisting of a linear array of coaxial circular coils, and a secondary which is a cylindrical conductive sleeve concentric with the primary. Each primary is installed along the entire length of the launch structure, but is divided into sections. These sections are energized by polyphase electric currents, thereby producing a traveling wave of magnetic flux density. This flux is coupled to the passive secondary and induces in it an azimuthal system of currents. The interaction between the primary and secondary currents creates a longitudinal force component used for propulsion, and a strong radial centering force component used for levitation and guidance. The frequency of the primary currents increases from one section to the other to provide constant acceleration of the launch vehicle. The energy is supplied by flywheel motor/generator sets.

The main feature of the concentric arrangement of the primary and secondary is that propulsion, guidance and levitation are provided by the same set of drive coils. Also the magnetic flux is confined, being carried by the inner core and closing mainly in the cylindrical gap between primary and secondary. This permits the elimination of the iron cores without increasing unduly the magnitude of the magnetization current needed for the establishment of the magnetic field. Another feature deriving from the cylindrical symmetry of the primary and secondary is that all portions of the current-carrying conductors contribute to the generation of useful forces. This tends to give high efficiency with reduced material stress and small physical dimensions, and to minimize the cost of the apparatus. As another feature of this system, operation in the asynchronous mode eliminates the need for synchronization between the moving vehicle and the traveling magnetic wave.

The LIL, then, operates as a linear induction motor; hence, its name. A prototype assembled at the Polytechnic with components borrowed from the U.S. Army Electronics Technology and Devices (ET&D) Lab in Fort Monmouth, New Jersey, achieved design performance in 1993, accelerating a 137-gram aluminum (sleeve) cylindrical tube to a velocity of 476 m/s with an acceleration of 19 kGee's, thus validating our computer simulation codes.[3]

Also, in 1993, two of the authors of this paper (ZZ, EL) obtained a U.S. Patent on a spin-off of the LIL, a novel air-cored motor for magnetically levitated (Maglev) trains.[4] Unlike the LIL, the energized coils are inside the sleeve, which is split longitudinally, parallel to the axis, to allow for mechanical support of the coils. The coils are energized at industrial frequency (60 Hz, for example) and provide levitation and guidance, as well as propulsion. The system, of which a close-up view is shown in Fig. 1, is compatible with ordinary steel-wheel rail railroads. The vehicle uses two aluminum rail guides, and it may have four air core motors.

If desired, the same concept could be applied to Maglift for ETO.

As was already mentioned, we propose vertical take-off. However, in order to decouple the diameter of the payload from that of the barrel and in order to limit the voltage impressed on the coils, we propose to use a cluster of barrels and split sleeves, as shown in Fig. 2, instead of a single barrel. The payload is accelerated by means of several, three in Fig. 2, split sleeves, affixed to it, forming a rigid assembly, and arranged in a star-shaped, geometry. The direction of movement of this assembly -- the payload, the housing, and its three split sleeves -- is intended, in the Figure, to be directed into the page (i.e., away from the reader).

In view of the general trend towards lighter satellites, "smallsats," we have also modified the specifications to be more in line with those of a minimal craft, such as Clementine, which carries a 235 kg payload and 223 kg of fuel.

According to a preliminary design, these modified specifications can be met with a launcher having the dimensions and design parameters shown in the next sections.

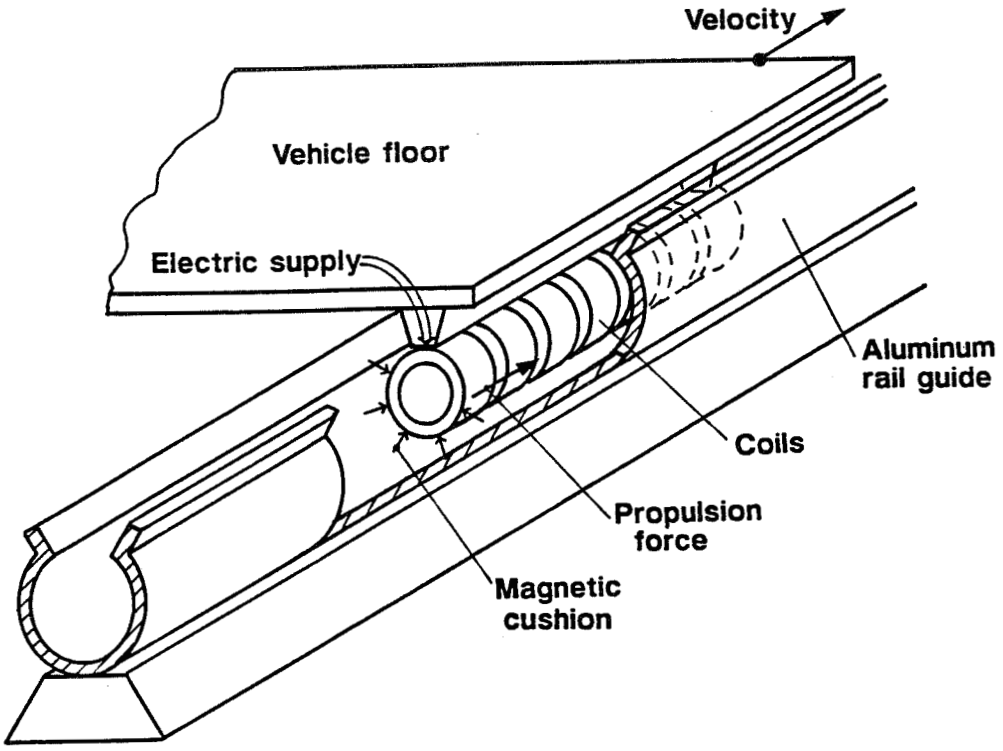

Figure 1. Close-up view of propulsion, suspension and guidance system.

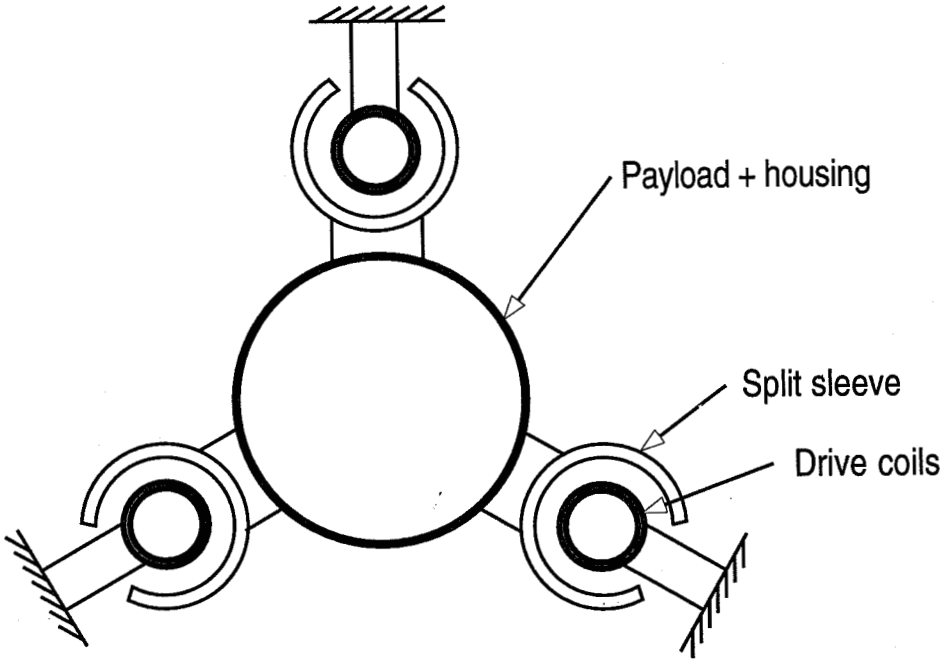

Figure 2. Cluster of barrels using a novel topology.

VERTICAL TAKE-OFF ETO LAUNCHER

A preliminary design (see Table 1 below) made according to Refs. 5-8 and Appendix 1 indicates that a launcher for a final velocity of 5 km/s and a weight payload + housing + sleeves of 500 kg should be visualized as a tower about 50 meters high, consisting of six columns (the six barrels) and 38 levels (one for each section of the launcher). On each level would be placed six flywheel motor/generator sets, which energize the appropriate sections (of the six barrels) that correspond to that level. Initially, in preparation for the launch, all of the flywheels would be brought up to speed using each of the synchronous machines on each level as a motor powered by an adjustable speed drive. Then, during launch, the same machines, working now as generators, would be sequentially switched on at each level, from the lowest to the uppermost, to energize the 38 sections of each barrel.

In the table below is given a set of ETO specifications, followed by a list of the results of the preliminary design of an ETO launcher.

Table 1. ETO Specifications and Preliminary Design for Vertical Take-Off

ETO specifications:

Final velocity:	5	km/sec
Acceleration:	25,000	Gee's
Weight, payload + housing + sleeves:	500	kg
Payload diameter:	as needed	
Armature fraction: (sleeve weight/total weight)	66%	
Cycle time:	~ 500	per week

ETO preliminary design parameters:

Structure:	vertical	(cluster of barrels)
Length of barrel:	50.4	m (height of tower)
No. of barrels:	6	
No. of sections:	38	(one per tower level)
No. of phases:	12	
Pole pitch:	0.36	m
Ampere turns per coil:	$6.78 \cdot 10^6$	AT
Peak volt per turn:	77	kV *
OD of each barrel:	0.192	m
Air-gap clearance:	0.025	m

Length of sleeve:	0.72	m
OD of each sleeve:	0.237	m

* A change in the number of barrels and of their dimensions would reduce the voltage per turn to more acceptable values.

ELECTROMECHANICAL STORAGE

As already mentioned, it is proposed to use electromechanical storage to power the ETO launcher. The mechanism consists of a flywheel/motor-generator set in which the flywheel would be brought up to speed using the synchronous machine as a motor, powered by a variable frequency drive. The density of kinetic energy stored in a cylindrical flywheel is $e_{kin} = \left(\frac{v}{2}\right)^2 \frac{\text{joule}}{\text{kg}}$ where v is the peripheral velocity of the flywheel. The present speed record is held by a flywheel built at Oak Ridge with a peripheral velocity of 1370 m/s.[9] This yields an energy density $e_{kin} = 4.7 \cdot 10^5 \frac{\text{joule}}{\text{kg}}$ which for ETO, requiring a stored energy of $10.4 \cdot 10^3$ MJ, corresponds to a total mass m = 44 tonnes. When this mass is divided by the number of barrels, which is 6, and the number of sections, which is 38, the dimensions of the individual flywheels become quite reasonable. Each flywheel must serve also as a motor/generator set. In the first low-energy sections, the flywheels could consist of a set of permanent magnets embedded in a carbon-fiber composite, similar to those being developed by American Flywheel Systems Inc.[10] for use in electrical vehicles. In the high energy sections, however, the cost of the permanent magnets would become prohibitive. There are other ways to provide excitation to the rotor without the need to resort to sliding contacts and brushes which, due to the high speed, would not be reliable (see Refs. 11, 12).

In the 1970's the authors of this paper developed a homopolar inductor motor for Maglev under sponsorship of the U.S. Department of Transportation[11, 12]. They designed a full-scale motoring unit which was built and successfully tested by the General Electric Company in Schenectady, NY. The unit was mounted on a flywheel rotating at a peripheral velocity of 134 m/s, which corresponds to a train speed of 300 miles/h. In view of the experience gained with this project, we propose to adopt this type of machine in the last sections of the ETO launcher.

Although flywheels are quite adequate for storing large amounts of energy, its delivery at the extremely large rate, which is required by the generator, presents a challenge. To illustrate the fundamental problem in electrical terms, one can look at the equivalent circuit of a unit mass of the flywheel in a motor generator set (Fig. 3).[13, 14] The equivalent dielectric constant $\varepsilon_{eq} = \xi/B^2$ where ξ is the mass density and B is the magnetic flux density, is so huge that also the discharge time constant $\tau = \xi/\gamma B^2$ of the material is very large. Here γ is the conductivity, J is the current density, f_m is the mechanical force density, E is the field intensity and v is the linear velocity.

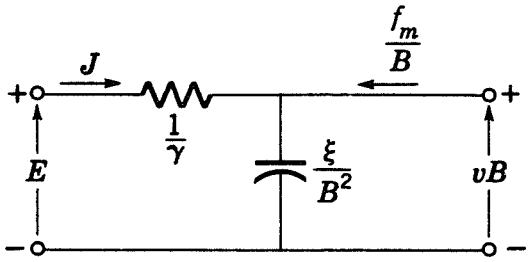

Figure 3. Equivalent circuit of unit volume of conducting material.

INCLINED TAKE-OFF ETO LAUNCHER

The power level required for heavy payloads limits the acceleration rates and, therefore, leads to unacceptable heights for vertical take-off launching towers. The solution is a Maglift, a spin-off of the magnetic levitation systems for high-speed transportation. It envisages an inclined racetrack on the slope of a mountain. Again, the centering forces in the motor elements and their symmetrical distribution around the payload afford the lateral stability that other systems lack.

Using preliminary calculations and design given in Appendix 2, in concept, a low acceleration launcher for a final velocity of 5 km/sec and an assembly weight of 2,000 kg should be visualized as a straight 900-meter-long track.

In Table 2 below is given a set of Maglift ETO specifications, followed by a list of the results of the preliminary design of an ETO launcher.

Table 2. ETO Specifications and Preliminary Design of Maglift ETO

Maglift ETO specifications:

Final velocity:	5	km/sec
Acceleration:	1,420	Gee's
Assembly weight:	2,000	kg
Payload diameter:	as needed	
Armature fraction: (sleeve weight/total weight)	66%	
Cycle time:	~ 500	per week

ETO preliminary design parameters:

Structure:	inclined	
Length of barrels:	900	m
No. of barrels:	4	
No. of sections:	46	
No. of phases:	12	
Pole pitch:	2	m
Ampere turns per coil:	$8.26 \cdot 10^5$	AT
Peak volt per turn:	18.8	kV
OD of each barrel:	0.21	m
Air-gap clearance:	0.025	m
Length of sleeve:	0.72	m
OD of each sleeve:	0.255	m

ETO power supply:

Flywheel/motor-generator sets		
Total stored energy	$41.6 \cdot 10^3$	MJ
Total mass of all sets	176	tonnes
Total number of sets	184 on 46 levels; 4 sets per level	

CONCLUDING REMARKS

The development of electromagnetic ETO launchers still presents challenging tasks. The preliminary designs contained in this paper indicate, however, that there do not appear to be any problems that cannot be surmounted with existing technology.

REFERENCES

1. Joint SDIO/IST, DARPA; held Feb. 8, 1990 at W. J. Schafer Associates, Arlington, VA.

2. Based on $(ma)l_b = \frac{1}{2}mv^2$ = kinetic energy of launch assembly.

3. Z. Zabar, X. N. Lu, E. Levi, L. Birenbaum, and J. Creedon, "Experimental Results and Performance Analysis of a 500 m/s Linear Induction Launcher," 7th EML Symp. San Diego, CA, April 20-24, 1994.

4. E. Levi and Z. Zabar, "Air-Cored, Linear Induction Motor for Magnetically Levitated Systems," U.S. Patent No. 5,270,539, Dec. 14, 1993.

5. Y. Naot, E. Levi, Z. Zabar, and L. Birenbaum, "Design and Power Conditioning for the Coilgun," IEEE Trans. Vol. MAG-24, pp. 627-631 (1989).

6. J. L. He, Z. Zabar, E. Levi, and L. Birenbaum, "Concerning the Design of Capacitively Driven Coilguns," IEEE Trans. on Plasma Science, Vol. 17, pp. 429-438 (1989).

7. J. L. He, Z. Zabar, E. Levi, and L. Birenbaum, "Transient Performance of Linear Induction Launchers Fed by Generators and Capacitor Banks," IEEE Trans. on Magnetics, Vol. 27, pp. 585-590 (1991).

8. J. L. He, Z. Zabar, E. Levi, and L. Birenbaum, "Analysis of Induction-Type Coilgun Performance Based on Cylindrical Current Sheet Model," pp. 579-584, Ibid.

9. M. L. Wald, "Flywheels to Power Vehicles," p. D2, New York Times, June 22, 1994.

10. "Transportation," IEEE Spectrum, pp. 62-63, Vol. 31, No. 1, Jan. 1994.

11. E. Levi, "Linear Propulsion," Section 23, Pars. 271-309, Standard Handbook for Electrical Engineers, 11th Edition, McGraw-Hill, 1978. Revised 1985.

12. E. Levi, Polyphase Motors: A Direct Approach to Their Design, John Wiley, New York, 1984.

13. E. Levi and M. Panzer, Electromechanical Power Conversion, McGraw-Hill, New York, 1966. Second Corrected Edition, Dover, 1974; New Printing, Robert E. Krieger, 1982 (Russian Translation, Mir Press: Moscow USSR, 1969.

14. E. Levi and Z. Zabar, "Novel Scheme for Space Power Generation and Energy Storage," IEEE Trans. on Magnetics, Vol. 25, pp. 331-334 (1989).

APPENDIX 1

Preliminary Design for Vertical ETO Launcher

Specifications: muzzle velocity: $v_m = 5 \times 10^3$ m/s; acceleration: $a = 2.5 \times 10^5$ m/s^2

assembly weight: $w_{pr} = 500$ kg.; armature fraction: $\frac{1}{\nu} = \frac{2}{3}$

The length of the barrels is: $l_b = \frac{1}{2}\frac{v_m^2}{a} = \frac{1}{2}\frac{25 \times 10^6}{2.5 \times 10^5} = 50$ m.

We assume a pole pitch: $\tau = 0.36$ m and we round the length of the barrel to $l_b = 50.4$ in order to have an integer number of pole pairs. We choose $l_b = 50.4$ m, in order to have an even number of pole pairs. We choose a cluster of 6 barrels, so that we have available for each sleeve a weight $w_s = \frac{1}{\nu}\frac{w_{pr}}{6} = 55.55$ kg. We assume a sleeve length $l_s = 2\tau = 0.72$ m and a thickness $a_s = 2$ cm, so that the average radius is

$$r_s^{ave} = \frac{w_s}{\xi_s \times 2\pi \times a_s \times l_s} = \frac{55.55}{2.7 \times 10^3 \times 2\pi \times 2 \times 10^{-2} \times 0.72} = 0.227\text{m}.$$

The inside radius is then: $r_s^i = r_s^{ave} - \frac{a_s}{2} = 0.227 - \frac{0.02}{2} = 0.217$ m.

We assume an air-gap length $g_a = 0.025$ m, so that the outside radius of the barrel is $r_b^0 = r_s^i - g_a = 0.217 - 0.025 = 0.192$. We assume that the thickness of the barrel coils is $a_b = 0.04$ m. The effective air gap is then:

$$g = \frac{2+4}{2} + 2.5 = 5.5\text{ cm};\ \beta g = \frac{\pi}{0.36} \times 5.5 \times 10^{-2} = 0.48;\ coth\,\beta g = 2.241$$

Letting the critical slip be s_c and the synchronous speed be v_s we have

$$s_c v_s = \frac{1 + coth\,\beta g}{a_s\,\gamma_{400}\,\mu_o} = \frac{1 + 2.241}{2 \times 10^{-2} \times 1.338 \times 4\pi} = 9.63\text{ m/s}.$$

Letting θ be the temperature rise and Γ the ratio of peak to minimum power, we then have

$$\theta/\Gamma = \frac{\nu\xi_s v_m s_c v_s}{c} = \frac{1.5 \times 2.7 \times 10^3 \times 5 \times 10^3 \times 9.63}{2.68 \times 10^6} = 72.76.$$

where ν is the inverse of the armature fraction, ξ_s is the specific weight of the sleeve material and c is the heat coefficient per-unit volume.

Let $\theta = 500$K, so that $\Gamma = 6.84$ and the number of sections is

$$n = \frac{v_m}{2 s_c v_s \sqrt{\Gamma^2 - 1}} = \frac{5 \times 10^3}{2 \times 9.63 \sqrt{6.84^2 - 1}} = 38.$$

The kinetic energy is $E_{kin} = \frac{1}{2} w_{pr} v_m^2 = \frac{1}{2} \times 500 \times 5^2 \times 10^6 = 6.25 \times 10^9$ J.

The average force is $F_{ave} = \frac{E_{kin}}{l_b} = \frac{6.25 \times 10^9}{50.4} = 1.24 \times 10^8$ N.

The increment of kinetic energy in the last section is

$$\Delta E_{kin} = Pt = P\frac{\Delta v}{a} = \frac{1}{2}(v_f^2 - v_i^2) = \frac{1}{2} m\Delta v\,(2v_f - \Delta v) = ma(v_f - \frac{\Delta v}{2}).$$

Assuming $\Delta v = \text{const} = \frac{v_m}{n} = \frac{5 \times 10^3}{38} = 131$ m/s, we get in the last section

$$P = 1.44 \times 10^8 \times (5 \times 10^3 - \frac{131}{2}) = 7.105 \times 10^{11}.$$

Assuming PF = 0.7; efficiency $\eta = 0.6$ and 12 phases per barrel, we need switches with a handling capacity of $\frac{7.105 \times 10^{11}}{6 \times 12 \times 0.7 \times 0.6} = 2.35 \times 10^{10}$ VA.

Such switches are commercially available. Now we calculate the voltage and current:

$$F_{ave} = \frac{F_m}{\sqrt{\Gamma^2 - 1}} ln\,(\Gamma + \sqrt{\Gamma^2 - 1}) = \frac{F_m}{6.76} ln\,(6.84 + 6.76) = 0.386\, F_m$$

$$F_m = \frac{F_{ave}}{0.386} = 3.21 \times 10^8 \text{ N}.$$

The average force density is then:

$$< f_m > = \frac{F_m/6}{2\pi r_b^o \times l_s} = \frac{3.21 \times 10^8/6}{2\pi \times 0.192 \times 0.72} = 6.16 \times 10^7 \text{ N/m}^2$$

$$K_b = 2\, e^{\beta g} \sqrt{\frac{< f_m >}{\mu_o}} = 2 \times e^{0.48} \sqrt{\frac{6.16 \times 10^7}{4\pi \times 10^{-7}}} = 2.26 \times 10^7 \text{ A/m}$$

Assuming that the width of the coil is $w_c = \frac{0.36}{12} = 0.03$ m

$$NI = 0.03 \times 2.26 \times 10^7 = 6.78 \times 10^5 \text{ AT}$$

$$B_1 = \frac{1}{2}\mu_o K_b = \frac{1}{2} 4\pi \times 10^{-7} \times 2.26 \times 10^7 = 14.2\,\mathrm{T}\,.$$

In the last section we have:

$$E = v_s B = 5.05 \times 10^3 \times 14.2 = 71.7\,\mathrm{kV/m}$$

$$\frac{V}{N} = 2\pi \times r_b^{ave} \times E = 2\pi(0.192 - 0.02) \times 71.7 \times 10^3 = 77.48\,\mathrm{kV}$$

This voltage is a little on the high side but is acceptable.

APPENDIX 2

Preliminary Design for Inclined ETO Launcher

Specifications: muzzle velocity: $v_m = 5 \times 10^3$ m/s; acceleration $= 1.39 \times 10^4$ m/s

projectile weight: $w_{pr} = 2{,}000$ kg.; armature fraction: $\frac{1}{\nu} = \frac{2}{3}$

The length of the barrels is: $l_b = \frac{1}{2}\frac{v_m^2}{a} = \frac{1}{2}\frac{2.5 \times 10^6}{1.39 \times 10^4} = 900$ m

We assume a pole pitch: $\tau = 2$ m

We choose a cluster of 4 barrels, so that we have available for each sleeve a weight $w_s = \frac{1}{\nu}\frac{w_{pr}}{4} = \frac{2}{3}\frac{2000}{4} = 333$ kg. We assume a sleeve length $l_s = 2\tau = 4$ m and a thickness $a_s = 2$ cm, so that the average radius is

$$r_s^{ave} = \frac{w_s}{\xi_s \times 2\pi \times a_s \times l_s} = \frac{333}{2.7 \times 10^3 \times 2\pi \times 2 \times 10^{-2} \times 4} = 0.245 \text{ m.}$$

The inside radius is then: $r_s^i = r_s^{ave} - \frac{a_s}{2} = 0.245 - \frac{0.02}{2} = 0.235\, m.$

We assume an air-gap length $g_a = 0.025$ m, so that the outside radius of the barrel is $r_b^0 = r_s^i - g_a = 0.235 - 0.025 = 0.21$ m. We assume that the thickness of the barrel coils is $a_b = 0.04$ m. The effective air gap is then:

$$g = \frac{2+4}{2} + 2.5 = 5.5 \text{ cm} \quad \beta g = \frac{\pi}{2} \times 5.5 \times 10^{-2} = 0.086; \; coth\, \beta g = 11.65$$

$$s_c v_s = \frac{1 + coth\, \beta g}{a_s\, \gamma_{400}\, \mu_o} = \frac{1 + 11.65}{2 \times 10^{-2} \times 1.338 \times 4\pi} = 37.61 \text{ m/s.}$$ We then have

$$\theta/\Gamma = \frac{\nu \xi_s\, v_m\, s_c\, v_s}{c} = \frac{1.5 \times 2.7 \times 10^3 \times .5 \times 10^3 \times 37.61}{2.68 \times 10^6} = 284\,.$$

Let $\theta = 500$K, so that $\Gamma = 1.76$ and

$$n = \frac{v_m}{2\, s_c\, v_s \sqrt{\Gamma^2 - 1}} = \frac{5 \times 10^3}{2 \times 37.61 \times \sqrt{1.76^2 - 1}} = 45.9 \sim 46\,.$$

The kinetic energy is $E_{kin} = \frac{1}{2} w_{pr} v_m^2 = \frac{1}{2} \times 2000 \times 5^2 \times 10^6 = 2.5 \times 10^{10}$ J.

The average force is $F_{ave} = \frac{E_{kin}}{l_b} = \frac{2.5 \times 10^{10}}{900} = 2.77 \times 10^7$ N.

The increment of kinetic energy in the last section is

$$\Delta E_{kin} = Pt = P\frac{\Delta v}{a} = \frac{1}{2}(v_f^2 - v_i^2) = \frac{1}{2} m\Delta v\,(2v_f - \Delta v) = ma(v_f - \frac{\Delta v}{2}).$$

Assuming Δv = const = $\frac{v_m}{n} = \frac{5 \times 10^3}{46} = 108.7$ m/s, we get in the last section

$$P = 2.77 \times 10^7 \times (5 \times 10^3 - \frac{108.7}{2}) = 1.367 \times 10^{11}.$$

Assuming PF = 0.7; η = 0.6 and 12 phases per barrel, we need switches with a handling capacity of $\frac{1.367 \times 10^{11}}{4 \times 12 \times 0.7 \times 0.6} = 6.78 \times 10^9$ VA.

Such switches are commercially available. Now we calculate the voltage and current:

$$F_{ave} = \frac{F_m}{\sqrt{\Gamma^2 - 1}} ln\,(\Gamma + \sqrt{\Gamma^2 - 1}) = \frac{F_m}{1.448} ln\,(1.76 + 1.448) = 0.805\,F_m$$

$$F_m = \frac{F_{ave}}{0.805} = 3.44 \times 10^7 \text{ N}$$

$$< f_m > = \frac{F_m/6}{2\pi r_b^o \times l_s} = \frac{3.44 \times 10^7}{2\pi \times 0.21 \times 4} = 6.5 \times 10^6 \text{ N/m}^2$$

$$K_b = 2\,e^{\beta g}\sqrt{\frac{< f_m >}{\mu_o}} = 2 \times 1.09\sqrt{\frac{6.5 \times 10^6}{4\pi \times 10^{-7}}} = 4.96 \times 10^6 \text{ A/m}$$

Assuming that the width of the coil is $w_c = \frac{2}{12} = 0.167$

$$NI = 0.167 \times 4.96 \times 10^6 = 0.826 \times 10^6 \text{ AT}$$

$$B_1 = \frac{1}{2}\mu_o K_b = \frac{1}{2} 4\pi \times 10^{-7} \times 4.96 \times 10^6 = 3.116 \text{ T}.$$

In the last section we have:

$$E = v_s B = 5.05 \times 10^3 \times 3.116 = 15.73 \text{ kV/m}$$

$$\frac{V}{N} = 2\pi \times r_b^{ave} \times E = 2\pi \times 0.19 \times 15.73 = 18.78 \text{ kV}$$

A quite acceptable voltage.

Session 17 -- Applications of Superconductivity

Chairman: Justin Schwartz
National High Magnetic Field Laboratory (NHMFL)

A 2 TESLA FULL SCALE HIGH PERFORMANCE PERIODIC PERMANENT MAGNET MODEL FOR ATTRACTIVE (228KN) AND REPULSIVE MAGLEV

Z. J. J. Stekly, C. Gardner, P. Domigan, J. Baker,
M. Hass, C. McDonald, C. Wu, R. A. Farrell
Intermagnetics General Corporation

Two 214.5 cm. long high performance periodic (26 cm period) permanent magnet half-assemblies were designed and constructed for use as a wiggler using Nd-B-Fe and vanadium permendur as hard and soft magnetic materials by Field Effects, a division of Intermagnetics General Corporation. Placing these assemblies in a supporting structure with a 2.1 cm pole to pole separation resulted in a periodic field with a maximum value of 2.04 T. This is believed to be the highest field ever achieved by this type of device.

The attractive force between the two 602 kg magnet assemblies is 228 kN, providing enough force for suspension of a 45,500 kg vehicle. If used in an attractive maglev system with an appropriate flat iron rail, one assembly will generate the same force with a gap of 1.05 cm leading to a lift to weight ratio of 38.6, not including the vehicle attachment structure. This permanent magnet compares well with superconducting systems which have lift to weight ratios in the range of 5 to 10.

This paper describes the magnet assemblies and their measured magnetic performance. The measured magnetic field and resulting attractive magnetic force have a negative spring characteristic. Appropriate control coils are necessary to provide stable operation. The estimated performance of the assemblies in a stable repulsive mode, with eddy currents in a conducting guideway, is also discussed.

The development of this concept and overall configuration was internally funded by Intermagnetics. The design and construction of the permanent magnet assemblies was performed under a U.S. Department of Energy subcontract from the Stanford Synchrotron Radiation Laboratory (Stanford University Contract No. 7144.)

INTRODUCTION

Commercial development of magnetic suspension and propulsion systems in Japan[1] and Europe[2] have utilized resistive coils in the vehicle as part of a magnetic circuit that

includes the guideway. These systems have a relatively small gap of the order of 1 cm or less. The limitation on resistive coils is generally the power dissipated in the coils.

Superconducting coils, with no resistive losses, have been selected for the new high speed Yamanashi test line now under construction in Japan[3]. These coils will operate at a gap of 11 cm. The only resistive losses in superconducting systems are in the guideway. In general, the magnetic suspension has little damping by itself and power must be supplied to achieve acceptable dynamics.

Permanent magnets may be used to supply the steady component of force thereby reducing resistive coil system power levels. Power to correct for negative spring constants in attractive systems as well as other dynamic requirements will still be required.

The permanent magnet wiggler periodic arrays built and described in this paper have large force capability and can be tailored in length by adding or subtracting poles. They can also be placed in multiple parallel arrays to achieve varying width. Thus, the design provides flexibility which may be utilized for maglev applications. The significant features of the magnetic arrays are discussed in this paper, followed by a review of their potential for use as maglev system elements.

WIGGLER MAGNET PROGRAM SUMMARY

A unique 2.04 T hybrid wiggler was designed and fabricated for Beamline 9 of the Stanford Synchrotron Radiation Laboratory (SSRL) by Field Effects, a division of Intermagnetics General Corporation[4]. The wiggler, a periodic array composed of permanent magnets and magnetic poles, provides a high strength alternating magnetic field that bends an electron beam to generate synchrotron radiation. The 16 milliradian fan of high energy x-rays produced is utilized for research in structural molecular biology and other scientific disciplines. The basic SSRL performance specifications [5] include a magnetic field at minimum gap of at least 1.9 T. The 2.04 T achieved exceeded this specification.

The magnetic structure makes use of Neodymium-Iron-Boron (Nd-Fe-B) permanent magnet materials and vanadium permendur for the pole pieces in a compact pole design. This configuration uses considerably less magnet pole material than conventional hybrid or wedge pole designs [6,7,8].

The large magnetic forces at minimum gap, and the need to operate reproducibly at lower magnetic fields and lower forces with larger gaps, required an overall mechanical design that was suitably rigid with provisions for accurate, reproducible gap adjustment. While this system was built for other purposes, it is a full-scale permanent magnet model

of a type which may be used for magnetic levitation. That is, its measured performance can be used as a basis for permanent magnet suspensions for other applications.

Wiggler Configuration And Operation

A schematic of the overall configuration of the wiggler is contained in Figure 1. Dimensions and weights are given in Table I. Figure 2 shows a photo of the completed assembly. The Wiggler consists of upper and lower permanent magnet arrays mounted on backing beams. The backing beams are connected by cross beams to four precision rotating ball screws which provide symmetrical parallel vertical motion to the upper and lower moveable assemblies (magnets, backing beams and cross beams).

The large magnetic forces at minimum gap are transmitted through the four rotating ball screws which are chain driven by a single stepper motor through gear reducers. This includes a brake assembly to prevent unplanned motion. The gap position is determined by an encoder mounted on one of the ball screws which is calibrated over the full range of gaps using laser measurement techniques.

The overall assembly is designed to provide the large magnetic forces at minimum gap (over 228 kN) with minimal deflections, support gravity and seismic loads, and allow accurate installation of the wiggler onto the electron beam.

A remotely-controllable drive system opens and closes the wiggler. The drive system consists of a motor, gearbox and brake, and is capable of continuous or intermittent scanning using a computer control. The drive system is capable of movement through the full gap range of 2.1 to 21 cm in 55 seconds.

A laser interferometer system was used to initially measure and calibrate gap as a function of encoder count. This system has a resolution of 10 nanometers. The gap is varied from approximately maximum to minimum in 20 encoder count steps. This establishes the calibration and reproducibility of position versus encoder count. The repeatability error over the full range of gaps was determined to be $\pm$ 24 μm and $\pm$ 31 μm in two sets of measurements. Most of this variation is due to a load reversal at one location. If this is neglected, the repeatability is $\pm$ 15 μm.

Wiggler Magnetic Characteristics

The wiggler consists of an upper and lower array of 15 physically identical full strength pole assemblies each. Each pole assembly is one half of a period length. There are half strength integrated field lower strength poles to provide appropriate transitions along the beam path at both ends.

For each of the arrays, the pole assemblies are arranged in alternating polarity on a stainless steel backing beam to support the large magnetic forces, as shown in Figure 3. The polarity of the upper and lower magnetic pole arrays are such that their magnetic fields add. The upper and lower pole face arrays must be parallel and precisely positioned in the directions parallel and perpendicular to the beam.

The pole design and assembly process allows measurement and mechanical adjustment of individual poles prior to assembly. Further magnetic measurement and adjustment of individual poles in the assembled array is also possible. Using this approach three adjacent poles in the end regions, one of half and two of full strength were adjusted. Figure 4a gives the values of magnetic field after correction as a function of position along the beam. Figure 4b provides the details for a single pole. These corrections resulted in a final on-axis pole to pole peak field variation at minimum gap of 0.48%. The principal magnetic parameters are listed in Table II.

The peak on-axis magnetic field is 2.04 T at the minimum gap of 2.1 cm. We believe this to be the highest reported magnetic field for a permanent magnet wiggler at this time.

Figure 5 compares predicted and measured magnetic field as a function of gap, indicating excellent agreement. The field estimates were made using 2D finite element software [9], 3D analytical techniques, and a 1/3-scale, 1/2-period model which was fabricated to confirm field characteristics. Figure 6 illustrates the rapid increase in attractive force between the upper and lower assemblies as the gap decreases and clearly demonstrates the negative spring characteristic. This figure utilizes calculated force which was subsequently confirmed by measured magnetic field versus gap data. Figure 6 can be converted to a lift-to-weight ratio by dividing by the appropriate magnetic structure weights.

Maglev Magnet Analysis

Although the previously described wiggler system was not intended for attractive or repulsive suspension, the adjustable gap feature allows magnetic field and magnetic force

to be varied. The as-built system is configured in an attractive mode, where the polarity of the upper poles are opposite those of the facing lower pole pieces and both add to the magnetic field in the central gap as illustrated in Figure 3.

A repulsive force could be achieved with the wiggler by shifting the assembled arrays horizontally one half period so that the polarity in the pole pieces on both sides of the gap is the same. Alternately, the polarity of one array can be switched mechanically, again resulting in like polarity poles aligned to each other across the gap, as indicated in Figure 7.

For the purposes of maglev analysis, the wiggler minimum achievable gap (2.1 cm) and magnet structure assembly weight (602 kg) is utilized for levitation calculations. This represents maximum lift to weight performance. Wiggler field measurements were made in the attractive mode configuration using Intermagnetics' - built computer-positioned Hall probes or coils. Repulsive mode performance was computed using 2D finite element magnetic field calculations.

Magnetic fields were determined for various gaps, using two boundary conditions:
1. Magnetic field perpendicular to the central plane - attractive condition.
2. Magnet field parallel to the axis on the central plane - repulsive condition.

Physically, the first boundary condition represent either a single array with a magnetic guideway, Figure 8, or two permanent magnet arrays in a attractive mode at twice the pole to magnetic guideway gap, Figure 3. The magnetic field estimates for the magnetic guideway case would be valid at any practical speed provided the guideway was appropriately designed to minimize eddy currents. Permanent magnets in the guideway generally would not work well at other than zero speed because of the periodic character of the arrays. The exception to this is when the periodic array is placed transverse to the direction of motion.

The second boundary condition represents either a single array operating above a highly conducting guideway, Figure 9, or two opposing permanent magnet arrays, Figure 7, at twice the pole to guideway distance. Because the repelling eddy currents move with the array, it represents a practical maglev configuration. As in the attractive case, with permanent magnets in the guideway, the guideway magnets must be placed transverse to the direction of motion because of the periodicity of the array.

It is possible to design a nonperiodic array (in the direction of motion) to operate in either attractive or repulsive modes by using an appropriate non-periodic permanent magnet guideway.

Table III summarizes the maximum performance at minimum gap conditions for each of the operating conditions of the two permanent magnet arrays discussed above. Maximum performance as previously discussed corresponds to minimum gap between the two arrays. Alternatively, it assumes infinite permeability or conductivity, as appropriate for the guideway.

The two attractive conditions indicated in Table III result in lift-to-weight ratios approaching 40 in both cases. The table clearly points to the fact that an "energized" permanent magnet guideway in an attractive mode has twice the operating gap of the "passive" magnetic guideway. We can also conclude that for equal gaps, permanent magnets in the guideway will result in about twice the lift-to-weight ratio.

The two repulsive modes each have a lift-to-weight ratio of just below 6, compared with about 40 for the attractive modes. The main reason for this is the somewhat less than optimum design for repulsion. Figure 10 illustrates the calculated magnetic field in the gap. For the attractive case (solid curve), the magnetic field is over 2 T at the center of the pole in the region of the vanadium permendur magnetic pole. For the repulsive case (dotted curve), the field under the soft magnetic pole is very small, and rises to a maximum of less than 1 T in the region away from the pole.

Figure 11 compares the calculated, normalized performance of the attractive and repulsive system (all the forces are divided by the attractive force at minimum gap). Although it is only in the region below 15 cm gap that the repulsive force differs significantly from the attractive force, this is not of much practical use because the forces at this point are of the order of 0.01 times the maximum value. If the attractive case at a minimum gap to 1.0 cm is considered, i.e., a lift to weight ratio approaching 40, then a relative force of 0.1 represents a lift to weight ratio of 4. If we take this as a lower value, comparable to a superconducting system, a permanet magnet attractive system could operate at gaps of about 9 cm. The corresponding gap for a repulsive system is approximately 5 cm.

With regard to implementing the approach of magnets in the guideway, it is not necessary to have the highest performance, expensive materials in the guideway. The US Bureau of Mines has successfully demonstrated a system with lower performance and cost ferrite permanent magnets in the guideway.[10]

Maglev System Optimization

Vehicles considered for magnetic suspension range from about 45,500 kg at 300 mi/hr for high speed ground transportation[11] to 230,000 kg to 360,000 kg at 600 mi/hr for magnetically-assisted launch space vehicles[12]. The two permanent magnet arrays built for the wiggler are capable of lifting nearly all anticipated high speed ground vehicles, and 13 to 20% of the magnetically-assisted launch space vehicle at the minimum gap.

The availability of essentially full size individual permanent magnet components with high lift-to-weight capability is a significant milestone for the demonstration of full scale permanent magnet suspension systems. However, optimization of system

performance and costs must be carried out that includes adequate consideration of the guideway and system dynamics over the required range of velocities. For stability, the suspension must have at least four locations to support the vehicle on the guideway. These supports must be able to handle 25% of the vehicle weight plus dynamic loads.

An alternate is a system having eight suspension locations that handle 12.5% of the total load. The cross section for this guideway is considerably smaller. The optimization carried out under the National Maglev Initiative for a high speed 44,000 kg transportation vehicle resulted in a large number of magnetic supports[13]. The lift-to-weight ratio of the superconducting levitators for the optimum system was significantly lower than that required with four high lift levitators.

Control coils will probably be required to varying extents depending on the system. The repulsive systems are stable vertically, however, control may be required to provide adequate ride quality for passengers, or to limit the maximum dynamic loads in other instances. Attractive systems have a negative spring constant and control coils are required to counter this effect. In addition the control system, as well as other system elements that influence dynamics, must provide for acceptable overall system dynamic performance.

Magnetic systems using permanent or superconducting magnets have essentially no loss. As a result, these systems have no damping. This must be taken account of in overall system design.

SUMMARY

The design and construction of a unique wiggler magnet for the Stanford Synchrotron Radiation Laboratory has been described. All critical design parameters were met or exceeded. The high magnetic forces achieved in this system demonstrate that permanent magnets have the potential for high performance in attractive suspension systems.

The particular wiggler configuration built works well for attractive systems, and compares well with superconducting systems. However, optimization is needed for repulsive mode operation. A periodic magnet array can also serve as part of a linear motor propulsion element. A non periodic array in the direction of motion may be beneficial if permanent magnets are part of the guideway.

The feasibility of utilizing permanent magnets for maglev application has been demonstrated at full scale. The potential advantages for maglev are reduced power consumption, relative to resistive systems, and no cryogenic requirements, relative to superconducting systems.

ACKNOWLEDGMENTS

The assistance of Ms. Denise Silva and Ms. Julia Saia in preparing this manuscript is gratefully acknowledged.

REFERENCES

1. HSST Magnetically Levitated Train, HSST Development Corp., Tokyo, Mar., 1995.
2. Maglev Transportation Technology, Thyssen Henschel, Munich, June 1994
3. Tanaka, H., Q. Rep. Railway Technical Research Institute, 1992, 33 (3) 160.
4. Z.J.J. Stekly, et. al., *Design and Performance of a 2T Permanent Magnet Wiggler for the Stanford Synchrotron Radiation Laboratory*, presented at Synchrotron Radiation Instrumentation October, 1995, Argonne, IL, to be published in Review of Scientific Instruments.
5. RFP No. 7144 for a Beamline 9 Wiggler Stanford Synchrotron Radiation Lab, Stanford University, 1993
6. Halbach, Klaus, *Permanent Magnet Undulators*, Proceedings 1982 Bendor FEL Conference, Journal de Physique 44, p. 1-211, 1983E. Hoyer, Review of Scientific Instruments 66 (2) 1995, p. 1902-1903
7. U5.0 Conceptual Design Rept., Accelerator and Fusion Res. Div. Lawrence Berkeley Laboratory Publication - 5256, U of California Nov., 1989.
8. N. A. Vinokurov, Nuclear Instrum. Meth., A246 1986, p. 105
9. POISSON (Super Fish Reference Manual LA-UR-87-126 LANL Code Group MSH829, LANL, N.M.) Jan, 1987
10. K. Hanna, J. Geraghty, Bureau of Mines, Denver, CO., *"Maglev Technology for Frictionless Movement of Materials, People, and Equipment"*, Nov., 1995
11. Grumman Aerospace Corporation, *System Concept Definition of a Superconducting Maglev Electromagnetic System*, National Maglev Initiative Rept., Sept. 1992.
12. NASA Technical Interchange Meeting on Highly Reusable Space Transportation. July 25-27, 1995. Huntsville, AL.
13. Z.J.J. Stekly, E. Gregory, *"Applications for High Temperature Superconductors"*, Chapter in High Temperature Superconducting Materials Science & Technology, Editor Donglu Shi, Pergamon Press, Elsevier Science, Tarrytown, N.Y., 1995.

TABLE I

DIMENSIONS AND WEIGHTS

Approximate Dimensions

Magnetic Structure

Individual Full Strength Pole

Height	21.4 cm
Width	21.8 cm
Along Beam	13.0 cm
Overall Length	214.5 cm

Overall Dimensions

Height	199 cm
Width	108 cm
Along Beam	220 cm
Beam Height from floor	106.7 cm

Weights

Weight of each full strength pole	36.4 kg	(80 lbs.)
Assembled Magnetic Structure *	602 kg	(1325 lbs.)
Backing Beam*	367 kg	(806 lbs.)
Magnetic Structure with backing beam*	970 kg	(2131 lbs.)
Total System	3295 kg	(7250 lbs.)

** Weights of one assembly*
- Two required one upper and one lower

TABLE II

MAGNETIC CHARACTERISTICS

Characteristic	
Period Length (λ)	26 cm
Number of full-strength periods	7.5
Integrated field for each full-strength pole at 2.1 cm	17.816 T-cm
Length of each half-strength end pole	9.83 cm
Integrated field for each half-strength pole at 2.1 cm	8.902 T-cm
Width	21.8 cm
Total Length	214.5 cm
Minimum gap	2.100635 cm
Maximum gap	22 cm
On-axis peak field at minimum pole gap	2.0428 T
On-axis pole-to-pole peak field variation at min. gap	0.48%
Integrated field rolloff at min. gap (+/- 2.8 cm transverse offset)	3.79% Max.
On-axis peak field at maximum gap	1466 G
Relative integrated field strength of untuned end poles	50 +/- 0.33%

TABLE III

Maximum Performance Estimate for Permanent Magnet (PM) Arrays For Vehicle Application

	Weight (kg)	Force (kN)	Gap (cm)	Lift-to-weight Ratio
One PM array in vehicle Attracted to PM in guideway	602	228	2.1	38.6
Two PM arrays in vehicle Attracted to ferromagnetic guideway	1204	456	1.05	38.6
One PM array in vehicle repulsed by P.M. in guideway	602	34.5	2.1	5.85
Two PM arrays in vehicle repelled by conductive guideway	1204	69	1.05	5.85

Lift-to-weight - Force (kN)/[Weight (kg) g (m/sec^2)]

LIST OF FIGURE CAPTIONS

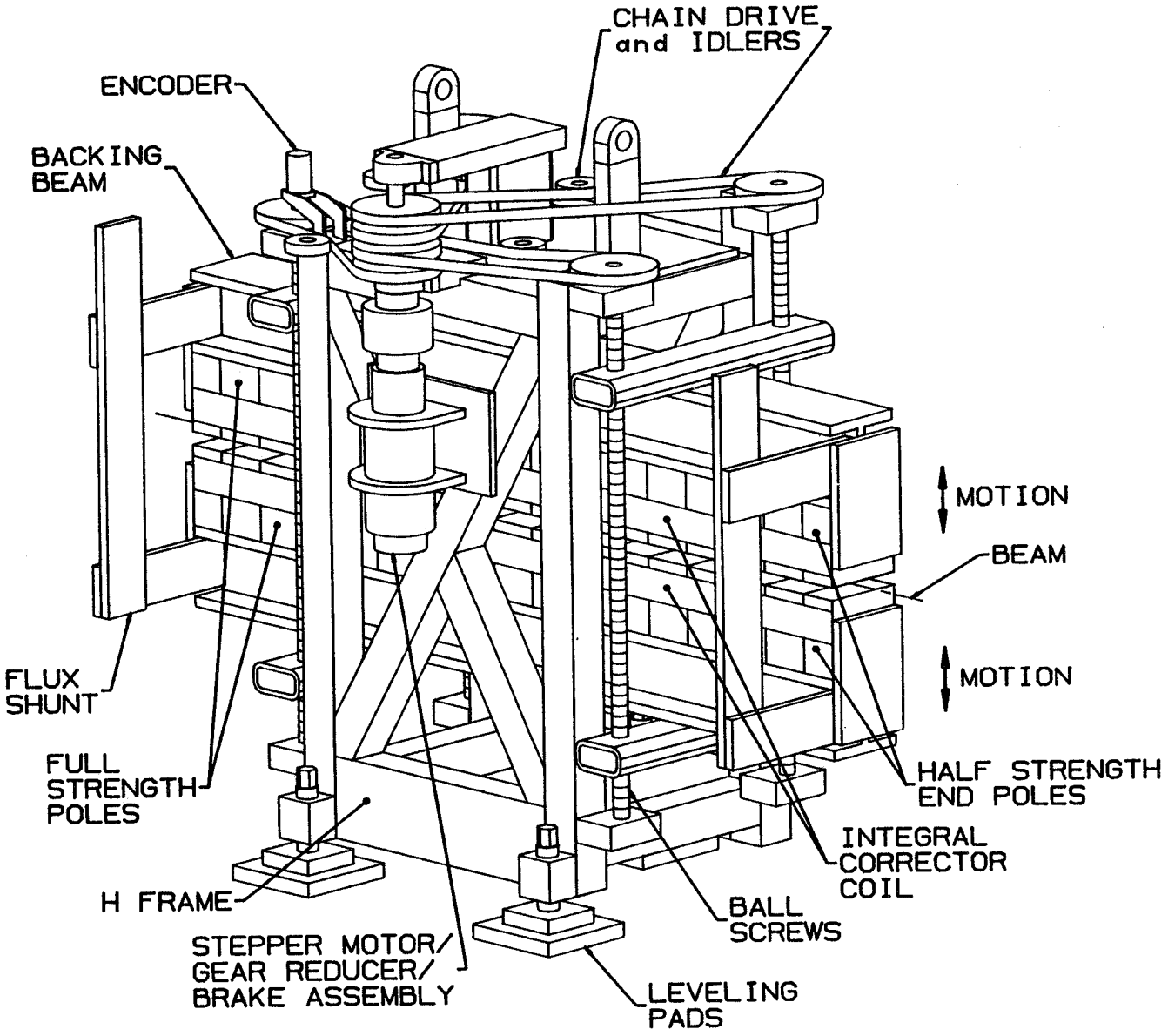

Figure 1

2.04 T SSRL Beamline 9 Wiggler Schematic

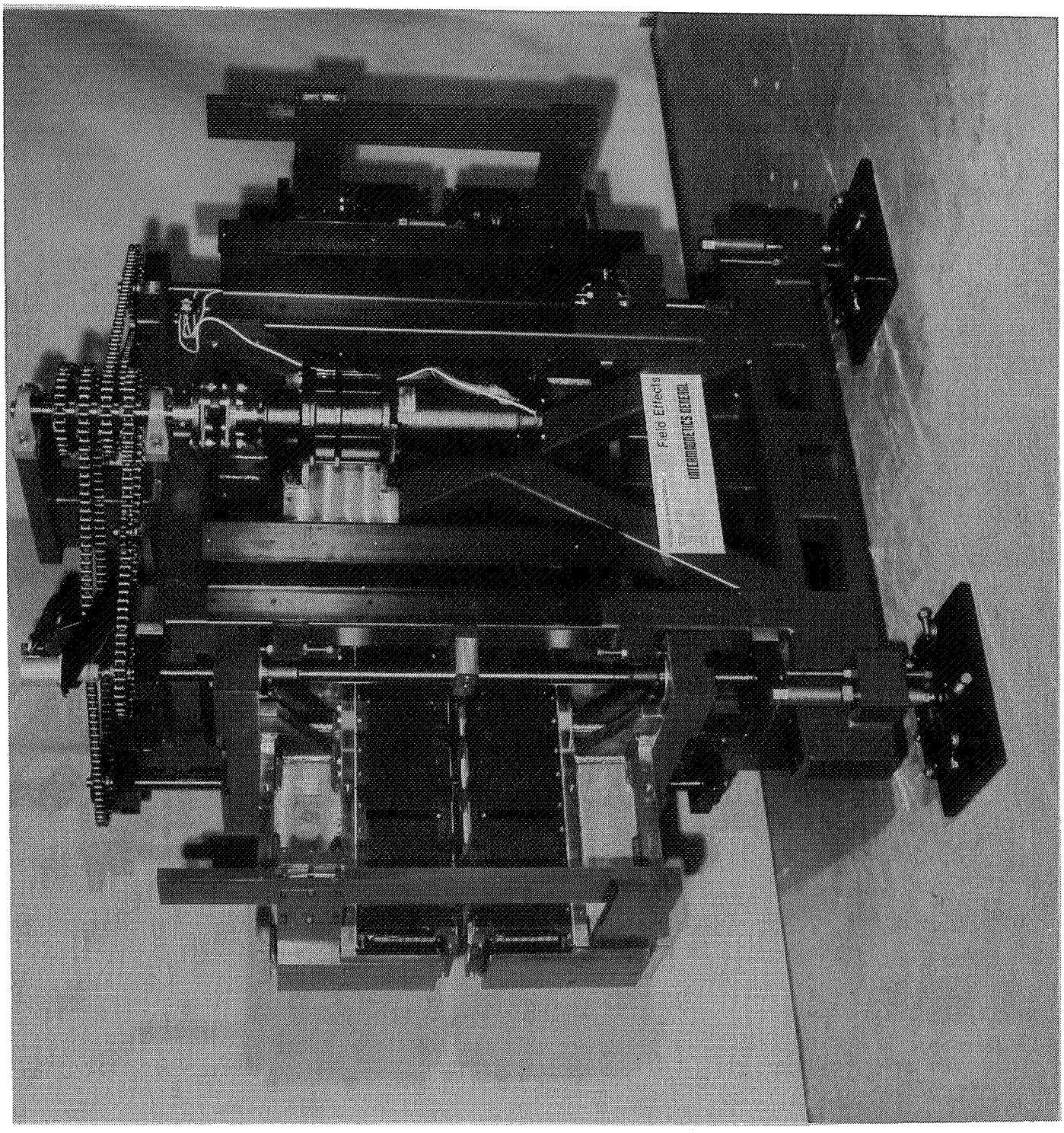

Figure 2
2.04 T Beamline 9 Wiggler

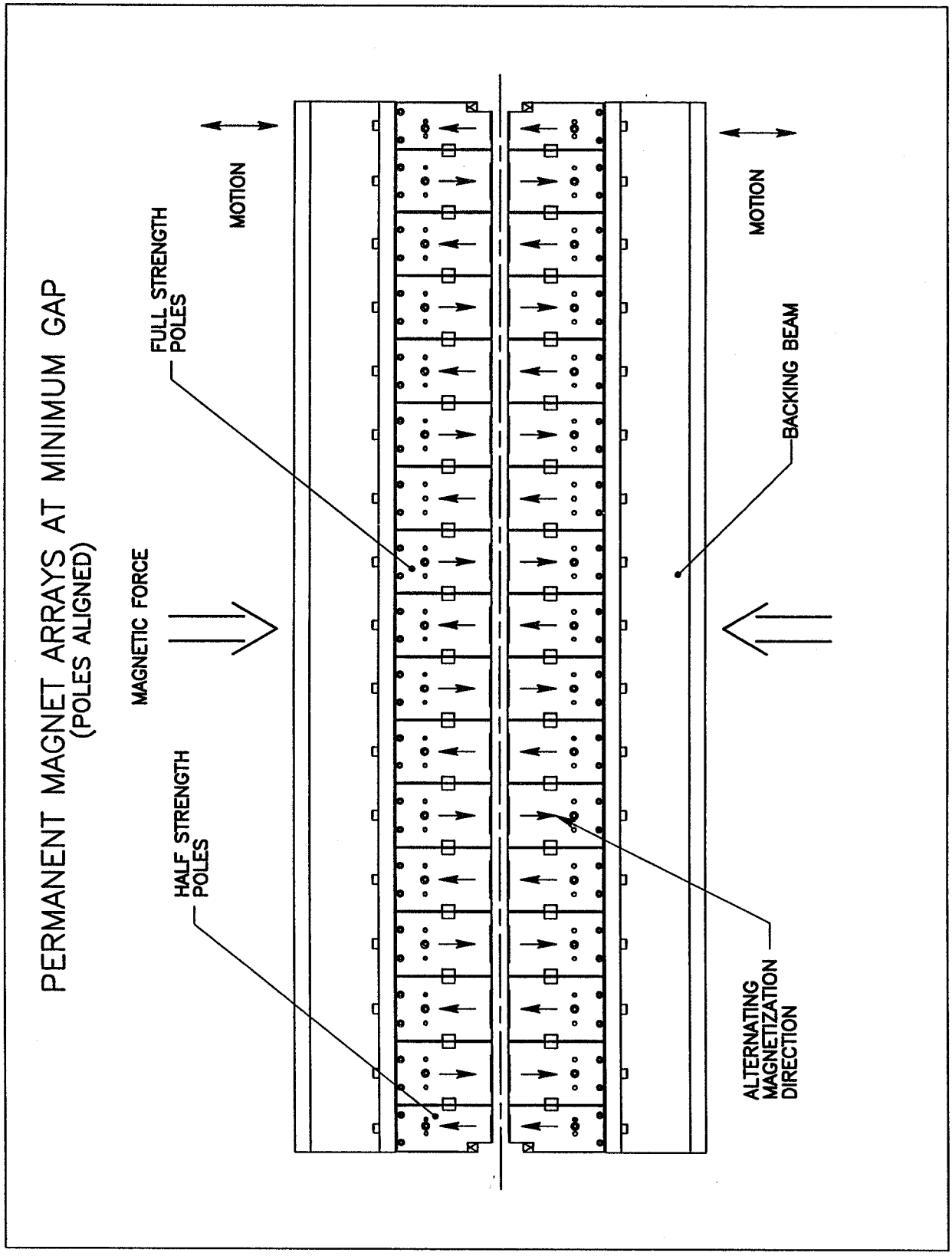

Figure 3

Permanent Magnet Arrays at Minimum Gap (Poles Aligned)

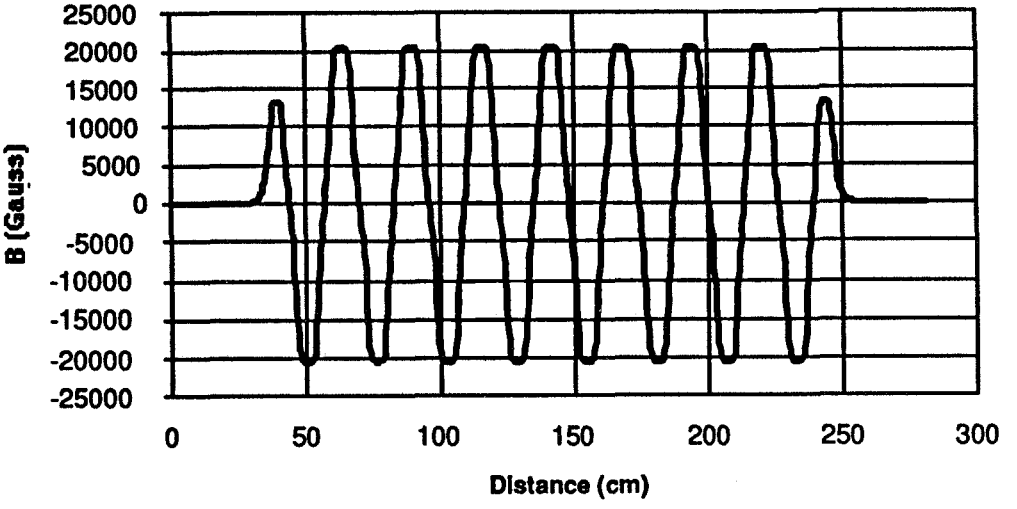

Figure 4a

Wiggler Corrected Magnetic Field Parallel to the Beam

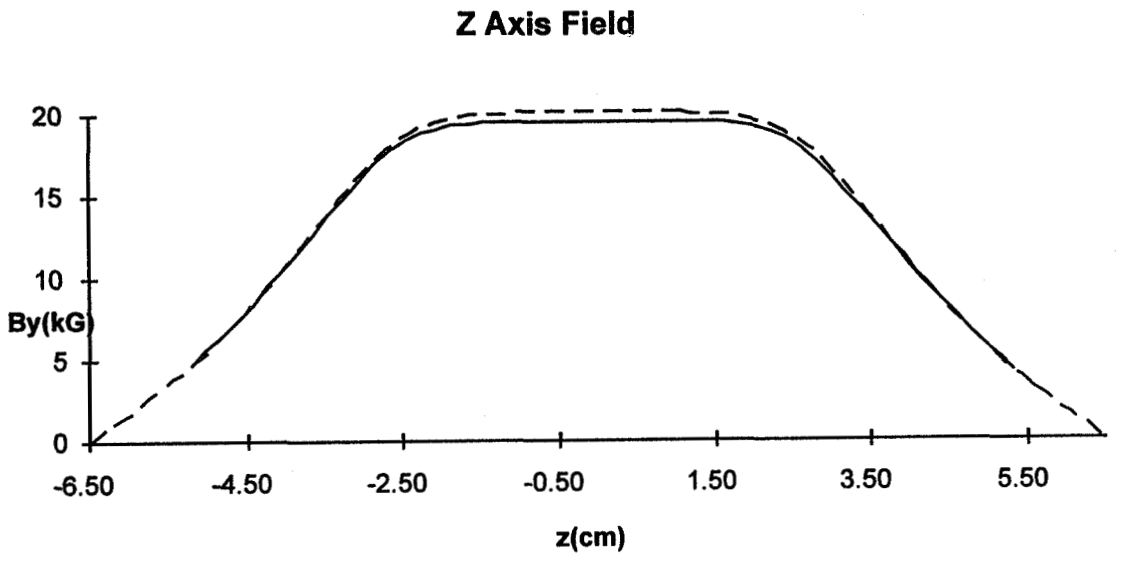

Figure 4b

Comparison of Measured (solid) to Computed (dashed) Wiggler On Axis Field for One Half Period

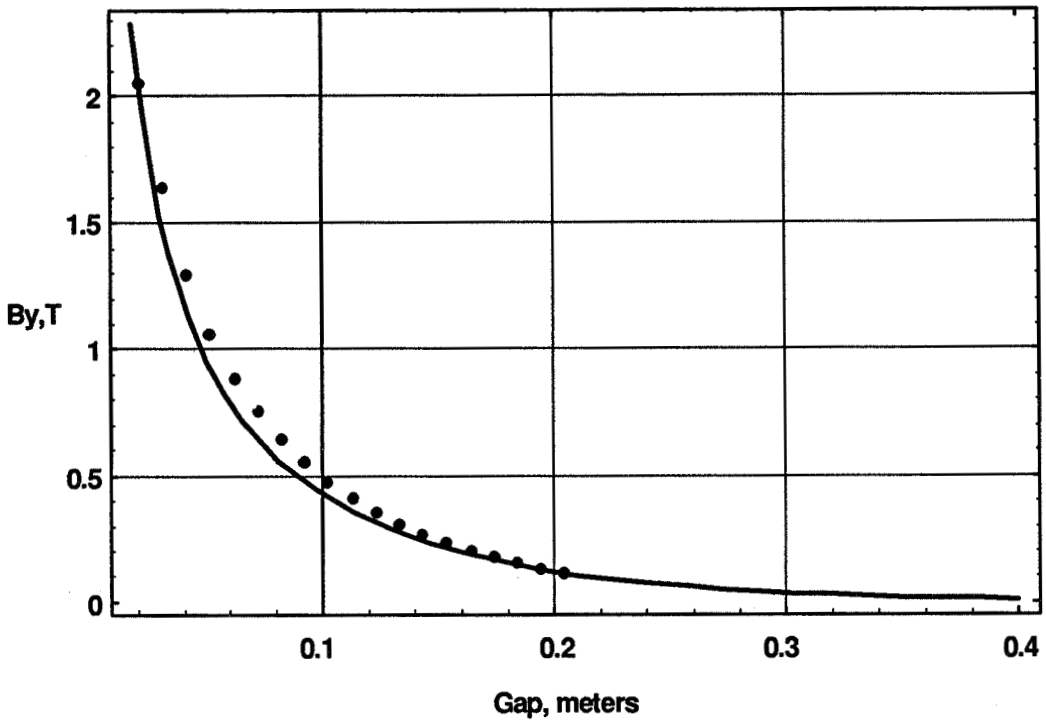

Figure 5

Comparison of Predicted (solid), to Measured (dots)
Wiggler Peak on Axis Field in the Gap

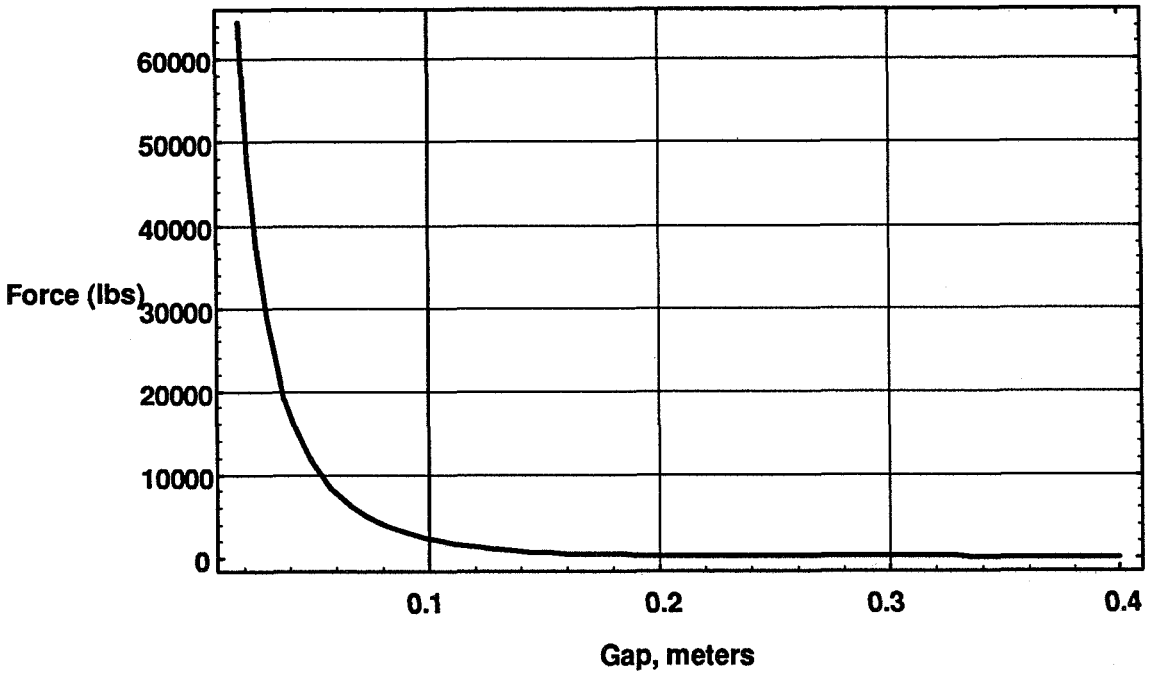

Figure 6

Predicted Wiggler Magnetic Force as a Function of Gap

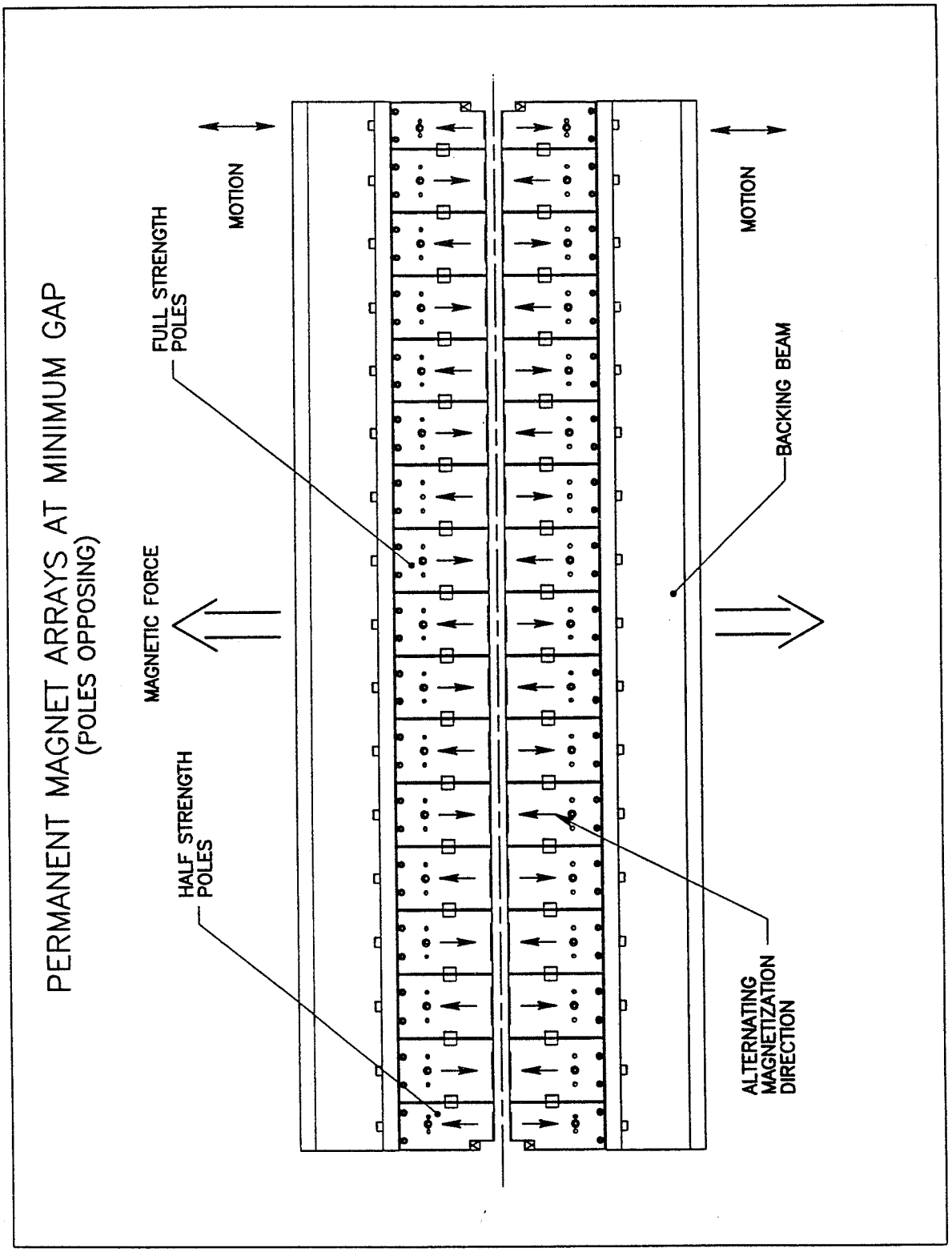

Figure 7

Permanent Magnet Arrays at Minimum Gap (Poles Opposing)

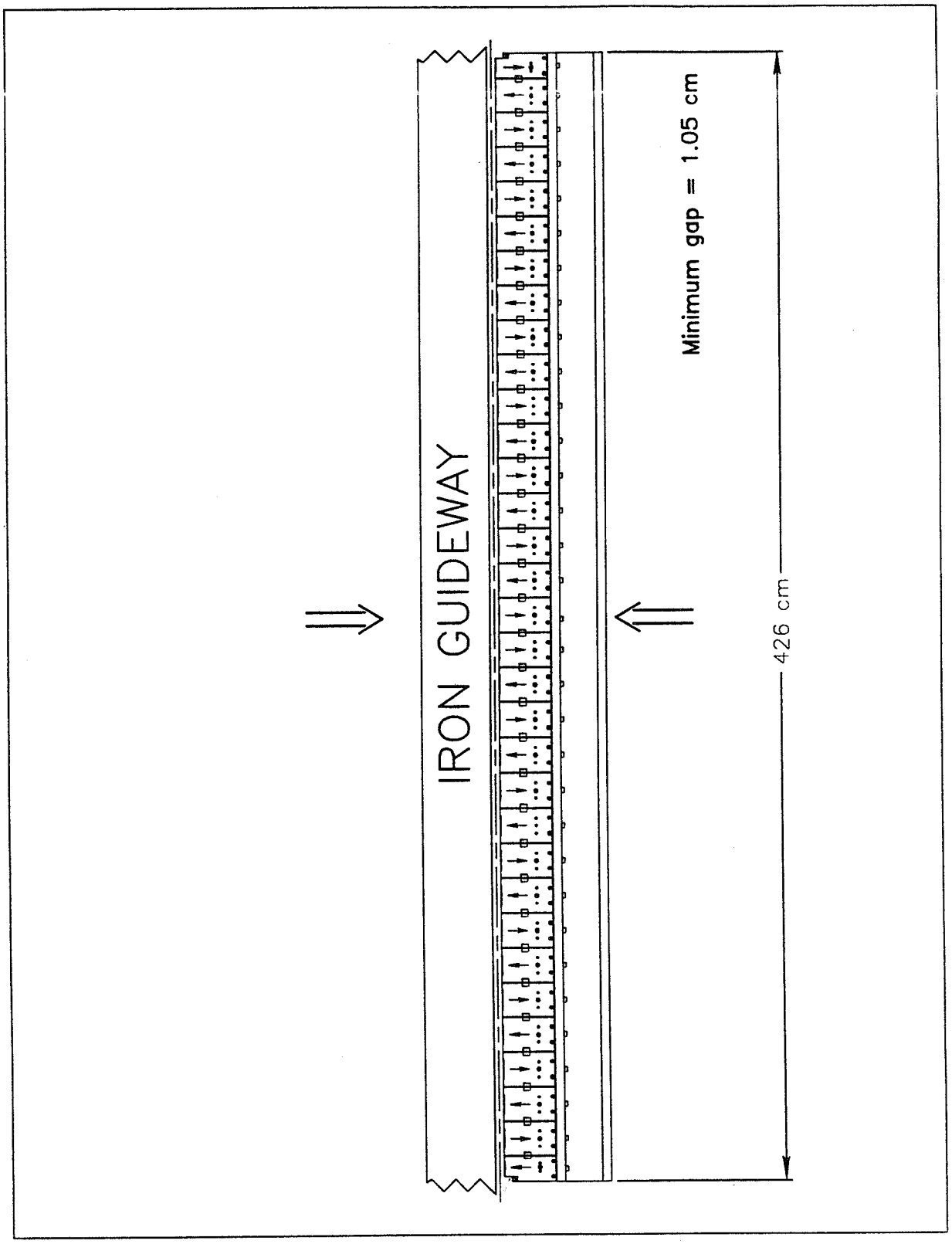

Figure 8

Permanent Magnet Arrays Attracted to Iron Guideway

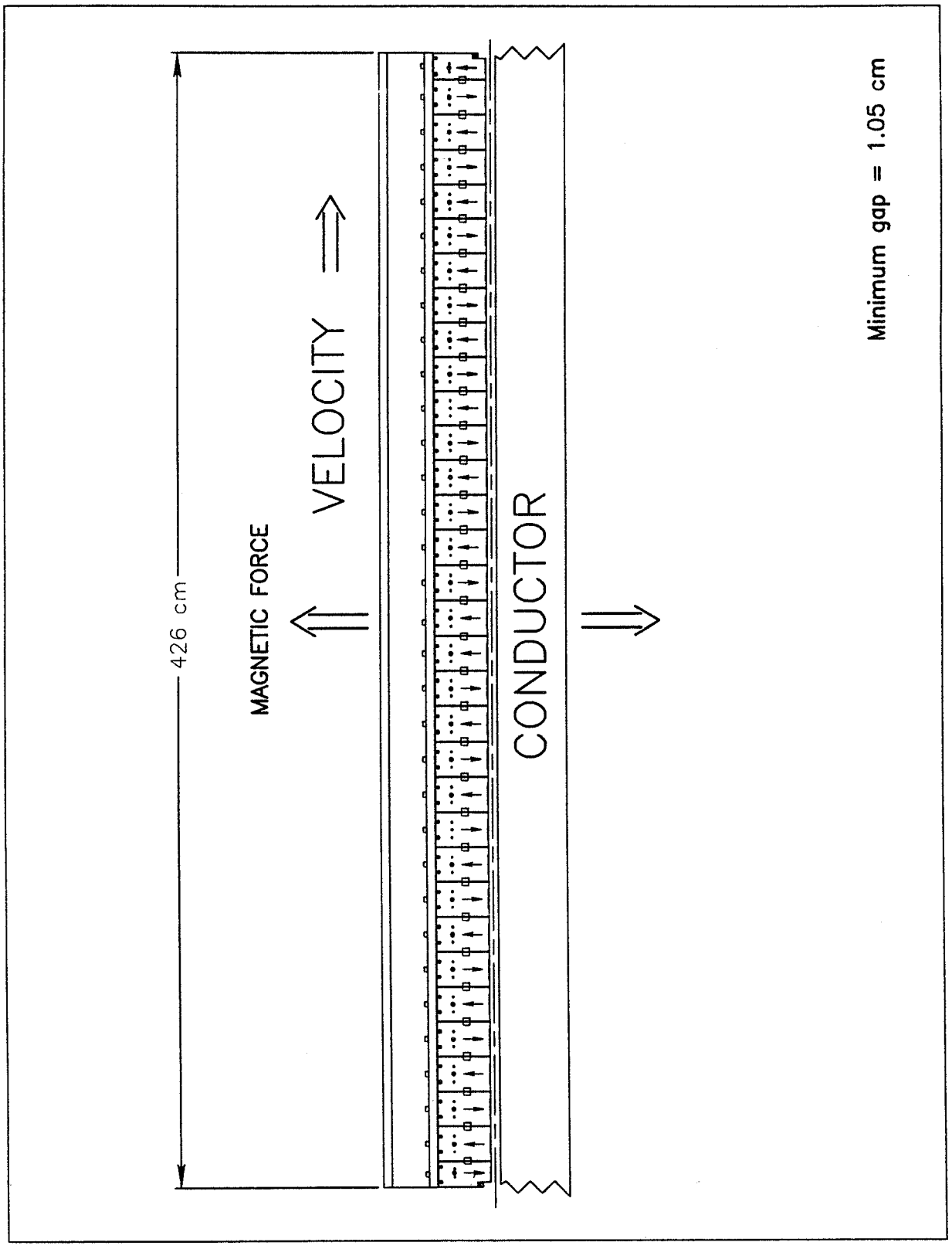

Figure 9

Permanent Magnet Arrays Repelled by Conducting Guideway

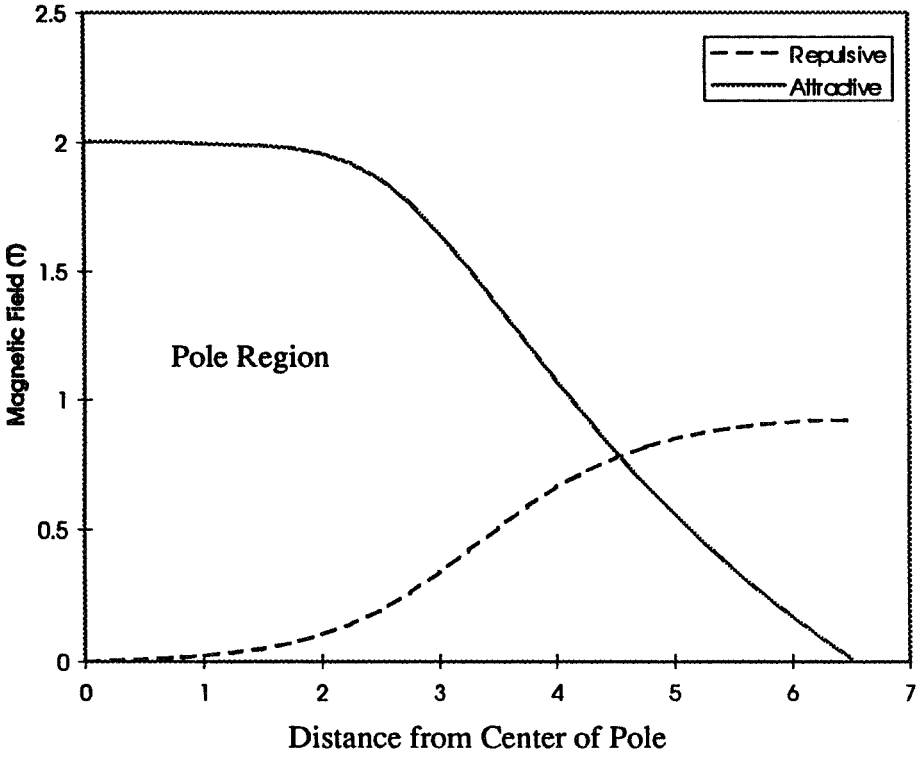

Figure 10

Magnetic Field at a Gap of 2.1 cm

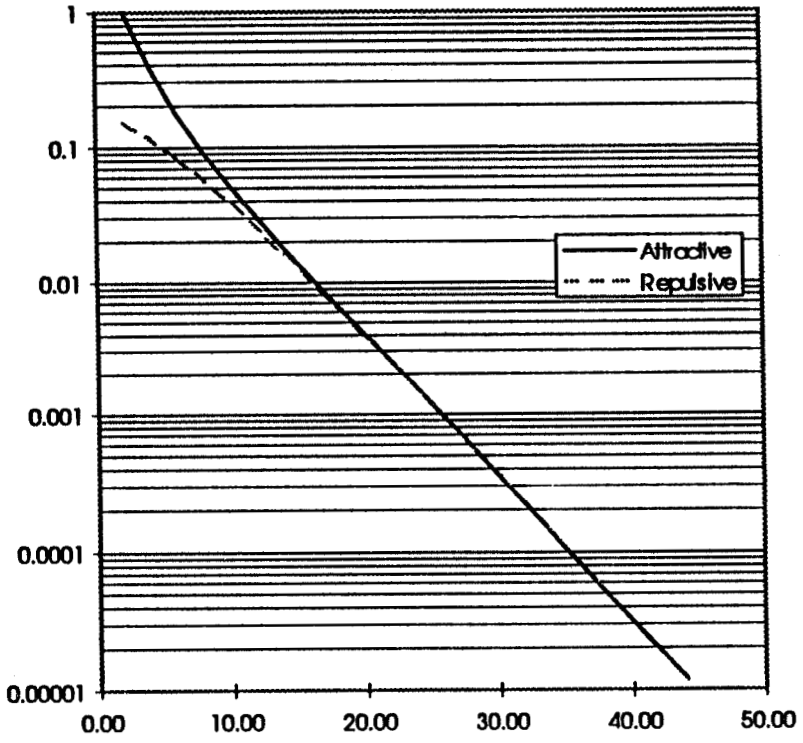

Figure 11

Relative Force as a Function of Gap for Attractive and Repulsive Magnetic Systems

FABRICATION OF LARGE DOMAIN $YBa_2Cu_3O_x$ FOR MAGNETIC SUSPENSION APPLICATIONS

S. Sengupta, J. Corpus, J. R. Gaines, Jr.
Superconductive Components, Inc.
Columbus, OH

V. R. Todt, X. Zhang, and D. J. Miller
Materials Science Division
Argonne National Laboratory
Argonne, IL

ABSTRACT

Large domain $YBa_2Cu_3O_x$ levitators have been fabricated using a seeded melt processing technique. Depending upon the seed, either a single or five domained sample can be obtained. The grain boundaries separating each domains in the five domain levitator are found to be 90 degrees. Similar levitation forces can be observed for single and five domained samples. After thermal cycling, however, a small decrease in the levitation force of the five domain levitator was observed as a function of thermal cycles while nearly no change in force was observed in the single domain levitator. Finally it is shown that both, single and five domain YBCO, behave similarly as a function of sample thickness.

INTRODUCTION

A stable levitation or suspension of a magnet is one of the fascinating properties of a superconductor. Unlike active suspension between magnets, the suspension of a magnet by a superconductor is completely passive. A magnet can be suspended above as well as below a type II superconductor (Fig. 1 & 2). A large number of applications are envisioned utilizing this unique property. These applications include rotary motion bearings, cryopumps, cryocoolers, cryoflowmeters, energy storage devices, contactless transportation, and vibration isolators.[1]

The stable suspension of superconducting materials was first demonstrated by Arkadiev.[2,3] Although the levitation by the superconducting material was studied in

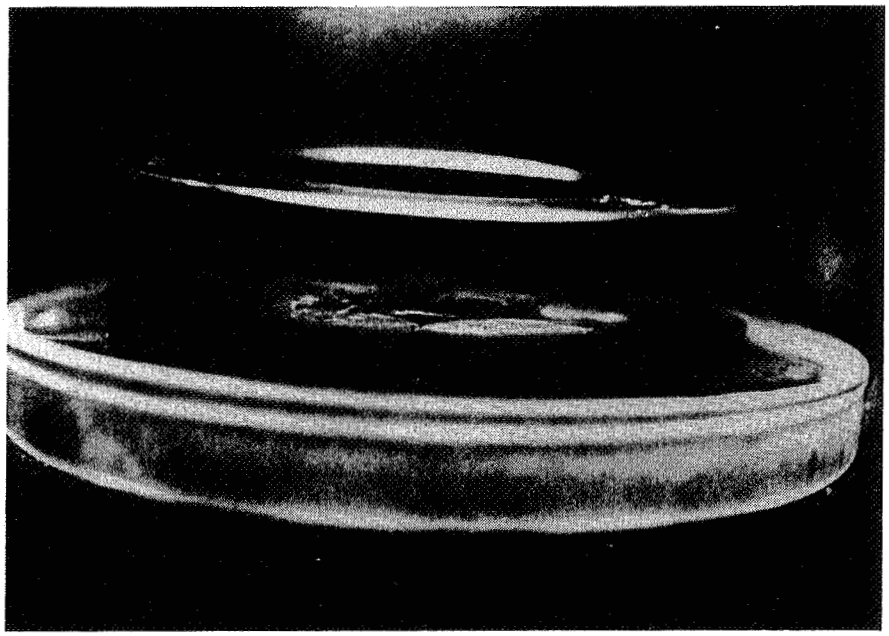

Figure 1. A ring magnet is suspended above a group of large domain levitators.

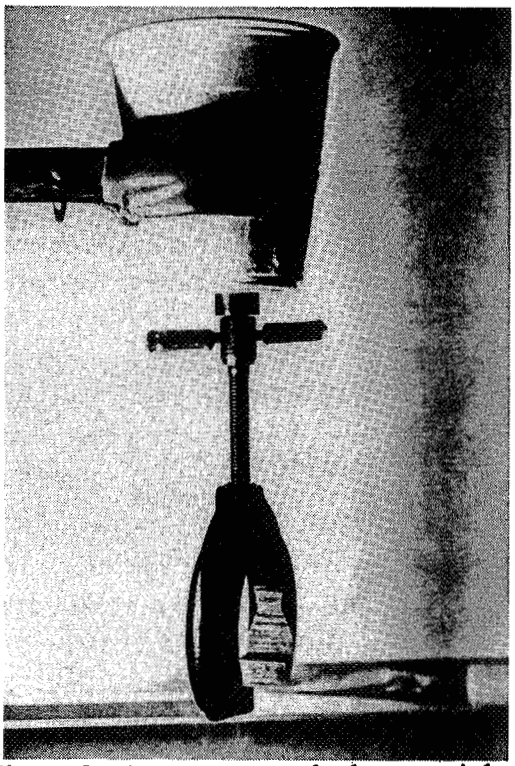

Figure 2. A magnet attached to a weight is suspended below a single large domain levitator (in cup).

1950s and 60s, the necessity of using expensive liquid helium (Temp.= 4.2 K) greatly hindered further development.[4] The discovery of a high T_c superconductor with transition temperatures above liquid nitrogen (77 K) renewed the interest in superconducting levitation.[5] Devices based on the principle of superconducting levitation are now being developed at various laboratories all over the world.[6-10] The levitation force on a magnet due to a superconductor is an integrated parameter which depends on the characteristics of the magnet as well as the superconductor. These factors include:

1. the distribution and the intensity of the magnetic field.
2. the local critical current density, J_c, of the superconductor, and
3. the characteristic length scale, d, of the induced current loop in the superconductor.

For a given magnet and for superconductors with similar dimensions, the levitation force can be enhanced by increasing J_c and/or d of the superconductor. The critical current density can be improved by introducing defects that can act as flux pinning centers, and d can be increased by increasing the size of the strongly linked regions.

The melt processing technique offers an attractive way to fabricate strongly linked $YBa_2Cu_3O_x$ (YBCO).[11-19] Moreover, defects like Y_2BaCuO_5 inclusions and other structural defects (like dislocations and stacking faults) can be incorporated during processing that can further enhance the current carrying capability in these materials.[17-19] In a typical melt processing method, YBCO is heated above its peritectic point where it melts incongruently into Y_2BaCuO_5 and a Ba- and Cu-rich liquid. The semi-solid melt is cooled slowly to obtain aligned grains of YBCO. The grains are aligned, however, only in small regions called domains. Within the domain the superconductor is mostly strongly linked. The domains are separated by large angle grain boundaries which act as weak links, thereby reducing the current carrying capability in the presence of magnetic fields (Only under some special situations like 90 degree grain boundaries, may the boundary act as strongly linked and be able to carry currents comparable to that within a domain).

In a melt processed YBCO sample the levitation force can be enhanced by increasing the domain size or by developing samples with strongly linked large angle boundaries. One way to increase the domain size is by initiating grain growth by using a seed crystal. In presence of a favorable temperature gradient the seed not only ensures a single nucleation site but also permits controlled orientation of the grains. Using the seeding technique along with a controlled temperature gradient YBCO domains as large as that of the sample size (single domain) can be fabricated. Seeding with a single crystal of MgO, Al_2O_3, $SmBa_2Cu_3O_x$ and $Nd_{1+x}Ba_{2-x}Cu_3O_y$ have been reported by various groups.[20-24] The seed can be added to the coldest point of the sample prior to heating or after an extra melting step. The addition of the seed prior to heating is preferable as it reduces the difficulty of mass production.

In this paper, fabrication of large domain levitators using a $Nd_{1+x}Ba_{2-x}Cu_3O_y$ seed is considered. A five domain or a single domain levitator can be produced based on the type of seed crystal used. The properties of the five domain as well as single domain levitators are also considered.

PREPARATION AND PROPERTIES OF THE SEED CRYSTALS

$Nd_{1+x}Ba_{2-x}Cu_30_y$ crystals are used as seeds in order initiate grain growth in melt processed YBCO. The crystals are prepared by using a self flux method. Specifically, a Barium and Copper rich mixture of Nd_2O_3, $BaCO_3$, and CuO are mixed and heated in Al_2O_3 crucibles above the peritectic point of $NdBa_2Cu_3O_x$. The melt was then slowly cooled and the excess liquid drained after adequate crystal growth. The crystals were then collected and cleaned for seeding.

Two types of seeds were obtained depending upon the amount of flux in the melt. When the amount of flux is low, the crystals obtained have a cubic appearance. These crystals are, however, not single crystals and do have a unique microstructure as shown in Figure 3. The crystal clearly shows five different regions. The central region is surrounded by four differently oriented crystals of the same crystal structure. Transmission electron microscopic studies have revealed that the surrounding crystals are rotated 90 degrees with respect to the central crystal. Furthermore, the surrounding crystals are also rotated by 90 degrees with respect to its adjacent crystal. The flat seeds on the other hand are single crystals. No special microstructure was observed as shown in Figure 4.

Figure 5 shows the X-ray diffraction of the crushed seeds (both cubic and flat) and near phase pure $NdBa_2Cu_3O_x$ produced by calcination in low partial pressure O_2 atmosphere. As evident from the figure, both the cube and the flat seeds have lattice structure similar to that of $NdBa_2Cu_3O_x$ powder.

Energy dispersive x-ray analysis showed an average cation composition of Nd:Ba:Cu of 1.25:1.85:2.4 with about 6 % Al contamination from crucible reactions for flat crystals. A composition of Nd:Ba:Cu of 1.35:1.75:2.8 with about 2 % Al contamination for the center of the cube shaped crystal was found, while the surrounding crystals showed a composition of Nd:Ba:Cu of 1.3:1.7:2.5 with about 6 % Al contamination. These compositional differences, especially those in Al-contamination, can be explained by differences in the initial phase composition and by processing during heat treatment. During the growth of the flat seeds a relatively larger contact between the crucible and its content existed. For the growth of cubic seeds, the contact of the melt with the crucible wall was less, leading to a reduction of contamination of the central crystal. The reason for the stronger contamination of the surrounding crystals may be due to the prolonged

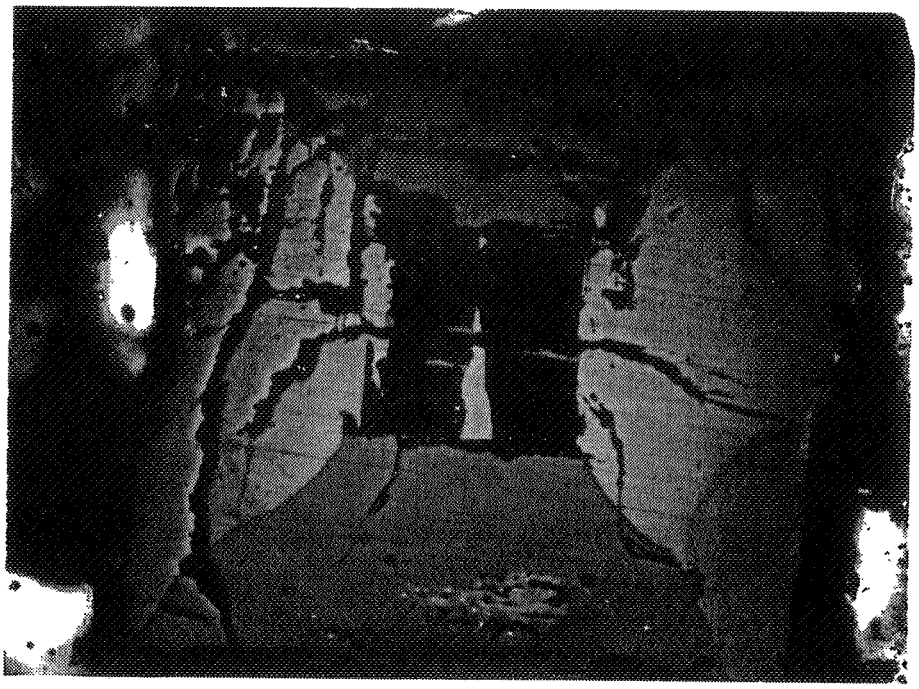

Figure 3. Photomicrograph of a "cubic" seed consisting of a central crystal and four surrounding single crystals.

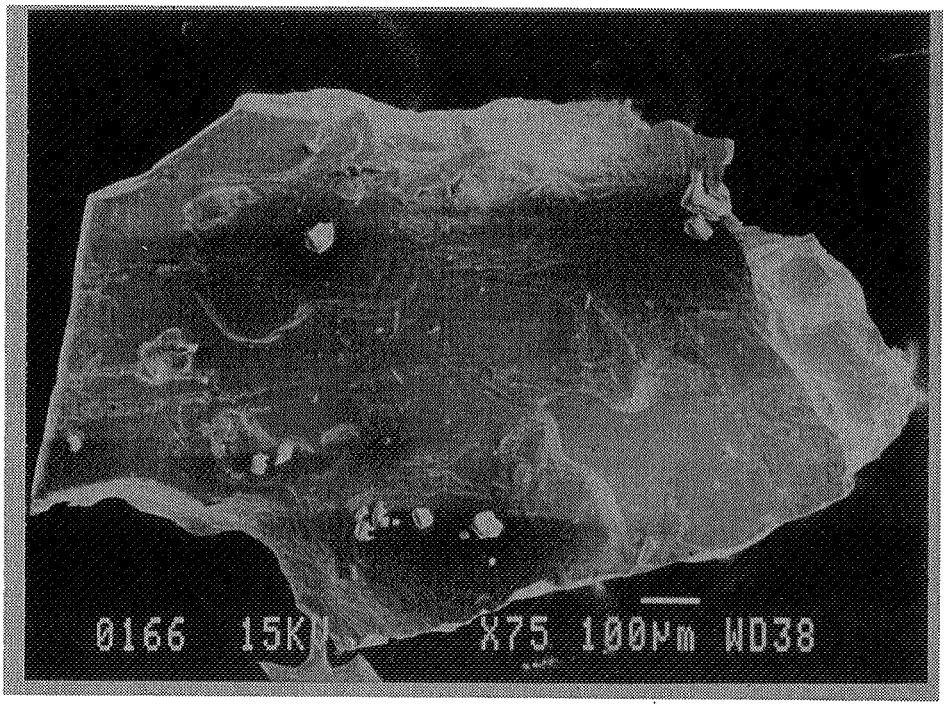

Figure 4. SEM photo of a flat, single crystal seed.

processing at the elevated temperatures. This in turn may account for the increased Al dissolution and diffusion through the content of the crucible.

A crystal can only work as a seed to initiate grain growth in melt processed YBCO, if the seed has a melting point higher than that of YBCO. Figure 6 shows the DTA of crushed flat and cube crystals. As evident from the figure, the crystal melts at about 1120 °C, which is considerably higher than the melting point of YBCO (~ 1010 °C). Interestingly, near phase pure $NdBa_2Cu_3O_x$ prepared by calcination in low partial pressure O_2 atmosphere melts at about 1070 °C. This difference in the melting point may be related with the surface energy of the faceted structure of the seeds. The higher melting point of both the cube and flat seeds thus open the possibility of using them as seeds for melt processing $NdBa_2Cu_3O_x$ itself.

FABRICATION AND PROPERTIES OF THE LEVITATORS

A top seeding method is used to melt process YBCO levitators. As mentioned earlier both cubic and flat shaped crystal were used for seeding. The details of the method have been reported previously.[24,25] Figure 7 shows some of the melt -processed YBCO levitators. Samples seeded with cubes as well as flat crystals showed similar appearance. However, a difference in the structure was obvious after polishing. A five domain structure was observed when the levitator was seeded with a cube seed (Fig. 8). Seeding with flat seeds, however, resulted in a single domain sample (Fig. 9). The melt processed YBCO levitators are therefore observed to replicate the feature of the seed used to initiate grain growth.

Transmission electron microscopy has been used to study the grain boundaries developed between two domains in a five domain levitator. Two kinds of grain boundaries were observed as shown in Figures 10 & 11. The first kind of grain boundary was observed between two domains that are rotated 90 degrees about a common [100/010] axis with both [001] axes lying in the plane of the paper. The boundary plane is always very sharp, free of secondary phases and shows macroscopical facetting. The boundary plane varies macroscopically from a symmetrical configuration - predominantly in the upper part of the pellet - to configurations where the grain boundary lies perpendicular to the [001] direction of one of the domains. The grain boundary is often inclined and meandering in the third dimension (into the paper plane) as well. The second kind of grain boundary is observed between two domains that are rotated 90 degrees about a common [100/010] axis with one [001]-axis normal to the plane of the paper and one [001]-axis contained within the plane of the paper. This type of grain boundary has been reported to support a high critical current density in thin film superconductors.

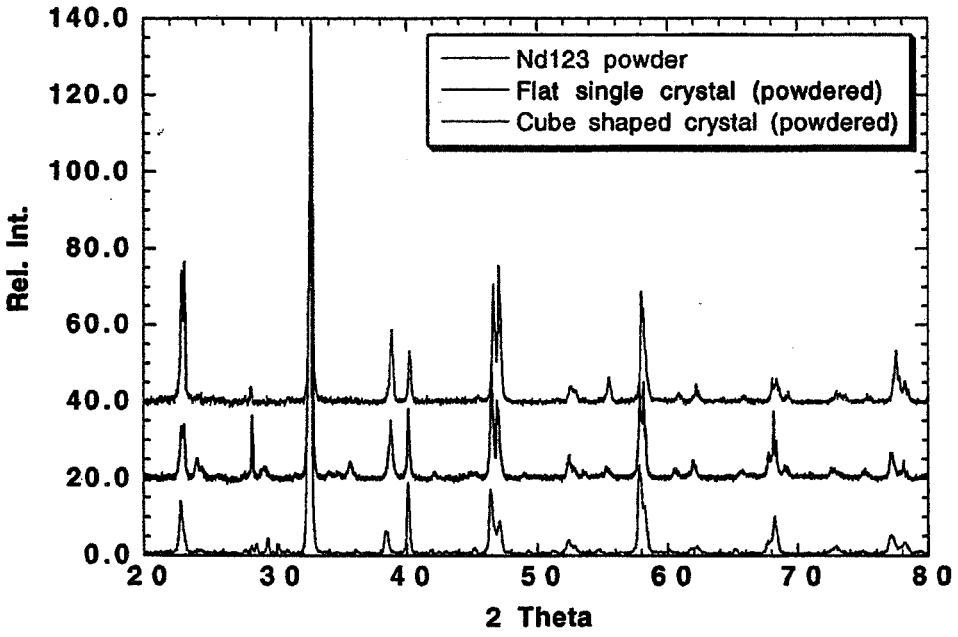

Figure 5. X-ray diffraction of $NdBa_2Cu_3O_x$ powder, crushed single crystals, and crushed cubed crystals. (in order from top to bottom)

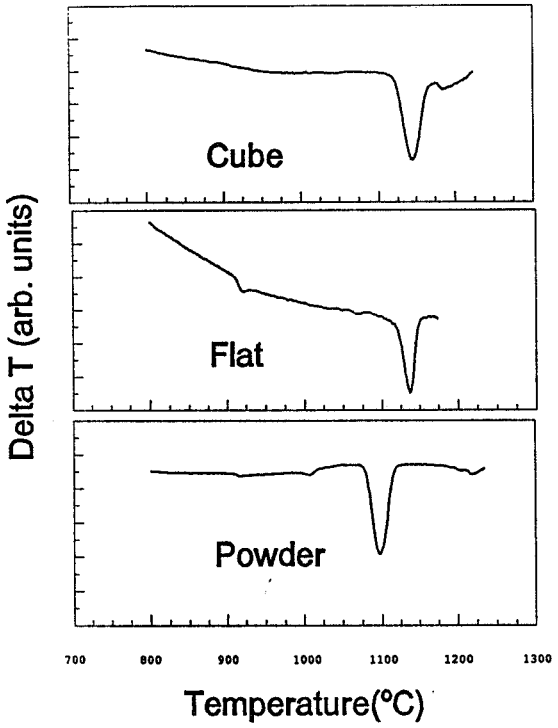

Figure 6. Differential thermal analysis of cubed crystals, flat single crystals, and Nd123 powder.

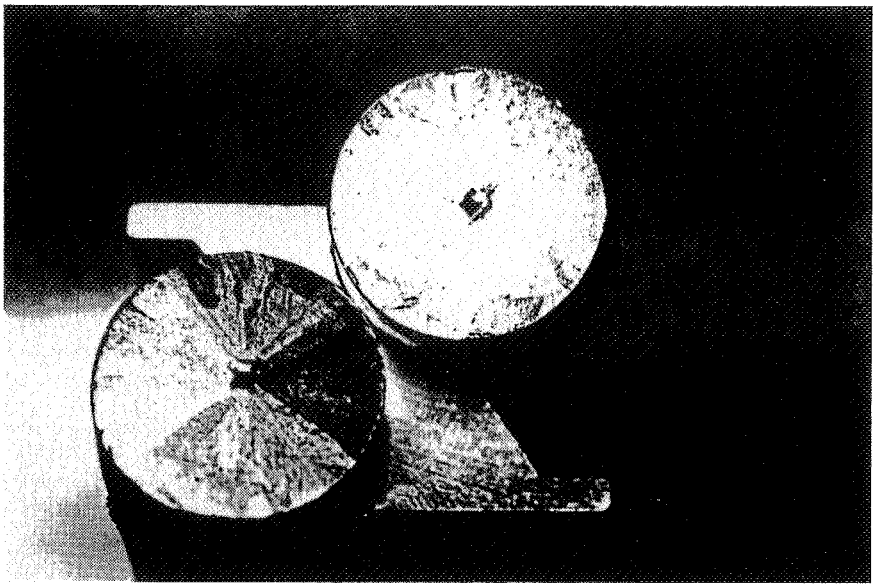

Figure 7. Photo of two melt-processed YBCO levitators.

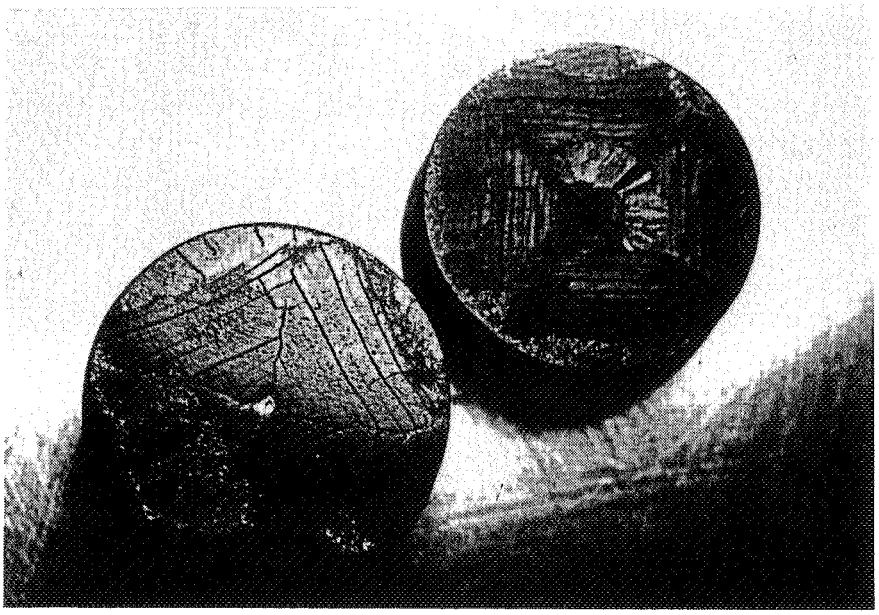

Figure 8. Photo of two polished, five domain levitators processed using cube seeds.

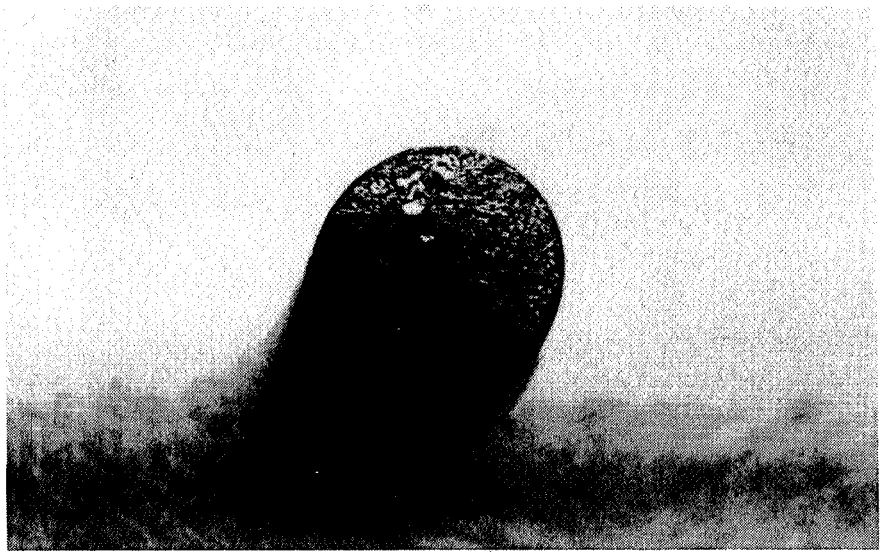

Figure 9. Photo of a single domain levitator processed using flat seeds.

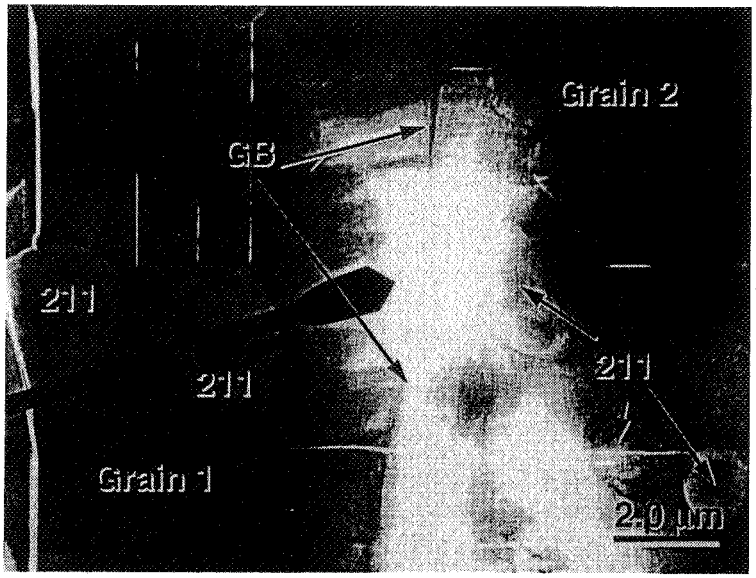

Figure 10. Transmission electron micrograph of two domains with both [001] axes lying in the plane of the paper.

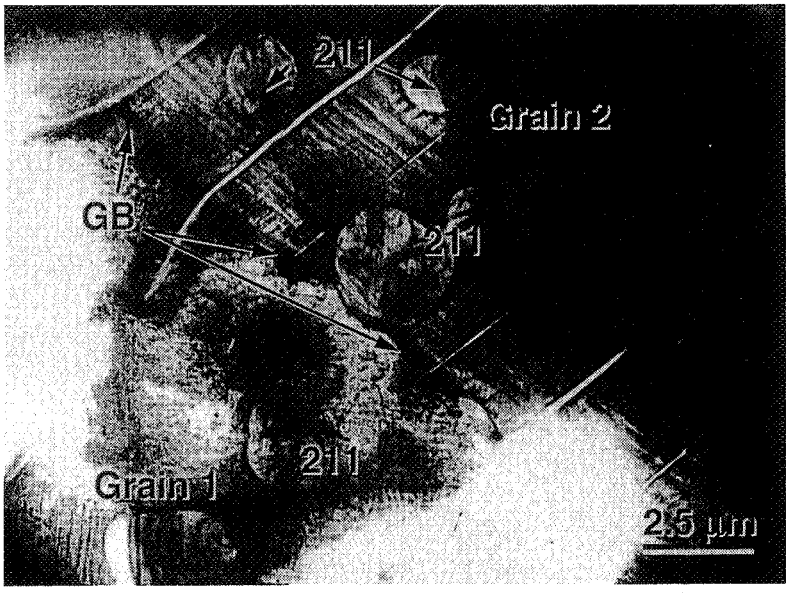

Figure 11. Transmission electron micrograph of two domains with one [001]-axis normal to the plane of the paper and one [001]-axis contained within the plane of the paper.

The levitation forces of a single domain and five domain levitator are plotted in Figure 12. As can be seen from the figure, similar levitation forces were observed for both samples. This result suggests that the 90 degree grain boundaries in the five domain levitator may be acting as strongly linked boundaries. Recent transport measurements across the these boundaries further confirms our results.[26]

In order to further investigate the properties of these two types of levitators (five domain and single domain) the levitation forces as a function of thermal cycling were studied. The levitators were cooled to liquid nitrogen temperature and then heated rapidly by using a copper block as a heat source. Figure 13 shows the zero distance levitation force of a five domain and a single domain levitator as a function of thermal cycling. As can be seen from the figure, only a small decrease (~10 %) in the levitation force of the five domain levitator was observed after 60 thermal cycles. Nearly no change was observed for the single domain sample. The result can be explained by considering the anisotropic nature of the thermal expansion in YBCO. This anistropy may lead to the development of microcracks during thermal cycling in a five domain levitator thereby reducing the levitation force.

Figure 14 shows the levitation force as a function of sample thickness for a five domain and a single domain levitator. In both cases the samples are sliced from the bottom. As evident from the figure, a small decrease in the levitation force is observed for both levitators with decreasing thickness. The force however drops rapidly once the thickness is reduced beyond 0.5 cm. The single domain levitators also show different behavior depending upon the position of the cut. The forces decrease much more rapidly when the levitator is cut from the top in comparison to that of the levitator cut from the bottom. This result shows the deleterious effect of the reaction from the crucible.

CONCLUSIONS

Large domain $YBa_2Cu_3O_x$ levitators have been fabricated using a seeded melt processing technique. Two types of seed crystals were prepared by a self flux method. The levitator was found to replicate the type of seed used to initiate grain growth. Based on the seed type, the levitators were either single domained or five domained. The levitation force for the single as well as five domain levitators were found to be similar. The grain boundaries separating two domains in the five domain levitator were found to be 90 degrees. Only a small change in the levitation force was observed as a function of thermal cycling in a five domain levitator. Nearly no change in the force was observed for the single domain levitator. The result can be explained by the anisotropic nature of the thermal expansion in YBCO. Finally, both single domain and five domain YBCO showed similar behavior as a function of thickness.

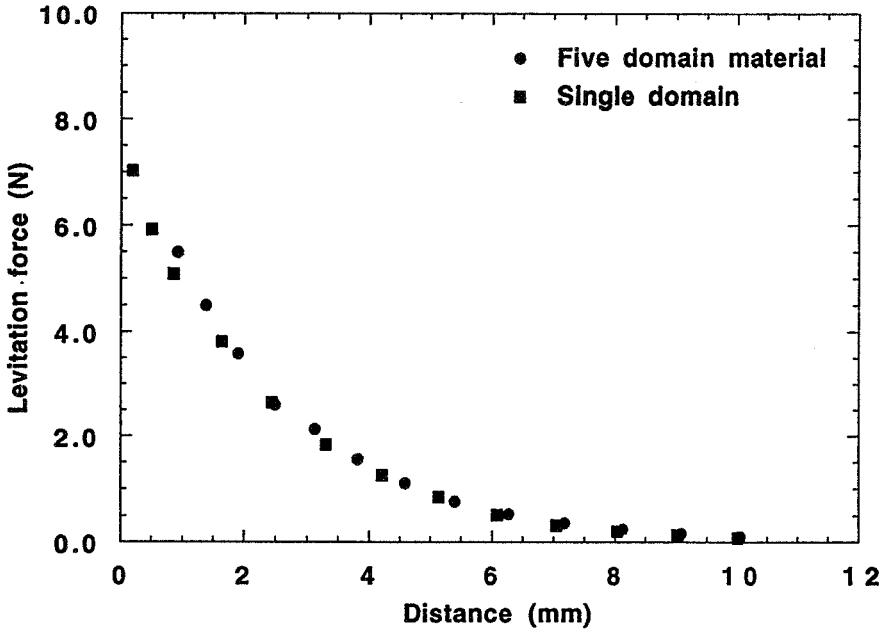

Figure 12. Levitaion force as a function of distance is plottted for a single and five domain levitator.

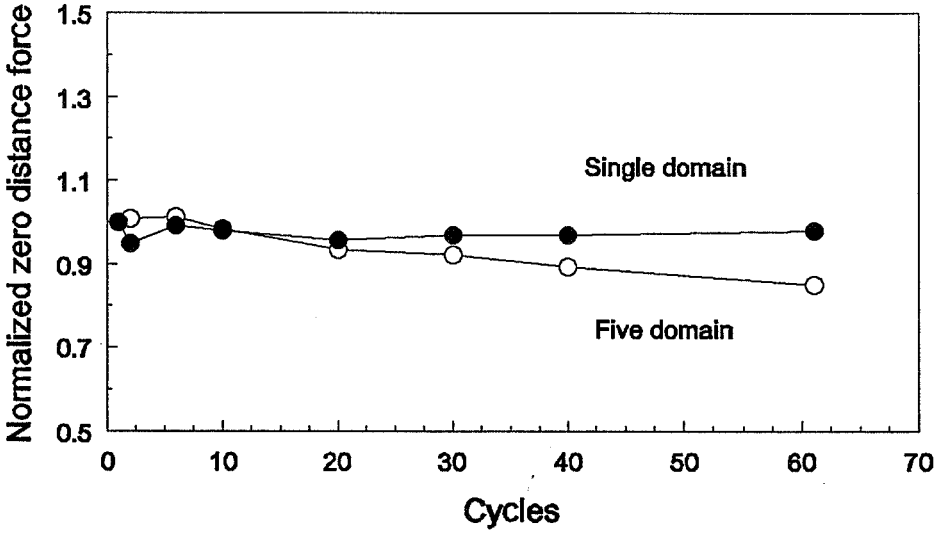

Figure 13. Zero distance levitation force as a function of thermal cycling is plotted for a single and five domain levitator.

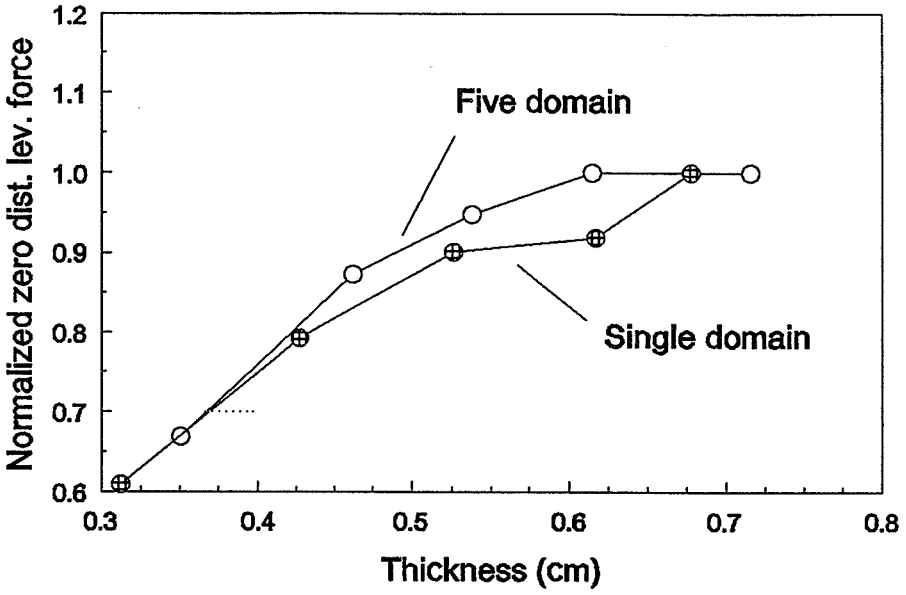

Figure 14. Levitation force as a function of thickness is plotted for a single and five domain levitator

ACKNOWLEDGMENTS

The work at Argonne National Laboratory is partially supported by the US Department of Energy, Division of Basic Energy Science-Materials Sciences, Conservation and Renewable Energy Utility Concepts-Superconductivity Technology Program, under Contract # W-31-109-ENG-38.

REFERENCES

1. F. C. Moon, *Superconducting Levitation, Applications to Bearings and Magnetic Transportation*, John Wiley & Sons, Inc. (1993).

2. V. Arkadiev, J. Phys. (Moscow) **9**(2), 148 (1945).

3. V. Arkadiev, Nature 160, 330 (1947).

4. P.J. Geary, *Magnetic and Electric Suspensions*, British Scientific Instrument Research Association, (1964).

5. C.W. Chu, P.H. Hor, R. L. Meng, L. Gao, Z.J. Huang, and Y. Q. Wang, Phys. Rev. Letts. **4**, 405 (1987).

6. F. C. Moon, and P. Z. Chang, Appl. Phys. Lett. **56**, 397 (1990).

7. H. Takaichi, Melt-Processed High-Temperature, ed. M. Murakami, World Scientific, London, 320 (1990).

8. C. K. McMichael, R. S. Colley, Q. Y. Chen, K. B. Ma, M. A. Lamb, R. L. Meng, C. W. Chu, and W. K. Chu, *Proc. 2nd Int. Symp. on Magnetic Suspension Technol.*, Seattle (1993), NASA CP-3247.

9. J. R. Hull and R. B. Poeppel, *HTS Materials, Bulk Proc. and Bulk Appl.*, World Scientific, Singapore, 484 (1992).

10. H. J. Bornemann, R. Zabka, P. Boegler, C. Urban, and H. Rietchel, *Proc. Second International Symposium on Magnetic Suspension Technology*, Seattle (1993), NASA CP-3247.

11. S. Jin, T. H. Tiefel, R. C. Sherwood, M. E. Davis, R.B. van Dover, G. B. Kammlott, R. A. Fastnacht, and H. D. Keith, Appl. Phys. Lett. **52**, 2074 (1988).

12. K. Salama, V. Selvamanikam, L. Gao, K. Sun, Appl. Phys. Lett. **54**, 2352 (1989).

13. A. J. Bourdillon, N. X. Tan, N. Savvides, and J. Sharp, Mod. Phys. Lett. B **3**, 1053 (1989).

14. P. J. McGinn, W. Chen, and M. A. Black, Physica C **161**, 198 (1989).

15. M. Murakami, M. Morita, K. Miyamoto, and H. Hamada, Jpn. J. Appl. Phys. **28**, L 399 (1989).

16. S. Kuaruangraong, and J. Taylor, J. Am. Ceram. Soc. **74**, 1964 (1991).

17. M. Murakami, Supercon. Sci. Technol. **5**. 185 (1992).

18. S. Sengupta, Donglu Shi, Z. Wang, A. C. Biondo, U. Balachandran, and K. C Goretta, Physica C **199**, 43 (1992).

19. D. F. Lee, V. Selvamanikam, and K. Salama, Physica C **202**, 83 (1992).

20. M. Morita, L. Trouilleux, S. Takebayashi, K. Kimura, M. Tanaka, K. Miyamoto, and M. Hashimoto, Proc. Inter. Workshop Super. RI-1, June23-26 (1992).

21. K. Y. Blohowiak, D. F. Garrigus, T. S. Luhman, K. E. McCray, M. Strasik, I. A. Aksay, F. Dogan, W. B. Hicks, J. Liu, and M. Sarikaya, IEEE Trans. Appl. Supercond **3**, 1049 (1993).

22. H. M. Jang, K. W. Moon, and S. Baik, Jpn. J. Appl. Phys. **28**, L 1223 (1989).

23. U. Balachandran, W. Zhong, and C. A. Youngdahl, and R. B. Poeppel, J. Electron. Mat. **22**, 1285 (1993).

24. V. R. Todt, S. Sengupta, Donglu Shi, P. R. Sahm, P. J. McGinn, R. B. Poeppel, and J. R. Hull, J. Electron. Mater. **23**, 1127 (1994).

25. V. R. Todt, S. Sengupta, and D. J. Miller, Appl. Supercond. **3**, 175 (1995).

26. V. R. Todt, X. F. Zhang, and D. J. Miller, Matls. Res. Soc. Mtg., (1995).

ADVANCED MANUFACTURING OF SUPERCONDUCTING MAGNETS

Mark W. Senti
Advanced Magnet Lab, Inc.
Palm Bay, FL

SUMMARY

The development of specialized materials, processes, and robotics technology allows for the rapid prototype and manufacture of superconducting and normal magnets which can be used for magnetic suspension applications. Presented are highlights of the Direct Conductor Placement System (DCPS) which enables automatic design and assembly of 3-dimensional coils and conductor patterns using LTS and HTS conductors. The system enables engineers to place conductors in complex patterns with greater efficiency and accuracy, and without the need for hard tooling. It may also allow researchers to create new types of coils and patterns which were never practical before the development of DCPS. The DCPS includes a custom designed eight-axis robot, patented end effector, CoilCAD™ design software, RoboWire™ control software, and automatic inspection.

INTRODUCTION

The "Direct Conductor Placement System" (DCPS) was developed to provide a low-cost and high precision automated manufacturing process for 3-dimensional conventional and superconducting wire, cable and other conductor forms, and electromagnetic devices. The system allows the fully automatic design and manufacture of complex, multi-layer, and splice free coils. Through the use of sophisticated software design tools and state-of-the-art automation, the DCPS can drastically reduce R&D and product development cycles. The end result is a flexible, cost effective, and high quality process.

The ability to automatically transform coil geometry's into precise wire forms eliminates the need for expensive and complex tooling. Another major benefit to DCPS is that scientists and engineers have greater freedom to design and prototype complex coil and conductor devices. The technology even permits the implementation of design changes at almost any time during the production process.

DIRECT CONDUCTOR TECHNOLOGY

Originally developed at the Superconducting Super Collider Laboratory (SSCL), "Direct Wire" technology as it was called, has been successfully applied to the manufacturing of multipole magnets, such as dipoles, quadrupoles, sextupoles, and decapoles for accelerator applications. At the time, the process involved use of a CNC (computer numeric control) machining center, specially coated wire and substrate, and a special "wiring head" to position and bond the wires. The SSCL team utilized the technique to construct 2.5 Tesla dipole magnets that exhibited excellent performance characteristics.

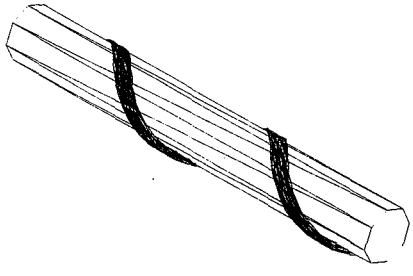

Figure 1. Helical coil directly wound.

The "Direct Wire" technique used a computer controlled coil assembly process to place wires with an accuracy of ±0.025mm. Coated wires used in the process were wound on an insulated support tube. Due to the precise placement, a high conductor packing density was achieved. The conductors in the finished wire matrix support each other, and the magnets show outstanding quench performance and random field errors are minimized. Precision manufacturing techniques and advanced material properties are required to build such magnets since wire movements of a few μm are sufficient to initiate a quench in these magnets.

The close-out of the SSCL resulted in license of the "Direct Wire" technology to the American Composites Education, Inc. (ACE) an advanced materials, manufacturing, and technology development firm. The state of the development of the technology was limited to the equipment and resources which were available during the last months of the SSCL. The ACE quickly recognized that for general industrial applications it would require collaboration with companies who had experience in robotics and automated manufacturing. As a result, the Advanced Magnet Laboratory, Inc. (AML) was created to offer a complete manufacturing system which integrates specialized materials, processes, and robotics technology.

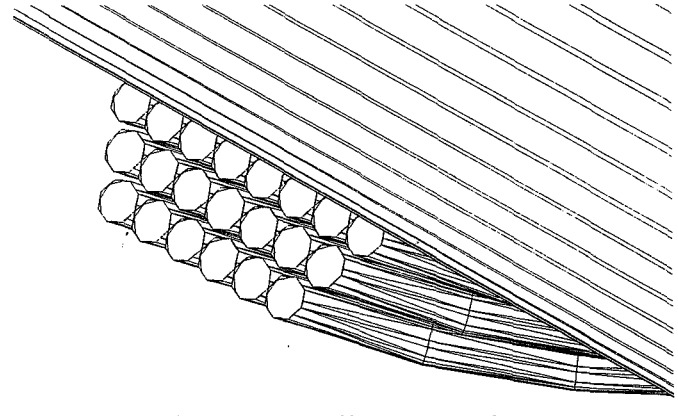

Figure 2. Three layer coil cross-section.

DIRECT CONDUCTOR PLACEMENT SYSTEM

The DCPS includes a custom designed eight-axis robot, patented end effector, CoilCAD™ design software, RoboWire™ control software, and vision inspection. The system is the result of a private collaboration between experts in superconducting magnet design, materials and manufacturing processes, and automation.

Computer Aided Coil Design

CoilCAD™

CoilCAD™ is a complete coil design package, with an easy to use Graphical User Interface (GUI) that runs under the popular Microsoft® Windows™ 3.1 environment. Running on an inexpensive PC, CoilCAD™ is capable of creating 3-dimensional spacial paths for complex and multi-layered conductor forms. Output from CoilCAD™ provides the complete set of robot path and associated control coordinates for the DCPS robot.

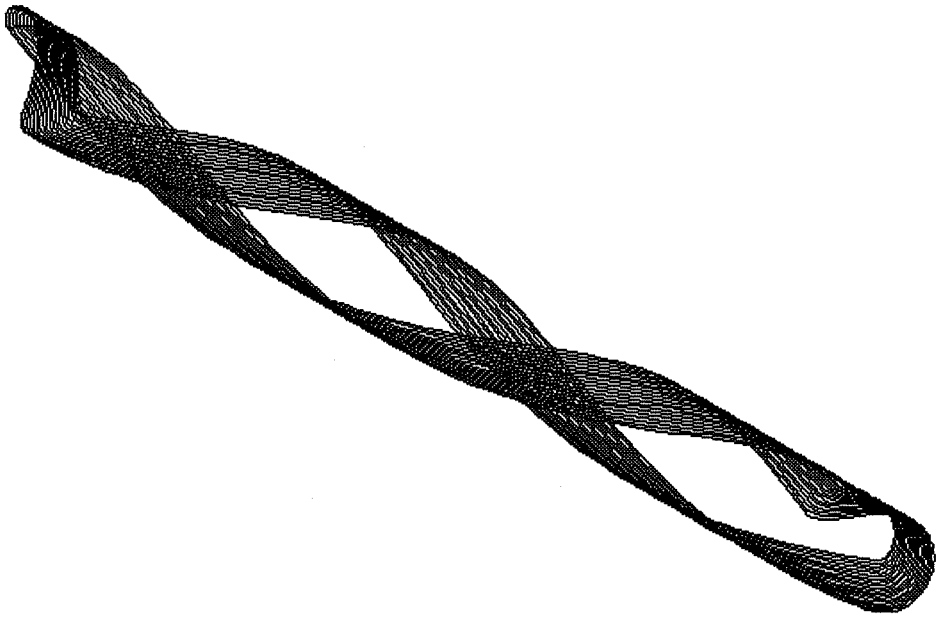

Figure 3. A 3-dimensional spacial curve created from CoilCAD™.

The "Direct Conductor" technique allows manufacturing of precise 2- and 3-dimensional conductor forms. In this assembly process a multi-axes Cartesian robot is used to accurately position and bond the conductor on to a support structure or another conductor layer. The process is ideally suited to the manufacturing of wire, cable and

other conductor-wound superconducting or normal conducting multipole magnets (dipole, quadrupole, sextupole, etc.) needed for accelerators and light sources.

In order to position the conductor in this winding process the 3-dimensional space curve of the conductor path of the coil or conductor pattern has to be defined in order to create the robot path. Even for simple dipole magnets these space curves are rather complex due to the coil ends where the conductor has to cross from one side to the other (see fig. 3). A special software program, called CoilCAD™ has been developed to generate the space curves for a large variety of magnet types and to prepare the coordinate files which are loaded into the DCPS controller and executed by RoboWire™ control software. This software was developed by internationally recognized scientists from the SSCL who are now a part of the AML.

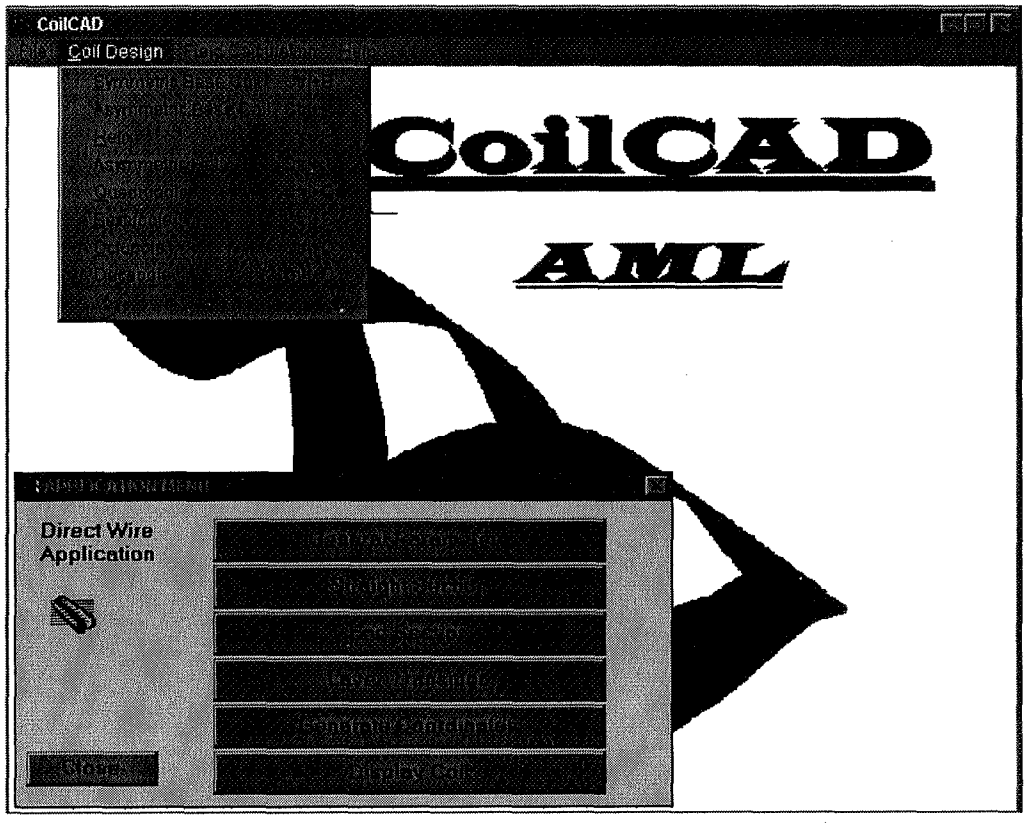

Figure 4. CoilCAD™ Graphical User Interface (GUI).

CoilCAD™ is a menu driven computer program with a powerful GUI. The user specifies the standard parameters of the conductor form to be created, like coil type (magnet, motor or other winding), coil length and diameter, conductor dimensions, and conductor spacing. The user can choose various shapes of coil ends to meet the special requirements of the application. The program generates the 3-dimensional space curve describing the coil geometry. For multi-layer coils the conductors are perfectly nested which is of particular importance for the performance of superconducting magnets.

The complete knowledge of the space curve describing the conductor path in the coil enables a precise calculation of the magnetic field of the coil. Even small effects like layer-to-layer crossings of the conductor and coil lead wires, which are normally neglected in field calculations, are automatically taken into account in this method of field calculation. CoilCAD™ is therefore not only a powerful tool to design magnets for the Direct Conductor process and to generate the coordinate files for the DCPS robot, but also to optimize the magnetic field of magnets with various goals like overall field homogeneity or field strength enhancements in the coil ends.

Direct Conductor Placement System Robot

System Flexibility

The system can be configured to produce round, square, rectangular, hexagonal, or other geometric coils. Flat conductor patterns utilize a vacuum frame for fixturing the coil substrate. Cylindrical patterns are achieved by the use of an additional robot axis for coordinated rotation of the coil support structure. CoilCAD™ allows the user to create or change coil types easily. RoboWire™ control software provides a means for changing or offsetting conductor patterns real-time during the manufacturing process.

Robot Manipulator

The DCPS is designed to manufacture a broad range of 3-dimensional or spacial patterns. The system features include (a)eight axis coordinated Robot Manipulator, (b)patented end effector, (c)RoboWire™ software, (d)vacuum frame table top for flat patterns, (e)rotational tube for 3-dimensional patterns, and (f)real-time vision/video feedback option.

The DCPS robot incorporates eight axes of coordinated control and is capable of placing conductors over a large envelope. The current AML system work area allows placement of conductor over an area of 1.5m X .3m. AML is planning to increase the envelope to 3m to accommodate large helical dipole magnets under development for the Brookhaven National Laboratory (BNL). The eight axes are X, Y, Z, rotation (Theta), support tube rotation (C), conductor feed (A), bonding feedback (T), and drum rotation (D).

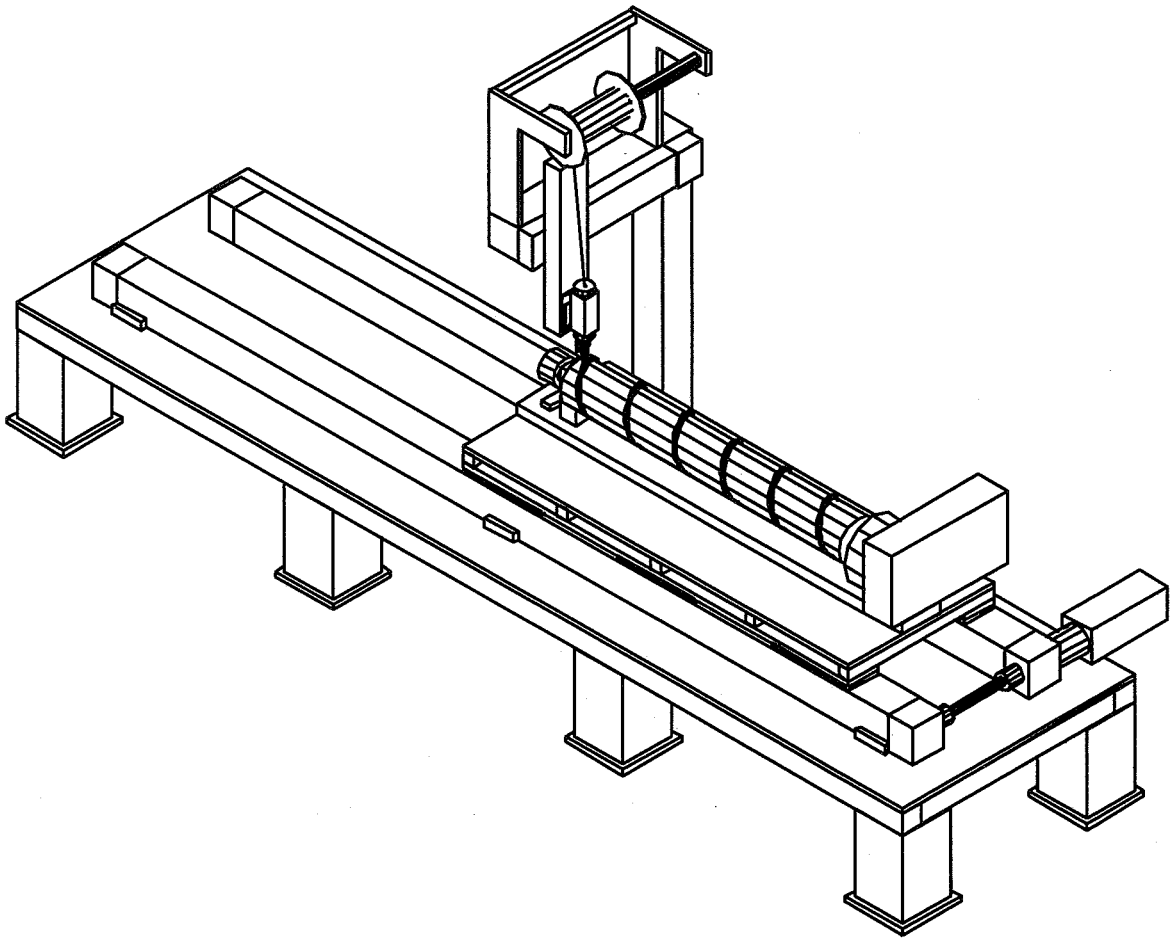

Figure 5. Direct Conductor Placement System.

Table 1. Current DCPS Robot Specifications

X-axis stroke	= 1.5m
Y-axis stroke	= .3m
Z-axis stroke	= .3m
Theta axis stroke	= Unlimited
C axis (Tube rotation)	= 540°
A axis (Feed)	= Unlimited
T axis (Temp control)	= Unlimited
D axis (Wire drum control)	= Unlimited
Accuracy (X, Y, Z, θ, C)	= ±0.025 mm
Speed Max.	= 254 mm/sec.

End Effector. This is where the tire hits the road. The development of the end effector is the most critical part of the robot and manufacturing process. The DCPS end effector provides for continuous rotation and real-time feedback of the placement process. The theta axis provides unlimited rotation for the conductor feed allowing the system to follow a circular path. The feed axis controls the amount of conductor to pay out during the conductor placement process. The bonding control allows the system to vary the adhesive process used to bond the conductor. During conductor placement, the specially designed end effector monitors the conductor tension. This is of particular importance in the coil end radii to assure precise conductor placement.

Special end effectors which allow the automatic winding process with controlled conductor tension are presently under development. The end effectors are important, for example, for winding solenoid magnets.

Video/Vision. Live magnified video can be used to monitor the process real-time. This can be especially helpful during the initial set-up and debug of coil patterns. Vision feedback can be used to inspect newly completed runs. The camera rides behind the placement head and looks at the placement of conductor real-time. Good images can be stored to disk and used to compare to those in process.

The vision system (see fig. 6) also allows quality analysis of coil patterns. For example, image analysis could be performed after placement of each conductor layer/pattern. This would prevent the operator from covering a "poor" or defective pattern.

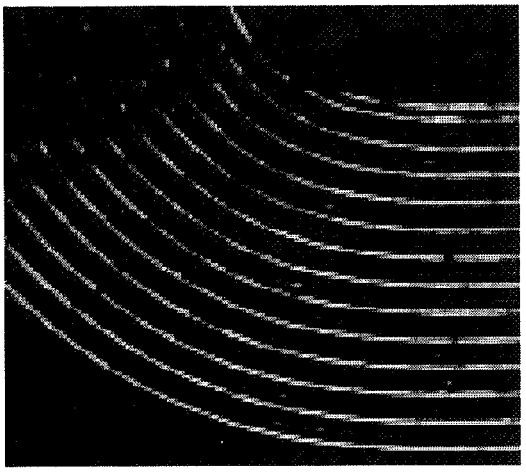

Figure 6. Vision Inspection of Coil.

RoboWire™ Controller

The DCPS controller is built around a standard 486-66 PC, advanced motion controller board, and Micro-PLC machine-I/O control. This provides three levels of dedicated control working asynchronously and simultaneously. Essentially, we have divided up robot control into three dedicated controllers - each with their own processor and firmware. The result is a powerful multi-tasking controller. While RoboWire™ is managing the "system" control, the motion controller can concentrate on motion control and the PLC handles I/O operation.

RoboWire™ SOFTWARE

RoboWire™ provides the overall management of the robot control and includes numerous features for setup, programming, security, peripheral control, factory networking and program execution. RoboWire™ is used as the front-end interface and provides transparent control of the conductor placement process and machine control.

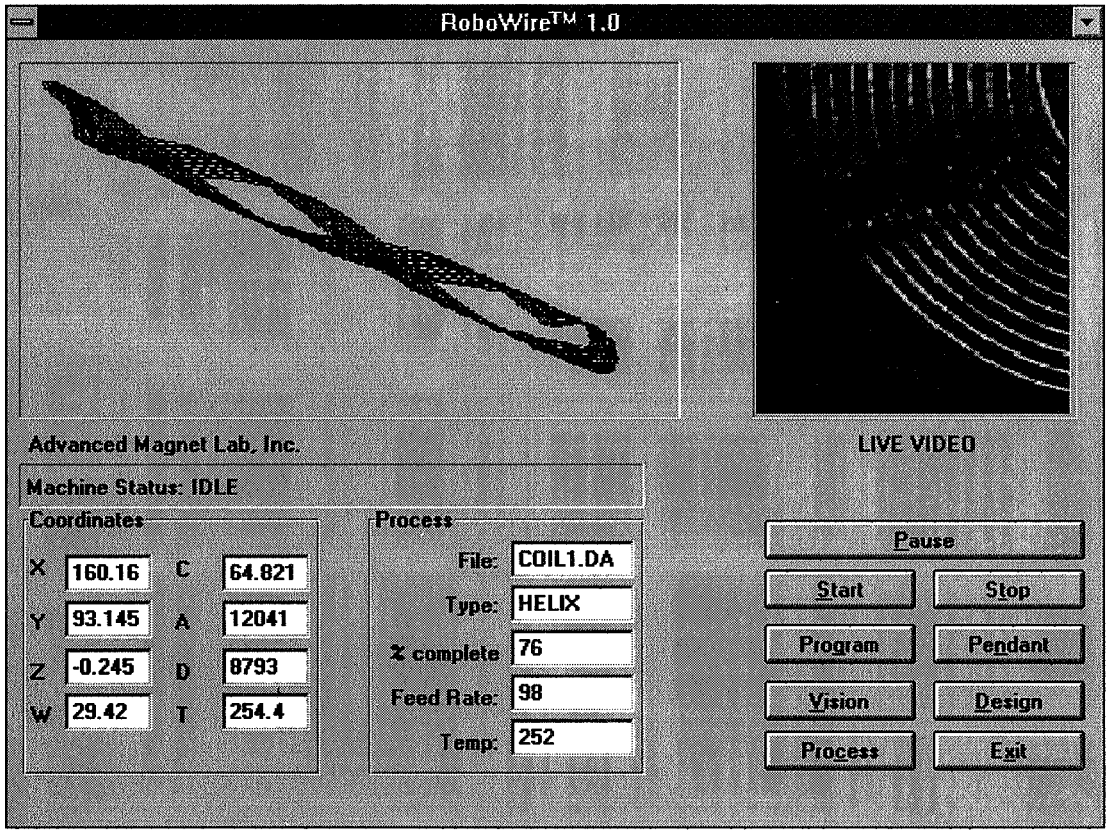

Figure 7. RoboWire™ Control Software Interface.

RoboWire™ is a complete Graphical User Interface (GUI) designed as an easy to use, graphical, motion control package that runs under the popular Microsoft® Windows™ 3.1 environment. Running on a low-cost PC, RoboWire™ is capable of controlling robots with multiple axes using a powerful set of motion control tools. The user interface is fully menu and icon driven and includes full on-line help and documentation. In addition to motion control, RoboWire™ also provides full support for CoilCAD™, binary I/O and serial communications. RoboWire™ also includes capabilities for performing other robotics related functions, such as axis calibration, vision-based inspection and laser calibration.

Bonding Technologies

There are three primary methods currently used for bonding conductors: (a)heat transfer, (b)ultrasonic heating, and (c)direct adhesive.

The **heat transfer** method was used at the SSCL successfully on 3-dimensional coils. It can handle a large variety of conductor types and diameters. Disadvantage of this process is the increased material costs because it requires the conductor to be coated with special adhesive. The **ultrasonic heating** has been successfully implemented for use in manufacturing single layer and 2-dimensional coils. This process has limitations when handling miniature superconducting cables which are made of several strands or large diameter or cross-section conductors.

Direct adhesive provides significant cost benefits to the DCPS technology and this patent pending technology is based upon advanced polymeric materials and process techniques. It also reduces process variables and tooling (end effector) requirements.

APPLICATIONS FOR DCPS

The use of DCPS is already being internationally well received in academia, government, research laboratories, and industry. This includes a broad range of applications such as a variety of superconducting magnets, solenoid magnets, linear induction and other motors, transformers, medical MRI and several proprietary developments.

DCPS Application Examples

Spin Rotators. The Advanced Magnet Lab and Brookhaven National Laboratory are working together to design and build helical "spin rotator" dipole magnets in industry for the RHIC (Relativistic Heavy Ion Collider). Benefits of the DCPS design approach for dipole magnets include: (a)compact coil design to optimize mechanical stability of the conductor matrix, (b)optimized coil-end design keeps peak field in magnet to a minimum, (c)experiences from prototype testing can be easily incorporated.

Particle Storage Ring Corrector and Trim Magnets. The Large Hadron Collider (LHC) presently under construction at CERN, Geneva, Switzerland has very similar technical requirements as the SSCL, where the Direct Wire technique was successfully used. The AML is also collaborating with the BNL to utilize Direct Conductor technology to build corrector coils for the "g-2" project.

MRI Correctors. The DCPS is very adaptable to MRI applications. This could allow MRI manufacturers to directly place coil patterns on MRI tubes. Benefits include greater accuracy in coil placement, higher field qualities, reduced labor costs, reduced tooling and greater flexibility between product variations.

MAGLEV. American Maglev Star, Inc. is working with AML to develop and produce proprietary electromagnetic devices including superconducting magnetic suspension and propulsion conductor forms.

AML has been organized to handle applications that could develop through future programs such as the NASA MagLifter, Holloman Air Force Base Propulsion Sled and others. The DCPS could be used to automatically fabricate the advanced electromagnetic systems required for the smart guideways and magnet systems.

Motors. DCPS is well suited for the development and manufacturing of these applications. Due to the precise conductor placement the weight of such devices can be reduced.

Cornell University. Cornell is currently upgrading the magnet systems for the interaction region of the CESR e^+-e^--storage ring. The required correction magnets are proposed to be manufactured with the DCPS.

ACKNOWLEDGMENTS

The Direct Conductor technology could not have survived without the effort put forth by many individuals. These include but are not limited to: Rodney "Rex" Barrick, Walter "Wally" Czapla, Stu Geraghty, Paul Leppek, Dr. Rainer Meinke, John Morena, Michael M.D. Phelipa, John Skaritka, Gerry Stelzer, and Billy Yager. Other supporters of this technology include many individuals from the RHIC, AGS, and Magnet Divisions at Brookhaven National Laboratory, American Composites Education, Inc., InterTech, and American Maglev Star, Inc.

REFERENCES

1. R. Barrick, W. Czapla, R. Meinke, J. Morena, B. Yager, and Z. Yuping: *Recent Developments in Superconducting Wire Wound Magnet Technology.* Superconducting Super Collider Laboratory, Waxahachie, Texas.

Session 18 -- Modelling 2

Chairman: Gerald Foshage
Honeywell Corporation

COMPUTATIONAL ANALYSIS OF STATIC AND DYNAMIC BEHAVIOUR OF MAGNETIC SUSPENSIONS AND MAGNETIC BEARINGS

Dr. Colin P. Britcher
Department of Aerospace Engineering
Old Dominion University
Norfolk, VA 23529-0247

and

Nelson J. Groom
Guidance and Control Branch
Flight Dynamics and Control Division
NASA Langley Research Center
Hampton, VA 23681

ABSTRACT

Static modelling of magnetic bearings is often carried out using magnetic circuit theory. This theory cannot easily include nonlinear effects such as magnetic saturation or the fringing of flux in air-gaps. Modern computational tools are able to accurately model complex magnetic bearing geometries, provided some care is exercised. In magnetic suspension applications, the magnetic fields are highly three-dimensional and require computational tools for the solution of most problems of interest.

The dynamics of a magnetic bearing or magnetic suspension system can be strongly affected by eddy currents. Eddy currents are present whenever a time-varying magnetic flux penetrates a conducting medium. The direction of flow of the eddy current is such as to reduce the rate-of-change of flux. Analytic solutions for eddy currents are available for some simplified geometries, but complex geometries must be solved by computation. It is only in recent years that such computations have been considered truly practical. At NASA Langley Research Center, state-of-the-art finite-element computer codes, "OPERA", "TOSCA" and "ELEKTRA" have recently been installed and applied to the magnetostatic and eddy current problems.

This paper reviews results of theoretical analyses which suggest general forms of mathematical models for eddy currents, together with computational results. A simplified circuit-based eddy current model proposed appears to predict the observed trends in the case of large eddy current circuits in conducting non-magnetic material. A much more difficult case is seen to be that of eddy currents in magnetic material, or in non-magnetic material at higher frequencies, due to the lower skin depths. Even here, the dissipative behaviour has been shown to yield at least somewhat to linear modelling.

Magnetostatic and eddy current computations have been carried out relating to the Annular Suspension and Pointing System, a prototype for a space payload pointing and vibration isolation system, where the magnetic actuator geometry resembles a conventional

magnetic bearing. Magnetostatic computations provide estimates of flux density within air-gaps and the iron core material, fringing at the pole faces and the net force generated. Eddy current computations provide coil inductance, power dissipation and the phase lag in the magnetic field, all as functions of excitation frequency. Here, the dynamics of the magnetic bearings, notably the rise time of forces with changing currents, are found to be very strongly affected by eddy currents, even at quite low frequencies.

Results are also compared to experimental measurements of the performance of a large-gap magnetic suspension system, the Large Angle Magnetic Suspension Test Fixture (LAMSTF). Eddy current effects are again shown to significantly affect the dynamics of the system.

Some consideration is given to the ease and accuracy of computation, specifically relating to OPERA/TOSCA/ELEKTRA.

INTRODUCTION

The prediction of magnetostatic forces in small-gap magnetic suspensions, most notably magnetic bearings, has typically relied heavily on so-called "circuit models" [1,2]. Here, the magnetomotive force and reluctances around the closed flux path are equated to give the total flux in the circuit. Experience has shown that where the air-gap is small and the flux path is properly designed, these calculations are fairly reliable. Some cases arise, however, where extra precision is required, or where the variation of flux across the air-gap is of interest [3]. In large-gap magnetic suspension systems, no simple predictive model exists, due to the highly three-dimensional flux path [4,5]. Hence there is an increasing use of finite element, magnetostatic computer codes for design and analysis of both small-gap and large-gap systems.

Where the dynamics of magnetic actuators are of interest, it has been shown that eddy currents in conducting cores, metallic structures, etc., can cause significant departures from ideal behaviour [6,7]. Potentially the most troubling are restrictions on the bandwidth of such actuators. Here, the problem is sufficiently complex such that some form of finite element approach is recommended throughout.

APPLIED COMPUTATIONAL ELECTROMAGNETICS

Finite element methods are used extensively to obtain solutions to a wide range of engineering problems governed by partial differential, or integral equations. Numerical solutions become possible for problems with complex geometries, awkward boundary conditions and/or nonlinear behaviour. It is not the purpose of this paper to describe the difficulties of the approach, the formulations or numerical methods used in any detail, since a vast quantity of literature exists [8,9,10 etc.]. Rather, an existing "state-of-the-art" suite of codes is applied to real-world problems related to magnetic bearings and magnetic suspensions. The apparent accuracy of the solutions, with comparison to experimental data where possible, the practical problems encountered, and the weaknesses revealed in the codes, are all addressed from an applications perspective.

Magnetostatic fields can be expressed as a sum of a solenoidal component (where no current is flowing) and a rotational component (inside current-carrying conductors). In the solenoidal region, simple potential functions should describe the magnetic field, although a

difficulty arises exterior to current-carrying conductors, where the potential is multi-valued. This difficulty can be overcome by splitting the field into two parts, one representing the field due to magnetized volumes, and another representing the contribution of current-carrying conductors. A "reduced potential" can be defined to represent the former, and a "total potential" to represent the combination. The total potential can now be made single-valued in regions exterior to current-carrying conductors. The field due to prescribed currents (i.e. prescribed currents in electromagnet windings) is calculated in the reduced potential space using the Biot-Savart law. For practical eddy current problems, the governing equations are the zero-frequency limit of Maxwell's equations. This implies that the wavelength of any electromagnetic wave is very long compared to the characteristic physical dimension of the problem. These equations can be solved using a "vector potential" formulation, where $B = \nabla \times A$. The region containing an eddy current problem can therefore be subdivided into reduced, total and vector potential spaces as appropriate, with field continuity enforced on the boundaries between different potentials. The approach described is the one used in this work, but is far from being the only possibility.

OPERA-3D / TOSCA / ELEKTRA / VF-GFUN

OPERA-3D (OPerating environment for Electromagnetic Research and Analysis) comprises an interactive, graphical, pre-processor, for preparation of finite element problems, with a related post-processor, for analysis and display of results. Problems specified in the pre-processor are submitted to a variety of analysis packages for solution. These packages include TOSCA, for solution of magnetostatic and electrostatic problems using conventional finite-element methods, VF/GFUN, for solution of magnetostatic problems using integral equation methods, and ELEKTRA, for solution of eddy current problems using the finite-element method.

THE ANNULAR SUSPENSION AND POINTING SYSTEM

The Annular Suspension and Pointing System (ASPS) is a prototype for a high precision space payload pointing and vibration isolation system. A ferromagnetic rotor is magnetically suspended by five double-acting magnetic bearing stations, such that the orientation of the ring can be controlled in two "tilt" and three translational degrees-of-freedom, with a high level of isolation of base vibrations. The general configuration is illustrated in Figure 1, with the geometry of one of the "axial" bearing stations shown in Figure 2. Considerable hardware upgrades have been made recently, and the system now utilizes transistor switching power amplifiers and a simple digital controller [11]. Further details are presented elsewhere in this Proceedings [12].

THE LARGE-ANGLE MAGNETIC SUSPENSION TEST FIXTURE (LAMSTF)

In order to explore the technology required for the magnetic suspension of objects over large ranges of orientation, a small-scale laboratory development system, the Large Angle Magnetic Suspension Test Fixture (LAMSTF) was constructed at NASA Langley Research

Center. Possible applications for magnetic suspension systems of this general class include space payload pointing and manipulation, microgravity vibration isolation and wind tunnel model suspension. An important objective of this particular project is to investigate the dynamic modelling of large-gap magnetic suspension systems, so that future systems can be designed with higher levels of confidence.

The general configuration [13] is illustrated in Figure 3. Five room temperature copper electromagnets are mounted on an aluminum plate, each electromagnet driven by a transistor switching power amplifier. The suspended element consists of Neodymium-Iron-Boron permanent magnet material inside an aluminum tube. The direction of magnetization is along the axis of the cylinder, which is horizontal when suspended. The suspension height is 0.1m, measured from the axis of the suspended element to the top plane of the electromagnet conductor. Several different control systems have been developed and demonstrated, including several digital versions [14, 15].

MAGNETOSTATIC CALCULATIONS - SMALL AIR-GAPS

A simplified finite element representation of an ASPS axial bearing station is shown in Figure 4. Only one "side" of the real actuator is represented, corresponding to the present operational status where the rotor is suspended against gravity. It should also be noted that the rotor cross-section is considerably simplified, with the cylindrical inner flange and rotor curvature deleted. This permits more extensive symmetry in the problem and a reduction in solution time. A linear TOSCA solution for a current of 1 Amp in both coils and an iron relative permeability of 1000 is also seen in Figure 4.

A comparison of the predicted magnetic fluxes in the center of the air-gap is shown in Table A. The air-gap is 3.41 mm and the coil current 1 A for these cases. The discrepancy between the circuit model and both computational or experimental results is quite large and worrisome. The major problem is quickly found to be the improper assumption (in the circuit model) of uniform magnetic flux in the air-gap. The air-gap in ASPS is relatively large by the standards usually applied to magnetic bearings, the "aspect ratio" (diameter/gap) being between 6 (original design) and 12 (modified axial stations). Flux "fringing" around the periphery of the air-gap is, therefore, quite pronounced, as indicated in Figure 5.

TABLE A - Flux at gap centroid

TOSCA solution, μ=1000, Tesla	0.2385
Measured, Ni-Fe core, Tesla	0.2010
Circuit model, $\mu \rightarrow \infty$, Tesla	0.2985

It has previously been suggested that the predicted and actual magnetic forces would be in closer agreement, since the circuit model overpredicts gap flux, but confines the flux to an underpredicted area. The comparison between predicted, computed and measured forces does indicate improved agreement, but still significant discrepancies, as shown in Table B. The total flux crossing the air-gap is also compared between the circuit model and computations.

Studies were undertaken during the original development of ASPS to improve the accuracy of the circuit model by accounting for fringing and leakage path reluctances. Due to the difficulties and limited scope of this approach, the circuit model is now abandoned as a

viable, accurate tool in this case. Instead, further refinement of the finite element solution will be addressed.

TABLE B - Flux and forces per air-gap

	Total flux, Tm^2	Force, N
TOSCA, μ=1000	5.87e-4	44.47
Circuit model, $\mu \rightarrow \infty$	4.9e-4	58.2
Experimental, assuming rotor mass	*not available*	41.79

Once a basic finite element model has been established, the usual and proper procedure to establish a satisfactory confidence level in the results is to study the effects of variations of detail parameters within the model. The classic example is grid refinement, where a nearly stationary result with increasing refinement indicates that the grid is "sufficiently" fine. Here, this idea can be extended to introducing quadratic elements in critical regions, such as in and around the air-gap, and local refinement of the grid in regions of high field gradients. Further, a realistic BH curve can be invoked, the resulting solution being magnetically nonlinear. Typical results from these studies are shown in Table C. It is emphasized that the initial results from any finite element solution should be regarded with some scepticism. Studies of solution accuracy and realism are always a sensible investment of time and effort.

From a reliable solution, valuable qualitative design information is easily obtained, as illustrated in Figure 6. Here it is seen that the highest flux density in the magnetic circuit occurs at an interior corner of the flux return path. This corner should clearly be radiused to improve the linearity of the assembly close to overall saturation.

It should be noted that TOSCA is capable of solving problems with anisotropic materials. This capability is not, however, demonstrated here, since the ASPS core material is not laminated and is thought to be quite isotropic.

TABLE C - Flux at gap centroid

8008 linear elements, μ=1000	0.2385
8008 quadratic elements, μ=1000	0.2392
16,170 linear elements, μ=1000	0.23875
8008 linear elements, μ=mild steel	0.20587
8008 linear elements, μ=high grade steel	0.22677

MAGNETODYNAMIC CALCULATIONS - SMALL AIR-GAPS

A finite element model similar to that described above can be submitted to the ELEKTRA solver, for analysis of eddy currents induced in the iron cores by sinsusoidal currents in the electromagnets. Magnetically nonlinear or anisotropic problems are not presently soluble with ELEKTRA. Some care proved to be necessary to establish an effective combination of total, reduced and vector potentials. In this case, it was found to be necessary to "coat" the surface of the iron region with a layer of vector potential air, in order to improve the solution matrix conditioning in the presence of abrupt changes in magnetic and electrical properties at the iron-air interface. Establishing a valid configuration, favorable element

distributions, and the correct boundary conditions are practical problems that do require some familiarity with whichever codes are used, and a certain degree of skill and experience.

An effort to model, measure and compute the eddy current effects in the ASPS bearing stations has begun. Magnetic field in the air-gap is measured using a Hall-effect gaussmeter with the rotor locked in its datum position. Early experimental results indicate steadily falling magnetic field intensity in the air-gap and steadily increasing phase lag, as frequency is increased, as shown in Figure 7. The rate of roll-off is seen to be around 10 db/decade as suggested by application of classical theories [8,16,17,18]. There is also a strong indication of variations in relative amplitude and phase of the magnetic field across the air-gap, also shown in Figure 7. A typical eddy current distribution in the iron core is shown in Figure 8.

It should be noted that these computations require the specification of two material properties, namely magnetic permeability and electrical conductivity. Neither is easy to specify accurately for the nickel-iron alloy employed, partly due to the effect of heat-treatments. Since the observed break frequencies depend on the square-root of the product of these two parameters, this is seen to represent a significant practical problem.

Both computational and experimental results indicate an ASPS actuator bandwidth of perhaps 30 Hz. This happens to be well above the design system bandwidth of around 1 Hz, so is not a serious performance limitation. The low design value is due to the massive payloads envisioned (at least 600 kg for the original specifications, later increased).

MAGNETOSTATIC CALCULATIONS - LARGE AIR-GAPS

One of the earliest applications of the OPERA-3D suite of codes in this research was the computation of magnetic fields and field gradients in air, to permit the prediction of forces and moments on the suspended element in LAMSTF. Where the suspension coils are air-cored and the suspended element is a permanent magnet, no finite element solution is required. Instead, the field in air due to prescribed currents can be calculated directly by numerical integration of the Biot Savart law (by OPERA), to very high accuracy. When iron cores are present in the suspension coils, the magnetization must be determined as part of the solution. Extensive use has been made of VF/GFUN in this application. The integral equation approach used in VF/GFUN only requires the discretization of the iron regions and thus seems to be a more appropriate approach for this class of problem.

Computed fields have been compared to experimental measurements in a variety of cases. Typical agreement, such as shown in Figure 9, has been considered satisfactory, especially considering the considerable problems inherent in accurate experimental measurements of highly 3-dimensional fields. In fact, computations have often been regarded as more consistently reliable, particularly in estimating field gradients. Forces and moments on the suspended object can be calculated to good accuracy by integration of the Maxwell stress tensor on a control surface surrounding the object [5,9 etc.].

MAGNETODYNAMIC CALCULATIONS - LARGE AIR-GAPS

In the original design of LAMSTF, eddy-current circuits were deliberately introduced in three main areas: the position sensor structure, the electromagnet cores, and the aluminum baseplate. This was done so that it would be necessary to measure, analyze and model the eddy

current effects, rather than attempting to avoid their influence, as would have been the conventional practice. The fact that stable suspension was initially achieved rather easily was taken to indicate that the eddy current effects were not very significant. However, a consistent discrepancy was discovered in the dynamic behaviour in the "pitch" degree-of-freedom [7,13], when the metallic baseplate and sensor frame were used. This led to a careful analysis of the effects of eddy currents, which were subsequently confirmed to be the cause of the anomaly.

A typical result, relating to the eddy currents flowing in the position sensor ring is shown in Figure 10. Further results have been more fully described elsewhere [7,17]. Good agreement between experiment and computation is observed for simple geometries, but significant difficulties are encountered with more complex geometries.

DISCUSSION

No finite element code of this level of sophistication can be considered particularly easy to use by the novice. Potential users interested more in applications engineering than the codes themselves should exercise extreme care in interpretation of results and should be prepared to invest in training of some kind and experimental validation where possible. Further, the suite of codes employed here do lack certain desirable features. These include the ability to model hysteresis and the ability to model anisoptropic materials or rotational motion in magnetodynamic problems. Other commercially available codes have comparable weaknesses, although developments are proceeding at a rapid pace. It should be noted that currently available codes represent truly astounding advances in capability from anything available even a decade ago.

CONCLUSIONS

Contemporary software provides powerful tools for the analysis of magnetic fields, forces and moments, and eddy currents in magnetic suspensions and magnetic bearings. Results compare reasonably well to experimental measurements, provided care is exercised and accurate material properties are available.

ACKNOWLEDGEMENTS

This work was supported by NASA Langley Research Center under Grant NAG-1-1056. The Technical Monitor was Nelson J. Groom of the Guidance and Control Branch, Flight Dynamics and Control Division. The first author would also like to express gratitude to a number of graduate students who have contributed to this work, notably Mehran Ghofrani, Lucas Foster, Daniel Neff and Yan Yang.

REFERENCES

1. Schweitzer, G.; Bleuler, H.; Traxler, A.: Active Magnetic Bearings. vdf Hochschulverlag

AG, 1994
2. Moon, F.C.: Superconducting Levitation. Wiley, 1994
3. Knight, J.D.; Xia, Z.; McCaul, E.B.: Forces in Magnetic Journal Bearings: Nonlinear Computation and Experimental Measurement. 3rd International Symposium on Magnetic Bearings, Alexandria, VA, July 29-31, 1992.
4. Groom, N.J.; Britcher, C.P.: Open-Loop Characteristics of Magnetic Suspension Systems Using Electromagnets Mounted in Planar Arrays. NASA TP-3229, November 1992.
5. Britcher, C.P.: Large-gap Magnetic Suspension Systems. International Symposium on Magnetic Suspension Technology, August 1991, published as NASA CP-3152, 1992.
6. Kim, C.; Palazzolo, A.B.; Tang, P.; Manchala, D.; Kascak, A.; Brown, G.; Montague, G.; Klusman, S.: Field Lag Effects on the Vibrations of Active Magnetic Bearing Levitated Rotors. 4th International Symposium on Magnetic Bearings, Zurich, Switzerland, August 23-26, 1994.
7. Britcher, C.P.; Foster, L.: Some Further Developments in the Dynamic Modelling of the Large-Angle Magnetic Suspension Test Fixture. 2nd Int. Symposium on Magnetic Suspension Technology, Seattle, WA, Aug.1993. NASA CP-3247, May 1994.
8. Binns, K.J.; Lawrenson, P.J.; Trowbridge, C.W.: The Analysis and Computation of Electric and Magnetic Fields. Wiley, 1992.
9. Ida, N.; Bastos, J.P.A.: Electromagnetics and Calculation of Fields. Springer Verlag, 1992.
10. Allaire, P.E.; Rockwell, R.; Kasarda, M.E.F.: Magnetic and Electric Field Equations for Magnetic Bearing Applications. MAG'95, Alexandria, VA, August 10-11, 1995.
11. Britcher, C.P.; Groom, N.J.: Current and Future Development of the Annular Suspension and Pointing System, 4th International Symposium on Magnetic Bearings, ETH, Zurich, August 1994.
12. Neff, D.J.; Britcher, C.P.: Design and Implementation of a Digital Controller for a Vibration Isolation and Vernier Pointing System. 3rd International Symposium on Magnetic Suspension Technology, Tallahassee, FL, December 1995.
13. Britcher, C.P.; Ghofrani, M.: A Magnetic Suspension System with a Large Angular Range. Review of Scientific Instruments, Volume 64, No. 7, July 1993.
14. Cox, D.E.; Groom, N.J.; Implementation of a Decoupled Controller for a Magnetic Suspension System using Electromagnets Mounted in a Planar Array. 2nd International Symposium on Magnetic Suspension Technology, Seattle, WA, Aug.1993. NASA CP-3247, May 1994.
15. Lim, K.; Cox. D.E.: Robust Tracking Control of a Magnetically Suspended Rigid Body. 2nd International Symposium on Magnetic Suspension Technology, Seattle, WA, Aug.1993. NASA CP-3247, May 1994.
16. Zmood, R.B.; Anand, D.K.; Kirk, J.A.: The Influence of Eddy Currents on Magnetic Actuator Performance. IEEE Proceedings, Vol.75, No.2, February 1987.
17. Britcher, C.P.; Groom, N.J.: Eddy Current Computations Applied to Magnetic Suspensions and Magnetic Bearings. MAG'95, Alexandria, VA, August 1995.
18. Stoll, R.L.: The Analysis of Eddy Currents. Clarendon, 1974

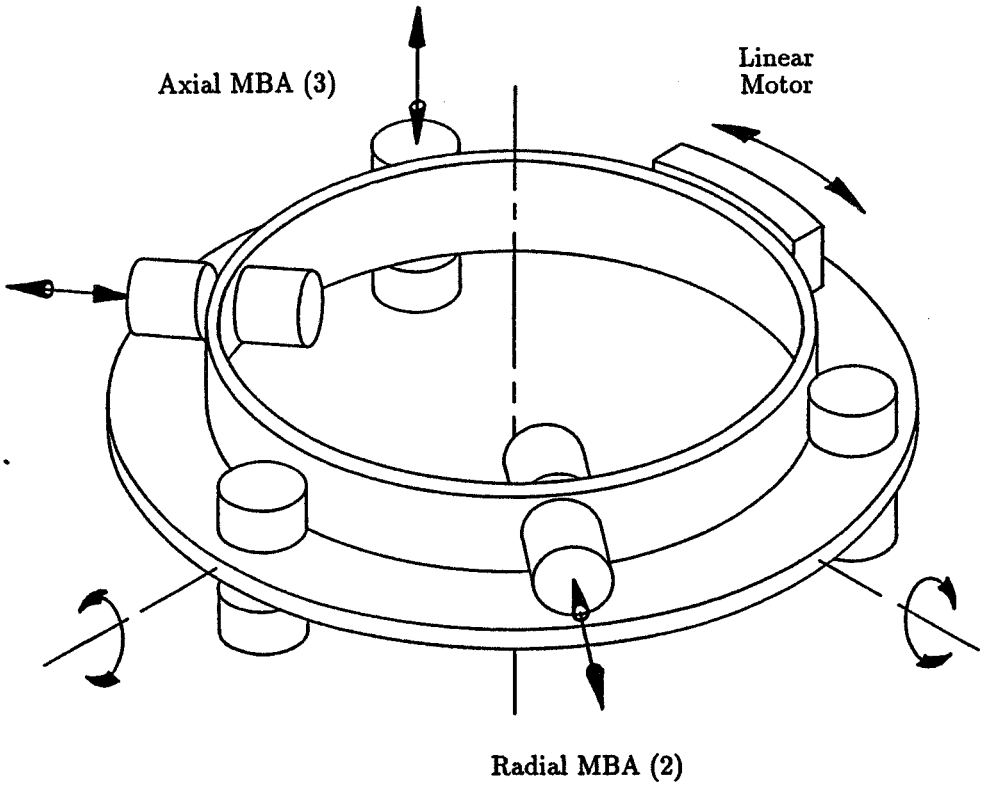

Figure 1 - Geometry of the Annular Suspension and Pointing System

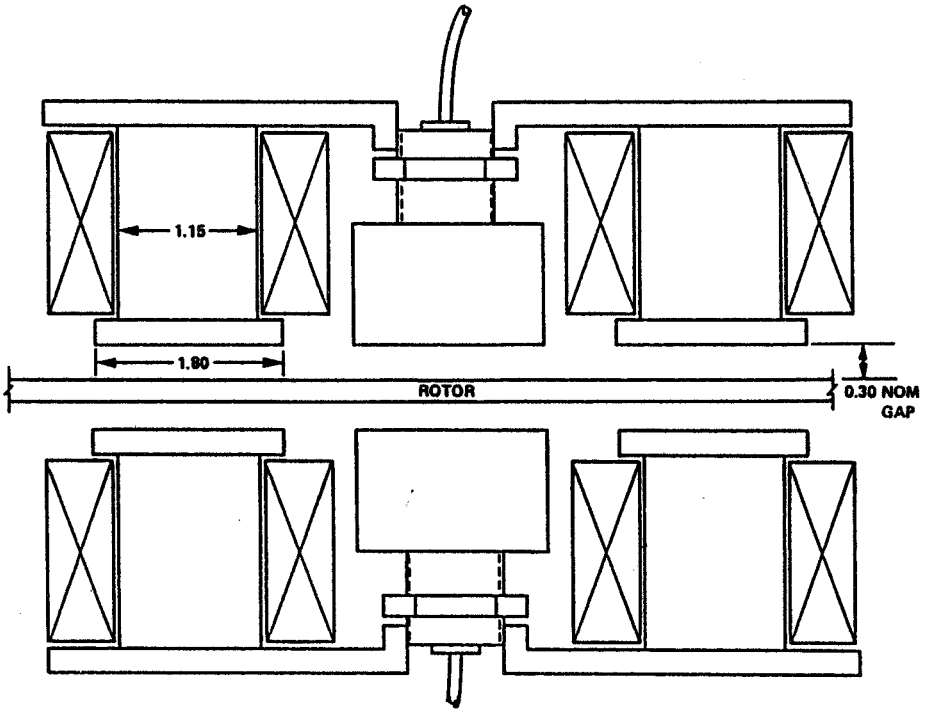

Figure 2 - ASPS Axial Bearing Station (dimensions in inches)

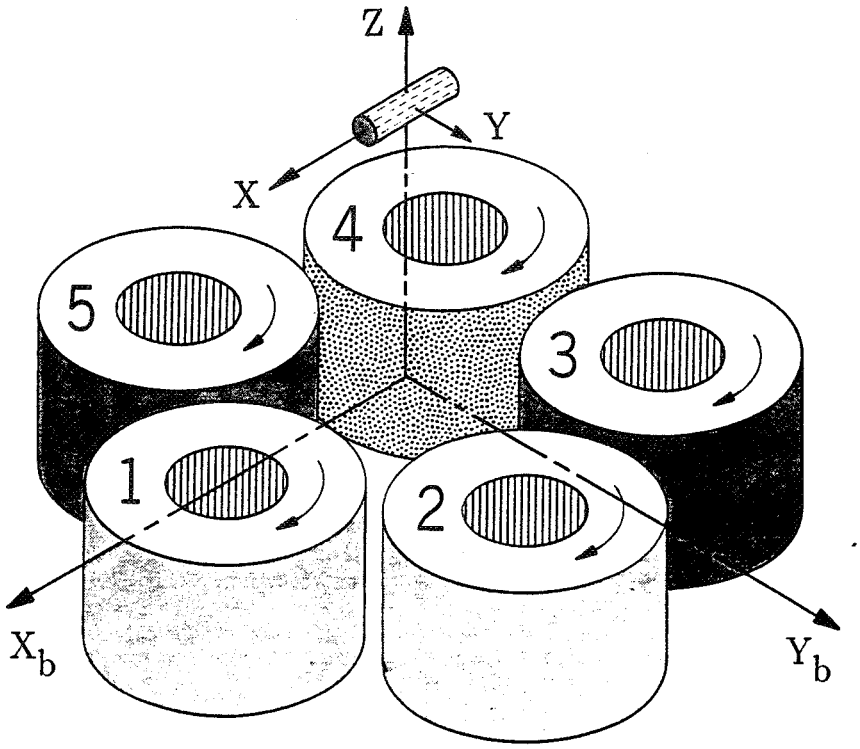

Figure 3 - General Arrangement of the Large Angle Magnetic Suspension Test Fixture

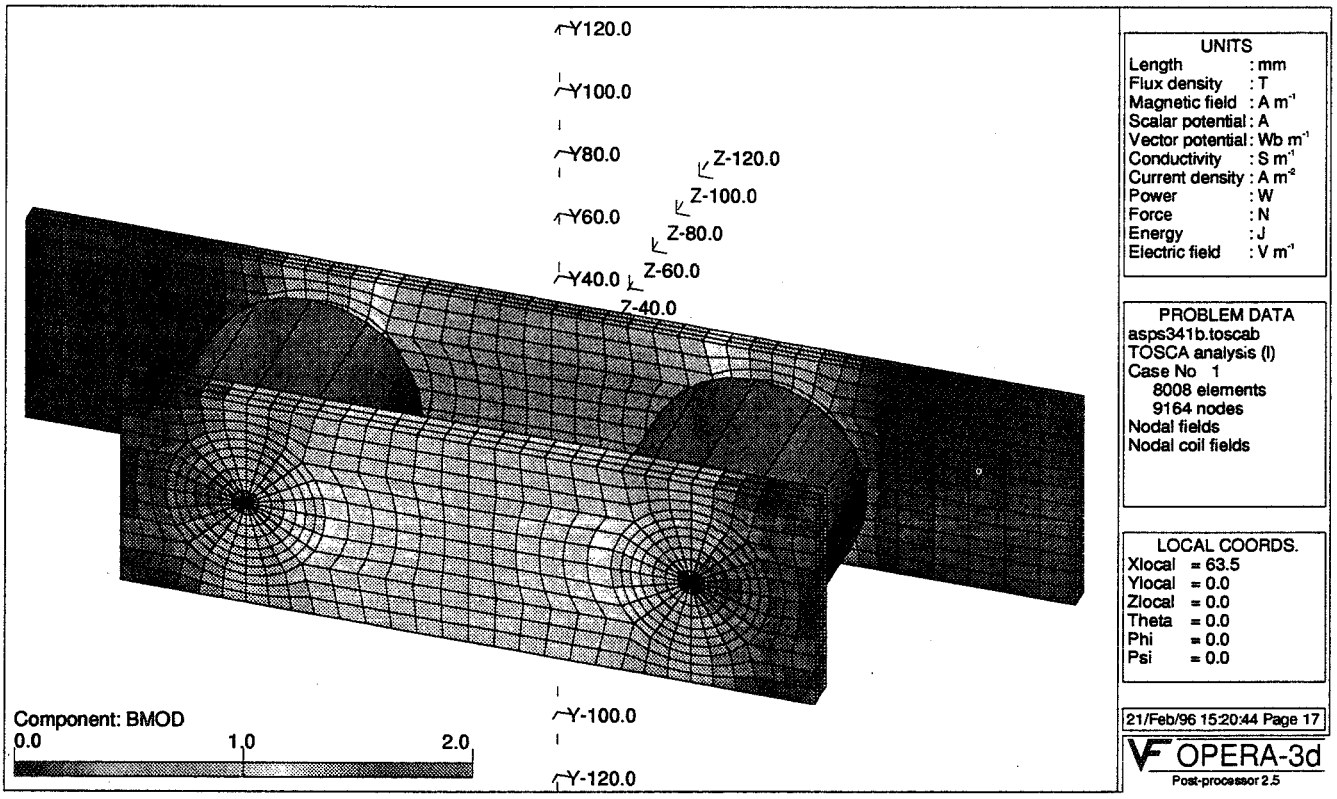

Figure 4 - ASPS Finite Element Model, with TOSCA Solution, μ_r=1000

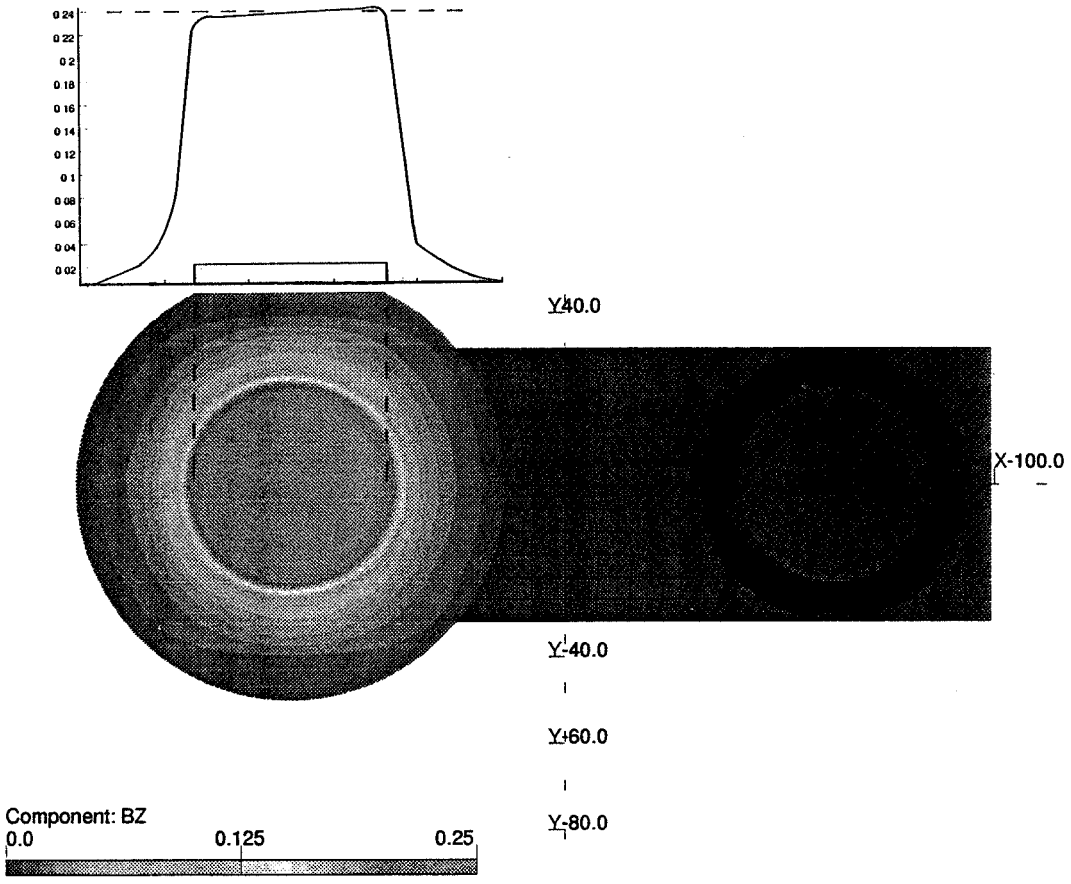

Figure 5 - Computed Magnetostatic Field in Air-Gap, showing flux fringing

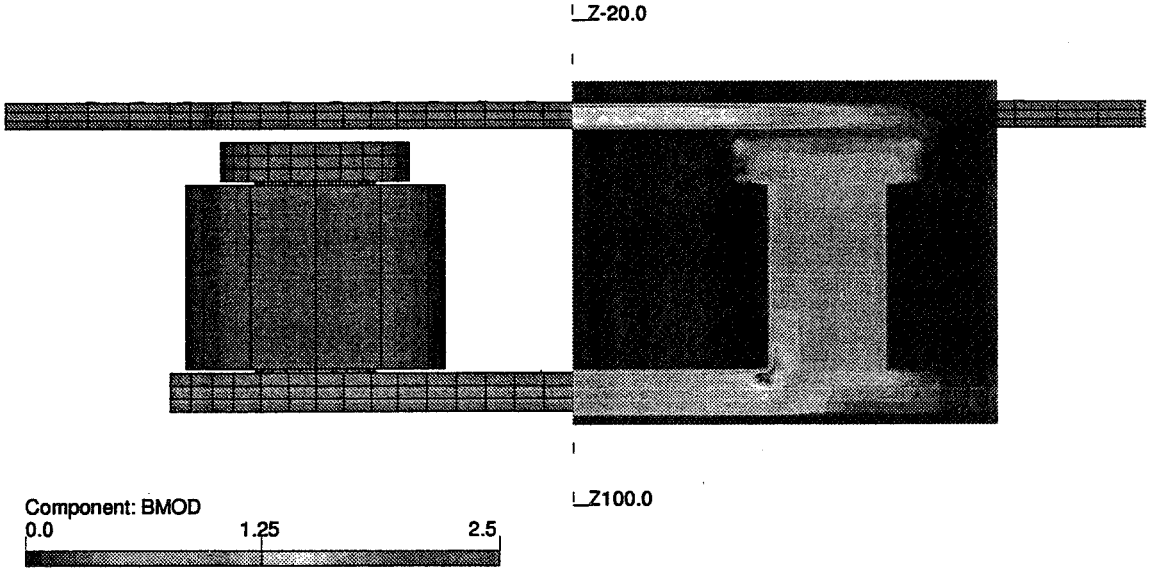

Figure 6 - Magnetic Flux in ASPS Iron Circuit

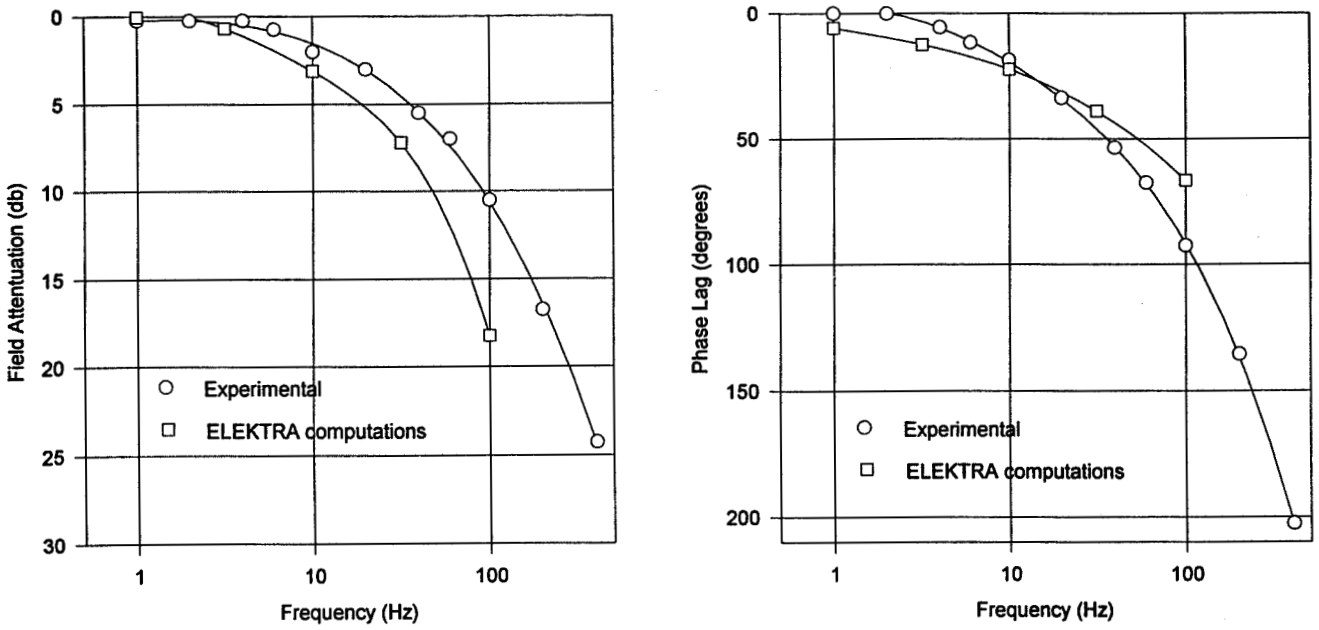

a) Measured and computed fields at gap centroid

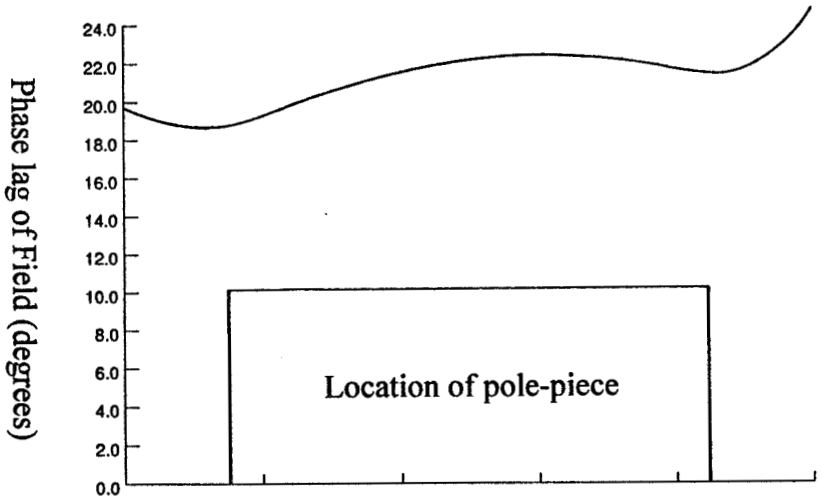

b) Computed phase variation across gap

Figure 7 - Magnetic Fields in the Air-Gap of an ASPS Bearing Station

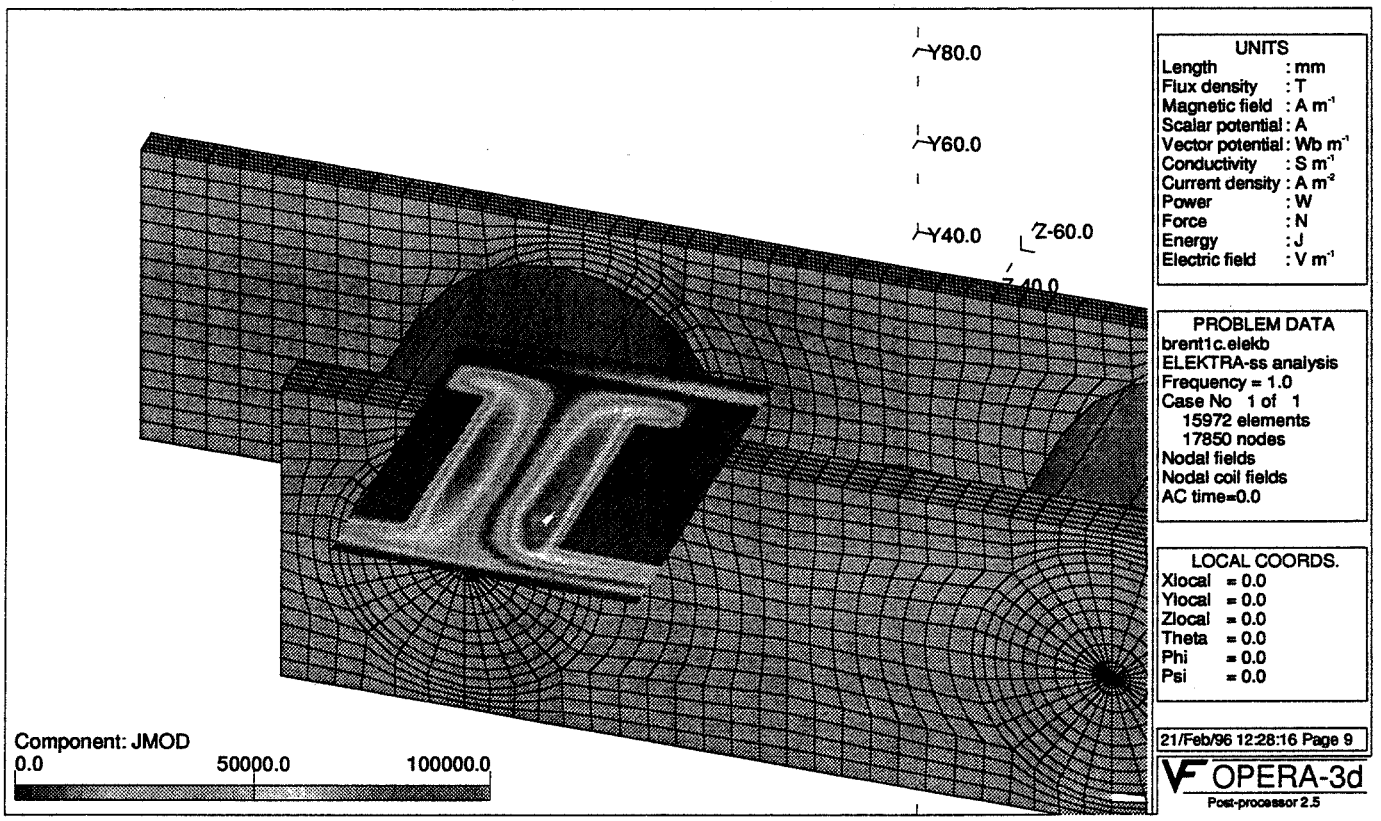

Figure 8 - Eddy Current in ASPS Iron Core

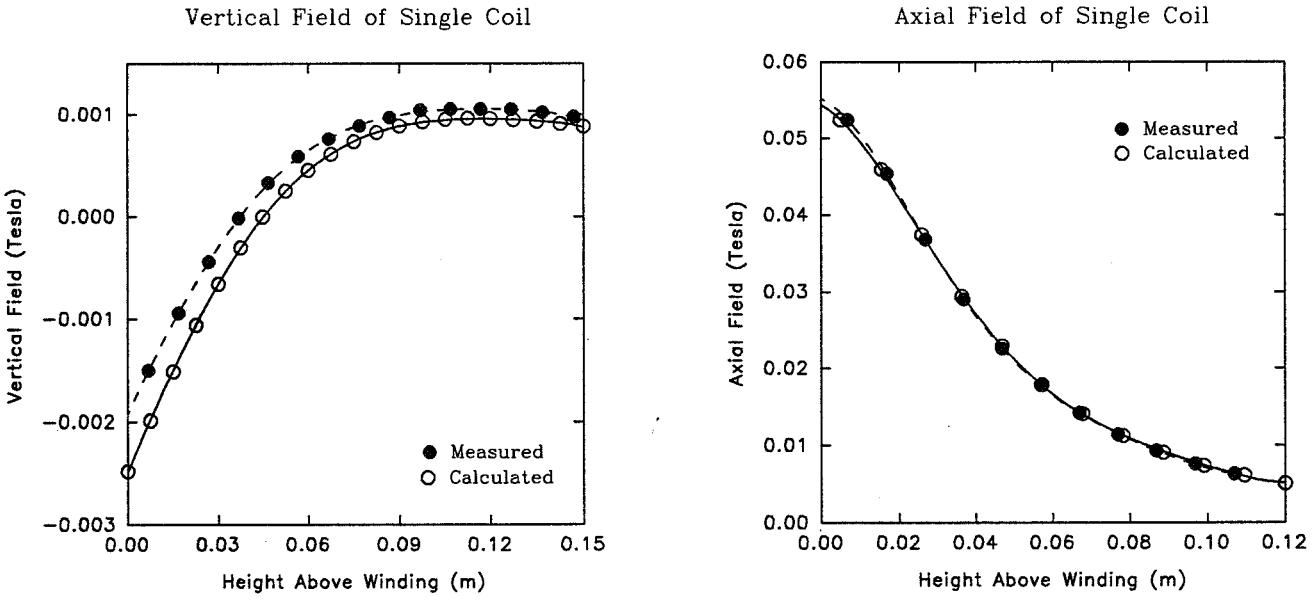

Figure 9 - Typical Air Fields from VF/GFUN

DYNAMICS OF PERMANENT-MAGNET BIASED ACTIVE MAGNETIC BEARINGS

Satoru Fukata
Department of Energy and Mechanical Engineering, Kyushu University
Fukuoka 812-81, Japan.

Kazuyuki Yutani
Graduate Student, Kyushu University
Fukuoka 812-81, Japan.

SUMMARY

Active magnetic radial bearings are constructed with a combination of permanent magnets to provide bias forces and electromagnets to generate control forces for the reduction of cost and the operating energy consumption. Ring-shaped permanent magnets with axial magnetization are attached to a shaft and share their magnet stators with the electromagnets. The magnet cores are made of solid iron for simplicity. A simplified magnetic circuit of the combined magnet system is analyzed with linear circuit theory by approximating the characteristics of permanent magnets with a linear relation. A linearized dynamical model of the control force is presented with the first-order approximation of the effects of eddy currents. Frequency responses of the rotor motion to disturbance inputs and the motion for impulsive forces are tested in the non-rotating state. The frequency responses are compared with numerical results. The decay of rotor speed due to magnetic braking is examined. The experimental results and the presented linearized model are similar to those of the all-electromagnetic design.

INTRODUCTION

Active magnetic bearings that consist of permanent magnets giving bias flux and electromagnets generating control flux have been considered for the reduction of the high cost and the running energy consumption in the all-electromagnetic design. Reference 1 reviewed works related to this subject, but only a few reports are available to the authors. A key to this subject is the construction of magnetic circuits of the combined magnet system. Allaire et al.[1] discussed the design, construction and testing of a set that have permanent magnets in the stators. They also presented an analysis of the magnetic circuits. Their construction may be advantageous in use at high speeds. In addition, it is possible to combine a radial bearing with a thrust bearing.[1] However, because the permanent-magnetic bias-flux is not canceled out by the electromagnetic flux, the control force may be restricted.

This paper considers another construction in which the permanent magnets are attached to a shaft and their magnet stators are all shared with the electromagnets. This construction has a feature that it is possible to cancel out the bias flux with the electromagnetic flux. This point is a property similar to the all-electromagnetic design. However, since the composition of the rotor becomes complicated, there may be some problems to the rigidity of the shaft and to the elaborate machining of the rotor. This magnetic composition seems similar to an all electromagnetic case consisting of two independent magnet coils that are wound around the same poles and are assigned the separate functions of bias and control.

The magnet cores of the experimental setup are made of solid iron for simplicity of manufacturing. A simplified magnetic circuit of the combined magnet system is analyzed with the linear circuit theory by approximating the characteristics of permanent magnets with a linear relation. A linearized dynamical model of the control force is presented with a first-order approximation of the effects of eddy currents. The control systems are designed with simple analog PID compensators. Frequency responses of the rotor motion to disturbance inputs and the motion for impulsive force are tested in the non-rotating state. The decay of rotor speed due to magnetic brake is examined. The frequency responses are compared with numerical results.

PERMANENT-MAGNET BIASED RADIAL MAGNETIC BEARINGS

Figure 1 shows the mechanical part of the experimental setup of five-axis-control magnetic bearing system supporting a symmetric rotor in the horizontal direction. The radial bearings are composed of permanent magnets (ferrite) for biasing and electromagnets for control. The permanent magnet rings with axial magnetization are attached to a shaft of aluminum and are held between two iron rings each. The electromagnets are constructed with a pair of magnet coils that are wound around the stators positioned on the radially opposing sides: the pair of magnet coils are connected in series and are driven by a single power amplifier. The magnet poles in the vertical direction are one-fourth wider than those in the horizontal direction to supply larger bias flux for the suspension of the dead weight of the rotor. Four displacement sensors of the eddy current type are used to measure the radial motion of the rotor. The magnet cores are made of solid iron for simplicity of manufacturing. The rotor mass is 0.90kg, the airgap length is about 0.5 mm and the diameter of the rotor core is 40mm. The primary data are given later in Table 1.

A thrust bearing is positioned in the center of the setup using an electromagnet in place of the permanent magnet, for simplicity. Two magnet coils are wound around the inner core of the stator, one is for biasing and the other for control. The two opposing magnet coils on the left and right sides of the disc (the rotor of the thrust bearing) are connected in series to give similar magnetic circuits to the radial bearing. The rotor rotation is provided by compressed air blown onto teeth on the edge of the disc.

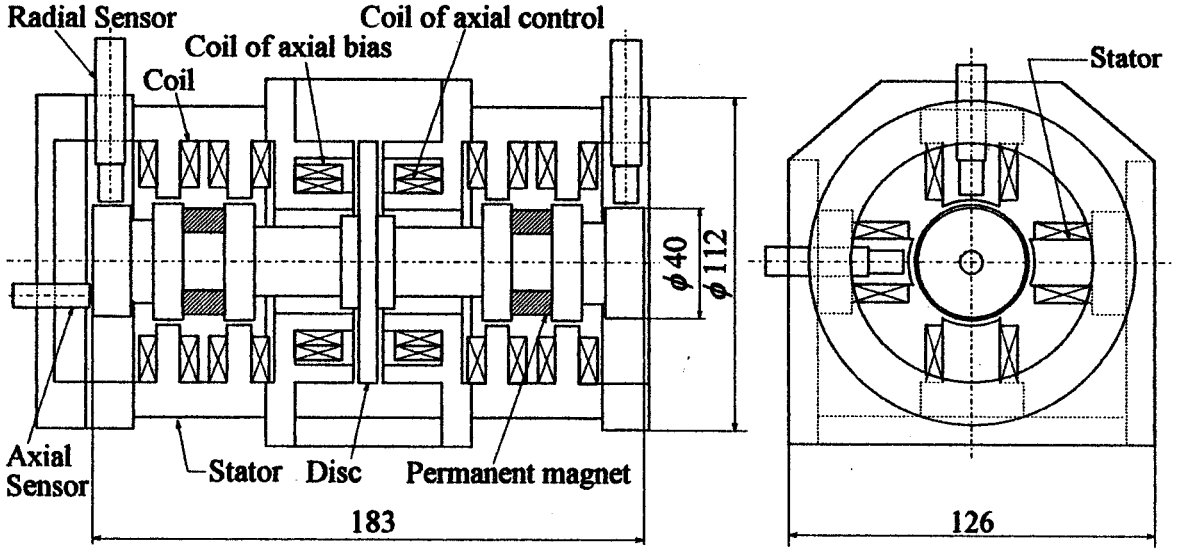

Figure 1. Construction of permanent-magnet biased magnetic bearing.

Figure 2 gives the magnetic flux paths of the radial bearing, neglecting leakage flux. The permanent magnetic flux, providing bias flux, flows radially in the iron-core ring and goes into the four poles of the stators through the airgaps, and passes through the stators along the axial direction to return to the rotor via the other airgaps. The electromagnetic flux generating from the upper and lower magnet coils passes down through the rotor along the radial direction on one side, and passes up through the other side. Thus, if the total flux increases in the lower side, then it decreases in the upper side. The difference of the flux produce a control force. With this construction, we can cancel out the bias flux with the electromagnetic flux. This is a point similar to the all-electromagnetic case. The configuration of the rotor, however, may be disadvantageous in use at high speeds, and there may be some problems in manufacturing the rotor.

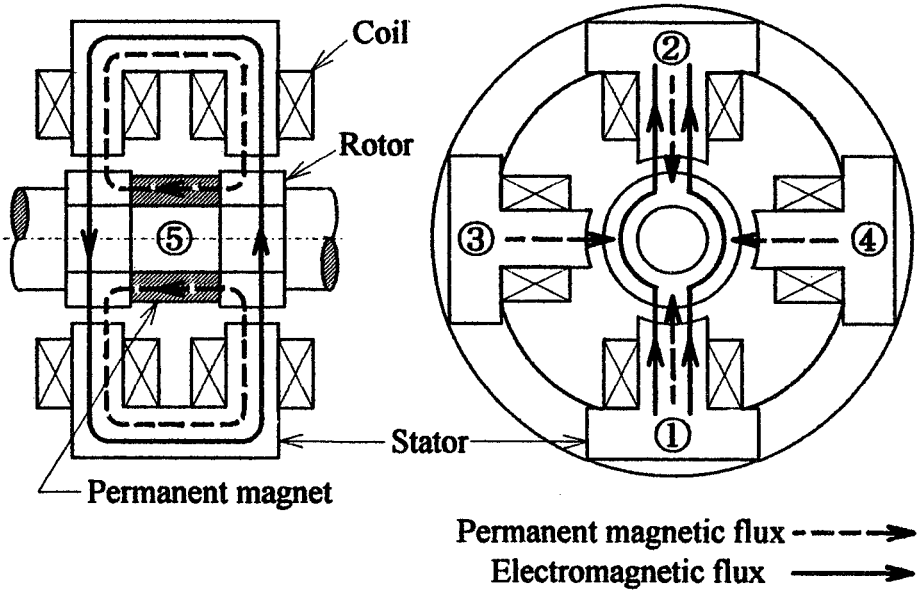

Figure 2. Magnetic flux paths of radial bearing.

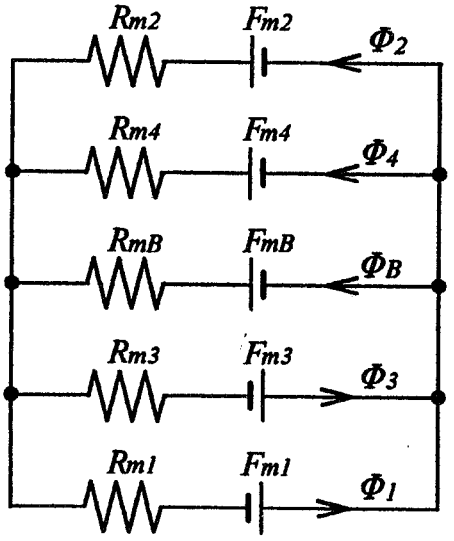

Figure 3. Simplified magnetic circuit.

ANALYSIS OF MAGNETIC SYSTEM

Magnetic Circuit of Radial Bearing

The characteristics of permanent magnets are considered based on the demagnetization curve. This curve may be quite linear for permanent magnets useful in practice such as ferrite magnets and rare-earth material magnets. Here, we approximate the demagnetization curve with a linear relation, using imaginary magnetomotive force and magnetic internal resistance. Then, as a model of the magnetic system of the radial bearing we consider the magnetic circuits in Fig. 3, where flux leakage is neglected. In the figure, F_{mj} is magnetomotive force, R_{mj} is magnetic resistance and Φ_j is magnetic flux associated with a stator numbered j in Fig. 2 and with the permanent magnet with B. The imaginary magnetomotive force F_{mB} and the magnetic internal resistance R_{mB} may be described as[2]

$$F_{mB} = l_m \frac{B_r}{\mu_r}, \qquad R_{mB} = \frac{l_m}{\mu_r A_m} \tag{1}$$

where B_r is the residual flux density, μ_r the recoil permeability, l_m, the thickness and A_m is the area. For this circuit we have the following relations.

$$\begin{aligned} F_{m1} + F_{m2} &= R_{m1}\Phi_1 + R_{m2}\Phi_2 \\ F_{m1} - F_{m3} &= R_{m1}\Phi_1 - R_{m3}\Phi_3 \\ F_{m1} + F_{m4} &= R_{m1}\Phi_1 + R_{m4}\Phi_4 \\ F_{m1} + F_{mB} &= R_{m1}\Phi_1 + R_{mB}\Phi_B \\ \Phi_1 &= \Phi_2 - \Phi_3 + \Phi_4 + \Phi_B \end{aligned} \tag{2}$$

The magnetic resistances are estimated by

$$R_{mj} = \frac{2l_{mj}}{\mu_0 A_j} \tag{3}$$

where l_{mj} is an equivalent airgap length considering the magnetic path in the magnet core, μ_0 is the permeability of air, and A_j is the area of a magnet pole. Then, from eq. (2) we obtain the relations

$$\begin{aligned} R_{m1}\Phi_1 &= F_{m1} - \Delta F_{12} - \Delta F_{34} + \alpha_B F_{mB} \\ R_{m2}\Phi_2 &= F_{m2} + \Delta F_{12} + \Delta F_{34} - \alpha_B F_{mB} \\ R_{m3}\Phi_3 &= -\Delta F_{12} + F_{m3} - \Delta F_{34} + \alpha_B F_{mB} \\ R_{m4}\Phi_4 &= \Delta F_{12} + F_{m4} + \Delta F_{34} - \alpha_B F_{mB} \\ R_{mB}\Phi_B &= \Delta F_{12} + \Delta F_{34} + (1-\alpha_B) F_{mB} \end{aligned} \tag{4}$$

where

$$\Delta F_{12} = \alpha_1 F_{m1} - \alpha_2 F_{m2}, \qquad \Delta F_{34} = \alpha_3 F_{m3} - \alpha_4 F_{m4}$$

$$\alpha_j = \frac{R_T}{R_{mj}}, \quad j = 1 \sim 4, B; \qquad \frac{1}{R_T} = \sum_{j=1}^{4,B} \frac{1}{R_{mj}}$$

In the following, we take the center of the bearing as the nominal position of the rotor, and in place of the flux we use variables defined by

$$Q_j = \frac{R_{m10}}{N}\Phi_j, \quad j = 1,2; \qquad Q_j = \frac{R_{m30}}{N}\Phi_j, \quad j = 3,4 \tag{5}$$

where R_{mjo} are the nominal magnetic resistances, and N is the coil turns that are all the same here. The variables have the same dynamical characteristics as the flux and the unit of current, and give coil currents if the eddy-current effects are negligible. The variable was introduced first to simplify the description of electromagnet systems,[3] and effectively used in modeling the systems with eddy-current effects.[4] Then, we rewrite eq. (4) as follows:

$$\begin{aligned} c_{m1}Q_1 &= (1-\alpha_1)f_{m1} + \alpha_2 f_{m2} - \bar{f}_{34} + Q_B \\ c_{m2}Q_2 &= \alpha_1 f_{m1} + (1-\alpha_2)f_{m2} + \bar{f}_{34} - Q_B \\ c_{m3}Q_3 &= -\bar{f}_{12} + (1-\alpha_3)f_{m3} + \alpha_4 f_{m4} + Q_B \\ c_{m4}Q_4 &= \bar{f}_{12} + \alpha_3 f_{m3} + (1-\alpha_4)f_{m4} - Q_B \\ c_{mB}Q_B &= \bar{f}_{12} + \bar{f}_{34} + (1-\alpha_B)f_{mB} \end{aligned} \tag{6}$$

where

$$c_{mj} = \frac{R_{mj}}{R_{mj0}}, \quad f_{mj} = \frac{F_{mj}}{N}, \quad j = 1,2,3,4,B$$

$$Q_B = \alpha_B (F_{mB}/N)$$

$$\bar{f}_{12} = \alpha_1 f_{m1} - \alpha_2 f_{m2}, \quad \bar{f}_{34} = \alpha_3 f_{m3} - \alpha_4 f_{m4}$$

We refer the initial steady-state values with subscript 0. In the steady state without initial load in the horizontal direction, we have

$$\begin{aligned} Q_{10} &= I_{10} + Q_B, \quad Q_{20} = I_{10} - Q_B, \\ Q_{30} &= -Q_{40} = Q_B, \\ f_{m10} &= f_{m20} = I_{10}, \quad f_{m30} = f_{m40} = I_{30} = 0 \end{aligned} \tag{7}$$

In the following, we assume that
(1) The displacement of the rotor is sufficiently small.
(2) The incremental magnetic flux is sufficiently small.
We consider the increments

$$\begin{aligned} q_j &= Q_j - Q_{j0}, \quad \Delta f_{mj} = f_{mj} - f_{mj0}, \\ \Delta\alpha_j &= \alpha_j - \alpha_{j0} \end{aligned} \tag{8}$$

We write the magnetic resistance as

$$\begin{aligned} R_{m1} &= R_{m10}(1+k_{m1}), \quad R_{m2} = R_{m10}(1-k_{m1}), \\ R_{m3} &= R_{m30}(1+k_{m3}), \quad R_{m4} = R_{m30}(1-k_{m3}) \end{aligned} \tag{9}$$

where k_{mj} is the relative variation of the magnetic resistance. Then, the parallel magnetic resistance R_T defined under eq. (4), is expressed as

$$R_T \cong R_{T0}\left[1 - 2\left(\alpha_{10}{k_{m1}}^2 + \alpha_{30}{k_{m3}}^2\right)\right] \cong R_{T0} \tag{10}$$

where α_{10} and α_{30} are the nominal values. This implies that the parallel resistance is nearly constant under the assumption (1). This gives the increments of α_j as follows:

$$-\Delta\alpha_1 = \Delta\alpha_2 = \alpha_{T10}k_{m1}, \quad -\Delta\alpha_3 = \Delta\alpha_4 = \alpha_{30}k_{m3} \tag{11}$$

Substituting eq. (11) into the incremental equations of eq. (6), and neglecting the second-order terms of the increments, we obtain the following relations.

$$q_1 + Q_{10}' k_{m1} = (1-\alpha_{10})\Delta f_{m1} + \alpha_{10}\Delta f_{m2} - \alpha_{30}\Delta f_{m34},$$
$$q_2 + Q_{20}' k_{m1} = \alpha_{10}\Delta f_{m1} + (1-\alpha_{10})\Delta f_{m2} + \alpha_{30}\Delta f_{m34} \quad (12)$$
$$q_3 + Q_B k_{m3} = (1-\alpha_{30})\Delta f_{m3} + \alpha_{30}\Delta f_{m4} - \alpha_{10}\Delta f_{12},$$
$$q_4 + Q_B k_{m3} = \alpha_{30}\Delta f_{m3} + (1-\alpha_{30})\Delta f_{m4} + \alpha_{10}\Delta f_{12} \quad (13)$$

where

$$Q_{10}' = Q_{10} - 2\alpha_{10} I_{10} = (1-2\alpha_{10})I_{10} + Q_B,$$
$$Q_{20}' = -Q_{20} + 2\alpha_{10} I_{10} = -(1-2\alpha_{20})I_{10} + Q_B \quad (14)$$
$$\Delta f_{12} = \Delta f_{m12} - 2I_{10} k_{m1}, \quad \Delta f_{m12} = \Delta f_{m1} - \Delta f_{m2},$$
$$\Delta f_{m34} = f_{m3} - f_{m4} \quad (15)$$

Dynamical Linearized Equation of Incremental Flux

We discuss the vertical direction whose special case gives the results of the horizontal direction. We apply a model presented in Reference 3, considering the first-order effect of eddy currents. This model describes the electric and magnetic coupling system composed of the two stator-coils in series as

$$V_1 = R_{12} I_1 + N(\dot{\Phi}_1 + \dot{\Phi}_2) \quad (16)$$
$$\left(R_e i_e + L_e \dot{i}_e + N\dot{\Phi}\right)_j = 0, \quad \left(R_L i_L + N\dot{\Phi}\right)_j = 0, \quad j = 1,2 \quad (17)$$
$$F_{mj}/N = f_{mj} = I_1 + (i_e + i_L)_j, \quad j = 1,2 \quad (18)$$

where V_1, R_{12} and I_1 are the input voltage, resistance and current of the magnet coil; i_{ej} and i_{Lj} are the eddy currents in the magnet cores, R_{e1} $(= R_{e2})$ and R_{L1} $(= R_{L2})$ are the resistances, and L_{e1} $(= L_{e2})$ is the inductance of the equivalent eddy current loop; F_{mj} are the magnetomotive forces. Here, we take the coil current positive when it increases the flux in the stator 1 (in the lower side). For a power amplifier with output current control, we suppose that the input voltage is expressed as

$$V_1 = p(b' E_1 - I_1) \quad (19)$$

where E_1 is an input voltage to the amplifier, p is the control loop gain, and b' is a constant. In this case, eq. (16) is replaced by

$$pb' E_1 = (p + R_{12})I_1 + N(\dot{\Phi}_1 + \dot{\Phi}_2) \quad (20)$$

Using the variables defined by eq. (5) simplifies eqs. (17) and (19) as follows:

$$I_1 = b_1 E_1 - T_{R1}(\dot{Q}_1 + \dot{Q}_2) \quad (21)$$
$$\left(i_e + T_e \dot{i}_e\right)_j = -T_{0ej}\dot{Q}_j, \quad i_{Lj} = -T_{0Lj}\dot{Q}_j, \quad j = 1,2 \quad (22)$$

where

$$b_1 = \left(\frac{p}{p+R_{12}}b'\right)_1, \quad T_{R1} = \frac{L_{10}}{(p+R_{12})_1}, \quad L_{10} = \frac{N^2}{R_{m10}},$$

$$T_{0e1} = \frac{L_{10}}{R_{e1}}, \quad T_{0L1} = \frac{L_{10}}{R_{L1}}, \quad T_{e1} = \frac{L_{e1}}{R_{e1}} \tag{23}$$

Eliminating I_1, i_{ej} and i_{Lj} from eqs. (18), (21) and (22), we obtain the following equations.

$$\begin{aligned} T_{e1}\dot{f}_{m1} + f_{m1} &= b_1\left(T_{e1}\dot{E}_1 + E_1\right) - T_{21}\ddot{Q}_1 - T_{11}\dot{Q}_1 - T_{R1}\left(T_{e1}\ddot{Q}_2 + \dot{Q}_2\right), \\ T_{e1}\dot{f}_{m2} + f_{m2} &= b_1\left(T_{e1}\dot{E}_1 + E_1\right) - T_{21}\ddot{Q}_2 - T_{11}\dot{Q}_2 - T_{R1}\left(T_{e1}\ddot{Q}_1 + \dot{Q}_1\right) \end{aligned} \tag{24}$$

where

$$T_{21} = \left(T_R + T_{0L}\right)_1 T_{e1}, \qquad T_{11} = \left(T_R + T_{0L} + T_{0e}\right)_1$$

The interacting magnetomotive forces in eqs. (12) and (13), Δf_{m12} and Δf_{m34}, which are zero if there is no effect of eddy currents, make the analysis quite complicated. We suppose that these influences are secondary, and we will make a rough approximation. From the incremental relations of eq. (24), we have

$$\begin{aligned} T_{e1}\Delta\dot{f}_{m12} + \Delta f_{m12} &= -T_{0L1}T_{e1}\dddot{\bar{q}}_{12} - T_{0Le1}\ddot{\bar{q}}_{12}, \qquad \bar{q}_{12} = q_1 - q_2, \\ T_{0Le1} &= T_{0L1} + T_{0e1} \end{aligned} \tag{25}$$

This relation suggests that the interactions are dynamical, i.e. statically zero. On the other hand, eqs. (12) and (13) give the relations

$$\begin{aligned} \bar{q}_{12} &= -\bar{Q}_{12}'\,k_{m1} + (1-2\alpha_{10})\Delta f_{m12} - 2\alpha_{30}\Delta f_{m34}, \\ \bar{q}_{34} &= 4\alpha_{10}I_{10}k_{m1} + (1-2\alpha_{30})\Delta f_{m34} - 2\alpha_{10}\Delta f_{m12}, \qquad \bar{q}_{34} = q_3 - q_4 \end{aligned} \tag{26}$$

where

$$\bar{Q}_{12}' = Q_{10}' - Q_{20}' = 2(1-2\alpha_{10})I_{10}$$

Substituting eq. (26) into eq. (25) and a similar equation of Δf_{m34}, and taking the lowest derivative terms of the variables, we have the approximation

$$\begin{aligned} \Delta f_{m12} &= \bar{Q}_{12}'\,T_{0Le1}\dot{k}_{m1}, \\ \Delta f_{m34} &= -4\alpha_{10}I_{10}T_{0Le3}\dot{k}_{m1} \end{aligned} \tag{27}$$

We eliminate Δf_{m1} and Δf_{m2} from eq. (12) with (27) for Δf_{m34} and the incremental equations of eq. (24). Since the results have higher derivatives of k_{m1} and are so complicated, we neglect the higher derivatives than the first. Thus, we obtain the following results.

$$\begin{aligned} \tilde{T}_{21}\ddot{q}_1 + \tilde{T}_{11}\dot{q}_1 + q_1 + \left(\gamma_1 + Q_{10}'\,T_{e1}\right)\dot{k}_{m1} + Q_{10}'\,k_{m1} &= b_1\left(T_{e1}\dot{e}_1 + e_1\right), \\ \tilde{T}_{21}\ddot{q}_2 + \tilde{T}_{11}\dot{q}_2 + q_2 + \left(-\gamma_1 + Q_{20}'\,T_{e1}\right)\dot{k}_{m1} + Q_{20}'\,k_{m1} &= b_1\left(T_{e1}\dot{e}_1 + e_1\right) \end{aligned} \tag{28}$$

where

$$\begin{aligned} \tilde{T}_{21} &= \left(2T_{R1} + T_{0L1}\right)T_{e1}, \qquad \tilde{T}_{11} = 2T_{R1} + T_{0L1} + T_{0e1} + T_{e1}, \\ \gamma_1 &= 2I_{10}\left[(1-2\alpha_{10})T_{R1}' - 2\alpha_{10}\alpha_{30}T_{0Le3}\right], \qquad T_{R1}' = T_{R1} + \alpha_{10}(T_{0L1} + T_{0e1}) \end{aligned} \tag{29}$$

The time constants $\tilde{T}_{21}$ and $\tilde{T}_{11}$ are the same values that are given when we take the two opposing stator-coils to be one. This natural fact is easily confirmed with the definition of the time constants in eq. (23). Thus, the above results are similar to those of the all-electromagnetic cases,

except for the term with γ_1. This term appears without eddy current effect. We can see that its first term with T_{R1}' results from the effect of the opposite-side stator-coil system with a bias current. We note that this term is reduced by the second term that is due to the interaction from the horizontal direction.

Similar equations are derived for the horizontal direction, but it may be simpler to take another way. Adding the two equations of eq. (13) gives the equation without interaction to the summing variable as

$$2q_{30} + 2Q_B k_{m3} = \Delta f_{m3} + \Delta f_{m4}, \quad 2q_{30} = q_3 + q_4 \tag{30}$$

Then, using relations similar to the incremental form of eq. (24), we have

$$\tilde{T}_{23}\ddot{q}_{30} + \tilde{T}_{13}\dot{q}_{30} + q_{30} + Q_B\left(T_{e3}\dot{k}_{m3} + k_{m3}\right) = b_3\left(T_{e3}\dot{e}_3 + e_3\right) \tag{31}$$

In a similar way, the difference variable $\bar{q}_{34}$, with Δf_{m12} in eq. (27) we obtain the approximated equation

$$(1-2\alpha_{30})T_{0L3}T_{e3}\dddot{\bar{q}}_{34} + \left[(1-2\alpha_{30})T_{0Le3} + T_{e3}\right]\ddot{\bar{q}}_{34} + \dot{\bar{q}}_{34} + \bar{q}_{34} = 4\alpha_{10}I_{10}\left\{\left[T_{e3} - (1-2\alpha_{10})T_{0Le1}\right]\dot{k}_{m1} + k_{m1}\right\} \tag{32}$$

Then, we have the expression of the decoupled form

$$q_3 = q_{30} + \bar{q}_{34}/2, \quad q_4 = q_{30} - \bar{q}_{34}/2 \tag{33}$$

Similar to the case in the vertical direction, the interaction due to the term Δf_{m12} reduces the effect of $\dot{k}_{m1}$.

The above results suggest that the interactions are primarily due to the bias current combined with the airgap variation in the biasing direction, and that this interaction into the horizontal direction becomes smaller at higher frequencies. The results become quite simple in the case of laminated magnet cores.

We will obtain the time constants in eqs. (28) and (31), experimentally, because it is difficult to estimate theoretically the time constants of the eddy current effects, defined in eq. (23). For the fixed airgap of the nominal length ($\dot{k}_{m1} = k_{m1} = 0$), we write eq. (28) with the parallel combination of two first-order time-lag systems, using the Laplace transforms, as

$$\frac{Q(s)}{bE(s)} = \frac{T_e s + 1}{\tilde{T}_2 s^2 + \tilde{T}_1 s + 1} = \frac{k_1}{T_1 s + 1} + \frac{1 - k_1}{T_2 s + 1} \tag{34}$$

where we omitted the subscript 1, and where

$$\tilde{T}_2 = T_1 T_2, \quad \tilde{T}_1 = T_1 + T_2, \quad T_e = (1-k_1)T_1 + k_1 T_2 \tag{35}$$

To give γ_1, the other time-constants, T_{0L1} and T_{0e1}, are calculated from these results and the theoretical value of T_{R1} with the relations in eqs. (29).

LINEARIZED EQUATIONS OF ROTOR MOTION

Linearized Equation of Control Force

The magnetic force acting between two pole faces with the magnetic flux Φ may be expressed as $F = (A_h / 2\mu_0)(\Phi / A)^2$, where A is the area of the pole face and A_h is its projected area on the plane perpendicular to the sense of the force. Applying this to the two poles with the same face area and using the variables of eq. (5), we have the resultant magnetic force acting on the rotor on the opposing sides as

$$F_{12} = c_{F1}\left(Q_1^{\,2} - Q_2^{\,2}\right), \quad c_{F1} = \frac{\mu_0 A_h}{4}\left(\frac{N}{l_{m10}}\right)^2 \tag{36}$$

Then, the net force is given by

$$\Delta F_{12} = F_{12} - F_{120} = f_1 + c_{F1}\left(q_1^{\,2} - q_2^{\,2}\right) \tag{37}$$

with the first-incremental force

$$f_1 = (k_{F1}/2)(q_1 + c_{Q1} q_2) \tag{38}$$

where

$$k_{F1} = 4c_{F1}Q_{10} = 4\frac{F_{10}}{Q_{10}}, \qquad c_{Q1} = \frac{-Q_{20}}{Q_{10}} \ (>0) \tag{39}$$

When the rotor approaches stator 1 with displacement z, the relative variation of the magnetic resistance, k_{m1}, may be approximated under the assumption (1) as

$$k_{m1} \cong -\frac{z}{l_{m10}} \tag{40}$$

Using eqs. (28) with this relation, and replacing $(q_1 + c_{Q1}q_2)/2$ by a new variable q_1, we write eq. (31) with the dynamical form as follows:

$$f_1 = k_{F1} q_1, \qquad \tilde{T}_{21}\ddot{q}_1 + \tilde{T}_{11}\dot{q}_1 + q_1 - a_{11}\dot{z} - a_{01} z = \beta_1 b_1 (T_{e1}\dot{e}_1 + e_1) \tag{41}$$

where

$$a_{11} = a_{01}\left(\tilde{T}_{R1}' + T_{e1}\right), \qquad a_{01} = \frac{Q_{10}'}{2l_{m10}}\left(1 + c_{Q1}c_{Q1}'\right),$$

$$\beta_1 = \frac{1}{2}\left(1 + c_{Q1}\right), \qquad c_{Q1}' = \frac{Q_{20}'}{Q_{10}'}, \tag{42}$$

$$\tilde{T}_{R1}' = \frac{(1 - c_{Q1})(1 - c_{Q1}')}{1 + c_{Q1}c_{Q1}'}\left(T_{R1}' - \tau_{0Le3}'\right), \qquad \tau_{0Le3}' = \frac{2\alpha_{10}}{1 - 2\alpha_{10}}\alpha_{30} T_{0Le3},$$

For the horizontal force, the result is directly obtained by application of eq. (31) to eq. (38) with $c_{Q1} = 1$ as follows:

$$f_3 = k_{F3} q_3, \qquad \tilde{T}_{23}\ddot{q}_3 + \tilde{T}_{13}\dot{q}_3 + q_3 - \frac{Q_B}{l_{m30}}\left(T_{e3}\dot{y} + y\right) = b_3\left(T_{e3}\dot{e}_3 + e_3\right) \tag{43}$$

where y is the displacement toward stator 3.

The above results are almost all the same as those of the all-electromagnetic case,[4] if we regard the equivalent bias flux Q_B as an equivalent bias current. The term with $\tilde{T}_{R1}'$ is inherent in the magnet system consisting of two opposing stator-coils with bias current. We see through the derivation that the interaction appears separately on each of the two opposing sides, but that their resultant effect becomes smaller, and is canceled out in the horizontal direction. In this way, our analysis may seem to be a waste of labor and space. The analysis, however, gives a deeper understanding of the phenomena, and shows the complexity of the magnetic system.

Linearized Equations of Rotor Motion

The radial position of the rotor is controlled by the resultant forces and resultant moments of the incremental forces in the two bearings. We number the bearings 1 and 2 on the left and right sides, respectively, and use these numbers in the subscript of the variables if necessary, for simplicity. We take the sense of the rotor displacement to be positive when going down, as in the above, and the sense of the conical motion to be positive when going down more in bearing 1 than in bearing 2. We rewrite the conical motions with the equivalent displacements at the bearing,[5] for convenience, and neglect the interactions due to the gyroscopic effects. Applying eq. (41) to the two radial bearings having the same characteristics and supporting a symmetric rotor, we obtain the linearized equations that are similar in form each other, for the rigid-rotor motion in the vertical direction, as follows:

Translatory motion:

$$m\ddot{z} = k_{F1}q_z + d_z,$$
$$\tilde{T}_{21}\ddot{q}_z + \tilde{T}_{11}\dot{q}_z + q_z - a_{11}\dot{z} - a_{01}z = \beta_1 b_1\left(T_{e1}\dot{e}_z + e_z\right) \tag{44}$$

Conical motion:

$$m_C\ddot{z}_C = k_{F1}q_{zC} + d_{zC},$$
$$\tilde{T}_{21}\ddot{q}_{zC} + \tilde{T}_{11}\dot{q}_{zC} + q_{zC} - a_{11}\dot{z}_C - a_{01}z_C = \beta_1 b_1\left(T_{e1}\dot{e}_{zC} + e_{zC}\right) \tag{45}$$

where d_z is disturbance force, and m_c and d_{zC} are the equivalent mass and force of the conical motion.[5] The control variables e_z and e_{zC} are related to the actual control inputs as

$$2e_z = e_{11} + e_{21}, \qquad 2e_{zC} = e_{11} - e_{21} \tag{46}$$

If the control variables are given, then the inputs, e_{11} on the left side and e_{21} on the right side, are determined by

$$e_{11} = e_z + e_{zC}, \qquad e_{21} = e_z - e_{zC} \tag{47}$$

Similar equations of the horizontal direction are obtained with $c_{Q1} = c_{Q1}' = 1$ in the above results.

EXPERIMENTAL AND NUMERICAL RESULTS

The primary data of the experimental setup are shown in Table 1. We mounted the setup by pressing on to a block of modelling clay. Experimental data are obtained in the non-rotating state except for the decay of rotation. We will show the results in the vertical direction; similar results are obtained in the horizontal direction.

Table 1 Data of Setup

Rotor		
Mass (PM contained)	$m = 0.90$	kg
Diameter	$D = 40.0\times10^{-3}$	m
Moment of inertia of conical motion	$J = 2.31\times10^{-3}$	kgm^2
Polar moment of inertia	$J_P = 3.51\times10^{-4}$	kgm^2
Distance between bearing centers	$l_1 = 111\times10^{-3}$	m
Distance between two gap-sensors	$l_2 = 174\times10^{-3}$	m
Stator (Radial)		
Magnet coil: Turns	$N = 200$	Turns
Resistance	$R = 0.62$	Ω
Area of pole face (Vertical)	$A_V = 1.60\times10^{-4}$	m^2
Area of pole face (Horizontal)	$A_H = 1.28\times10^{-4}$	m^2
Air gap length	$l_0 = 0.5\times10^{-3}$	m
Thrust bearing		
Bias coil : Turns	$N = 100$	Turns
Bias current	$I_0 = 1.0$	A
Control coil: Turns	$N = 100$	Turns

Magnetic Characteristics

It is difficult to theoretically estimate the time constants of our model. We examine the dynamical generation of the incremental flux by obtaining its frequency response to an input into the power amplifier. The generating voltage in a search coil gives the frequency response of the rate of the flux. We have the response of the flux by numerically multiplying $1/j\omega$ to this result represented in complex number, where j is the complex factor and ω is an angular frequency. The result measured with a 4-turn search coil is shown in Fig. 4 by the solid lines in the vertical direction, for the fixed airgap length of 0.5mm and the non-biasing input of the amplitude corresponding to the coil current of 0.38A statically. The phase in low frequencies is considered to be incorrect (the authors guess this is due to FFT analysis in the analyzer). The response has a characteristic that the phase lag in higher frequencies is small compared with the decay of the gain. We may understand this result with a first-order time-lag model in such a way that the increase in the magnetic resistance, due to the eddy current effects, decreases the incremental flux, but reduces the time constant that is inversely proportional to the resistance: the ratio of the inductance to the resistance.

To approximate the characteristics, we apply the model of eq. (34), and try curve fitting by selecting the two time constants and the weighting. The fitness depends on the range because of the low-order model. A result is shown in Fig. 4 by the broken lines; with this curve, we have T_1 = 0.17ms, T_2 = 1.88ms and k_1 = 0.40. The static gain of -84.4dB is given by the theoretical value

calculated with $b_1 = 0.36$ and $l_{m0} = 1.05$ x (airgap length) without flux leakage nor fringing effect. The lines zigzag through the experimental results, and may be unsatisfactory: the gain is larger in frequencies of about 15 to 100Hz, and the phase lag is smaller as a whole; however it seems difficult to have much more improvement. A similar result was obtained in the all-electromagnetic case.[6]

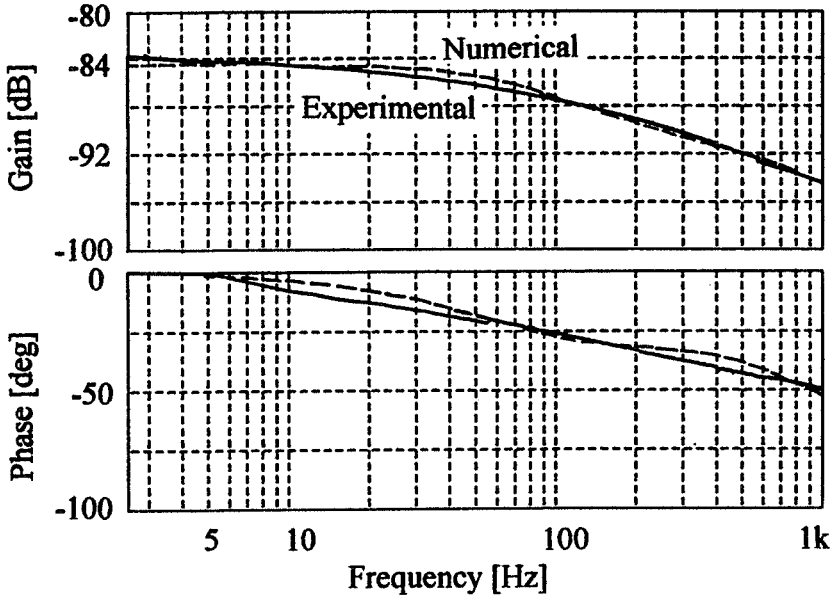

Figure 4. Frequency characteristics of incremental flux.

Control System

The control systems are constructed as in Fig. 5, for each of the vertical and horizontal motions, neglecting the interactions of the conical motions due to gyroscopic effects. This construction decouples the control of the translatory and conical motions into two single variable systems within the linearity. The input variables z_1 and z_2 are displacements of the rotor on the left and right sides. The outputs e_1 and e_2 are control inputs given to the electromagnet systems on the left and right sides. The variables z and z_c are displacements of the translatory and conical motions, u and u_c are control variables, and $C(s)$ and $C_c(s)$ are transfer functions of the compensators. The inputs u_0 and u_{0c} are used for the measurement of frequency responses of the control system. We used analog PID compensation.

Gains of the PID controllers were adjusted experimentally to give desirable characteristics of the control system. The selected gains gave the phase margin of about 35 deg. at 80~90Hz, and the gain margin of 15~18 dB at around 400Hz in the open-loop characteristics. The control inputs e_1 and e_2, including the bias input, are limited to a value corresponding to the static coil current of about 1.5A.

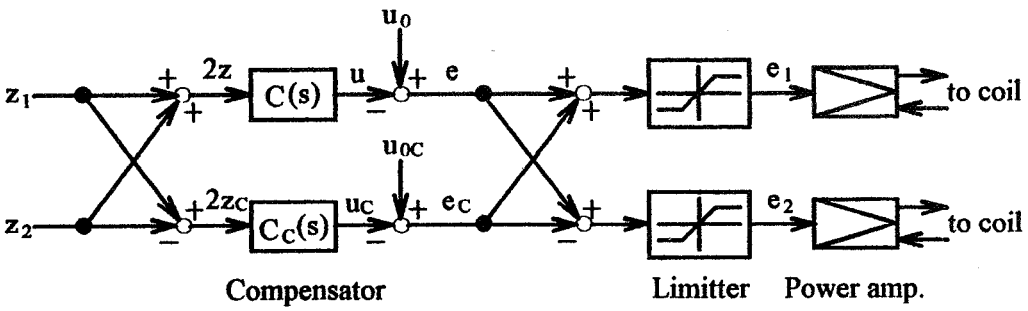

Figure 5. Control system.

Frequency Responses of Rotor Motion

Frequency responses of the rotor motion are measured for a sinusoidal input of amplitude 0.5V, corresponding to the coil current of about 0.19A statically. Figure 6 shows the responses of the vertical

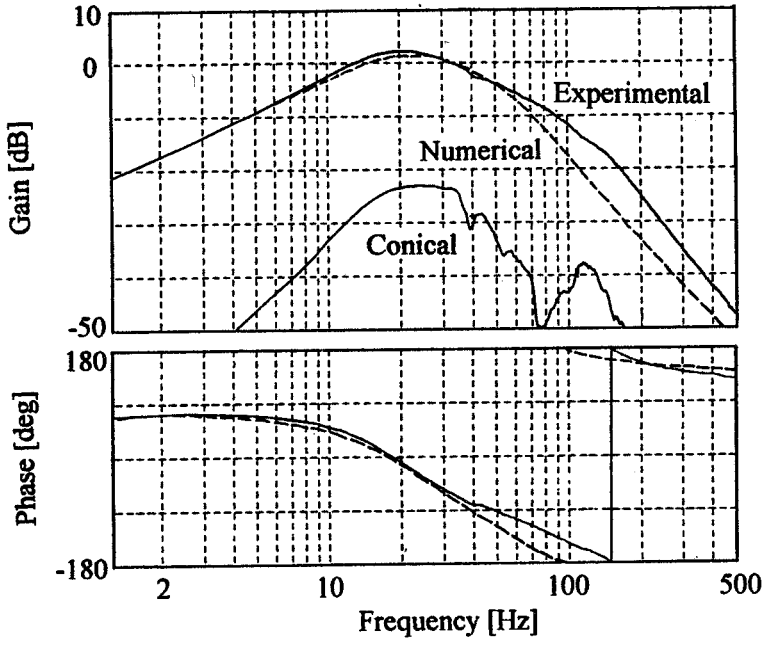

Figure 6. Frequency responses to translatory input.

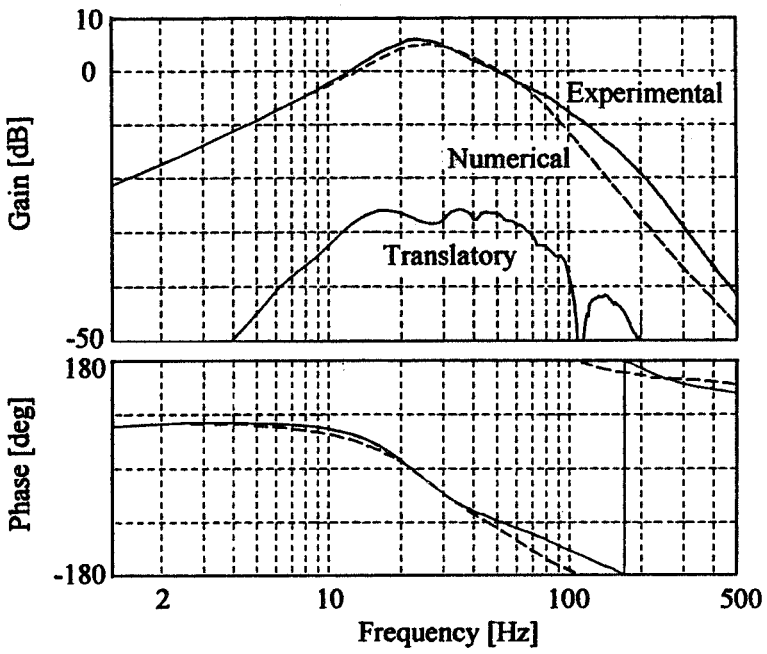

Figure 7. Frequency responses to conical input.

motion to the disturbance input of the translatory system. The phase is given only for the translatory motion. The maximum displacement in frequency about 20Hz is about 0.13mm, about one-fourth of the airgap length, (the output gains of the displacement sensor are 5.0×10^3 V/m for the translation, and 7.8×10^3 V/m for the conical motion). The induced conical motion is small as expected, but may have some information in higher frequencies. The responses to the input into the conical system are given in Fig. 7. The results are similar to the above results with a small translatory motion induced. The maximum displacement is about 0.13mm.

It was difficult to measure the permanent magnetic flux density in the airgap 0.5mm, therefore we guessed roughly 0.2T from the other measurement data. This flux density corresponds to an equivalent coil current of 0.84 A ($Q_B = 0.84$) and estimates the forces of 5.7N and 4.6N in the vertical and horizontal directions, respectively. In this case, the bias coil current in the vertical direction is calculated as 0.19 A ($I_{10} = -0.19$). The data necessary for the numerical analysis and the time constants obtained from the experiment, excluding data given in Table 1, are summarized in the followings.

$$b_1 \cong 0.36 \text{ A/V}, \quad p \cong 140 \text{ V/A}$$

$$\alpha_{10} = 0.25, \quad \alpha_{30} = 0.20, \quad \alpha_{TB} = 0.11, \quad R_{m10} = 5.0 \times 10^6 \text{ A/Wb}$$

$$T_{R1} = 0.057 \text{ ms}, \quad T_{0L1} = 0.26 \text{ ms}, \quad T_{0e1} = 0.82 \text{ ms}, \quad T_{e1} = 0.85 \text{ ms}$$

$$a_{01} = 2.11 \times 10^3 \text{ A/m}, \quad a_{11} = 1.83 \text{ As/m}, \quad c_{Q1} = 1.59, \quad c_{Q1}' = 1.26$$

We use T_{0Le1} in place of T_{0Le3} in eq. (42) because we have no data for it at present; however the authors suppose that this approximation is unimportant in this case.

The broken lines in Figs. 6 and 7 give the numerical results based on the linearized model. The results fit fairly well with the experimental results in lower frequencies, but poorly at frequencies higher than 150Hz. A further examination is required to explain this inconsistency. We guess at present that the primary cause is in the stiffness of the stators and in the supporting of the experimental setup.

Motion for Impact

Figure 8 gives the translatory motion and the actual control input for vertical impulsive force added at the center of the rotor for the maximum displacement of about 70% of the airgap. The shapes of the transient responses were similar for smaller motions, which is a result of the lower control gains.

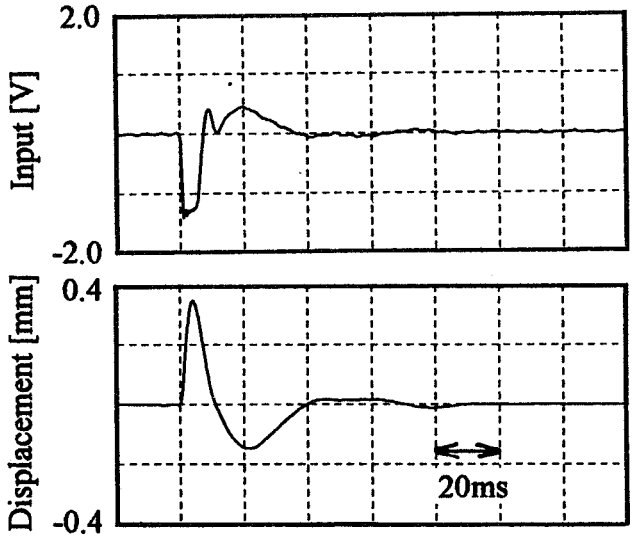

Figure 8. Translatory motion for vertical impact.

Decay of Rotation due to Magnetic Braking

We had a maximum rotating speed of a little more than 7,000 rpm, which was restricted by tolerable whirling of the rotor. The decay of the rotor speed starting from 7,000 rpm is observed as in Fig. 9. The rotor stopped completely after about 55s. A line connecting the points is approximated by the equation $\dot{\omega} + c\omega = -\tau_b$, $c = 0.046\,\text{rad/s}$, $\tau_b = 72\,\text{rad/s}^2$.

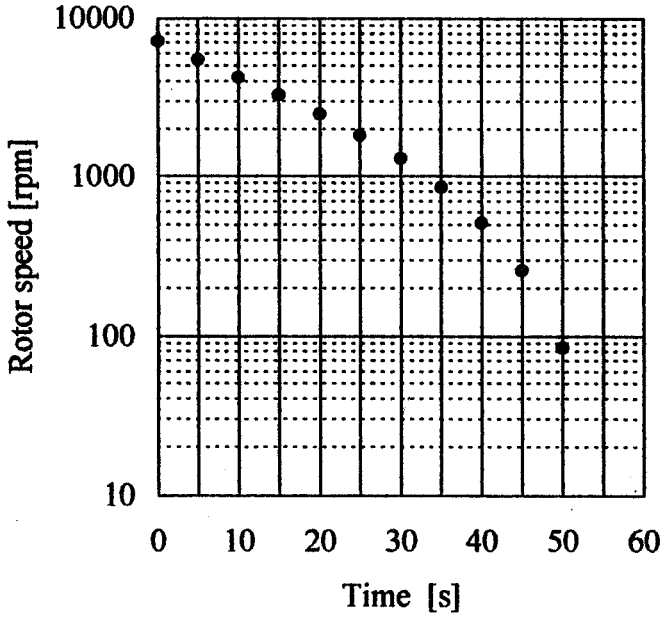

Figure 9. Decay of rotation.

CONCLUSIONS

Active magnetic radial bearings were considered with the combination of permanent magnets to give bias force and electromagnets to generate control force. The ring-shaped permanent magnets with axial magnetization are attached to a shaft and share all the magnetic poles with the electromagnets, so that the control flux may cancel out the bias flux. All the magnet cores are made of solid iron for simplicity of manufacturing. This, however, caused much complicated analysis. The simplified magnetic circuits were analyzed and the linearized dynamical model of control force was presented with the first-order effect of eddy currents. Frequency responses of the rotor motion to disturbance inputs and the motion for impulsive force are tested in the non-rotating state. The frequency responses are compared with the numerical results in some disagreement. The decay of rotor speed due to magnetic brake was examined. The experimental results and the presented linearized model are similar to those of the all-electromagnetic design.

We considered larger, but the same-size magnet poles in the vertical direction supporting the deadweight of the rotor, to reduce a decrease of the resultant bias force on the lower side. It may be reasonable to design different-size poles so that the permanent magnet may supply different bias fluxes to support a part or all of the initial load. In this case, however, the analysis of the magnetic circuits becomes much more complicated. Our approach may be a step towards this case.

The authors thank Mr. S. Fujino for help in making the experimental setup.

REFERENCES

1. Allaire, P.E.; *et al*: Permanent Magnet Biased Magnetic Bearings-Design, Construction, and Testing. *Proc. 2nd International Symposium Magnetic Bearings*, pp. 175-182, Tokyo, June 1990.

2. Ookawa, K.: *Introduction to Magnetic circuits of Permanent Magnets* (in Japanese), pp. 108-109, Sogo-Denshi Pub., Tokyo, 1994.

3. Fukata, S.; Kouya, Y.; and Tamura, H.: Dynamics of Active Magnetic Bearings, *Trans. Japan Soc. Mech. Eng.* (in Japanese), Vol. C-53, No. 490, pp. 1201-1207, 1987.

4. Fukata, S.: Linearized Model and Control Systems of Active Magnetic Bearings with Magnet Core in the Shape of a Cone. *Trans. Japan Soc. Mech. Eng.* (in Japanese), Vol. C-58, No. 551, pp.2081- 2088, 1992.

5. Fukata, S.; and Kouya, T.: Control Systems of Active Magnetic Bearings Based on Decoupling of the Motion of Rigid Rotor, *Technology Report of Kyushu Uni.*, Vol. 60, No. 2, pp. 185-191, 1987.

6. Fukata, S.; and Kouya, T.: Dynamics of Active Magnetic Bearings with Magnet Cores in the Shape of a Cone, *Proc. 3rd Inter. Sympo. Magnetic Bearings*, pp. 339-348, Alexandria, July 1992.

INTERACTION FORCES BETWEEN MULTIPLE BODIES IN A MAGNETIC FIELD

Benjamin Joffe
Jet Propulsion Laboratory
Pasadena, California

SUMMARY

Some of the results from experiments to determine the interaction forces between multiple bodies in a magnetic field are presented in this paper. It is shown how the force values and the force directions depend on the configuration of the bodies, their relative positions to each other, and the vector of the primary magnetic field.

A number of efficient new automatic loading and assembly machines, as well as manipulators and robots, have been created based on the relationship between bodies and magnetic fields. A few of these patented magnetic devices are presented. The concepts involved open a new way to design universal grippers for robots and other kinds of mechanisms for the manipulation of objects. Some of these concepts can be used for space applications.

INTRODUCTION

In the paper presented by the author earlier at the First International Symposium on Magnetic Suspension [1] an overview was provided of the parameters of magnetic fields and single bodies positioned in the magnetic fields that apply force and torque to the bodies. It is much more complicated to evaluate the interacting force value applied to a single body when that body is one of a group of bodies within the magnetic field. This is so because both the force and torque on the single body are now dependent not only on the parameters of the magnetic field and the body itself but also on the magnetic flux contribution from the other bodies being positioned in the primary magnetic field. All of these contribute to the total value and direction of the force being applied to the single body within a group.

There are some publications on this subject [2–5]. Some experimental research results on forces acting on bodies in a group were published in [2], [4], and [5], and some theoretical work was presented by Sermons [3]. This paper provides an overview of some of the results of these previous publications, as well as some patented concept designs based on these research results. The force effects between bodies in a magnetic field are illustrated using a simple group of objects. The first section of the paper discusses the interaction force effects between ferromagnetic bodies, and the second section illustrates the force effects between nonferromagnetic current-conductive bodies.

INTERACTION FORCES BETWEEN FERROMAGNETIC BODIES IN A MAGNETIC FIELD

The force effects between the bodies in a magnetic field can be illustrated using a group of three balls being positioned in a homogeneous permanent field, as shown in Figure 1, cells 1 and 3. For simplicity, the field distortion due to the presence of these ferromagnetic bodies is not shown. The bodies drawn with solid lines show their initial positions, prior to the effects of the magnetic field. The bodies drawn with dotted lines show the direction of motion resulting from the interaction of forces.

Let us analyze a few extreme conditions. First, let us look at the condition in which the magnetic permeability of the bodies is equal to the magnetic permeability of the primary magnetic field area. In this condition the bodies will have no distortion effects upon the field, and there will be no magnetic interaction forces between the bodies. In the second condition, which is typical for ferromagnetic bodies, the magnetic permeability of the bodies is much greater than that of the field area. The result is that the primary magnetic field flux distribution will change to minimize energy losses, since the field uses the ferromagnetic bodies as a pathway, creating interaction forces. The character of the direction of the forces applied to the bodies in the group is illustrated in Figure 1.

In this condition, when the induction vector of the field is colinear with the group of bodies and the field is homogeneous, as shown in Figure 1, cell 1, the interaction force between the bodies will have a tendency to bring the bodies into contact. When the induction vector of a homogeneous field is normally directed toward the stream of the bodies (see Fig. 1-3), the interaction force between the bodies will tend to separate them. In a

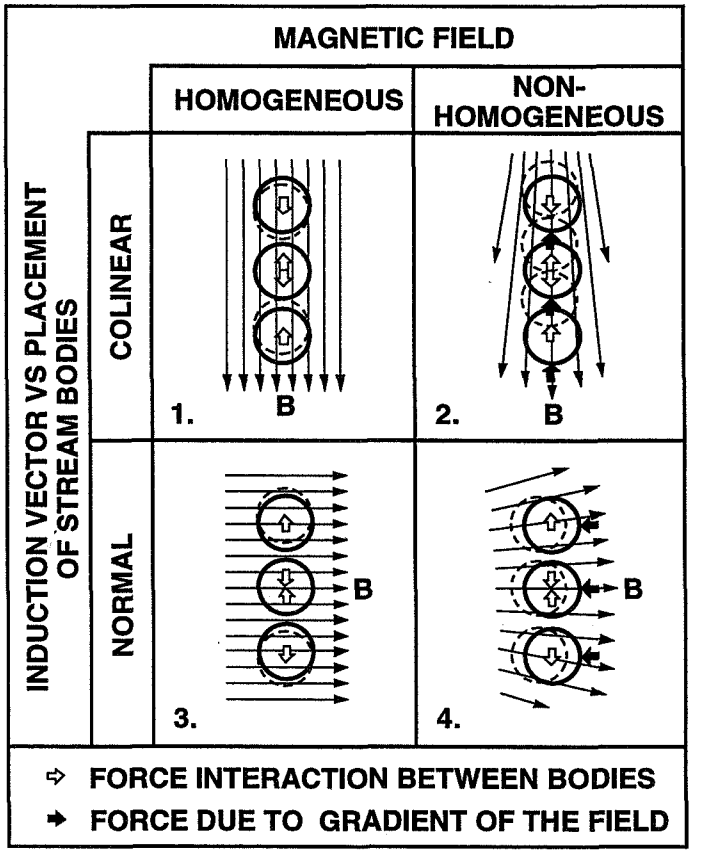

Figure 1. Four simplified sketches showing the interaction forces between ferromagnetic bodies, which are dependent on the angle between the magnetic field induction vector and the direction of the stream of bodies. For simplicity, the field distortion due to the presence of these ferromagnetic bodies is not shown. The bodies drawn with solid lines show their initial positions, prior to the effects of the magnetic field. The bodies drawn with dotted lines show the direction of motion resulting from the interaction forces.

condition of a colinear nonhomogeneous magnetic field (see Fig. 1-2), or a condition of a normally directed nonhomogeneous field (see Fig. 1-4), the interaction force between the bodies still tends to bring the bodies into contact or separate them, respectively. In addition, however, in both of these cases it tends to move the group of bodies toward the area of more concentrated magnetic flux, due to forces created by the gradient of the primary magnetic field.

By experimenting with different configurations and sizes of bodies in magnetic fields [4] some interesting effects were discovered. One of them is illustrated in Figure 2, which shows how the magnitude and direction of the interaction force changes as two bodies—ferromagnetic cylinders—are shifted in relation to each other within the field. Figure 2 uses cylinders for illustration, but this effect is similar for other types of bodies, as well. For ferromagnetic bodies, the magnetic saturation effect is a very important factor, because it limits the possibilities of increasing the interaction force between bodies. If the saturation effect begins to occur, the next increase of the magnetic flux value will not create the same increase in interaction force as before, and if the full saturation effect takes place the next interaction force increase will not occur at all. From the design standpoint, this knowledge provides a positive benefit. What it indicates is that the appropriate magnet system need only be powerful enough to provide magnetic flux up to, but not exceeding, the onset of the saturation effect for the type of parts being manipulated. This permits designing systems that are efficient in terms of weight and size of the magnets and energy consumption.

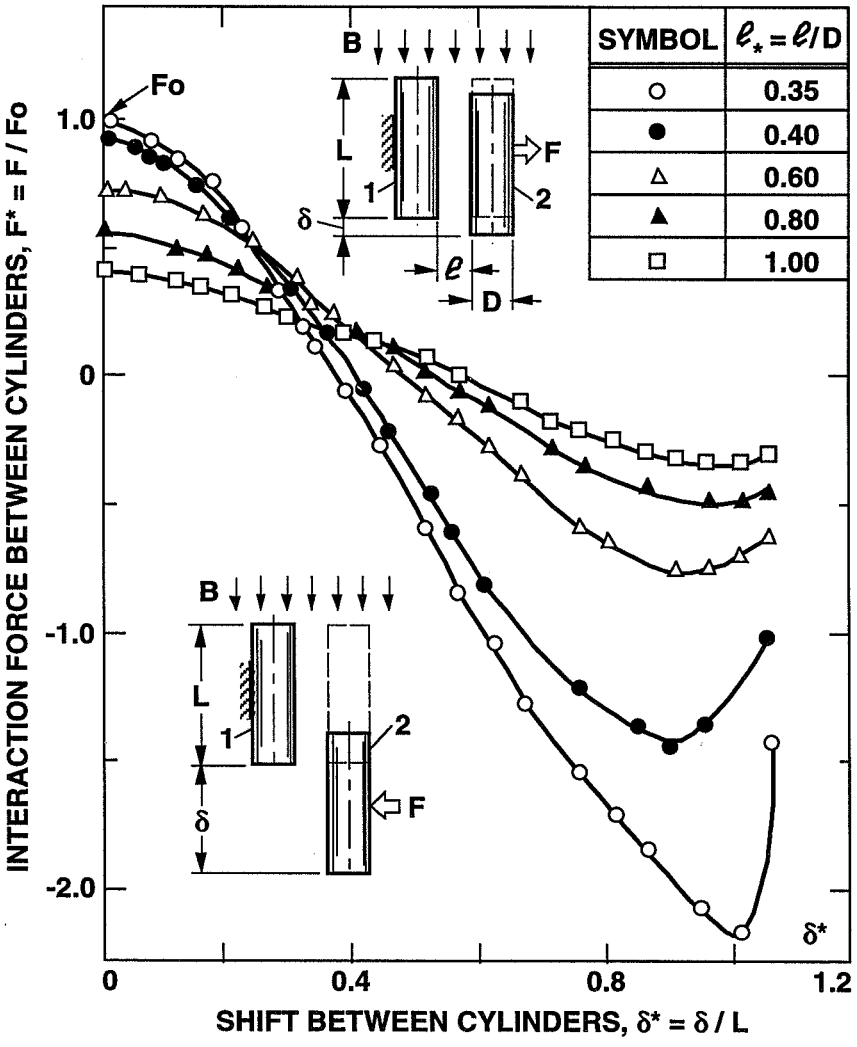

Figure 2. Magnitude of interaction forces between two ferromagnetic cylindrical bodies, based on the shift of the bodies relative to each other and the gap between them in a permanent magnetic field, with the magnetic induction (flux density) B = constant.

The saturation effect can also be observed in experiments where the gap of a permanent magnet is filled with ferromagnetic cylinders. The interaction force relation between the bodies, as shown in Figure 3, is dependent upon the quantity of bodies within the field, or the coefficient of fill. Prior to saturation, the interaction force increases in a relatively linear way as more bodies are added to the field. After saturation starts to occur, which is at a coefficient of fill close to 0.5 in Figure 3, the increase in the interaction force with the addition of more bodies begins to fall off. The interaction force can be calculated using the formula in the upper left corner of Figure 3, in which F_i is the interaction force on an individual body; P_i is the magnetic pressure, which is the result of the square of the induction field; and S_i is the area of the body in the field direction. These experimental results allowed the design of magnetic devices for various applications, two of which are described in patents [6] and [7].

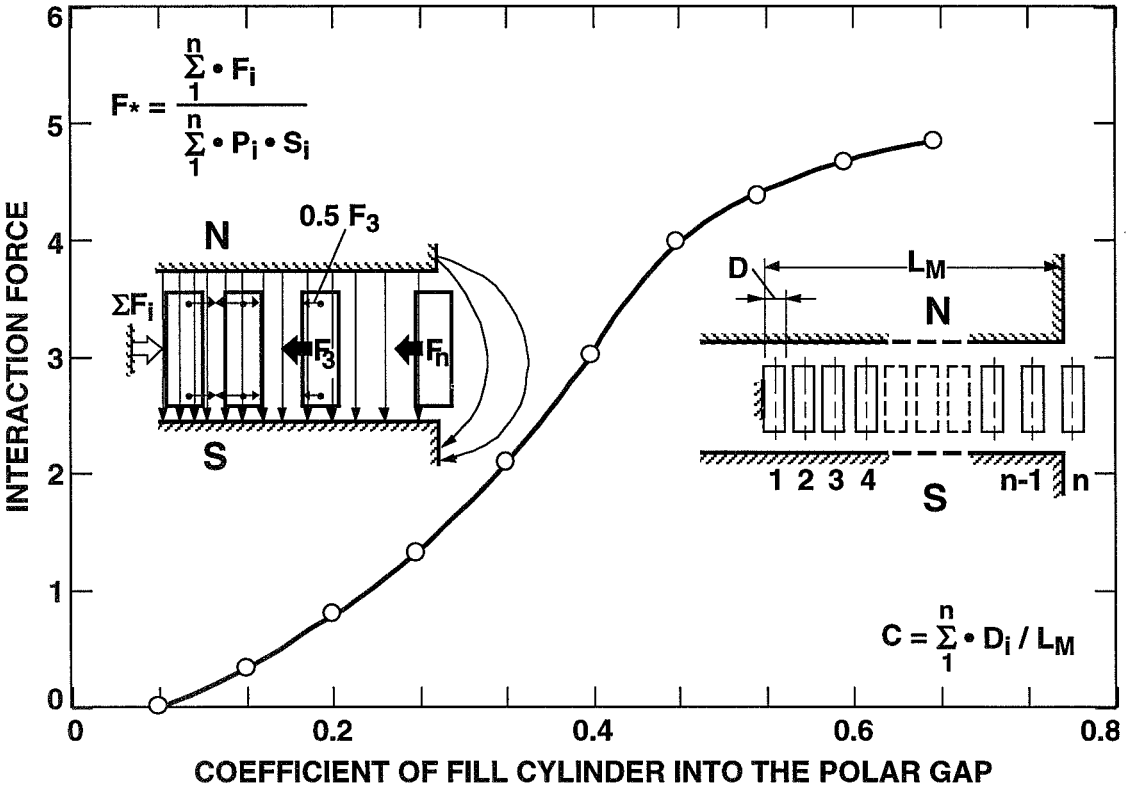

Figure 3. The dependency of the magnitude of forces acting on a single cylinder placed in the polar gap of a permanent magnet (B = constant) on the coefficient of fill (i.e., the number of cylinders that fits in the magnetic gap).

To provide the maximum possible force on ferromagnetic bodies, the magnetic field can be concentrated in the area where it is desired that the bodies be positioned. This can be done using different techniques. One of them, which is very well known, involves choosing a particular configuration of the magnetic poles that concentrates the flux in the desired area [8], [9]. Another way to achieve this is illustrated in Figure 4, which shows how the magnetic field can be concentrated in the gap between the poles (1) and (2) in order to position ferromagnetic bodies (3). In this polegap area, a system of electric wires (4 thru 7) is positioned. The powered wire system adds magnetic flux to the primary magnetic field in some areas and dislocates the flux of the primary field in other desired areas. Figure 4b shows how concentrations of the magnetic flux occur using this technique, allowing parts to be positioned in such concentrated flux areas by the magnetic forces.

If the wire system is configured with more than one layer, powering those layers one at a time can create a gradient of magnetic field that generates a force greater than the force of gravity, allowing the parts to be moved, for instance, in a vertical direction. This is a new way that multiple ferromagnetic parts can be assembled with nonferromagnetic components [10].

Another technique for achieving the same kind of effect is shown in patents [11] and [12], which describe how the concentrations of magnetic flux can be localized in desired areas. This is based on using an alternating electromagnetic field, with a system of conductive plates located between the magnetic poles. The primary

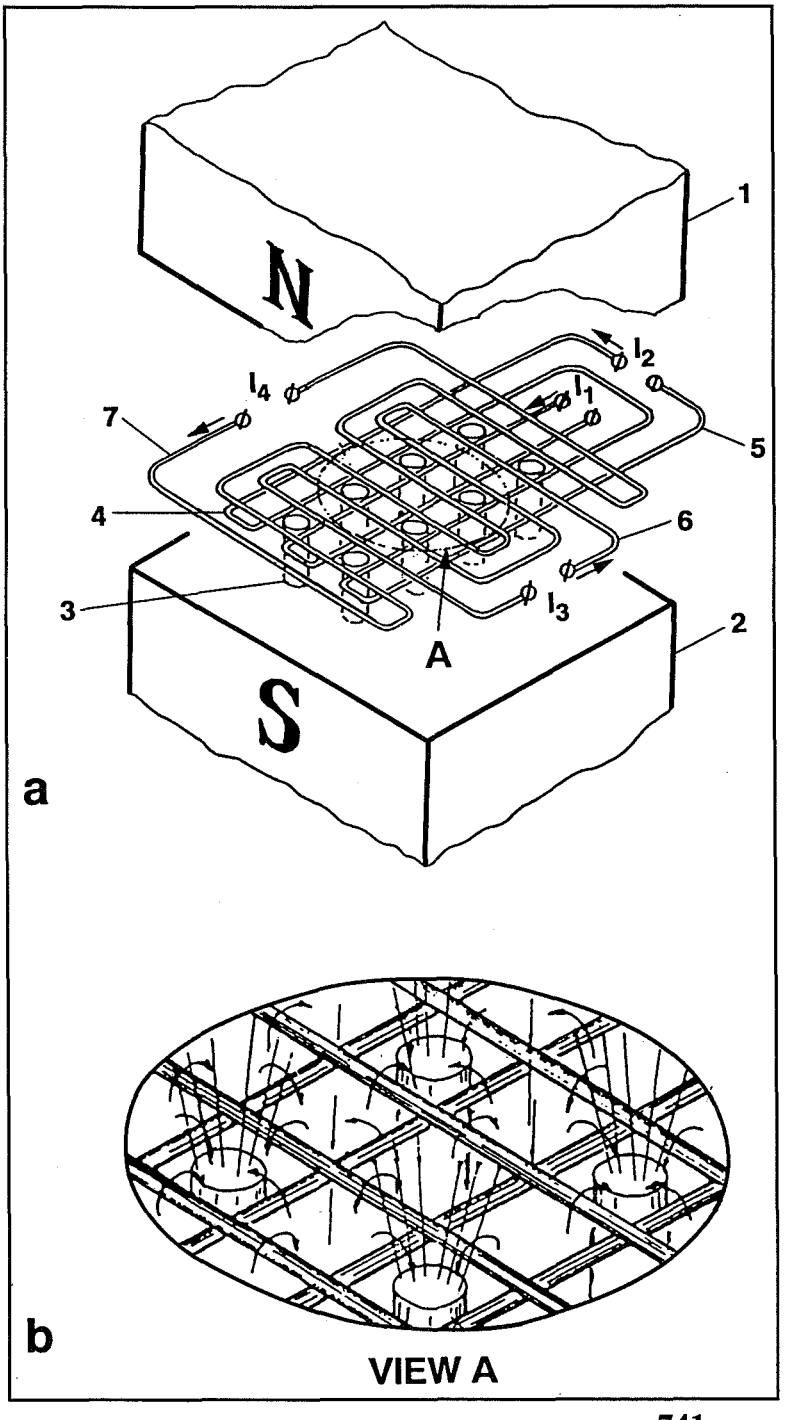

Figure 4. An example of the generation of localized zones with concentrated magnetic flux created by a system of conductors (wires) carrying current. Such a method of generating localized gradients of flux density can be utilized for moving ferromagnetic bodies along complex paths to the desired locations.

Figure 4a shows an overview of the system (1,2 – magnet poles; 3 – ferromagnetic body; 4,5,6,7 – wire system).

Figure 4b represents a close-up view of the electric wire system with concentrated flux lines.

magnetic field induces a current in the conductive plates, and the secondary magnetic field created by this current interacts with the primary magnetic field, creating extra flux in the same manner as was described above for the wire system configuration. This concentrates magnetic flux in areas where ferromagnetic parts are to be positioned. Such a system can be used for the efficient assembly of parts.

INTERACTION FORCES BETWEEN NONFERROMAGNETIC CONDUCTIVE BODIES IN A MAGNETIC FIELD

As is known, the mechanism for the creation of forces acting on current-conducting bodies in alternating magnetic fields is based on the interaction of secondary fields with the primary field, as was described in [1] and [2]. The interaction force effect between two bodies is illustrated in Figure 5. The induced current (i) in the conductive rings generates a secondary magnetic field that creates resistance to the primary field, with the result that the primary field is bowed out from the ring areas. As a result, on the ring periphery, zones of increased concentration of magnetic flux are created and form electrodynamic forces (F). Because the concentration of flux is greatest between the rings, the interaction forces are strongest in this area. The tendency, then, will be for the rings to move away from each other until the forces between the rings and on the outboard sides are equal.

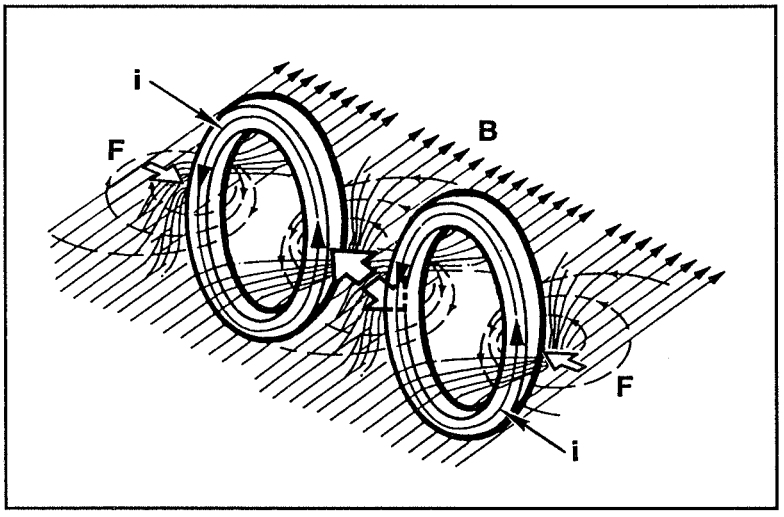

Figure 5. Shown are the interaction force effects between two nonferromagnetic conductive rings, in coplanar positions, in an alternating magnetic field. For clarity, the primary magnetic field, with induction B, and the secondary magnetic fields created by induced currents (i) are shown in only one plane. F represents the electrodynamic force.

The experimental measurement of such electrodynamic forces between two conductive bodies was done in a homogeneous alternating magnetic field to avoid any influence on the measurement from a gradient of the primary field. The electrodynamic forces between two identical cylinders in a homogeneous field are shown in Figure 6, which includes plots for cylinders of copper, aluminum, and brass. This illustrates the direct dependence of the electrodynamic forces on the conductivity of the bodies.

Figure 7a gives the relative coefficients (K_1) characterizing the effects of form on the magnitude of the electrodynamic forces between two identical bodies. For a baseline, the forces between two balls are established as $K_1 = 1.00$. From the coefficients in this table, it is possible to determine the electrodynamic interaction forces for other configurations of bodies. Figure 7b shows the coefficients characterizing the effects of relative positioning on the magnitude of electrodynamic forces. It should be noted that the coefficients for solid cylinders (not shown) and hollow cylinders are the same. Using the information from Figure 6 and coefficients such

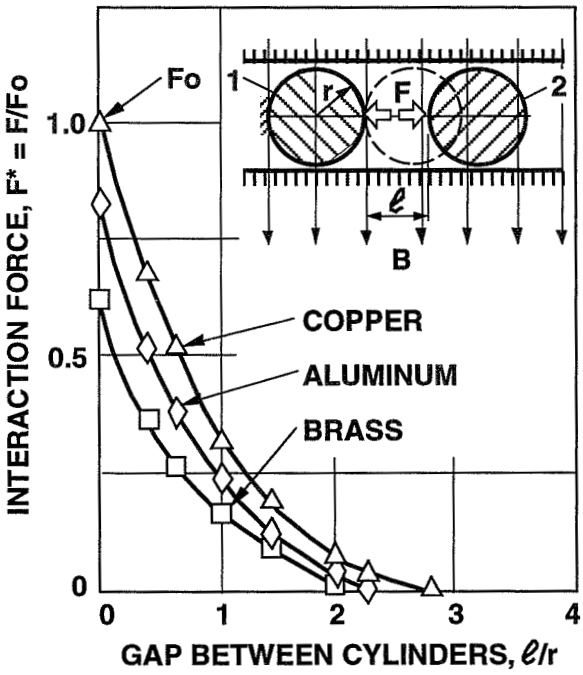

Figure 6. The magnitude of the interaction forces between two nonferromagnetic conductive cylinders in a homogeneous alternating magnetic field depends upon the gap between the cylinders.

TABLES OF COEFFICIENTS CHARACTERISING THE EFFECTS OF FORM AND RELATIVE POSITIONING ON INTERACTION FORCES BETWEEN TWO BODIES

	BODIES / COEFF.	B, F, F, D	H, H, H	δ = H/2, H, H	D, H	d = D/2, H
a	K_1	1.00	1.21	1.90	0.67	0.57

	BODIES / COEFF.	d = D/2, H			δ = H/2, H, H		
b	K_2	1.00	1.90	2.20	1.00	0.25	1.30

Figure 7a. Coefficients characterizing the effects of form on the magnitude of electrodynamic forces between two identical bodies.

Figure 7b. Coefficients characterizing the effects of relative positioning of two identical bodies on the magnitude of electrodynamic forces.

as those shown in Figure 7, it is possible to predict the electrodynamic interaction forces for various types of bodies within magnetic fields. Based on this research, several new methods were developed for separating bodies for automation [13], [14], [15], [16].

It is well known that when the magnetic field is nonhomogeneous, the gradient of the field will have a direct influence on the force value between the bodies. The difference between nonferromagnetic conductive bodies and ferromagnetic bodies is that the force directions relative to the gradient of the field are opposite. In the case of ferromagnetic bodies, the force direction is toward the area of highest flux concentration, and with conductive bodies the force direction is toward areas of lower flux concentration.

Now, let us look at the case of two non-coplanar rings in a magnetic field. The interaction force effect between two such bodies is shown in Figure 8. As with the coplanar rings described above, the induced current (i) in the rings (1) and (2) generates a secondary magnetic field that creates resistance to the primary field, with the result that the primary field is bowed out from the ring area. On the ring periphery, zones of increased field induction are generated and form electrodynamic forces (F_y) that tend to move the rings toward contactless convergence and centering on the same axis (X).

Figure 8. Shown are the interaction force effects between two nonferromagnetic conductive rings, in non-coplanar positions, in an alternating magnetic field. For clarity, the primary magnetic field and the secondary magnetic fields created by induced currents (i) are shown in only one plane.

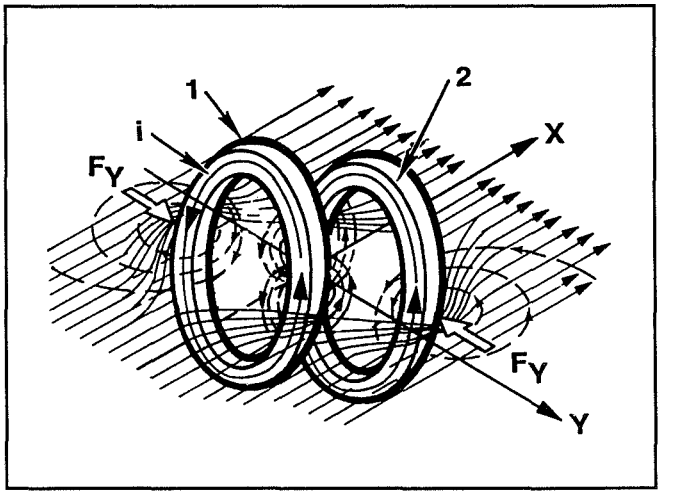

Based on this effect, different kinds of methods and devices for automation were created. One of them, which is illustrated in Figure 9, involved the alignment of multiple objects (1) positioned on a nonconductive plate (3) in which is mounted numerous conductive targets (2). The targets are mounted in the plate in the configuration in which the objects are to be positioned after alignment. Because of the interactive force effects, the objects and the conductive targets interact in the same manner as the two non-coplanar rings in Figure 8.

Using this technique, many applications can be developed. An increase in the alignment effect can be achieved by placing the objects between two nonconductive plates with conductive targets [17]. In fact, multiple layers of plates and objects to be aligned can be configured. Creating the target as a conductive coil with a switch that can open and close the loop provides still more opportunities for the manipulation of objects. Some of these design possibilities are illustrated in patent [18].

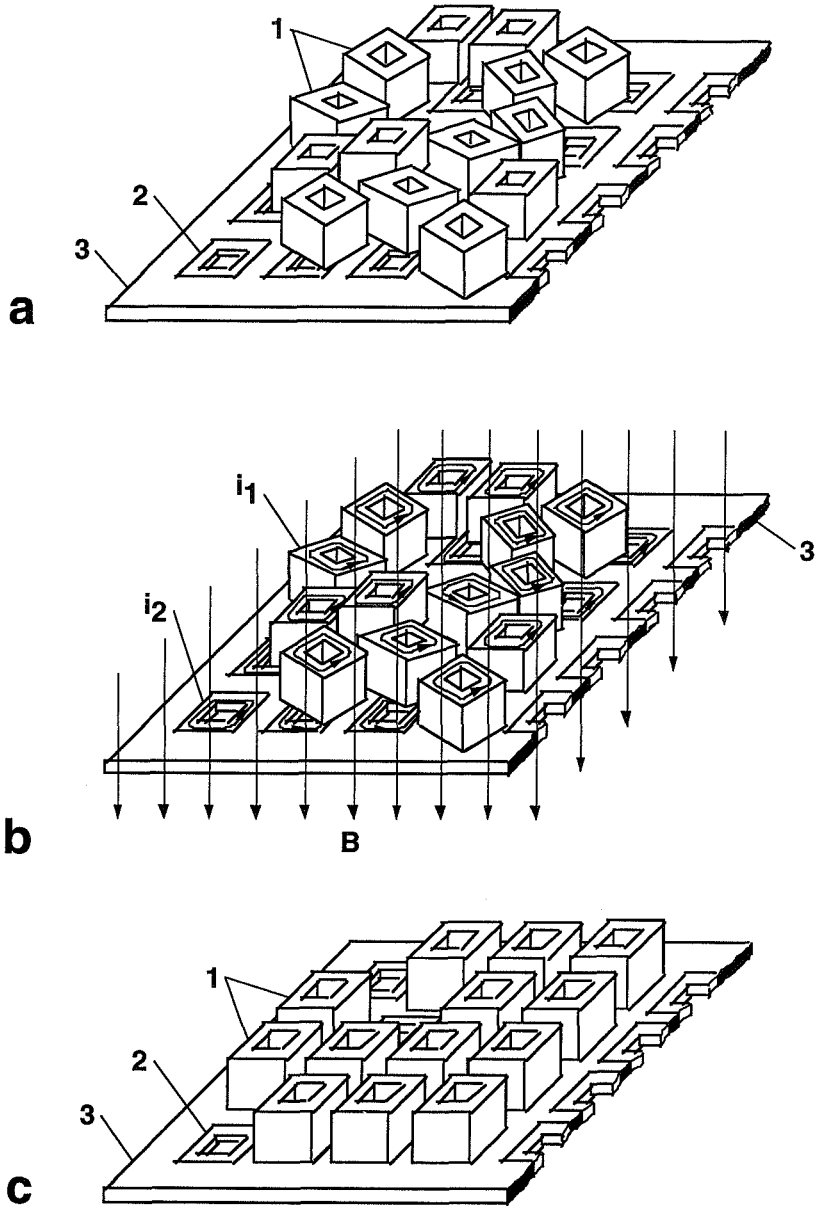

Figure 9. Illustration of alignment of a group of bodies, which can be achieved by interaction of electrodynamic forces between the bodies (1) in the group and between the bodies (1) and the conductive targets (2) mounted in a plate (3).

Figure 9a shows a disorganized group of bodies on a plate before the primary magnetic field is generated.

Figure 9b shows the induced currents in the bodies and the conductive targets as a result of the primary alternating magnetic field being applied.

Figure 9c shows the organized, aligned group of bodies as a result of the acting of the electrodynamic forces.

An example of such a concept design is presented in Figure 10. The object to be manipulated (1) is positioned between four coils (2,3,4,5). When a primary electromagnetic field (B) is applied, a current (i_1) is induced in the object. When the switches (6,7) for both sets of coils are open, as shown in Figure 10a, no interaction force occurs between the object and the coils. If, for example, the switch (6) for one pair of coils (2,3) is closed (Figure 10b), the primary field induces a current (i_2 and i_3) in that set of coils. As a result of the interaction between the currents in the object and the coils, an electrodynamic force is created that moves the object to the left. If the switch (7) for the other set of coils (4,5) is closed while the other switch is open, as is shown in Figure 10c, the opposite effect occurs, resulting in an electrodynamic force that moves the object toward the right. For simplicity, Figure 10 does not show the magnetic flux interactions among the primary alternating magnetic field (B), the magnetic field-induced currents in the movable object (1), and the coil system (2,3 and 4,5). Some of these interactions are shown in Figure 8 and in Figure 11 below.

By creating such designs with multiple coils, the manipulation effects on the object can be made more complex. A coil system could also be designed for remote operation of the switches, either manually or by computer programs, for contactless positioning of objects. These kinds of devices could be used for many automation applications, including nonmanned object manipulation on spacecraft.

Figure 10. The concept design of an electromagnetic device for manipulation of an object (1) by electrodynamic force (F).

Figure 10a shows an overview of the concept design.

Figures 10b and 10c present a cross-section view of the object and the coil system (2,3,4,5), showing how the electrodynamic force applied to the movable object changes as a result of closing and opening the loop of the coil system by operating the switches (6,7).

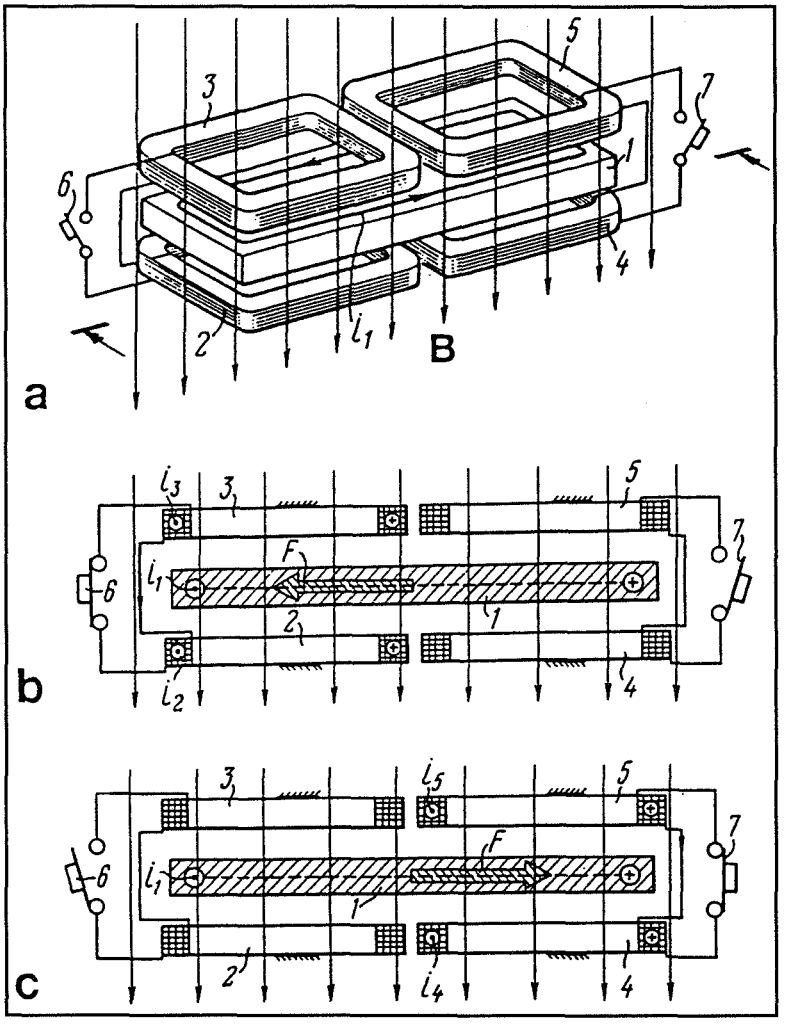

The force relations between non-coplanar bodies within a magnetic field can also be used for more complicated manipulations of objects, including the contactless assembly of parts [19].

Another example of the use of interaction forces between non-coplanar conductive bodies in a magnetic field is shown in Figure 11. A conductive plate (1) can be used as a contactless screen for separating a subset of conductive bodies from a larger set of bodies (2). The magnetic flux at the edges of the plate in relation with the induced current in the bodies creates interaction forces that separate the bodies at the edges of the plate from those under the plate. This technique can be used, for example, for preparing groups of parts for packaging.

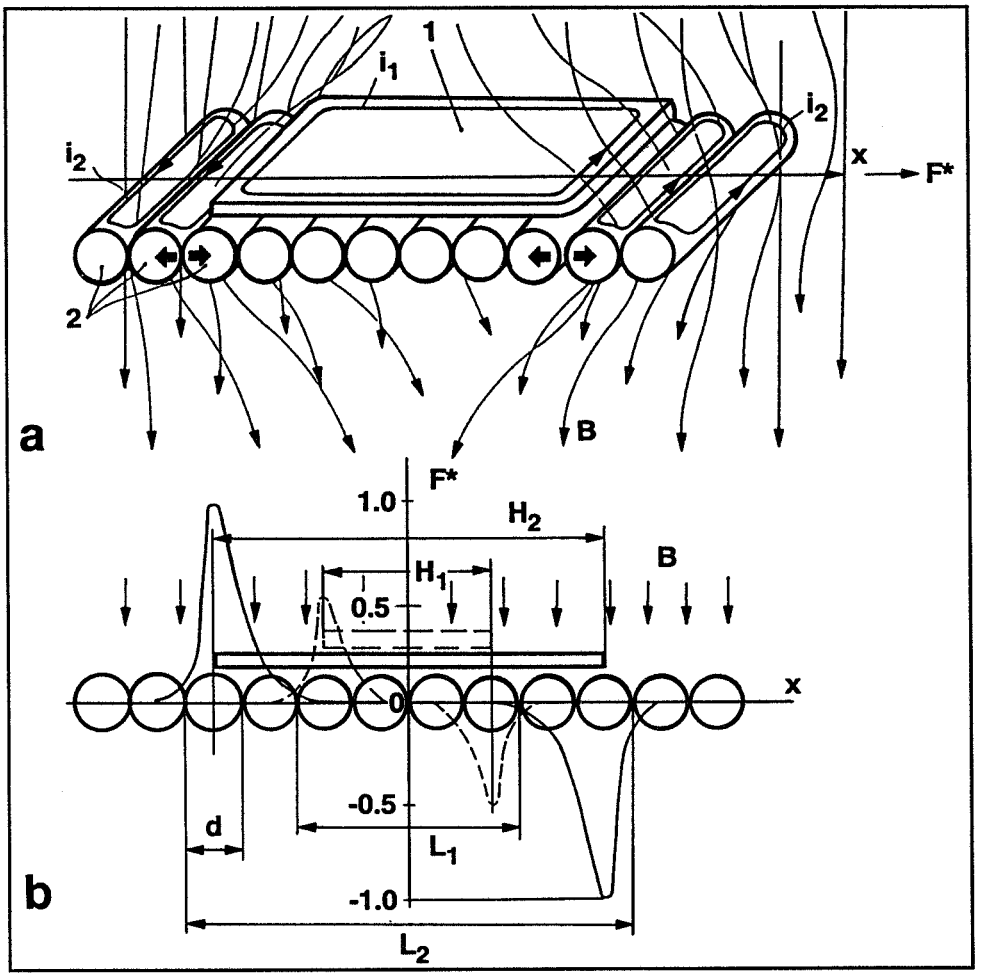

Figure 11a illustrates the use of a conductive plate (1) as a screen for separating a subset of conductive bodies (2) from a larger set of bodies in an alternating magnetic field.

Figure 11b shows the characteristics of magnitude and direction of electrodynamic forces (F) generated by the interaction of a primary magnetic field and secondary fields induced in the screen (1) and the bodies (2).

Force magnitude at the screen edges is shown for two different screen sizes, H1 and H2.

The forces created by the interaction between the primary field and induced fields in the bodies can be used not only for providing linear motion of bodies in relation to one another but also for achieving rotation. This effect is illustrated in Figure 12, which shows a cylindrical conductive body (1) located inside a conductive frame (2). Applying an alternating primary magnetic field (B) to this system induces currents, and consequently secondary magnetic fields, in both the cylinder and the frame. The induced current in the cylinder is generated ninety degrees from the direction of the primary field. The current position of the frame is dependent upon the angle position of the frame. The induced current in the cylinder has a tendency to align itself with the induced current in the frame. If the frame is oriented at some angle such as that shown in Figure 12a and 12b, counterclockwise rotation will result. If the frame location has the opposite angle position, as shown in Figure 12c, the cylinder rotation will be clockwise.

From this we can see that varying the position of the frame allows the manipulation of the torque, speed, and direction of rotation of the cylindrical body. To increase the interaction forces, a second conductive frame can be placed on the opposite side of the cylinder from the first one [20]. It is also understood that by organizing the primary field with a gradient, a levitation effect for the cylinder can be achieved, as well, thus reducing the friction force between the body and the frame. The torque value can also be increased by using a multi-winding coil instead of a solid frame loop. This concept can be used to develop electric motors and, for example, such things as devices for polishing surfaces [21].

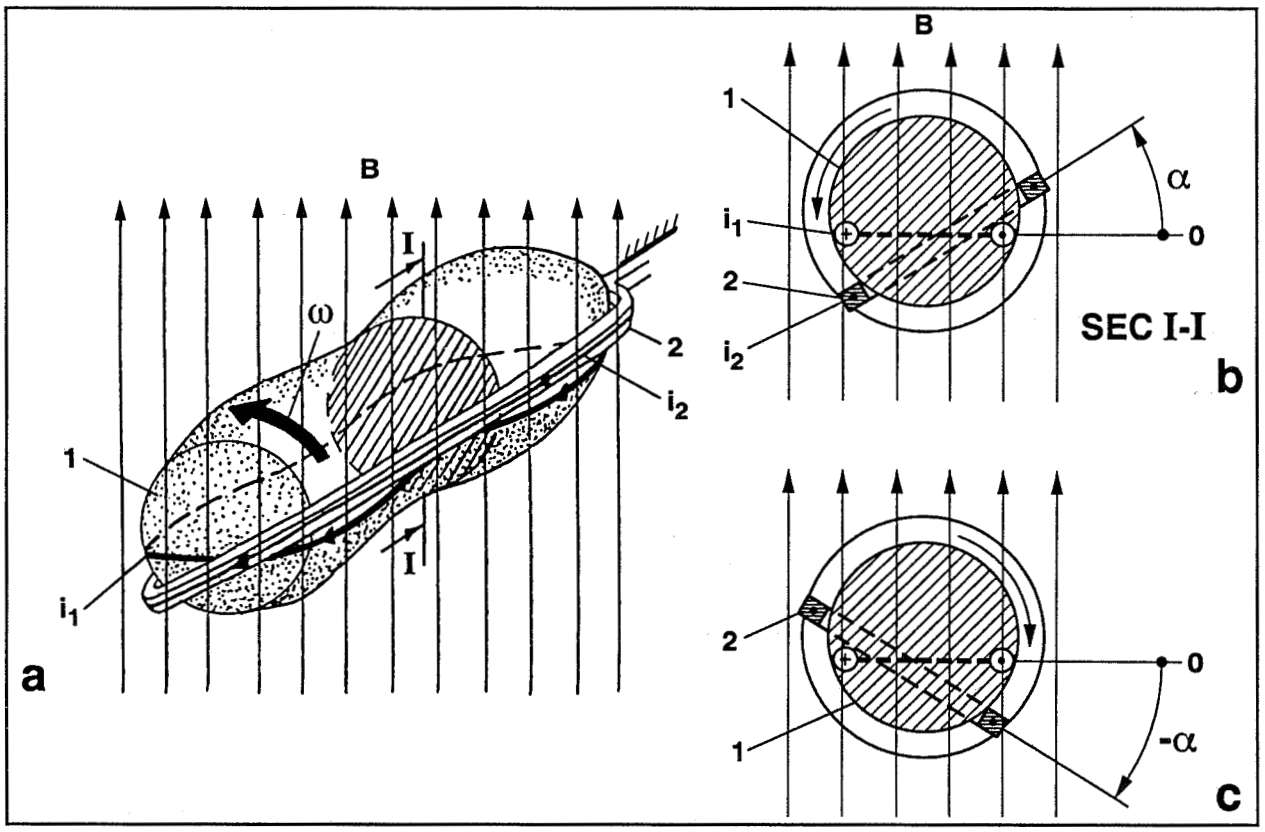

Figure 12a shows the effects of interaction between a cylindrical conductive body (1) and its encompassing conductive frame (2), both of which are in the alternating magnetic field. The interaction force relation between the induced currents in the two bodies creates torque that results in the rotation of the cylindrical body.

Figure 12b gives a cross section I–I from Figure 12a.

Figure 12c is the same as 12b, except that it shows a different frame angle (a) position relative to the induced current in the cylindrical body. This results in the opposite torque direction, creating a different direction of rotation for the cylinder.

CONCLUSION

This paper has presented only a brief overview of the interaction forces between ferromagnetic and current-conducting bodies positioned in simple groups. The results of the investigations of these groups were sufficient to provide an understanding of the dependence among the bodies and to allow the creation of new types of devices, some of which were described in this paper.

In the next presentation the author plans to provide some interaction force calculations as well as to analyze the force relations for more complex groups of bodies.

It is also of special interest to analyze the dependence of the interaction forces between magnetized bodies or permanent magnets. Some information about these forces, which depend upon the types of magnetic materials used, the sizes of the bodies, and their configuration, is already available. With regard to more complicated configurations of magnetized bodies, which have already been used in designs of new kinds of mechanisms and machines [21], specific information on the interaction forces still needs to be gathered. A related area of investigation would be to analyze the interaction forces when other movable components, made from different kinds of materials, are involved in the mechanism along with magnetized bodies. Examples of such mechanisms are contained in patent [22].

From the research presented here it is clear that designs based on these concepts could have applications in a wide variety of areas, including the space program. Specifically, the use of magnetic interaction forces would allow the production of lightweight, efficient, multi-functional mechanisms for remotely controlled, nonmanned spacecraft applications, where durability and versatility of the designs are extremely important.

REFERENCES

1. Joffe B. "Manipulation and Identification of Objects by Magnetic Forces." Presented to the International Symposium on Magnetic Suspension Technology, Hampton, Virginia, August 19-23, 1991. NASA Conference Publication 3152, Part 2, 1992, pp. 617-638.

2. Joffe B.A., Kalnin R.K. Orientation of Parts by Electromagnetic Field. Riga, "Zinatne," Latvian Academy of Sciences Publishing House, 1972.

3. Sermons G.Y. Dynamics of Rigid Bodies in Electromagnetic Field. Riga, "Zinatne," Latvian Academy of Sciences Publishing House, 1974.

4. Baltvilks A.T., Joffe B.A., Kalnin P.K. "Force Interaction of Ferromagnetic Cylinders and Disks by Magnetic Field," in Automation of Assembly Processes, Installment 6. Riga, Polytechnic Institute, 1977, pp. 7-22.

5. Baltvilks A.T., Joffe B.A., Kulberg A.Y. "Investigation of Magnetostatic Force Interaction of Ferromagnetic Parts in the Zone of Magnetic Saturation Applicable to Solution of Problems of Assembly," in Automation of Assembly Processes, ISSN 0320-6963. Riga, Polytechnic Institute, 1978, pp. 47-59.

6. Joffe B.A., et al. "Device for Contactless Separation of Individual Ferromagnetic Components from a Flow of Components," U.S. Patent No. 4,113,142, Class 271/171.

7. Joffe B. "Rotating Drive Magnetically Coupled for Producing Linear Motion," U.S. Patent No. 5,331,861, Class 74/89.15.

8. Kulberg A.Y., Joffe B.A., et al. "Device for Arranging Ferromagnetic Components at Preset Distance from One Another," U.S. Patent No. 4,153,151, Class 198/456.

9. Joffe B.A., et al. "Automatic Assembly Device," U.S.S.R. Patent No. 518,318, Class B23p.

10. Joffe B.A. "Assembly of Elongated Ferromagnetic Components," U.S.S.R. Patent No. 737,189, Class B23.

11. Kalnin R.K., Joffe B.A., et al. "Device for Assembly of Ferromagnetic and Nonmagnetic Components," U.S.S.R. Patent No. 707,189, Class B23p.

12. Joffe B.A., et al. "Device for Assembly of Ferromagnetic and Nonmagnetic Components," U.S.S.R. Patent No. 812,499, Class B23p.

13. Joffe B.A. "Method for Separation of Parts," U.S.S.R. Patent No. 442,979, Class B65h.

14. Joffe B.A., et al. "Apparatus for the Simultaneous Contactless Separation of Individual Nonmagnetic Electrically Conductive Bodies from a Continuous Flow," U.S. Patent No. 3,661,241, Class 198/33.

15. Joffe B.A., Kalnin R.K. "Method of Dismantling Units," U.S. Patent No. 4,109,366, Class 29/427.

16. Kern I.I., Joffe B.A., Graubin Y.J. "Method for Multiple Directional Distribution of Nonsymmetric Parts," U.S.S.R. Patent No. 441,763, Class 62-229.6Y.

17. Joffe B.A., et al. "Device for Making Sets of Nonmagnetic Current-Conducting Components," U.S. Patent No. 4,144,637, Class 29/739.

18. Joffe B.A., et al. "Method of Oriented Feeding of Nonmagnetic Current-Conducting Components and Devices for Effecting the Same," U.S. Patent No. 4,077,027, Class 335/219.

19. Kalnin R.K., Joffe B.A., et al. "Method of Assembly of Nonmagnetic Current-Conducting Components," U.S. Patent No. 4,238,658, Class 219/9.5.

20. Kern I.I., Joffe B.A., Summer V.A. "Device for Rotation of Parts," U.S.S.R. Patent No. 420,441, Class 62-837.

21. Joffe B.A., et al. "Machine for Lapping Flat Surfaces of Parts," U.S.S.R. Patent No. 804,402, Class 621.923.5.

22. Joffe B. "Rotating Drive Magnetically Coupled for Producing Linear Motion," U.S. Patent No. 5,331,861, Class 74/89.15.

Session 19 -- Sensors

Chairman: Colin P. Britcher
Old Dominion University

A MAGNETICALLY SUSPENDED WHEEL FOR A MINIATURE GYRO MADE USING PLANAR FABRICATION TECHNOLOGIES*

Charles R. Dauwalter
Milli Sensor Systems and Actuators, Inc.
West Newton, MA

SUMMARY

The technical feasibility of a magnetically suspended rotating wheel for miniature gyro applications was investigated under a NASA SBIR contract. A concept for a configuration for a system of compact, lightweight magnetic actuators capable of generating the necessary suspension forces and fabrication using millimachining planar fabrication technologies was developed. Both capacitive and electromagnetic position sensing concepts were developed for implementing a closed loop control system for supporting the wheel. A finite difference technique, implemented in a spreadsheet environment, for analyzing the force characteristics of the actuator was used and the results verified with Finite Element Analysis.

INTRODUCTION

Electrostatic actuators have been widely studied and applied to microfabricated devices, not only because of their relatively simple fabrication requirements (due to their planar nature), but because in micro-sized devices, where very small gaps are practical, their maximum force capability can be higher than for magnetic devices. However, for devices in the centimeter size range, magnetic actuators are the only real choice. Our group is pursuing the development of inertial instruments, such as gyros and accelerometers, that can be fabricated through the use of many of the technologies widely used for micro-devices, but adapted for application to larger devices. We have termed these fabrication technologies "millimachining"; they are briefly discussed below. Consequently, we chose to investigate the application of magnetic suspension techniques for the support of a spinning wheel that can function as the angular momentum generator of a gyro. The basic wheel configuration we considered was a disk approximately 1 centimeter diameter and of the order of one to several millimeters thick. Several types of motor were initially considered to drive the wheel into rotation, including permanent magnet, hysteresis and reluctance types but, because of the unavailability of suitable materials that we were confident could be fabricated by the millimachining techniques we intended to exploit, we settled on a reluctance motor, of the type investigated by Ahn and Allen[1], having the required rotor features on the rim of the wheel, leaving most of the face areas of the disk for the magnetic suspension actuators and position sensors. The motor will not be discussed further in this paper.

* The majority of the work described was supported by NASA SBIR Contract NAS 7-1340

The proposed magnetic suspension system is expected to implement active control of the actuators by feedback of position information generated by suitable sensors; the actuators themselves can provide the sensing function also, if a time sharing mode of operation is utilized. Otherwise, separate electromagnetic sensors could be used, but these require the allocation of some of the volume that could otherwise be used to improve the forcing performance. A third reasonable option is capacitive sensing which is planar in nature and can be implemented in much less additional volume than separate electromagnetic sensors. Completely passive suspension control, without independent position sensors or control loops, is possible and has found wide use in floated inertial instruments developed at Draper Laboratory[2], but is not seen as practical for the spinning wheel at this time due to the lack of a practical passive method for providing damping to stabilize operation.

MILLIMACHINING

Millimachining is a design philosophy and fabrication approach that MSSA is developing from a merging of the traditional technologies and the emerging micro-machining technology, and applying it to devices in the size range between macro and micro. Millimachined inertial instruments are expected to realize higher performance than micro instruments due to larger angular momentum. Millimachined devices can also be expected to be less expensive and more reliable than conventionally fabricated macro-sized instruments because they can take advantage of the economy and reproducibility of batch processing and dispense with most of the expensive, time consuming and unreliable hands-on human labor. Millimachining, as we use the term, subsumes applicable portions of traditional macromachining with those from the emerging micromachining field into an effective and efficient technology for designing and manufacturing milli-sized instruments.

The approach we are pursuing in the development of millimachined instruments is to reduce well-understood three-dimensional traditional components to pseudo-two dimensional planar configurations with equivalent or better functionality. Complete instruments then become multi-layered in form and may be assembled simply and automatically by stacking and bonding the layers. The individual layers, each containing components for a number of instruments, are batch fabricated, tested if necessary, and finally stacked into a complete block containing many instruments, which can then be separated into individual ones.

MAGNETIC SUSPENSION ACTUATOR CONFIGURATIONS

Once the rim of the wheel had been allocated to the motor function, it was necessary to identify an efficient way to provide magnetic forces in the plane of the wheel as well as normal to it. Magnetic actuators capable of developing independently controllable forces in two orthogonal directions simultaneously were the subject of research in the mid-1970s for application to magnetically levitated high speed ground transportation systems[3] and we selected a variation of that idea for further development. Figure 1a shows a cross sectional view of a magnetically suspended wheel employing actuators of conventional construction which can simultaneously develop both vertical and horizontal forces; only half of the wheel system is

shown, the other half to the left of the centerline is a mirror image of the illustrated right-hand side. Each of the actuators is pie-shaped in form, occupying a quadrant of space, and has a number of concentric circumferential slots on both the stator and wheel portions to provide both normal and tangential forces; this is illustrated more clearly in Figure 3.

The relative dimensions illustrated in Figure 1a are approximately correct; the stator back iron width, b, and the rotor back iron width, d, must be approximately 4 times the tooth width, since (neglecting leakage) they carry the flux of 4 teeth. Dimension c is greater than b to provide space for the coil, which can either be wound around the back iron, as shown, or around the actuator stator legs above the teeth.

IMPROVED ACTUATOR CONFIGURATION

Figure 1b shows an actuator configuration (patent applied for) that was developed during this work and which, because of its essentially planar geometry, lends itself well to millimachining fabrication. It offers exactly the same functionality as the conventional construction illustrated in Figure 1a, but with significant functional and fabrication advantages for implementing a magnetically suspended wheel system. Since both actuator configurations illustrated have the same number of teeth and slots, and the same surface area, the maximum attainable tooth saturation limited force is approximately the same for each. However, the volume of iron, and thus weight, of both the stator and rotor structures is very much less for the planar actuator in Figure 1b than for the conventional construction in Figure 1a. This is made possible by distributing the exciting electrical conductors in the slots of the planar stator sections that were provided to enable tangential force generation, rather than winding them around the back iron or stator legs. As was the case for Figure 1a, the relative dimensions in Figure 1b are approximately correct. Dimensions b', the stator back iron thickness, and d', the rotor back iron thickness, are approximately half of dimension a', the tooth width, because each carries half of the tooth flux. Figure 2 is an enlarged section view of the planar actuator showing the conductor insulation; it should be apparent that, with the same fabrication process, the single conductor per slot could be subdivided into a number of conductors insulated from each other and the stator core to reduce the required excitation current.

WHEEL MAGNETIC SUSPENSION SYSTEM

The integration of the actuators described above into a complete magnetic suspension system for the spinning wheel is shown in Figure 3. The upper half of the figure depicts an assembly of the eight stator actuator sectors, four on each side of the wheel, that are required to implement the magnetic suspension of the wheel; in the lower half of the Figure, the four actuator sections on one side of the wheel have been rotated away from the wheel as a unit to expose the circumferential grooves on the wheel and the conductors embedded in the slots of the stator segments.

x and y axis forces: The magnetic forces generated by the actuator sections can be independently controlled, to provide complete three-dimensional suspension as follows; Figure 4 will be helpful in

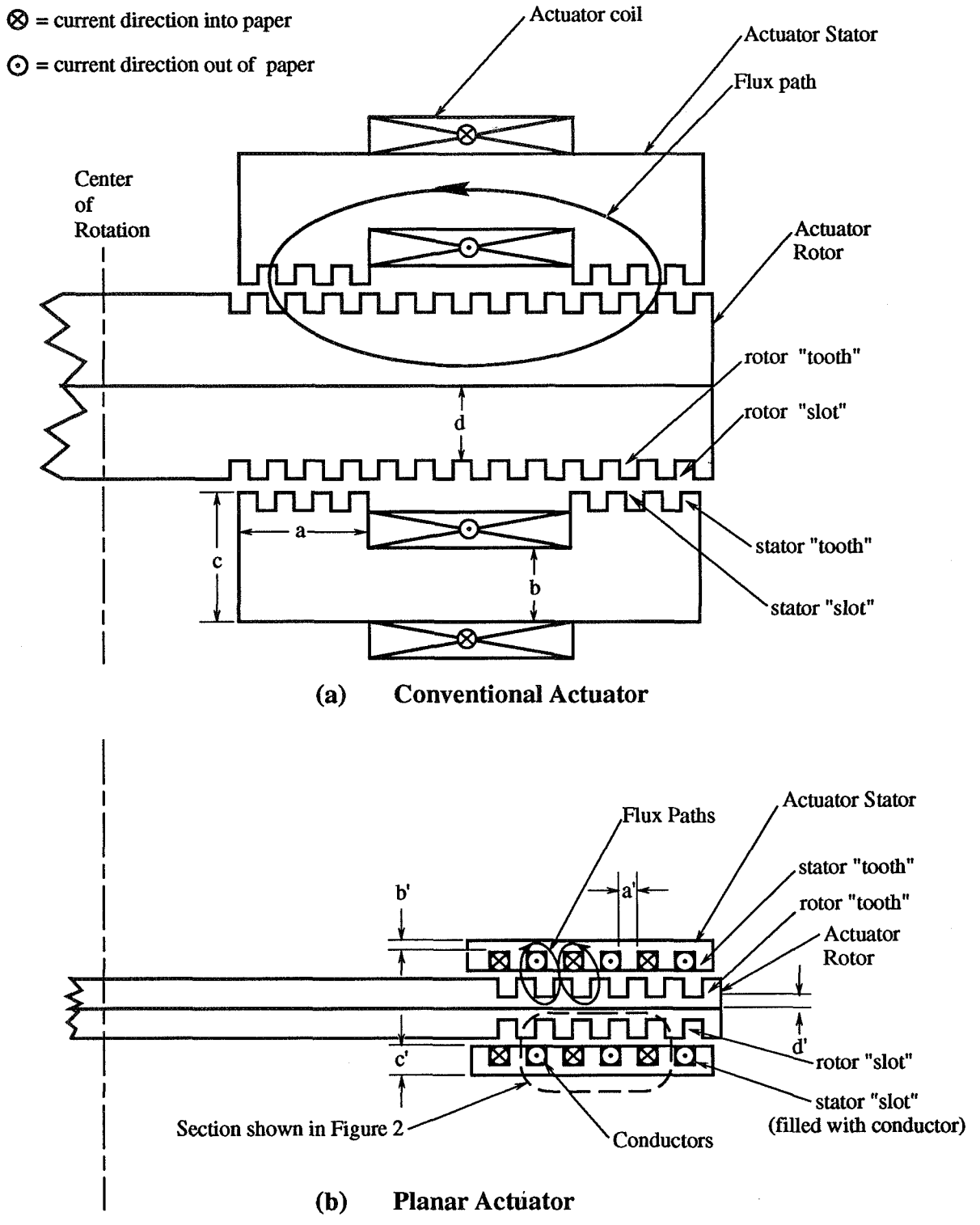

Figure 1 Conventional and Planar Actuators

understanding the operational concept. First, a selected quiescent, or bias, current is passed through all of the conductors, creating essentially identical forces in each actuator sector; the z direction attractive force

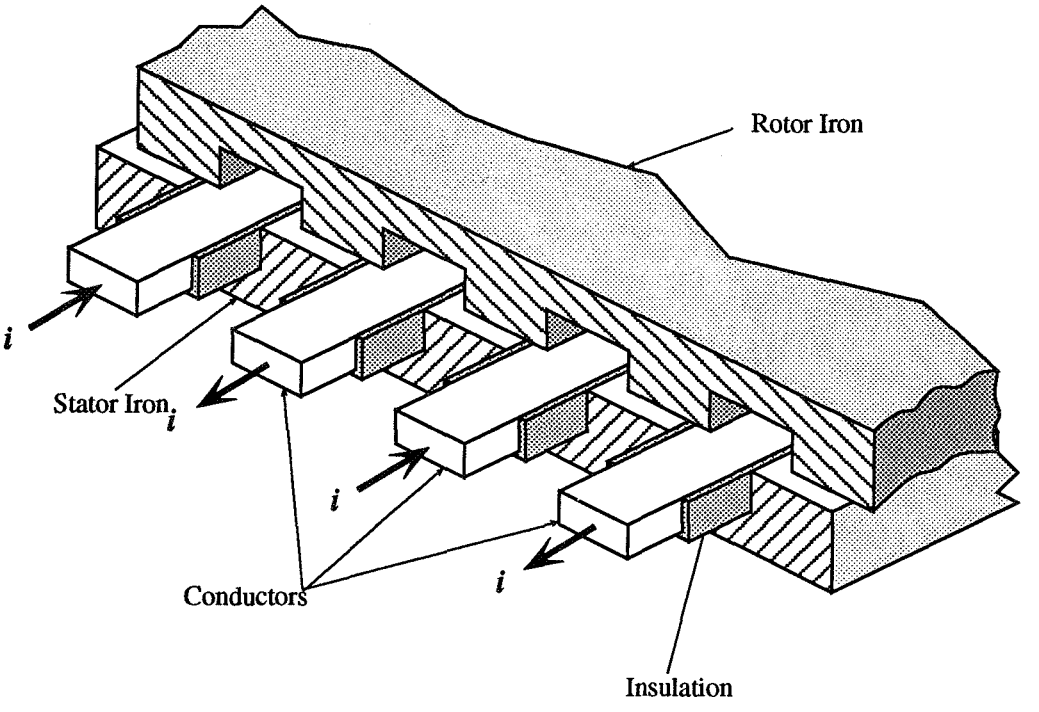

Figure 2 Enlarged View of Planar Actuator

of the actuator labeled B_{top} is equal to, but opposite in sign, that of the actuator labeled B_{bottom} while the x forces are equal and in the same direction (-x direction). The +z direction attractive force of the actuator, labeled D_{top}, is equal to, but opposite in sign, that of the actuator D_{bottom}, while the x forces are equal and in the same direction (+x direction). Thus, no net force is developed on the rotor. A similar situation applies to the y-axis forces. +x-axis force only, without affecting the other forces and moments, is generated by increasing the current in the actuator conductors of, D_{top} and D_{bottom}, by Δi and decreasing that in the conductors of B_{top} and B_{bottom} by Δi. y-axis forces are generated in a similar fashion.

z-axis forces: +z-axis force only, without affecting the other forces and moments, is generated by increasing the current in the conductors of actuator sectors A_{top}, B_{top}, C_{top} and D_{top}, by an amount Δi, while decreasing the current in the conductors of A_{bottom}, B_{bottom}, C_{bottom} and D_{bottom}, by Δi; the net x and y-axis forces and moments are unchanged.

Moments about x- and y-axes: Counterclockwise torque on the rotor, $+M_x$, about the x-axis is generated by increasing the current in the conductors of A_{top} and C_{bottom} by Δi and decreasing the current in the conductors of A_{bottom} and C_{top} by Δi; the x, y and z forces are unchanged. Clockwise torque on the rotor, $-M_x$, is generated by decreasing the current in the A_{top} and C_{bottom} conductors by Δi and increasing the current in the A_{bottom} and C_{top} conductors by Δi; the x, y and z forces are again unchanged. Torques about the y-axis are generated similarly.

The control logic is summarized in Table 1. In addition to making independent control of the forces and torques possible, the bias current provides the benefit of linearizing the force vs. control current relationship, which would otherwise be quadratic.

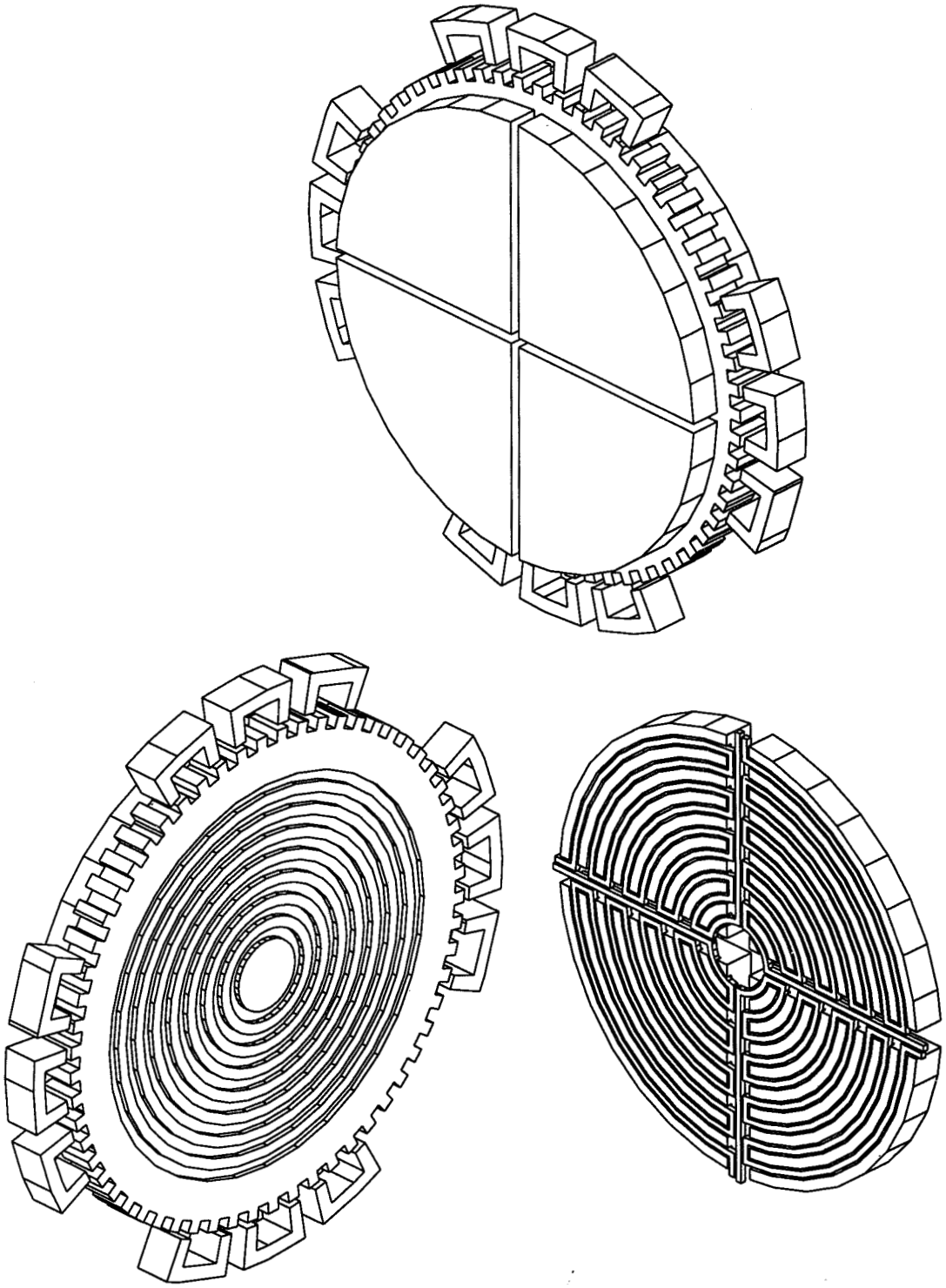

Figure 3 Assembled Magnetic Suspension Stator Sectors And Gyro Wheel

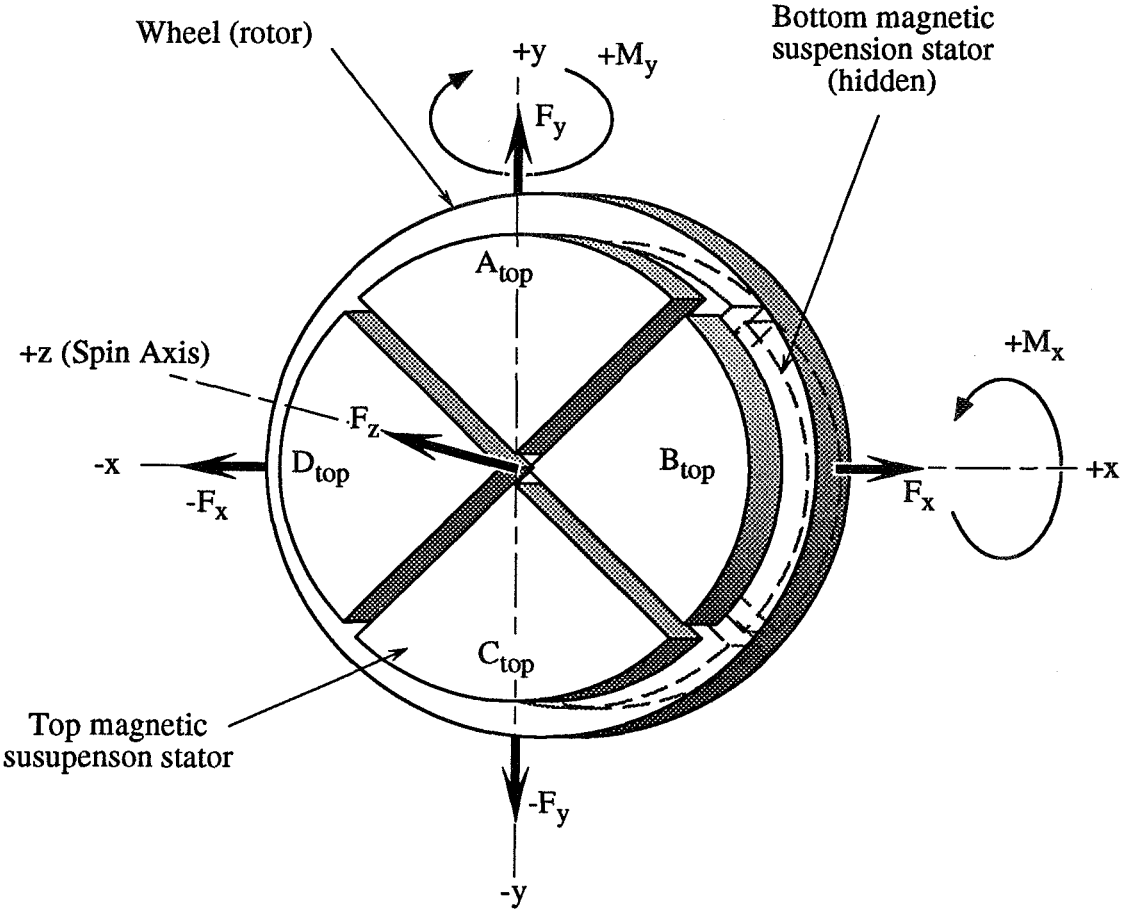

Figure 4 Magnetically Suspended Wheel

Table 1 Magnetic Suspension Control Logic

Sector	$+F_x$	$-F_x$	$+F_y$	$-F_y$	$+F_z$	$-F_z$	$+M_x$	$-M_x$	$+M_y$	$-M_y$
A_{top}	$+\Delta i$	$-\Delta i$	$+\Delta i$	$-\Delta i$	$+\Delta i$	$-\Delta i$	$+\Delta i$	$-\Delta i$		
B_{top}					$+\Delta i$	$-\Delta i$			$-\Delta i$	$+\Delta i$
C_{top}			$-\Delta i$	$+\Delta i$	$+\Delta i$	$-\Delta i$	$-\Delta i$	$+\Delta i$		
D_{top}	$-\Delta i$	$+\Delta i$			$+\Delta i$	$-\Delta i$			$+\Delta i$	$-\Delta i$
A_{bottom}			$+\Delta i$	$-\Delta i$	$-\Delta i$	$+\Delta i$	$-\Delta i$	$+\Delta i$		
B_{bottom}	$+\Delta i$	$-\Delta i$			$-\Delta i$	$+\Delta i$			$+\Delta i$	$-\Delta i$
C_{bottom}			$-\Delta i$	$+\Delta i$	$-\Delta i$	$+\Delta i$	$+\Delta i$	$-\Delta i$		
D_{bottom}	$-\Delta i$	$+\Delta i$			$-\Delta i$	$+\Delta i$			$-\Delta i$	$+\Delta i$

POSITION SENSING APPROACHES

Practical approaches to implementing the position indication needed for an active suspension control system can be described only briefly here, due to space limitations; they are described in considerable detail in the contract Final Report. Briefly, four techniques for position sensing were explored, one using the variation of capacitance with position of capacitors fabricated on the tips of the stator teeth and three using the variation of the stator segments' inductance with position: 1) adding capacitor electrodes to the actuator stator structure to implement capacitive position sensing, as schematically illustrated in Figure 5, 2) continuously sensing the inductance of the actuators while they are being used to generate force and 3) periodically time sharing the actuators so that they are used for forcing for a part of the period and then as sensors for the balance of the period; the latter reduces the maximum force that could be developed, 4) sharing the space allocated to the sensor and actuator stators, providing a portion for forcing and using the balance for sensing. This, like time sharing, would also decrease the maximum force, but might be practical for situations not requiring maximum force capability, and it would reduce the effect of the interaction of magnetic material nonlinearities and forcing current variations on accuracy of position sensing.

The actuators themselves can be effectively used for sensing the position of the rotor because their self-inductances change with both tangential and normal motion; an output voltage proportional to change in inductance, and thus in position, results when the actuators are used in a suitable bridge circuit. The sensing sensitivity will be maximum when the geometry is selected for maximum developed force because both position sensing sensitivity and the developed force are directly proportional to the rate of change of inductance with position.

All of the position sensing approaches described above provide ideal collocation of the sensing and forcing functions, avoiding the control system complications caused by non collocation.

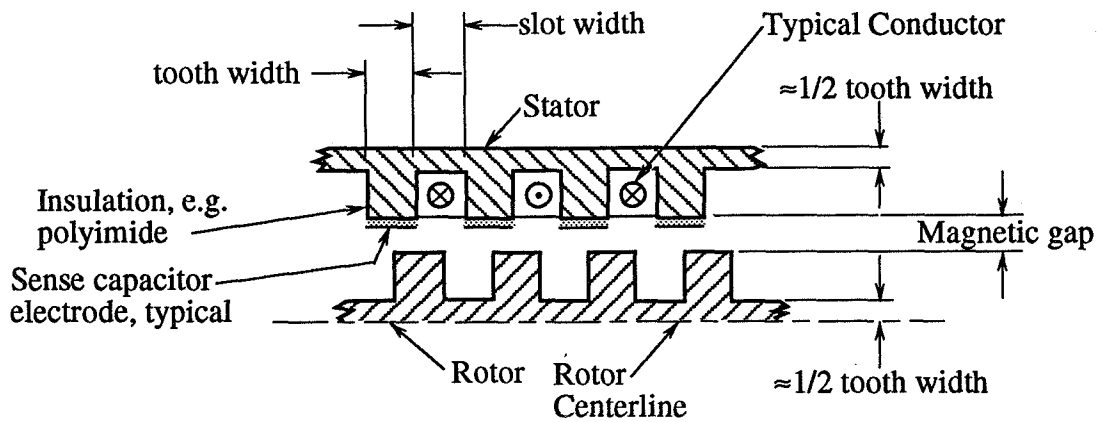

Figure 5 Actuator With Position Sensing Capacitors

Zero Current Regions

In a region devoid of electric currents, the magnetic field can be derived from a magnetic scalar potential Φ:

$$\overline{H} = -\overline{\nabla}\Phi \tag{1}$$

where Φ satisfies Laplace's equation

$$\nabla^2\Phi = 0 \tag{2}$$

In the two dimensional case considered here,

$$\overline{B_x} = \mu_0 \overline{H_x} = -\mu_0 \frac{\partial \Phi}{\partial x} \text{ and } \overline{B_y} = \mu_0 \overline{H_y} = -\mu_0 \frac{\partial \Phi}{\partial y} \tag{3a, 3b}$$

Non-Zero Current Regions

In a region containing electric currents, the scalar potential formulation is invalid; the magnetic field can be obtained from a magnetic vector potential $\overline{A}$:

$$\overline{B} = \overline{\nabla} \times \overline{A} \tag{4}$$

where $\overline{A}$ satisfies Poisson's equation

$$\nabla^2 \overline{A} = -\mu_0 \overline{J} \tag{5}$$

In the two dimensional cases considered here, $\overline{J}$ and $\overline{A}$ have only a z component, perpendicular to the x-y plane, with the result that

$$B_x = \frac{\partial \overline{A}}{\partial y} \text{ and } B_y = -\frac{\partial \overline{A}}{\partial x} \tag{6a, 6b}$$

The Finite Element Method has been highly developed for the analysis of magnetic field problems, and a number of programs are commercially available for that purpose; some, such as ANSYS, as a subset of a more general purpose package for engineering analysis. While these programs are now very sophisticated and have excellent capabilities, they are generally expensive, making them difficult to afford for very small organizations and individuals. Also, because of their broad capabilities, they tend to be rather complex, requiring substantial familiarization efforts by the user. Finite difference approximations to Laplace's and Poisson's equations can be used in conjunction with widely available spreadsheet programs, such as Excel® for useful analysis of a limited class of magnetic analysis problems, which includes the actuator discussed here. Since many engineers already have spreadsheet programs and use them extensively for engineering analysis, cost is not an impediment, and the simple nature of the procedures requires negligible effort for familiarization with their use.

Finite Difference Approximations of Laplace's and Poisson's Equations

If a discretized square coordinate grid is superimposed on the problem region with a grid spacing of $\Delta x=\Delta y$, then Laplace's equation in two dimensions can be approximated[4] by

$$\phi_1 + \phi_2 + \phi_3 + \phi_4 - 4\phi_0 \cong 0 \tag{7}$$

with the result that

$$\phi_0 = \frac{1}{4}\left(\phi_1 + \phi_2 + \phi_3 + \phi_4\right) \tag{8}$$

where ϕ_0 is the value of Φ at a particular node and ϕ_1, ϕ_2, ϕ_3, ϕ_4 are the values of Φ at the surrounding nodes. This simple equation is the basis for the field solutions using a spreadsheet; actually, the spreadsheet contains only this equation, repeated, and the relevant boundary conditions.

Similarly, Poisson's equation in two dimensions can be approximated by

$$\overline{A}_1 + \overline{A}_2 + \overline{A}_3 + \overline{A}_4 - 4\overline{A}_0 \cong -\mu_0 \overline{J} \tag{9}$$

with the result that

$$\overline{A}_0 = \mu_0 J + \frac{1}{4}\left(\overline{A}_1 + \overline{A}_2 + \overline{A}_3 + \overline{A}_4\right) \tag{10}$$

applies to those nodes of the problem region which contain currents; Equation (8) applies elsewhere.

Boundary Conditions

Four types of boundary conditions are applicable to the type of problem being discussed here. The first is the Dirichlet boundary condition in which a prescribed value of the potential function is applied to the boundary. The second is the Neumann boundary condition in which field is specified on the boundary; in this case, the field has no components normal to the boundary. The third consists of symmetry relationships; this type appears in problems, like the present one, in which the overall geometry consists of repeating sub-units. In this type, for example, the potential value at the first node to the left of the left-hand boundary is specified to be the same as the value at the first node to the left of the right-hand boundary and vice-versa. The field may have in this case components normal to the boundary. A fourth boundary condition, used in vector potential models where iron of infinite (or relatively high) permeability is assumed, is the specification that the normal derivative be zero. This results in zero field parallel to the iron surface, a consequence of the infinite permeability; in scalar potential models, this is a natural consequence of the Dirichlet boundary conditions used.

Force Calculations Using Maxwell's Stress Tensor

The Maxwell's stress tensor[5] can be used to obtain expressions for the normal stress, σ, and the shear stress, τ, on a differential surface area, ds, that is produced by the magnetic field, H, at that surface. These expressions provide a convenient and powerful method for calculating the magnetic forces exerted on a body, and are commonly used in finite element magnetics programs. If H_x and H_y are the magnetic field components parallel and normal, respectively, to the surface, ds, then the magnetic stresses on ds are

$$\tau = \mu_0 H_x H_y \tag{11}$$

and

$$\sigma = \frac{\mu_0}{2}\left(H_y^2 - H_x^2\right) \tag{12}$$

The total force and torque on a body are calculated by integrating the stresses along a closed contour in the space surrounding the body.

Solution Technique

The solution technique utilized for obtaining the potentials from which the fields are derived is a relaxation method, the Gauss-Seidel method. To implement this in a spreadsheet, the calculation option is set to allow iteration. With iteration enabled, recursive calculations are permitted; i.e., the equations for the calculations in a cell are allowed to contain parameters which depend upon the results of the calculation, e.g. x=x+1; without iteration enabled a "circular reference" error would result. A suitable limit on the number of iterations allowed is set, and a value for maximum change set. Then, the calculation proceeds until either the maximum number of iterations is reached, or the maximum change in the value of any cell for one cycle of calculations is less than the specified value. The accuracy of the result depends both upon the specified maximum change in cell value per iteration and the fineness of the subdivision of the problem region. The adequacy of the fineness of the net can be assessed by comparing the values of Φ for the problem with net spacing $\Delta x=\Delta y=h$ with the results with net spacings $\Delta x=\Delta y=h/2$. Karplus[6] describes a useful extrapolation which determines the potential distribution of a model with a mesh at least as fine as $\Delta x=\Delta y=h/4$:

$$\Phi_{\Delta x=\Delta y=h/4} = \Phi_{\Delta x=\Delta y=h/2} - \frac{1}{3}\left(\Phi_{\Delta x=\Delta y=h} - \Phi_{\Delta x=\Delta y=h/2}\right) \tag{13}$$

Typical Spreadsheet Implementing Finite Difference Equations

Figure 6 shows a typical spreadsheet set up to solve for the vector potential of a problem. The actuator configuration discussed in this paper is illustrated, but with a relatively small number of cells to permit the equations for the cells to be shown more clearly on the sheet. The

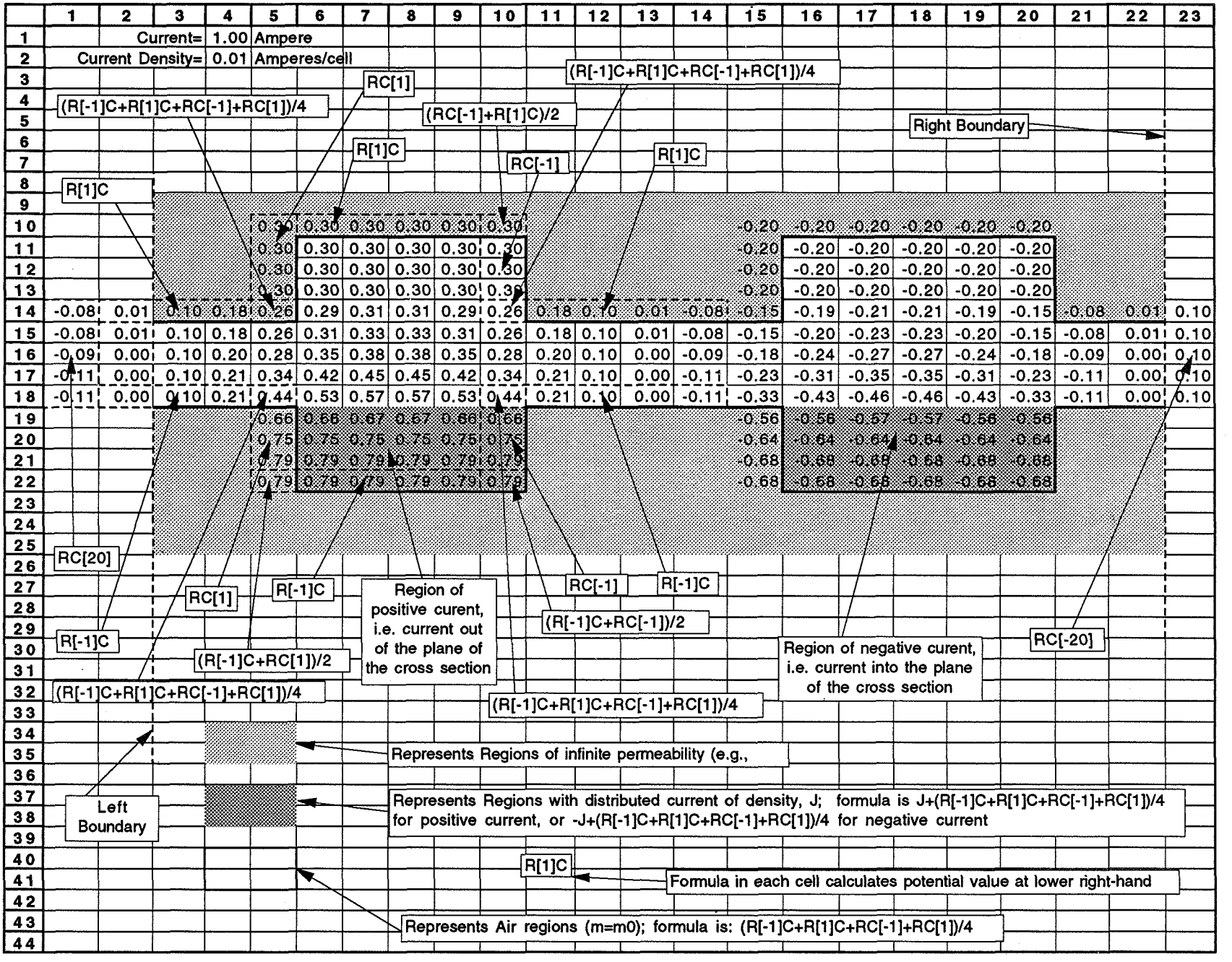

Figure 6 Example Spreadsheet Actuator Analysis

regions representing the iron and the current carrying conductors is shaded, as indicated by the key on the Figure, to facilitate ready visualization of the geometry being modeled; the boundary between the iron and air is indicated by a heavy black line. On the left-hand side of the sheet, cells containing the same equations are enclosed in dotted boxes; arrows connect those regions with the equations that they contain; this identification is omitted on the right side, except for the boundary condition. The intersections of the individual cell walls correspond to nodes of the square grid superimposed on the problem region to discretize it for finite difference analysis. The equation which an individual cell contains calculates the value of the node at its lower right-hand corner.

As discussed above, Equation (10) is implemented in all cells in regions where current is not zero, and Equation (8) in all other cells except at the boundaries. At the right and left-hand boundaries, the symmetry condition discussed above, under boundary conditions, is applied to reflect that the actuator consists of repeating sets of the basic configuration of two teeth and two slots. On the remaining boundaries, representing the iron portions of the actuator, the boundary values are set to equal those of the nearest adjacent non-boundary node, so that the normal derivative of the potential is zero; this reflects the effect of the assumed infinite permeability of the iron, which results in a zero value for the field gradient parallel to the boundary (i.e., the magnetic flux lines are normal to the boundary.) In the equations for the cells of regions containing current, j is the current density in the region.

Field Visualization

It is sometimes helpful in magnetics design problems to be able to visualize the field distribution; this may readily be done with the spreadsheet solution approach. Visualization is almost trivial for problems utilizing the vector potential formulation, since the magnetic field is parallel to equipotentials of $\overline{A}$, and many spreadsheet programs have a built-in facility for easily plotting equipotentials. This function is provided by the Contour Chart format of the 3-D Surface Chart type in Excel®. Producing a field plot is somewhat more involved for scalar potential problems, since the field lines are orthogonal to the equipotentials. If the problem is reformulated with the appropriate Dirichlet boundaries replaced by Neumann boundaries and vice versa, the desired result is obtained. For problems such as the configuration shown in Figure 1a, in which the stator and rotor surfaces are properly Dirichlet boundaries and the boundaries of the repeating element are the symmetry boundary described above, it is necessary for correct results to ensure that the problem is set up such that the symmetry boundaries are located in a region where the field lines are parallel to those boundaries. This requires some intuition and/or experience and is not possible, except very approximately, for some problems.

ANALYSIS RESULTS

The results of the analysis of the force characteristics of the planar actuator are shown in Figures 7 and 8, which show tangential and normal forces vs. tangential displacement for various air gap values. The forces indicated are those for the repeating unit of two teeth and two slots, per meter of actuator length. The configuration that was analyzed is the lower half of the planar

actuator illustrated in Figure 1b and Figure 2. Both the tooth and slot widths were 32 mm and the slot depth was 16 mm for the finite element analyses and 32 mm for the spreadsheet analysis. The purpose of the analyses was to provide an initial understanding of how the normal and tangential forces depend upon the design variables, in particular the air gap relative to the stator tooth and slot widths. No attempt was made to explore the effect of varying the tooth to slot width ratio to yield more optimum characteristics; such an optimization study will be appropriate for future work.

The maximum tangential force, for all air gaps in the range studied, occurs when the normal force is approximately half-way between its maximum and minimum values; since the tangential force, for the proportions studied, was always smaller than the normal force (by a factor of approximately 5), designs for applications would likely be chosen to operate in this region. It is considered likely that higher ratios of tangential to normal forces can be attained by modifying the ratio of the tooth to slot widths used, quite arbitrarily, in this study; the latter ratio is also important in influencing the power dissipation since making the slot wider allows a larger conductor cross-section area resulting in lower total resistance and power. Figure 9, which compares the results of the FEM and spreadsheet analyses for one value of air gap, demonstrates that the spreadsheet method of analysis produces predictions that are close, but not identical to those of the finite element analysis method. Some of the difference may be due to the assumption of infinite material permeability in the spreadsheet analysis (a permeability of 4,000 was assumed in the finite element analyses) and that the slot depth used for the FEM analysis that was half the value used for the spreadsheet analysis.

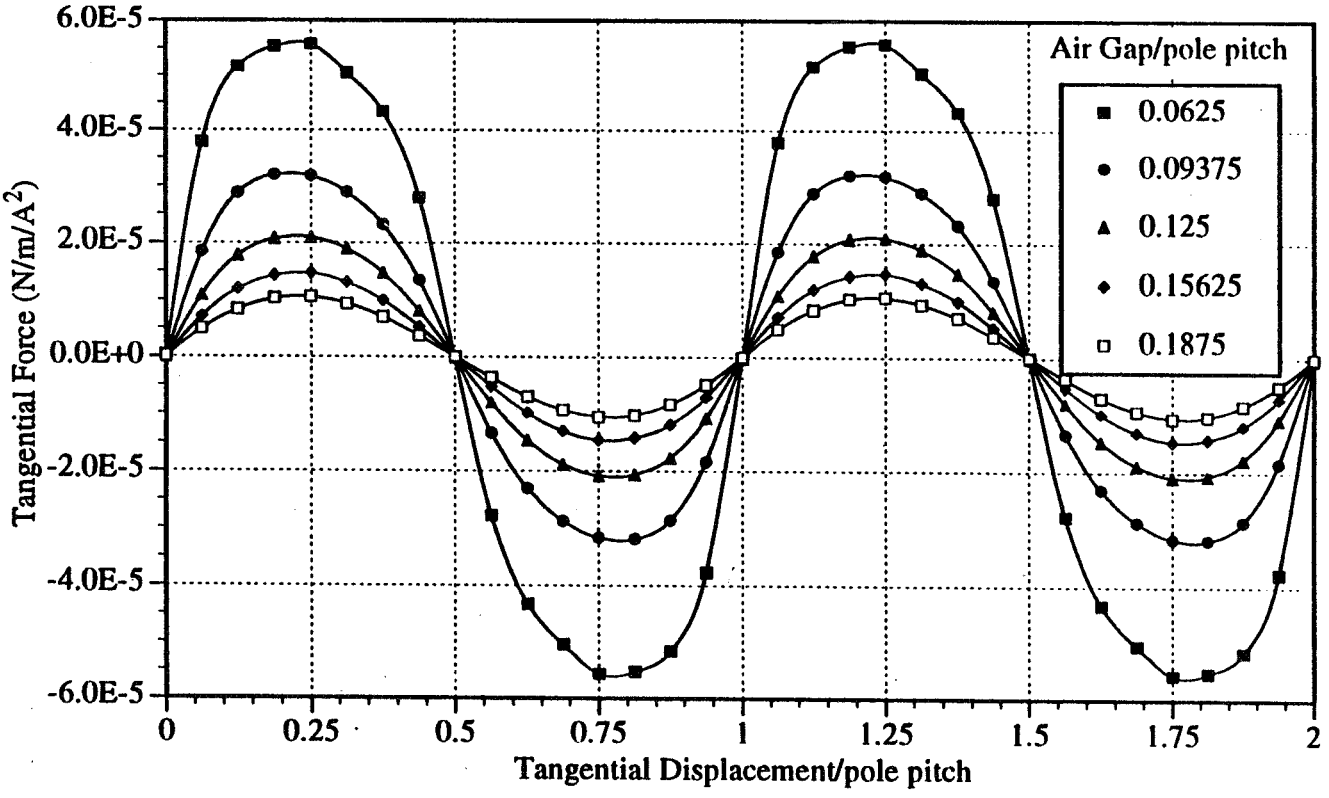

Figure 7 Tangential Force vs. Tangential Displacement and Air Gap, FEM

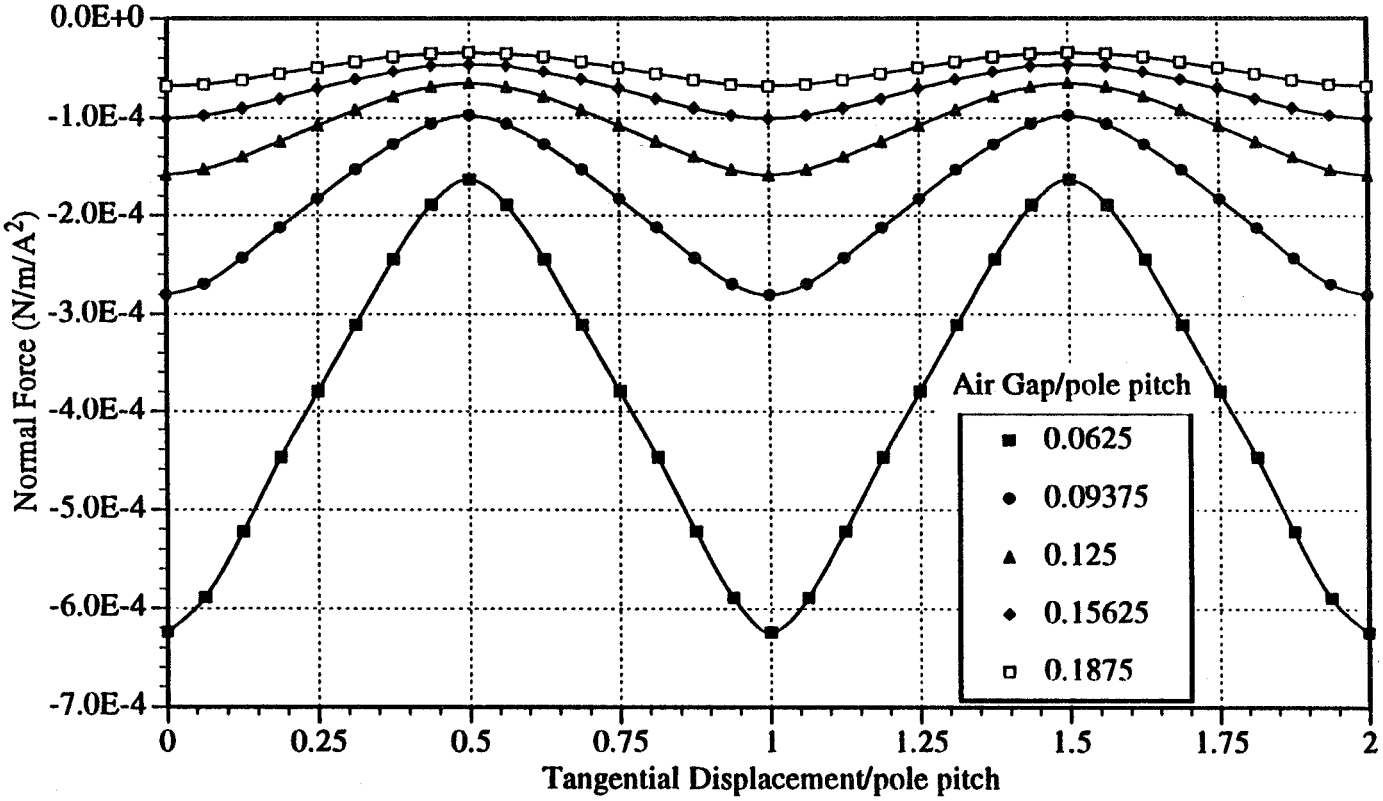

Figure 8 Normal Force vs. Tangential Displacement and Air gap, FEM

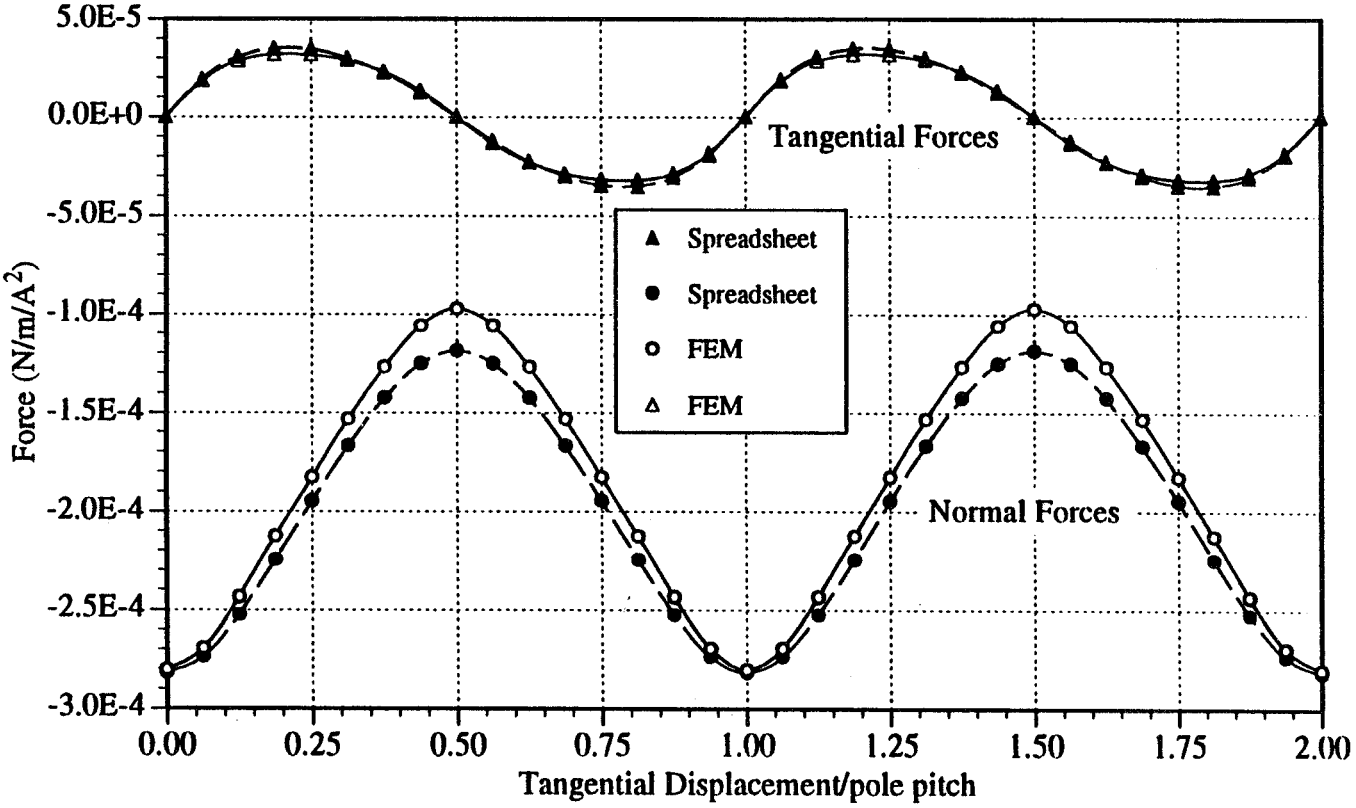

Figure 9 Spreadsheet/FEM Comparison: Force vs. Displacement

Conclusions

The work described established the technical feasibility of a magnetically suspended spinning wheel for applications such as a miniature gyro. The planar actuator configuration that was developed appears to be well suited to fabrication by millimachining processes as well as making lighter weight and more volume efficient actuator designs possible. The fabrication of the planar actuator was confirmed by supporting work at Georgia Institute of Technology, where it was possible to fabricate a proof-of-concept miniature actuator stator assembly in only a few weeks after the design was identified. Performance analysis of electromagnetic devices using finite difference approximations to the relevant field equations in a spreadsheet environment was shown to be a convenient and reasonably accurate alternative to finite element analysis programs, at least for relatively simple geometry's and for preliminary design purposes. Further work may improve the spreadsheet analysis capabilities, in particular permitting finite material permeability and axi-symmetric geometry's to be handled.

ACKNOWLEDGMENTS

The author gratefully acknowledges the assistance provided by the following: Dr. Randy Bartman, contract Technical Monitor at JPL, for support, encouragement, and helpful discussions of potential NASA applications of the technology, Dr. Raymond Carroll of MSSA for timely and helpful discussions of the field solutions, Kevin Hinckley and Joseph Nicolaisen of the Equipment Division of Dynamics Research Corp. for finite element analyses, and Prof. Mark G. Allen and his student, William P. Taylor, at Georgia Institute of Technology for their expert advice on actuator design considerations for millimachining fabrication and the fabrication of proof-of-concept devices.

REFERENCES

1. Ahn, C. H. and Allen, M. G.: A Fully Integrated Micromagnetic Actuator with Multilevel Meander Inductive Core. Proc. IEEE Solid State Sensor and Actuator Workshop, Hilton Head, SC, June 1993.

2. Frazier, R. H.; Gilinson, P. J., Jr.; and Oberbeck, G. A.: *Magnetic and Electric Suspensions.* MIT Press, Cambridge, MA, 1974, pp. 147 et seq.

3. Wormley, D. N, et. al: Noncontacting Suspension and Propulsion for Ground Transportation. Report DOR/RSPA/DPB-50/79/34, Department of Transportation, Research & Special Programs Administration, Washington, DC, 1979 (Available NTIS, Springfield, VA).

4. see, e.g., Karplus, W. J.: *Analog Simulation*, McGraw-Hill, New York, 1958, pg. 92-94.

5. Ida, Nathan and Bastos, Joao, P. A.: *Electromagnetics and Calculation of Fields*, Springer-Verlag, New York, 1992, pp. 188-195.

6. Karplus, *op. cit.*, pp. 200.

DESIGN AND APPLICATION OF A COLLOCATED CAPACITANCE SENSOR FOR MAGNETIC BEARING SPINDLE

Dongwon Shin, Seon-Jung Liu, Jongwon Kim

Seoul National University
Seoul, Korea

SUMMARY

This paper presents a collocated capacitance sensor for magnetic bearings. The main feature of the sensor is that it is made of a specific compact printed circuit board (PCB). The signal processing unit has been also developed. The results of the experimental performance evaluation on the sensitivity, resolution and frequency response of the sensor are presented. Finally, an application example of the sensor to the active control of a magnetic bearing is described.

INTRODUCTION

A magnetic bearing is a contact-free machine element which can support a spinning shaft by active control of electromagnetic forces. The advantages of magnetic bearings are that they are free from the problem of lubrication, wear, sealing, etc. and that it can actively suppress shaft vibration. However, since the magnetic bearing system is inherently unstable, a feedback controller is necessary. To implement a feedback controller, a displacement sensor is used for on-line measurement of the gap between the rotor and the magnetic bearing pole.

The problem this paper deals with is the location of the sensor. The sensors which are most frequently used are eddy current displacement sensors. This type of sensor is, however, so easily influenced by the magnetic fields generated by the magnetic actuator coils that it should be installed outside the coils (ref. 1). This causes a noncollocation problem of the sensor. The capacitance type sensor is also applied to magnetic bearings (ref. 2). However, commercial capacitance sensors are relatively expensive and are not so compact as to be collocated in the magnetic actuator coils of the magnetic bearing system.

Since the noncollocation problem of the gap sensor means inconsistency of the location of gap measurement with that of magnetic actuator coils, it is natural that the measured gap data include an indispensable error which is proportional to the offset distance of the gap sensor from the center of magnetic actuator coil. Moreover, Maslen *et al.* (ref. 3) and Barrett *et al.* (ref. 4) have verified that the noncollocated magnetic bearing might generate unstable motions with a flexible rotor shaft.

The objective of the research is to develop a collocated sensor system for magnetic bearings. The

main ideas are based on two points. One point is that the developed sensor is of the capacitance types rather than an eddy current type, considering the robustness to electrical noise induced by magnetic fields. The other point is that it is made of a small piece of printed circuit board (PCB) so that it could be both cost-effective and compact enough to be built into the center of the magnetic actuator coils of the magnetic bearing.

The mechanism of gap measurement by using a capacitance type sensor has been well demonstrated by Chapman (ref. 5). Chapman designed a circular sensor plate on which a thin brass layer is coated. He installed this sensor plate at the end of the spindle nose of a milling machine in such a way that the sensor plate and the spindle nose maintain a sub-mm gap from each other. He used this sensor system in on-line measurement of the gap, thus ultimately measuring the rotational motion accuracy of the spindle axis.

The research approach used in this paper is based on Chapman's method. What has been enhanced is that the sensor size can be reduced by the order of more than 1: 200 by adopting PCB manufacturing technology instead of a man-made brass layer. Additionally, the signal processing unit is refined for improving the resolution and bandwidth of the sensor system, which becomes more critical as the sensor size gets smaller.

This paper is organized as follows. In the next section, the detailed design of the collocated capacitance sensor system is described. Then, the following section presents the experimental setup and the results of the experimental evaluation of the developed sensor system. Finally, the experimental results of the sensor system application to magnetic bearing control are included.

DESIGN OF A COLLOCATED CAPACITANCE SENSOR SYSTEM

The overall shape and location of the gap sensor plate is illustrated below in figure 1. The base material of the sensor plate is epoxy resin FR4 with a copper layer coated on it. The coating thickness is 0.1 mm.

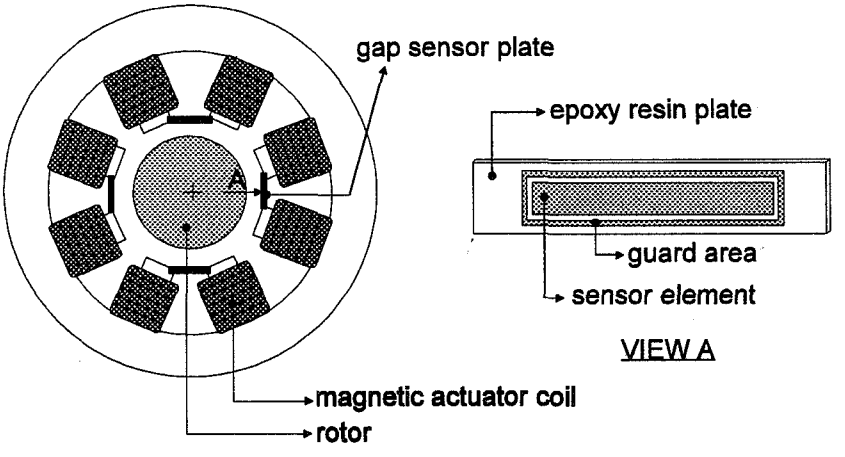

Figure 1. Cross section of the magnetic bearing and the overall shape and location of the gap sensor plate.

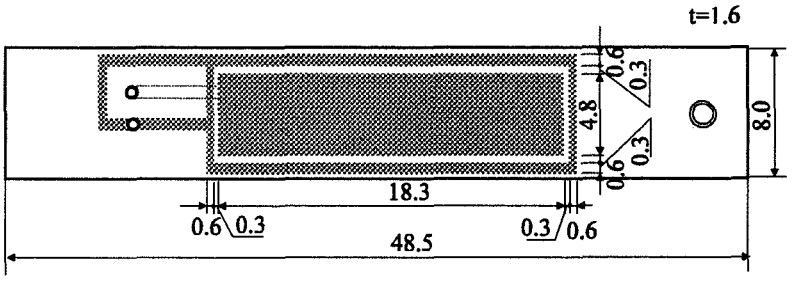

Figure 2. Detail geometric dimensions in mm of the gap sensor plate.

The copper layer is then cut out to the desired pattern through the etching process, which is an identical technology to the manufacture of printed circuit boards (PCB's). The copper layer pattern is composed of a sensor element and a guard area. The guard area, surrounding the sensor element, protects the sensor element from the influence of the electromagnetic fields outside the sensor plate. As shown in figure 1, a sensor plate is embedded into each of the magnetic actuator coils in order. The location of the sensor plate in the center position of the magnetic actuator coil eliminates definitely the noncollocation problem of the sensor.

Figure 2 shows the detailed geometric dimensions of the gap sensor plate developed. Currently, sensor plate of width 8.0 mm, length 48.5 mm and thickness 1.6 mm are manufactured. The capacitance of the sensor is 1.95 pF when the gap between the rotor and the sensor is 0.4 mm. Finally, the surface of the sensor plate is coated with an insulator.

Two pairs of gap sensors are connected to one signal processing unit as shown in the schematic diagram of figure 3. Each of x and y axis gap displacements is measured by each pair of gap sensors located opposite to each other. The signal processing unit consists of two parts : (1) four channels of capacitance to voltage converters (C/V's), sample and holders (S/H's), low pass filters (LPF's), offset and gain adjustment circuits (OGA's), and (2) two channels of differential circuits (DIFF's), offset and gain adjustment circuits (OGA's).

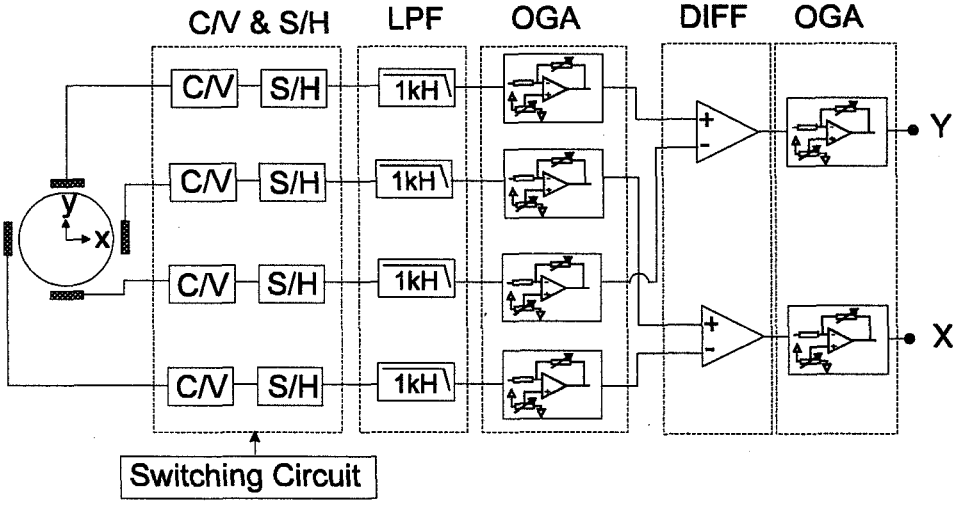

Figure 3. Schematic diagram of the signal processing unit.

The C/V converter charges the sensor element of the sensor plate during a fixed charging time interval T_C, and then measures and holds the charged voltage V_P of the sensor element. After sampling and holding V_P it discharges remaining electric charges on the sensor element during a fixed discharging time interval T_d. The C/V converter repeats this charging, sampling and holding, and discharging routine during a total time interval T. Figure 4-a. shows the signal flow chart of the C/V converter.

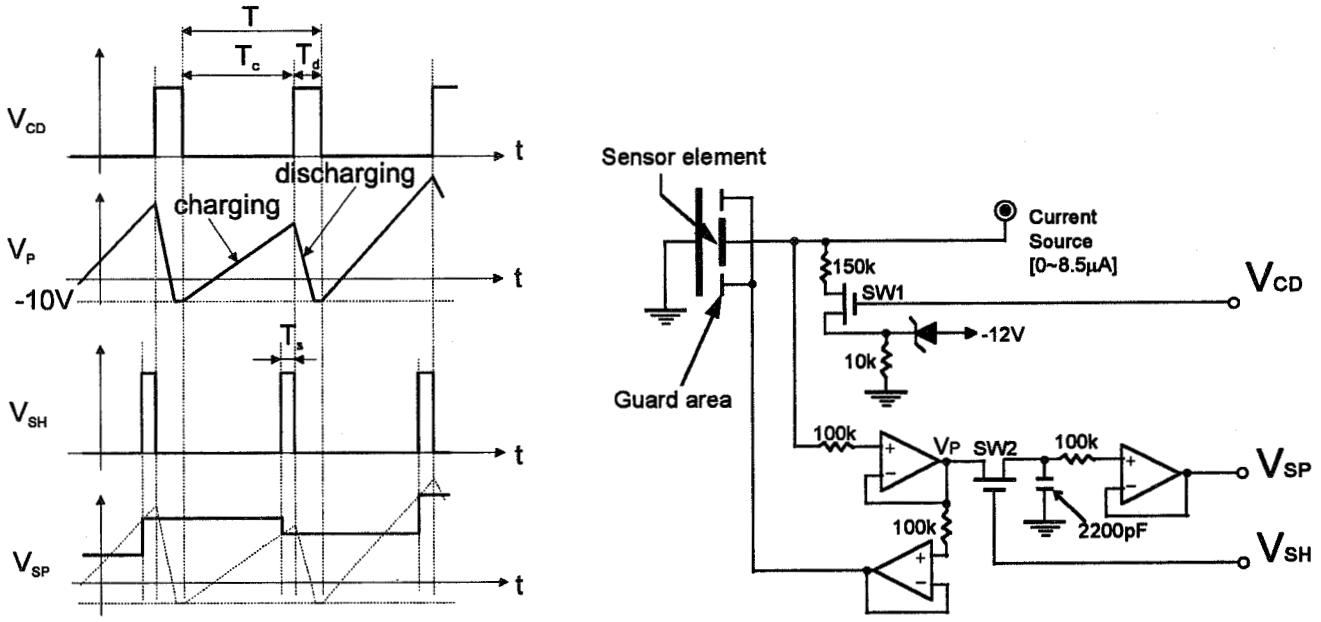

(a) Signal flow chart (b) Detail circuits of C/V and S/H

Figure 4. Signal flow chart and detail circuits of the C/V and S/H of the signal processing unit.

The gap between the rotor and the magnetic actuator coil, denoted by x, is related to the fixed charging time interval T_C and the charged voltage V_P of the sensor element as following :

$$V_p = \frac{Q_{T_c}}{C_s} \equiv \frac{\int_0^{T_c} i_s \, dt}{\kappa \varepsilon_0 A_s} x \quad \text{or} \quad V_p = \frac{i_s T_c x}{\kappa \varepsilon_0 A_s} \tag{1}$$

where

Q_{Tc} : electric charges accumulated during T_c
C_s : capacitance of the sensor element
i_s : current input to the sensor element
κ : dielectric constant
ε_0 : permittivity constant
A_s : total area of the sensor element

From equation (1), the displacement gap x is measured indirectly from the charged voltage V_p. Figure 4-b illustrates the detailed circuits of the C/V and S/H of the signal processing unit. In order to charge the sensor element, Chapman (ref. 6) used a constant voltage source. With a constant voltage source, the rate of growth of the charged voltage V_p decreases during the charging time interval T_c,

resulting in the deterioration of measurement resolution as the gap x becomes larger. For this reason, a constant current source circuit is adopted in order to maintain a linear increase of V_p during T_c. The driving signal V_{CD} synchronizes the charging and discharging cycle of the sensor element by turning on and off switch #1 (SW1) in the circuit as shown in figure 4. On the other hand, the sample and hold driving signal V_{SH} turns on and off switch #2 (SW2) in the circuit. Therefore the maximum value of the charged voltage V_p of the sensor element is sampled and held, thus being transformed to the output signal V_{SP} of the C/V and S/H circuit. The typical values of cycle time T, discharging time T_d, sample and holding time T_s are 50-100 μsec, 15 μsec, and 440 nsec, respectively.

The low pass filter (LPF) of the signal processing unit (see figure 3) eliminates the switching noise component of the output signal V_{SP} with the cutoff frequency of 1 kHz. The function of the offset and gain adjustment circuit (OGA) is to compensate for the inherent tolerance of the geometric dimension of the sensor element and for the electric properties of each channel in the signal processing unit.

As shown in figure 3, a pair of gap sensors is assigned to each axis gap measurement. Each pair of sensors is located in the opposite direction from each other. What is necessary to obtain from this sensor system for magnetic bearing control is the relative displacement of the rotor from the fixed reference of frame. That is, the difference between the output signals from the sensor elements of the same pair is important for magnetic bearing control. Hence, the output signals from the sensor elements constituting a pair are finally differentiated, and then, amplified by the differential circuits (DIFF's) of the signal processing unit, resulting in V_x and V_y.

EXPERIMENTAL EVALUATION OF THE DEVELOPED SENSOR SYSTEM

As the performance measures of the developed sensor system, the sensor sensitivity and bandwidth subject to static and dynamic gap displacement variations, respectively, are evaluated.

Sensor Sensitivity to the Static Gap Displacement Variation

An experimental setup has been implemented such that a sensor plate is attached to the moving part of a micrometer which retains the positioning accuracy of 0.01 mm resolution. The sensor plate is able to be positioned accurately from the rotor shaft in radial direction by using the micrometer. For each positioning point of the sensor plate, that is, for each known gap displacement, the output signals of the signal processing unit are measured. The experimental results are shown in figure 5.

The sensitivity plots shown in figure 5 are obtained from two series of experiments in cases of the cycle time T of 97 μsec and 65 μsec, respectively. The discharging time T_d is 15 μsec for both cases. The constant current i_S supplied to the sensor element is also varied from 3.0μA to 7.0 μA. From the plots, sensitivity characteristics can be easily verified as follows :

(1) As the cycle time T increases, the range of the sensor increases,
(2) as the output of the current source i_S increases, the range of the sensor increases, and
(3) the rate of growth of the output signal V_x decreases as the gap displacement x increases.

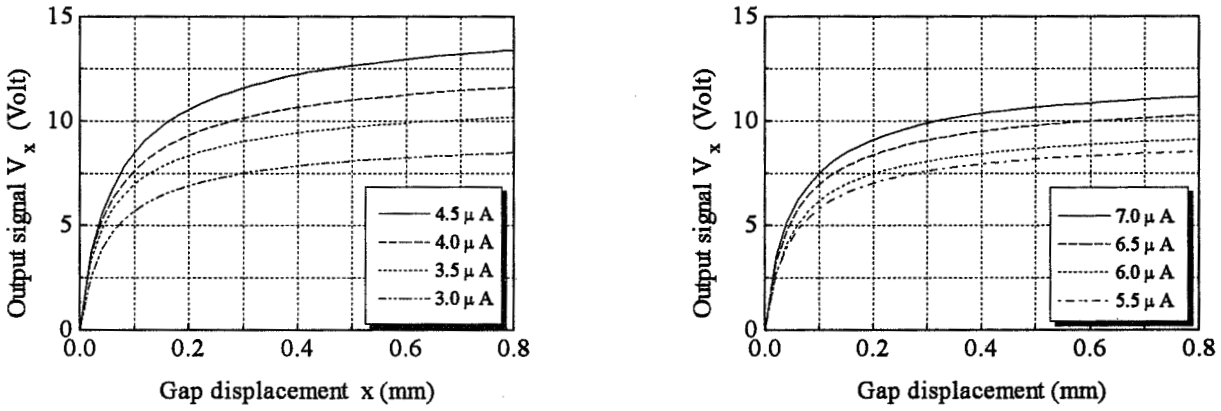

(a) In case of T=97μsec

(b) In case of T=65μsec

Figure 5. Sensor sensitivity to the static gap displacement variation.

Since the relationship between the output signal V_x and the gap displacement x is not linear, a look-up table method or an interpolation algorithm should be used when utilizing indirect measurement data to practical control issues.

Bandwidth to the Dynamic Gap Displacement Variation

The bandwidth of the sensor is also important when it is used for magnetic bearing control at such high rotational speeds above 10,000 rpm. To test the bandwidth of the sensor, the gap displacement x has to be varied in such a way to generate a sinusoidal signal. For this purpose, a special rotor shaft has been designed and manufactured. The cross section of the specially designed rotor shaft is shown in figure 6.

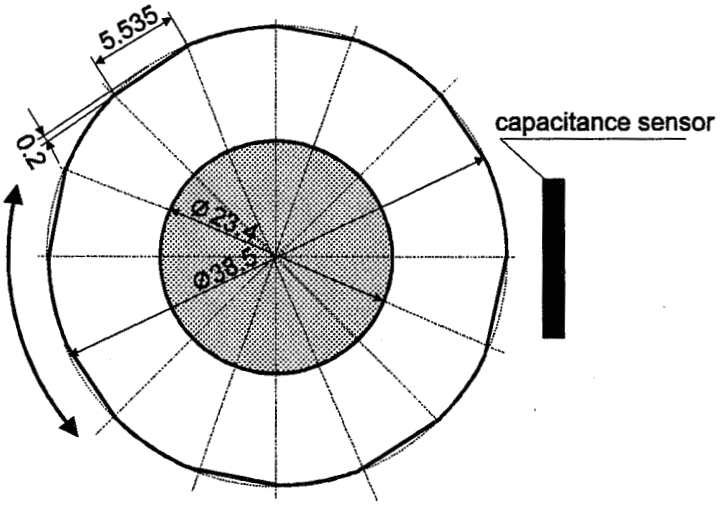

Figure 6. Cross section of the specially designed rotor shaft for the sensor bandwidth test[unit : mm]

Eight segments of the perimeter of the rotor shaft with the diameter of 38.5 mm have been flat end-milled at equiangular intervals with the width and the maximum depth-of-cut of 5.535 mm and 0.2 mm, respectively. Thus, the specially designed rotor shaft is able to generate quasi-sinusoidal gap displacement signals of the maximum frequency of 1.6 kHz when its spinning speed is 12,000 rpm.

The frequency response plots of the output signal V_x are shown in figure 7. The Bode plots shown in figure 7 are obtained from the three series of experiments in cases of the cycle time T of 97, 65 and 57 μsec, respectively. The discharging time T_d is 15 μsec, and the constant current i_s is 4.5, 7.0 and 7.5μA, respectively. From the plots, frequency response characteristics can be easily verified as follows :

(1) As the cycle time T decreases, the bandwidth of the sensor increases, and

(2) the bandwidth of the sensor with T of 97 μsec is around 7,500 rad/sec (or 1.2 kHz).

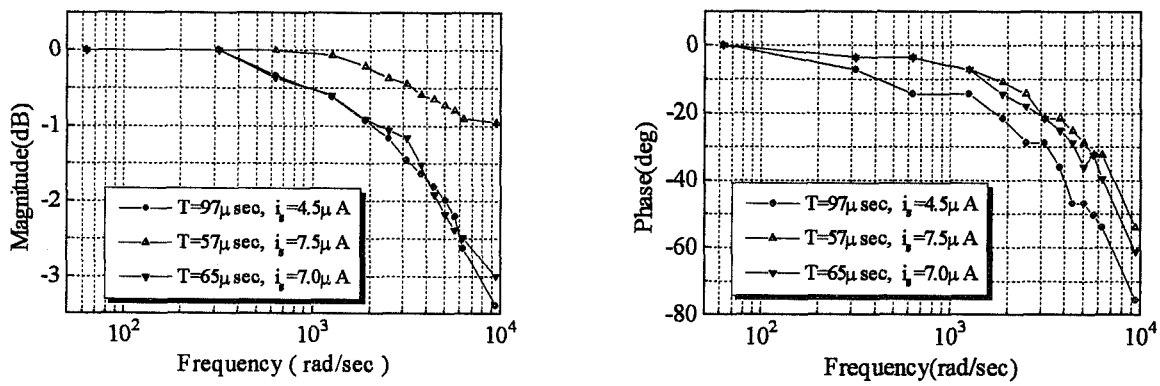

(a) magnitude (b) phase

Figure 7. Frequency response of the output signal V_x

If higher bandwidth is desired, a lower value of the cycle time T should be selected. In this case, the static sensitivity is decreased as shown in figure 5. From further experimental results, of which data are not shown in the paper, it has been also verified that the bandwidth of the sensor is independent of both the output of the current source i_s and the total area of the sensor element A_s.

SENSOR APPLICATION TO A MAGNETIC BEARING SPINDLE

The collocated sensor system has been equipped into a testbed of a magnetic bearing spindle as shown in figure 8 on the next page. The vertical rotor shaft is supported by a radial angular contact ball bearing at the lower part and by a radial magnetic bearing at the upper part. Thus, without the magnetic bearing, the rotor shaft would behave like a vertical pendulum. The rotor is connected to a brushless DC motor through a universal coupling. From the built-in encoder in the DC motor, the spinning speed of the rotor shaft is measured. There is a backup ball bearing at the uppermost part of the rotor for both idle and emergency states.

The feedback control algorithm is run by a digital signal processor (DSP) based controller where a TMS320C40 CPU chip is embedded with a 12-bit analog-to-digital (A/D) converter and a 12-bit digital-to-analog (D/A) converter. The DSP board is installed into a personal computer 486 class. PC 486 can share the selected internal states with the DSP board through a dual port random access memory (RAM) of the DSP board. Based upon the output of the DSP board, a pulse width modulation (PWM) current amplifier generates each of the control inputs into two pairs of magnetic actuator coils which drive independently the x and y-axis radial motions of the rotor shaft, respectively.

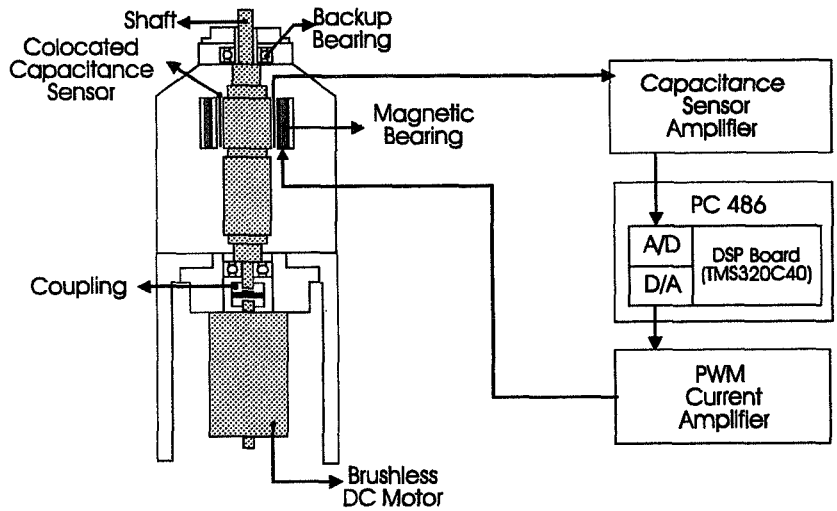

Figure 8. Schematics of a testbed for the magnetic bearing control experiment by using the collocated gap displacement sensor.

The feedback control algorithm adopted for magnetic bearing control is one of modified PID controllers, which might be called an 'I-Lead' feedback controller :

$$\frac{I_j(s)}{V_j(s)} = K_c \frac{s+b}{s+a} + \frac{K_I}{s}; \qquad j = x, y \tag{2}$$

where $I_j(s)$: Laplace transform of the variation of control inputs to magnetic actuator coils
$V_j(s)$: Laplace transform of the variation of gap displacement signals
K_c, K_I : Controller gains

In the experiment, the controller parameters are selected as K_c = 21,000 A/m, a = 9,545 rad/sec, b = 1,363 rad/sec, K_I = 1,500 A/m-sec, and the control sampling time T_{cn} = 0.1 msec. Among the output signals from the sensor signal processing unit, the maximum bound of the noise signal has been measured to be around 30 mV, which corresponds to the gap displacement of 2.3μm. This value is the final resolution of the collocated sensor system.

Figure 9 on the next page shows the experimental results of the magnetic bearing control where the developed collocated sensor system has been utilized. Figure 9-a presents the orbit of the rotor

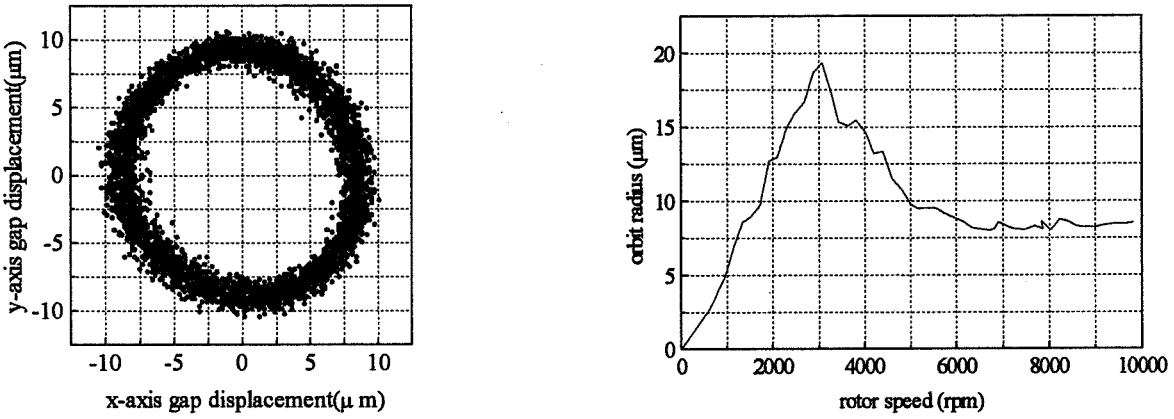

(a) Rotor orbit at 5,800rpm

(b) Orbit radius with varying rotor speed

Figure 9. Experimental results of the magnetic bearing control by using the collocated gap displacement sensor.

shaft center when it is spinning at 5,800 rpm. The average orbit radius is around 9 μm. The average orbit radii have been recorded as the rotational speed is varied up to 10,000 rpm as shown in figure 9-b. At the natural frequency of 320 rad/sec (that is, at the spinning speed of 3,060 rpm), the average orbit radius reaches the maximum value of 19 μm.

CONCLUSIONS

(1) A collocated sensor system has been developed for magnetic bearing control application. It consists of a capacitance type gap sensor plate constructed by applying PCB manufacturing technology and a signal processing unit for measuring and amplifying the charged voltages of the sensor element of the sensor plate during a cycle time of less than 100 μsec.

(2) The sensor sensitivity and bandwidth subject to static and dynamic gap displacement variations, respectively, are measured in the experiments. The bandwidth of the sensor is measured to be 1.2 kHz when the cycle time is 97 μsec.

(3) The experimental works have been executed to verify the function of the collocated sensor system. The sensor has been embedded into a vertical magnetic bearing spindle system. The average orbit radii of the rotor shaft center have been obtained increasing the rotor rotational speed up to 10,000 rpm, with the maximum value of 19 μm at the speed of 3,060 rpm.

REFERENCES

1. Allaire, P. E.; and Humphris, R. R.: Dynamics of a Flexible Rotor in Magnetic Bearings. *4th Workshop on Rotor Dynamics Instability Problems in High Speed Turbomachinery*, Texas A&M Univ., June 1986.
2. Ortiz Salazar; A., Dunford; W., Stephan, R.; and Watanabe, E.: A Magnetic Bearing Systems Using Capacitive Sensor for Position Measurement. *IEEE Trans. on Magnetics*, Vol. 26, No. 5, Sept. 1990, pp2541-2543.
3. Maslen, E. H.; and Lefante, V. S.: Transfer Function Zeros in Noncollocated Flexible Rotor Models. *Proceedings of the 3rd International Symposium on Magnetic Bearings*, 1992, pp242-252.
4. Barrett, L. E.; Brockett, T. S.; and Maslen, E. H.: Analysis of Rotors with Non-Collocated Magnetic Bearings Using Transfer Matrices. *Proceedings of MAG'92*, 1992, pp144-154.
5. Chapman, P. D.: A Capacitive Based Ultra-precision Spindle Error Analyzer. *J. of Precision Engineering*, Vol. 7 No. 3, July 1985, pp29-536.

VELOCITY-CONTROLLED MAGNETIC BEARINGS WITH SOLID CORES

H. Ming Chen & James Walton
Mohawk Innovative Technology, Inc.
Niskayuna, NY

SUMMARY

A methodology for designing velocity-controlled magnetic bearings with laminated cores has been extended to those with solid cores. The eddy-current effect of the solid cores is modeled as an opposing magnetomotive force. The bearing control dynamics is formulated in a dimensionless fashion which can be readily reviewed on a root-locus plot for stability. This facilitates the controller design and tuning process for solid core magnetic bearings using no displacement sensors.

INTRODUCTION

To make inexpensive active magnetic bearings, there have been developing efforts to spare displacement sensors in the bearing control. The displacement sensors not only are costly, but also are reliability burden and the source of non-collocation instability. Recently, Chen [1] has developed a method for designing this type (commonly called self-sensing or sensorless) of magnetic bearings. Chen's method divides the bearing control system into three major parts with independent functions. These parts are called velocity feedback controller (VFC), velocity estimator (VE) and self-starter (SS). The design approach has clearly shown that the bearings without displacement sensors, apply in essence the feedback control of rotor velocity. The velocity can be estimated by analog or digital means based on the current and back EMF measurements at the magnetizing coils, or even measured directly using an inexpensive velocity sensor. Any effort attempting to re-create the rotor absolute displacements seems unnecessary, because there naturally exist a reference of the absolute displacement for the control. This reference is at a location in the bearing clearance where all static forces balance each other.

The other control method utilizes observers [2] to estimate the system states, i.e., the rotor displacement, velocity and dynamic current, based on similar measurements at the magnetizing

coils. There are five or six unknown observer parameters for each control axis. Thus, tuning the controller with the observers is difficult. Chen's method which utilizes a separate velocity estimator reduces the number of unknowns to three in the tuning process. Most importantly, it retains the physical insight during that process.

It is the purpose of this paper to extend Chen's method and apply it to the magnetic bearings with solid cores. Specifically, the formulation of VFC and VE will be modified to accommodate the retarded control response due to eddy currents in solid cores. Also it will be demonstrated, via an numerical transient simulation of a flywheel thrust bearing design, that SS is easy to design and works well, contrary to many beliefs.

VELOCITY FEEDBACK CONTROL FORMULATION

A thrust magnetic bearing such as the one shown in Figure 1 usually has solid cores because it is difficult to make the bearing with silicon steel laminations aligned in the radial direction. There is also a great incentive for many industrial applications to make radial magnetic bearings with solid cores in order to reduce manufacturing cost. Figure 2 shows such a bearing with a homopolar

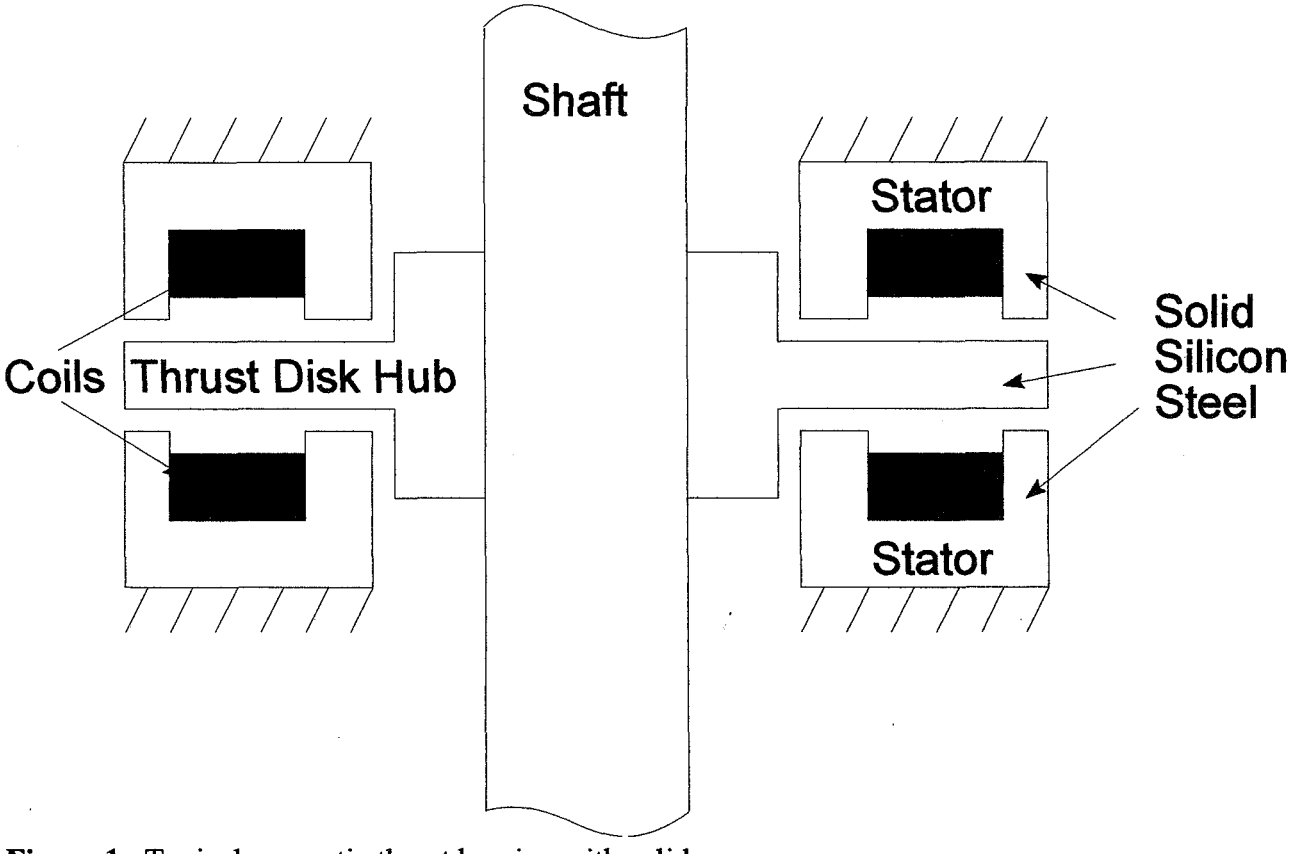

Figure 1. Typical magnetic thrust bearing with solid cores.

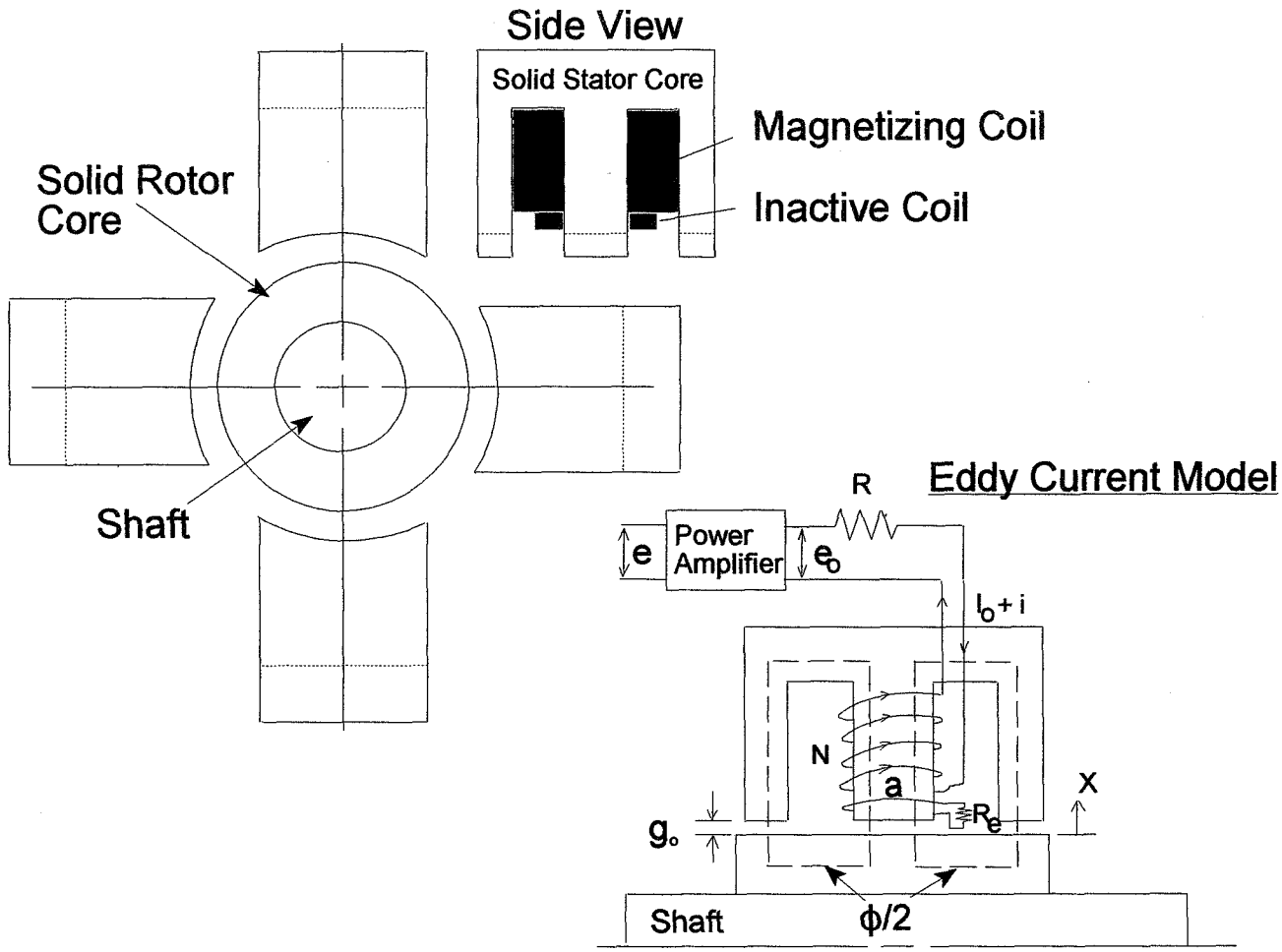

Figure 2. Radial bearing with homopolar solid cores.

configuration. Without laminations, there will be eddy current generated in the cores when dynamic (control) current is applied to the magnetizing coils and the eddy current effect in retarding the bearing response should be considered. The retarding effect is usually measured in terms of gain reduction and phase lagging of magnetic flux with respect to the excitation current applied to the magnetizing coils. Both the gain and phase are functions of excitation frequency and the phase lagging is a serious concern for control. For example, a phase lag of 16 degrees at 40 Hz was recorded in [3]. A similar measurement of 30.5 degrees at 100 Hz was made for a steel core material in [2]. Close examination of these and other similar data has revealed that the eddy-current retarding effect may be approximated by the dynamics of a half-order pole. However, for controlling the low frequency modes of magnetic bearings, a linear approximation is preferred and proper. Thus, the eddy current has been modeled as an opposing magnetomotive force [2,4] by assigning to the solid cores a coil turn with an equivalent resistance. According to [4], the feedback of coil current in the power amplifier itself, i.e., the mechanism providing a current source, is not capable of improving the time lag due to the eddy current. The dynamics of the sub-system (Figure 2) including the power amplifiers, magnetizing coils and the eddy currents in solid cores, can be represented by the following equation:

$$T(dq/dt) + q + (hT)(dx/dt) = G_a e \qquad (1)$$

where T = time constant of eddy-current effect, sec
t = time, sec
q = quasi-current, A
h = a constant related to bias currents and gaps of opposing poles, A/in
x = rotor displacement, in
G_a = power amplifier sensitivity, A/volt
e = power amplifier input, volt.

Without considering bending modes, the rotor equation of motion can be represented by (2).

$$M(d^2x/d^2t) = K_i q + K_m x \qquad (2)$$

where M = rotor mass at the bearing, lb-sec^2/in
K_i = current stiffness, lb/A
K_m = magnetic stiffness, lb/in

A velocity-controlled magnetic bearing axis can be represented by the block diagram of Figure 3 including the dynamics of equations (1) and (2). For a radial magnetic bearing, there are two independent controlled axes as such, and for a thrust bearing, there is one. Note that in reference [1] the VFC for laminated cores includes a first-order low-pass filter for trimming the velocity input in high frequency range. The purpose of the filter was to control the high frequency noise and/or

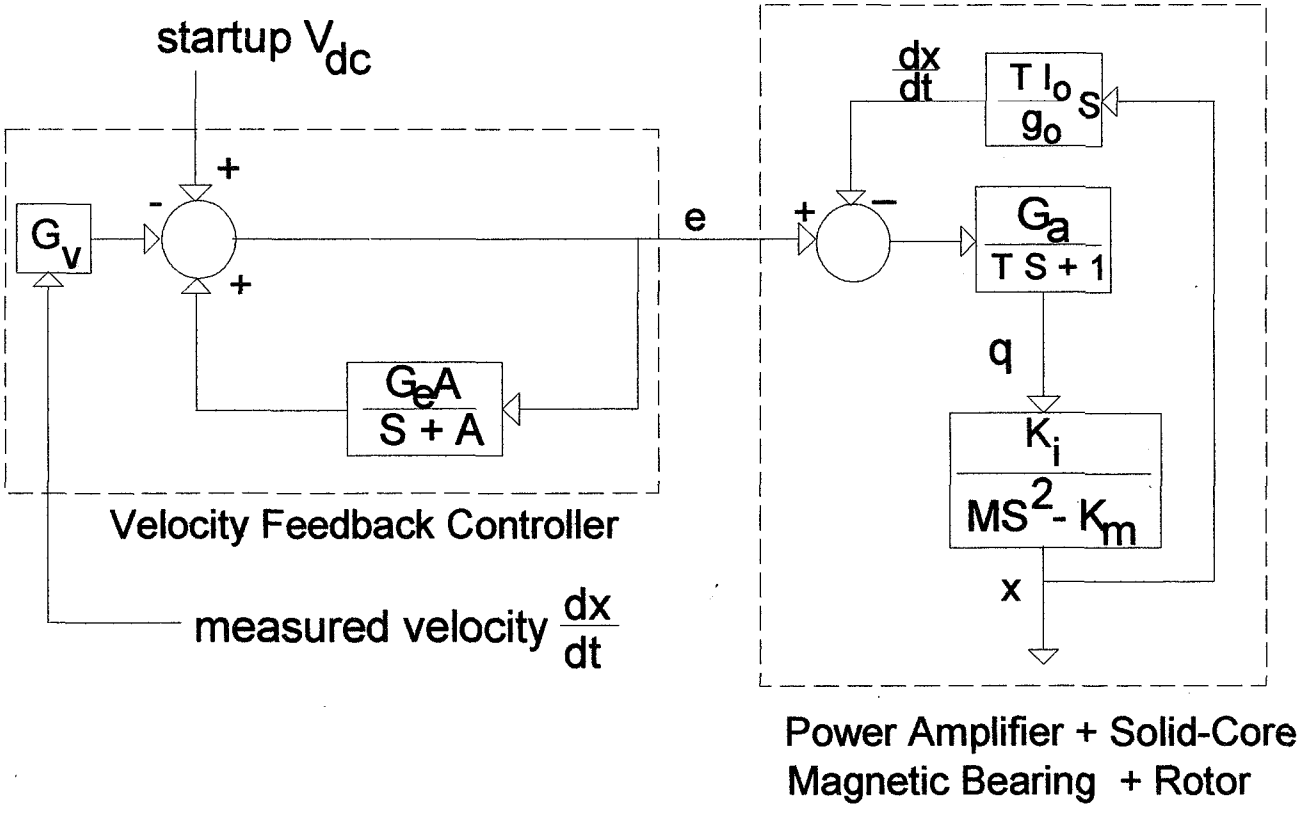

Figure 3. Velocity-controlled magnetic bearing axis with solid cores.

structural resonances. However for bearings with solid cores, the response retarding effect of eddy current is naturally a low-pass mechanism. Therefore, there is no need for an additional low-pass filter in VFC, and it is thus eliminated. The key element of VFC is an inner loop with a positive feedback. The loop contains a low-pass filter with a gain G_e and a time constant 1/A. The corresponding characteristic equation of the controlled axis is:

$$1 + KS(S+A)/[TS^3+S^2+T(H-1)S-1](S-A_r) = 0 \qquad (3)$$

where S = Laplace variable
$A_r = (G_e-1)A$
$K = K_i G/MB$
$H = K_i h/MB^2$
$G = G_a G_v$
$B = \sqrt{K_m/M}$

The parameters S, A, A_r in (3) are all normalized by the artificial parameter B called the bias frequency which is a measure of the strength of the bias flux in the magnetic bearing. Also, the time constant T is normalized by 1/B and it is partly due to the eddy-current effect and partly due to inductance of the coils. For a magnetic bearing with laminated cores and using current-source power amplifiers, the time constant T becomes small and the pole terms in the square parenthesis of (3) is reduced to $[S^2-1]$ as expected.

SELECTION OF VELOCITY FEEDBACK CONTROLLER PARAMETERS

The time constant T can be experimentally determined by clamping down the rotor concentrically in a bearing and measuring magnetic flux versus the applied sinusoidal excitation currents at different frequencies. The measured data are then fitted to a first-order low-pass network to determine the values of G_a and T. For example, based on the gain and phase lag data of [2], the time constant due to eddy current is estimated as 0.001 second for a steel material.

The constant h is a function of bias current (I_o) and nominal air gap (g_o). For simplicity, equal bias currents for the opposite electromagnet coils will be assumed subsequently. It can be readily shown that:

$$h = I_o/g_o \quad \text{and} \quad K_i/K_m = g_o/I_o \qquad (4)$$

Therefore, the normalized h value is : $H = K_i h/MB^2 = K_i/K_m h = 1.0$.

The VFC has three parameters to be determined and they are A, G_e and G_v. Instead of using G_e and G_v, the parameters A_r and K of (3) will be used in the following discussion for convenience. The selection process of VFC parameters can be assisted by using root-locus plots of the

characteristic equation. To illustrate the process, we shall use a design example of a magnetic thrust bearing for an energy storage flywheel rotor as follows.

Shown in Figure 4 is the flywheel rotor with two passive radial magnetic bearings and an active thrust magnetic bearing. The latter is the subject of our discussion. The rotor axial velocity is

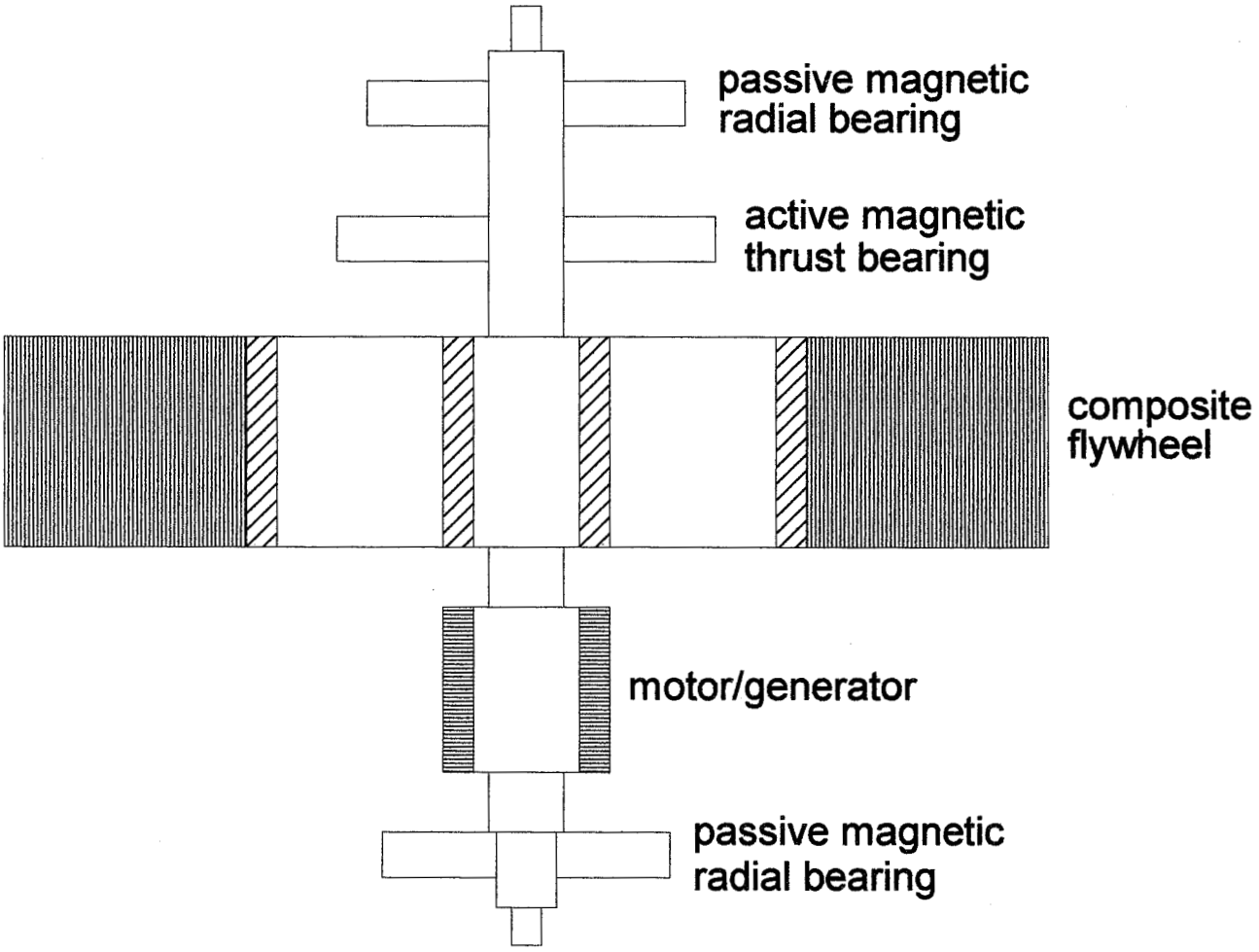

Figure 4. Flywheel rotor.

measured by using a variable reluctance (magnetic) sensor which is commercially available and inexpensive.

The pertinent data for the thrust bearing VFC design are listed in Table 1. Note that the passive radial magnetic bearings are made of permanent magnetic rings, and each has an axial magnetic (negative) stiffness of 7.0×10^5 N/m. Their total value is represented by K_{mb} in Table 1.

Table 1 - Pertinent Data For Thrust Bearing VFC Design

Rotor weight	22Kg
Load capacity	1000 N
Outer diameter	100 mm
Inner diameter	50 mm
Bias current I_o	3 A
Nominal air gap g_o	0.38 mm
Current stiffness K_i	363 N/A
Magnetic stiffness K_{ma}	2.85×10^6 N/m
Axial stiffness of radial bearings K_{mb}	1.40×10^6 N/m

To use equation (3) for determining the VFC unknown parameters, we shall first calculate the bias frequency B using the data of Table 1.

$$K_m = 2.85 \times 10^6 \text{ N/m} + 1.40 \times 10^6 \text{ N/m} = 4.25 \times 10^6 \text{ N/m}$$

$$B = \sqrt{K_m/M} = \sqrt{4.25 \times 10^6 / 22} = 440 \text{ rad/sec} = 70 \text{ Hz}$$

Taking the eddy current time constant for the bearing solid cores as 0.001 sec, then its normalized value is:

$$T = (0.001 \text{ sec})(B) = 0.44$$

Choosing the normalized values A=0.8 and $A_r = 0.4$, The root loci of (3) with the above T and H values are plotted in Figure 5. For the normalized gain K =2.5, the system shows two pairs of complex conjugate roots:

$$-0.25 \pm j\,0.42 \qquad \text{and} \qquad -70 \pm j\,1.84$$

Both modes are reasonably damped. The first mode frequency is 29.4 Hz (=0.42 x 70 Hz) and the second mode frequency is 129 Hz (=1.84 x 70 Hz). Apparently the second or the mode with higher frequency is more affected by the eddy current in solid cores. The selection of the values of A and A_r determines the locations of a pole and a zero for K = 0. The selection dictates the shapes of the root loci. One may choose the desired shapes from a pre-calculated, non-dimensional data bank and determine the unknown K, A and A_r. It is basically a pole placement design method. For this particular example, using different values of A and A_r may result in a set of more damped roots with lower modal frequencies.

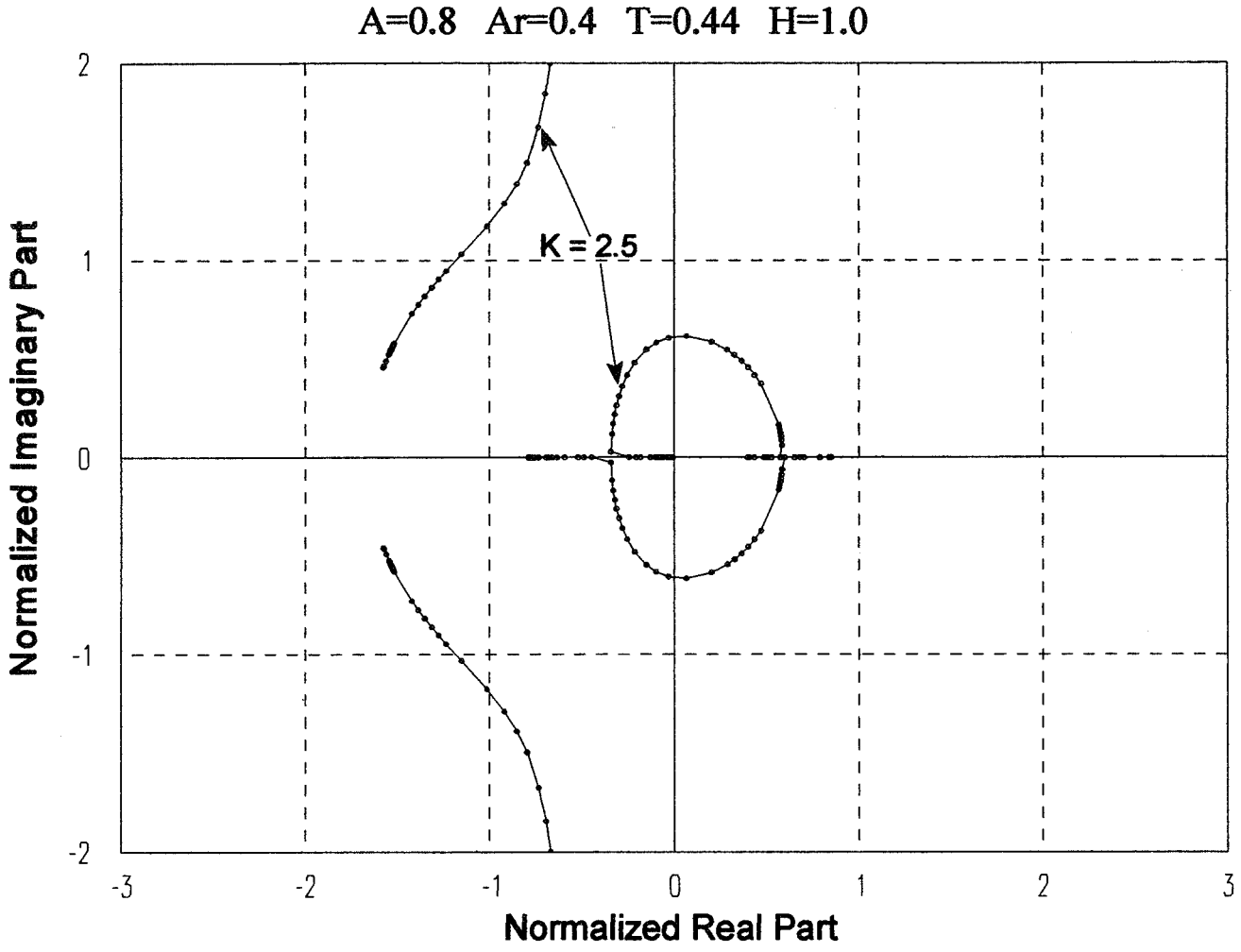

Figure 5. Root loci for a solid core bearing control axis.

A hidden design issue is how high the bias frequency B should be set. A high value of B implies a large static stiffness K_m which is desirable. However, for the solid-core bearings, the normalized time constant T is increased and the control system is likely to have one lightly damped mode. With the normalized root-locus method described above, this design issue can be easily examined in details for each application.

It should be emphasized that high-frequency bending modes in active magnetic systems are dealt with similarly regardless as to whether the bearings are conventionally PID-controlled or velocity-controlled. In other words, gain and phase compensations such as using notch-filters or lead-lag circuits, are provided in high-frequency range to stabilize these modes, if necessary.

VELOCITY ESTIMATOR FORMULATION

Similar to (1), the following equation [4] relates the voltage across the coil (e_o), the quasi-current (q) and the rotor vibration velocity (dx/dt):

$$T_o(dq/dt) + q + (hT_o)(dx/dt) = e_o/R \quad (5)$$

where

$T_o = (N^2/R + 1/R_e)/R_m$
N = coil turns
R = coil electric resistance
R_e = equivalent electric resistance of eddy current in solid cores
R_m = air gap reluctance = $2g_o/\mu_o a$
μ_o = air permeability
a = pole area.

Unlike the coil current (I_o+i of Figure 2), the quasi-current q is an artificial term not directly measurable. But, it can be readily shown [2] that

$$q = I(1+\Delta) - e_o\Delta/R \quad (6)$$

where

$\Delta = R/N^2 R_e$

Combining (5) and (6), it is straightforward to make a velocity estimator for the solid core magnetic bearing. However, such a scheme suffers the common drawback of being sensitive to the coil temperature [1], because the resistance varies significantly with the coil temperature. While temperature compensation is one of the possible solutions, it complicates the estimator design.

Another possible solution of less complication is to measure the flux using an inactive coil [1]. There is no current flowing in the inactive coil, and its resistance and thus the temperature has no bearing to the measured voltage signal. The voltage across the inactive coil is:

$$V = -n(d\phi/dt) \quad (7)$$

where

ϕ = dynamic magnetic flux
n = inactive coil turns.

It is also readily shown from the solid core model that:

$$T_o(d\phi/dt) + \phi + (hN/R_m)x = (N/R\,R_m)e_o \quad (8)$$

Combining (7) and (8), the rotor velocity of a solid core bearing can be estimated using a scheme presented in Figure 6.

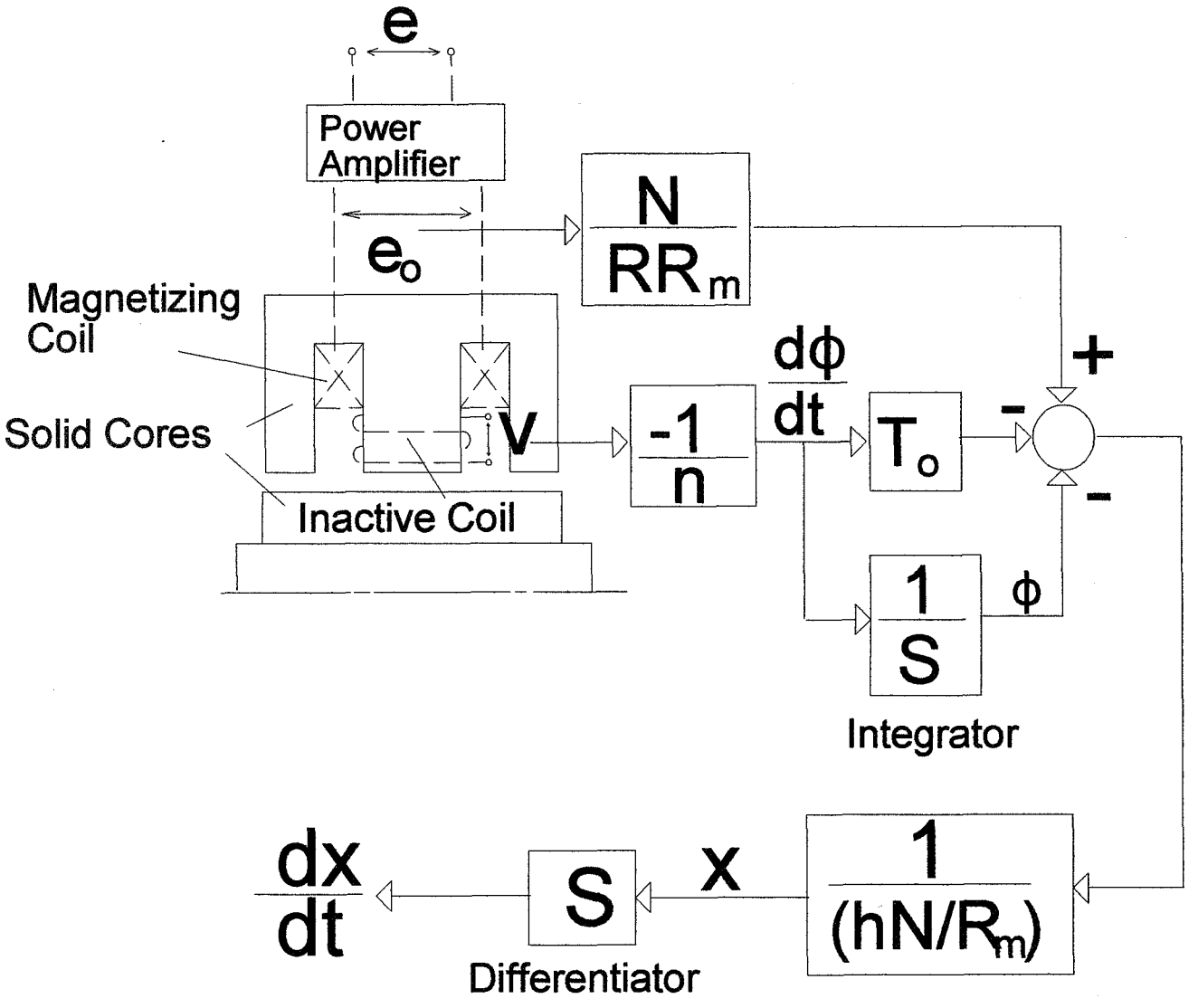

Figure 6. Velocity estimator for magnetic bearings with solid cores.

SELF-STARTER DESIGN AND SIMULATED PERFORMANCE

Contrary to what many may believe, the velocity-controlled magnetic bearings are easy to start. As shown in Figure 3, a small DC voltage V_{dc} is injected at the velocity input terminal of VFC for the startup. One should know that the VFC by itself is unstable. Its output "e" is usually saturated or latched to ± maximum output. Therefore, the output is electrically grounded before any startup. The electrical ground is then turned off simultaneously when the DC voltage is injected. The polarity of the injected voltage depends on which side of the backup bearing the rotor initially rests.

It is straight forward in designing a magnetic bearing to ensure that the rotor is made to rest on a predetermined side before its lift-off. The DC voltage is turned off after the rotor is levitated.

A transient analysis simulating the dynamics of the thrust bearing and the flywheel rotor (Figure 4) lifting off the bottom backup bearing has been performed. The rotor axial velocity was assumed to be measured directly using a velocity sensor. The rotor initially rests at the bottom backup bearing which is located at a half of the air gap below the thrust bearing center. According to the above startup procedure, a positive DC voltage of 0.010 volt is injected at the VFC input terminal. The controller will integrate the DC voltage and *kick* the rotor upward and *grab* it in the air, so to speak. The simulation result is presented in Figure 7. The results of three cases with different rotor

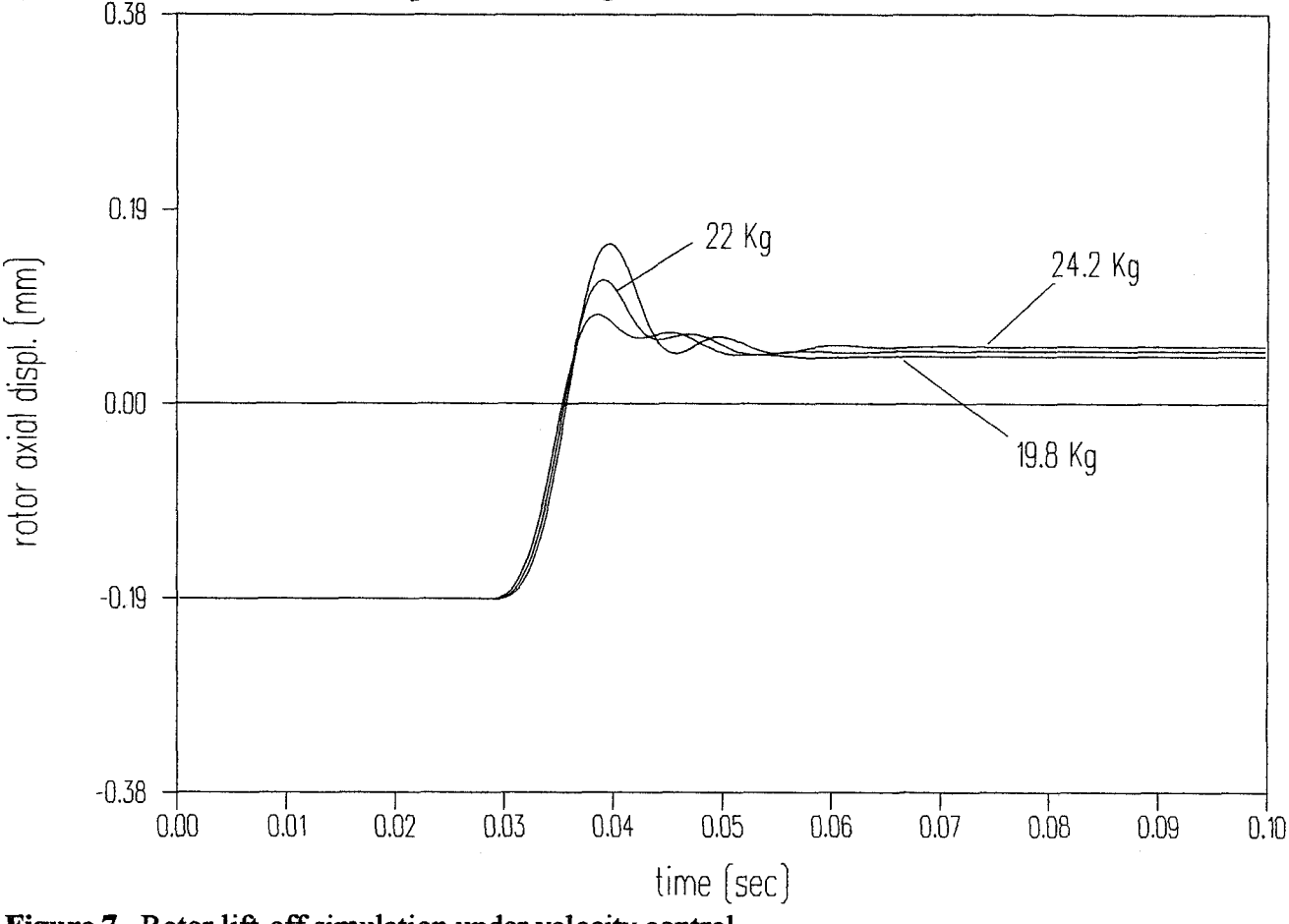

Figure 7. Rotor lift-off simulation under velocity control.

weights, i.e., 22 kg, 10% less and 10% more, are overlapped in the figure for comparison. The results indicate three remarkable aspects:

- The rotor settles above the thrust bearing center. In other words, the thrust runner is closer to the top electromagnet than to the bottom. This is due to our choice of equal bias currents for both the top and bottom coils.

- A heavier rotor would settle at a higher axial position or closer to the top electromagnet, and a lighter rotor would do the opposite. Both this and the previous result show that the rotor will settle at an axial position in the clearance where all the static forces balance each other.
- The rotor response ripples at lift-off are indicative of light damping associated with the second mode. The light damping is due to the solid core eddy current effect.

CONCLUSIONS

Magnetic bearings with solid cores, like those with laminated cores, can be controlled using velocity feedback. The control for a solid core bearing also involves three parts, i.e., Velocity Feedback Controller, Velocity Estimator and Self Starter which have independent functions and can be separately designed. The separation is intended to simplify the control design and tuning process. For the solid core bearings, the VFC is not required to have a low-pass filter and thus simpler. A dimensionless root-locus analytical procedure has been formulated to facilitate the selection of three key parameters of VFC. The VE formulation is quite different from those of laminated cores, because of the eddy-current effect. The SS design is the same as for those laminated bearings.

Finally, using a thrust bearing with solid cores as an example, it has been shown by numerical simulation how the rotor would lift off a backup bearing with the velocity controller and how it would automatically settle at a location in the bearing clearance where all the static forces on the rotor balance each other.

REFERENCES

1. Chen, H. Ming: Design and Analysis of a Sensorless Damper. Presented at *ASME TURBO EXPO 95*, Houston, June 5-8, 1995, 95-GT-180.

2. Mizuno, T., et al: An Industrial Application of Sensorless Magnetic Bearings. *Proceedings of the 4th International Symposium on Magnetic Bearings*, pp317-320, 1994.

3. Allaire, P.E., et al: Eddy Currents, Magnetic Flux and Force in Solid Magnetic Thrust Bearings. *Proceedings of the 4th International Symposium on Magnetic Bearings*, pp. 157-163, 1994.

4. Fukata, S., et al: Dynamics of Active Magnetic Bearings Composed of Solid Cores and Rotor. *Memoirs of the Faculty of Engineering, Kyushu University*, Vol. 46, No. 3, September 1986.

SUPERCONDUCTING REBALANCE ACCELEROMETER*

R. P. Torti, M. Gerver, K. J. Leary, S. Jagannathan, D. M.Dozer
SatCon Technology Corporation
Cambridge, MA

SUMMARY

A multi-axis accelerometer which utilizes a magnetically-suspended, high-T_c proof mass is under development. The design and performance of a single axis device which is stabilized actively in the axial direction but which utilizes ring magnets for passive radial stabilzation is discussed. The design of a full six degree-of-freedom device version is also described.

INTRODUCTION

There have been a number of instruments developed which utilize levitation of a superconducting proof mass as the basis for sensing acceleration and gravity gradients[1,2,3,4]. The advantages of these approaches at liquid-helium temperature include reduction of electrical and mechanical fluctuations by a factor of 10, while superconducting operation implies negligible dissipation from current carrying elements. Use of instrumentation such as SQUIDs which depend upon significant quantum effects at low temperatures becomes practical. Furthermore, the flux trapping properties of superconductors allows stable field control. For applications such as gravimeters, where the devices must detect small changes against a 1 G background, a superconducting coil can be used to levitate the proof mass with high long term stability since a low decay rate persistent current in the levitation coil is used to cancel gravity[1].

A serious disadvantage with conventional superconductors is the requirement to cool to 4.2 K which is both expensive and requires more volume relative to operation at 77 K. The use of high-T_c materials does not retain all the advantages of conventional superconductors, but nonetheless brings with it lower than room temperature thermal noise, insignificant electrical power dissipation in coils, and the advantages of flux trapping.

This work was approached as an examination of the feasibility for using a superconducting proof mass in conjunction with low noise displacement sensors in the development of a multi-axis acceleration sensor. Major efforts were undertaken along three lines: 1) Development of an extremely low-noise displacement sensor operating at RF frequency, 2) testing of a one degree-of-freedom test device which uses a high-T_c proof mass and 3) design and operation of full 6 degree-of-freedom proof-of-principle multi-sensor.

---

*Work done on contract for NASA Langley Research Center, NAS1-19938.

APPROACH

The conceptual design is for a multi-sensor which detects linear and angular acceleration along six axes. In operation, a measurement of the displacement of a fully magnetically-suspended mass is detected in conjunction with an active control system which "rebalances" to the original position. The necessary drive to accomplish this is processed into the corresponding output signal. Use of a rebalance scheme minimizes non-linearities in displacement sensors and actuators. The limited proof-mass motion inherent in a rebalance system also allows more accurate position measurements to be made and improves performance. A suspended proof-mass device, while more complex than spring-restraint systems, has the further advantage of active control of the different stiffness and damping characteristics at different frequencies. This allows better vibration isolation from external disturbances.

A conceptual drawing of the sensor is shown in Figure 1. It consists of a cubically shaped high temperature superconducting proof-mass whose position is sensed and controlled by a set of co-located capacitive sensors and control coils fixed to a support structure cooled to liquid nitrogen temperature. The control coils are actuated by an electronic control system to maintain a constant cube position based upon outputs from displacement sensors. From the mass dynamics of the cube and the actuator control signals, three accelerations and three angular rates can be determined. In this prototype, six sensors and actuators are sufficient to control the six degrees-of-freedom of the cube although other workers have used more for averaging and redundancy[4]. The cube, sensors, and control coils are contained in an evacuated vessel with the coils and sensors mounted to the internal cooled support jacket.

The device has several features that should enhance performance. First, high frequency capacitive sensors can yield position sensitivities of 10^{-3} angstroms/$\sqrt{Hz}$. Second, the proof mass, sensors and coils are cooled to 77 degrees Kelvin which reduces mechanical thermal noise to approximately half that at room temperature. Third, the use of a superconducting 1 G levitation coil generates very little heat in the system, reducing thermal gradients which would degrade precision. Fourth, operation at 77 K brings with it the possibility for substitution of a bulk high-T_c material disc for the wire coil. This "coil" could be charged inductively and operated persistently.

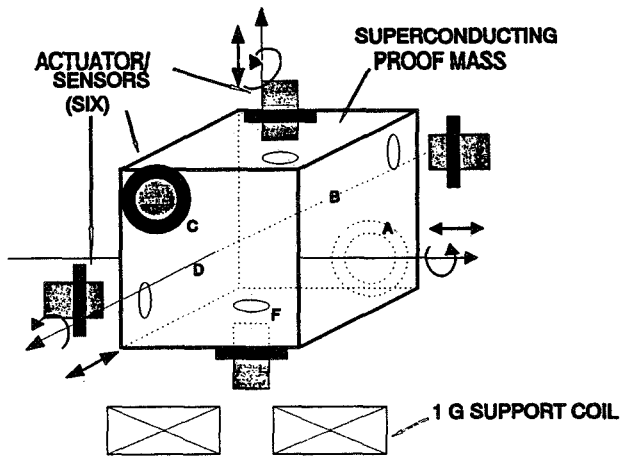

Figure 1. Schematic of Multi-sensor Illustrating Principle of Operation.

Configured in this optimal way, the device would have stand alone resolution of 0.1 μg acceleration and 10^{-5} rad/sec^2 angular acceleration and would drift 75 angstroms and 5 x 10^{-5} degrees in one hour due to sensor noise. These numbers are based on a bandwidth of 100 Hz, the use of capacitive position sensors with noise of 1.5 x 10^{-3}Å/$\sqrt{Hz}$ and a cube of diameter 2 cm. The drift is assumed to be a random walk, with time step ($10^{-2}/2\pi$) seconds, and spatial step equal to the sensor noise at 100 Hz. Any systematic (non random) drift would be in addition to drift from sensor noise.

ONE DEGREE-OF-FREEDOM TEST DEVICE

The design of the full multi-sensor accelerometer involves the integration of at least three demanding technologies: bulk and wire superconductor fabrication, cooling with liquid cryogens through a vacuum, and active electronic control. Especially significant for latter are flux pinning and hysteretic effects observed in high-T_c materials, which can make the operating point dependent upon magnetizing history affecting both magnetic spring constant and damping.

To provide information for the design of the six degree-of-freedom device, a simpler device involving a fully suspended proof mass but with only one degree-of-freedom has been built and is currently under testing. This is shown in block form in Figure 2. A magnetic geometry is utilized which is passively stable in all directions except axially. Magnetization of ring magnets either normal to their face or radially will produce axially symmetric, radial forces. The sense of the magnetization can be chosen so that the movable element can then be positioned axially so that it is in a radial but not axial potential well. The axial position is then controlled by the active magnetic repulsion generated between the control coil and superconductor and sensed by the displacement sensor.

This is implemented as shown in Figure 3. For mechanical simplicity, sensing functions have been separated from coil/superconducting disc functions. This is accomplished by attaching the proof mass, ring magnets and sensor target to a rod which is part of the suspension. At its top the proof mass is completely re-entrant into the liquid nitrogen reservoir. Dual magnet rings sets are incorporated for alignment stability. This arrangement will also allow maximization of the vacuum gap between cold regions and vessel walls with sensor at room temperature. The entire support assembly is placed in a "bell jar" consisting of a Nalgene cover and stainless steel base plate. Liquid coolant is forced through a copper baffle into the stainless reservoir by tank-pressurized liquid nitrogen. A vent to the liquid chamber allows access for vacuum pumping to decrease temperature below 77 K. With the superconducting and suspended proof mass re-entrant into the reservoir and facing the cold baffle below, effective cooling has been achieved.

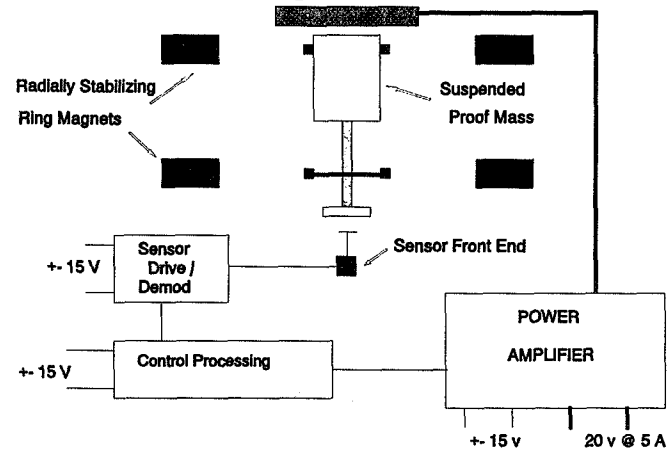

Figure 2 Block diagram of single-axis device.

Test Device Sizing

The mass is sized at about 75 gm to correspond to the full 6 degrees-of-freedom cube. The two sets of permanent magnets are mounted in such a way that only one degree-of-freedom (vertical motion) will be unstable, while the horizontal motion and tilting degrees of freedom are stable. If the vertical separation distance between the two sets of rings is at least a few times the radial separation

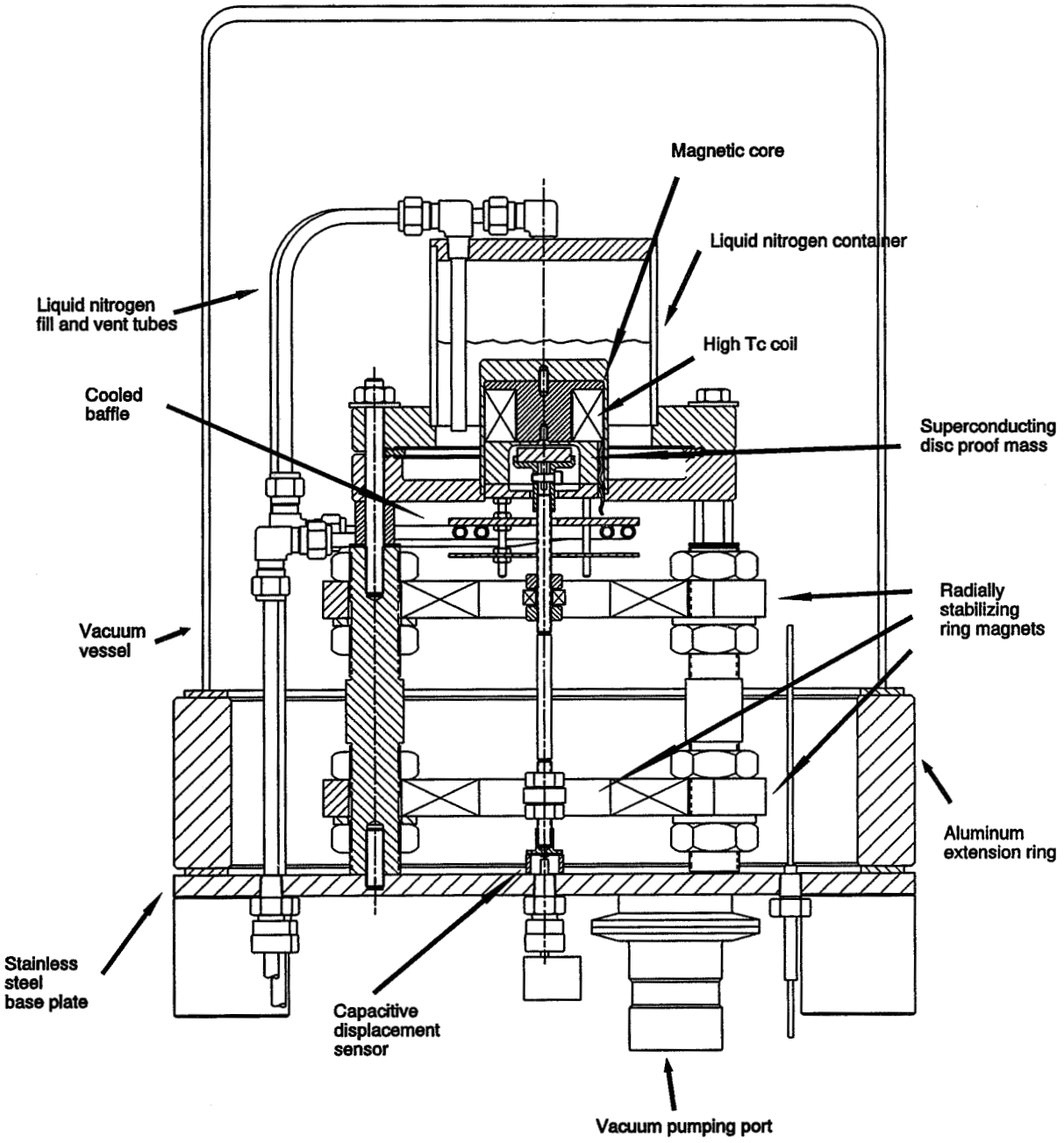

Figure 3. One degree-of-freedom test device.

within each set, then the two sets will not exert appreciable forces on each other.

The rings of each set are magnetized vertically with radial thickness w_i and w_o for the inner and outer rings, average radius r_i and r_o, and height h_i and h_o (see Figure 4). The forces between the inner and outer rings may be calculated by assigning an effective magnetic monopole surface charge to the top and bottom surfaces of each ring and integrating the forces, assuming that the force between two magnetic monopole charges q_1 and q_2, separated by a distance r. It is given by

$$F = q_1 q_2 / 4\pi\mu_0 r^2$$

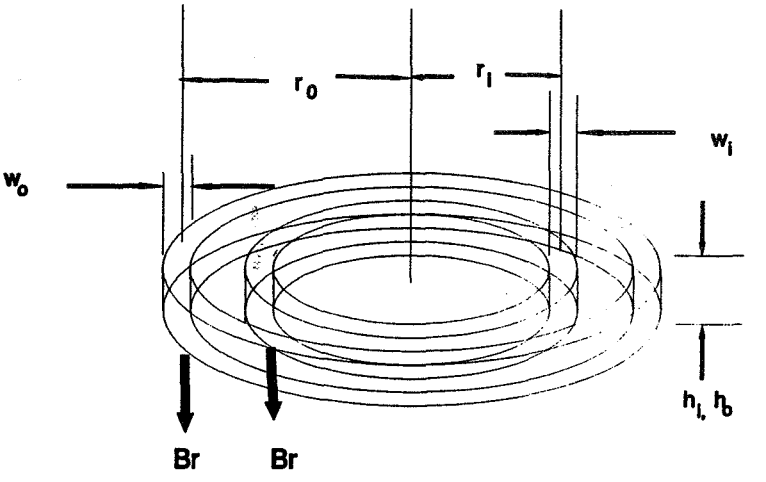

Figure 4. Magnet geometry.

in analogy to electrostatic forces. The effective magnetic charge density is then equal to the divergence of the intrinsic magnetization, which is always close to B_r, regardless of the magnet dimensions, for rare earth magnets. So the magnetic surface charge is B_r for the north pole surface of each ring, and $-B_r$ for the south pole surface. The forces take a particularly simple form if

$$w_o, w_i \ll \max(r_o - r_i, |h_o - h_i|) \ll r_o, r_i$$

Then, if the inner and outer magnets are both magnetized in the same direction, we find the vertical spring constant for one set of rings is

$$\frac{\partial F_z}{\partial z} = \frac{B_r^2}{\mu_0} w_i w_o (r_i + r_o) \left(\frac{(r_o - r_i)^2 - (h_o - h_i)^2/4}{[(r_o - r_i)^2 + (h_o - h_i)^2/4]^2} - \frac{(r_o - r_i)^2 - (h_o + h_i)^2/4}{[(r_o - r_i)^2 + (h_o + h_i)^2/4]^2} \right)$$

$$\frac{\partial F_x}{\partial x} = \frac{\partial F_y}{\partial y} = -\frac{1}{2}\frac{\partial F_z}{\partial z}$$

To suspend a 70 gm proof mass with a 0.5 cm displacement between the magnet sets the required spring constant is

$$\frac{70g \times 9.8 m/\sec^2}{0.5\ cm} = \frac{7 \times 10^2 \times 9.8}{5 \times 10^{-3}} = 1.4 \times 10^2 N/m$$

for each ring.

It can be shown that similarly sized rings with small radial spacings make too stiff a spring. Making magnets much smaller, or making $(r_0-r_i) \approx (h_0-h_i)$, makes the spring constant very sensitive to dimensions and position while making w_0, w_i much smaller is difficult mechanically.

A soft enough spring can be achieved with low intensity (B_r) magnets and large radial spacings. Ceramic magnets with $B_r \approx 0.38$ tesla were used with:

$$w_0 = 3.5 \text{ cm}, w_i = 0.6 \text{ cm}, r_i = 0.6 \text{ cm}, r_0 = 4.7 \text{ cm}, h_i = 0.6 \text{ cm}, \text{ and } h_o = 1.6 \text{ cm},$$

This gives a spring constant $\approx$ 110 N/m per ring set which can easily support approximately 100 gm of proof mass and magnets over an axial range of 0.5 cm.

Superconductors

Two high-T_c superconducting components are used in this device. A single fixed coil provides both bias against the magnetic spring and active control while the suspended proof mass comprises a ring magnet support rod, the sensor target, and disc of bulk YBCO which interacts with the coil to produce a repulsive (levitating) force. The sole rationale for the coil was minimization of a heat source close to the levitated superconductor since a coil/core set capable of canceling 1 G dissipates approximately 40 W.

The coil, fabricated by American Superconductor Co. of Westborough, MA, operates in zero background field at 77 K at 3000 Amp-turns. Coil size is approximately 53 mm outside diameter 23 mm long with a 25 mm bore. The superconductor is Lead Bismuth Strontium Calcium Copper Oxide. The coil dissipates ~0.04 W at full current.

The suspended disc is a 25 mm diameter by 6.4 mm thick "YBCO large-domain levitator" fabricated by Superconductive Components, Inc. of Columbus Ohio.

Displacement Sensing

The initial multi-sensor concept device included operation in conjunction with fast, high precision capactive placement sensors. For shot noise limited resolution, the fractional position sensitivity limit is

$$\delta d/d = \sqrt{(2e/I)} \cdot (\sqrt{Hz})^{-1}.$$

Here I is the bias current and the electronic charge. δd can be reduced by increasing the drive frequency which is the rationale for high frequencies.

Although the current multi-sensor is designed primarily for proof-of-principle operation due to cost constraints, and not optimized for precision or bandwidth, a single high-precision RF driven

capacitive displacement sensor prototype was designed, built and tested. The sensor is based upon circuity designed by RCA[5] for capacitive video disc reader. The principle has also been developed by a group at JPL[6].

As conceived by RCA, a drive signal of nearly 1 GHz is imposed upon a resonator which includes the capacitance of the electrode gap to be measured. Displacement is read as a change in RF tune since the detected signal amplitude moves along the tuning curve as the resonance frequency changes. Sensitivity is enhanced by operation around the sharp slope of the resonance curve. Active control via a voltage controlled oscillator (VCO) fixes the operating point. Unlike the RCA implementation, which used stripline technology, this design employs a miniature coaxial cable as both transmission line and resonator.

Resonant frequency and Q were determined by measurement of the AC amplifier output voltage vs. frequency with the modulators disabled and 10% AM on the master oscillator output. The quantity dV_o/df (derivative of operating point voltage with frequency) was measured by changing the master oscillator frequency with the modulator operating and measuring the DC output of the 1.0 kHz low pass filter. The master oscillator, an HP8656B capable of $1:10^8$ in frequency, provides oscillator drive and frequency readout. The peak-to-peak noise was estimated by an oscilloscope from the filter output. Auxiliary measurements of V_o and/or oscillator frequency for null V_o were taken for various test capacitor plate separations, recorded as actuator micrometer readings.

The measured dV_o/df was combined with a simulated model of the resonator to compute a V_o/C, in volts/pF, which was then used to compute a noise equivalent capacitance change from the measured noise. With 2mm x 2mm plates and 0.1 mm spacing, the nominal capacitance is 0.35 pF and separation sensitivity about 3.5×10^{-9} F/m. Dividing the noise equivalent capacitance by this number gives an rms position error of 2.5×10^{-11} m (2.5×10^{-12} m/$\sqrt{\text{Hz}}$). In a 100 Hz bandwidth this is approximately a sensitivity in acceleration 1×10^{-5} m/s^2 or 10^{-6} g.

Force Calculations

In order to limit the size and expense of the superconducting suspension coil, it was found necessary to include a soft magnetic core and optimize core and coil geometry with finite element calculations. Calculated levitation forces produced by a permanent magnet and melt-process YBCO levitators were higher by about a factor of 2.5 compared to data provided by Superconducting Components, Inc. This was discrepancy was corroborated by measurements at SatCon and included in core and coil sizing designs.

Control

The operation of the multi-sensor is based on measurement of forces and moments required to restore the proof mass, i.e., the superconducting cube, to a center zero orientation. A

force/moment rebalance controller with a displacement feedback is the basis for achieving this measurement. The principle is illustrated with a single degree-of-freedom force rebalance system as shown in Figure 5.

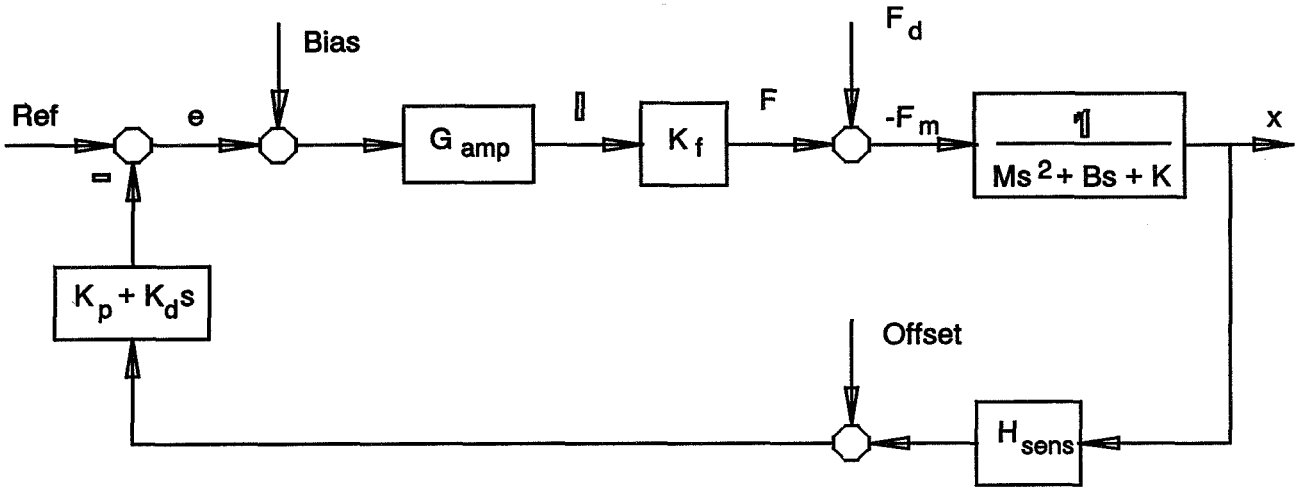

Figure 5. One axis, closed-loop control block.

Closed Loop Design

The controlled system is closely approximated by a second-order system of mass M, equivalent viscous damping B, and stiffness K. The equivalent viscous damping occurs as a result of the motion of pinned flux. This pinned flux is also responsible for a portion of the overall system stiffness K.

The overall system stiffness has contributions from two equivalent spring constants. The first contribution results from the interaction between permanent magnets mounted on the proof mass and the stationary dewar. Ideally, the system can be stabilized at this (unstable) equilibrium point and the contribution to the overall spring rate is zero. However, in practice, a negative contribution to the overall rate is observed. The second contribution to the overall spring rate is due to flux pinning which allows the proof mass to be stabilized at an otherwise unstable equilibrium point.

The block diagram illustrates the closed-loop system. Both a control force F_e and a disturbance force F_d may be applied to the multi-sensor proof mass. The disturbance force is proportional to the acceleration of the multi-sensor. In a suitably small neighborhood of the operating point, the control force is proportional to the applied current through the force constant K_f. A current controlled amplifier with adjustable gain G_{amp} is used to provide a current proportional to the compensated error signal e. Displacement feedback is received through the frequency dependent gain H_{sens}.

Since the system closely resembles a second order oscillator, the simplest stabilizing controller is a proportional plus derivative (PD) controller. As shown in the figure, proportional K_p and derivative K_d gain terms appear in the feedback path. In theory, this control structure allows

independent control of the system damping and stiffness through the adjustment of K_d and K_p, respectively. The compensated error signal is proportional to the required restoring force and may be used for the sensor output.

The closed-loop transfer functions of merit are given below.

$$\frac{x(s)}{F_d(s)} = \frac{1}{Ms^2 + (B + G_{amp}K_fH_{sens}K_d) + (K + G_{amp}K_fH_{sens}K_p)}$$

$$\frac{e(s)}{F_d(s)} = \frac{-H_{sens}(K_{dS} + K_p)}{Ms^2 + (B + G_{amp}K_fH_{sens}K_d) + (K + G_{amp}k_fH_{sens}K_p)}$$

Controller Implementation

A practical analog implementation of the control circuit is shown in Figure 6. A practical differentiator is constructed from an LM318. For stability and noise reduction, second order poles are placed at 270 and 330 Hz. Inverting gain stages provide variable derivative and proportional gains for damping and stiffness adjustment. A unity gain inverting summer provides a variable reference and produces the compensated error signal used to drive the adjustable gain current amplifier.

Performance

Open-loop frequency scans of proof-mass displacement at constant forcing current indicate a peak with highly non-linear behavior between 10 and 20 Hz which is in the range of the resonance expected with the designed magnetic spring and measured proof mass. Current efforts involve observing the effects of varying ring magnet alignment, the level of frozen-in flux, and circuit gains on closed loop performance.

SIX DEGREE-OF-FREEDOM PROTOTYPE

The multi-axis device has six degrees of freedom, namely x,y,z translation and θ_x, θ_y, and θ_z rotations as shown in Figure 7. The actuator coils and capacitive sensors are collocated. There can be one or two sensors and actuators reacting against each face of the cube shaped proof mass (six or twelve total). Each actuator coil and sensor pair is located on a diagonal of the face. The cube faces are identified as A,B,C,D,E,F with the corners defining the faces. By virtue of the location of the actuator coil/sensor pair, each pair can generate a force along one translational axis and a moments around two rotational axis. If the forces generated by the actuator coils are defined by a vector

$$F_{act} = [F_a, F_b, F_c, F_d, F_e, F_f]^{-1}$$

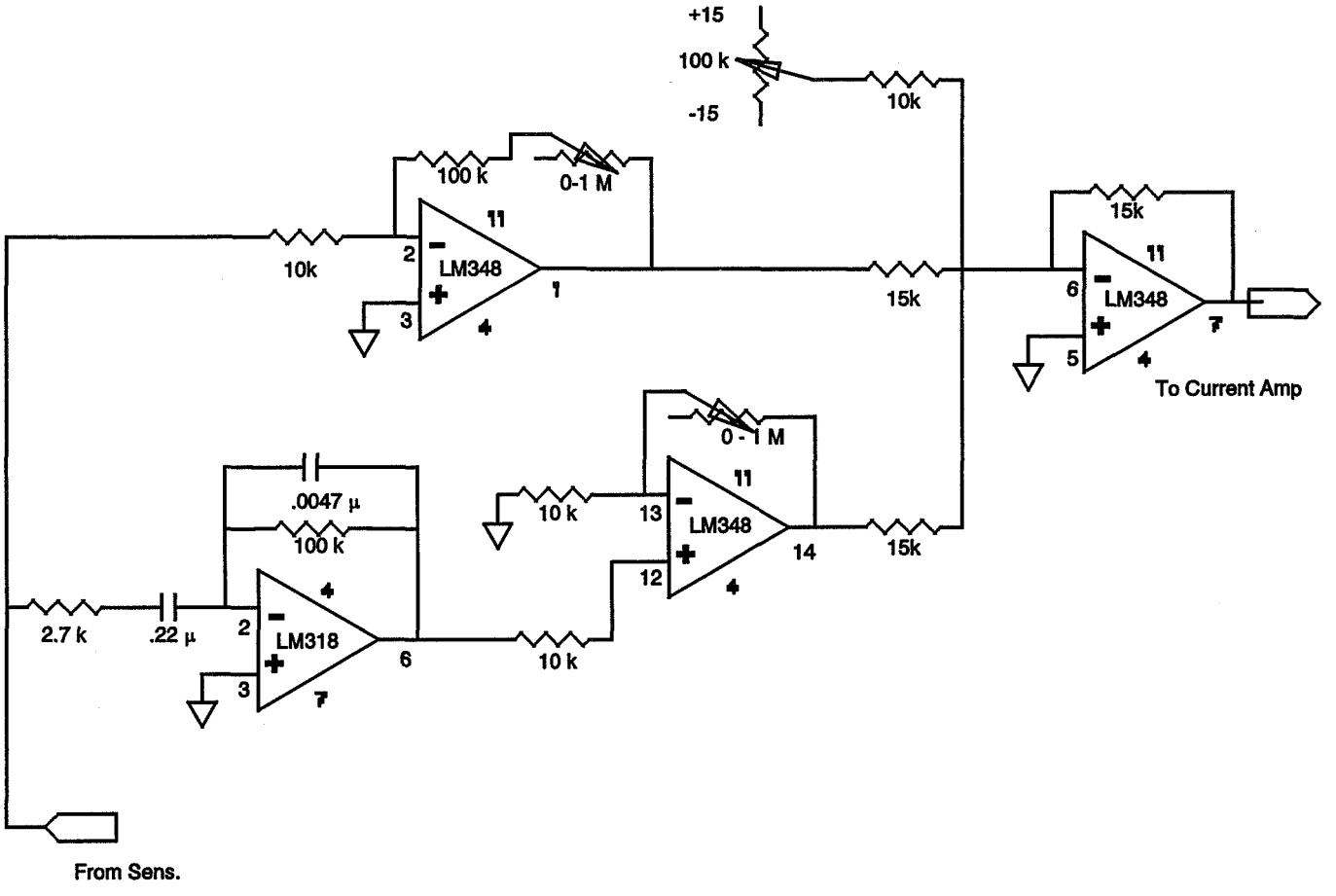

Figure 6. Single axis electronics implementation.

then a transformation can be found which relates F_{act} the forces and moments

$$FM = [F_x, F_y, F_z, M_x, M_y, M_z]^{-1} = [T]*F_{act}$$

As the sensors are collocated with the actuator coils, the displacements measurement "d" at each sensor can be transformed to translations and rotations using the same matrix [T], i.e.,

$$[X, Y, Z, \theta_x, \theta_y, \theta_z]^{-1} = [T][d_a, d_b, d_c, d_d, d_e, d_f]^{-1}$$

Use of the transform [T] and $[T]^{-1}$ allows the controller to be six decoupled compensators, one for each degree-of-freedom. The compensation is then tailored to meet the frequency response requirements of the sensor system.

A functional block of the multi-axis device is shown in Figure 8. Six displacement sensors are used in conjunction with six normal control coils. A single superconducting coil is used to continuously cancel 1 G of the proof mass. The normal control coils operating at 77 K produce about 4 W when

rebalancing 0.3 G.

The mechanical implementation of this device is shown in Figure 9. The vacuum vessel configuration is the same as the single axis test device. The liquid nitrogen container is of aluminum, bored for six sensor/coil pairs entering the shell at oblique angles. Steel magnetic cores are used to tailor the fields. The 1 G support coil is imbedded in the base of the container and faces upward to repel the cubical proof mass oriented vertically along an axis which includes a set of diagonally opposed vertices.

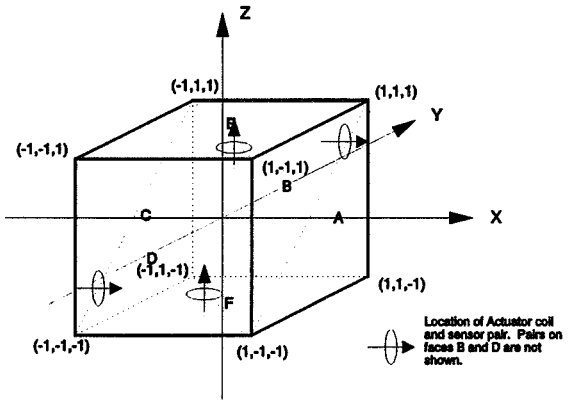

Figure 7. Sensor and actuator location nomenclature.

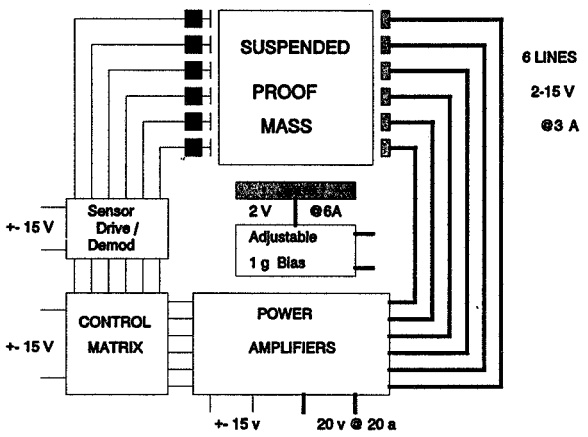

Figure 8. Block of six degree-of-freedom prototype.

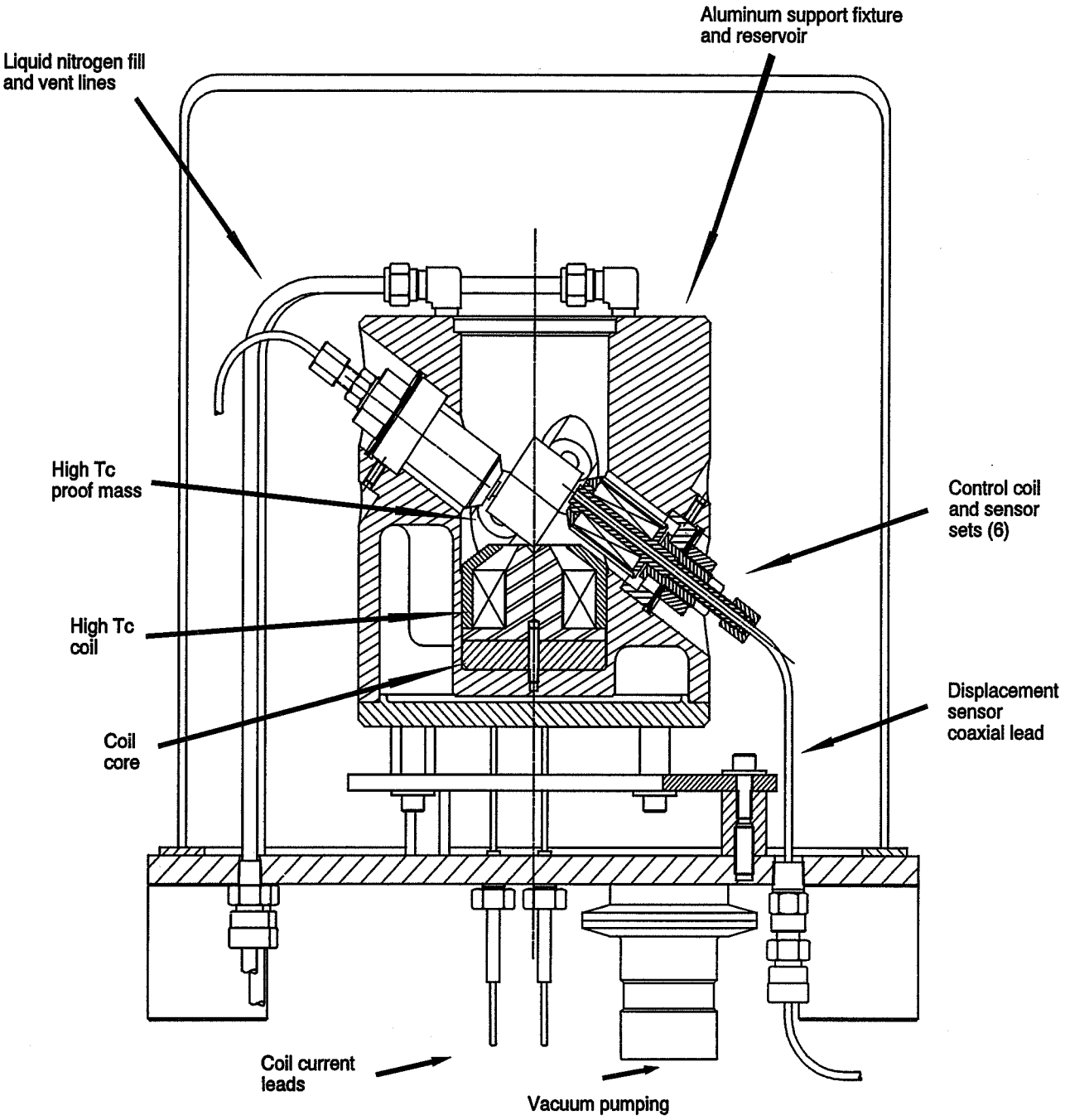

Figure 9. Six degree-of-freedom test device.

REFERENCES

1. J. M. Goodkind and R. J Warburton, "Superconductivity Applied To Gravimetry," IEEE Trans. on Magnetics, **MAG-11**, 708 (1975).

2. J.M. Goodkind, P.V. Czipott, A.P. Mills,Jr., M. Murakami, P.M. Platzman, C.W. Young, D.M. Zuckerman, "Test of the Gravitational Inverse-square Law at 0.4 to 1.4 m Mass Separations," Phys. Rev. D, **47**, 1290 (1993).

3. M.V. Moody and H.J. Paik, "Gauss's Law Test of Gravity at Short Range," Phys. Rev. Lett. **70**, 1195 (1993).

4. Ho Jung Paik, Edgar R. Canavan, Benjamin Backrach, Hans J Haucke, "Development of Superconducting Technology for Inertial Guidance, Gravity Survey, and Fundamental Gravity Experiments," Report PL-TR-94-2222, (1994).

5. R.C. Palmer, E.J. Denlinger, and H. Kawamoto, "Capacitive-Pickup Circuitry for VideoDiscs," RCA Review **43** 194 (1982).

6. T. R. Van Zandt, T. W. Kenny, W. J. Kaiser, "Ultra-High-Frequency Capacitive Displacement Sensor," NASA Tech Briefs, **18** (1994) 42.

REPORT DOCUMENTATION PAGE

Form Approved
OMB No. 0704-0188

1. AGENCY USE ONLY *(Leave blank)*	2. REPORT DATE	3. REPORT TYPE AND DATES COVERED
	July 1996	Conference Publication

4. TITLE AND SUBTITLE

Third International Symposium on Magnetic Suspension Technology

5. FUNDING NUMBERS

WU 505-64-70-03

6. AUTHOR(S)

Nelson J. Groom and Colin P. Britcher, Editors

7. PERFORMING ORGANIZATION NAME(S) AND ADDRESS(ES)

NASA Langley Research Center
Hampton, VA 23681-0001

8. PERFORMING ORGANIZATION REPORT NUMBER

L-17591B

9. SPONSORING/MONITORING AGENCY NAME(S) AND ADDRESS(ES)

National Aeronautics and Space Administration
Washington, DC 20546-0001

10. SPONSORING/MONITORING AGENCY REPORT NUMBER

NASA CP-3336
Part 2

11. SUPPLEMENTARY NOTES

Nelson J. Groom: Langley Research Center, Hampton, VA; Colin P. Britcher: Old Dominion University, Norfolk, VA

12a. DISTRIBUTION/AVAILABILITY STATEMENT

Unclassified–Unlimited
Subject Category 18
Availability: NASA CASI (301) 621-0390

12b. DISTRIBUTION CODE

13. ABSTRACT *(Maximum 200 words)*

In order to examine the state of technology of all areas of magnetic suspension and to review recent developments in sensors, controls, superconducting magnet technology, and design/implementation practices, the Third International Symposium on Magnetic Suspension Technology was held at the Holiday Inn Capital Plaza in Tallahassee, Florida on December 13–15, 1995.

The symposium included 19 sessions in which a total of 55 papers were presented. The technical sessions covered the areas of bearings, superconductivity, vibration isolation, maglev, controls, space applications, general applications, bearing/actuator design, modeling, precision applications, electromagnetic launch and hypersonic maglev, applications of superconductivity, and sensors. A list of attendees appears on page xv of the document.

14. SUBJECT TERMS

Magnetic bearings; Magnetic suspension; Large gap magnetic suspension; Small gap magnetic suspension; Maglev; Sensors; Superconducting magnetic suspension systems; Control systems

15. NUMBER OF PAGES

444

16. PRICE CODE

A19

17. SECURITY CLASSIFICATION OF REPORT	18. SECURITY CLASSIFICATION OF THIS PAGE	19. SECURITY CLASSIFICATION OF ABSTRACT	20. LIMITATION OF ABSTRACT
Unclassified	Unclassified	Unclassified	